Autoignition Modeling and a Generalized Hot Surface Ignition Criterion

Thesis by
Branson William Davis

In Partial Fulfillment of the Requirements for the
Degree of
Doctor of Philosophy



CALIFORNIA INSTITUTE OF TECHNOLOGY
Pasadena, California

2026
Defended August 14th, 2025

© 2026

Branson William Davis
ORCID: 0000-0002-5288-7913

All rights reserved except where otherwise noted

ACKNOWLEDGEMENTS

I am deeply grateful to my advisor, Professor Joseph Shepherd, for his unwavering support, intellectual rigor, and friendship throughout my time at Caltech. He has profoundly shaped the way I approach science and engineering. It has been an honor to be his final Ph.D. student as a small part of a remarkable academic legacy. Thank you for your mentorship, your trust, and for giving me the freedom to explore.

I have had the privilege of working with several past and present members of the Explosion Dynamics Laboratory: Drs. Charline Fouchier, Michael Wadas, Donner Schoeffler, Conor Martin, Rémy Mével, Ken Matsuoka, and Yunliang Qi. Thank you for your friendship and for all the help navigating roadblocks over the years. I also want to thank the past and present members of the Caltech Hypersonics Group: Alex Acosta, Michael Stramenga, Ying Luo, William Feasey, Jorge Rodríguez Gutiérrez, and Dr. Wesley Yu for the many productive interactions and friendships that emerged from our shared spaces and close collaboration. I'm grateful to Drs. Liam Heidt and Jimmy Ragan as well as my high school friends: Mohith Manohara, Philip Lin, and Jamb Lamb for game nights every week that provided a much-needed mental reset. Special thanks to our group administrator, Liza Bradulina, for her vital help navigating logistics, and to Noel Esparza-Duran for his technical expertise and enduring friendship. I would also like to thank my committee members, Professors Joanna Austin, Hans Hornung, and Tim Colonius, for critically evaluating this work and for their insightful discussions and encouragement.

I am also grateful to our collaborators at The Boeing Company for supporting this research through the Strategic Research and Development Relationship Agreement (CT-BA-GTA-1). In particular, I want to thank Dr. Jason Damazo, Dr. Philipp Boettcher, Dr. Brad Moravec, and Dominic Martinez for their thoughtful feedback and engaging conversations during our many meetings.

To Meredith—thank you for being by my side through the inevitable highs and lows of this Ph.D. journey. You make me a better person and bring so much joy to my life. I will always be most grateful for your endless love and support.

Finally, none of this would have been possible without the continuous support from my whole family. To my parents, Cyndi and Mark—thank you for nurturing my love for science from an early age and for always believing in me. I strive every day to be the person you raised me to be.

ABSTRACT

This work investigates the fundamental physics and predictive modeling of thermal ignition in heated volumes and near hot surfaces. Three-dimensional simulations of the ASTM-E659 apparatus revealed how natural convection and fuel stratification influence ignition timing and location, highlighting key limitations in standardized AIT testing. A one-dimensional analog further demonstrated the impact of radial temperature gradients on ignition behavior.

To isolate the core mechanisms of thermal runaway, a canonical hot surface ignition problem was analyzed, showing that inclusion of low-temperature chemistry induces two-stage ignition and lowers critical surface temperatures. Building on insights from classical theory, a novel ignition model was developed based on chemical and thermal length scales. The model collapses ignition data across a wide range of configurations and defines a critical Damköhler number. Despite some limitations for NTC fuels and catalytic effects, this unified framework represents a major advance over existing models.

PUBLISHED CONTENT AND CONTRIBUTIONS

Davis, B., C. Fouchier, and J. E. Shepherd (2024). "Fluid Motion and Heat Transfer in Autoignition Testing". In: *Proceedings of the 15th International Symposium on Hazards, Prevention and Mitigation of Industrial Explosions (ISHPMIE)*. DOI: 10.5281/zenodo.12621001.

B.D. participated in the conception of the project, designed and conducted the numerical simulations and experiments, designed and implemented software for data processing, led analysis of results, and was the lead author in writing the manuscript.

Davis, B., C. Fouchier, and J. E. Shepherd (2025). "Fluid motion and heat transfer in an ASTM-E659 apparatus". *Journal of Loss Prevention in the Process Industries* 94, p. 105558. DOI: 10.1016/j.jlp.2025.105558.

B.D. participated in the conception of the project, designed and conducted the numerical simulations and experiments, designed and implemented software for data processing, led analysis of results, and was the lead author in writing the manuscript.

Davis, B. and J. E. Shepherd (2025). "Numerical Modeling of Gaseous n-Hexane Autoignition in an ASTM-E659 Apparatus". *Under consideration for Fuel*.

B.D. participated in the conception of the project, designed and conducted the numerical simulations and experiments, designed and implemented software for data processing, led analysis of results, and was the lead author in writing the manuscript.

TABLE OF CONTENTS

Acknowledgements . . . iii
Abstract . . . iv
Published Content and Contributions . . . v
Table of Contents . . . v
List of Illustrations . . . ix
List of Tables . . . xxii
Chapter I: Introduction . . . 1
1.1 Motivation . . . 1
1.2 Studies on autoignition and hot surface ignition . . . 3
1.3 Ignition threshold correlations . . . 10
1.4 Thesis outline . . . 12
Chapter II: Numerical modeling of autoignition testing apparatus . . . 14
2.1 Motivation . . . 14
2.2 Experimental methods . . . 15
2.3 Numerical methods . . . 16
2.4 Results and discussion . . . 20
2.5 Implications for AIT experiments . . . 33
2.6 Conclusions . . . 34
Chapter III: Numerical modeling of n-hexane autoignition . . . 37
3.1 Motivation . . . 37
3.2 Numerical methods . . . 37
3.3 Results and discussion . . . 46
3.4 One-dimensional analog . . . 69
3.5 Implications for AIT experiments . . . 75
3.6 Conclusions . . . 76
Chapter IV: Hot surface thermal ignition . . . 78
4.1 Motivation . . . 78
4.2 Numerical model . . . 78
4.3 Ignition results . . . 80
4.4 Conclusions . . . 94
Chapter V: An analytical model for ignition near a hot surface . . . 95
5.1 Motivation . . . 95
5.2 Thermal explosion theory . . . 95
5.3 The theory of thermal ignition near a hot surface . . . 99
5.4 An analytical model for ignition near a hot surface . . . 109
5.5 Summary and conclusions . . . 112
Chapter VI: Numerical calculation of Λ_c and ℓ_k . . . 113
6.1 The characteristic thermal layer thickness, Λ_c . . . 113
6.2 The characteristic ignition kernel thickness, ℓ_k . . . 124

6.3 The line of criticality . . . 132
6.4 Model limitations: fuels with low-temperature chemistry . . . 134
6.5 Summary and conclusions . . . 138
Chapter VII: Ignition model validation . . . 139
7.1 Application to numerical simulations . . . 139
7.2 Application to experiments . . . 147
7.3 Summary and conclusions . . . 176
Chapter VIII: Ignition near a 12.7 cm hot vertical cylinder . . . 179
8.1 Motivation . . . 179
8.2 Experimental apparatus . . . 179
8.3 Temperature measurements . . . 180
8.4 Test conditions and procedure . . . 185
8.5 Numerical model . . . 187
8.6 Predicted ignition temperature and location . . . 191
8.7 Experimental results . . . 195
8.8 Ignition temperature comparison . . . 200
8.9 Summary and conclusions . . . 201
Chapter IX: Conclusions and Future Work . . . 203
9.1 Conclusions . . . 203
9.2 Future work . . . 207
Bibliography . . . 209
Appendix A: Effects of 1,2,4-trimethylbenzene on the ignition of n-decane . . . 220
A.1 Motivation . . . 220
A.2 Zero-dimensional ignition results . . . 221
A.3 Chemical analysis . . . 224
A.4 Summary and conclusions . . . 226
Appendix B: Reduced nC_6H_{14} kinetic mechanism (LTC + HTC) . . . 228
Appendix C: Additional data: hot surface ignition of dimethyl ether/air . . . 238
Appendix D: One-dimensional diffusing thermal layer configurations . . . 243
Appendix E: Convergence of the reaction order, n, and activation energy, E_a . . . 245
E.1 First-, second-, and fourth-order differencing schemes . . . 245
E.2 Empirical determination of T' and ρ' . . . 247
Appendix F: τ_i, T_a, and κ computations . . . 249
F.1 H_2/air mixtures . . . 250
F.2 CO/H_2/air mixtures . . . 260
F.3 CH_4/air mixtures . . . 262
F.4 CH_2O/air mixtures . . . 267
F.5 C_2H_4/air mixtures . . . 268
F.6 nC_5H_{12}/air mixtures . . . 275
F.7 nC_6H_{14}/air mixtures . . . 276
F.8 NH_3/air mixtures . . . 281
Appendix G: Additional data: two-dimensional ignition simulations . . . 282
G.1 nC_6H_{14}/air . . . 283
G.2 H_2/air . . . 289
G.3 CH_4/air . . . 290

G.4 NH_3/air 291
Appendix H: 50C experimental shot log 292

LIST OF ILLUSTRATIONS

Number *Page*

1.1 Canonical problem of ignition near a hot surface. 7

1.2 Inverse of ignition surface temperature plotted against sphere diameter on a log scale for heated spheres in three mixtures. 10

1.3 Ignition surface temperature plotted against surface area for a wide range of previous studies. 11

2.1 Experimental apparatus. 15

2.2 Numerical modeling of the ASTM apparatus. 16

2.3 Height-varying temperature boundary condition. 19

2.4 Grid convergence profiles for average temperature, $\bar{T}$, and fluctuation intensity, T'_{rms}, along the vertical center line. 21

2.5 Average temperature along the vertical center line of the flask, comparing simulation and experiment. 22

2.6 Comparison of temperature fluctuations at selected heights between the simulation (solid lines, –) and experiment (dashed lines, - -). . . . 23

2.7 Average temperature field and projected (surface) streamlines along a vertical cross-section of the domain for the three holder heights. . . 25

2.8 Average temperature profile along the vertical center line for the three holder heights. 26

2.9 Average vertical velocity along the vertical center line for the three holder heights. 27

2.10 Flask average temperature probability distributions for the three holder configurations. Flask center temperatures, T_4, are also indicated. . . . 28

2.11 C_2H_4 mole fraction temporal evolution on a vertical cross-section within the flask. 29

2.12 nC_6H_{14} mole fraction temporal evolution on a vertical cross-section within the flask. 30

2.13 $nC_{12}H_{26}$ mole fraction temporal evolution on a vertical cross-section within the flask. 30

2.14 Coefficient of variation, Eq. (2.9), over time for C_2H_4, nC_6H_{14}, and $nC_{12}H_{26}$ initialized at flask ambient temperature. Results are also provided for C_2H_4, nC_6H_{14} initialized at room temperature. 32

2.15 Number of fuel moles normalized by the initial value within the flask over time. 33
3.1 τ_i vs. $1000/T$ and absolute error plot in % for nC_6H_{14}/air at 1 bar using CaltechMech and the reduced mechanism. 39
3.2 1D flame model solution for T_u = 300 K and ϕ = 1 at 1 bar using the reduced CaltechMech mechanism for a nC_6H_{14}/air mixture. 42
3.3 Laminar burning velocity, S_L, vs. equivalence ratio, ϕ, for CaltechMech, the reduced mechanism, and four experimental studies. 43
3.4 Laminar burning velocity, S_L and flame thickness, ℓ_f vs. equivalence ratio, ϕ, for the two mechanisms at T = 520 K. 44
3.5 Vertical cross-section of the background temperature field and projected (surface) streamlines (left) and nC_6H14 fuel sphere initialization (right). 46
3.6 Maximum temperature vs. time for the three grid resolutions. 47
3.7 Ignition delay time, τ, cool flame temperature, T_{CF}, and vertical ignition location, y_{ign} for the three grid resolutions. 47
3.8 nC_6H_{14} volume field inside the flask during the cooking phase (0-10 s). 49
3.9 Q, $OC_6H_{11}OOH$, C_2H_4, and H_2O_2 volume fields inside the flask at 10 s. 50
3.10 3D ignition kernel evolution and instantaneous streamlines near the ignition event. 52
3.11 Temperature profile through the ignition kernel for different instances in time for (a) the 1st stage and (b) the 2nd stage. 53
3.12 Two 36 gauge thermocouples attached to formed nitinol wire. 54
3.13 Thermocouple temperature traces from an ASTM-E659 experiment with injection of 80 μL nC_6H_{14}. 55
3.14 Ignition particle trajectory. 56
3.15 nC_6H_{14} mole fraction over the entire simulation time. The temperature (- -) is also shown. 57
3.16 Major species mole fraction during the two stage ignition event along the ignition particle. The temperature (- -) is also shown. 58
3.17 Total heat release of the top reactions for the first ignition stage. . . . 59
3.18 Heat release and rate of production (ROP) of OH, HCO, and CH_3 along the ignition particle for the top reactions during the second stage. 61
3.19 Total heat release of the top reactions for the second ignition stage. . . 62

3.20 Flame front isosurface (T = 1500 K) with surface normal vectors and nC_6H_{14} mole fraction on a vertical cross-section through the flame. . 64
3.21 Projected velocity (-) and temperature (–) along the horizontal line across the flame front at height, y = 6.25 cm and time, t = 16.35065 s. 64
3.22 Computed S_L (left) and ℓ_k (right) surface maps for 300 K < T_u < 600 K and 0.5 < ϕ < 1.9 for nC_6H_{14}/air mixtures at 1 bar. 65
3.23 Colormaps of (a) temperature, (b) nC_6H_{14}, (c) CO_2, and (d) H_2 mass fractions along a vertical slice during the flame propagation. 67
3.24 One-dimensional spherical model and simplified computational grid. 70
3.25 Temporal evolution of the temperature profile in the thermal diffusion problem using the spherical and OpenFOAM solutions. 71
3.26 Temporal temperature profiles for ΔT = 0 K during the (left) first stage ignition event and (right) second stage ignition event 72
3.27 Temporal temperature profiles for ΔT = 7 K during the (left) first stage ignition event and (right) second stage ignition event. 73
3.28 Radial temperature profiles at the time of ignition for the four ΔT cases and the three-dimensional ASTM simulation. 74
4.1 Zero-dimensional ignition delay times for stoichiometric nC_6H_{14}/air at 1 bar with three detailed kinetic mechanisms. 79
4.2 Schematic of the forced convection boundary layer across a hot surface. 80
4.3 Maximum temperature in the domain over time. 80
4.4 Temperature field evolution during the ignition event. Instantaneous streamlines are overlaid. 81
4.5 Trajectory of the massless particle that ignites through the thermal layer up until ignition. 82
4.6 Mole fraction of the top 9 species of the ignition particle. Temperature is shown on the right axis. 83
4.7 Energy equation terms along a surface normal line through the center of the ignition kernel at various instances in time. 84
4.8 Maximum temperature in the domain over time. 86
4.9 Temperature field evolution and instantaneous streamlines during the first and second stage ignition events. 87
4.10 Massless particle that (top) pass through the 1st stage ignition event and (bottom) ignites the second stage ignition event. 88
4.11 Mole fraction of the top 10 species of a particle passing through the first stage ignition event. Temperature is shown on the right axis. . . . 89

4.12 Mole fraction of the top 9 species of the 2nd stage ignition particle. Temperature is shown on the right axis. 89
4.13 Energy equation terms along a surface normal line through the center of the ignition location at various time instances for the two stage ignition event. 90
4.14 Heat release comparison at the second stage ignition time for the two kinetic mechanisms. 92
4.15 Comparison of surface normal temperature distributions over time for the two ignition events using the two kinetic mechanisms. 93
5.1 $\phi(t)$ vs. t. 98
5.2 Thomas and Bowes critical solutions of θ vs. z for various values of θ_0. 103
5.3 Comparison of Zeldovich and Thomas and Bowes critical solutions, θ vs. z for various values of θ_0. 104
5.4 Nondimensional temperature gradient evaluated at the cold wall, $-\frac{d\theta}{dz}|_{z=2}$ vs. $-\theta_0$ (left) and the percent difference vs. $-\theta_0$ (right). . . . 104
5.5 Thermal layer structure as formulated for a large activation energy flammable mixture 106
5.6 $(\theta + \chi)_{\chi\to\infty}$ vs. Δ. Upper and lower branches of Eq. (5.60) are indicated by (- -) and (−), respectively. 108
5.7 Procedure for determining the critical length scales, Λ_c and ℓ_k for a reacting system. 111
6.1 The Thomas and Bowes problem. 113
6.2 Subcritical solution for a mixture of stoichiometric nC_6H_{14}/air at 1 bar with $T_H = 1000$ K, $T_C = 300$ K, $L = 0.976174$ cm. 114
6.3 Supercritical solution for a mixture of stoichiometric nC_6H_{14}/air at 1 bar with $T_H = 1000$ K, $T_C = 300$ K, $L = 0.976178$ cm. 115
6.4 Maximum heat release, Q, over time for $L = 0.976174$ cm (subcritical) and $L = 0.976174$ cm (supercritical) cases. 115
6.5 Maximum temperature, $T_{\max}$ vs. time for cases near L_c for a mixture of stoichiometric nC_6H_{14}/air at 1 bar, $T_H = 1000$ K and $T_C = 300$ K. . 116
6.6 Ignition classification vs. L for a mixture of stoichiometric nC_6H_{14}/air at 1 bar with $T_H = 1000$ K and $T_C = 300$ K. 117
6.7 Chemically frozen steady-state temperature profile and temperature gradient vs. L for the critical spacing, $L_c = 0.976176$ cm. 118
6.8 Schematic of the one-dimensional diffusing thermal layer problem. . 119

6.9 Temperature distributions for the diffusing thermal layer problem at various times for (a) reacting and (b) chemically frozen. 120
6.10 Temperature gradient at the hot wall, $dT/dx|_H$, vs. time from the chemically frozen diffusing thermal layer shown in Figure 6.9b. . . . 121
6.11 Reacting and frozen temperature profiles at the time of ignition, τ, for four fuel/air mixtures at 1 bar and $T_H = 1000$. 122
6.12 Computed Λ_c vs. T_H for all mixtures, wall temperatures, and pressures for the one-dimensional diffusing thermal layer model. 124
6.13 Mole fractions of the top 7 species during a 0D adiabatic, CP ignition simulation of nC_6H_{14}/air with $T_0 = 1000$ K at 1 bar. 125
6.14 Computed ignition delay times as a function of initial temperature for 7 fuel/air mixtures and 3 pressures. 127
6.15 Computed thermal diffusivity, κ, as a function of initial temperature for 7 fuel/air mixtures and 3 pressures. 128
6.16 Savitzky-Golay filter applied to activation temperature for stoichiometric H_2/air at 0.2 bar. 129
6.17 Computed activation temperature, $T_a = E_a/R$, as a function of initial temperature for 7 fuel/air mixtures and 3 pressures. 131
6.18 Computed ℓ_k vs. T_H for all mixtures, wall temperatures, and pressures for the one-dimensional diffusing thermal layer model. 132
6.19 Critical values of Λ_c and ℓ_k for the diffusing thermal layer model plotted in $\Lambda - \ell_k$ space. 133
6.20 Temporal temperature profiles for the LTC + HTC kinetic mechanism, nC_6H_{14}, $T_H = 1000$ K, $T_C = 300$ K, and 1 bar. 135
6.21 Temporal temperature profiles for the LTC + HTC kinetic mechanism, nC_6H_{14}, $1000 < T_H < 1500$ K, $T_C = 300$ K, and 1 bar. 136
6.22 Ignition delay time, t^*, vs hot wall temperature for 0.2, 1, and 5 bar for the HT mechanism as well as the LTC + HTC mechanism. 136
6.23 Critical (ℓ_k, Λ_c) points for nC_6H_{14}/air simulations using both the HTC mechanism (circles) and LTC + HTC mechanism (diamonds). . 137
7.1 Schematics of the forced and natural convection as well as the stagnation point flow configurations. 140
7.2 Temperature field during an ignition event in a forced and natural convection boundary layer and a stagnation point flow. 142
7.3 Maximum temperature in the domain over time for all two-dimensional simulation cases. 142

7.4 Temporal evolution of (ℓ_k, Λ) pairs at every location along the hot surfaces for the three simulations described by Figure 7.2. 144
7.5 Temporal evolution of Λ/ℓ_k at every location along the hot surfaces for the three simulations described by Figure 7.2. 145
7.6 Ignition model predicted ignition temperature, T_{model} vs. measured ignition temperature from the detailed ignition simulations, $T_{measured}$. 146
7.7 Combustion vessel with 10 mm heated cylinder mounted vertically. . 148
7.8 Time- and spatially-varying temperature boundary condition used on the surface of the heated vertical cylinder and ends. 148
7.9 Velocity magnitude and temperature fields for the chemically frozen numerical model of the 10 mm cylinder ignition experiment. 149
7.10 Comparison of the temperature field for a stoichiometric H_2/air mixture at $T_H = 1000$ K between simulation and experiment. 150
7.11 Surface normal temperature distribution at the center of the hot surface, $y = 0$ mm. 151
7.12 Temporal evolution of (ℓ_k, Λ) pairs for a stoichiometric C_2H_4/air mixture at every surface location for a temperature $T > 900$ K. 152
7.13 Temporal evolution of the ratio, Λ/ℓ_k at every location on the heated cylinder for $T > 900$ K and a stoichiometric mixture of C_2H_4/air. . . 153
7.14 Experimentally measured and model predicted hot surface ignition temperature for (a) H_2/air, (b) C_2H_4/air, and (c) nC_6H_{14}/air mixtures. 154
7.15 Time- and spatially-varying temperature boundary profiles for (a) an isothermal holder temperature and (b) an adiabatic holder temperature. 156
7.16 Intersections pairs, (ℓ_k, Λ_c) of the numerical solutions with the line of criticality. 157
7.17 Numerical model of a square hot surface suddenly exposed to a cold CH_4/air mixture. 158
7.18 Temperature field on a $y-z$ cross-section of the 18x18 mm hot surface at 1402 K suddenly exposed to an 8.0% CH_4/air mixture at 300 K. . . 159
7.19 Surface normal temperature gradient, $\partial T/\partial z_{wall}$ on the hot surface for $T_H = 1402$ K. 160
7.20 $|\partial T/\partial z|$ in the center of the hot surface over time for the 18x18 mm surface with $T_H = 1402$ K. 161
7.21 Temporal evolution of (Λ, ℓ_k) pairs at the center of the hot surface for seven surface temperatures. 18x18 mm hot spot, 8.0% CH_4/air. . . 161

7.22 Experimentally measured and model predicted ignition temperature for various CH_4/air mixtures on the 3x3 mm and 18x18 mm surfaces. 162
7.23 Schematic for the falling sphere experimental setup and testing procedure. 164
7.24 Temperature, instantaneous streamlines, and H_2 mass fraction fields for the falling hot sphere simulation. 165
7.25 Temporal evolution of the H_2 mass fraction at the front stagnation point and separation point along the sphere for $\Phi = 1.0$, $\beta = 9$. 166
7.26 Temporal evolution of (ℓ_k, Λ) pairs at every sphere location for T_H = 998 K, with $\Phi = 1.0$ and $\beta = 9$. 168
7.27 Temporal evolution of the ratio, Λ/ℓ_k at every sphere location for T_H = 998 K, with $\Phi = 1.0$ and $\beta = 9$. 169
7.28 Temporal evolution of the H_2 mass fraction at the front stagnation point and separation point along the sphere. 170
7.29 Autolite 1110 glow plug schematic. 171
7.30 Temporal evolution of the temperature field near the glow plug for a stoichiometric mixture of C_2H_4/air. 171
7.31 Temporal evolution of (ℓ_k, Λ) pairs at every location on the glow plug for a stoichiometric mixture of C_2H_4/air and $T > 900$ K. 172
7.32 Temporal evolution of the ratio, Λ/ℓ_k at every location on the glow plug for a stoichiometric mixture of C_2H_4/air and $T > 900$ K. 174
7.33 Experimental, numerical, and model predicted glow plug ignition temperatures for (a) H_2/air and (b) C_2H_4/air mixtures. 175
7.34 T_{model} vs $T_{measured}$ for all experiments and numerical simulations in this chapter. 177
8.1 Heated cylinder experimental setup. 180
8.2 Pyrometer calibration setup. 183
8.3 Pyrometer calibration. 184
8.4 Heating test pyrometer and thermocouple temperature measurements over time. 185
8.5 50C axisymmetric computational domain. 187
8.6 Temperature over time at the center, top, and on the copper support during a heating test. 188
8.7 Steady heat equation solutions for a surface temperature at the center of 800 K for various values of ϵ_{ss}. 189

8.8 Temporal evolution of the temperature from Eq. (8.9) for $I = 235$ A and $\epsilon_{ss} = 0.8$. 190
8.9 Temperature field near the hot vertical cylinder for C_2H_4/air mixtures at 0.2 bar, 0.5 bar, and 1 bar after 60 s of heating. 191
8.10 Temporal evolution of (ℓ_k, Λ) pairs at every location on the heated portion of the vertical cylinder for C_2H_4/air at 0.5 bar and $T > 900$ K. 192
8.11 Temporal evolution of Λ/ℓ_k at every location on the heated portion of the vertical cylinder for C_2H_4/air at 0.5 bar and $T > 900$ K. 193
8.12 Predicted ignition temperatures from the model for all four fuel/air mixtures and three pressures. 194
8.13 Visualization of an ignition event in shot 16. The mixture is stoichiometric C_2H_4/air at 0.5 bar. 195
8.14 Ignition height for shot 18. The mixture is stoichiometric C_2H_4/air at 0.5 bar. 196
8.15 Pyrometer temperature measurements for three tests with at the same condition: stoichiometric C_2H_4/air at 0.5 bar. 197
8.16 Pressure increase over time for the four fuel/air mixtures during ignition at (a) 0.2 bar, (b) 0.5 bar, and (c) 1 bar 199
8.17 Ignition model predicted and experimentally measured ignition temperatures for all four fuel/air mixtures and three pressures 201
8.18 T_{model}, vs $T_{measured}$ for the 50C ignition experiments. All data from Chapter 7 is also included. 202
9.1 T_{model}, vs $T_{measured}$ for all 60 configurations examined in this work. . 206
A.1 Experimental autoignition temperature distributions in °C for SPK and two batches of Jet A. 220
A.2 Internal report of reaction delay time in an ASTM-E659 test for various amounts of 1,2,4-trimethylbenzene in nC_9H_{20}. 221
A.3 0D mole fractions of major species for a stoichiometric mixture of 70% $nC_{10}H_{22}$/30% 1,2,4-TMB in air with $T_i = 525$ K and $P = 1$ bar. . 222
A.4 0D ignition delay times for stoichiometric mixtures of 1,2,4-TMB, n-decane, and air for initial temperatures 483 K < T_i < 525 K. 223
A.5 Reaction pathway diagram following efflux of H atoms from HO_2. . . 224
A.6 Rate of production of 1,2,4-TMB for top reactions before and during the first stage ignition event. 225
A.7 Visualization of the oxidation pathway of 1,2,4-TMB before and during the first stage ignition event. 226

C.1 Zero-dimensional ignition delay times for stoichiometric DME/air at 1 bar. 238
C.2 Temperature field evolution and instantaneous streamlines. T_H = 1000 K, P = 1 bar, U_∞ = 0.1 m/s, and L = 0.09 m. 240
C.3 Heat release field evolution and instantaneous streamlines. T_H = 1000 K, P = 1 bar, U_∞ = 0.1 m/s, and L = 0.09 m. 240
C.4 OH mass fraction field evolution and instantaneous streamlines. T_H = 1000 K, P = 1 bar, U_∞ = 0.1 m/s, and L = 0.09 m. 241
C.5 CH2O mass fraction field evolution and instantaneous streamlines. T_H = 1000 K, P = 1 bar, U_∞ = 0.1 m/s, and L = 0.09 m. 241
C.6 Temperature field evolution and instantaneous streamlines. T_H = 925 K, P = 1 bar, U_∞ = 0.1 m/s, and L = 0.09 m. 242
C.7 Heat release field evolution and instantaneous streamlines. T_H = 925 K, P = 1 bar, U_∞ = 0.1 m/s, and L = 0.09 m. 242
E.1 Variation of T_a with initial temperature for stoichiometric nC_6H_{14}/air at 1 bar for the three differencing schemes. 246
E.2 Reaction order, n, variation with initial temperature for a mixture of stoichiometric CH_2O/air at 1 bar for different values of $\rho' = \Delta\rho$. . . . 247
E.3 Activation temperature, $T_a = E_a/R$, variation with initial temperature for a mixture of stoichiometric CH_2O/air at 1 bar for different values of $T' = \Delta T$. 248
F.1 Computed zero-dimensional ignition delay time τ_i(top), activation temperature $T_a = E_a/R$ (middle), and thermal diffusivity κ (bottom) for 10% H_2/air. 250
F.2 Computed zero-dimensional ignition delay time τ_i(top), activation temperature $T_a = E_a/R$ (middle), and thermal diffusivity κ (bottom) for 20% H_2/air. 251
F.3 Computed zero-dimensional ignition delay time τ_i(top), activation temperature $T_a = E_a/R$ (middle), and thermal diffusivity κ (bottom) for stoichiometric H_2/air. 252
F.4 Computed zero-dimensional ignition delay time τ_i(top), activation temperature $T_a = E_a/R$ (middle), and thermal diffusivity κ (bottom) for 40% H_2/air. 253
F.5 Computed zero-dimensional ignition delay time τ_i(top), activation temperature $T_a = E_a/R$ (middle), and thermal diffusivity κ (bottom) for 45% H_2/air. 254

F.6 Computed zero-dimensional ignition delay time τ_i(top), activation temperature $T_a = E_a/R$ (middle), and thermal diffusivity κ (bottom) for 70% H_2/air. 255
F.7 Computed zero-dimensional ignition delay time τ_i(top), activation temperature $T_a = E_a/R$ (middle), and thermal diffusivity κ (bottom) for 75% H_2/air. 256
F.8 Computed surfaces for the zero-dimensional ignition delay time τ_i(top), activation temperature $T_a = E_a/R$ (middle), and thermal diffusivity κ (bottom) for a $H_2/O_2/N_2$ mixture as a function of β for an equivalence ratio, $\Phi = 0.39$. 257
F.9 Computed surfaces for the zero-dimensional ignition delay time τ_i(top), activation temperature $T_a = E_a/R$ (middle), and thermal diffusivity κ (bottom) for a $H_2/O_2/N_2$ mixture as a function of β for an equivalence ratio, $\Phi = 1.0$. 258
F.10 Computed surfaces for the zero-dimensional ignition delay time τ_i(top), activation temperature $T_a = E_a/R$ (middle), and thermal diffusivity κ (bottom) for a $H_2/O_2/N_2$ mixture as a function of β for an equivalence ratio, $\Phi = 1.35$. 259
F.11 Computed zero-dimensional ignition delay time τ_i(top), activation temperature $T_a = E_a/R$ (middle), and thermal diffusivity κ (bottom) for CO/0.25%H_2/air. 260
F.12 Computed zero-dimensional ignition delay time τ_i(top), activation temperature $T_a = E_a/R$ (middle), and thermal diffusivity κ (bottom) for CO/1%H_2/air. 261
F.13 Computed zero-dimensional ignition delay time τ_i(top), activation temperature $T_a = E_a/R$ (middle), and thermal diffusivity κ (bottom) for stoichiometric CH_4/air. 262
F.14 Computed zero-dimensional ignition delay time τ_i(top), activation temperature $T_a = E_a/R$ (middle), and thermal diffusivity κ (bottom) for 5.6%, 5.7%, and 6.0% CH_4/air at 1 bar. 263
F.15 Computed zero-dimensional ignition delay time τ_i(top), activation temperature $T_a = E_a/R$ (middle), and thermal diffusivity κ (bottom) for 7.1%, 8.0%, and 8.3% CH_4/air at 1 bar. 264
F.16 Computed zero-dimensional ignition delay time τ_i(top), activation temperature $T_a = E_a/R$ (middle), and thermal diffusivity κ (bottom) for 9.1%, 10.6%, and 10.8% CH_4/air at 1 bar. 265

F.17 Computed zero-dimensional ignition delay time τ_i(top), activation temperature $T_a = E_a/R$ (middle), and thermal diffusivity κ (bottom) for 12.3% and 12.4% CH_4/air at 1 bar. 266
F.18 Computed zero-dimensional ignition delay time τ_i(top), activation temperature $T_a = E_a/R$ (middle), and thermal diffusivity κ (bottom) for stoichiometric CH_2O/air. 267
F.19 Computed zero-dimensional ignition delay time τ_i(top), activation temperature $T_a = E_a/R$ (middle), and thermal diffusivity κ (bottom) for stoichiometric C_2H_4/air. 268
F.20 Computed zero-dimensional ignition delay time τ_i(top), activation temperature $T_a = E_a/R$ (middle), and thermal diffusivity κ (bottom) for 2.8% C_2H_4/air. 269
F.21 Computed zero-dimensional ignition delay time τ_i(top), activation temperature $T_a = E_a/R$ (middle), and thermal diffusivity κ (bottom) for 4% C_2H_4/air. 270
F.22 Computed zero-dimensional ignition delay time τ_i(top), activation temperature $T_a = E_a/R$ (middle), and thermal diffusivity κ (bottom) for 10% C_2H_4/air. 271
F.23 Computed zero-dimensional ignition delay time τ_i(top), activation temperature $T_a = E_a/R$ (middle), and thermal diffusivity κ (bottom) for 12.5% C_2H_4/air. 272
F.24 Computed zero-dimensional ignition delay time τ_i(top), activation temperature $T_a = E_a/R$ (middle), and thermal diffusivity κ (bottom) for 15% C_2H_4/air. 273
F.25 Computed zero-dimensional ignition delay time τ_i(top), activation temperature $T_a = E_a/R$ (middle), and thermal diffusivity κ (bottom) for 21.9% C_2H_4/air. 274
F.26 Computed zero-dimensional ignition delay time τ_i(top), activation temperature $T_a = E_a/R$ (middle), and thermal diffusivity κ (bottom) for stoichiometric nC_5H_{12}/air. 275
F.27 Computed zero-dimensional ignition delay time τ_i(top), activation temperature $T_a = E_a/R$ (middle), and thermal diffusivity κ (bottom) for stoichiometric nC_6H_{14}/air. 276
F.28 Computed zero-dimensional ignition delay time τ_i(top), activation temperature $T_a = E_a/R$ (middle), and thermal diffusivity κ (bottom) for 1% nC_6H_{14}/air. 277

F.29 Computed zero-dimensional ignition delay time τ_i(top), activation temperature $T_a = E_a/R$ (middle), and thermal diffusivity κ (bottom) for 1.5% nC_6H_{14}/air. 278
F.30 Computed zero-dimensional ignition delay time τ_i(top), activation temperature $T_a = E_a/R$ (middle), and thermal diffusivity κ (bottom) for 3% nC_6H_{14}/air. 279
F.31 Computed zero-dimensional ignition delay time τ_i(top), activation temperature $T_a = E_a/R$ (middle), and thermal diffusivity κ (bottom) for 3.5% nC_6H_{14}/air. 280
F.32 Computed zero-dimensional ignition delay time τ_i(top), activation temperature $T_a = E_a/R$ (middle), and thermal diffusivity κ (bottom) for stoichiometric NH_3/air. 281
G.1 Natural convection: Temperature field evolution during the ignition event. $P = 1$ bar, $L = 0.01$ m. 283
G.2 Natural Convection: Temperature field evolution during the ignition event. $P = 1$ bar, $L = 0.05$ m. 283
G.3 Stagnation point: Temperature field evolution during the ignition event. $P = 1$ bar, $L = 0.09$ m, $U_\infty = 0.01$ m/s. 284
G.4 Stagnation point: Temperature field evolution during the ignition event. $P = 1$ bar, $L = 0.09$ m, $U_\infty = 0.1$ m/s. 284
G.5 Forced convection: Temperature field evolution during the ignition event. $P = 1$ bar, $L = 0.01$ m, $U_\infty = 0.1$ m/s. 285
G.6 Forced convection: Temperature field evolution during the ignition event. $P = 1$ bar, $L = 0.01$ m, $U_\infty = 0.5$ m/s. 285
G.7 Forced convection: Temperature field evolution during the ignition event. $P = 1$ bar, $L = 0.09$ m, $U_\infty = 0.1$ m/s. 286
G.8 Forced convection: Temperature field evolution during the ignition event. $P = 1$ bar, $L = 0.09$ m, $U_\infty = 0.5$ m/s. 286
G.9 Forced convection: Temperature field evolution during the ignition event. $P = 0.2$ bar, $L = 0.01$ m, $U_\infty = 0.1$ m/s. 287
G.10 Forced convection: Temperature field evolution during the ignition event. $P = 5$ bar, $L = 0.01$ m, $U_\infty = 0.1$ m/s. 287
G.11 Forced convection: Temperature field evolution during the ignition event. $P = 5$ bar, $L = 0.01$ m, $U_\infty = 0.5$ m/s. 288
G.12 Forced convection: Temperature field evolution during the ignition event. $P = 1$ bar, $L = 0.01$ m, $U_\infty = 0.1$ m/s. 289

G.13 Forced convection: Temperature field evolution during the ignition event. $P = 1$ bar, $L = 0.01$ m, $U_\infty = 0.5$ m/s. 289
G.14 Forced convection: Temperature field evolution during the ignition event. $P = 1$ bar, $L = 0.018$ m, $U_\infty = 0.1$ m/s. 290
G.15 Forced convection: Temperature field evolution during the ignition event. $P = 1$ bar, $L = 0.018$ m, $U_\infty = 0.1$ m/s. 291

LIST OF TABLES

Number *Page*

2.1 Geometric holder configurations. 19
2.2 Statistical analysis of temperature at the center of the flask for the three holder heights. 26
2.3 Molecular weight, Lennard-Jones parameter, fuel sphere density, Schmidt number, and Froude numbers for the three tested fuels. . . . 30
7.1 Predicted ignition temperature from the model for the three tested temperature boundary conditions for stoichiometric H_2/air mixture. . 157
7.2 Equivalence ratio, Φ, and N_2 fraction, β for the three mixtures of H_2-O_2-N_2. The initial composition is specified as $2\Phi H_2 + O_2 + \beta N_2$. 164
8.1 Summary of temperatures at the center of the vertical cylinder at the time of ignition for the four fuels and three initial pressures. 198
A.1 Experimentally measured and numerically estimated AITs for varying amounts of 1,2,4-trimethylbenzene in n-decane/air. 223
B.1 Comprehensive list of the 265 elementary reactions used in the reduced nC_6H_{14} mechanism. 229
B.2 Subset of reactions that include fall-off behavior, showing low-pressure limit Arrhenius coefficients and TROE parameters. 236
B.3 List of third-body enhanced or reduced efficiencies (α_j) specified for collisional stabilization or deactivation. 236
D.1 A full list of one-dimensional diffusing thermal layer configurations. The gas mixtures are initially set to 300 K. 243
H.1 50C vertical cylinder shot log. 292

Chapter 1

INTRODUCTION

1.1 Motivation

Industries such as chemical storage and processing, mining, nuclear power, and transportation are essential to modern infrastructure but frequently operate under conditions where flammable atmospheres exist. In these settings, uncontrolled ignition can lead to severe economic, environmental, and human consequences. History offers numerous examples where fires and explosions initiated by thermal, electrical, or mechanical ignition sources have resulted in catastrophic consequences.

Among the earliest and most illustrative of such hazards are the methane-fueled explosions that occurred in 19th and 20th-century coal mining operations. Disasters such as the 1812 Felling Colliery explosion, which was one of the first well-documented cases of firedamp (primarily methane) ignition, underscore the historical importance of controlling ignition sources in flammable environments. An investigation into the disaster published in 1882 attributed the explosion to ignition of firedamp likely by an open flame lamp (Galloway, 1882). Throughout the 19th and 20th centuries, methane and coal dust were frequently ignited by open flames, hot lamp housings, and frictional heating which often led to devastating chain-reaction explosions. Other notable examples include the Haswell colliery incident (1844), Oaks Colliery disaster (1867), Dixonville explosion (1891), Scofield disaster (1900), Fraterville disaster (1902), Courrières disaster (1906), Monongah disaster (1907), and the Senghenydd colliery disaster (1913).

In the chemical storage and processing industry, similar incidents have been extensively reported. In the Deepwater Horizon disaster (2011), methane gas released from a failed well surged to the surface and likely ignited upon contact with hot machinery, triggering a catastrophic explosion and fire that killed 11 workers and resulted in the largest marine oil spill in U.S. history that cost over $70 billion in clean up costs that are ongoing to this day. Similarly, the Buncefield explosion (2005) in the UK occurred after a hydrocarbon vapor cloud generated by an overflowing fuel tank encountered an ignition source, likely a hot surface or electrical equipment. The blast was felt over 125 miles away and the British Geological Survey registered the primary explosion at a 2.4 on the Richter scale. The Texas City refinery explo-

sion (2007), the Valero refinery fire (2010), and the Toulouse chemical plant disaster (2002) each involved flammable vapor releases that ignited in the presence of poorly controlled hot surfaces or thermal energy sources. Even more dramatically, the PEPCON explosion (1990) and the Beirut port disaster (2020) demonstrate how accumulated energetic materials, subjected to heat buildup or welding operations, can undergo runaway reactions and detonate. A comprehensive investigation of historical disasters in the chemical process industry can be found in Lees (2012) and Kletz and Amyotte (2019). These events collectively highlight the recurring and deadly role of ignition in environments where flammable gases, vapors, or energetic solids are present.

The aviation industry has also experienced several high-profile disasters. In 1963, Pan Am Flight 214 exploded midair after a lightning strike ignited fuel vapors in the aircraft's left wing fuel tank (1964). The incident report from the Civil Aeronautics Board posited that the strike either created a localized hot spot in the fuel tank or that lightning current caused a spark discharge that ignited the flammable mixture of air and jet fuel vapor. Decades later, in 1996, TWA Flight 800 suffered a catastrophic explosion of its center wing fuel tank. The National Transportation Safety Board investigation concluded that the likely ignition source was an electrical short circuit in the fuel system, allowing sufficient energy to arc inside the tank (2000). Compounding the hazard, air conditioning packs mounted below the tank had elevated the tank temperature and fuel vapor concentration. Both incidents further highlight the vulnerability of flammable mixtures to ignition when exposed to energy sources.

Collectively, these disasters demonstrate the critical need to understand and mitigate ignition hazards in systems where flammable vapors or gases may be present. A key aspect of this effort involves determining the conditions under which ignition occurs, such as the autoignition temperature and the surface temperature thresholds required to initiate thermal runaway. Extensive research over the past several centuries has been devoted to characterizing these ignition parameters under controlled laboratory conditions. The following section reviews foundational and recent studies aimed at understanding autoignition and hot surface ignition phenomena, highlighting the methods used to measure these thresholds and the physical variables that influence ignition behavior.

1.2 Studies on autoignition and hot surface ignition

The term “ignition” refers to the onset of exothermic chemical reaction leading to observable indicators of combustion. Ignition can occur through several mechanisms including spark, flame, compression, and thermal heating. In this thesis, we focus specifically on thermal ignition, where combustion is initiated solely by heating. In the case of autoignition, fuels are placed in a heated volume to determine the lowest temperature at which thermal runaway can occur, typically identified by light emission and a sudden temperature rise. In hot surface ignition studies, ignition refers to the localized development of a reacting gas kernel adjacent to a heated surface, also characterized by thermal runaway and light emission.

1.2.1 Historical background

The earliest published work on ignition dates back to the 1700s. Henry Cavendish demonstrated spark-induced ignition of inflammable air (what we now call hydrogen) in one of the first controlled gas ignition experiments (Cavendish, 1766). This motivated later spark ignition work by Alessandro Volta on methane/air mixtures through his invention of the "Volta Cannon" where methane and oxygen were placed in a metal vessel sealed with a cork (Volta, 1777). A small spark was used to ignite the mixture and pop the cork off the vessel. Several decades later and motivated by the 1812 Felling Colliery disaster previously discussed, Sir Humphry Davy investigated ignition of hydrogen, ethylene, carbon monoxide, and methane from a heated iron rod (Davy, 1815). He found that hydrogen ignited at "the lowest visible heat of iron." Both ethylene and carbon monoxide ignited at iron "heated to redness." Davy was unable to ignite methane from any temperature iron rod, however, found that replacement of the hot rod with a burning rod resulted in ignition. From his findings, he invented a safety lamp that isolated the wick from the surroundings via a mesh screen that functionally acted as a flame arrestor.

1.2.2 Autoignition testing and standardization

More quantitative investigations on ignition, specifically in heated vessels, were conducted in the late 1800s. Mallard and Le Chatelier (1880) conducted the first heated vessel ignition tests where mixtures of oxygen with hydrogen, carbon monoxide, and methane were filled into a vessel at some temperature measured by an air thermometer. They reported the lowest vessel temperatures resulting in ignition as 555°C for hydrogen, 655°C for carbon monoxide, and 650°C for methane which occurred after a time lag. This was an early experiment demonstrating the coupling

of chemical reaction with temperature and heat transfer. The experiment was the first attempt to determine a minimum temperature at which a fuel and oxidizer would spontaneously ignite in a heated volume. This is commonly referred to today as the autoignition temperature (AIT).

Freyer and Meyer (1893) further studied the minimum ignition temperature via two methods: the first was a slow flowing reactor set in a hot bath maintained a constant temperature and the second was a sealed glass bulb of fuel and air at atmospheric pressure suddenly set in the temperature controlled bath. Several mixtures were studied, but of interest to this work the following ignition temperatures were obtained. For methane and oxygen, the ignition temperature was between 650-730°C in the slow flowing reactor and between 606-730°C for the sealed bulb. For ethane and oxygen, the ignition temperature was between 606-650°C in the slow flowing reactor and between 530-606°C for the sealed bulb. For ethylene and oxygen, the ignition temperature was between 606-650°C in the slow flowing reactor and between 530-606°C for the sealed bulb. Lastly for carbon monoxide and oxygen, the ignition temperature was between 650-730°C in the slow flowing reactor and between 650-730°C for the sealed bulb. Experiments the same year by Meyer and Münch (1893) on the ignition of fuel/oxygen mixtures in a heated glass bulb found minimum temperatures between 656-678°C for methane and oxygen, 605-622°C for ethane and oxygen, and 577-590°C for ethylene and oxygen mixtures.

Dixon and Coward (1909) was concerned with oxidation of the fuel prior to reaching the desired temperature in the previously reported studies. They ran heated vessel experiments where the fuel and oxidizer were heated separately and then allowed to mix at an exit nozzle into an enclosure set at the same temperature. They reported average ignition temperature thresholds for hydrogen and oxygen as 585°C [580-590°C], carbon monoxide and oxygen as 650°C [637-658°C], ethane and oxygen as 575°C [520-630°C], ethylene and oxygen as 510°C [500-519°C], and methane and oxygen as 628°C [556-700°C].

The ignition results from Mallard and Le Chatelier (1880), Freyer and Meyer (1893), Meyer and Münch (1893), and Dixon and Coward (1909) demonstrated significant variability in the ignition temperature. As Mason and Wheeler (1924) write,

> "In general, ignition is so dependent upon the experimental method used that records of 'ignition temperatures' of different mixtures obtained by these means have only relative significance."

Subsequent studies on ignition in hot volumes have focused on the potential contributing role of convection on variability during filling and ignition, emphasizing the localized temperature variation associated with the onset of exothermic reaction. Experimental studies by Tyler (1966) and later by Ashmore et al. (1967) examined the effect exothermic chemical reaction had on heat transfer in closed spherical vessels held at a constant temperature. For faster reaction rates, the large increase in local temperature caused significant convection to occur that caused an asymmetry of the vertical temperature profile. Tyler and Tuck (1967) demonstrated experimentally using inert gases (H_2, N_2, CO_2) that temperature differences as small as 5 K between the gas and walls could induce significant natural convection in 280 and 1100 cm^3 spheres. They proposed that the onset of natural convection could be correlated with using a Rayleigh number of 600, consistent with the observations of temperature profiles observed in the reacting tests (Tyler, 1966; Ashmore et al., 1967).

Numerical simulations (Jones, 1974; Kee et al., 1975; Silakova et al., 2006; Campbell et al., 2007) demonstrate that for modest values of the Rayleigh number ($\geq$ 600), natural convection in a reacting flow results in a toroidal vortex within a closed flask. Heated gas from chemical reaction rises through through the center and falls along the outer surfaces of a cylinder or spherical container. The implications of heat-release generated convection on autoignition was explored through numerical simulation by Silakova et al. (2006), Liu et al. (2010a), Liñán et al. (2016), Sánchez et al. (2016), and Iglesias et al. (2017) and most recently by Melguizo-Gavilanes et al. (2019).

Setchkin (1954) and Zabetakis et al. (1954) recognized the variability of published ignition temperatures and sought to develop a standardized test for autoignition, driven by the need to regulate the shipping and handling of combustible liquids to minimize fire hazards. These initial studies developed methodology and apparatus that have evolved into the modern day ASTM-E659 (2005) standard in North America and the comparable international standard ISO/IEC (2017). During testing, a small quantity of liquid fuel is injected into a glass flask containing hot air at atmospheric pressure. Modifications are prescribed in the standards for testing with gaseous fuels. The AIT is classified as the minimum temperature for which ignition is observed within a limited time period in a series of trials varying the fuel amount and flask temperature following the procedure set out in the standard. Both the tests immerse the flask within a temperature-controlled oven and inject fuel through the

open mouth of the flask. The top of flask remains open during testing to enable visualization of light emission associated with ignition.

The ASTM-E659 standard and the related ISO standards such as EN 14522 and DIN 51794 (ISO/IEC, 2017) have been extensively used to characterize AITs for various fuels. The reported AITs are tabulated in combustion safety databases, such as the Chemical Hazard Response Information System (CHRIS) and CHEMSAFE (Guard, 1999; Zakel et al., 2019). While significant improvements from the early work in the late 1800s and early 1900s were made with the ASTM-E659 standard, recent experimental results of Martin and Shepherd (2021) emphasize that a wide range of ignition behaviors can still occur, which could be categorized into at least four distinct modes. Measured AITs are also found (Lüth et al., 2014; Johnson and Mashuga, 2023) to be sensitive to the specifics of the measurement technique, with variability often exceeding the precision of published data.

1.2.3 Hot surface ignition studies

Throughout the experiments of the 1900s, a separate problem became apparent, where ignition temperatures had considerably larger variation between differing experiments. In this problem a cold, flammable atmosphere is exposed to a hot surface resulting in ignition. Ignition near hot surfaces represents another fundamental combustion problem that is more representative of many thermal ignition hazards in industrial applications that were outlined previously, such as the Deepwater Horizon (ignition of methane by exposure to hot machinery) accident or Pan Am Flight 214 accident (ignition of jet fuel by a local hot spot induced by a lightning strike).

Unlike autoignition in heated volumes, surface-induced ignition introduces steep temperature gradients, strong thermal stratification, much more significant energy losses, and convection driven species transport, all of which influence the ignition behavior. Figure 1.1 shows a schematic of the canonical problem. A thermal layer develops within a cool, flammable atmosphere at T_C near a heated surface at some higher temperature, T_H. The thermal layer thickens over time as heat diffuses away from the surface. Simultaneously, a velocity boundary layer develops due to the no-slip condition at the wall, altering the transport of heat and reactive species. In the case of forced convection problems (like a boundary layer flow or stagnation point flow), the layer is sustained by a constant inflow of gas at some velocity and temperature. In the case of natural convection problems, the heated gas near the hot surface becomes less dense than the surrounding gas and a buoyancy-induced

boundary layer develops. In either scenario, the hot surface introduces energy into the adjacent gas and thermal diffusion/convection dissipate the energy to the surroundings. At elevated temperatures, chemical reaction can further increase the local gas temperature above the surroundings. This region is emphasized in the figure as a bump in the temperature profile. If the temperature is sufficiently high such that heat release from chemical reaction exceeds the losses from thermal diffusion and convection, the system experiences a rapid rise in temperature in what is known as thermal runaway and ignition.

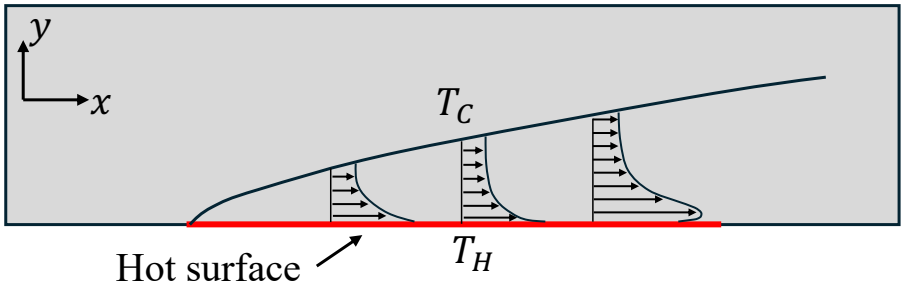


Figure 1.1: Canonical problem of ignition near a hot surface.

The canonical problem can be easily extended to other scenarios and several experiments have been performed for better understanding. For example, to replicate the scenario of firedamp ignition in mines, Silver (1937) studied the ignition of heated spheres between 10-50 mm diameter shot through a flammable mixture of methane/air at varying velocities up to 5 m/s. Paterson (1940) conducted a similar experiment with smaller 1.5-3 mm spheres of both platinum and quartz in coal gas/air. Several conclusions were made from this study. The first was that as the injection speed of the hot sphere increased, the surface temperature required to trigger ignition increased. Similarly, as the concentration of firedamp was decreased, the surface temperature required to trigger ignition increased. For a fixed flow velocity, the ignition temperature decreased with an increasing sphere diameter. Experiments with both the platinum and quartz yielded similar surface temperatures for ignition. They found ignition temperatures ranging from 850-1300°C. Note these temperature have a 450°C range and are substantially higher than the ignition temperatures reported by previous authors in the hot volume experiments. Subsequent work by Roth et al. (2014) and Zirwes et al. (2017) studied ignition of sub-millimeter scale hot spheres both experimentally and numerically, respectively. Similar trends were observed, where ignition temperature was found to decrease as the sphere diameter

was increased. Ignition temperatures were determined to be between 775-1125°C for H_2/air mixtures and between 1425-1725°C for CH_4/air mixtures. Coronel (2016) studied ignition of millimeter-scale falling spheres in n-hexane/air mixtures. The same trends in ignition temperatures with sphere diameter were found ranging from 875-1125°C. Additional analysis found that the ignition kernel evolved from the separation region on the backside of the sphere.

Similar work has been performed near rapidly heated plates. Rae et al. (1964) studied ignition of methane/air mixtures near millimeter-scale hot metal squares mounted at various angles in a combustion box. They found that as the squares got larger in size, the ignition temperature decreased for all configurations. Similarly, as the concentration of methane increased, the ignition temperature also increased. Overall, ignition temperatures ranged from 985-1335°C. Cutler (1974) and Cutler (1978) later studied ignition on rapidly heated tungsten strips 57 mm in length and with variable width. Of the tested mixtures of ethylene, propane, and methane in air, ethylene had the lowest ignition temperature and methane had the highest ignition temperature with all critical temperatures ranging from 850-2000°C. As the width of the strip was increased, the ignition temperature decreased. Similar ignition results for methane/air mixtures near heated strips were found by Laurendeau (1982).

The effect of natural convection on hot surface ignition temperatures has also been a topic of recent research. In this scenario, the heated surface induces a significant buoyancy-driven flow in the surrounding gas. Ono et al. (1976) studied ignition of methane, propane, ethanol, and diethyl ether air mixtures on steel plates mounted vertically. The dimensions were 40 mm in width and the height was varied between 5-30 mm. Cairnie et al. (1981) and Harrison and Cairnie (1988) studied ignition of diethyl ether and acetaldehyde, respectively, on even larger vertical plates (114 mm and 170 mm metal squares). Even more recently at Caltech, thorough investigation of ignition near glow plugs (Boettcher, 2012) and vertical cylinders of varying size from 10 mm to 254 mm in length for hydrogen, ethylene, and n-hexane (Melguizo-Gavilanes et al., 2016; Boeck et al., 2017; Jones, 2021; Martin, 2023) revealed thermal runaway behavior and critical surface temperature thresholds for each respective experiment.

1.2.4 Theoretical models

Quite separately from the experimental and numerical approaches, a substantial body of theoretical analyses have been developed to understand the underlying physics of hot volume and hot surface thermal ignition.

Early work dates back to the late 1800s. Jacobus van't Hoff was interested in understanding the influence of temperature change on chemical reaction. He developed an equation which we now refer to as the van't Hoff equation, that relates the change in chemical reaction equilibrium constant to change in temperature (van't Hoff, 1884). The relation implied that chemical systems are exponentially sensitive to temperature, especially when heat release is substantial. This was among the first formulations linking chemical kinetics and thermodynamics and inspired many ideas, including the Arrhenius rate law that is commonly used today to treat reaction rate sensitivity (Arrhenius, 1889). In van't Hoff's own words,

> "The ignition temperature is the temperature at which the initial loss of heat, due to conduction etc., is equal to the heat evolved in the same time by the chemical reaction."

The idea of balancing heat generation with thermal losses in modeling ignition problems was later utilized in numerous combustion theories and in the context of hot surface thermal ignition, the point of adiabaticity (what is now commonly referred to as the van't Hoff condition).

The first theoretical models in the 1920s and 1930s treated ignition as a self-heating phenomenon where thermal feedback between exothermic chemical reaction competes with heat transfer to create critical conditions for ignition. Semenoff (1929) considered stirred batch reactors and later, his student, Frank-Kamenetskii (1939b) considered conduction in a stationary material with heat transfer modeled by engineering correlations at the boundaries of the vessel.

In the same year, Zeldovich (1939) used Frank-Kamenetskii's ideas about approximating the Arrhenius chemical reaction term in the energy equation to model ignition between two slabs of differing temperature. The assumptions and conclusions made by Zeldovich were later critically analyzed by Thomas and Bowes (1961) and found to be accurate within the limit of large activation energy, the minimum energy needed to initiate chemical reaction. Throughout the 1970s-1990s, theoretical models for ignition near a hot surface used the method of matched asymptotic expansions to formulate the problem as a boundary layer, where a thin reactive-diffusive region

near the wall was matched to a convective-diffusive region far away from the wall (Law, 2010). This formulation has been used to study ignition in many different problems including near hot spherical particles (Law, 1978a), stagnation point flows (Law, 1978b), as well as boundary layers (Mendez et al., 1986; Treviño and Méndez, 1991).

1.3 Ignition threshold correlations

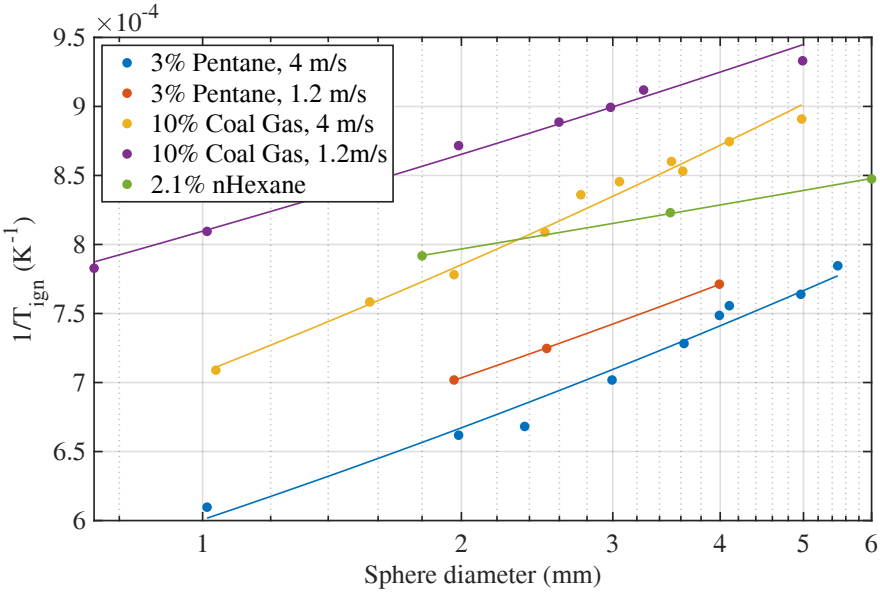


Figure 1.2: Inverse of ignition surface temperature plotted against sphere diameter on a log scale for heated spheres in three mixtures. Data from the coal gas and pentane mixtures are summarized in Laurendeau (1982) and the n-hexane data is from Coronel (2016).

While theoretical models offer insight into the mechanisms driving ignition, empirical correlations remain essential for practical application and design. Correlations of ignition data yield insight to the physical processes underlying thermal runaway and can further be used to motivate safe design criteria for industrial systems. Many authors have developed such correlations. Khitrin and Goldenberg (1957) balanced heat transfer with chemical reaction to propose a correlation of the Nusselt number, Nu, and the inverse of the surface temperature for flat heated walls and spherical bodies. Ono et al. (1976) extended these results to natural convective flows around vertical flat plates. Laurendeau (1982) developed a similar correlation based on ignition temperature, pressure, surface size, and flow velocity. These correlations often yield an inverse-log relation, plotting $\log(L)$ against $1/T_{\text{ign}}$ where L is a char-

acteristic length scale defined by the size of the hot surface being studied. Figure 1.2 presents this formulation for heated sphere ignition data summarized in Laurendeau (1982) and Coronel (2016). A near linear dependence can be extrapolated for each series of data. However, wide variations in ignition temperature over 1000 K can be seen depending on the fuel used and the flow velocity.

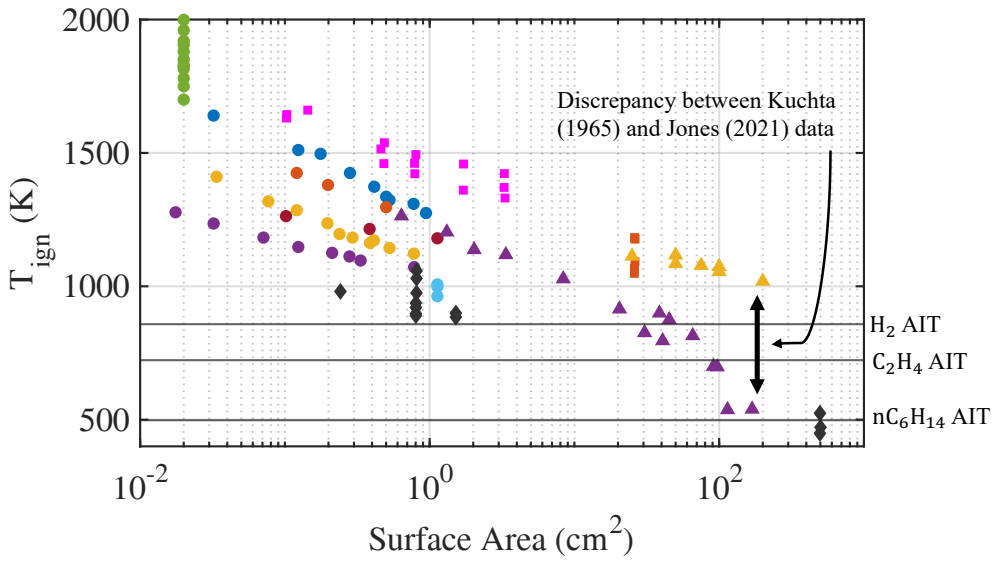


Figure 1.3: Ignition surface temperature plotted against surface area for a wide range of studies. Legend: Circles are for ignition studies on spheres where blue, orange, yellow, purple, green, cyan, and red are studies with hydrogen, methane, coal gas, pentane and n-hexane (Laurendeau, 1982; Coronel, 2016; Zirwes et al., 2017; Jones et al., 2019). Squares are for ignition studies on hot plates where magenta is a study with methane (Laurendeau, 1982) and orange is a study with n-hexane (Smyth and Bryner, 1997). Purple triangles are from Kuchta et al. (1965) with n-hexane. Yellow triangles are from Jones (2021). Lastly, black diamonds are from glow plug and heated vessel experiments with n-hexane (Boettcher, 2012). Three lines denote tabulated AITs for H_2, C_2H_4, and nC_6H_{14} (ISO/TC 197, 2015; USGC, 1999).

The usefulness of correlating data conventionally with a characteristic length scale, such as the diameter of a sphere shown in Figure 1.2, or the length of a hot plate/cylinder is limited in its applicability since the characteristic length scale is dependent on the particular geometry of interest. In addition, it is only valid for a single composition and thermodynamic state. Kuchta et al. (1965) proposed surface area as the critical correlation parameter for hot surface ignition in an attempt to collapse data with similar composition, but differing geometries. Select results from experiments presented in the previous sections are summarized in Figure 1.3

which plots the ignition temperature against surface area covering several fuels and geometric configurations from numerous studies. A general trend of decreasing ignition temperature with increasing surface area is observed. However, this trend is inadequate as significant scatter can still be seen in the data with large variability in critical surface temperatures across different experiments. Recent experiments by Jones (2021) critically examined the surface area conclusion proposed by Kuchta for n-hexane/air mixtures near vertical cylinders of varying surface area up to 200 cm^2. She found that the surface area conclusion was erroneous, reporting ignition temperatures 300-500 K above what Kuchta found for the same composition and surface area in a different experiment. This result is highlighted in the figure. Across the entire range, trends in the data are largely only seen for the same family of experiments with overall ignition temperatures ranging from 480 K to 2000 K.

Echoing the early observations from Mason and Wheeler (1924), the consensus in the combustion community is that ignition is *highly* dependent on the configuration. To date, there exist no correlations that collapse ignition data from systems of varying geometry, composition, and thermodynamic state. This presents a significant challenge because deviation in industrial design from controlled experiments with published ignition thresholds have an unknown and potentially hazardous effect on the safety of a system. Three-dimensional simulation with detailed chemistry or controlled experimentation on the critical surface temperatures for ignition of a particular system can be time and resource intensive. As a result, industries use tabulated AITs as a blanket solution for designing and certifying systems, even though many configurations (as extensively discussed in this section) exhibit critical temperatures that are substantially higher as shown in Figure 1.3. For these purposes, AITs measured from standardized tests, such as the ASTM-E659 (2005), are widely adopted in industry. These limitations underscore the need for a generalizable ignition framework that can account for diverse geometries, compositions, and thermodynamic states, bridging the gap between standardized test data and real-world applications.

1.4 Thesis outline

This thesis is organized into several parts that collectively aim to advance understanding of autoignition and hot surface ignition phenomena. Chapter 2 presents the numerical modeling of an experimental apparatus used for measuring autoignition temperatures in accordance with the ASTM-E659 standard, with a focus on understanding sources of variability in reported AIT values. Chapter 3 extends this

analysis by modeling the ignition behavior of n-hexane within the same apparatus, providing insight into the fluid mechanics and chemical processes governing thermal runaway in a test. Chapter 4 introduces the fundamental physics governing ignition near a hot surface, including thermal boundary layer development and energy transport mechanisms, and extends the analysis to assess the influence of low-temperature chemistry for heavy hydrocarbons. In Chapter 5, the important conclusions from theoretical models of ignition are analyzed in detail. These important conclusions motivate the development of an analytical model describing ignition near hot surfaces, incorporating fundamental transport and kinetic concepts. In Chapter 6, the characteristic length scales that underpin the ignition model are computed numerically. Chapter 7 presents validation of the proposed model against a wide range of high-fidelity reacting flow simulations and experimental data on hot plates, cylinders, spheres, and glow plugs. Finally, Chapter 8 applies the validated model to predict ignition behavior near a 12.7 cm hot vertical cylinder where substantial surface temperature variation exists for numerous fuels and pressures. By refining ignition modeling approaches and identifying robust scaling laws, this work aims to support safer design of systems operating in combustible environments, with further implications for improved standardized testing development and hazard assessment.

Chapter 2

NUMERICAL MODELING OF AUTOIGNITION TESTING APPARATUS

2.1 Motivation

Autoignition temperature (AIT) testing is a critical tool for evaluating the ignition risk of flammable substances and plays a key role in determining AITs for various fuels in safety standards such as ASTM-E659 (2005) and comparable international protocols (ISO/IEC, 2017). In these tests, a small quantity of liquid fuel is introduced into a heated flask containing air at atmospheric pressure, and the AIT is recorded as the lowest temperature at which ignition is observed within a defined time period. Though standardized, these methods still allow for variation in experimental facility design, and all require an open flask mouth to enable optical detection of ignition.

Despite the standardization, reported AIT values in chemical databases (Guard, 1999; Zakel et al., 2019) exhibit significant variability across laboratories and testing protocols. Prior studies have shown that measured AITs are sensitive to the measurement technique (Lüth et al., 2014; Johnson and Mashuga, 2023). Experiments by Martin and Shepherd (2021) further revealed that ignition can occur in multiple distinct modes under similar test conditions. Recent work by Fouchier and Shepherd (2025) significantly improved measurement diagnostics in ASTM-E659 testing and automated the fuel injection process resulting in more repeatable results.

Our own observations revealed substantial surface temperature variation in the experimental apparatus itself. In addition, gas temperature measurements inside the flask revealed strong buoyancy-driven convection, driven by the open-top geometry and temperature gradients. These non-reactive flow features are present even before fuel injection and may play a significant role in the observed variability in published AITs. A major limitation of previous modeling efforts is the assumption of a closed, well-mixed system with idealized initial conditions (Jones, 1974; Kee et al., 1975; Silakova et al., 2006; Campbell et al., 2007; Liu et al., 2010a; Liñán et al., 2016; Sánchez et al., 2016; Iglesias et al., 2017; Melguizo-Gavilanes et al., 2019).

This chapter addresses that gap by numerically modeling the flow field inside our own ASTM-E659 test apparatus in three dimensions, using experimentally measured temperature boundary conditions for validation. We then conduct a parametric study

of three different flask configurations permitted under the standard to understand how geometry influences the internal flow and temperature distribution. Finally, we analyze the non-reacting mixing behavior of three different fuels of varying molecular weights and thermophysical properties. These studies highlight how purely physical effects, such as buoyancy and diffusion, can potentially contribute to variability in ignition behavior and reported AITs.

2.2 Experimental methods

For our study, we adapted the experimental setup used by Martin and Shepherd (2021) for the characterization of the AITs for Jet A and surrogate jet fuels. This apparatus was constructed following the ASTM-E659 (2005) standard. Figure 2.1 shows a picture and a cross-section drawing of the setup.

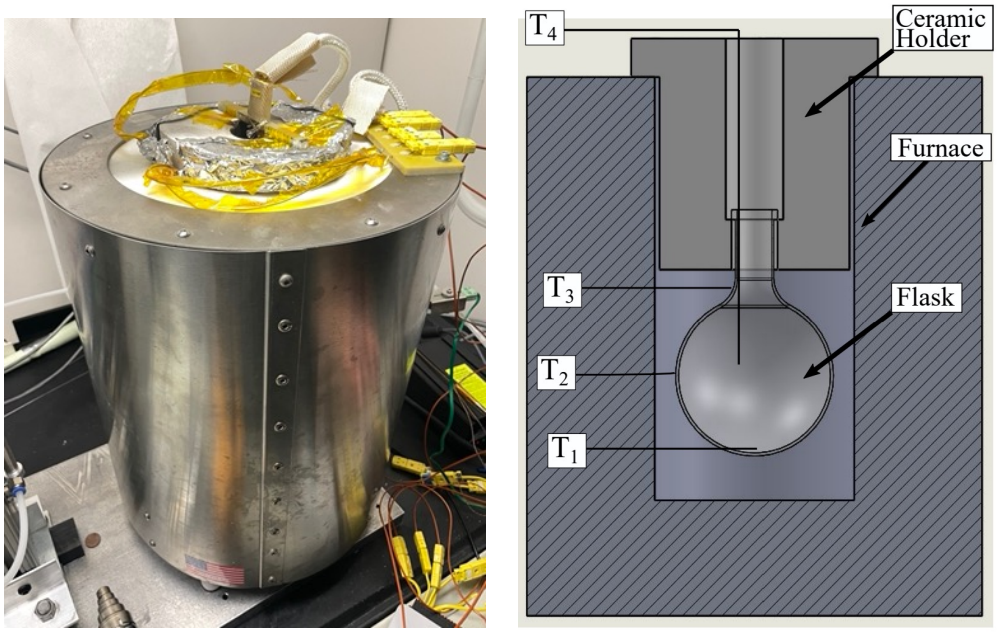


Figure 2.1: Experimental apparatus.

The apparatus is composed of a Mellen CV12 crucible furnace with a 133 mm diameter and 200 mm deep cylindrical volume, which controllably heats a 500 mL round bottom, borosilicate flask up to 1250 °C with a PID controller (Love Controls series 16B) system accurate to 1 °C. The flask is suspended in the furnace by a ceramic holder molded from silica-based Cotronics Rescor 750. The flask and ceramic holder are covered by aluminum foil to reflect the radiation inside the flask and reduce heat loss.

The temperature of the flask surface is measured with three 34 gauge, type K thermocouples inside a mineral-insulated metal sheath, set at positions T_1, T_2, and T_3 (see Figure 2.1). The thermocouple conventionally used to measure the air temperature, T_4, in ignition experiments was removed and replaced with a 36 gauge, type K thermocouple attached to a Velmex slide (NEMA 17, 155 mm travel) capable of precise vertical resolution. This allowed temperature measurements to be taken at various heights within the apparatus. The temperature variation is recorded with a NI 9213 16-channel, 24-bit, 75 Hz thermocouple data acquisition module from National Instruments, connected to a cDAQ-9171 CompactDAQ Chassis. We sampled each height for 120 s and waited an additional 120 s between measurements to allow unsteadiness effects caused by the movement of the internal thermocouple to dampen.

2.3 Numerical methods

The transient, three-dimensional fluid motion, heat transfer, and mixing were numerically simulated directly by solving the Navier-Stokes equations of a multi-component ideal gas mixture.

2.3.1 Geometric model and meshing

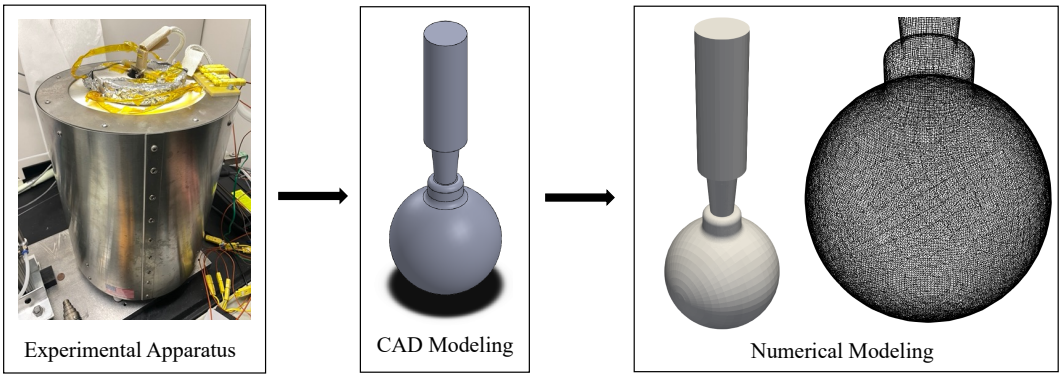


Figure 2.2: Numerical modeling of the ASTM apparatus.

The flask and ceramic holder of the ASTM setup shown in Figure 2.1 were carefully measured and modeled in Solidworks to provide a suitable framework for simulation. This process is shown in Figure 2.2. The interior geometry was then meshed in three dimensions using the OpenFOAM tool, *snappyHexMesh*, prioritizing uniform hexahedral cells. A grid-independent solution, as determined from a statistical

analysis of the unsteady flow, could be achieved for a grid of 6 million cells resulting in cell sizes of approximately 600 μm. In addition to modeling the flask and ceramic holder, a rectangular region above the flask (not shown in Figure 2.2) with open boundaries was included to model the exchange of gas between the flask and the surrounding atmosphere.

2.3.2 Governing equations

The governing equations we simulated were the variable-density Navier-Stokes equations for a Newtonian fluid with temperature-dependent transport properties and buoyancy forces in the momentum equation as

$$\frac{\partial \rho}{\partial t} + \nabla \cdot (\rho \mathbf{u}) = 0\,, \tag{2.1}$$

$$\frac{\partial}{\partial t}(\rho \mathbf{u}) + \nabla \cdot (\rho \mathbf{u}\mathbf{u} + p\mathbf{I}) = \nabla \cdot \tau + \rho \mathbf{g}\,, \tag{2.2}$$

$$\frac{\partial}{\partial t}(\rho Y_i) + \nabla \cdot (\rho Y_i \mathbf{u}) = -\nabla \cdot (\rho Y_i \mathbf{V}_i) + \dot{\Omega}_i \quad i = 1, 2, \ldots, K\,, \tag{2.3}$$

$$c_P \frac{\partial}{\partial t}(\rho T) + c_P \nabla \cdot (\rho \mathbf{u} T) = -\nabla \cdot (\lambda \nabla T) - \rho \nabla T \cdot \sum_{i=1}^{K} c_{P,i} Y_i \mathbf{V}_i - \sum_{i=1}^{N} h_i \dot{\Omega}_i\,, \tag{2.4}$$

where t is time, ρ is the mixture density, p is the pressure, u is the velocity, g is the acceleration due to gravity, T is the temperature, c_P is the specific heat at constant pressure, λ is the mixture thermal conductivity, Y is the mass fraction, $\mathbf{V}$ is the correction diffusion velocity, $\dot{\Omega}$ is the net volumetric mass production rate, h is the specific enthalpy, and τ is the viscous stress tensor written as

$$\tau = \mu\left[\nabla \mathbf{u} + (\nabla \mathbf{u})^T\right] - \frac{2}{3}\mu(\nabla \cdot \mathbf{u})\mathbf{I} \tag{2.5}$$

where $\mathbf{I}$ is the identity matrix. The subscript, i, indicates the individual species, and K is the total number of species. For simulations in air, the species conservation equation and mass diffusion term in the energy equation were omitted. The ideal gas equation of state was used to calculate the density of the mixture.

The diffusion velocities are calculated according to Chapman and Cowling (1990) using Fick's law, including a contribution by thermodiffusion (Soret effect) as:

$$\mathbf{V_i} = -\frac{D_i}{Y_i}\nabla Y_i - \frac{D_i \Theta_i}{X_i}\frac{1}{T}\nabla T \tag{2.6}$$

where X_i is the mole fraction, and Θ_i is the thermodiffusion ratio of species i. The individual-species mixture-averaged diffusion coefficients, D_i, are calculated

according to Curtiss and Hirschfelder (1949) as

$$D_i = \frac{1 - Y_i}{\sum_{j \neq i}^{N} \frac{X_i}{\Gamma_{ji}}} \tag{2.7}$$

where Γ_{ji} are the binary diffusion coefficients. To ensure the conservation of mass, a correction diffusion velocity is applied to $\mathbf{V}_i$ in Eqs (2.3) and (2.4) as described by Coffee and Heimerl (1981) as

$$\mathbf{V}_i^C = \mathbf{V}_i + \mathbf{V}_C \ . \tag{2.8}$$

Standard CFD methods using segregated algorithms are typically unsuitable for reacting flow problems involving large chemical mechanisms due to high stiffness and nonlinearities of the species and energy transport equations. Operator-splitting techniques can instead be used to separate the terms associated with nonstiff processes (convective and diffusive transport) from those associated with stiff processes (chemical reactions). Eqs (2.1)-(2.4) were numerically integrated in the OpenFOAM framework with the open-source *laminarBuoyantPimpleSMOKE* solver which uses the pressure implicit with splitting of operators (PISO) algorithm and the Strang splitting scheme (Strang, 1968; Issa, 1986). Second-order central differencing was employed to compute the spatial derivatives. More information about the solver can be found in Cuoci et al. (2013a) and Cuoci et al. (2013b).

Eqs (2.1)-(2.4) are the governing equations that described the low Mach number reacting flow solver used for the simulations presented throughout this work. The buoyancy term is only included in the momentum equation and is omitted from the energy equation as it is several orders of magnitude smaller than the other energy equation terms. This is conventionally done in other reacting flow solvers. For brevity, it will not be rewritten in the following chapters. In this chapter, we only considered non-reacting flow to characterize the test apparatus. Thus, the reacting terms were set to zero in the species and energy equations.

2.3.3 Initial and boundary conditions

Figure 2.3 shows the temperature boundary condition on the flask and holder as a function of height. A piece-wise linear profile in height z was imposed on the surface of the flask and was assumed constant in the holder section due to the large ceramic mass being held inside the furnace. These temperatures correspond to experimentally measured flask surface temperatures $T_1 = 521$ K, $T_2 = 527$ K, and $T_3 = 518$ K. A no-slip condition was imposed on the walls.

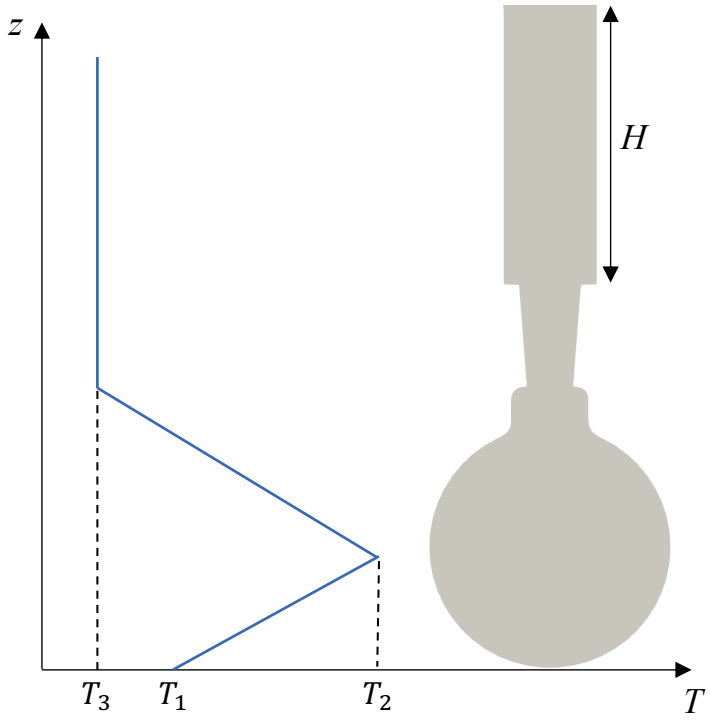


Figure 2.3: Height-varying temperature boundary condition.

The simulations were initiated from rest at room temperature and continued until the temporal flow field became statistically stationary. Flow characterization and mixing simulations used this resultant flow field as an initial condition.

2.3.4 Test conditions

The initial and boundary conditions were used to characterize a dry air flow field for various height ceramic holder pieces. Varying the holder height parametrically can alter the effect of buoyancy and overall flow structure. This is important because the ASTM-E659 standard only specifies a minimum furnace size to house the glass flask. Thus, varying furnace sizes will affect the length holder necessary to suspend the flask inside. The inner diameter for all holders was 38.1 mm.

Table 2.1: Geometric holder configurations.

Case	**Holder Height H (mm)**
A	57.15
B	114.3
C	228.6

Case B corresponds to the dimension of the ceramic holders used in our laboratory and was used to numerically examine fuel mixing within the flask for gaseous ethene (C_2H_4), n-hexane (nC_6H_{14}), and n-dodecane ($nC_{12}H_{26}$). The ASTM-E659 standard with an open flask is intended for liquid or solid substances. Ethene was examined in order to investigate the effect of lighter, more diffusive fuels on the mixing process and efflux. Although the ASTM standard uses a closed flask for gas testing, the ISO/IEC (2017) international standard allows the testing of gas in an open flask similar to the ASTM liquid apparatus. The syringe injection process was not simulated, but instead, a 15 mm sphere of fuel was initialized into a fully established flow field at both the internal flask temperature as well as room temperature (300 K). The 15 mm fuel sphere diameter was selected as it roughly corresponds to the amount of liquid fuel typically injected during an experiment. The resulting evolution of the composition (without reaction) was characterized as a function of time and space.

2.4 Results and discussion

2.4.1 Numerical verification

A grid convergence study was performed to ensure the flow solution was adequately resolved, especially in the flask portion of the apparatus where chemical physics occurs during a test. The three grids are at 600 μm, 1200 μm, and 2400 μm for fine, medium, and coarse grids, respectively.

Figure 2.4 plots the average temperature and and fluctuation intensity along the vertical center line through the domain for the three grid resolutions. Statistics were taken once the flow became fully developed (~15 s) and was averaged for 120 s of simulation time. From 2.4a, the average temperature increases as the grid is refined. The difference between medium and fine grids was on average 0.3%, with the largest differences (0.7%) occurring outside the flask. Looking at the fluctuations, the opposite trend was observed with a decreasing fluctuation intensity for all positions as the grid was refined. The average difference between medium and fine grids was on average 3.2% with the largest differences occurring outside the flask where the flow is more unsteady. A similar analysis was carried out for velocity variables and at numerous portions in the domain to ensure convergence. From the results, it was concluded that the flow physics could be properly resolved. The fine grid of 600 μm was used for further analysis and subsequent simulations.

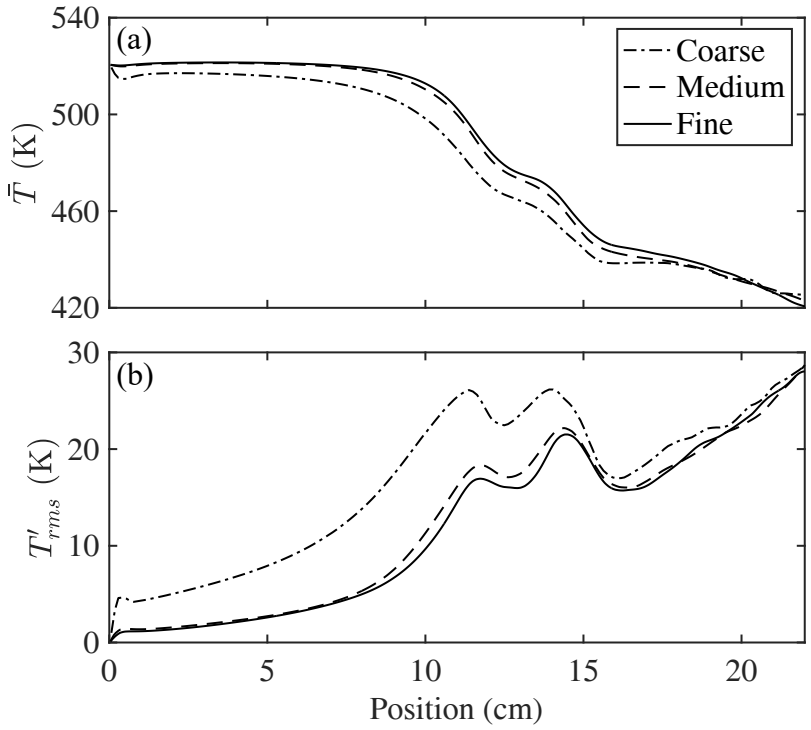


Figure 2.4: Grid convergence profiles for (a) average temperature, $\bar{T}$, and (b) temperature fluctuation intensity, T'_{rms} along the vertical center line for three grid resolutions.

2.4.2 Experimental validation

To validate the numerical model, temperature measurements were digitally recorded and temporally averaged for a series of points on the vertical center line of the experimental apparatus and compared with values from the equivalent numerical simulation of case B. The position 0 mm corresponds to the bottom of the flask. Figure 2.5 compares the average temperature between the experiment and the simulation. The vertical dashed lines indicate the top of the lower, spherical part of the flask (98 mm) and the upper neck of the flask (159 mm). A variation of 4 K was seen across the lower portion of the flask. Through the neck, a more significant 75 K temperature variation was seen due to the mixing region at the exit of the flask and within the ceramic holder. Above the flask, the temperature decreases with increasing height, approaching the value of the cold ambient air above the setup.

Comparing the average temperature between the simulation and the experiment within the lower part of the flask, the maximum deviation was only 1.5 K for any measured position. However, larger deviations in the temperature profile inside

the ceramic holder can be observed. The surface temperature profile within the ceramic holder was not measured and was assumed to be spatially uniform in the simulation. This assumption is likely the source of discrepancy between simulation and experiment in this region.

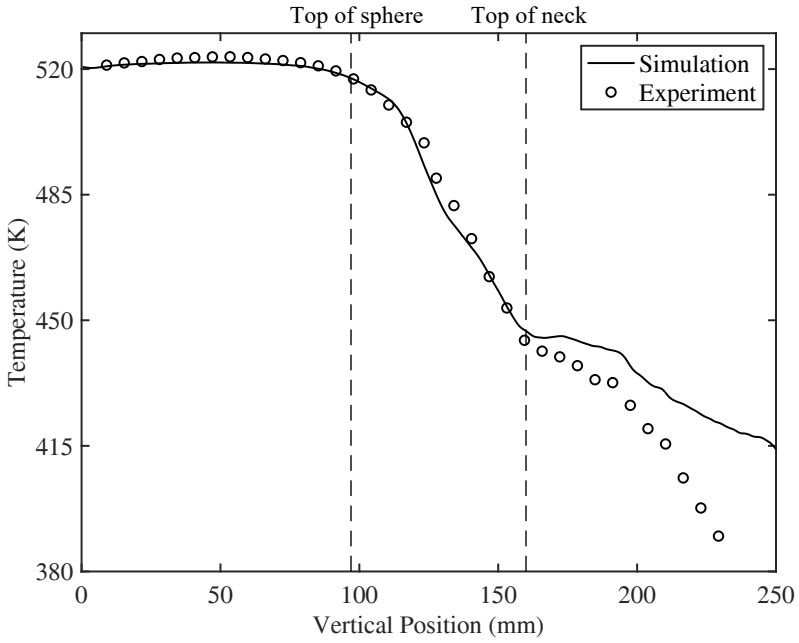


Figure 2.5: Average temperature along the vertical center line of the flask, comparing simulation and experiment.

Computed and observed temporal temperature fluctuations are shown in Figure 2.6 at heights of 9, 47.1, and 159.5 mm along the flask center line. These heights correspond to the bottom, middle, and region immediately above the top of the flask. In the simulations, fluctuations up to 5 K are observed at the bottom of the flask and up to 12 K at the center of the flask. Immediately above the top of the flask, the flow is unsteady. Fluctuations up to 80 K are observed with durations of approximately 0.1 s. The experimentally measured fluctuations for all heights are significantly less than those simulated, only 20 K at most above the flask in the ceramic holder. This difference is due to the slow response time of the thermocouple used for the measurements, estimated to have a characteristic step response time of $\tau = 1$ s to reach 67% of the final value. This is at least an order of magnitude slower than the fluctuations observed in the simulations and accounts for the observed differences.

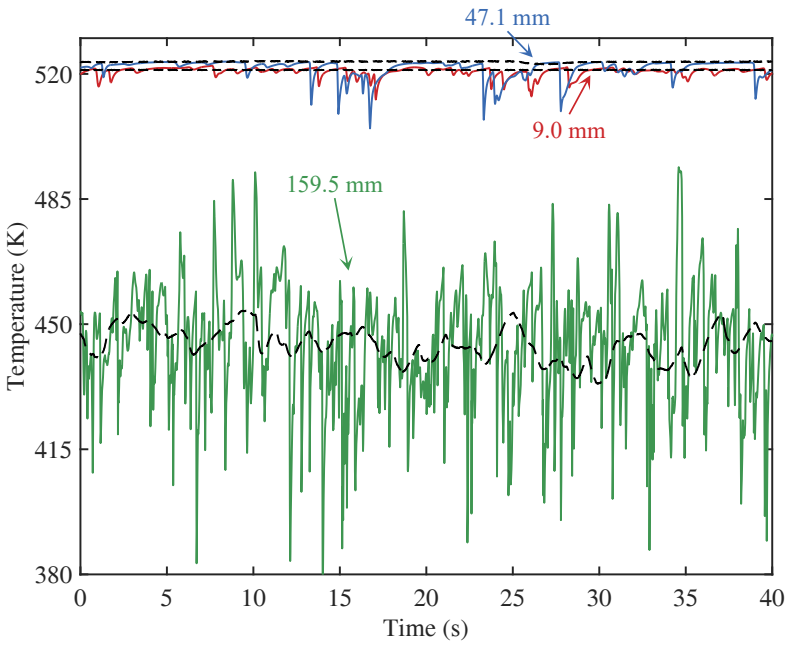


Figure 2.6: Comparison of temperature fluctuations at selected heights between the simulation (solid lines, –) and experiment (dashed lines, - -).

2.4.3 Effects of holder height

The ASTM standard allows users flexibility in the construction of the apparatus and in particular, the dimensions of the ceramic holder and the location of the flask within the furnace. We examined the influence of the three insulating holder heights shown in Table 2.1 on the fluid motion. The motion was simulated for 50 seconds after stationary statistics were achieved that were independent of start-up behavior. Figure 2.7 plots on a vertical cross-section through the center line the average temperature field and projected (surface) streamlines. For all three cases, a toroidal vortex is observed within the bottom of the flask where air sinks through the center and rises along the walls. The calculated Rayleigh and Reynolds numbers based on the flask radius and maximum temperature difference is computed as $Ra_r = 8.3 \cdot 10^4$ and $Re_r = 60$. Thus, sufficient convection resulting in a toroidal structure is consistent with the critical Rayleigh number threshold, $Ra_c \approx 600$, described in the literature for closed spherical vessels (Tyler and Tuck, 1967; Jones, 1974; Kee et al., 1975; Silakova et al., 2006; Campbell et al., 2007). Flow is driven by both the surface temperature distribution on the flask and, more importantly, the unsteady flow of colder, more dense air penetrating down the ceramic holder through the center of the flask and an upward counterflow of hot air circulating

from the bottom portion of the flask upward along the hot walls. Circulation cells commonly observed in natural convection flows within nonuniformly heated slots or cavities are observed above the flask within the ceramic holder. As the holder height is increased, the number of cells increases, from 2 to 10. The averaged flows are approximately axisymmetric but evidence of unsteadiness, three-dimensional motion, and symmetry-breaking can be observed in the surface streamline patterns in the holder section which can be attributed to both Rayleigh-Taylor and Kelvin-Helmholtz instabilities of the buoyancy-driven flow in a sufficiently tall volume. The Rayleigh numbers chracterizing the flow in the holder section for the three cases are calculated using the height of the apparatus as $3.7 \cdot 10^7$, $7.2 \cdot 10^7$, and $2.3 \cdot 10^8$ for cases A, B, and C, respectively which place the physical problem well within the transition to turbulence regime (Churchill and Chu, 1975; Chenoweth and Paolucci, 1986) that propagates down into the flask itself.

The results from Figure 2.7 show the existence of an unsteady toroidal vortex which is evidence of convection independent from any chemical reaction. In contrast to vortical motion observed in self-heating tests and computations that are discussed in Chapter 1, the vortex rotates in the opposite direction and is a direct consequence of nonreactive flow, the intrusion of cold air downward through the open mouth of the flask. The sinking cold air mixes with the hot air in the entrance to the flask, penetrates on the center line into the main volume and creates an average vortical motion within the flask, with hot air rising along the side walls.

Examining the average temperature field, an unstable vertical stratification is apparent within the holder, with temperature decreasing with increasing height, as shown in Figure 2.8. Modest variations in temperature can be observed within the spherical portion of the flask, case A was on average 7 K lower than case C. The temperature variations within the neck of the flask decrease with the increasing height of the ceramic holder. This is due to the increased mixing and longer residence time of the cold ambient gas as it plunges down through the longer holders into the flask. The cold air above the furnace has to travel further to reach the flask in case C compared to case A. The average downward velocity, Figure 2.9, is lower in case C than in case A leading to a longer mixing time and greater heat transfer. Therefore, larger average temperatures are observed as the holder height increases. Transverse velocities along the center line (not shown) are two orders of magnitude smaller than the vertical component.

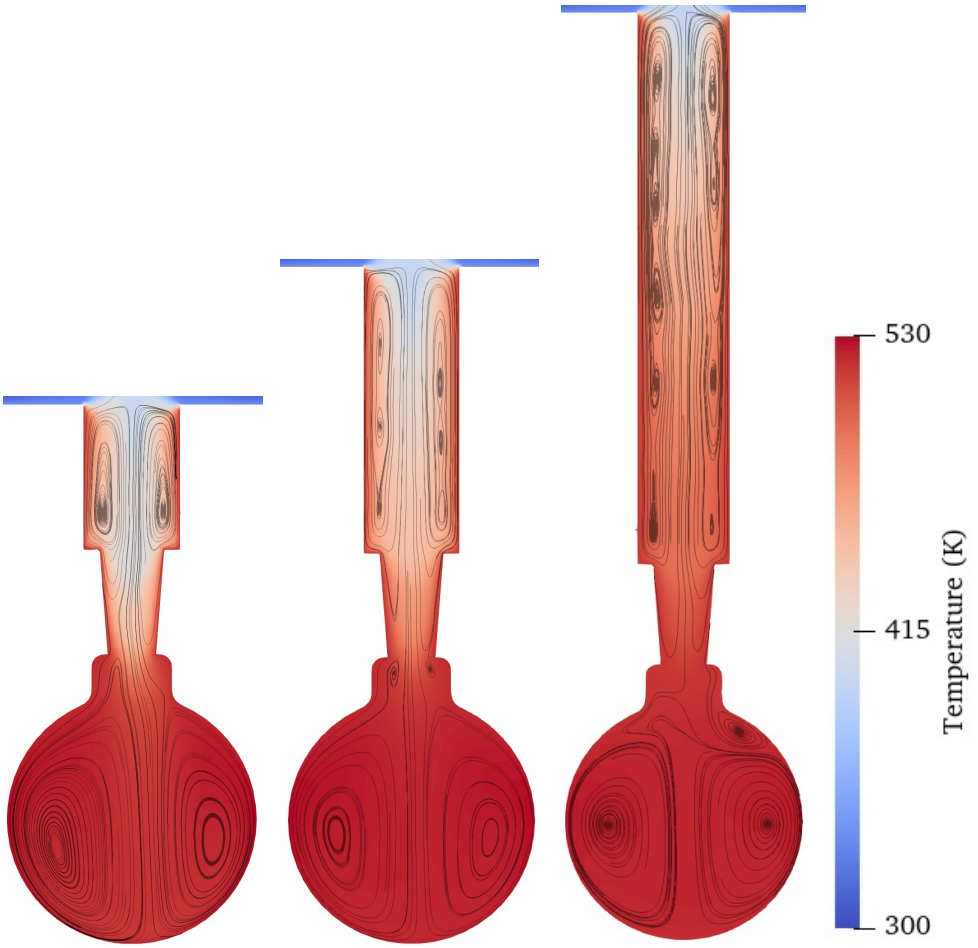


Figure 2.7: Average temperature field and projected (surface) streamlines along a vertical cross-section of the domain for the three holder heights.

While averages can be informative about the large-scale features of the flow, temperature fluctuations are important for unsteady reactive flow problems since reaction rates strongly depend on temperature. Table 2.2 gives the temporal temperature statistics in the center of the flask. This location is consistent with the nominal location of thermocouple T_4, used by the ASTM-E659 standard to monitor and characterize the temperature within the flask during ignition experiments. Case A had the largest temperature standard deviation (8 K) and largest absolute fluctuation size (38 K), while case C had the smallest standard deviation (0.9 K) and absolute fluctuation size (3 K). This is expected since the residence times of downward moving cold air are smaller in the shorter flask holder as compared to the taller holders.

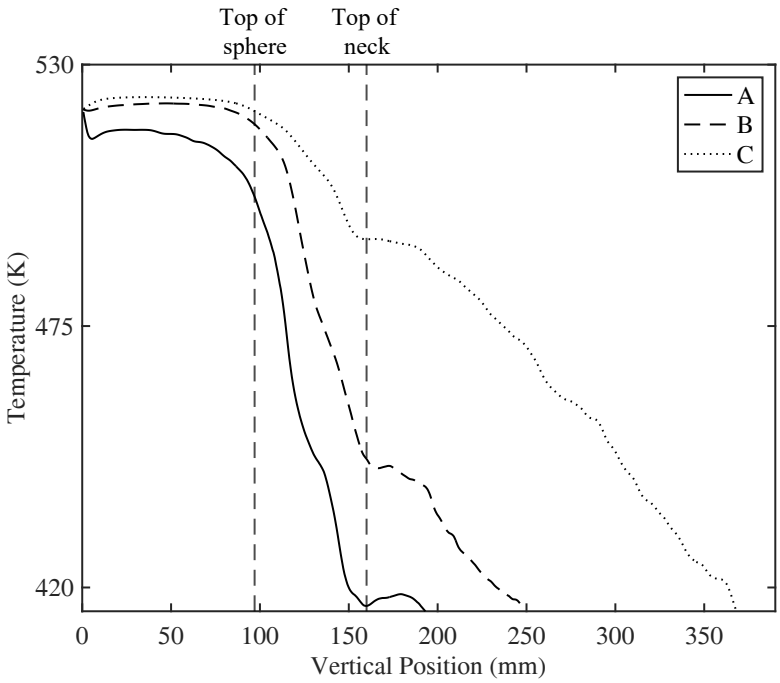


Figure 2.8: Average temperature profile along the vertical center line for the three holder heights.

Table 2.2: Statistical analysis of temperature at the center of the flask for the three holder heights.

Case	T_{avg} (K)	T_{std} (K)	T_{min} (K)	T_{max} (K)
A	515.6	8.00	477.2	522.1
B	520.6	3.30	494.3	523.6
C	522.8	0.90	519.7	524.1

The temporal average temperature was computed for all cells within the spherical portion of the flask. A histogram was obtained by binning the average temperature field. This is directly related to the probability distribution as the computational volumes are essentially identical in size and uniformly distributed. Figure 2.10 plots the distributions for the three holder heights. The location of the temperature at the center of the flask, T_4, is indicated with vertical lines. For the shortest holder, case A, the distribution is broadest, spanning 15 K, whereas cases B and C are narrower, spanning 9 and 8 K, respectively. These trends are consistent with the fluctuations reported in Table 2.2. With decreasing holder height, the flow fields become less

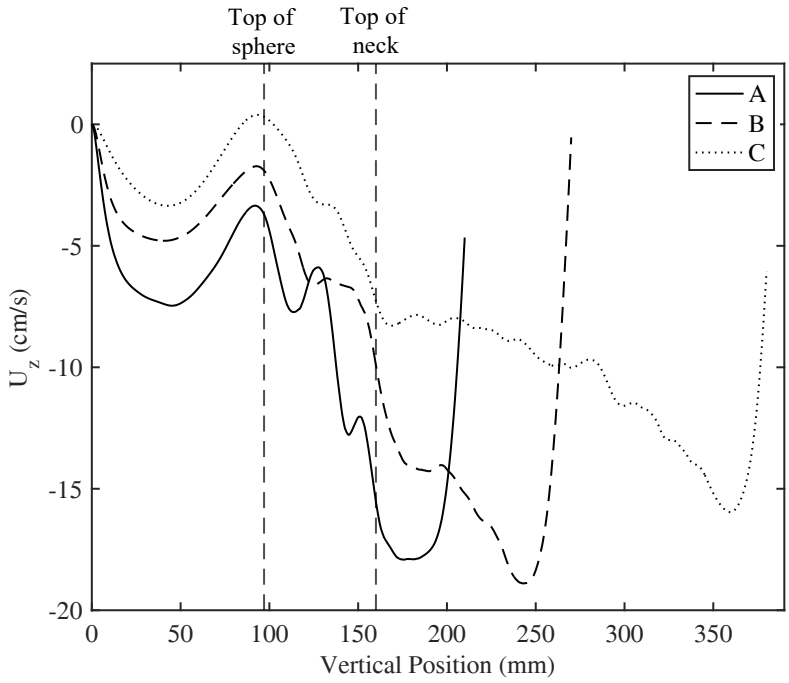


Figure 2.9: Average vertical velocity along the vertical center line for the three holder heights.

steady and more cold air enters the flask, broadening the temperature probability distribution. For all holders, T_4 is on the left tail of their respective distributions with values of T_4 up to 5 K less than the median temperature. The implications for reported AITs are discussed in Section 2.5.

2.4.4 Fuel Mixing

During an ignition experiment, fuel is injected from a syringe through a thin needle into the flask. Depending on the temperature, ignition can occur at a range of times following injection and with different extents of mixing depending on the fuel density and diffusivity. Understanding how the fuel distribution evolves within the flask following injection is also relevant to explaining the various modes of ignition that have been observed (Martin and Shepherd, 2021).

To study the effect of mixing, a ball of fuel in its gaseous phase was initialized near the bottom of the flask in an established dry air flow field. The temperature of the fuel sphere was set to be equal to the local air temperature at the time of injection. An initial fuel temperature closer to room temperature (300 K) was also examined and mixing behavior for these cases are briefly discussed. All presented results besides

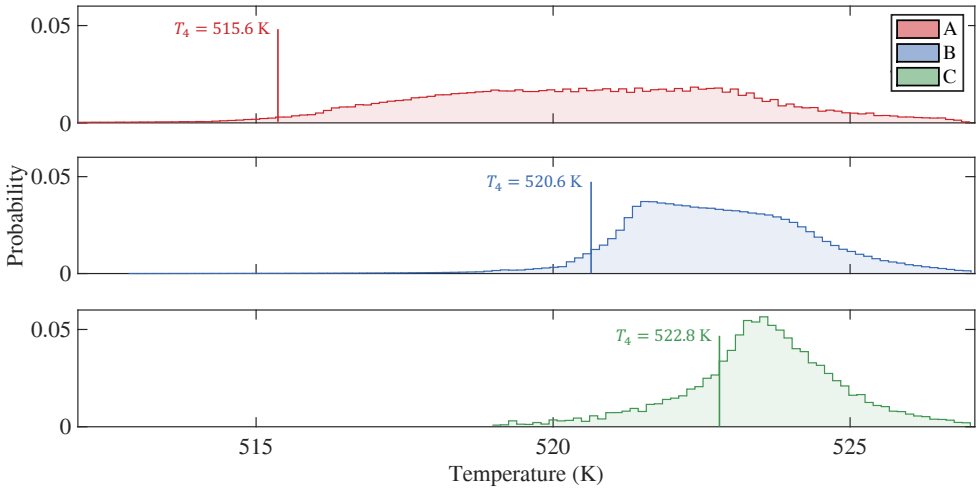


Figure 2.10: Flask average temperature probability distributions for the three holder configurations. Flask center temperatures, T_4, are also indicated.

the blue curves in Figure 2.14 are for the flask ambient temperature fuel initialization cases. We acknowledge that a more complicated situation exists for liquid fuels, with droplets and two-phase mixtures emerging from the needle. The flow momentum, droplet vaporization, impact on the flask surface, and droplet dynamics, including the Leidenfrost effect, will influence the mixing behavior. Chemical reactions will also begin to take place concurrent with the mixing process. We have drastically simplified the problem to enable a preliminary analysis. The effect of chemical reaction will be studied further in Chapter 3.

The evolution of fuel concentration over time was computed for three fuels of different sizes and molecular weights. Figures 2.11, 2.12, and 2.13 plot the mole fractions of C_2H_4, nC_6H_{14}, and $nC_{12}H_{26}$ on a vertical cross-section through the center of the flask over time. The color bar is updated at every instance in time so that the mixing characteristics can be visualized. For the C_2H_4 case, the fuel initially rises slightly before being fully mixed in the flask within 30 seconds. The nC_6H_{14} and $nC_{12}H_{26}$ cases mix differently than C_2H_4. For the heavy molecules, the fuel initially sinks to the bottom of the flask before diffusing upwards and becoming fully mixed over a much longer period. While the mixing behaviors are similar between n-hexane and n-dodecane, the larger n-dodecane molecule diffuses more slowly and thus, has a longer time to fully mix in the domain. For n-hexane, it takes approximately 130 s to reach equilibrium whereas for n-dodecane, it takes 185 s.

The effect of varying the fuel molecular weight and temperature can be characterized by the density of the fuel sphere, ρ_F, the Froude number based on peak center line speed U, flask diameter d, and density normalized density difference $\Delta\rho/\rho_F = (\rho_F - \rho)/\rho_F$ between the fuel volume and surrounding air

$$Fr = \frac{U}{\sqrt{gd|\Delta\rho|/\rho_F}} \cdot \text{sign}(\Delta\rho_F)\,,$$

and the Schmidt number based on the mixture viscosity μ and fuel diffusivity D_F in the surrounding fuel-air mixture

$$Sc = \frac{\mu}{\rho D_F}\,.$$

Representative values for each fuel are shown in Table 2.3.

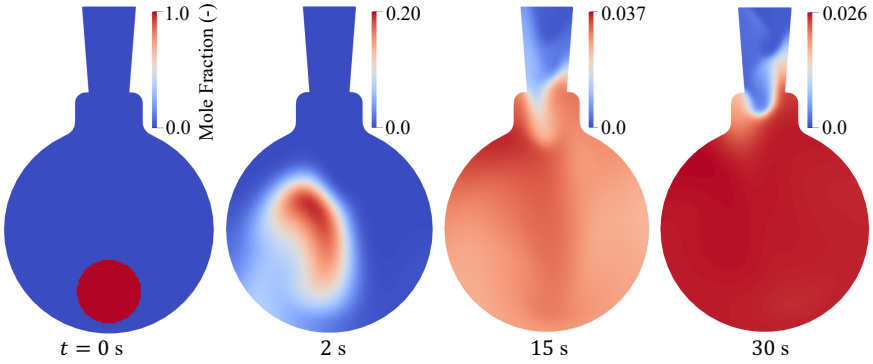


Figure 2.11: C_2H_4 mole fraction temporal evolution on a vertical cross-section within the flask.

Because all the cases were initialized at the same temperature and pressure, the initial density of the ethene sphere is slightly smaller than the ambient air density (0.69 kg·m^{-3}) and the initial density of the n-hexane and n-dodecane spheres are larger than ambient. As a consequence, ethene is slightly buoyant with $Fr < 0$ and the flow is dominated by convection. The unstable fuel sphere is convected throughout the flask and the distorted volume rapidly mixes by diffusion. The n-hexane and n-dodecane are dominated by buoyancy with $1 \gg Fr > 0$. The initial negative buoyancy results in the fuel spheres settling to the bottom of the flask and then slowly diffusing upward with a stable interface between the fuel-air mixture and air.

The degree of "mixedness" can be studied to quantitatively assess how quickly the fuels mix within the flask. The intensity of segregation can be defined in terms of

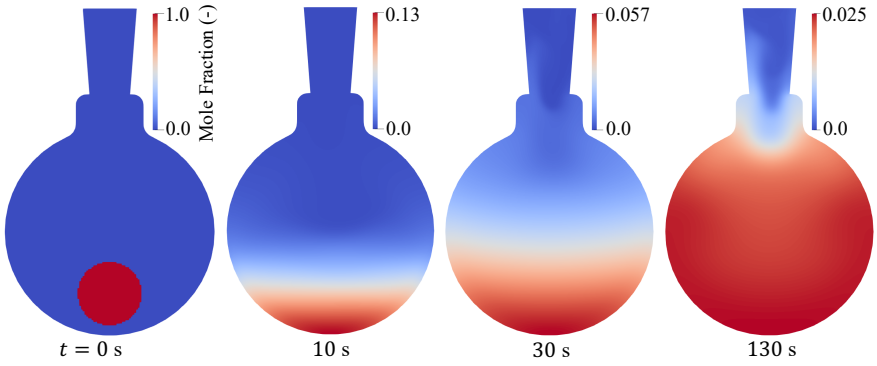


Figure 2.12: nC_6H_{14} mole fraction temporal evolution on a vertical cross-section within the flask.

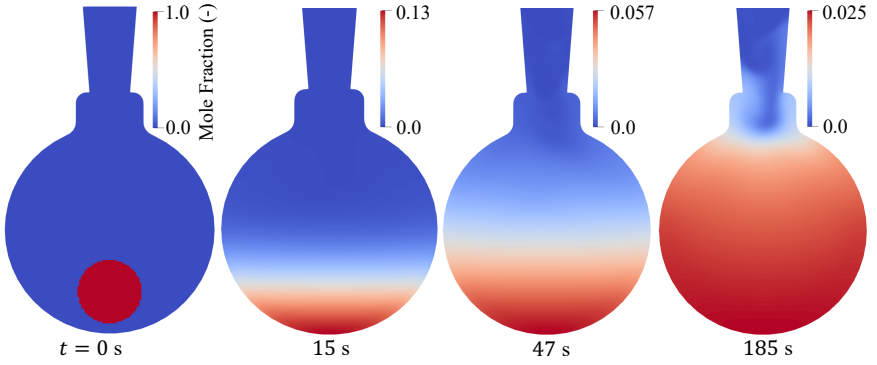


Figure 2.13: $nC_{12}H_{26}$ mole fraction temporal evolution on a vertical cross-section within the flask.

Table 2.3: Molecular weight, Lennard-Jones parameter, fuel sphere density, Schmidt number, and Froude numbers for the three tested fuels.

Fuel	W_F [kg· kmol^{-1}]	σ_F [nm]	ρ_F [kg·m^{-3}]	Sc	Fr
C_2H_4	28	0.39	0.65	0.93	-0.27
nC_6H_{14}	86	0.59	2.00	1.8	0.059
$nC_{12}H_{26}$	170	0.76	3.95	2.6	0.053

the coefficient of variation as described in Kukukova et al. (2009) as:

$$c_v = \sqrt{\frac{1}{N}\sum_{i=1}^{N}\left(\frac{X_i - \overline{X}}{\overline{X}}\right)^2} \tag{2.9}$$

where X_i is the fuel mole fraction for a given computation cell, $\overline{X}$ is the volume

average fuel mole fraction, and N is the total number of cells in the domain. The coefficient of variation, c_v, can be normalized by the initial $c_v(0)$ to obtain a value between 0 and 1. Given that c_v computes the standard deviation over the mean, the value is largest for a perfectly unmixed state and will decay to 0 for a completely homogeneous mixture. As c_v is dimensionless, it can be readily compared between the different fuel cases. Figure 2.14 plots c_v against time for the three fuels. In early times, the mixedness of n-hexane and n-dodecane decays more rapidly than ethene. This is caused by the strong buoyancy force that immediately drives the heavier fuels to the bottom of the flask. However, as time continues, ethene c_v reaches a steady value near zero significantly faster than for n-hexane and n-dodecane.

The effect of diffusivity on mixing can be understood by examining the estimated Schmidt numbers, Sc, in Table 2.3. The increase in Sc with increasing fuel molecular weight is primarily due to the decrease in diffusivity with increasing fuel molecule size, although there is a small contribution (15%) from the difference in mixture kinematic viscosity. For example, consider how the binary diffusion coefficient (Kee et al., 2005) depends on both the molecular weights W_i and effective collision cross sections σ_{FA}^2

$$D_{FA} \propto \frac{1}{\sigma_{FA}^2}\sqrt{\frac{1}{W_F}+\frac{1}{W_A}}$$

where $\sigma_{FA} = (\sigma_F + \sigma_A)/2$ and $\sigma_A = 0.35$ nm. The increase in molecular size σ_F and decrease in diffusivity for the larger fuel molecules results in an increase in the time to mix, all other factors being the same. This accounts for the differences in the mixing rate of n-hexane and n-dodecane.

Taking a 5% level of c_v conventionally used in industry to characterize mixing time, the time to mix was = 11, 59, and 104 s for C_2H_4, nC_6H_{14}, and $nC_{12}H_{26}$, respectively. Previous work from Martin (2023) shows that nC_6H_{14} and $nC_{12}H_{26}$ can ignite before these times in some ASTM test conditions. In those cases, it is probable that ignition occurs before the fuel is fully mixed inside the flask.

A mixing investigation of C_2H_4 and nC_6H_{14} fuel spheres initialized at room temperature was also carried out. The results are presented in blue in Figure 2.14. The lower temperature, higher density C_2H_4 sank to the bottom of the flask, similar to what was observed for the heavy hot fuels. The lower temperature, higher density nC_6H_{14} sank to the bottom of the flask with a greater acceleration compared to the flask ambient temperature case. This additional buoyancy induced acceleration seen for both cold fuels resulted in greater mixing during the initial transient (< 10 s).

For the faster mixing C_2H_4, this resulted in a reduction in the time to mix from 11 s to 7 s. Later in time for the nC_6H_{14} case (> 20 s), after the initial transient damps, the fuel layer is stably stratified and the subsequent mixing is primarily through molecular diffusion. This resulted in a time to mix that remained at 59 s for both the room temperature and the flask ambient temperature n-hexane fuel case.

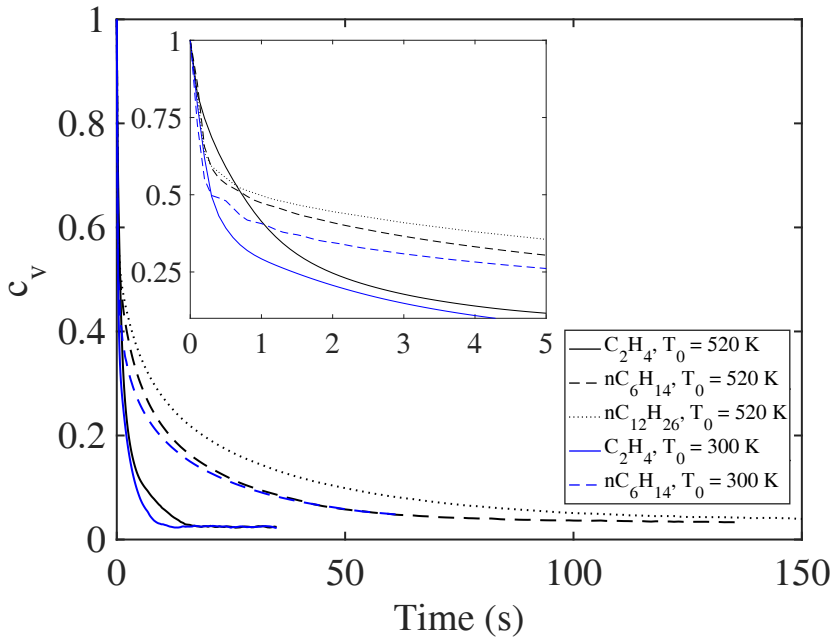


Figure 2.14: Coefficient of variation, Eq. (2.9), over time for C_2H_4, nC_6H_{14}, and $nC_{12}H_{26}$ initialized at flask ambient temperature. Results are also provided for C_2H_4, nC_6H_{14} initialized at room temperature.

The number of fuel moles, n, within the flask can also be tracked over time by integrating spatially over the number of cells. This is shown in Figure 2.15. Since the same volume, pressure, and temperature were initialized, n is initially the same for all three cases. After 3 seconds, ethene molecules begin leaving the flask and the number of moles rapidly decreases over the next several seconds. After 26 s, 10% of the fuel has escaped into the holder and ambient air above. For n-hexane and n-dodecane cases, a 10% loss of fuel takes significantly longer at 117 and 173 s, respectively. The much slower loss of the larger, heavier fuel molecules is a consequence of the stable stratification, resulting in a much longer time for the fuel-air interface to reach the top of the flask, diffuse into the neck of the flask, and, ultimately, escape. For all cases, the time to lose 10% of the fuel molecules is longer than the time for the intensity of segregation to drop below 5%. Thus, the

fuel molecules remain mostly within the flask prior to complete mixing, even for the smaller, lighter C_2H_4 case. Martin (2023) observed ignition of n-hexane and n-dodecane up to approximately 70 and 170 seconds, respectively. It's probable that less than 10% of the fuel leaves the flask before he observed ignition.

The mixing results presented are for a highly idealized fuel initialization. For liquid fuels, such as nC_6H_{14} and $nC_{12}H_{26}$, rapid vaporization of the fuel droplets is expected to create a substantial transient velocity field inside the flask due to the volume displacement of air within the flask. For gaseous fuels, such as C_2H_4, the momentum of the jet of injected fuel will also induce flow and displacement. In both cases, the initial distribution of fuel composition and temperature will be quite different than the idealized spherical ball. Our simulations are intended to guide the understanding of the effects of the initial flow field on the composition at later times characteristic of a long duration autoignition test.

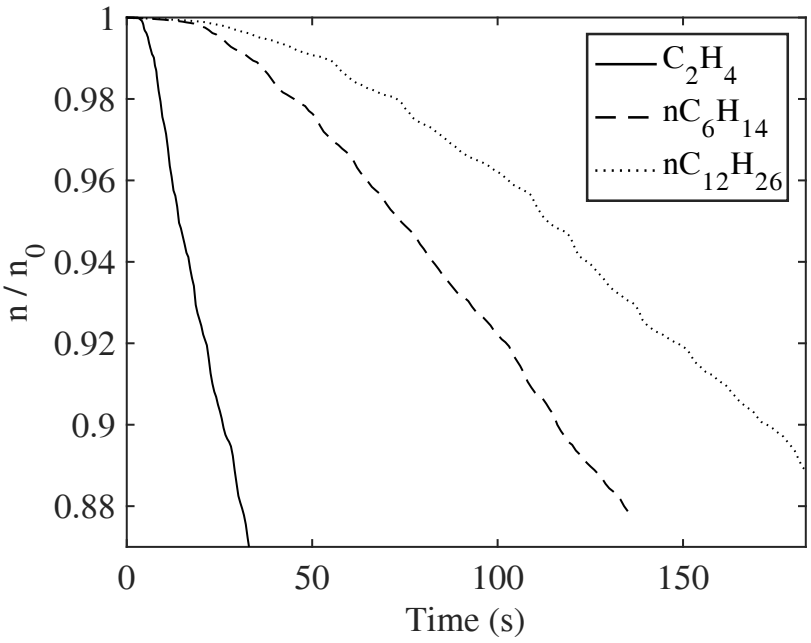


Figure 2.15: Number of fuel moles normalized by the initial value within the flask over time.

2.5 Implications for AIT experiments

Our results (Figures 2.5 - 2.10) indicate that various setups conforming to the ASTM-E659 (2005) standard exhibit a dominant toroidal vortex within the flask, driven by cold plumes of air sinking through the center of the flask from the open top. This

effect is a feature of buoyancy driven nonreactive flow and is distinct from the vortical flows produced by exothermic chemical reaction. The vortex rotation direction in a closed spherical vessel undergoing self-heating is the opposite direction and a different order of magnitude (smaller) than that due to the cold air intrusion.

The downward sinking cold air will be a feature of any test apparatus that is open to the surrounding atmosphere at the mouth of the flask. This is the case not only for an ASTM-E659 flask, but also the IEC and DIN apparatus outlined in the ISO/IEC (2017) standard which include an open top in a shorter neck and smaller flask volume than the E659 standard. For long duration, up to 600 s, tests used to define the AIT, temperature variations induced by the sinking cold air intruding through the open neck of the flask may be comparable to those due to buoyancy effects associated with to energy release and temperature variations on flask surface.

The temperature and composition fluctuations created by influx and mixing of cold air will influence the self-heating process, an additional source of variability in reported AIT values. The results presented in Figure 2.10 further indicate that variations in the implementation of the ASTM-E659 standard can have significantly different temperature distributions. A range of temperatures can exist within the flask and will not be captured by the single point of measurement at T_4. Further, the size of fluctuations and general unsteadiness are different for the three cases we considered. This indicates that investigation and consideration of variations between apparatus construction is needed when evaluating reported results. The existence of a range of temperatures within the test flask indicates that care is needed in interpreting the values of AIT based only on the measurements of T_4.

We observe that fuel dispersion inside the flask is affected by the flow field and the fuel's physical properties, such as the density and diffusion coefficient. For short-duration tests, ignition could occur in a poorly mixed, stratified atmosphere, while for long-duration tests, loss of fuel could influence the AIT. Competing mixing and chemical timescales could cause AIT comparisons between different fuels to be misleading unless these factors are taken into account.

2.6 Conclusions

Experimental measurements and three-dimensional numerical simulations with realistic transport properties were used to characterize the nonreactive flow field inside our ASTM-E659 Autoignition Temperature (AIT) facility. Within the test flask, the downward movement of air through the center of the neck create a single dominant

toroidal vortex that transports gas upwards along the walls and downward along the center line. The observed toroidal vortex is counter-rotating and exists in a non-reacting flow compared to results from numerous previous studies in closed spherical vessels. This is a direct consequence of the open flask configuration used in AIT testing in order to visualize emission from the flame.

Temperature measurements were made along the vertical center line in our AIT facility and were compared to a numerical simulation of the same geometry. A maximum variation of 4 K (0.7%) was observed in the average temperature within the flask. Above the flask, larger deviations between the simulation and experiment were observed due to the isothermal boundary condition used on the numerical model. For all measured locations, experimental temperature fluctuations were significantly smaller than those seen in the simulation at the same location, These differences are attributed to the slow response time of the thermocouple used in the experimental measurements.

A parametric study of the ceramic holder heights was carried out numerically to observe the effect on the resultant flow field. While the same toroidal vortex pattern was seen within the bottom of the flask for all cases, the strength decreased with increasing holder height as the cold plume influx to the flask decreased in these cases. As a result, the average temperature for any given location along the vertical center line increased with increasing holder height. At the center of the flask, the average temperature for case A (shortest) was 7 K lower than for case C (tallest). Similarly, the absolute fluctuation size decreased from 8 K with the shortest holder to 0.9 K for the tallest holder.

A parametric study was also carried out to observe the effect of varying fuel molecule size and molecular weight on the mixing process within the flask. For the smallest molecule, ethene, complete mixing can occur in only 11 s due to minimal buoyancy effects and small Schmidt number. Heavier fuels, such as n-hexane and n-dodecane, consequently have much smaller, positive Froude numbers. Therefore, gravity initially plays a dominant role in forcing the fuel to the bottom of the flask. With significantly larger Schmidt numbers, these fuels diffuse much more slowly in air with mixing times of 59 and 104 s respectively, compared to ethene. A 10% loss of fuel molecules was observed after 25, 119, and 180 s for ethene, n-hexane, and n-dodecane, respectively. Therefore for all fuels studied, significant loss of fuel from the flask only occurs after complete mixing is obtained. The mixing character for ethene was found to be affected by the initial fuel temperature whereas for n-hexane, the time to mix was unchanged with a changing initial fuel temperature.

In this chapter, a number of factors were identified that are important to consider in interpreting AIT data from the ASTM-E659 apparatus. We observe that both the construction of the apparatus (with the allowable specification of the standard) and the fluid motion induced by buoyancy through the open top can have a significant influence of gas inside the flask prior to fuel injection as well as chemical reaction progress after injection. The observed variability in temperature and fuel concentration may have an influence on the measured autoignition temperatures and ignition delay times with implications for application to hazard assessment.

Chapter 3

NUMERICAL MODELING OF N-HEXANE AUTOIGNITION

3.1 Motivation

This chapter extends the fluid mechanic, heat transfer, and fuel mixing results presented in Chapter 2 on the ASTM-E659 testing apparatus in our laboratory to include chemical reaction in modeling an actual autoignition test. For these purposes, nC_6H_{14} was selected as a suitable surrogate for Jet A, a commonly used fuel in the commercial aviation industry. Additional analysis and the effects of aromatic compounds found in Jet A on the oxidation of straight chain alkanes can be found in Appendix A. First, a kinetic mechanism for nC_6H_{14} oxidation suitable for low-temperature ignition simulation was reduced and validated with the parent mechanism against zero-dimensional ignition delay times and one-dimensional freely propagating flame calculations. Then, the autoignition of nC_6H_{14} was simulated and compared with experimental results. The ignition process in this configuration proceeds through several distinct stages that were analyzed in detail: i) fuel dispersion and stratification following injection, ii) a pre-ignition "cooking phase" marked by slow low-temperature reactions, iii) a multi-stage ignition event driven by coupled chemical-thermal runaway, iv) transition to high-temperature reactions with subsequent flame propagation shaped by the evolving composition and flow field. While the present simulations assume an initially gaseous fuel distribution, the actual ASTM-E659 test involves a two-phase jet injection, including droplet breakup, vaporization, and liquid–wall interactions, which are not considered in the current analysis.

3.2 Numerical methods

3.2.1 Geometric model and meshing

The same geometry, governing equations, and boundary conditions as case B (corresponding to the setup in our laboratory) discussed in Chapter 2 was used for this study. In this case, reactions were enabled and the reaction terms included in the species and energy equations.

3.2.2 Kinetic modeling

Mechanism reduction and ignition delay time validation

Autoignition experiments for liquid hydrocarbon fuels often take place at very low temperatures (< 800 K) as shown in Martin and Shepherd (2021) and Fouchier and Shepherd (2025). It is well understood that the chemical reaction pathways for heavy n-alkane oxidation in this temperature regime differ from those at more elevated temperatures (< 1000 K) as evident from the observed "negative temperature coefficient" (NTC) region as shown in Westbrook and Dryer (1984) and Battin-Leclerc (2008) along with many other studies. Thus, both high- and low-temperature reaction pathways must be included when simulating such an environment. For these purposes, the CaltechMech full mechanism (Blanquart et al., n.d.) was selected for creating a reduced mechanism to use in multidimensional reacting flow studies. The CaltechMech mechanism was validated against extensive experimental datasets including laminar premixed flames, laminar diffusion flames, and homogeneous reactors for a wide range of temperatures and pressures making it a good source mechanism to use for reduction. The reduction was carried out for n-hexane/air ignition studies and has been verified with the CaltechMech full mechanism for $500 < T < 1500$ K and $0.2 < P < 5$ bar. The automatic method proposed by Davidenko et al. (2011) to reduce reaction mechanisms under autoignition conditions was employed. Briefly, the procedure consists in removing one reaction at a time from the detailed model and evaluating its impact on the zero-dimensional adiabatic constant-pressure (CP) auto-ignition process. More detail about the zero-dimensional model can be found in Chapter 6. After each CP simulations, several quantities are verified, including the time to peak or the maximum heat release rate, defined as

$$\dot{q}_{max} = -\sum_{i=1}^{N} h_i \dot{\Omega}_i, \tag{3.1}$$

the equilibrium temperature and mean molar mass, as well as the profiles of heat release, temperature, and mean molar mass. For each quantity, the deviation induced by the reaction removal must be below a specific threshold, as defined in Table 1 of Davidenko et al. (2011), for the reaction to be considered as “unimportant”. Otherwise, the reaction is classified as “important”. After all the reactions have been evaluated, the reaction inducing the lowest variation is definitely removed from the mechanism. The procedure is repeated until only important reactions remain. The resultant reduced mechanism consists of 54 species and 265 reactions. Coefficients for all elementary reactions can be found in Appendix B.

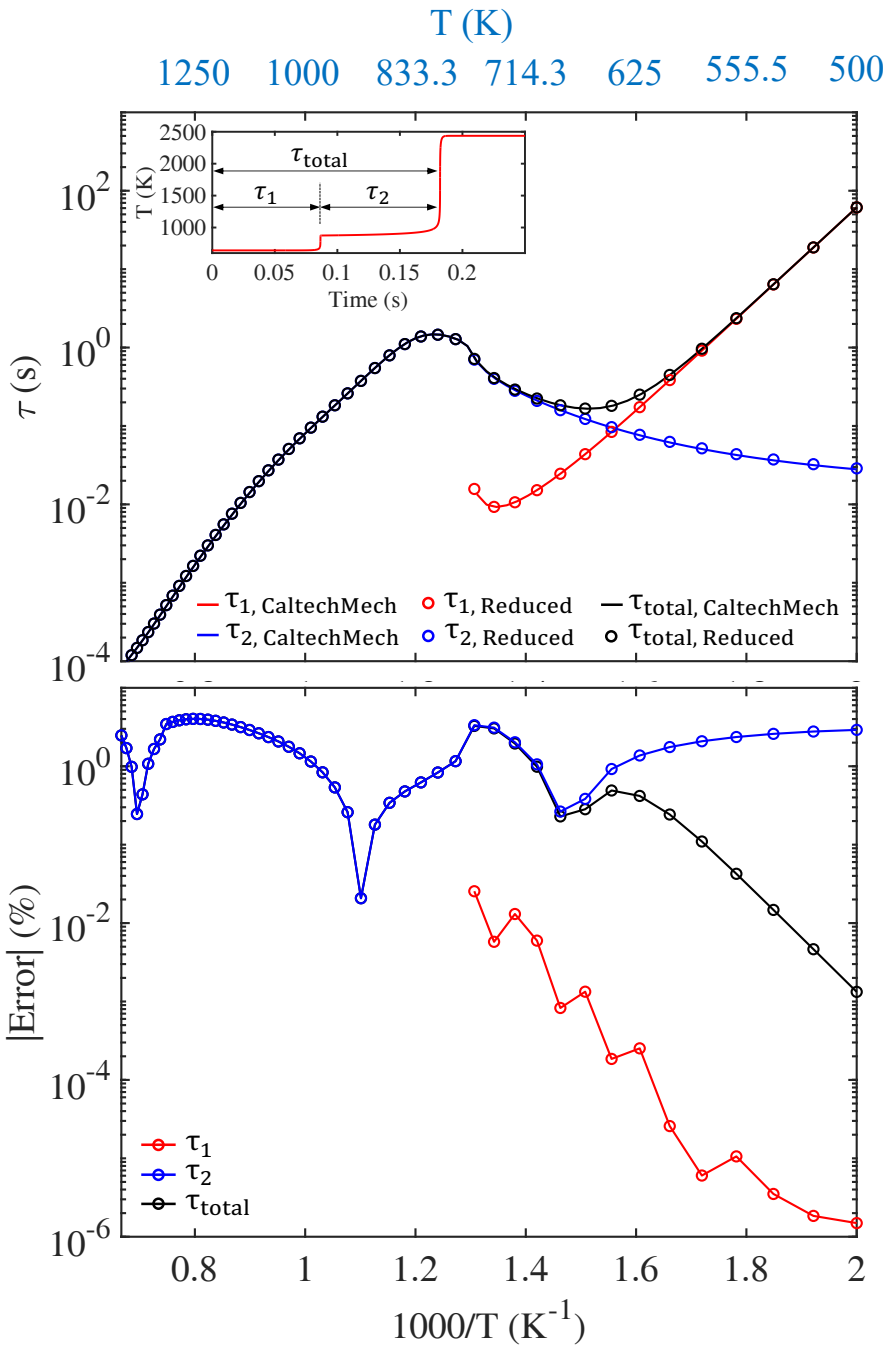


Figure 3.1: Comparison of the ignition delay times for CaltechMech and the reduced mechanism. (Top) Ignition delay time vs. the inverse of temperature for stoichiometric nC_6H_{14}/air oxidation at 1 bar. Delay times for the first stage, τ_1, the second stage, τ_2, and the total delay, τ_{total}, for both CaltechMech and the reduced mechanism are shown. (Bottom) The absolute error in % of the ignition delay times computed from the reduced mechanism compared to CaltechMech.

Figure 3.1 (top) plots the ignition delay times against the inverse of temperature computed from zero-dimensional adiabatic constant pressure simulations at 1 bar for stoichiometric nC_6H_{14}/air (C_6H_{14} + 9.5 (O_2 + 3.76 N_2)) in Cantera (Goodwin et al., 2021). The first stage delay, τ_1, the second stage delay, τ_2, and total delay, τ_{total} as defiend in the figure for both the CaltechMech full mechanism and reduced mechanism are shown. In general, as the initial temperature is increased, τ_{total} decreases due to the exponential dependence of the reaction rate constant on temperature. However, the characteristic NTC region associated with a shift in dominant reaction pathways can be seen between 650 K and 800 K where an increase in τ_{total} with temperature is observed. For a given delay time, τ_{total} = 0.4 s, three distinct situations can exist depending on the initial temperature. At T_i = 600 K, τ_1 is much longer than τ_2. At this temperature, the low-temperature chemistry is much slower than the mid- and high-temperature chemistry. Therefore, most of τ_{total} is effected by τ_1. At T_i = 745 K, τ_1 becomes much shorter than τ_2 as the important reactions shift. Finally, at T_i = 908 K, the two-stage behavior disappears entirely and ignition occurs over a single event. This behavior as the initial temperature is increased is captured by the reduced mechanism, which can be further seen in Figure 3.1 (bottom). The absolute error of τ_1, τ_2, and τ_{total} is shown for the zero-dimensional simulations shown in Figure 3.1 (bottom). The mean error of the reduced mechanism from the CaltechMech mechanism for τ_1, τ_2, and τ_{total} is 0.0038%, 1.96%, and 1.65%, respectively and the maximum error was 0.026%, 4.02%, and 4.02%.

One-dimensional flame validation

While the reduced kinetic mechanism was developed specifically for ignition simulations, the quality in reproducing laminar burning velocities and flame thickness from the source mechanism can also assessed. In a flame-fixed coordinate system, the 1D freely propagating, premixed flame can be modeled assuming constant pressure with the steady-state equations for continuity, energy, and species in an infinite spatial dimension $-\infty < x < \infty$ as

$$\frac{d(\rho u)}{dx} = 0 \tag{3.2}$$

$$\rho u \frac{dY_i}{dx} = -\frac{d(\rho Y_i \boldsymbol{V}_i)}{dx} + \dot{\Omega}_i \tag{3.3}$$

$$\rho c_P u \frac{dT}{dx} = \frac{d}{dx}\left(\lambda \frac{dT}{dx}\right) - \rho \frac{dT}{dx} \sum_i^N c_{P,i} Y_i \boldsymbol{V}_i - \sum_i^N h_i \dot{\Omega}_i \tag{3.4}$$

where ρ is the density, u is the velocity, c_P is the specific heat capacity at constant pressure, T is the temperature, and λ is the thermal conductivity. Y is the mass fraction, $\dot{\Omega}$ is the formation rate, h is the enthalpy, and $\boldsymbol{V}$ is the diffusion velocity. The subscript i denotes properties relating to species i and N is the total number of species.

Fickian diffusion was employed using mixture-averaged diffusion coefficients, D_i, calculated according to Curtiss and Hirschfelder (1949) as

$$D_i = \frac{1 - Y_i}{\sum_{j \neq i}^{N} \frac{X_i}{\Gamma_{ji}}} \tag{3.5}$$

where Γ_{ji} are the binary diffusion coefficients. The diffusion velocity can then be calculated as:

$$\boldsymbol{V}_i = -\frac{D_i}{Y_i}\frac{dY_i}{dx} \tag{3.6}$$

The ideal gas equation of state was used to calculate the density of the mixture using the specific gas constant and mixture-averaged molecular weight.

Eqs. (3.2)-(3.4) are solved employing central differencing with the following boundary conditions

$$T(x = 0) = T_u \tag{3.7}$$

$$Y_i(x = 0) = Y_{i,u} \tag{3.8}$$

$$\frac{dT}{dx}(x \to \infty) = 0 \tag{3.9}$$

$$\frac{dY_i}{dx}(x \to \infty) = 0 \tag{3.10}$$

where the subscript u represents the unburnt gas state.

In practice, the solution is calculated on a finite domain $0 < x < L$ such that the spatial gradients at the boundary are ≈ 0. The model was implemented in Python based on Cantera's *adiabatic_flame.py* example code. The solution technique is a modified Newton's method to implicitly solve for u, T, ρ, Y_i, as well as the constant mass flux (Goodwin et al., 2021; Bane, 2010). Automatic grid refinement is carried out by first obtaining a solution on a coarse grid size, w, and then inserting point in regions with sharp temperature or species gradients (i.e., within the heat release zone of the flame). Typical converged grids had 100-200 cells across the flame for nC_6H_{14}/air mixtures. An example of the typical flame structure can be seem in Figure 3.2 which plots the primary species and temperature profiles across the flame front for an unburnt gas temperature, $T_u = 300$ K and a stoichiometric nC_6H_{14}/air mixture

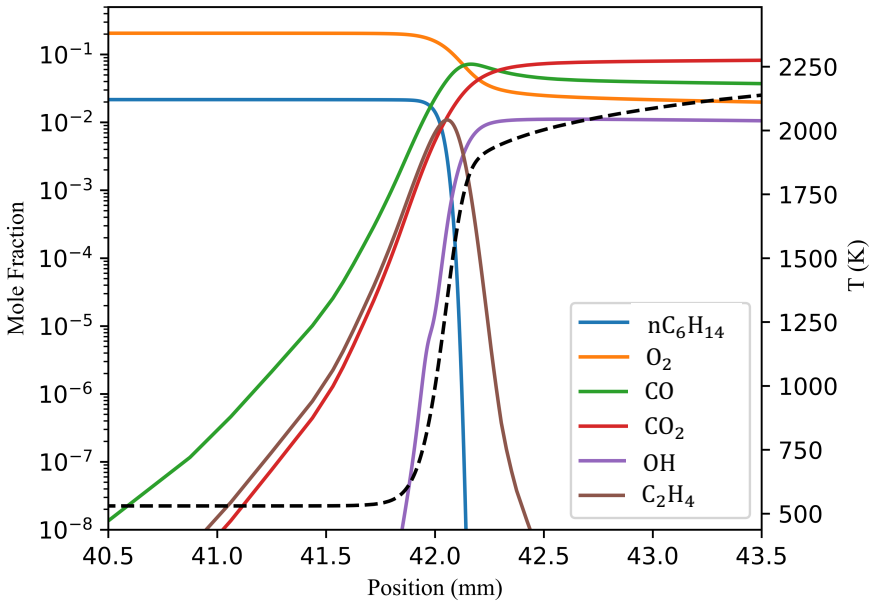


Figure 3.2: 1D flame model solution for T_u = 300 K and ϕ = 1 at 1 bar using the reduced CaltechMech mechanism for a nC_6H_{14}/air mixture.

(equivalence ratio, ϕ = 1) at 1 bar using the reduced CaltechMech mechanism described in Section 3.2.2. The position of the flame and domain size are arbitrary and depend on the solution scheme and grid refinement. Rapid oxidation of nC_6H_{14} into intermediates, such as C_2H_4 and CO, and finally into CO_2 by OH radicals can be seen across the flame.

With the unburnt u, and burnt, b, gas states, the flame propagates into the unburnt mixture at the laminar burning velocity, S_L, which can be computed from Eq. (3.2). Since the mass flow rate is constant through the domain, $\rho_u S_L = \rho_b u_b$ and S_L can be calculated as

$$S_L = \frac{\rho_b u_b}{\rho_u} \tag{3.11}$$

Of the many definitions of flame thickness, the most traditional definition is used to calculated ℓ_f according to Spalding and Jain (1961) as

$$\ell_f = \frac{T_b - T_u}{(dT/dx)_{max}} \tag{3.12}$$

Figure 3.3 compares the laminar burning velocity for different equivalence ratios between CaltechMech, the reduced mechanism, and experimental data. Both CaltechMech and the developed reduced mechanism exhibit similar structure, where

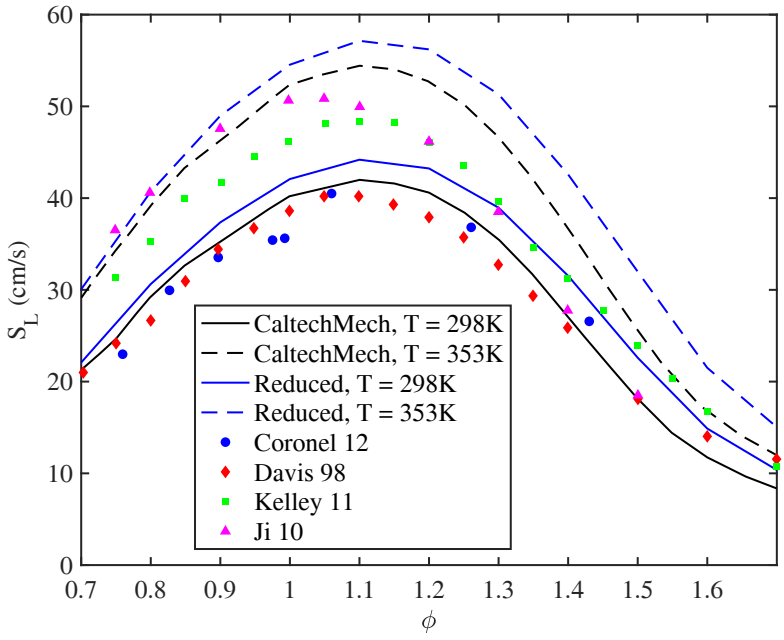


Figure 3.3: Laminar burning velocity, S_L, vs. equivalence ratio, ϕ, for CaltechMech, the reduced mechanism, and four experimental studies (Davis and Law, 1998; Ji et al., 2010; Kelley et al., 2011; Coronel et al., 2013) at two initial temperatures.

S_L is maximized near a stoichiometric composition. Lower S_L are observed for lean and rich mixtures as a consequence of inefficient combustion. The adiabatic flame temperatures are lower in these regions. This decreases the effective reaction rate, decreasing the laminar burning velocity. Both mechanisms over predict S_L slightly compared to the experimental results. The over prediction is worse for 353 K compared to 298 K and for larger ϕ. For all ϕ, the reduced mechanism over predicts the laminar burning velocity for both unburnt temperatures. This effect is more pronounced for larger values of ϕ, likely because of a shift to more complex reaction pathways not captured by the reduced mechanism. On average, the reduced mechanism over predicts S_L for a given ϕ by 10% for both unburnt gas temperatures.

It's useful to also check the reduced mechanism's performance at initial temperatures more relevant to autoignition studies for nC_6H_{14}. In this case, no experimentally measured values for S_L exist. However, the two mechanisms can be compared with each other. This is shown in Figure 3.4 which compares S_L and ℓ_f as a function of ϕ between CaltechMech and the reduced mechanism for an unburnt temperature, $T = 520$ K. The same S_L behavior is seen compared to the lower temperatures,

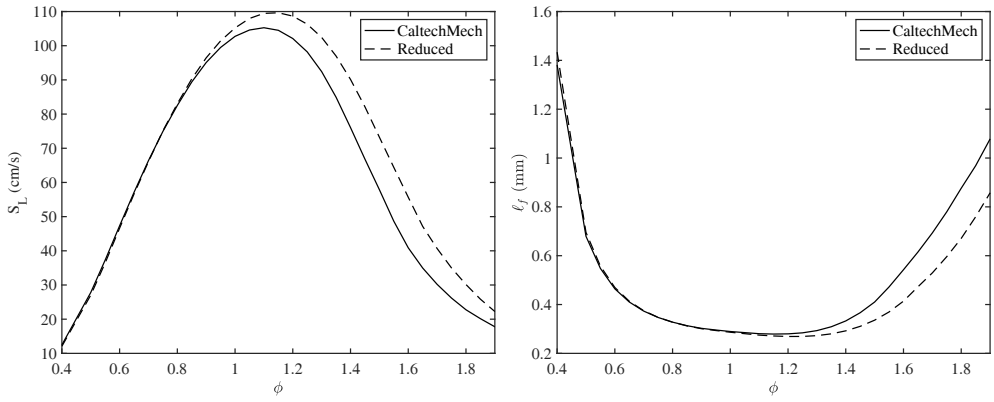


Figure 3.4: One-dimensional flame calculations for $T = 520$ K. (Left) Laminar burning velocity, S_L and (Right) flame thickness, ℓ_f vs. equivalence ratio, ϕ, for CaltechMech and the reduced mechanism at $T = 520$ K.

but shifted to large values since the reaction rate is higher. The flame thickness, ℓ_f, is quite thick for substantially rich and lean conditions. As ϕ moves towards stoichiometric, ℓ_f decreases to a minimum. Comparing the two mechanisms, good agreement is obtained for $\phi <= 1$. Here, the average difference between the two mechanisms is 0.3% for S_L and 0.04% for ℓ_f. For $\phi > 1$, the difference grows to 14% for both S_L and ℓ_f.

Surface reaction considerations

Surface reactions are also important to consider when discussing autoignition as they can significantly affect thermal runaway. Even Setchkin (1954) in his original development of a standardized autoignition test discussed the possibly of a catalytic influence, highlighting work by numerous studies. Callendar (1927) was interested in whether thermocouples had an effect on self-ignition. He tested the possible catalytic effect of various metals in a test tube and found that only platinum black had any effect on ignition. Subsequent work by Thompson (1929) and Matson and Dufour (1950) used different metals for the construction of the walls of a reaction chamber. Variation in the autoignition temperature with wall material was found, but the effects were attributed to changes in heat loss rather than to catalytic effects. Work by Smyth and Bryner (1997) studied thermal ignition of 19 hydrocarbon fuels of varying carbon number on 3 different heated surface materials at high temperatures (>1000 K). They found a moderate effect on the critical ignition surface temperature with stainless steel having the lowest value while nickel and titanium had a larger

catalytic effect. Larger hydrocarbons and higher equivalence ratios decreased the ignition temperature.

Studies on the catalytic effects of borosilicate glass or quartz on autoignition are quite sparse. Pfefferle et al. (1989a), Pfefferle et al. (1989b), and Griffin et al. (1992) studied the catalytic effect of platinum and quartz surfaces on boundary layers flows of ethane/air mixtures at temperatures greater than 1000 K using laser-induced florescence (LIF) to observe O and OH concentrations near the heated wall. The quartz surface was found to have minimal catalytic effects whereas the platinum surface had a more important influence on ignition. A more recent study by Johnson and Mashuga (2022) compared the autoignition of various hydrocarbons including nC_6H_{14} in an ASTM-E659 apparatus using a borosilicate glass and quartz flask. The AITs determined for each fuel were found to be nearly independent on the glassware type used, with variation well within the margin of error of the measurement.

Based on the sparse evidence of previous work, it is believed that the borosilicate glass used in the ASTM-E659 standard does not significantly influence the AIT for a given fuel. Therefore, surface reactions were not considered in this study. However, development and inclusion of a reliable surface reaction mechanism should be included in future work to validate this claim. The reduced mechanism discussed in this section was then implemented for a simulated ASTM-E659 test for gaseous nC_6H_{14}. Note, however, that while extensive validation datasets were compared, experimental data at the conditions of interest for AIT studies (T $\sim$ 500 K, P = 1 bar) are sparse. While the NTC region for heavy hydrocarbon fuels is well captured by the mechanism, there is uncertainty in the accuracy of the model in the relevant thermodynamic conditions range.

3.2.3 Initial conditions

Similar to the fuel mixing studies presented in Chapter 2, a 300 K sphere of gaseous nC_6H_{14} of radius r = 1.5 cm ($V_{liquid} \approx 86.5\mu$L) was initiated near the bottom of the flask into a fully developed unsteady flow field for pure dry air. This initial condition is shown in Figure 3.5. The vaporization process that occurs immediately after injection in an experiment is believed to enhance the initial mixing transient. However, it is not considered in this study.

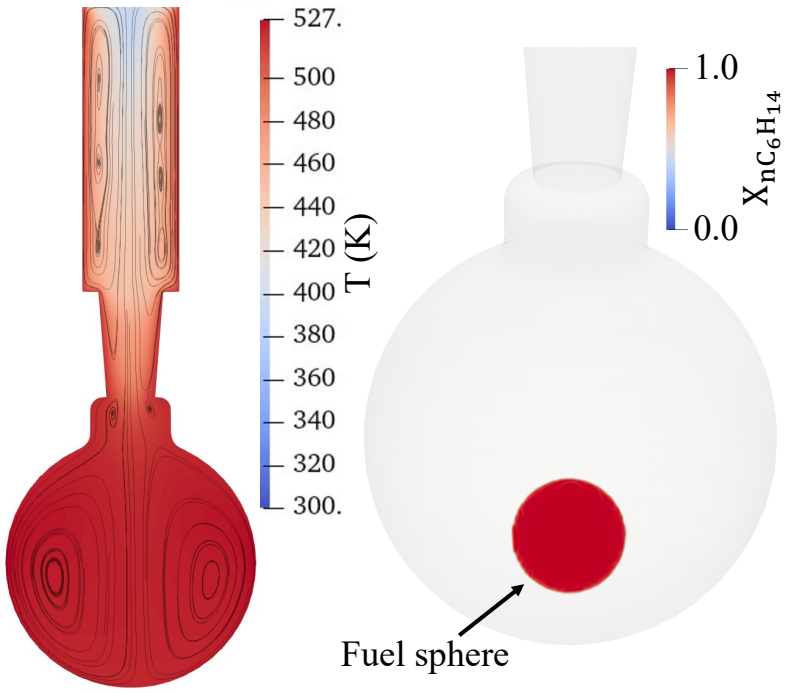


Figure 3.5: Vertical cross-section of the background temperature field and projected (surface) streamlines (left) and nC_6H14 fuel sphere initialization (right).

3.3 Results and discussion

3.3.1 Numerical verification

Grid convergence is an essential part of any numerical simulation. Standard techniques such as achieving stationary statistics for unsteady flows , as was performed for the flow fields in Chapter 2 cannot be used since thermal ignition is a single event (i.e., they are not fully developed flow problems). Instead, other metrics specific to thermal ignition have been used to assess grid convergence including the time to ignition, τ, the max temperature of the first ignition stage, T_{CF}, and the vertical location of the ignition event inside the flask, y_{ign}.

Figure 3.6 shows the maximum temperature in the domain over time, T_{max}, for three grids of varying fineness. Coarse, medium, and fine correspond to hexahedral cell sizes of 2400 μm, 1200 μm, and 600 μm, respectively. All three grids exhibit a two-stage ignition event around 16 s where the maximum temperature is the wall temperature up until the onset of thermal runaway. Convergence can be observed visually as a collapse of the time at which thermal runaway occurs.

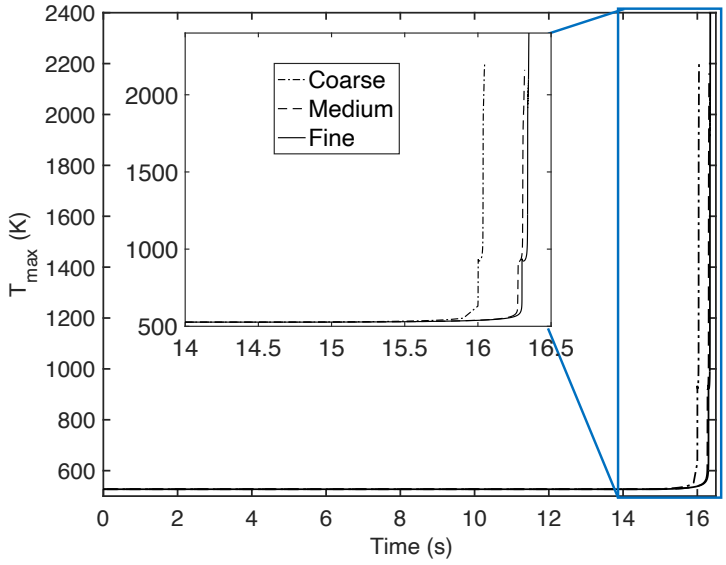


Figure 3.6: Maximum temperature vs. time for the three grid resolutions.

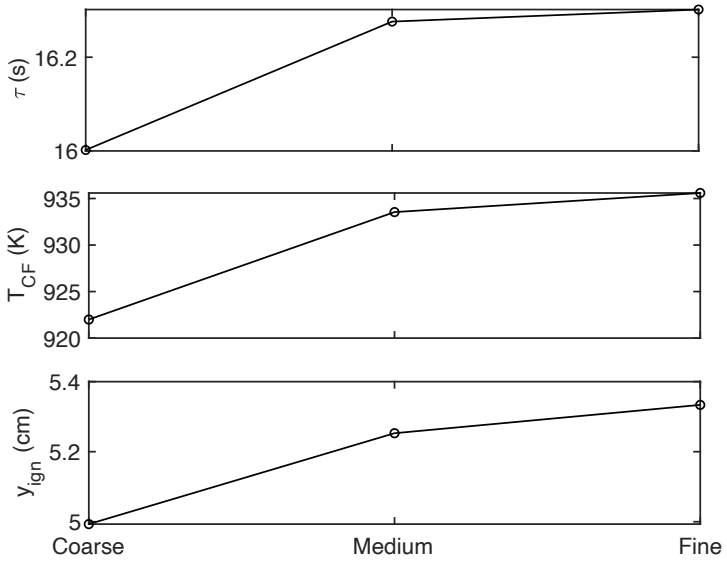


Figure 3.7: Ignition delay time, τ, cool flame temperature, T_{CF}, and vertical ignition location, y_{ign} for the three grid resolutions.

The grid convergence can be assessed quantitatively in Figure 3.7 which plots τ, T_{CF}, and y_{ign} for three grid resolutions. The difference between the medium and fine grids were 0.23% for τ, 0.12% for T_{CF}, and 1.52% for y_{ign}. While all three grids are relatively coarse in the context of typical flame propagation problems, the results indicate convergence of around 1% difference for grids at 600 μm for ignition behavior. This is possible because of the substantially thick thermal layers (~5 cm) characteristic in autoignition testing along with the exceedingly low temperature range (500 K). While the resultant flame propagation was not the focus of our study as quantitative analysis would require substantially finer grids (<100 μm), preliminary verification and qualitative insight is provided in Section 3.3.6.

3.3.2 Cooking phase

After the nC_6H_{14} sphere is initialized in the flask, the cooking phase begins where chemical reaction progresses slowly. In this phase, about 16 s passes without a rapid change in temperature or species. Figure 3.8 plots the nC_6H_{14} volume field in the flask at 4 instances in time through the cooking phase. Driven by buoyancy, the fuel initially sinks to the bottom of the flask. The fuel dispersion is mostly axisymmetric as seen by the volume field at 0.1 s, but with small asymmetry caused by the unsteady flow field induced by the open top. The effect this has on the ignition event will be discussed later. Later in time (5-10 s), a stable, stratified concentration of nC_6H_{14} can be seen that slowly diffuses upwards towards the top of the flask. This mixing characteristic of n-hexane is further discussed in Chapter 2.

Figure 3.9 plots the volume fields of the heat release, Q, as well as the mole fraction of three important intermediate products ($OC_6H_{11}OOH$, C_2H_4, and H_2O_2) at 10 s. For all quantities, a ring structure can be seen around the stable, nC_6H_{14}/air interface with most significant heat release and production of intermediates occurring near the walls. This is caused by the temperature distribution inside the flask. Gas temperatures near the walls can be 7 K warmer than gas near the center of the flask (Chapter 2). Thus, reaction progress occurs more quickly in these regions. Over time, this ring structure moves upwards in the flask as the bulk fuel diffuses upwards until the time of ignition. The slight lopsidedness of the ring can be attributed to the asymmetry in the initial mixing transient driven by the unsteady flow generated by the open top in the flask, the resultant variation in temperature within the gas, and the sloshing behavior of the fuel as it initially sinks to the bottom of the flask.

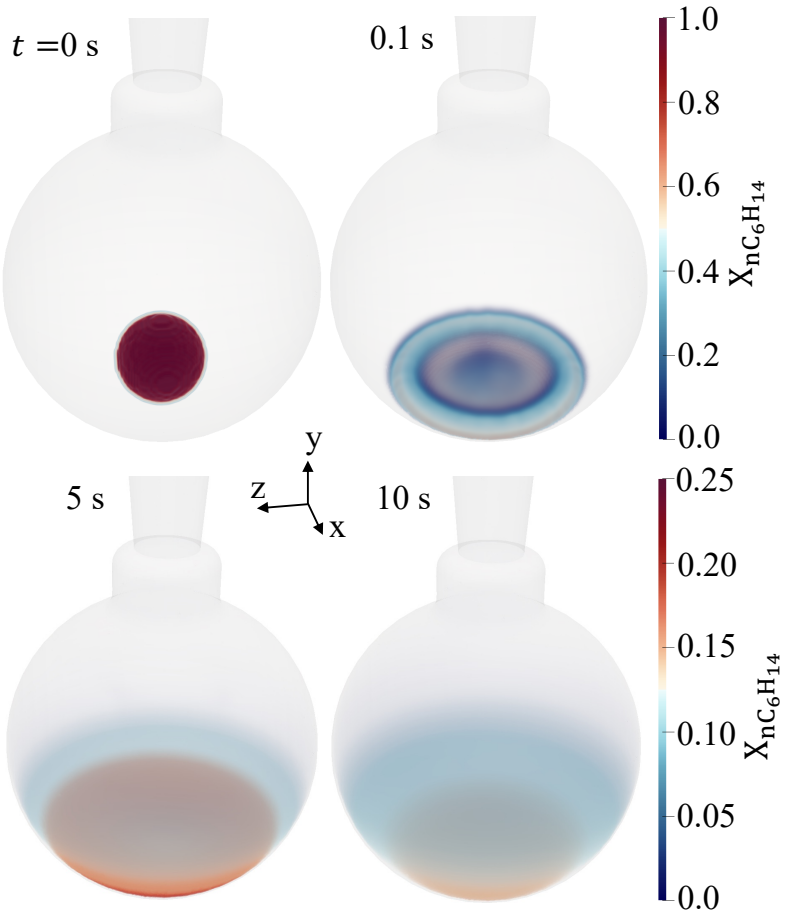


Figure 3.8: nC_6H_{14} volume field inside the flask during the cooking phase (0-10 s).

3.3.3 Ignition dynamics

As time progresses past 10 s, signs of a coupled chemical-thermal runaway process can be observed. Figure 3.10 shows the temperature volume field and instantaneous streamlines inside the flask during the ignition event. Only temperatures above the wall temperature are colored to emphasize the characteristics of thermal ignition. As early as 14.775 s, local gas temperatures surpass the wall temperature. This time instance is omitted from the visualization as it would be a single pixel, but is important to distinguish as it marks the onset of the ignition kernel. At 15.9 s, a ring kernel can be seen near the walls around the vertical midpoint of the flask where exothermic chemical reaction causes the gas temperature to exceed the wall temperature by up to 100 K prior to ignition. The ring retains its lopsided structure remaining from the initial fuel mixing transient and influences the location of the

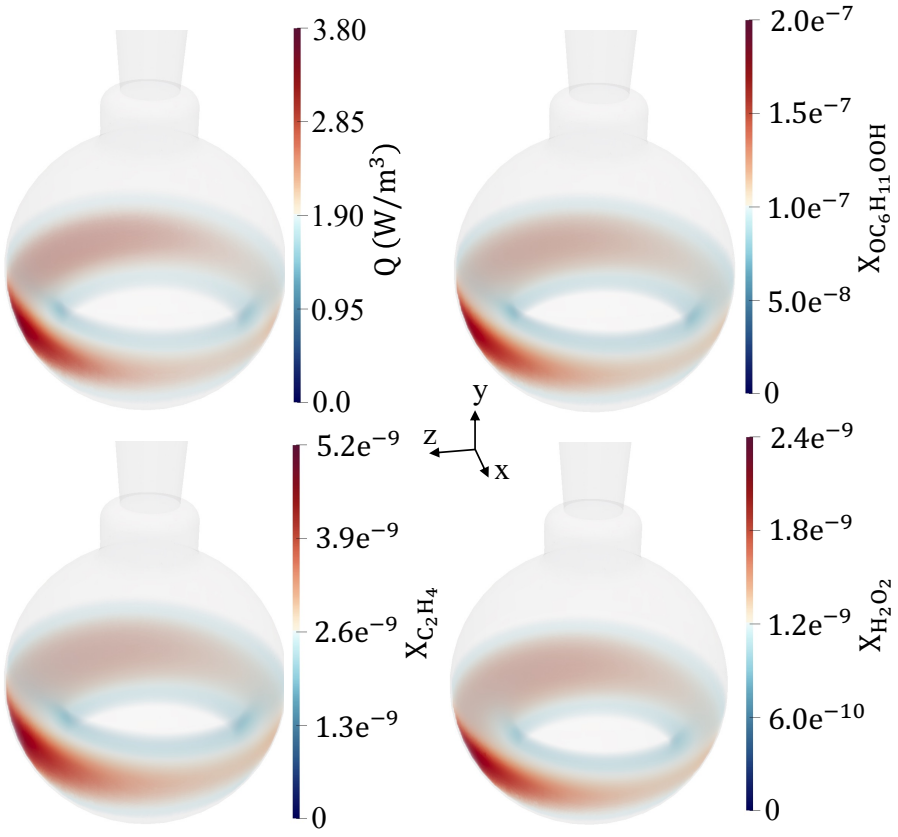


Figure 3.9: Q, $OC_6H_{11}OOH$, C_2H_4, and H_2O_2 volume fields inside the flask at 10 s.

localized ignition event. The toroidal vortex flow pattern discussed in Chapter 2 can be seen, driven by downward movement of cold air through the center of the open neck and upward movement near the walls as the gas heats up through conduction, convection, and chemical reaction. The Rayleigh number based on flask radius increases by a factor of 7 to $Ra_r = 6.0 \cdot 10^4$ compared to the flow characterization solely in air, which can be attributed to natural convection induced by exothermic chemical reaction. Progressing to 16.3316 seconds, the ring kernel has grown in size as the initial stages of the runaway process develop. The first stage of the ignition event can be seen propagating from a localized section of the flask with a peak temperature of 935 K. The resultant cool flame moves outwards, favoring propagation azimuthally through the ring kernel as the local temperatures are higher than near the center of the flask. Natural convection driven by chemical reaction from the first stage is evident by a further increase in the Rayleigh number to $Ra_r = 1.2 \cdot 10^5$. The streamlines propagate out the top of the flask indicating

gas expansion caused by the modest temperature rise of the first stage ignition event. Around 16 ms later, at 16.3476 s, the second and final stage of ignition can be seen with a rapid and substantial increase in temperature to 2000 K. The significant increase in temperature leads to substantial gas expansion, where the speed of reactants being pushed up out the neck of the flask reach 14 m/s through the smallest cross-sectional area portion.

The two stage ignition event can also be shown graphically in Figure 3.11 which plots the horizontal temperature profiles through the ignition event and the center of the flask for the two stages. From Figure 3.11a, the formation of the ring kernel is seen. For early times (t = 0.1 s) after the fuel sphere initialization, there is an asymmetric disturbance to the temperature field. This is caused by the asymmetric mixing immediately after the nC_6H_{14} sphere is initialized in the domain that occurs because of the unsteady flow field induced by the open top. At 10 s, after the initial transient has dampened, the hottest point remains at the wall, and a smoother temperature profile is seen with the toroidal vortex bringing colder air down through the center. Note there remains a slight asymmetry in this profile caused by small differences in reaction progress brought by the initial transient. This difference grows as time continues and the reaction progresses. At 16.3025 s, the kernel has a peak temperature ~60 K above the wall temperature which is localized to a single part of the flask. The opposing side of the flask has peak temperature that is only 10 K above the wall temperature at the time of the first stage thermal runaway. The first stage thermal runaway can be seen from Figure 3.11b between 16.3025 s and 16.3105 s characterized by a rapid increase in temperature to 935 K. The temperature profile at 16.3025 s is repeated to illustrate the range of temperatures that exist between the ring kernel formation and thermal runaway process that evolves into a propagating cool flame. The resultant cool flame propagates outwards and a localized second stage kernel forms between the wall and the cool flame front. The second stage kernel ignites ~40 ms after the first stage which is associated with a rapid increase in temperature to 2000 K and the subsequent second stage flame front chases and catches the first stage flame front.

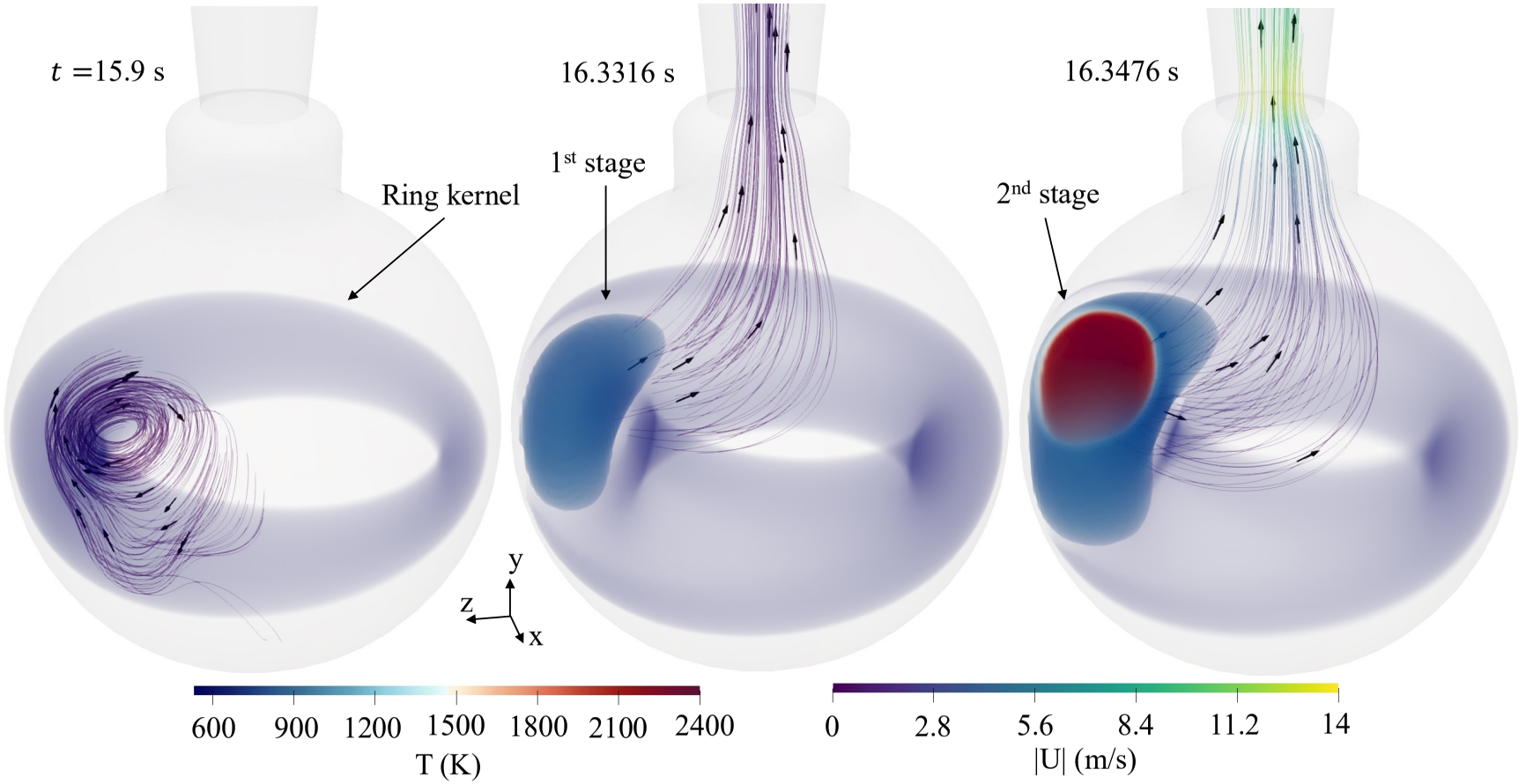


Figure 3.10: 3D ignition kernel evolution inside the flask. Temperatures above the wall temperature are colored as well as instantaneous streamlines near the ignition event.

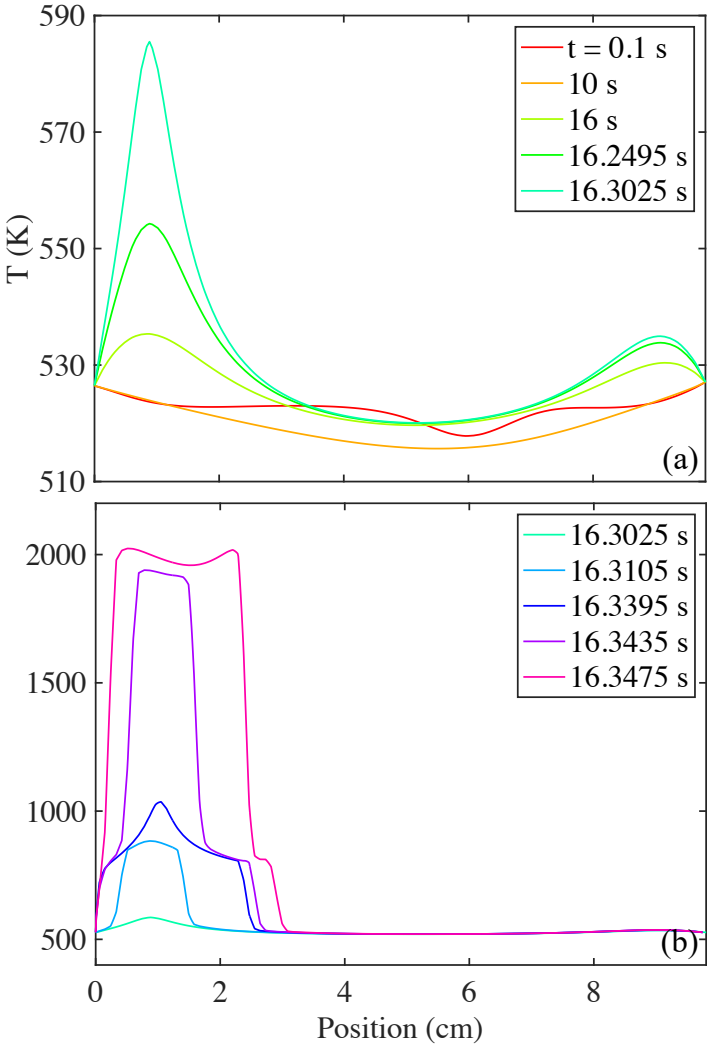


Figure 3.11: Temperature profiles along a horizontal line passing through the ignition event and the vertical center line of the flask for different instances in time for (a) the 1st stage and (b) the 2nd stage ignition event. The origin represents the flask wall closest to the ignition event.

3.3.4 Experimental validation

The resultant three-dimensional reacting flow solution can be compared with an equivalent experiment in our ASTM-E659 apparatus. The setup is further discussed in Chapter 2. Without good optical access, understanding where ignition occurs and how the flame propagates through the flask is difficult. To obtain more information, two additional bare-wire K-type 36 gauge thermocouples were inserted in the flask at the same height as the T_4 thermocouple, but much closer to the walls. This was achieved by attaching the thermocouples to formed nitinol wire at 90° angles made

with the vertical center line. The nitinol was formed using clamps and a heat gun. Because of the "shape memory" property of nitinol to return to its preset austenite phase from its martensite phase upon heating, the nitinol/thermocouple assembly can be inserted into the flask folded up. Once heated, the two thermocouples extend outwards near the walls of the flask. This process is shown in Figure 3.12. The idea is that with temperature measurements at three locations across the flask centerline, qualitative information about the relative location of the ignition event can be obtained and compared with the simulation results.

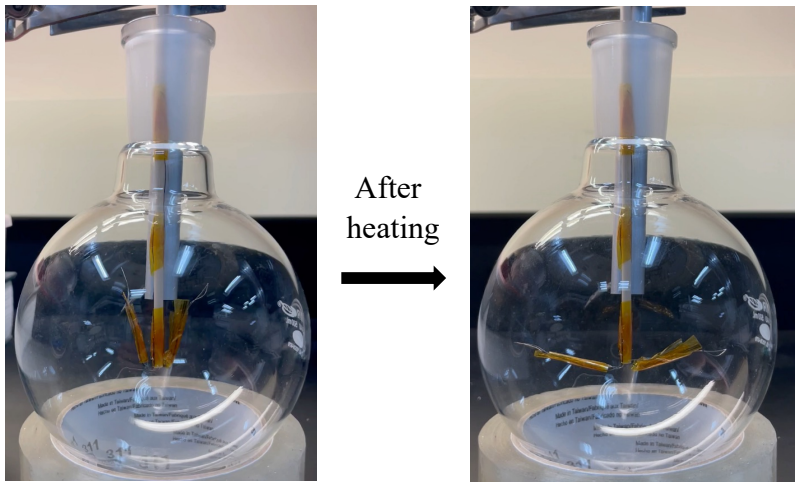


Figure 3.12: Two 36 gauge thermocouples attached to formed nitinol wire.

Figure 3.13 shows the results from an E659 experiment where 80 μL of liquid nC_6H_{14} is injected into a flask with a surface temperature, $T_2 = 527$ K, in accordance with the standard. These conditions were set to replicate what was simulated with gaseous nC_6H_{14}. Temperature traces are shown from three 36 AWG K-type thermocouples mounted in the center of the flask and near the walls at the same height 180° apart from each other (i.e., all three thermocouples are mounted on a horizontal line about the center of the flask). After injection, a dip in the temperature can be seen across the thermocouples, strongest on $TC_{offset,2}$ indicating an asymmetric injection, vaporization, and initial mixing transient, qualitatively similar to what was observed in the simulation presented in Figures 3.8 and 3.9. The ignition delay time τ_{delay} can be measured from the time of injection to the first instance of a sharp temperature rise, $\tau_{delay} \approx 17.7$ s. This is 1.35 s longer what is found in the 3D numerical simulation ($\tau_{ign} = 16.35$ s) and can be attributed to the additional time it takes for the fuel to vaporize prior to the onset of chemical reaction. The increase

in temperature seen by the thermocouples to 700-800 K is indicative of thermal ignition and flame propagation inside the flask. True flame temperatures (~ 2000 K) could not be obtained because of the 1 s response time of the thermocouples. The temperature recorded by $TC_{offset,2}$ prior to ignition in the cooking phase is larger and sees a sharp temperature rise 150 ms before $TC_{offset,1}$ and TC_{center}. This is further evidence of an ignition kernel forming near the walls and an off-center coupled chemical-thermal runaway event, as seen in the numerical simulation.

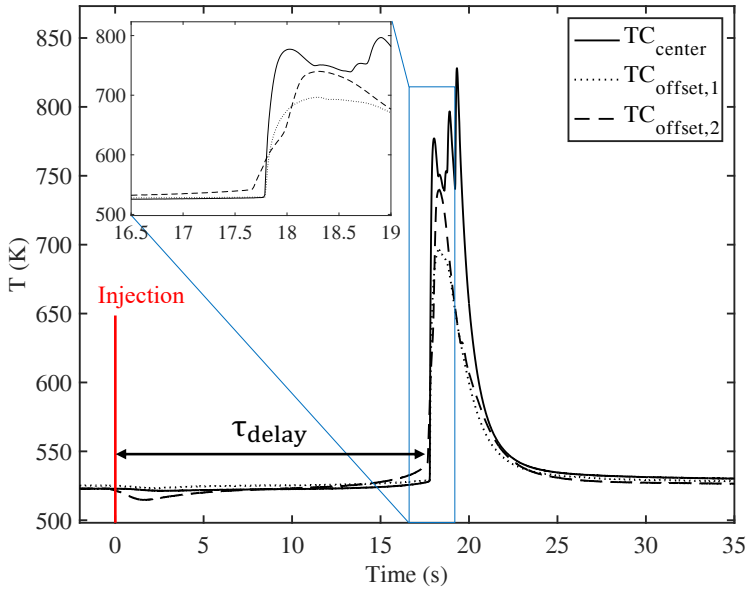


Figure 3.13: ASTM-E659 experiment with injection of 80 μL nC_6H_{14}. The three curves are from three 36 AWG K-type thermocouples mounted in the center of the flask and near the walls at the same height 180° apart from each other.

The small discrepancy in ignition delay time may be a consequence of omitting the liquid-phase and two-phase jet dynamics in the simulation. In the experiment, the injected liquid undergoes complex processes including surface impingement of the two-phase jet, spreading, and vaporization, all of which introduce a finite delay before a flammable vapor-air mixture is established. These effects, which depend on droplet breakup, heat transfer, and fuel-wall interactions, are not included in the present simulation, which assumes an initially gaseous fuel distribution. Other sources of uncertainty include the limited validation of the reaction mechanism at AIT thermodynamic conditions. Most importantly, experimental observations by Fouchier and Shepherd (2025) indicate that test-to-test variability in ignition delay times is observed even under carefully controlled testing conditions. The

discrepancy for this single comparison is smaller than the observed variability, indicating that further experimental studies with statistical quantification of the uncertainty are required before further interpretation of the discrepancy.

Nevertheless, the agreement between the measured and simulated ignition delays is remarkable, indicating that the dominant ignition physics governed by fluid motion, mixing, and chemical kinetics in the gaseous phase are well represented even in the absence of detailed liquid modeling. Prior studies have shown that liquid-fueled ignition systems can be sensitive to vaporization transients (Turns et al., 1996; Sirignano, 2010), and incorporating these effects could further improve quantitative accuracy in future work.

3.3.5 Lagrangian particle tracking

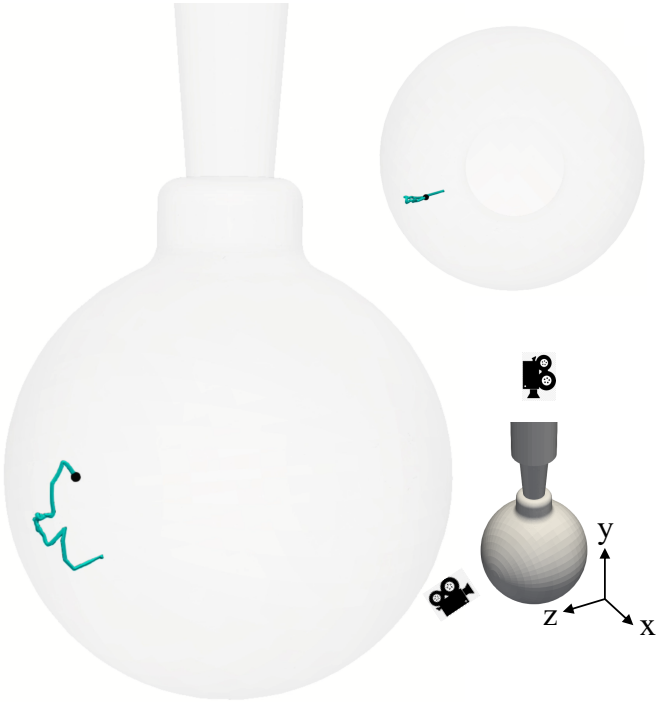


Figure 3.14: Ignition particle trajectory.

Particle tracking of the fluid parcel that ultimately ignites can provide insight on the important chemical pathways that lead to thermal ignition. Since the exact ignition location is not known a priori, a massless particle was injected at the time and location of ignition during post-processing. The three-dimensional numerical solution can then be integrated backwards in time to extract the approximate trajectory of the ignition particle over the entire duration of the simulation. The trajectory of the

ignition particle is shown in Figure 3.14 from the point of fuel initialization up to the time of ignition. The particle convects 5.6 cm upwards along the side of the flask as it heats up, following the toroidal vortex flow pattern discussed in Chapter 2.

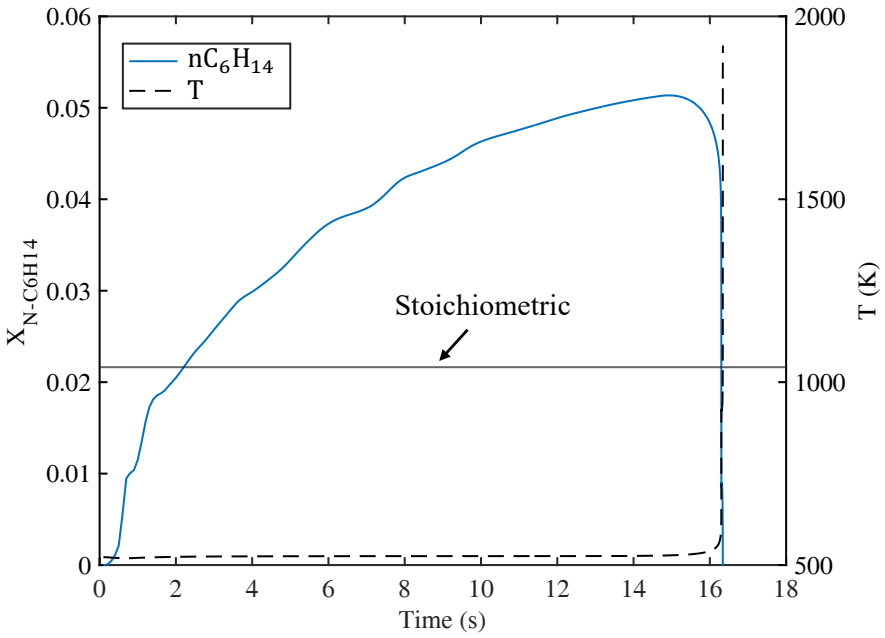


Figure 3.15: nC_6H_{14} mole fraction over the entire simulation time. The temperature (- -) is also shown.

Figure 3.15 plots the mole fraction of nC_6H_{14} fuel along the ignition particle. During the first 15 s during the cooking phase, the nC_6H_{14} concentration increases as it mixes with the surrounding air. The unsteady downwash of cold air through the neck of the flask can be seen through the small wobbles in fuel as time evolves. At 2.2 s, the fuel concentration passes through stoichiometric. The ignition event occurs in arich mixture (equivalence ratio, $\phi \approx 1.8$).

Figure 3.16 zooms in to two stage ignition event that occurs over ~5 ms. The top species mole fractions are shown. Across the first stage, a rapid conversion of nC_6H_{14} and O_2 into smaller intermediate products such as ethene, C_2H_4, formaldehyde, CH_2O, and hydrogen peroxide, H_2O_2, can be seen along with a temperature increase to 935 K. At this point, the ignition progression temporarily slows as the primary reaction pathways responsible for thermal runaway change. The second and final stage of ignition can then be seen with the increase in temperature to 1900 K and

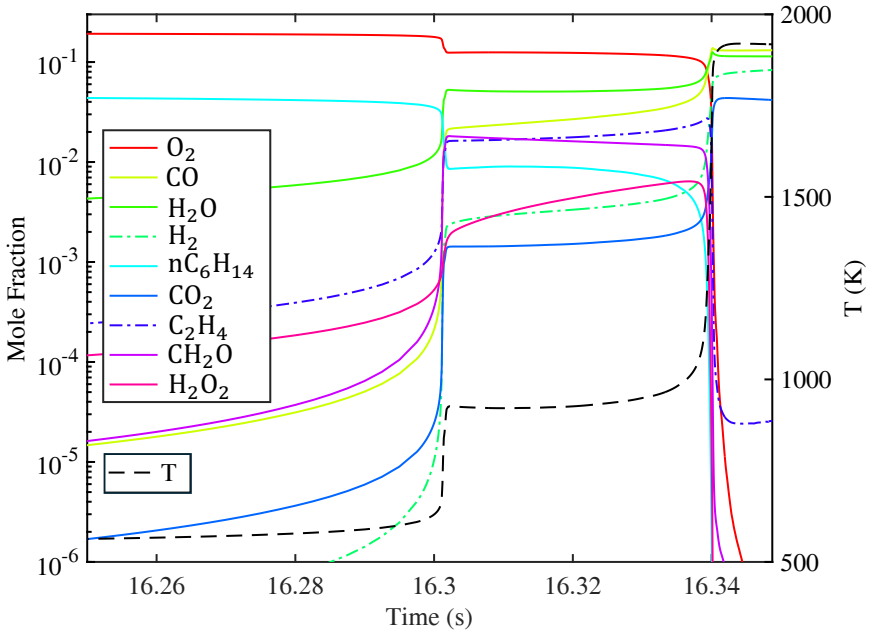


Figure 3.16: Major species mole fraction during the two stage ignition event along the ignition particle. The temperature (- -) is also shown.

the consumption of remaining fuel and intermediate products into CO, CO_2, H_2O, and H_2.

The reaction pathways responsible for the two stage ignition event can be identified by looking at the heat release associated with each reaction as well as rate of production of important species along the tracked particle path. The time-integrated heat release for top reactions across each ignition stage are shown in Figures 3.17 and 3.19. The following reaction pathway associated with the first stage ignition event can be seen from Figure 3.17

$$nC_6H_{14} + OH \rightarrow C_6H_{13} + H_2O \tag{R1}$$

The first step is the H-abstraction of the nC_6H_{14} fuel via an OH to produce a hexyl radical (C_6H_{13}) and H_2O.

$$C_6H_{13} + O_2 \rightarrow C_6H_{13}O_2 \tag{R2}$$

The C_6H_{13} then gets attacked by O_2 molecules. However, instead of further H-abstraction, the O_2 attaches to the C_6H_{13} to form $C_6H_{13}O_2$. This reaction is quite

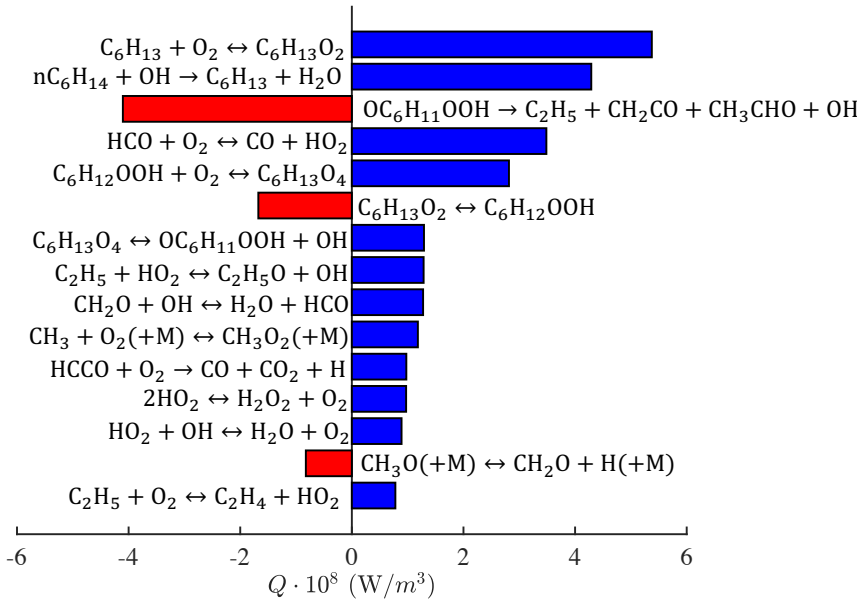


Figure 3.17: Total heat release of the top reactions for the first ignition stage.

exothermic and is the primary reaction responsible for the first stage heat release.

$$C_6H_{13}O_2 \rightarrow C_6H_{12}OOH \tag{R3}$$

$$C_6H_{12}OOH + O_2 \rightarrow C_6H_{13}O_4 \tag{R4}$$

An internal isomerization reaction followed by the addition of another O_2 onto the $C_6H_{12}OOH$ molecule produces hydroperoxyhexyl peroxy ($C_6H_{13}O_4$). While the isomerization reaction in this step is endothermic, the oxidation reaction makes this sequence of two reactions exothermic.

$$C_6H_{13}O_4 \rightarrow OC_6H_{11}OOH + OH \tag{R5}$$

$$OC_6H_{11}OOH \rightarrow C_2H_5 + CH_2CO + CH_3CHO + OH \tag{R6}$$

The final sequence involves decomposition of the $OC_6H_{13}O_4$ into $OC_6H_{11}OOH$ and another OH. The $OC_6H_{11}OOH$ molecule then breaks apart into smaller ketones and aldehydes, such as ketene (CH_2CO) and acetaldehyde (CH_3CHO). Along with the ethyl radical (C_2H_5), these ketones and aldehydes branch into many pathways that produce the stable intermediates seen behind the first stage ignition event (i.e., CO, C_2H_4, and CH_2O). This oxidation pathway is overall an exothermic sequence. Note that two OH molecules are produced from a single OH molecule the initiates the

reaction. Thus, this feedback leads to the multiplicative production of OH molecules that ultimately drive the first stage coupled chemical-thermal runaway. The first stage ignition event described by reactions (R1)-(R6) seen in the autoignition simulation is consistent with what has been discussed for nC_6H_{14} oxidation (Mével et al., 2019b) and more broadly for other heavy hydrocarbon fuels (Battin-Leclerc, 2008; Curran, 2019).

The second stage is evident from Figure 3.16 as a rapid temperature rise to 1900 K and completion of the reaction to form CO, CO_2, H_2O, and H_2. The 1900 K ignition temperature is significantly lower than what would be expected from a stoichiometric mixture of nC_6H_{14}/air (~2400 K). This can be attributed to the rich mixture (ϕ = 1.8) present at the time of ignition. The temporal heat release, Q, and rate of production (ROP) traces for the top reactions along the ignition particle path can be plotted for the second stage (Figure 3.18) which can broken up into two temperature ranges: 1.) 900 K < T < 1450 K and 2.) T > 1450 K.

We first examine the 900 K < T < 1450 K range. Looking at Figure 3.19, the oxidation reaction $HCO + O_2 \rightarrow CO + HO_2$ releases the most heat during the second stage. From the temporal heat release for the top reactions shown in Figure 3.18a, this reaction occurs early on while the temperature is below 1450 K. The reaction is sustained by the generation of HCO by the large amount of CH_2O produced from the first stage. This occurs primarily from the reactions $CH_2O + H \rightarrow H_2 + HCO$ and $CH_2O + OH \rightarrow H_2O + HCO$ as can be seen from the top reactions for the rate of production of HCO in Figure 3.18c. This reaction continues to release a significant amount of heat until around 1450 K. As the temperature continues to increase past 1450 K, the HCO molecules prefer to break apart into H and CO instead of reacting with the O_2. This decomposition does not release significant amounts of heat and instead, reaction pathways involving CH_3 and OH drive the temperature increase from this point on.

The temperature range, T > 1450 K, can be identified by an even sharper temperature rise associated with a shift in dominant reaction pathways from those with HCO to those involving CH_3 and OH carriers. The traditional mechanism for coupled chemical-thermal runaway of heavy alkanes by an OH carrier (Battin-Leclerc, 2008) can be seen from the second stage heat release and rate of production of OH shown in Figure 3.19 and Figure 3.18b. The prominent chain branching reactions H_2O_2 (+M) $\rightarrow$ 2OH (+M) and $H + O_2 \rightarrow O + OH$ can be seen followed by the exothermic chain terminating recombination reaction $CO + OH \rightarrow CO_2 + H$. However, because

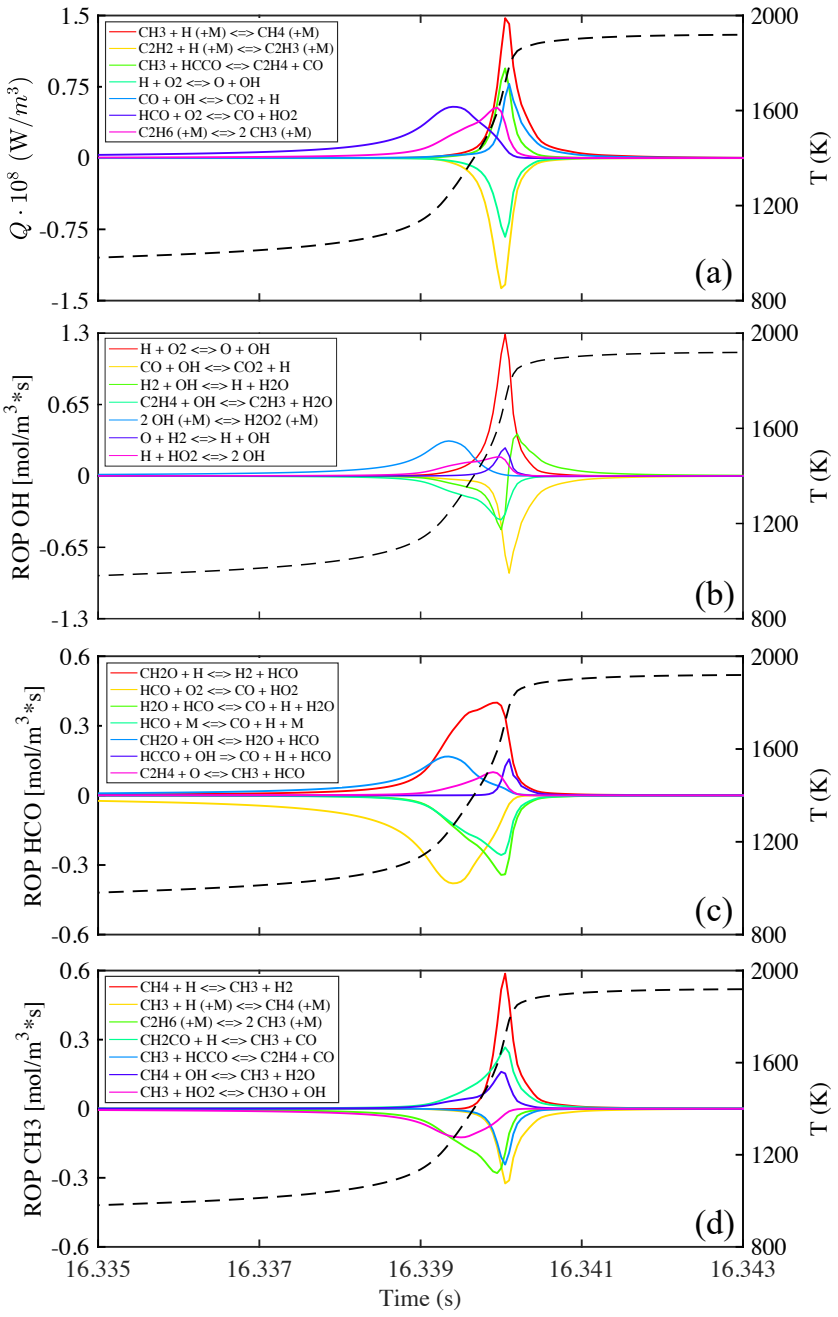


Figure 3.18: Heat release and rate of production (ROP) of OH, HCO, and CH_3 along the ignition particle for the top reactions during the second stage.

the ignition event occurs in a rich mixture, there are not as many oxygen atoms to drive the conversion from $CO \rightarrow CO_2$. As a result, it does not release as much heat during the second stage ignition process as would be expected from a stoichiometric analysis.

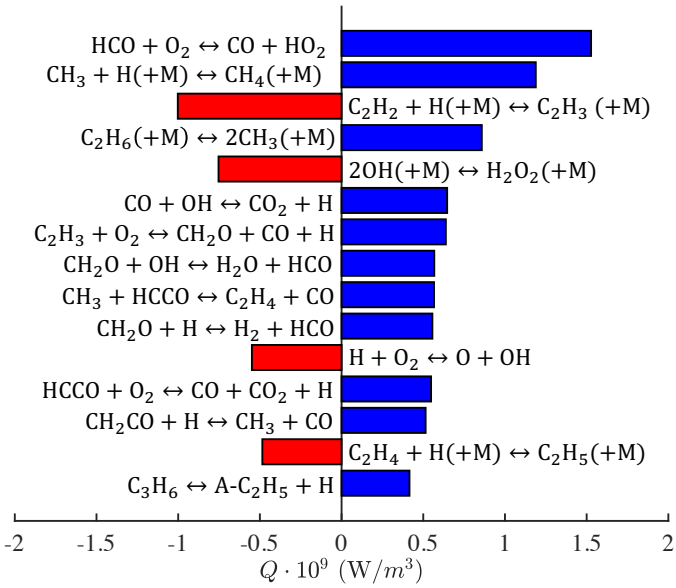


Figure 3.19: Total heat release of the top reactions for the second ignition stage.

Instead, reaction pathways involving methyl, CH_3, provide the most significant contribution to the heat release above 1450 K. This can be seen in Figure 3.19 and Figure 3.18d. The addition of an H atom onto CH_3 to produce CH_4 releases substantial heat followed by the combination of two CH_3 molecules into ethane, C_2H_6. These exothermic CH_3 reactions are sustained by the conversion of the C_2H_4 from the first stage ignition event into CH_3 through aldehydes and ketones, $C_2H_4 \rightarrow CH_2CHO \rightarrow CH_2CO \rightarrow CH_3$, as well as the feedback reaction $CH_4 + H \rightarrow CH_3 + H_2$ that produces H_2 as a byproduct.

The lack of oxygen present during the ignition event shifts the prominent reaction pathways critical for the second stage coupled chemical-thermal runaway. As a result, HCO and CH_3 reaction pathways become more significant. This leads to a decrease in ignition temperature and the more substantial amounts of CO and H_2 compared to CO_2 in the combustion products.

3.3.6 Flame propagation

While thermal ignition was the primary focus of this work, the subsequent flame propagation can provide further insight to the autoignition process and aid in developing more stringent testing standards.

Preliminary verification

The resultant flame propagation through the flask and holder section after the two-stage ignition event must be scrutinized, especially since the 600 μm grid size is quite coarse when discussing flames. However with limited optical access, experimental validation of the flame speed is challenging. Comparisons to the expected flame speed from well-resolved one-dimensional freely propagating laminar flame calculations provide an obtainable metric for preliminary verification. To this extent, one-dimensional flames were simulated in Cantera (Goodwin et al., 2021). More information about the modeling can be found in the Supplementary Material. Careful consideration of a number of factors must be made when comparing flame speeds between the three-dimensional autoignition simulation and a simplified one-dimensional laminar flame. The following two observations are made:

- At the time of ignition, the reactants are stratified throughout the flask which produces flame propagation through a vertically stratified mixture after ignition whereas the one-dimensional laminar flame calculations consider a homogeneous mixture.
- Two stage coupled chemical-thermal runaway in the autoignition simulation produces a transient two stage flame propagation for early times after ignition. This will not be captured by the steady one-dimensional laminar flame model

To best address these issues, a point in time and space is taken inside the flask where the flame propagation is horizontal and enough time has passed such that the second stage flame front has overtaken the first stage flame front. Because the injected nC_6H_{14} is mostly stratified after the initial mixing transient and prior to ignition as shown in Figure 3.8 and discussed in Chapter 2, locations of the flame that propagate horizontally are approximately homogeneous. Ensuring enough time has passed allows a single flame front to propagate into a reactant mixture that has not undergone significant chemical reaction. This can be easily initialized into the one-dimensional flame model. One possible horizontal line that satisfies these requirements is shown in Figure 3.20 at a height of y = 6.25 cm and at t = 16.35065 s where the local equivalence ratio is lean, $\phi \approx 0.80$. The velocity can then be projected onto and plotted along this axis. Figure 3.21 plots the projected velocity, U_{proj}, and the temperature along the chosen horizontal line. The flame speed can then be calculated as the velocity difference across the flame front as $\Delta u \approx 2.59$ m/s.

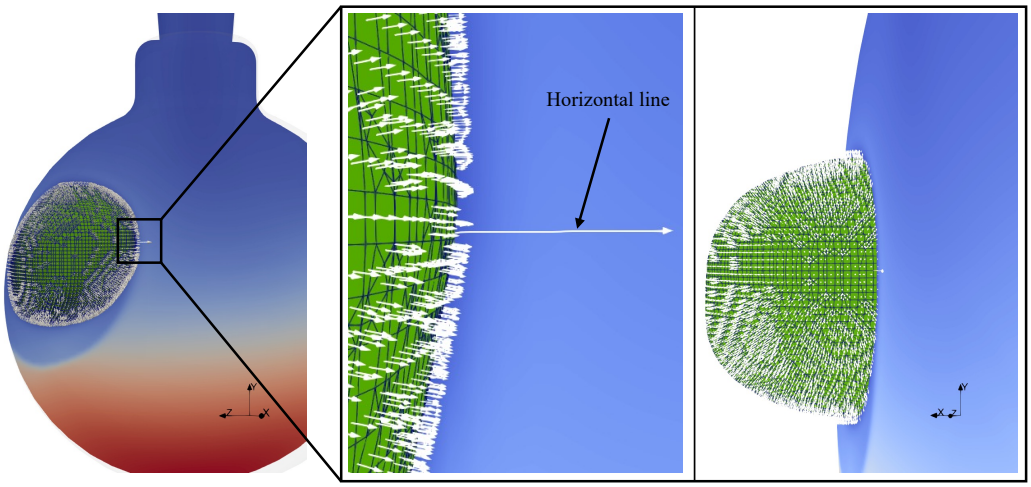


Figure 3.20: Flame front isosurface (T = 1500 K) with surface normal vectors and nC_6H_{14} mole fraction on a vertical cross-section through the flame. A horizontal line aligned with the flame propagation direction is shown.

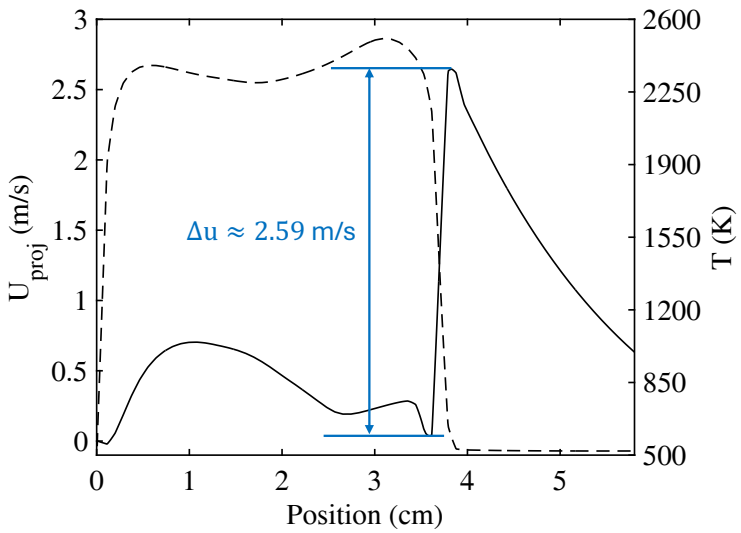


Figure 3.21: Projected velocity (-) and temperature (–) along the horizontal line across the flame front at height, y = 6.25 cm and time, t = 16.35065 s.

The estimated flame speed can easily be obtained from the 1D freely-propagating flame model through a mass balance as

$$u_f = u_b - S_L = \left(\frac{\rho_u}{\rho_b} - 1\right) S_L \tag{3.13}$$

where u_f is the estimated flame speed, u_b and ρ_b are the burnt gas speed and

density, respectively, ρ_u is the unburnt gas density, and S_L is the laminar burning velocity. Eqs. 3.11 and 3.12 can be used to compute the laminar burning velocity and estimated flame thickness for a wide range of initial conditions. This technique is modified from the results presented by Martin (2023) to instead explore the low temperatures and wide range of equivalence ratios that exist in autoignition studies. The relevant unburnt gas temperatures were well below 930 K observed to have convergence issues (Martin, 2023). Similarly, the equivalence ratio range was controlled to keep S_L much larger than 1 cm/s observed to also have convergence issues.

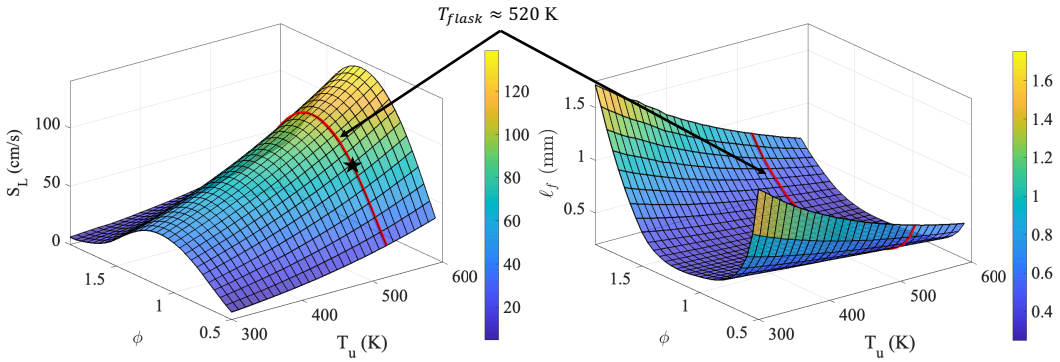


Figure 3.22: Computed S_L (left) and ℓ_k (right) surface maps for 300 K < T_u < 600 K and 0.5 < ϕ < 1.9 for nC_6H_{14}/air mixtures at 1 bar for the 1D freelying propagating flame model. The red line illustrates approximate gas temperatures inside the flask and the black star indicates the approximate condition compared to the 3D autoignition simulation.

Figure 3.22 plots the solution surfaces for S_L (left) and ℓ_f (right) for 300 K < T_u < 600 K and 0.5 < ϕ < 1.9 in nC_6H_{14}/air mixtures at 1 bar. The surfaces comprise approximately 1000 discrete simulations in the $\phi - T$ parameter space relevant to autoignition testing for nC_6H_{14}/air. A red line is traced along the surface at T = 520 K as this is approximately the temperature of the gas inside the flask for the present study. However, once the flame propagates out of the flask into the holder, gas temperatures down to nearly room temperature ($T \approx 300$ K) can exist. The black star on the laminar burning velocity plot corresponds to the condition used as verification for the 3D autoignition simulation. The inverse relation between S_L and ℓ_f can be seen over the range of unburnt gas temperatures and equivalence ratios as discussed in Martin (2023). For a fixed equivalence ratio, as the unburnt gas temperature is increased, the laminar burning velocity increased and the flame thickness decreased. For a fixed unburnt gas temperature, as the equivalence ratio

is increased, S_L increases to a maximum and ℓ_f decreases to a minimum at $\phi = 1.1$. As ϕ continues to increase, S_L then decreases and ℓ_f increases again.

Estimating the unburnt conditions from the 3D autoignition simulation ($T_u \approx 522$ K and equivalence ratio, $\phi \approx 0.80$), the following densities and laminar burning velocity are calculated from Cantera and Figure 3.22 as

- $\rho_u \approx 0.6966$ kg/m^3
- $\rho_b \approx 0.1665$ kg/m^3
- $S_L \approx 0.828$ m/s

Substituting these values into Eq. (3.13), the flame speed can be estimated as $u_f = 2.66$ m/s (2.7% difference to the 3D simulation flame speed).

For this condition, the estimated flame thickness computed from the 1D freely-propagating flame model results in Figure 3.22, $\ell_f \approx 300\mu$m. From Figure 3.21, the flame thickness calculated in 3D autoignition simulation is an order of magnitude larger at ~3.3 mm. This is most likely because the grid size of 600 μm is too large to adequately simulate the flame propagation after the ignition event and numerical diffusion artificially thickens the flame front. However, numerous studies of various fuel/oxidizer mixture flame thicknesses suggest that ℓ_f underestimates the actual flame thickness from experiments and numerical simulation. Bradley et al. (2000) suggest the true flame thickness measured by single shot OH planar laser-induced florescence (PLIF) of spherical explosions of iso-octane flames is larger than ℓ_f by a factor of 30. Other studies for methane/air flames suggest that the true flame thickness is between 3 and 50 times larger than ℓ_f (Bradley et al., 1996; Turner et al., 2021). While sparse data exists, if this is also the case for nC_6H_{14} flames, the estimated flame thickness and propagation from the presented simulation may be properly resolved.

Despite the coarse grid and expected numerical diffusion, the 3D autoignition simulation adequately reproduces the expected flame speed from the highly resolved 1D freely-propagating flame model. While a finer grid, likely < 100 μm, is necessary to quantitatively analyze the flame propagation after the ignition event, the solution is deemed sufficient to qualitatively assess flame development and behavior as time evolves.

Flame propagation

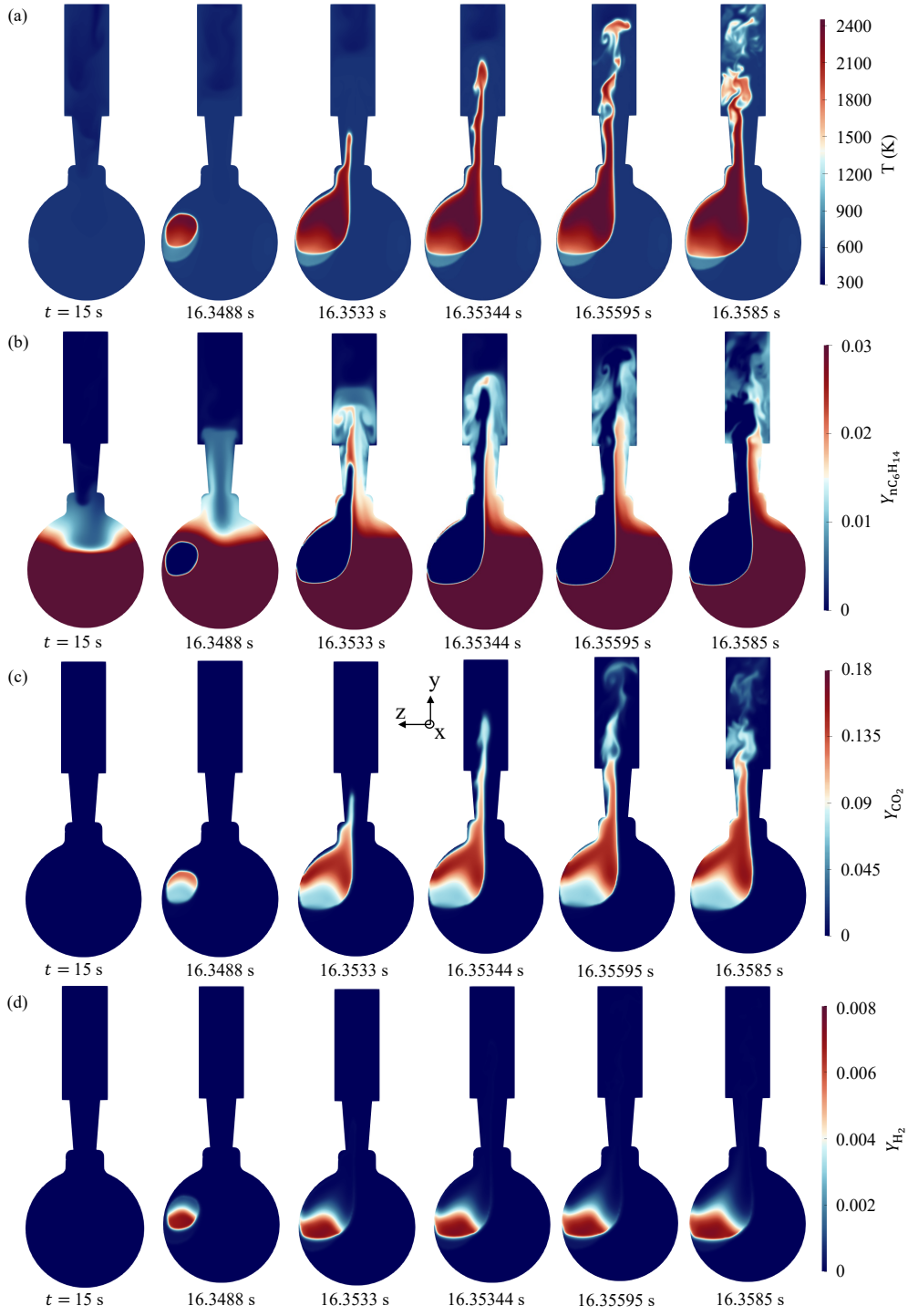


Figure 3.23: Flame evolution through the flask and holder along a vertical slice for (a) temperature, (b) colorbar-saturated nC_6H_{14} mass fraction to show fuel dispersion, (c) CO_2 mass fraction, and (d) H_2 mass fraction.

Figure 3.23 plots the temperature and colorbar-saturated nC_6H_{14} mass fraction as well as CO_2 and H_2 mass fraction fields on a vertical slice through the flask and holder at various times after the ignition event. The nC_6H_{14} mass fraction field is intentionally saturated to show the movement of fuel out of the flask. This occurs in a lean concentration and is most easily visible using a saturated colorbar. At early times in Figure 3.23a and 3.23b, the flame is ignited near the wall through a localized two-stage ignition event that was thoroughly analyzed in Section 3.3.1 - 3.3.5. As early as 16.3488 s, the nC_6H_{14} fuel can be seen being ejected from the flask as a jet through the neck as the gas rapidly expands from the ignition event. At 16.3533 s, the flame has expanded radially through the flask. Because the fuel is stratified at the time of ignition (see Figure 3.8), the nC_6H_{14} concentration at the bottom of the flask is rich and above the upper flammability limit (7.5% by volume, National Toxicology Program, 1992). Thus, the flame cannot propagate into this region. Instead, the flame is convected up out of the neck of the flask, rapidly accelerating and stretching into a thin front through one side of the constriction near the ignition event. The inability of the flame to propagate across the entire width of the neck is likely caused by the strong sheer created by the velocity gradients in the constriction due to the expelling of gas through the flask top. A similar effect was observed by Iida et al. (1985) for premixed flame propagation into a narrow channel. The propagation of the flame out of the flask is only possible because of the ejected unburnt fuel caused by the ignition event itself. Later in time, at 16.35344 s, the flame can be seen expanding into the holder section above the flask and becoming unsteady. This is a consequence of the highly unsteady flow that already exists in this region of the apparatus (Chapter 2). Progressing to 16.35595 s and later, 16.3585 s, the flame front can be seen breaking apart into numerous smaller flamelets that are convected upwards and eventually out of the flask in what has been observed and identified in experiments as "Mode I" ignition with a visible flame (Martin and Shepherd, 2021). This breakup of the flame can be attributed to numerous factors including unsteady mixing mixing, heat loss to the cooler surrounding gas, stretching of the flame surface caused by differential velocities, and localized regions of lean fuel concentrations below the lower flammability limit. This transition is consistent with known flame-flow interactions, where curvature and strain can wrinkle or fragment the flame surface (Law and Sung, 2000; Poinsot and Veynante, 2005; Bane et al., 2010a).

The differences in reaction pathways discussed in Section 3.3.5 as a result of the fuel stratification in the flask at the time of ignition can also be seen from Figures 3.23a, 3.23c, and 3.23d. After the ignition event in a fuel-rich region ($\phi \approx 1.8$), the flame front that got convected upwards reaches a maximum temperature around 2400 K where the fuel concentration is close to stoichiometry near the top of the flask. This rapid temperature rise coincides with a peak in the exothermic chain terminating recombination reaction CO + OH $\rightarrow$ CO_2 + H (further shown in Figure 3.18b) which dominates the conversion of CO into CO_2 and confirms that it is the dominant contributor to heat release in this region. Although the peak temperature decreases to around 1800 K, this pathway remains the dominant mechanism for heat release as the flame propagates into a lean mixture ($\phi < 1$) up through the neck of the flask and into the holder.

The downward propagating flame front occurs in a rich mixture ($\phi > 1.8$). The lower peak temperature of around 1600 K and significantly higher concentration of H_2 up to 9% mole fraction (compared with $\approx$ 1% mole fraction in the stoichiometric and fuel lean regions) in the products shown in Figure 3.23 is a result of an alternative dominant reaction pathway involving CH_3 as further discussed in Section 3.3.5. This flame front moves only 2 cm downwards from the ignition location before being quenched as it reaches a very rich fuel/air mixture ($\phi >> 1.8$).

3.4 One-dimensional analog

The three-dimensional simulation presented in this chapter provide a high-fidelity view of ignition behavior within the ASTM-E549 apparatus, where ignition occurs off-center from the vertical centerline, closer to the hot wall. To better understand this effect, a spherically symmetric one-dimensional analog was developed to isolate the role of temperature gradients on the ignition behavior.

3.4.1 Numerical implementation

The spherically symmetric one-dimensional problem was implemented in OpenFOAM. Figure 3.24 shows a visualization of the one-dimensional model in addition to a coarse grid to visualize computational cells. For the actual simulations, 5000 uniformly spaced cells ($\sim$10 μm) made up the computational grid. The dimensions of the computational domain were set to model a 500 mL closed spherical vessel, the same size as what is used in the ASTM-E659 (2005) standard. OpenFOAM 2023 uses the *wedge* boundary condition to simulate axisymmetry along a given axis when paired with a single computational cell in that axis direction. In the current

formulation, wedge boundaries were applied to the four surfaces encompassing the θ and ϕ dimensions and an angle between the wedge planes was selected to be 2.5° recommended for axisymmetric simulations in the documentation.

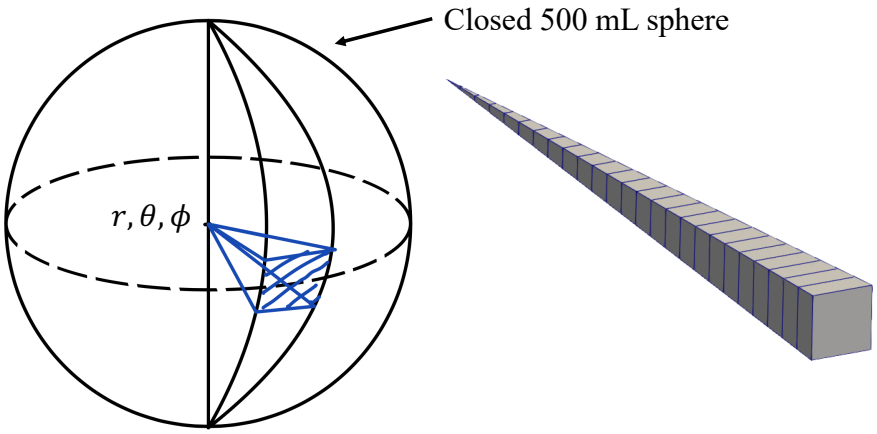


Figure 3.24: One-dimensional spherical model and simplified computational grid.

While numerous previous studies have used OpenFOAM to simulate a single axis of symmetry (Melguizo-Gavilanes et al., 2016; Zirwes et al., 2017; Schoeffler and Shepherd, 2023), no published work could be found employing two axes of symmetry required for a spherical implementation. For validation to ensure OpenFOAM properly solves the one-dimensional problem with spherical symmetry, a simple constant-property diffusion problem was solved in spherical coordinates using the method of lines and ODE15s in MATLAB and compared with the OpenFOAM solution. The spherical thermal diffusion problem is defined by

$$\rho c_p \frac{\partial T}{\partial t} = \frac{\lambda}{r^2} \frac{\partial}{\partial r} \left(r^2 \frac{\partial T}{\partial r} \right) \tag{3.14}$$

where the heat capacity at constant pressure, $c_p = 1000$ J/kg·K, the thermal conductivity, $\lambda = 0.03$ W/m·K, and the density, $\rho = 1$ kg/m^3. The gas was initialized at 300 K and the wall temperature fixed at $T_w = 527$ K to simulate the temporal diffusion problem.

Figure 3.25 plots the temporal evolution of the temperature profile for the diffusion simulation using the spherical and OpenFOAM formulation. As time evolves, the gas temperature rises for all radial locations, with the lowest temperature occurring in the center of the sphere. After 75 s, the temperature reaches a steady solution and equilibrates at the imposed wall temperature throughout the domain. Importantly,

the OpenFOAM solution matches the spherical coordinate solution to machine precision for all time instances. We conclude that OpenFOAM is a viable platform for running the one-dimensional spherically symmetric simulations.

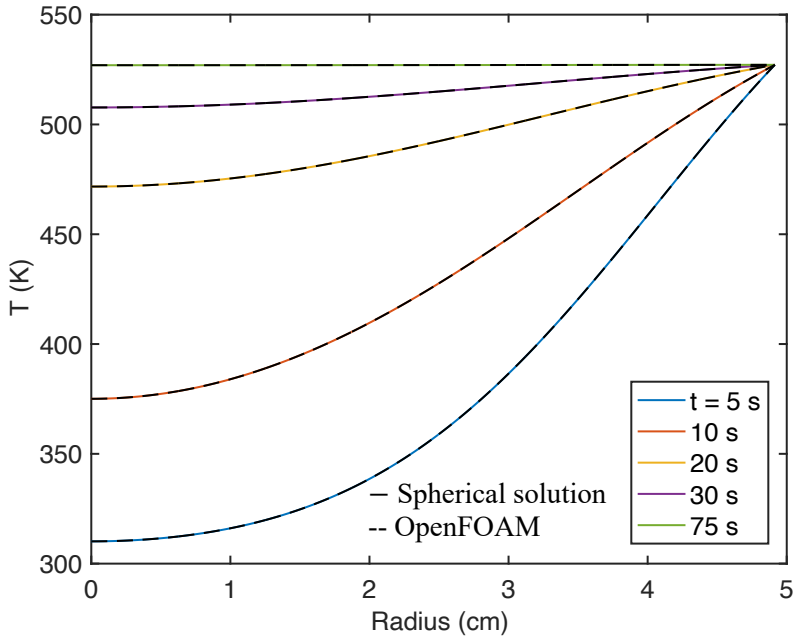


Figure 3.25: Temporal evolution of the temperature profile in the thermal diffusion problem using the spherical and OpenFOAM solutions.

The one-dimensional spherically symmetric model was then implemented and solved in OpenFOAM for ignition simulations. For these simulations, the wall temperature was fixed at $T_w = 527$ K corresponding to the maximum wall temperature used in the three-dimensional study previously examined in this chapter. The initial temperature of the mixture, T_i, was parametrically reduced to observe the effect on the ignition behavior. Specifically, $\Delta T = T_w - T_i = 0$, 0.1, 1, and 7 K were investigated. The $\Delta T = 7$ K case was selected as the largest temperature difference in the study as it corresponds to the approximate temperature range that exists in the case B configuration numerical solution presented in Chapter 2. The same reduced CaltechMech mechanism used for the three-dimensional simulation was used here and the mixture was initialized as homogeneous stoichiometric nC_6H_{14}/air.

We acknowledge that this one-dimensional model drastically simplifies the actual scenario modeled with the three-dimensional ignition simulation, removing effects from buoyancy, observed asymmetry in the flow field, and toroidal vortex driven by

the open top of the flask. However, the one-dimensional model is computationally efficient and can provide insight on the role temperature gradients that are known to exist in autoignition testing (Fouchier and Shepherd, 2025) have on ignition behavior.

3.4.2 Ignition results

ΔT = 0 results

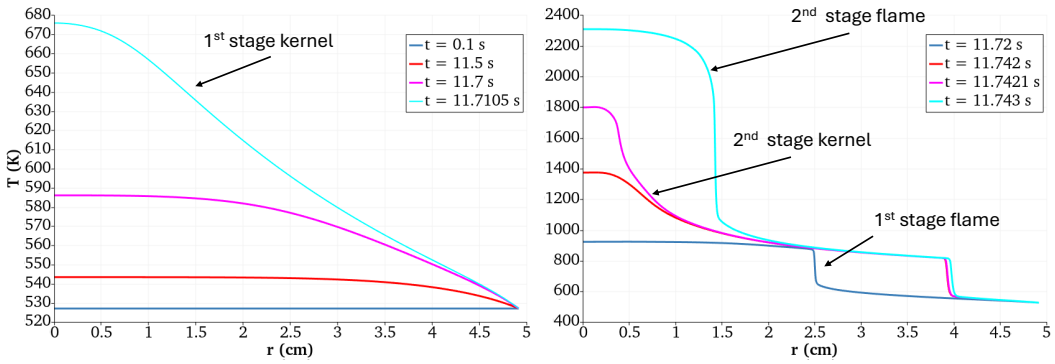


Figure 3.26: Temporal evolution of the temperature profile for $\Delta T = 0$ K during the (left) first stage ignition event and (right) second stage ignition event.

The first case examined was $\Delta T = 0$ K. That is, both the initial temperature in the domain and the wall temperature were set to 527 K. Figure 3.26 plots the radial temperature profile evolution over time . From Figure 3.26(left) for early times such as 0.1 s, the temperature distribution is nearly uniform. As time evolves, heat is released from chemical reaction and the temperature rises. The temperature maximum occurs exactly in the center of the sphere, when $r = 0$ cm. At 11.7105 s, a substantial increase in temperature is seen at $r = 0$ cm where the local gas temperature in the kernel exceeds the wall temperature by 150 K. From Figure 3.26(right) the first stage ignition event is evident at 11.72 s as a flame front propagating outwards towards the wall. Gas temperatures behind the front are around 935 K. Only 22 ms later at 11.742 s, evidence of the second stage kernel is seen as another local increase in gas temperature, maximized at $r = 0$ cm. This second stage ignites a short while after, at 11.7421 s. The second stage flame propagation can be seen propagating outwards towards the hot wall at 11.743 s.

The results in Figure 3.26 model a highly idealized combustion vessel that has zero temperature gradients initialized in the domain. Changes to the temperature distribution and subsequent ignition events are initiated from chemical reaction.

Ignition occurs in two stages at the center of the spherical volume (r = 0 cm). This conclusion is consistent with prior ignition modeling work in closed vessels (Kee et al., 1975; Campbell et al., 2007; Liu et al., 2010a; Melguizo-Gavilanes et al., 2019).

$\Delta T \neq 0$ results

The results using the one-dimensional model for ΔT = 7 K are shown in Figure 3.27 which show the temporal evolution of the radial temperature profile. From Figure 3.27(left), effects of thermal diffusion can be seen at 1 s where the hot wall heats the cooler gas. The temperature maximum at this time is at the hot wall. At 10 s, the gas continues to heat from thermal diffusion, but the wall temperature still exceeds the temperature at r = 0 cm by 2 K. At 12 s and 12.6 s, the first stage ignition kernel is evident from a temperature maximum within the gas at 3.8 cm. This is in contrast to the ignition kernel forming at the center of the sphere, r = 0 cm, for the ΔT = 0 K case. In Figure 3.27(right), the first stage ignition and radial flame propagation is seen between 12.836 s and 12.9 s. The second stage ignition kernel is seen as early as 12.838 s at 3.8 cm, characterized by a local temperature exceeding the first stage flame temperature. At 12.909 s, the second stage ignition event is observed propagating radially outwards. Interestingly, this ignition time is approximately 1.2 s slower than what was observed for the ΔT = 0 K case and can be attributed to the decreased initial gas temperature slowing down the self-heating process.

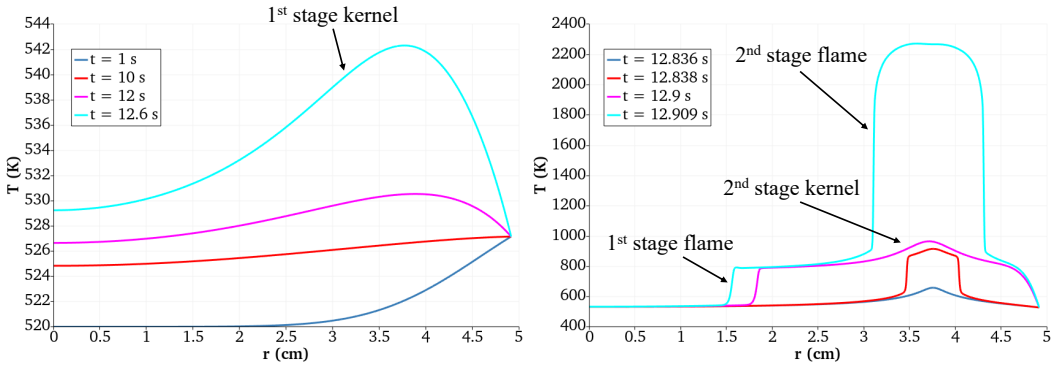


Figure 3.27: Temporal evolution of the temperature profile for ΔT = 7 K during the (left) first stage ignition event and (right) second stage ignition event.

Additional simulations were performed for $\Delta T = 0.1$ and 1 K. Figure 3.28 compares the radial temperature profiles at the time of ignition for the four one-dimensional cases and the three-dimensional ASTM simulation. For the $\Delta T = 0.1$ and 1 K cases, the radial ignition location was at 1.54 cm and 3.03 cm, respectively. For all cases, a two-stage ignition event as observed. However, the ignition times and locations are quite different. As ΔT is increased from 0 K to 7 K, the ignition delay time of the second stage shifted from 11.7 s to 12.9 s and the location shifted radially outwards towards the wall from $r = 0$ cm to $r = 3.8$ cm. For qualitative comparison, the ASTM 3D simulation is also shown at the time of ignition and exhibits similar structure and radial ignition location to the comparable one-dimensional case with $\Delta T = 7$ K.

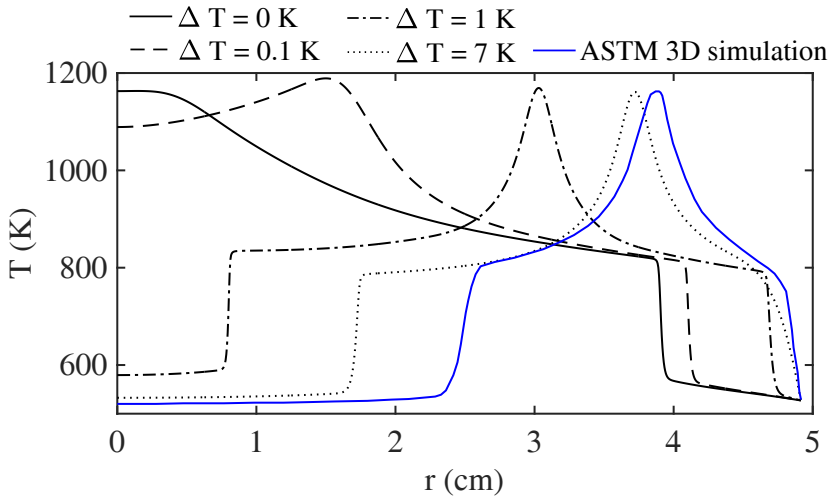


Figure 3.28: Radial temperature profiles at the time of ignition for the four ΔT cases and the three-dimensional ASTM simulation.

The conclusions from this analysis are that temperature differences in the gas, even as small as 0.1 K, lead to a difference in the ignition delay time and even more significant differences in the radial location of the ignition kernel. This is important because a non-uniform temperature distribution inevitably exists in any experiment and the ignition location is sensitive to this distribution. This can lead to variability in critical conditions for a given wall temperature and affect AIT results.

3.5 Implications for AIT experiments

The numerical autoignition simulation of nC_6H_{14} presented provide a first insight to the ignition process during an ASTM-E659 test.

The nonuniform temperature distribution within the flask brought about by small surface temperature differences inevitable in experiments and intrusion of cold gas through the open top through the center of the flask prescribed by the ASTM-E659 standard (ASTM-E659-24, 2024) leads to enhanced chemical reaction in a localized ring near the wall where the temperature is largest. In addition, the instantaneous temperature and velocity field inside the flask at the time of fuel injection drives a slightly asymmetric initial mixing transient that leads to a localized off-center ignition event. The highly unsteady fuel vaporization process not modeled in this work most likely also contributes to this phenomenon as well as additional variability in results (Fouchier and Shepherd, 2025). This highlights the sensitivity of the ignition behavior to the fuel injection technique and care should be taken to reduce the variability in results.

For short duration tests with heavy fuels (typically < 100 s, Chapter 2), as shown for nC_6H_{14} in this study, ignition occurs in a vertically stratified layer of fuel. The degree of stratification will depend on the amount of fuel injected as well as the surface temperature that can affect the ignition delay time and can have a substantial effect on the resultant flame propagation. For longer duration tests that are several minutes long, ignition will occur in a homogeneous mixture possibly through different specific reaction pathways.

For heavy hydrocarbons, such as nC_6H_{14}, that exhibit an NTC region, a two-stage ignition behavior is most likely present for temperatures slightly larger than the AIT as shown in this study, where substantial gas expansion pushes unburnt fuel and the flame out of the flask and holder assembly as a visible flame commonly referred to as "Mode I" ignition as defined by Martin and Shepherd (2021). Preliminary simulations suggest that slightly cooler surface temperatures significantly slow down the ignition process. Under these conditions, natural convection becomes more influential, causing the heated gas to rise and shifting the ignition location toward the neck of the flask. This upward movement, along with interactions between heat release and cooling effects from the surrounding air, appears to play a key role in the emergence of distinct ignition behaviors described by Martin and Shepherd (2021).

3.6 Conclusions

In this study, numerical modeling of gaseous nC_6H_{14} autoignition in our laboratory's ASTM-E659 apparatus was performed for a single test case corresponding to a given wall temperature distribution and injected fuel volume/temperature. A reduced kinetic mechanism suitable for multidimensional reacting flow simulations was developed for nC_6H_{14}/air oxidation including low temperature chemistry.

It was found that after initialization of the gaseous nC_6H_{14} sphere, the fuel immediately sinks to the bottom of the flask and begins to slowly diffuse upwards. Chemical reaction begins slowly and most prominently near the walls where the local gas temperature is the hottest, forming many intermediate species including $OC_6H_{11}OOH$, C_2H_4, and H_2O_2. The formation of intermediates is nearly symmetric in the azimuthal direction around the vertical center line in the flask, but small variations arise due to asymmetry in the initial mixing transient caused by the unsteady flow generated by the open top in the flask. These small variations grow over time during the cooking phase and ultimately lead to a localized ignition event. At 15.9 s, a lopsided ring kernel is seen near the walls around the vertical midpoint of the flask in a rich fuel-air mixture ($\phi \approx 1.8$) where exothermic chemical reaction causes the gas temperature to exceed the wall temperature by up to 100 K prior to coupled chemical-thermal runaway. Ignition follows in a two-stage sequence. The first stage occurs as a rapid increase in temperature to 935 K. The second stage follows from inside the gas processed by the first stage ~40 ms later with a conversion of the intermediate species into products and rapid increase in temperature to 1900 K.

Massless lagrangian particle tracking was performed on the fluid parcel that first ignites to understand the chemical pathways that occur prior to and during coupled chemical-thermal runaway. An exothermic low-temperature oxidation pathway $nC_6H_{14} \rightarrow C_6H_{13}O_2 \rightarrow C_6H_{13}O_4 \rightarrow OC_6H11OOH \rightarrow$ ketones + aldehydes was identified to be responsible for the first stage. Instead of the traditional high-temperature oxidation pathways converting $CO \rightarrow CO_2$ by OH radicals, oxidation of HCO molecules generated by the large amounts of CH_2O produced from the first stage was found to drive coupled chemical-thermal runaway of the second stage while $T < 1450$ K. Once $T > 1450$ K, reaction pathways involving recombination of CH_3 molecules become the primary process for heat release due to the lack of O_2 molecules present at the time of ignition. This results in higher concentration of CO and H_2 in the products compared to CO_2, as typically seen for mixtures closer to stoichiometry.

Lastly, a preliminary study of the flame propagation through the flask and holder after thermal ignition revealed agreement within 2.7% of the expected flame speed calculated from highly-resolved one-dimensional freely-propagating flame calculations, even though a coarse numerical grid artificially thickened the flame. The three-dimensional flame propagation solution was deemed sufficient for qualitative analysis. After ignition, gas expansion caused by the flame propagation ejects unburnt fuel in the flask out through the top of the flask as a jet. The flame, quenched at the bottom of the flask by a exceedingly rich mixture, is convected upwards, chasing the unburnt fuel. Upon entering the constriction in the neck of the flask, the flame rapidly accelerates and stretches into a long, thin front. The lean flame eventually becomes unstable and breaks apart into numerous smaller flamelets in the holder section because of unsteady mixing, heat loss, and stretching. These flamelets continue convecting upwards through the holder and out the top in what is believed to be experimentally observed as "Mode I" ignition.

In addition, a one-dimensional spherically symmetric analog was developed to isolate the influence of thermal gradients on ignition behavior. This model confirmed that even small radial temperature differences (as little as 0.1 K) can shift the ignition kernel location and affect the ignition delay time. The results support the conclusion that localized temperature gradients inherent to experimental conditions can have a strong influence on ignition behavior, consistent with the asymmetric off-center ignition observed in the three-dimensional simulation. This simple analog provides a computationally efficient framework for interpreting and generalizing the effects of spatial temperature non-uniformity in autoignition studies.

Chapter 4

HOT SURFACE THERMAL IGNITION

4.1 Motivation

As discussed in Chapter 1, hot surface ignition problems typically exhibit much higher critical surface temperatures for ignition compared with the autoignition studies presented in Chapter 3. In this chapter, we analyze the canonical hot surface ignition problem of a forced convection flow of nC_6H_{14}/air over a uniformly heated plate. The configuration provides a simplified, yet representative framework to examine the fundamental physics of hot surface thermal ignition, including the structure of the thermal boundary layer, formation of the ignition kernel, and roles of chemical heat release and energy transport. We first characterize ignition using a reduced kinetic mechanism using only high-temperature (> 900 K) chemistry, which is conventional in modeling of hot surface ignition problems (Liu et al., 2010b; Melguizo-Gavilanes et al., 2016; Schoeffler and Shepherd, 2023) as the surface temperatures required often exceed 1000 K (Boettcher, 2012; Coronel, 2016; Boeck et al., 2019; Jones et al., 2019; Jones, 2021; Martin, 2023). We then extend the analysis to include low-temperature chemistry (< 900 K) and asses the impact on species progression, thermal layer structure, and critical surface temperature.

4.2 Numerical model

4.2.1 Kinetic models

The two reduced kinetic mechanisms used and described by Figure 4.1 which plots the ignition delay times at 1 bar from 500 K to 1500 K from zero-dimensional constant pressure adiabatic simulations for three mechanisms. More information about the zero-dimensional simulation model can be found in Chapter 6. The first was a reduced mechanism from the Dagaut mechanism (Dagaut and Cathonnet, 2006). It consisted of 62 species and 230 reactions. This mechanism consists of high-temperature modeling and minimal low-temperature modeling, which can be seen as a decrease in the delay time slope around 833 K. However, the modeling is not sufficient to cause an inversion of the ignition delay time with decreasing temperature as is observed experimentally for heavy hydrocarbons (Ciezki and Adomeit, 1993; Fieweger et al., 1997). The second mechanism is the reduced mechanism from the CaltechMech mechanism developed in Chapter 3 consisting of 54 species and 265

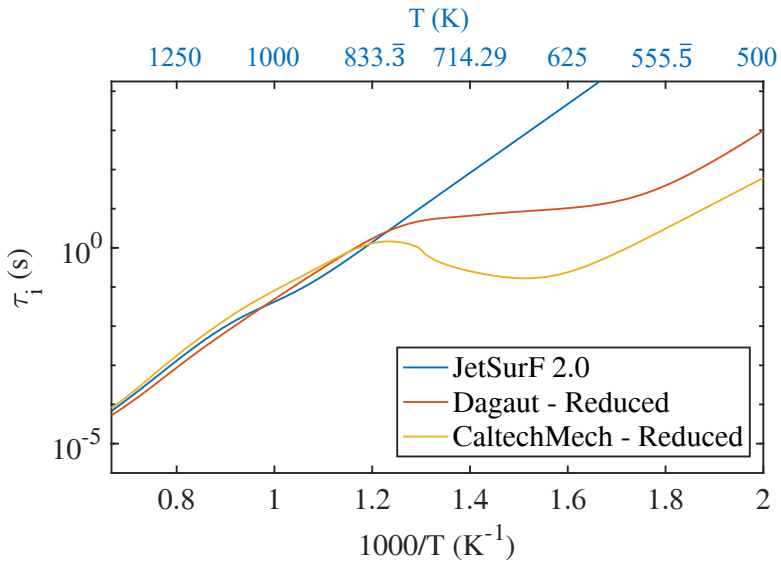


Figure 4.1: Zero-dimensional ignition delay times for stoichiometric nC_6H_{14}/air at 1 bar with three detailed kinetic mechanisms.

reactions. More care was taken to properly retain the low-temperature chemistry from the primary full mechanism in this reduced version. The result is a much more substantial dip in the delay time and the characteristic negative temperature coefficient (NTC) region where τ_i decreases with decreasing temperature. The y-axis is a log scale so the difference between the delay times for the two mechanisms is several orders of magnitude for some temperatures. For visual reference, the JetSurF 2.0 mechanism consisting of 348 species and 2163 reactions with no low-temperature modeling is included. For temperatures > 833 K, all three mechanisms have similar ignition delay times in magnitude and slope. For temperatures < 833 K, large and nonphysical ignition delay times exist for the JetSurF 2.0 and also for the reduced Dagaut mechanism compared to the reduced CaltechMech mechanism.

4.2.2 Geometry and flow configuration

The canonical problem is described by a two-dimensional forced convection boundary layer. Figure 4.2 shows a schematic of the geometry. The hot surface was $L = 1$ cm long with 0.5 cm cold surfaces kept at 300 K immediately adjacent on either side to move the relevant physics away from the computational domain boundaries. A 200 K/s ramp was imposed on the hot surface as to slowly heat the boundary layer until the mixture ignites. At the inlet on the left, the flow was fixed at $\boldsymbol{U}_\infty = (0.1, 0)$ m/s and $T_\infty = 300$ K. The top and right boundaries were set as outlets. Initially, the

gas was set at $T_i = 300$ K and with $\boldsymbol{U}_i = (0.1, 0)$ m/s to simulate sudden exposure to a hot surface. The pressure was set to $P = 1$ bar. A no slip condition was set on the hot surface and slip conditions were set on the adjacent cold surfaces to isolate the boundary layer development to the hot surface itself.

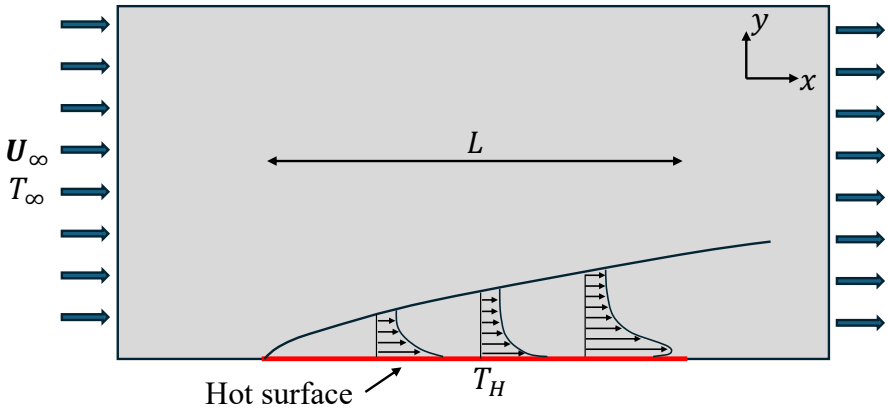


Figure 4.2: Schematic of the forced convection boundary layer across a hot surface.

This setup was selected to study, fundamentally, how the detailed nC_6H_{14} kinetic mechanisms behave in a reacting boundary layer. Grid convergence by way of unchanging critical surface temperatures and species profiles during ignition could be achieved for a grid of approximately 200,000 cells compressed in the wall normal direction. The local cell size near the wall was 20 μm.

4.3 Ignition results

4.3.1 High-temperature mechanism results

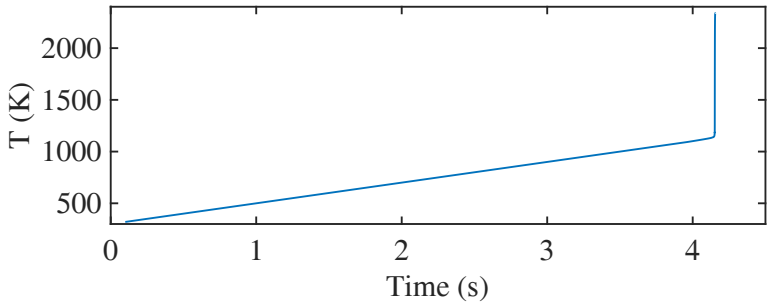


Figure 4.3: Maximum temperature in the domain over time.

The evolution of the maximum temperature in the domain is shown in Figure 4.3 for the reduced Dagaut mechanism, which includes only high-temperature kinetic pathways. For the first 4.15 seconds, the maximum temperature increases linearly, consistent with the imposed wall heating rate of 200 K/s. At t = 4.15 s, a rapid rise in maximum temperature is observed, exceeding 2000 K within milliseconds. This abrupt increase marks the onset of thermal runaway and ignition.

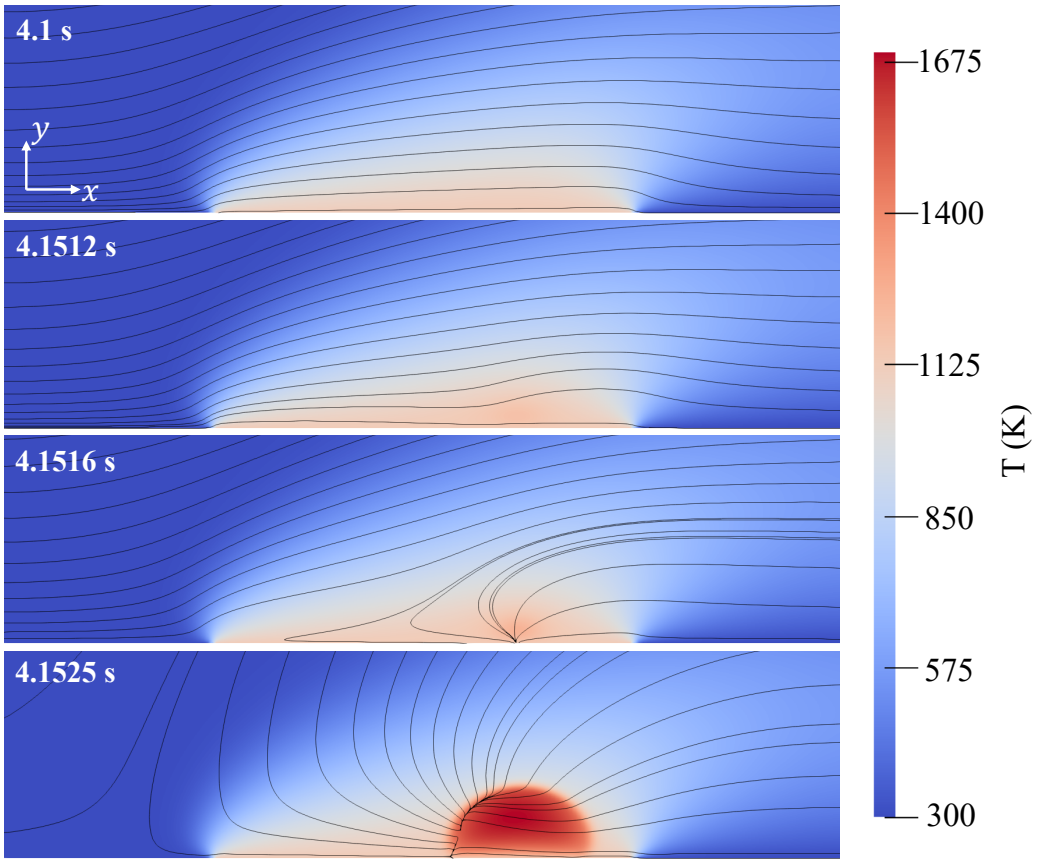


Figure 4.4: Temperature field evolution during the ignition event. Instantaneous streamlines are overlaid.

The ignition event is visualized in the spatial domain in Figure 4.4, which shows the temperature field and overlaid instantaneous streamlines. Before ignition, at 4.1 s, the thermal layer develops along the hot surface. There is a slight inflection of the instantaneous streamlines at the leading edge of the hot surface. At 4.1512 s, a localized region of elevated temperature appears near the wall, exceeding the wall temperature. A deviation of the instantaneous streamlines away from the kernel is a consequence of gas expansion. At 4.1516 s, the kernel can be visualized in the thermal layer as a small region at 7.6 mm along the hot surface where the gas

temperature exceeds the wall temperature by 150 K. Generally, the ignition location along the heated surface is largely influenced by the thickness of the thermal layer. This is discussed in more detail in the following chapters. The more significant temperature increase causes stronger gas expansion away from the kernel, such that upstream fluid reverses direction before being convected away downstream. The beginning of the flame front can be seen propagating outwards from the ignition location at 4.1525 s where temperatures exceed 1675 K. While not shown, this flame further propagates through the thermal layer and and out into the cold ambient gas in the rest of the domain.

The chemical pathways leading to ignition can be analyzed using Lagrangian particle tracking, similar to the analysis in Chapter 3. A massless particle is injected in post-processing to observe the important species that lead up to ignition. The particle analyzed is the ignition particle itself and its trajectory through the thermal layer until it ignites is shown in Figure 4.5. This must be done after the simulation has finished since the ignition location is not known a priori.

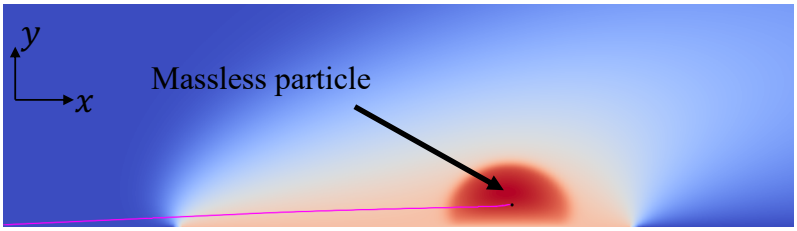


Figure 4.5: Trajectory of the massless particle that ignites through the thermal layer up until ignition.

Figure 4.6 plots the top 9 species along this particle as it progresses through the thermal layer and ignites. Between 3.8 s and 3.9 s, the particle enters the thermal layer where a rapid temperature increase is seen to 1000 K. The jaggedness of the profiles at these times are a result of low sampling rate well in advance of the ignition time to conserve storage. Over the next ~230 ms, the particle moves through the thermal layer and a steady decline of O_2 and nC_6H_{14} is converted into intermediate species as the temperature slowly rises. Accumulation of C_2H_4 and CH_2O intermediates is observed up until 4 s when the temperature is high enough to cause further conversion of these species to CO, H_2, and H_2O. From the zoomed in portion, ignition can be seen at 4.1522 s, where CO is converted to CO_2 exothermically by OH. A maximum temperature of 1621 K is seen by the ignition particle before exiting the thermal layer at 4.1537 s.

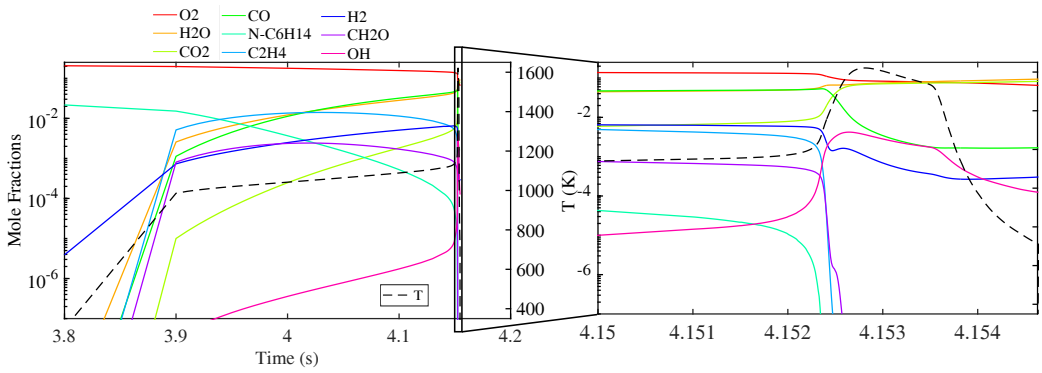


Figure 4.6: Mole fraction of the top 9 species of the ignition particle. Temperature is shown on the right axis.

In addition to the species evolution and intermediate product formation that lead to thermal ignition, it is important to also examine the transport phenomena that govern how energy is distributed in the thermal layer. The terms of the energy equation, convective transport, thermal diffusion, mass diffusion, unsteadiness, and heat release offer key insight into the thermal and fluid dynamic processes that lead to ignition. By analyzing these terms spatially at various instances in time, the interplay between localized chemical heat release and non-local energy transport can be investigated, thereby providing a comprehensive understanding of the ignition mechanism from both chemical and physical perspectives.

Figure 4.7 plots the five terms of the energy equation along a surface-normal line through the center of the ignition kernel, with the temperature profile overlaid on the right axis. At early times (2 s), thermal diffusion and convection dominate the energy balance across the thermal boundary layer, with peak magnitudes near 4 mm from the wall. This coincides with the location of maximum velocity in the developing boundary layer. Heat release from chemical reaction is negligible at this stage and the temperature smoothly decreases from the 700 K wall temperature to the 300 K ambient. By 3.7 s, the wall temperature has risen to 1040 K, and although the general diffusive-convective structure persists, the energy terms have roughly doubled in magnitude due to the elevated thermal gradients. Within the first millimeter from the wall, a modest contribution from chemical heat release becomes apparent, balancing thermal diffusion with minor influence from convection, mass diffusion, and unsteadiness. The local gas temperature in this near-wall zone is slightly elevated compared to the earlier profile. At 4.15185 s, the wall temperature reaches 1130 K, and a clear ignition kernel forms. A local gas temperature peak

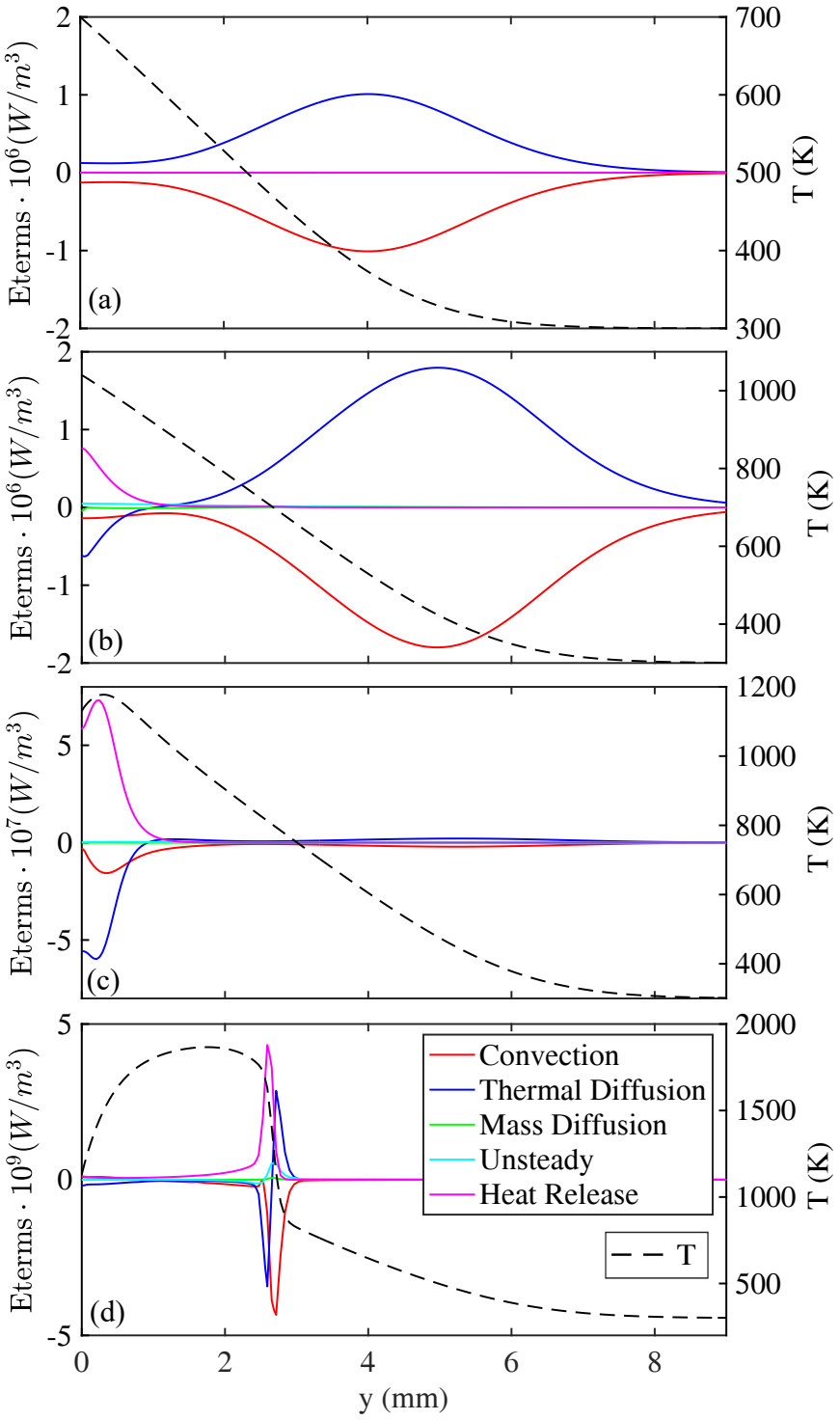


Figure 4.7: Energy equation terms along a surface normal line through the center of the ignition kernel at (a) 2 s, (b) 3.7 s, (c) 4.15185 s, and (d) 4.15291 s. Temperature is shown on the right axis.

appears just 0.29 mm from the surface, exceeding the wall temperature by 50 K. As the wall continues to heat, chemical heat release increases significantly. Eventually, thermal diffusion can no longer fully balance the heat release at the wall, and the temperature maximum shifts outward into the gas. The energy terms increase by another order of magnitude, and a dip in the convection term near the wall suggests local gas expansion effects near the ignition kernel. At 4.15291 s, thermal runaway becomes evident: the gas temperature surpasses 1800 K and the energy terms increase by two orders of magnitude. A flame front begins to propagate away from the wall, characterized by a convective-diffusive balance in the preheat zone followed by a diffusion-heat release balance in the energy release zone. A small unsteady contribution arises due to the transient motion of the flame front.

The results presented in Figure 4.7 highlight the role of various thermal and fluid dynamic processes that govern ignition near a hot surface. In particular, a near-wall region emerges where chemical heat release is locally balanced by thermal diffusion at elevated gas temperatures, while further into the gas, a balance of convection and diffusion dominates. The structure is consistent with what has been observed in prior studies of similarly configured systems with various fuels (Melguizo-Gavilanes et al., 2016; Melguizo-Gavilanes et al., 2017a; Melguizo-Gavilanes et al., 2017b; Coronel et al., 2018; Boeck et al., 2019). While the specific surface temperature required for ignition differs among studies due to varying fuels and boundary conditions, the underlying thermal processes that lead to ignition appear robust. This consistency suggests the potential for developing a generalized framework to model hot surface ignition across geometries and operating conditions, as explored in Chapter 5.

4.3.2 Influence of low-temperature chemistry

A key limitation of many past modeling efforts is the exclusion of low-temperature chemistry, particularly for heavy hydrocarbons such as the n-hexane used in this chapter. These fuels exhibit an NTC region (Figure 4.1) where competing reacting pathways significantly alter the zero-dimensional ignition delay times. Importantly, the thermal boundary layer near a hot surface spans a wide range of temperatures, from above 1000 K near the wall to the ambient 300 K, directly passing through the NTC region where several studies have observed significant low-temperature effects (Campbell et al., 2015; Zhao et al., 2016). An additional study was performed with stoichiometric dimethyl ether/air, another fuel that has an NTC region, in Appendix C where significant low-temperature effects were also observed. Here, the reduced CaltechMech mechanism including both low- and high-temperature chemistry is used to examine the influence of low-temperature reaction pathways on ignition

dynamics in the same canonical problem.

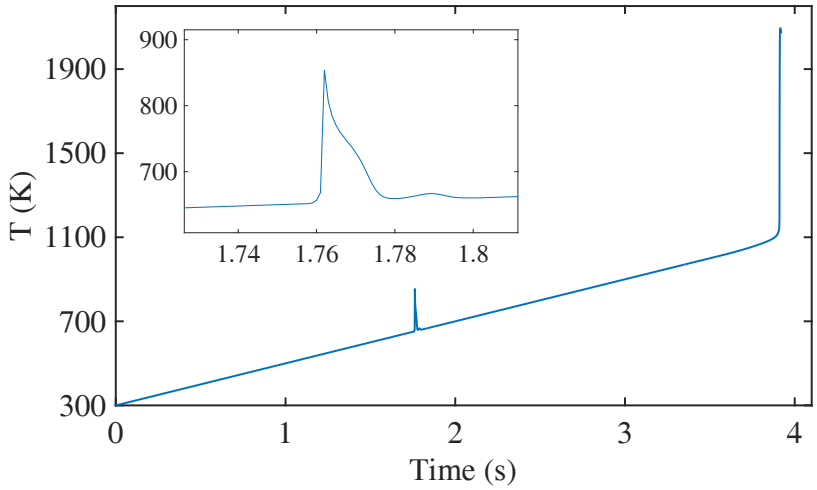


Figure 4.8: Maximum temperature in the domain over time.

Figure 4.8 plots the maximum temperature in the domain over time. At early times ($t < 1.5$ s), the maximum temperature follows the linear wall heating rate of 200 K/s and mirrors the behavior observed with the high-temperature mechanism. However, at 1.76 s, a rapid temperature increase occurs, from 652 K to 854 K over just 3 ms, followed by a slower recovery over the next 35 ms as the disturbance propagates through the thermal layer and dissipates. The temperature then resumes its linear rise due to the boundary condition. A similar pre-ignition temperature rise has been reported in simulations of n-heptane over a glow plug, where low-temperature reactivity is accurately captured (Menon et al., 2016). At 3.905 s, full ignition occurs with a sharp temperature increase exceeding 2000 K, marking the onset of flame propagation.

Figure 4.9 visualizes the two key ignition events. The left column shows the temperature field during the first-stage ignition event. At 1.7 s, a developing thermal boundary layer is apparent, with streamlines inflecting slightly near the heated wall. By 1.761 s, initial signs of exothermic reaction appear as streamlines deflect outwards, driven by local gas expansion at the end of the hot surface. At 1.76s, a localized first-stage ignition kernel forms at 7.6 mm along the 1 cm hot plate, characterized by thermal runaway of low-temperature chemical pathways. The gas expands outwards, disrupting the flow upstream. The flame front propagates within the thermal layer, as seen at 1.764 s, but notably never escapes it. At 1.78 s, the

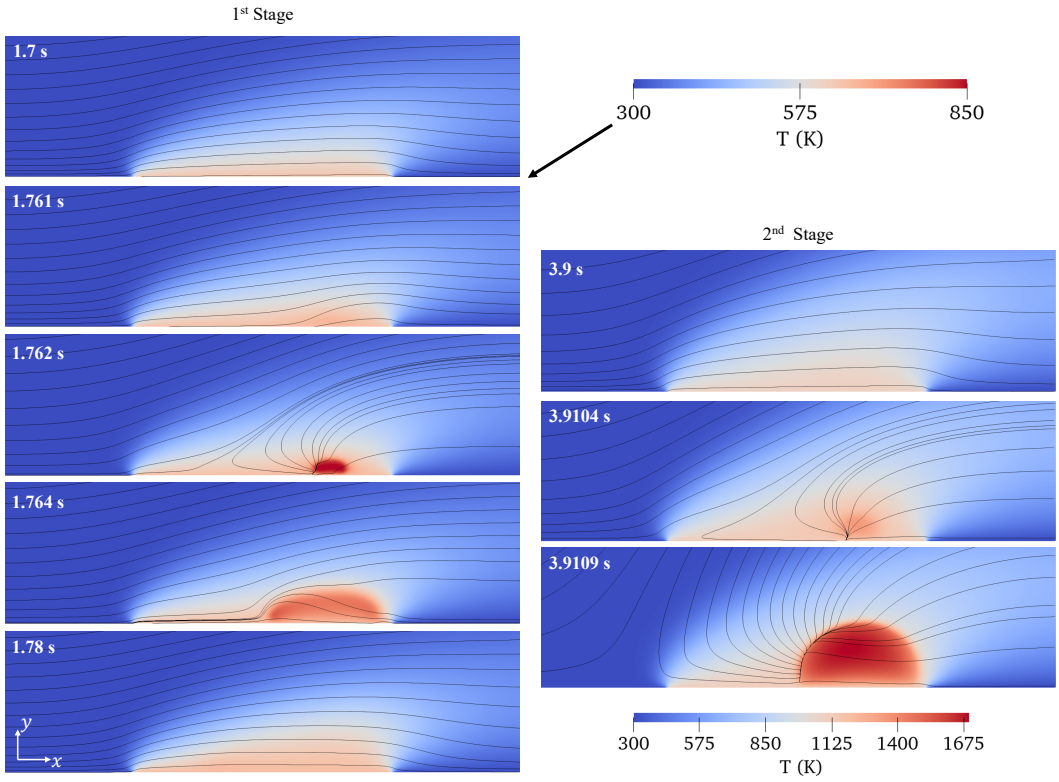


Figure 4.9: Temperature field evolution during the (left) first stage ignition event and (right) second stage ignition event. Instantaneous streamlines are overlaid.

propagation stalls, and the low-temperature reaction zone stabilizes as a persistent band of heat release in the lower-temperature portion of the thermal layer.

Several seconds later, at 3.9104 s, a second-stage ignition kernel initiates at the same axial location as the first stage. The associated temperature rise is more pronounced, causing significant gas expansion that pushes streamlines back towards the leading edge of the hot surface. At 3.9109 s, temperatures reach 1675 K, and flame propagation begins. While not shown, the second-stage flame ultimately exits the thermal layer and continues into the colder bulk gas. The behavior is qualitatively similar to that observed with the high-temperature chemistry mechanism, but the low-temperature capable mechanism allows for more extensive pre-ignition heat release.

Like what was performed for the high-temperature mechanism simulation, massless particles can be used to investigate the chemical evolution leading up to each ignition event. The two particles analyzed are shown in Figure 4.10 where the top image is a particle passing through the first-stage ignition event and the bottom image

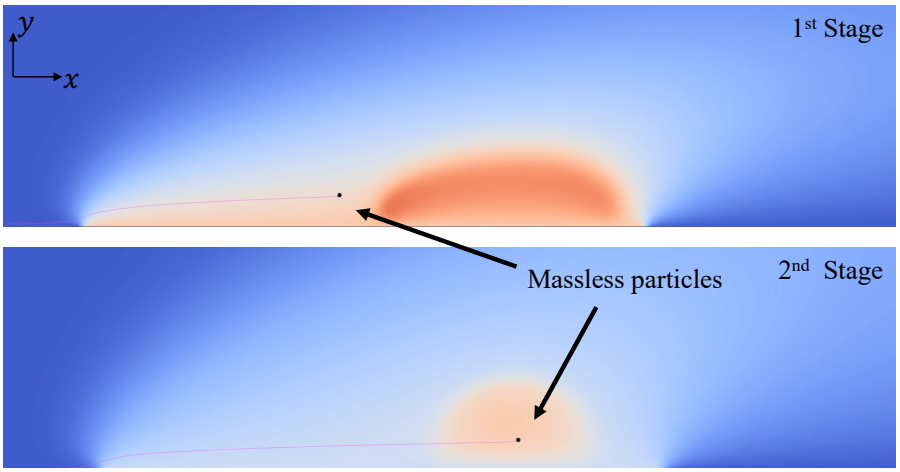


Figure 4.10: Massless particle that (top) pass through the 1st stage ignition event and (bottom) ignites the second stage ignition event.

shows the particle responsible for the second-stage ignition. In Figure 4.11, the top 10 species and temperature are plotted along the first-stage particle path. At 1.62 s, the particle enters the thermal layer, where its temperature increases to 550 K. Over the next 100 ms, the temperature rises by an additional 50 K with negligible chemical reaction. This is evident from the flat profiles of O_2 and nC6H14. At 1.764 s, the first-stage ignition passes over the particle, causing a temperature spike to 732 K and the sudden appearance of low-temperature intermediates such as CO, CH_2O, C_2H_4, CH_3CHO, and H_2O_2. These species are consistent with those reported in low-temperature first stage ignition of nC6H14 in Chapter 3 and prior studies (Westbrook and Dryer, 1984; Battin-Leclerc, 2008). They result primarily from decomposition of unstable OC6H11OOH intermediates, which accumulate along the exothermic low-temperature pathway: nC6H14 $\rightarrow$ C6H13 $\rightarrow$ $C6H13O_2$ $\rightarrow$ $C6H13O_4$ $\rightarrow$ OC6H11OOH. Only a small amount of O_2 is consumed, and the majority of the fuel is converted into reactive intermediates. H_2O forms via H-abstraction from nC6H14 by OH. The particle retains its composition until it exits the domain at 1.95 s.

Figure 4.12 shows the evolution of the particle responsible for second-stage ignition. At 3.62 s, it enters the domain, and by 3.67 s, enters the thermal layer, rapidly heating to 1000 K. As it traverses the persistent low-temperature heat release band, maxima in C_2H_4 and CH_2O appear. Unlike the first-stage case, however, the higher thermal environment leads to steady oxidation of O_2 and nC6H14 into intermediate species.

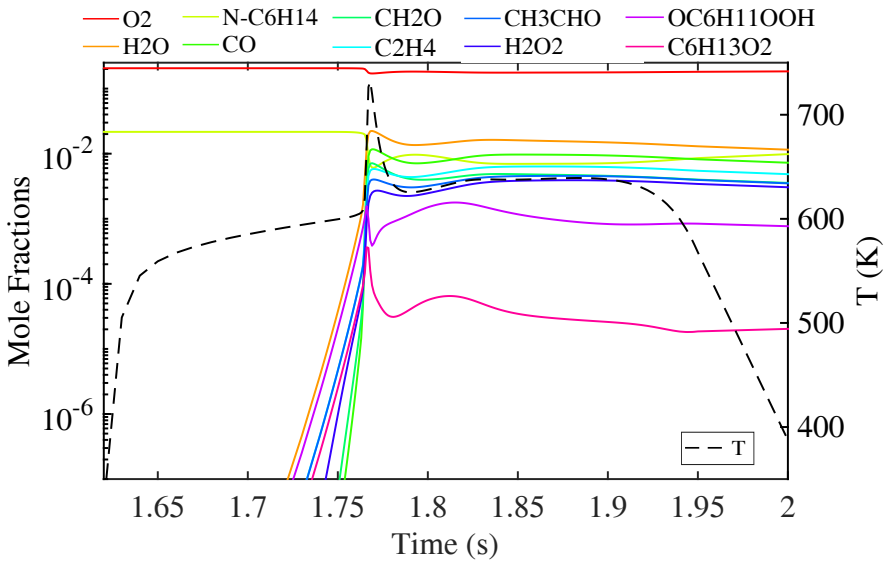


Figure 4.11: Mole fraction of the top 10 species of a particle passing through the first stage ignition event. Temperature is shown on the right axis.

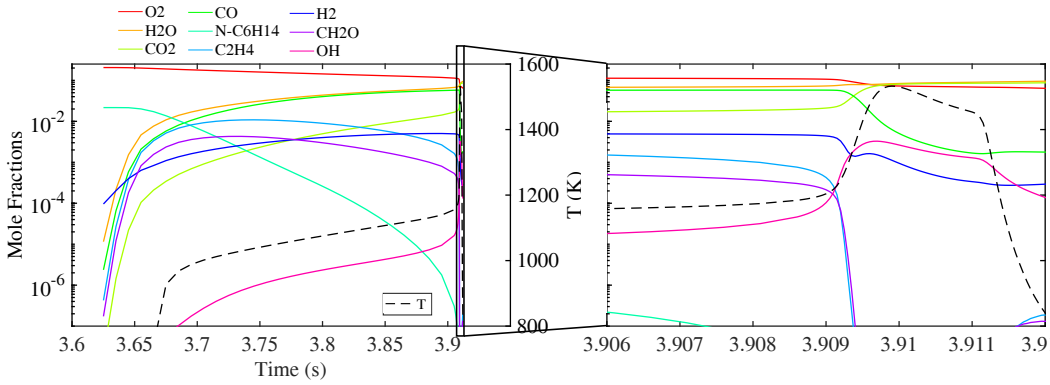


Figure 4.12: Mole fraction of the top 9 species of the 2nd stage ignition particle. Temperature is shown on the right axis.

CO and H_2O steadily accumulate until 3.909 s, when ignition occurs. A rapid exothermic conversion of CO to CO_2 via OH marks the second-stage ignition, with a peak particle temperature of 1533 K before exiting the thermal layer. While the final flame structure resembles that of the high-temperature mechanism simulation, the inclusion of low-temperature chemistry leads to significantly more oxidation of the initial nC6H14 into intermediates prior to ignition by over two orders of magnitude.

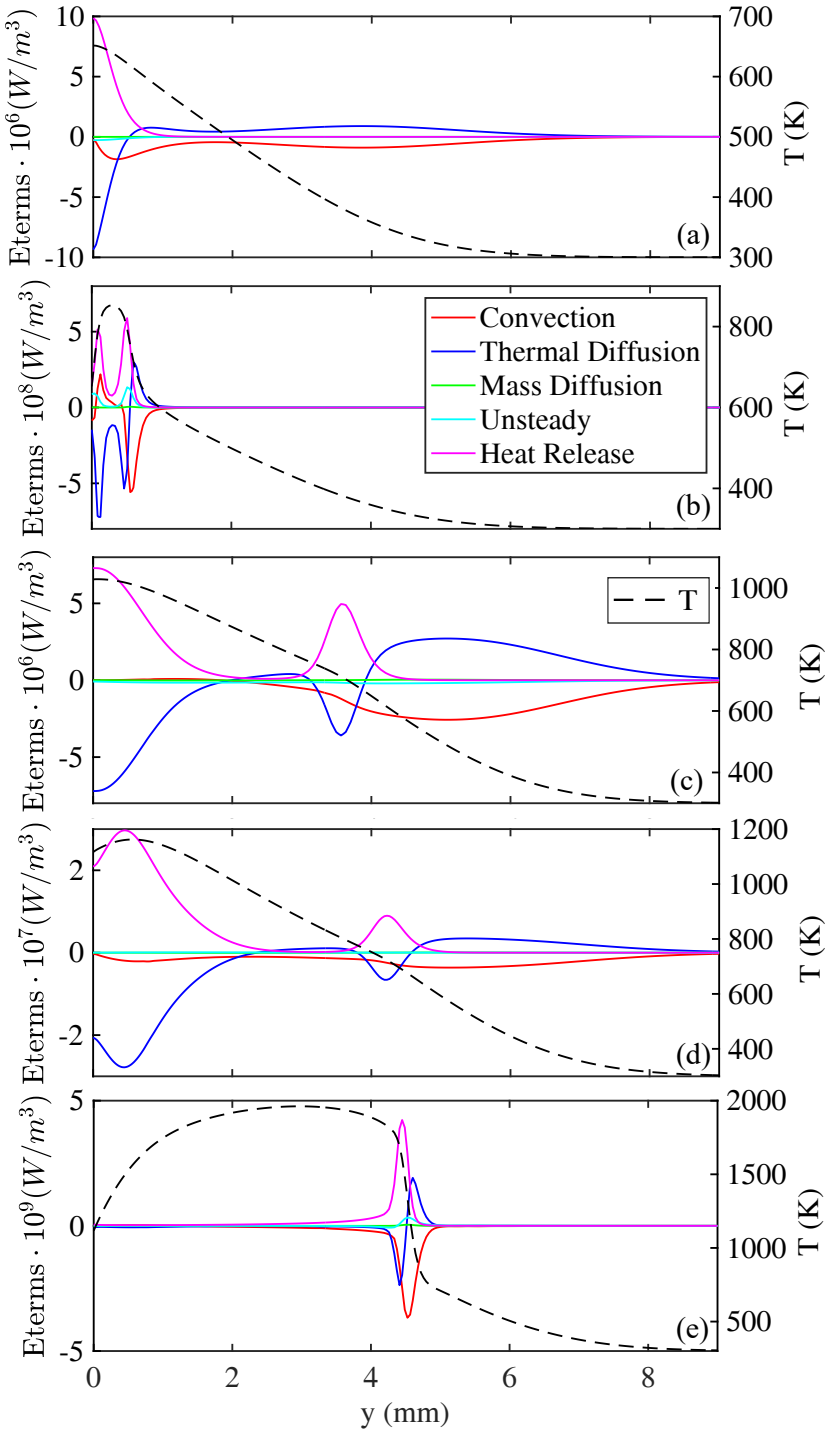


Figure 4.13: Energy equation terms along a surface normal line through the center of the ignition location for the two stage ignition event at (a) 1.758 s, (b) 1.762 s, (c) 3.64 s, (d) 3.908 s, and (e) 3.9112 s. Temperature is shown on the right axis.

Finally, Figure 4.13 shows the energy equation terms along a surface-normal line through the center of the ignition location for both ignition stages. At 1.758 s, heat release at the wall is balanced by thermal diffusion, with a convection–diffusion balance dominating the rest of the layer. The flat temperature distribution near the wall reflects local heat release, and a dip in the convection term is attributed to gas expansion. This mirrors the behavior of the high-temperature mechanism simulation at 1040 K but occurs here at only 652 K, illustrating the similarities of the first-stage ignition event with the high-temperature ignition event. At 1.762 s, the first-stage flame forms, and the front structure reveals a similar convective-diffusive preheat zone followed by a reactive-diffusive heat release zone. Unlike in the high-temperature case, the flame front does not escape the thermal layer. At 3.64 s, this structure evolves into a quasi-steady energy release band that shifts further from the wall as the temperature is increased and the thermal layer continues to grow. This heat release band is responsible for the "bump" in surface normal temperature distribution after the first-stage ignition event in Figures 4.13c and 4.13d. . The onset of the second-stage is seen in Figure 4.13c where thermal diffusion balances heat release from chemical reaction at the wall. Similar to the results in Figure 4.7c for the high-temperature mechanism results, heat release becomes too large to be balanced by thermal diffusion at the wall and the kernel gets pushed out into the gas with a temperature maximum 50 K above the wall temperature. Finally, at 3.9112 s, the second ignition stage has occurred and the initial stages of flame propagation can be seen as a significant increase in temperature behind the front to over 1950 K. The front is again, distinguished by a stronger convective-diffusive preheat zone followed by a reactive-diffusive heat release zone. This second stage flame overtakes the first stage heat release band in the thermal layer and continues outwards into the cold ambient gas throughout the rest of the domain.

4.3.3 Thermal layer comparison

The results using both the high-temperature reduced Dagaut mechanism and the reduced CaltechMech mechanism, which incorporates both low- and high-temperature chemistry, reveal strong similarities in the chemical composition and energy distribution near the wall during high-temperature ignition. However, a key distinction emerges in the form of a two-stage ignition process observed with the CaltechMech mechanism, in contrast to the single-stage ignition predicted by the Dagaut mechanism. The first-stage ignition in the CaltechMech solution produces a distinct band of heat release located away from the wall, contributing to the characteristic "bump"

observed in the temperature profile within the colder portion of the thermal layer. This feature is visualized in Figure 4.14, which compares the spatial distribution of heat release for the two mechanisms at their respective ignition times. In the CaltechMech simulation (top), a clear band of elevated heat release is observed originating near the leading edge of the hot surface and extending into the thermal layer. This feature is entirely absent in the Dagaut simulation (bottom), which shows only a localized region of heat release associated with the second-stage ignition kernel.

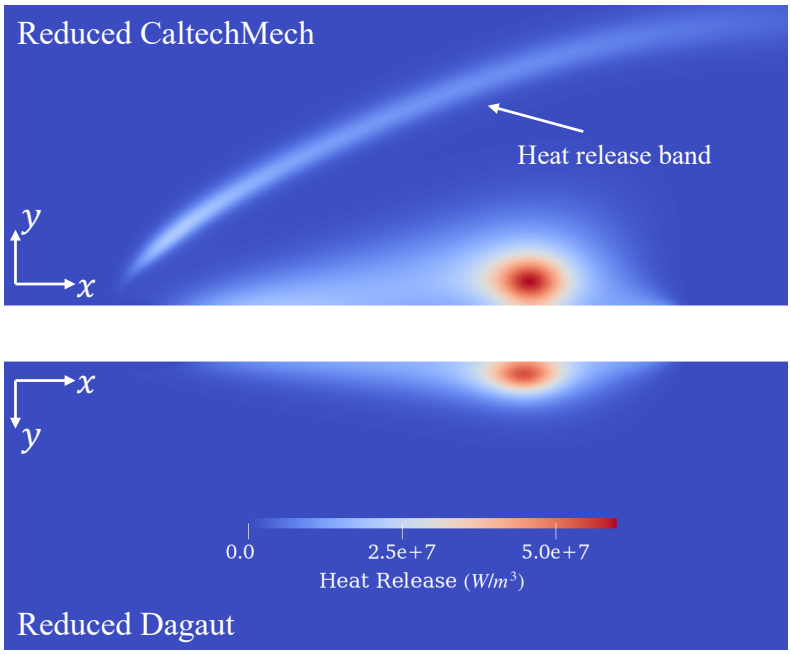


Figure 4.14: Heat release comparison at the second stage ignition time for (top) the reduced CaltechMech mechanism (t = 3.91 s) and (b) reduced Dagaut mechanism (t = 4.15 s).

To further compare the thermal layer evolution between the two mechanisms, Figure 4.15 plots the temperature distribution along a surface-normal line at a fixed axial location (7.6 mm from the leading edge). The top figure shows the first-stage ignition process, while the bottom panel highlights differences during the second-stage ignition. At t = 1.6 s, both mechanisms yield nearly identical temperature distributions, reflecting the purely conductive thermal development prior to ignition. At 1.76 s, however, the CaltechMech mechanism exhibits a clear local maximum in temperature due to the onset of the first-stage ignition event, while the Dagaut mechanism shows continued thermal diffusion with no apparent heat release. The first-stage heat release in the CaltechMech simulation subsequently forms a quasi-

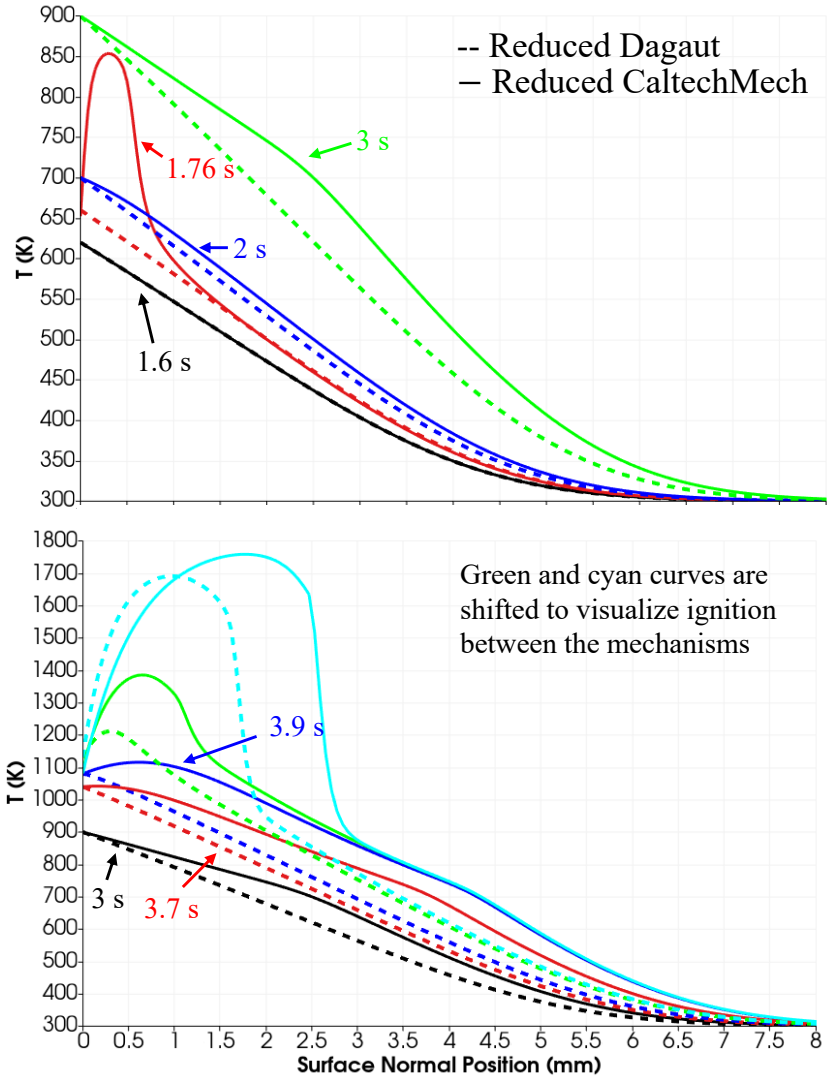


Figure 4.15: Comparison of surface normal temperature distribution over time between the HTC mechanism (reduced Dagaut) and LTC + HTC mechansim (reduced CaltechMech) at 7.6 mm from the leading edge of the hot surface. (Top) Temperature distributions for the first stage ignition event and (bottom) temperature distributions for the second stage ignition event. The green and cyan curves in the bottom figure are at different times to show ignition kernel structure between the two mechanisms. They are at different times because ignition does not occur at the same wall temperature.

steady energy band that persists as the thermal layer grows. This is evident at $t = 2.0$ s and $t = 3.0$ s, where the characteristic "bump" in the temperature profile appears only in the CaltechMech solution. At 2.5 mm from the wall, temperature differences between the two simulations exceed 75 K, emphasizing the impact of low-temperature chemistry on the thermal layer.

In Figure 4.15(bottom), the second-stage ignition event is compared. At $t = 3.9$ s, the ignition kernel for the CaltechMech solution is already visible, while the Dagaut mechanism has not yet ignited. This is the final synchronized time snapshot before divergence due to differing ignition times. The CaltechMech mechanism ignites shortly after, at $t = 3.91$ s, with a wall temperature of 1082 K. The reduced Dagaut mechanism does not ignite until $t = 4.15$ s, at a higher wall temperature of 1131 K. Thus, the inclusion of low-temperature chemistry reduces the required surface temperature for ignition by 49 K in this configuration. These differences underscore the importance of capturing low-temperature reaction pathways in modeling ignition of heavy hydrocarbons in thermal boundary layers.

4.4 Conclusions

Ignition near a hot surface emerges from a balance between localized chemical heat release and non-local energy transport mechanisms, such as thermal diffusion and convection. In the canonical forced convection boundary layer configuration studied in this chapter, these transport processes shape the thermal layer structure leading up to ignition. Once chemical heat release locally exceeds energy losses, an ignition kernel forms near the wall and subsequent thermal runaway occurs. The flame front structure exhibits a convective-diffusive preheat zone followed by a reaction-diffusion dominated energy release zone. These features qualitatively align with prior observations in experimental and computational studies of hot surface ignition across various fuels and geometric configurations, highlighting the generality of the underlying physical processes that will be investigated mathematically in Chapter 5.

A key finding of this chapter is the critical role of low-temperature chemistry in altering ignition behavior for heavy hydrocarbons such as n-hexane. Inclusion of low-temperature reaction pathways produces a first-stage ignition event and a persistent zone of heat release within the lower-temperature portion of the thermal layer. This added energy affects the temperature profile, flattening the wall-normal thermal gradient near the surface and thereby reducing thermal losses that would otherwise slow down the reaction. As a result, the surface temperature required for full ignition is significantly reduced, by 49 K in this case, compared to the simulation using only high-temperature chemistry. These results indicate that proper kinetic modeling of the negative temperature coefficient (NTC) region is essential for accurate modeling of hot surface ignition problems involving heavy hydrocarbons.

Chapter 5

AN ANALYTICAL MODEL FOR IGNITION NEAR A HOT SURFACE

5.1 Motivation

Quite separately from advancements in autoignition testing, as was shown in Chapters 2 and 3, ignition of a cold, flammable gas near a heated surface, as was investigated canonically in Chapter 4, has also remained an active area of research. As discussed in Chapter 1, there exist no correlations that collapse hot surface ignition data from systems of varying geometry, composition, and thermodynamic state. Empirical correlations are useful in system design, but are limited to the range of tested conditions. This presents a significant challenge because hot surface ignition problems are known to have extreme sensitivity to operational conditions ranging over 1500 K. These limitations highlight the need for a generalizable ignition framework that can account for diverse geometries, compositions, and thermodynamic states.

In this chapter, we seek to develop an analytical model based on theory for correlating and predicting critical ignition temperatures that can be generalized to arbitrary fuels, thermodynamic conditions, and geometries. The classical models of ignition from adiabatic reactors and hot surfaces will be critically analyzed. Important conclusions will then be utilized in formulating an analytical model for ignition near a hot surface.

5.2 Thermal explosion theory

The simplest model of ignition is described in zero dimensions. Here we consider the system of a lumped, adiabatic reactor where thermal losses of any kind are neglected. The formulation applies high activation energy asymptotic approximations (Frank-Kamenetskii, 1939b) as well as density variation through the reaction order to arrive at an analytical solution. The result is adapted from Bane et al. (2010b).

We start with writing the enthalpy, h, as a function of temperature, T, and mass fraction, Y, as

$$h = h(T, Y) \tag{5.1}$$

The enthalpy can then be differentiated with respect to time using the chain rule. For a constant pressure system, $dh/dt = 0$ and therefore,

$$\frac{dh}{dt} = \frac{\partial h}{\partial T}\frac{dT}{dt} + \frac{\partial h}{\partial Y}\frac{dY}{dt} = 0 \tag{5.2}$$

Noting that the heat capacity at constant pressure, $c_p = \partial h/\partial T$ and specific heat capacity, $q = \partial h/\partial Y$, Eq. (5.2) can be written as

$$c_p\frac{dT}{dt} + q_c\frac{dY}{dt} = 0 \tag{5.3}$$

We assume a one-step kinetic system where $R \rightarrow P$. Thus, only one mass conservation equation needs to be written. It is written for a reacting, zero-dimensional system as

$$\frac{dY}{dt} = \frac{\dot{\Omega}}{\rho} = \frac{W\dot{\omega}}{\rho} \tag{5.4}$$

where $\dot{\Omega}$ is the formation rate, $\dot{\omega}$ is the specific formation rate, and W is the molar mass. $\dot{\omega}$ is assumed to have an Arrhenius form as

$$\dot{\omega} = A[O]^{n_O}[F]^{n_F}\exp\left(-\frac{E_a}{RT}\right) \tag{5.5}$$

where A is the pre-exponential constant, [F] and [O] are the molar concentrations of fuel and oxidizer, respectively, and n_O and n_F are empirical reaction orders. Using the ideal gas law, the concentrations [O] and [F] can be written in terms of the species mole fraction and mixture density as

$$\dot{\omega} = A\left[\frac{x_O}{W_O}\rho\right]^{n_O}\left[\frac{x_F}{W_F}\rho\right]^{n_F}\exp\left(-\frac{E_a}{RT}\right) \tag{5.6}$$

After some algebraic manipulation, Eq. (5.6) can be substituted into Eq. (5.4)

$$\frac{dY}{dt} = \left(AW\frac{x_O^{n_O}x_F^{n_F}}{W_O^{n_O}W_F^{n_F}}\right)\rho^{n_O+n_F-1}\exp\left(-\frac{E_a}{RT}\right) \tag{5.7}$$

Defining the overall reaction order $n = n_O + n_F$, Eq. (5.3) can be rewritten as

$$\frac{dT}{dt} = \frac{q_c}{c_p}\left(AW\frac{x_O^{n_O}x_F^{n_F}}{W_O^{n_O}W_F^{n_F}}\right)\rho^{n-1}\exp\left(-\frac{E_a}{RT}\right) = \frac{q_c}{c_p}Z\rho^{n-1}\exp\left(-\frac{E_a}{RT}\right) \tag{5.8}$$

where $Z = AW\frac{x_O^{n_O}x_F^{n_F}}{W_O^{n_O}W_F^{n_F}}$.

Frank-Kamenetskii realized that under the assumption of a large activation energy, $E_a/RT >> 1$, the exponential term in Eq. (5.8) becomes sharply peaked and while temperature variations are small in absolute value, they are significant in the reaction rate (Frank-Kamenetskii, 1939a). Thus, by applying a small temperature rise, Eq. (5.8) can be linearized and solved analytically. The temperature is rewritten as:

$$T \approx T_0 + T' \tag{5.9}$$

where T' is a small perturbation around the initial temperature, T_0, and $T' << T_0$. Eq. (5.8) becomes

$$\frac{dT'}{dt} = \frac{q_c}{c_p} Z\rho^{n-1} \exp\left(- \frac{E_a}{RT_0 \cdot (1 + T'/T_0)} \right) \tag{5.10}$$

$1/(1 + \frac{T'}{T_0})$ can be Taylor-expanded about T_0 as

$$\frac{1}{1 + \frac{T'}{T_0}} = 1 - \frac{T'}{T_0} + \left(\frac{T'}{T_0}\right)^2 - \left(\frac{T'}{T_0}\right)^3 + \left(\frac{T'}{T_0}\right)^4 + \ldots \tag{5.11}$$

Taking the first two terms, we can approximate

$$\frac{1}{1 + \frac{T'}{T_0}} \approx 1 - \frac{T'}{T_0} \tag{5.12}$$

Eq. (5.12) can be substituted into Eq. (5.10) and rewritten in terms of the Frank-Kamenetskii parameter, $\frac{E_a}{RT_0^2}$, as

$$\begin{aligned} \frac{dT'}{dt} &= \frac{q_c}{c_p} Z\rho^{n-1} \exp\left[- \frac{E_a}{RT_0}\left(1 - \frac{T'}{T_0}\right)\right] \\ &= \frac{q_c}{c_p} Z\rho^{n-1} \exp\left(- \frac{E_a}{RT_0}\right) \exp\left(\frac{E_a}{RT_0^2} T'\right) \end{aligned} \tag{5.13}$$

Defining $\phi = \frac{E_a}{RT_0^2} T'$, Eq. (5.13) can be recast as

$$\frac{d\phi}{dt} = \left[\frac{q_c}{c_p} Z\rho^{n-1} \frac{E_a}{RT_0^2} \exp\left(- \frac{E_a}{RT_0}\right)\right] \exp(\phi) \tag{5.14}$$

$$= \left(\frac{1}{\tau_i}\right) \exp(\phi) \tag{5.15}$$

where the expression in front of the exponential is lumped into a single term, τ_i, as

$$\boxed{\tau_i = \frac{c_p}{q_c}\frac{RT_0^2}{E_a}\rho^{-n+1}\frac{1}{Z}\exp\left(\frac{E_a}{RT_0}\right)} \tag{5.16}$$

It is easy to see that from the differential equation defined by Eq. (5.14), ϕ will tend towards infinity in finite time. Integrating with the initial condition, $\phi(0) = \phi_0$,

$$\int \exp(-\phi)d\phi = \int \frac{1}{\tau_i}dt \rightarrow \exp(\phi) = \exp(-\phi_0) - \frac{t}{\tau_i} \tag{5.17}$$

$$\phi(t) = -\ln\left[\exp(-\phi_0) - \frac{t}{\tau_i}\right] \tag{5.18}$$

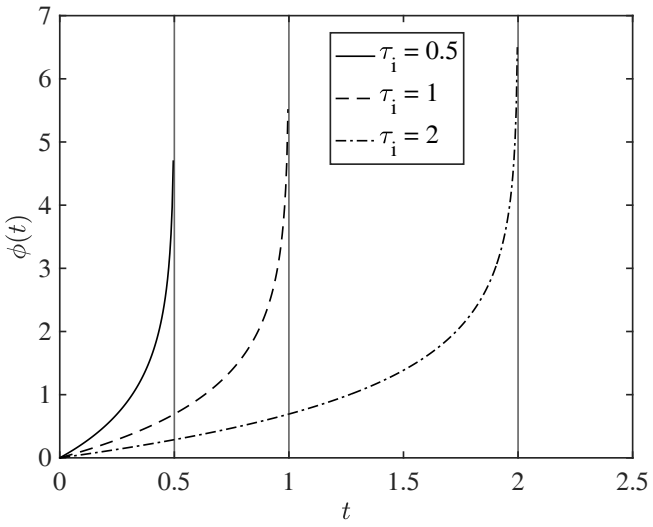


Figure 5.1: $\phi(t)$ vs. t.

Figure 5.1 shows the behavior of Eq. (5.18) for an initial condition $\phi_0 = 0$ and three constant values of τ_i. As τ_i is increased, the time when the singularity in the solution occurs increases. For a constant value of τ_i, $\phi(t) \rightarrow \infty$ as $t \rightarrow \tau_i$. Therefore, τ_i, is labeled as the *ignition delay time*.

Differentiating Eq. (5.16) with respect to ρ at constant T_0 and rearranging terms, the reaction order can be calculated as

$$\boxed{n = -\frac{\rho}{\tau_i}\left(\frac{\partial \tau_i}{\partial \rho}\right)_{T_0} + 1} \tag{5.19}$$

Similarly, E_a can be calculated by first using the ideal gas law to rewrite Eq. (5.16) as

$$\tau_i = \frac{c_p}{q_c}\frac{RT_0^{n+1}}{E_a}\left(\frac{p}{R}\right)^{-n+1}\frac{1}{Z}\exp\left(-\frac{E_a}{RT_0}\right) \tag{5.20}$$

Differentiating Eq. (5.20) with respect to T_0 at constant p and with algebraic manipulation, the activation energy can be written as

$$\boxed{E_a = RT_0\left[-\frac{T_0}{\tau_i}\left(\frac{\partial \tau_i}{\partial T_0}\right)_p + (n+1)\right]} \tag{5.21}$$

The usefulness of this model is in estimating the ignition delay time and reaction progression in systems where thermal energy transport can be neglected (i.e., shock tubes, rapid compression machines (RCMs), and stirred reactors). As will be discussed in Section 5.4, the formulation presented is still crucial in constructing an analytical model of ignition near a hot surface including detailed chemical kinetics where thermal losses exist.

5.3 The theory of thermal ignition near a hot surface

5.3.1 The Zeldovich solution

In 1939, Zeldovich was interested in expanding the ideas on thermal explosion presented in Section 5.2 to a gas slab between two different fixed temperatures, where critical conditions could be found from the steady-state energy equation. That is to say, for supercritical flammable system (i.e., it will ignite), a steady solution will not exist and therefore the critical state can be determined from balancing diffusion with heat release with specific boundary conditions (Zeldovich, 1939). He wrote the one-dimensional steady-state energy equation including chemical reaction and thermal diffusion with constant thermal properties as

$$0 = \lambda\frac{d^2T}{dx^2} + q_c\dot{\Omega} \tag{5.22}$$

where $\dot{\Omega}$ is the formation rate. While Zeldovich did not include the reaction order in his formulation, it is included in the derivation presented here for consistency with the adiabatic, lumped explosion theory presented in Section 5.2. It was assumed that reactant depletion was negligible in this analysis. $\dot{\Omega}$ can be written more generally with the effect from the reaction order as

$$\dot{\Omega} = A'\rho^n\exp\left(-\frac{E_a}{RT}\right) \tag{5.23}$$

where the new pre-exponential $A' = A \cdot (x_O^{n_O} x_F^{n_F})/(W_O^{n_O} W_F^{n_F})$ is defined in terms of the original A along with the mole fraction and molecular weight of the fuel and oxidizer. The steady-state energy balance then becomes

$$0 = \lambda \frac{d^2T}{dx^2} + q_c A' \rho^n \exp\left(- \frac{E_a}{RT} \right) \tag{5.24}$$

Zeldovich realized that the heat release near the hot wall was important and used the Frank-Kamenetskii (1939a) approximation of the Arrhenius term in Eq. (5.24), but expanded instead about the hot wall temperature, T_H. This was done by first assuming a small temperature rise from the hot wall temperature, and rewriting the temperature as

$$T \approx T_H + T' \tag{5.25}$$

Substituting this expression into Eq. (5.24), we obtain

$$0 = \lambda \frac{d^2T}{dx^2} + q_c A' \rho^n \exp\left(- \frac{E_a}{RT_H} \cdot \frac{1}{(1 + T'/T_H)} \right) \tag{5.26}$$

Taylor-expanding $1/(1 + \frac{T'}{T_H})$ about T_H and taking only the first two terms as

$$\frac{1}{1 + \frac{T'}{T_H}} = 1 - \frac{T'}{T_H} + \left(\frac{T'}{T_H} \right)^2 - \left(\frac{T'}{T_H} \right)^3 + \left(\frac{T'}{T_H} \right)^4 + \ldots \approx 1 - \frac{T'}{T_H} \tag{5.27}$$

Substituting Eq. (5.27) into Eq. (5.24), we obtain

$$\begin{aligned} 0 &= \lambda \frac{d^2T'}{dx^2} + q_c A' \rho^n \exp\left[- \frac{E_a}{RT_H} \left(1 - \frac{T'}{T_H} \right) \right] \\ &= \lambda \frac{d^2T'}{dx^2} + q_c A' \rho^n \exp\left(- \frac{E_a}{RT_H} \right) \exp\left(\frac{E_a}{RT_H^2} T' \right) \end{aligned} \tag{5.28}$$

Eq. (5.28) can be transformed using the dimensionless variables,

$$\theta = \frac{E_a}{RT_H} \cdot \frac{T' - T_H}{T_H} \quad ; \qquad \xi = x \cdot \left[\frac{E_a}{RT_H} \frac{q_c}{c_p T_H} \frac{A' \rho^{n-1}}{\kappa} \exp\left(- \frac{E_a}{RT_H} \right) \right] \tag{5.29}$$

into

$$\frac{d^2\theta}{d\xi^2} = -\exp(\theta) \tag{5.30}$$

Here we see that the inclusion of the reaction order in the formulation of the Arrhenius expression for the energy release merely changes the nondimensionalization of the spatial coordinate, ξ, and does not effect the mathematical conclusions that will emerge from the analysis. Zeldovich cleverly realized that

$$\frac{d^2\theta}{d\xi^2} = \frac{1}{2}\frac{d}{d\theta}\left(\frac{d\theta}{d\xi}\right)^2 \tag{5.31}$$

which allow for an exact first integral as

$$\frac{d\theta}{d\xi} = \pm\left[-2\int_0^\theta e^{\theta'}\,d\theta'\right]^{1/2} \tag{5.32}$$

where the point of adiabaticity at the hot wall (attributed to van't Hoff as the van't Hoff condition)

$$\left.\frac{d\theta}{d\xi}\right|_{\xi=0} = 0 \tag{5.33}$$

was assumed. The significance of this assumption is discussed in more detail in Section 5.3.2. The negative solution is taken in Eq. (5.32) as the physical solution. Carrying out the integration

$$\frac{d\theta}{d\xi} = -[2(1-e^\theta)]^{1/2} \tag{5.34}$$

The solution to Eq. (5.34) can be found via a substitution or by ansatz recognizing the functional form as

$$\theta(\xi) = -2\cdot\ln\left[\cosh\left(\frac{\xi}{\sqrt{2}}\right)\right] \tag{5.35}$$

The first integral described by Eq. (5.34) proves to be quite useful as describing critical conditions for the system. Observing that far from the hot surface, $\xi \to \infty$, $T \to T_C$ and $T_C << T_H$. In addition if E_a is large, in the limit, $\theta \to -\infty$. Thus,

$$\boxed{\lim_{\xi\to\infty}\frac{d\theta}{d\xi} = -\sqrt{2}} \tag{5.36}$$

Eq. (5.36) defines a critical temperature gradient far from the hot surface at the critical conditions for the self-heating quasi-steady state. Converting back to physical units,

$$\left.\frac{dT}{dx}\right|_c = \left.\frac{d\theta}{d\xi}\right|_c \cdot \frac{dT}{d\theta}\cdot\frac{d\xi}{dx} \tag{5.37}$$

$$= \sqrt{2}\cdot\left[\frac{RT_H^2}{E_a}\cdot\frac{q_c}{c_p}\cdot\frac{A'\rho^{n-1}}{\kappa}\exp\left(-\frac{E_a}{RT_H}\right)\right]^{1/2} \tag{5.38}$$

5.3.2 The Thomas and Bowes solution

A major assumption used in Zeldovich's analysis in Section 5.3.1 was that in the critical solution, the van't Hoff condition, $d\theta/d\xi|_{\xi=0} = 0$ was used. In practice, this has been shown to be incorrect (Bane et al., 2011; Boeck et al., 2019; Schoeffler and Shepherd, 2023). Instead, an ignition kernel forms close to the wall where the gas temperature exceeds the wall temperature prior to thermal runaway. Thomas and Bowes (1961) addressed this issue in the theoretical formulation. They solved the non-dimensionalized steady-state energy equation as

$$\frac{d^2\theta}{dz^2} = -\delta \cdot \exp(\theta) \tag{5.39}$$

where the Frank-Kamenetskii parameter,

$$\delta = \frac{E_a}{RT_H} \cdot \frac{q_c}{c_p T_H} \cdot \frac{A'\rho^{n-1}L^2}{\kappa} \exp\left(-\frac{E_a}{RT_H}\right) \tag{5.40}$$

was not expressed inside the independent variable as was done with the stretched spatial coordinate, ξ, in Zeldovich's analysis, $z = x/L$ is the nondimensional spatial coordinate, and

$$\theta = \frac{E_a}{RT_H} \cdot \frac{T' - T_H}{T_H} \tag{5.41}$$

is the same nondimensional temperature as Zeldovich. Once again, we include the reaction order in the Arrhenius term for consistency with the thermal explosion theory and Zeldovich's solution derived in Section 5.2 and 5.3.1, respectively. The inclusion only affects the nondimensionalization and does not change the mathematical conclusion. Thomas and Bowes applied the boundary conditions

$$\theta(z = 0) = 0 \tag{5.42}$$

$$\theta(z = 2) = \theta_0 \tag{5.43}$$

without the use of the van't Hoff condition. The exact solution is found as

$$\theta = \theta_m - 2 \cdot \ln\left[\cosh\left((z - z_m)\sqrt{\frac{\delta\exp(\theta_m)}{2}}\right)\right] \tag{5.44}$$

which is similar to the solution found by Zeldovich in Eq. (5.35) but instead allows for a temperature maximum, θ_m, at location, z_m, away from the wall.

For the case of an isothermal cold wall, the critical state was found as

$$\delta_c = \frac{P_c^2}{\sinh^2 P_c} \cdot \exp\left(-\frac{\theta_0}{2}\right) \cdot \left(\cosh P_c - \cosh\frac{\theta_0}{2}\right) \tag{5.45}$$

$$\cosh\frac{\theta_0}{2} = \cosh P_c + \frac{P_c \cdot \sinh P_c}{2(1 - P_c \cdot \coth P_c)} \tag{5.46}$$

$$\theta_m = \ln\left(\frac{P_c^2}{2\delta_c}\right) \tag{5.47}$$

$$z_m = 2 \cdot \frac{\cosh^{-1}\left[\exp\left(\theta_m/2\right)\right]}{P_c} \tag{5.48}$$

where $P_c = \sqrt{2\delta_c \exp(\theta_m)}$ and θ_0 is the nondimensional temperature at the cold surface. Solutions can be found by parametrically varying P_c and computing δ_c, θ_0, θ_m, and z_m to use in Eq. 5.44.

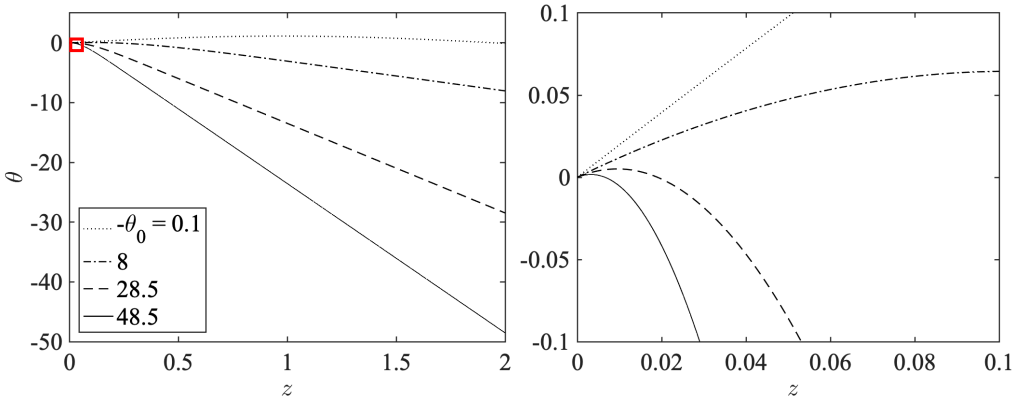


Figure 5.2: Thomas and Bowes critical solutions of θ vs. z for various values of θ_0 (left) and a zoomed in portion immediately next to the hot surface, denoted by a red box (right).

Figure 5.2 plots the critical Thomas and Bowes solutions for various values of $-\theta_0$. For small values of $-\theta_0$, the maximum occurs far from the wall. For example, when $\theta_0 = 0.1$, $z_m = 1$. However, as $-\theta_0$ increases, the temperature maximum becomes increasingly close to $\theta(z = 0)$ and z_m becomes exceedingly close to the wall.

The solutions by Thomas and Bowes can be compared to Zeldovich for various values of $-\theta_0$. This is shown in Figure 5.3. For the Zeldovich solution, the van't Hoff condition can be seen at $z = 0$ followed by a linear decrease in θ far away from the wall. This is consistent with Eq. (5.36). A maximum can be seen in θ for the Thomas and Bowes solution. Large differences can be seen when $-\theta_0 = 0.1$

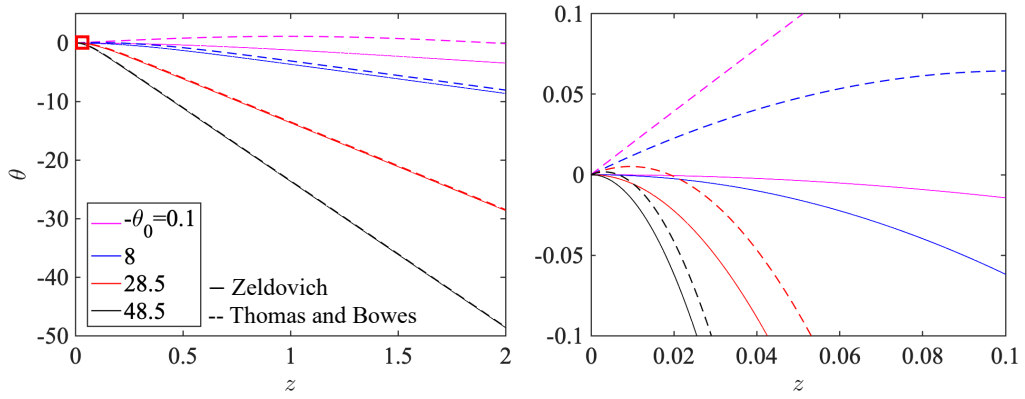


Figure 5.3: Comparison of critical solutions of θ vs. z for various values of θ_0 for Zeldovich and Thomas and Bowes (left) and a zoomed in portion immediately nex to the hot surface, denoted by a red box (right).

between the two solutions. However, as $-\theta_0$ is increased, the Thomas and Bowes solution becomes increasingly close to Zeldovich's solution. For shown curves at $-\theta_0 = 28.5$ and 48.5, the two solutions appear indistinguishable far away from the wall with small differences visible close to the wall when the van't Hoff condition is assumed.

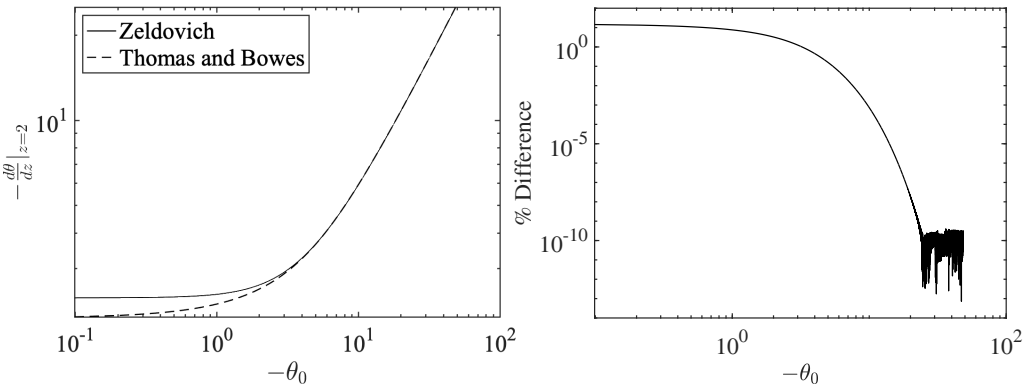


Figure 5.4: Nondimensional temperature gradient evaluated at the cold wall, $-\frac{d\theta}{dz}|_{z=2}$ vs. $-\theta_0$ (left) and the percent difference vs. $-\theta_0$ (right).

The conclusion presented from Zeldovich's analysis in Eq. (5.36) is that a critical temperature gradient exists far away from the hot wall. This conclusion can be investigated with the analysis from Thomas and Bowes. The nondimensional temperature gradient, $d\theta/dz$, can be evaluated at the cold wall for both solutions

as a function of θ_0. This is shown in Figure 5.4 which shows the absolute value of the gradient at the cold wall for the two solutions and the difference between the two. The negative of the gradient is taken to allow logarithmic presentation. For small values of $-\theta_0$, a difference in the critical gradient is seen with a maximum difference of 14.35%. However, as $-\theta_0$ is increased to even modest values, the critical gradients found from each solution collapse. From looking at the percent difference, this collapse is exponential, seeing small errors < 1% for $-\theta_0 > 3$ and bottoming out at machine precision. While omitted here for brevity, Thomas and Bowes find the asymptotic values of Eq. (5.45) - (5.48) for large values of $-\theta_0$ as $P_c \approx \theta_0/2$, $\delta_c \approx \theta_0^2/8$, $z_m \approx 8/\theta_0^2$, and $\theta_m \approx 4/\theta_0^2$. Differentiating Eq. (5.44), we recognize that in the limit as $-\theta_0 \to \infty$ evaluated far away from the hot wall, at $z = 2$

$$\lim_{-\theta_0\to\infty} \left.\frac{d\theta}{dz}\right|_{c,z=2} = \lim_{-\theta_0\to\infty} \left[-P_c \cdot \tanh\left(P_c - \frac{1}{2}P_c z_m\right)\right] = -\frac{\theta_0}{2} = -\sqrt{2\delta_c} \tag{5.49}$$

Rewriting Eq. (5.49) in terms of Zeldovich's stretched coordinate, ξ

$$\lim_{-\theta_0\to\infty} \left.\frac{d\theta}{dz}\right|_{c,z=2} = -\sqrt{2\delta_c} \to \boxed{\lim_{\xi\to\infty} \frac{d\theta}{d\xi} = -\sqrt{2}} \tag{5.50}$$

Eq. (5.50) is identical to the critical temperature gradient far from the wall found by Zeldovich using the van't Hoff condition in Eq. (5.36). The important conclusion found by Thomas and Bowes in relation to the present work is that as long as there is a sufficiently *large activation energy*, E_a, the use of the van't Hoff condition, as Zeldovich had assumed, is correct in the theoretical formulation of the problem. The subsequent mathematically analyses that show the existence of a critical temperature gradient are valid as long as E_a is large.

5.3.3 Boundary layer formulation

The classical work on ignition near a hot surface by Zeldovich and later by Thomas and Bowes solved a simple problem balancing heat release from a single-step chemical reaction with thermal diffusion. Theoretical work on ignition near hot surfaces was revisited more generally through the 1970s-1990s to extend to fluid flow systems by formulating the problem as a boundary layer solved with the method of matched asymptotic expansions. For a large activation energy, chemical reaction is confined to a thin, near-wall reactive-diffusive layer since the temperature drop even slightly away from the wall would prevent any chemical reaction. Thus, the inner reactive-diffusive layer is matched to a chemically frozen outer layer. As

was shown in the energy equation analyses presented in Chapter 4 and by several other authors (Melguizo-Gavilanes et al., 2016; Melguizo-Gavilanes et al., 2017a; Melguizo-Gavilanes et al., 2017b; Coronel et al., 2018; Boeck et al., 2019), this separation of regions is generally observed in practice. Figure 5.5 shows a schematic of this problem formulation which has been used to study ignition in many different problem including near hot spherical particles (Law, 1978a), stagnation point flows (Law, 1978b), as well as boundary layers (Mendez et al., 1986; Treviño and Méndez, 1991).

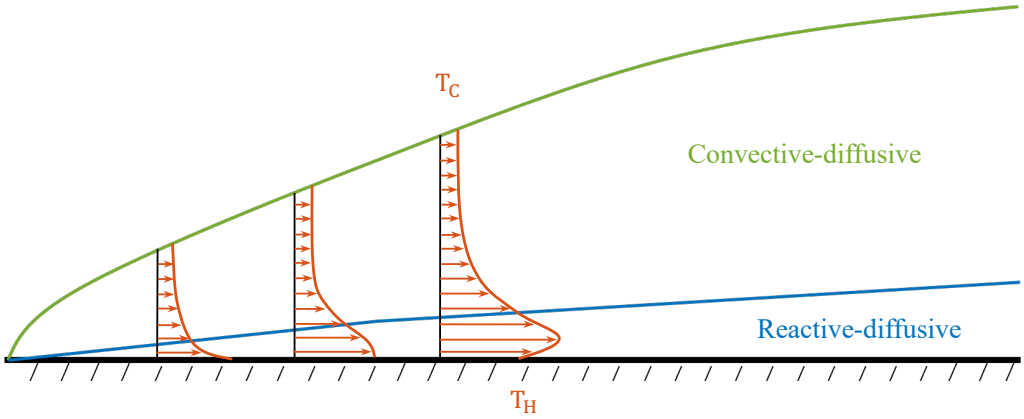


Figure 5.5: Inner reactive-diffusive region and outer convective-diffusive region of a reactive thermal layer as formulated for a large activation energy flammable mixture.

Inner expansion

Following Law's description (Law, 2010), the reactive-diffusive problem solved is identical to that solved previously be Zeldovich and Thomas and Bowes, but using an arbitrary normal direction, **n** as

$$0 = \lambda \frac{d^2 T_{in}}{d\mathbf{n}^2} + q_c \dot{\Omega} \tag{5.51}$$

Reactant consumption is considered negligible and the reacting layer is assumed to be quasi-planar. The inner solution is expanded as

$$T_{in} = T_H + \epsilon\theta(\chi) + O(\epsilon^2) \tag{5.52}$$

Law nondimensionalized Eq. (5.51) as

$$\frac{d^2\theta}{d\chi^2} = -\frac{\Delta}{2}\exp(\theta) \tag{5.53}$$

subject to $\theta(0) = 0$ where $\epsilon = RT_H^2/E_a$ is a small parameter and $\chi = \beta\mathbf{n}/\epsilon$ where $\beta = -(\partial T_0/\partial \mathbf{n})_0$ is introduced to simplfy matching to the outer expansion where T_0 is the leading order outer solution. β is the negative of the temperature gradient immediately at the hot surface in the chemically frozen limit where $E_a \to \infty$ and the thickness of the inner reactive-diffusive region $\to 0$. Notice the form of the nondimensionalization in Eq. (5.53) is nearly identical to the form solved by Zeldovich and Thomas and Bowes 60 years earlier.

Outer Expansion

Law expressed the outer solution as

$$T_{out} = T_0(\mathbf{x}, t) + \epsilon T_1(\mathbf{x}, t) + O(\epsilon^2) \tag{5.54}$$

To match the outer and inner solutions, the leading order term is expanded about $\mathbf{x} = 0$ in the direction of $\mathbf{n}$ and recast with the definition of χ as

$$T_0(\mathbf{n}, t) = T_0(0, t) + \mathbf{n}\left(\frac{\partial T_0}{\partial \mathbf{n}}\right)_0 + O(\mathbf{n^2}) \tag{5.55}$$

$$= T_H - \epsilon\chi + O(\epsilon^2) \tag{5.56}$$

The outer solution can then be finally expressed as

$$T_{out}(\chi, t) = T_H + \epsilon[T_1(0, t) - \chi] + O(\epsilon^2) \tag{5.57}$$

Matching and Solution

To solve Eq. (5.53), additional boundary conditions must be specified through matching of the inner and outer expansions. Formally, this is written as

$$(\theta + \chi)_{\chi\to\infty} = (T_1)_{n\to 0} \tag{5.58}$$

$$\left(\frac{d\theta}{d\chi}\right)_{\chi\to\infty} = -1 \tag{5.59}$$

Law solves the inner problem in Eq. (5.53) with the matching conditions and arrive at an expression for maximum temperature increase parameter, $(\theta + \chi)_{\chi\to\infty}$ as

$$(\theta + \chi)_{\chi\to\infty} = \ln\left\{\frac{4}{\Delta}\left[\frac{1 \mp (1 - \Delta)^{1/2}}{1 \pm (1 - \Delta)^{1/2}}\right]\right\} \tag{5.60}$$

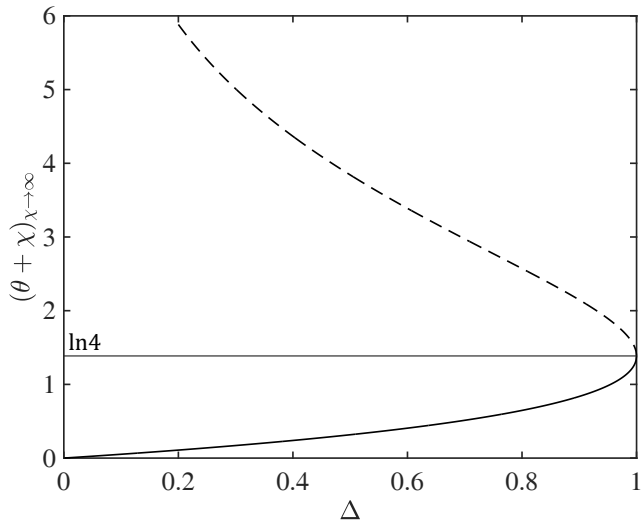


Figure 5.6: Maximum temperature increase parameter $(\theta+\chi)_{\chi\to\infty}$ vs. Δ. Upper and lower branches of Eq. (5.60) are indicated by (- -) and (−), respectively. Reproduced from Law (2010).

Figure 5.6 plots the upper and lower branches of $(\theta+\chi)_{\chi\to\infty}$ vs. Δ for the ignition of a combustible gas near a hot surface. Law asserts that ignition can occur when heat release from chemical reaction exceeds losses from the wall (the van't Hoff condition). From the Thomas and Bowes analysis, we know this assumption is justified for a large activation energy. That is, ignition can occur for $\Delta \geq 1$. Thus, he defines a critical Damköhler number as $\Delta_c = 1$, at $(\theta+\chi)_{\chi\to\infty} = \ln 4$. Converting back to dimensional variables, the critical condition can be written as

$$\left|\frac{\partial T}{\partial \mathbf{n}}\right|_c \cdot \left[\frac{2RT_H^2}{E_a}\cdot\frac{q_c}{c_p}\cdot\frac{A'\rho^{n-1}}{\kappa}\exp\left(-\frac{E_a}{RT_H}\right)\right]^{-1/2} = 1 \tag{5.61}$$

where the reaction order has been included in the rate law for consistency. This is identical to the large activation energy solutions first discovered by Zeldovich in Eq. (5.38) and later verified by Thomas and Bowes in Eq. (5.50). The significance of Law's solution is that the same result could be obtained from a boundary layer formulation where the critical temperature gradient conclusion could be prescribed from a generalized *chemically frozen* fluid mechanics flow solution immediately at the hot wall in the limit of infinite activation energy.

In 2023, Schoeffler and Shepherd (2023) interpreted the result as such and used the solution to define two characteristic length scales from the critical condition defined

in Eq. (5.61). The first was a heat transfer length scale described by the temperature gradient immediately at the wall from a chemically frozen flow and normalized by c_p/q_c as

$$\Lambda_c = \left(\frac{c_p}{q_c} \left| \frac{dT}{d\mathbf{n}} \right|_{\mathbf{n}=0} \right)^{-1} \tag{5.62}$$

and the second was a chemical length scale to describe the ignition kernel written as

$$\ell_k = \left[\frac{RT_H^2}{E_a} \cdot \frac{c_p}{q_c} \cdot \frac{A' \rho^{n-1}}{\kappa} \cdot \exp\left(-\frac{E_a}{RT_H} \right) \right]^{-1/2} \tag{5.63}$$

where in the critical solution the two length scales are related by $\Lambda_c = 1/\sqrt{2} \cdot \ell_k$. This theoretically defines the critical condition for ignition near a hot surface. Eqs. (5.62) and (5.63) suggest that the heat transfer length scale necessary to quantify critical conditions for ignition depends on the temperature gradient, something that is *intrinsic* to each hot surface ignition problem. This conclusion also provides an explanation as to why hot surface thermal ignition problems exhibit such variable results in critical surface temperatures as have been observed in the literature and the lack of ability of empirical correlations to extrapolate to a wide range of reacting flow systems.

5.4 An analytical model for ignition near a hot surface

Eqs. (5.62) and (5.63) are substantial in their implications for ignition near a hot surface. However, the range of application is still limited as the formulation is built on a one-step global chemical reaction and knowledge of kinetics and thermodynamic variables such as q_c and A' are necessary. Real systems can have hundreds of species and thousands of chemical reactions rendering direct application in their current form impossible. Here, we manipulate the equations and incorporate ideas from adiabatic thermal explosion theory discussed in Section 5.2 to recast Eqs. (5.62) and (5.63) in terms of measurable quantities from detailed kinetic mechanisms. We return to the critical condition in Eq. (5.61) and normalize the heat transfer length scale instead by the hot wall temperature, T_H, to simply the subsequent analyses as

$$\boxed{\Lambda_c \approx \frac{T_H}{\left| \partial T/\partial \mathbf{n} \right|_{\mathbf{n}=0,\text{frozen}}}} \tag{5.64}$$

where the expression is now approximate. This is because for real systems, a large but *finite*, activation energy, E_a, exists. This leaves us with a slightly different expression than Eq. (5.63) for the chemical length scale, which is now written as

$$\ell_k = \left[\frac{E_a}{RT_H} \cdot \frac{c_p T_H}{q_c} \cdot \frac{\kappa}{A' \rho^{n-1}} \cdot \exp\left(\frac{E_a}{RT_H} \right) \right]^{1/2} \tag{5.65}$$

where $\Lambda_c = 1/\sqrt{2} \cdot \ell_k$ still defines the theoretical critical condition for ignition near a hot surface. With some algebraic manipulation,

$$\ell_k = \frac{E_a}{RT_H} \cdot \left[\frac{RT_H}{E_a} \cdot \frac{c_p T_H}{q_c} \cdot \frac{\kappa}{A' \rho^{n-1}} \cdot \exp\left(\frac{E_a}{RT_H} \right) \right]^{1/2} \tag{5.66}$$

$$= \frac{E_a}{RT_H} \cdot \sqrt{\tau_i \kappa} \tag{5.67}$$

the chemical length scale can be expressed in terms of the asymptotic expression for the thermal explosion time,τ_i, derived in Section 5.2 in Eq. (5.16) where the initial temperature is taken as the wall temperature. Writing the activation energy in its reduced form, $\Theta = E_a/RT_H$, the final expression for ℓ_k is written as

$$\boxed{\ell_k = \Theta \cdot \sqrt{\tau_i \kappa}} \tag{5.68}$$

Reformulating the heat transfer and chemical length scales as Eq. (5.64) and (5.68) allow for application to systems with detailed chemical models. Figure 5.7 shows the procedure for applying the analytical model to realistic reacting systems and is adapted from Schoeffler and Shepherd (2023) to include zero-dimensional simulations in the formulation of ℓ_k. Chemically frozen flow solutions can be solved through CFD to compute Λ_c and θ, τ_i, and κ can be computed to determine ℓ_k from zero-dimensional adiabatic ignition simulations and thermodynamic/transport tables.

A number of assumptions go into the current presentation of the characteristic length scales that should be considered:

1. The activation energy must be sufficiently large. In particular, from the Thomas and Bowes analysis, $-\theta_0 > 3$ such that errors in assuming the van't Hoff condition are <1%
2. Negligible reactant depletion prior to ignition
3. The thin reactive-diffusive layer in the matched asymptotic expansion formulation is assumed to be quasi-planar
4. The reactive-diffusive layer is quasi-steady
5. Convective effects are negligible close to the hot surface

6. The fuel of interest does not have a negative temperature coefficient "NTC" region brought about by significant heat release in low temperature chemical reaction pathways

7. The hot surface is not catalytic

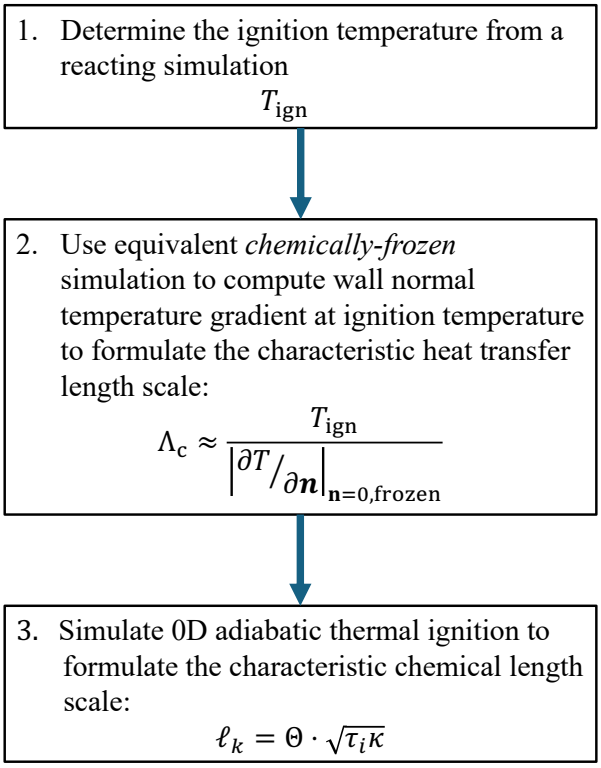


Figure 5.7: Procedure for determining the critical length scales, Λ_c and ℓ_k for a reacting system.

Formally, all of these conditions must be satisfied, although condition (1) is the most important of all as the entire theoretical framework for the problem relies on this assumption. Without it, the critical temperature gradient conclusion does not exist. Luckily, as will be shown in Section 6.2.4, condition (1) is generally satisfied quite easily for hydrocarbon and ammonia oxidation, although it is necessary to check for the fuel of interest. Conditions (2)-(5) are also often satisfied, but depend on the specifics of the problem being investigated. For example, if the wall temperature is high, but thermal losses are also high enough to prevent ignition, the fuel can rapidly deplete in the thin layer near the wall prior to reaching a point of criticality, violating condition (2). Condition (6) can be broken for heavy hydrocarbons that have low temperature energy release chemical pathways. This low temperature energy release

often does not occur near the wall and can effect the structure of the thermal layer, whereas the mathematics of the theory assume this region to be chemically inert. This is shown in Chapter 4. For the purposes of the developed analyses, condition (7) is assumed, but may not be true generally.

Provided that all seven conditions are met, it should be possible to correlate ignition data using Eqs. (5.64) and (5.68). As will be shown in the following chapters, the developed model will be used to predict critical conditions for various reacting flow systems. With knowledge of 5 parameters: T_H, Θ, κ, τ_i, and $dT/dx|_{H,\text{frozen}}$, the critical conditions for thermal ignition near a hot surface are fully defined.

5.5 Summary and conclusions

In this chapter, relevant classical theories of ignition are presented and discussed in the context of hot surface thermal ignition. First, analytical expressions for the activation energy, E_a, and ignition delay time, τ_i, for a zero-dimensional, adiabatic system are presented. Analysis of the theory of ignition near a hot surface, as first discovered by Zeldovich, revealed that a critical temperature gradient exists far away from the wall in the critical solution of a reacting-diffusive layer. Subsequent analysis by Thomas and Bowes showed that the use of the van't Hoff condition as well as the critical temperature gradient solution exists as long as the activation energy is large. In practice, we found that differences > 1% between the two solutions occur for values of $-\theta_0 < 3$. Formulating the problem as a boundary layer allows the critical temperature gradient to be defined by a chemically frozen flow solution.

Taking the critical solution from the theory, a novel analytical model was presented in terms of two characteristic length scales, Λ_c and ℓ_k, that describe a relation between heat transfer and chemical reaction. Incorporating the asymptotic expression for the ignition delay time, we develop a methodology for computing Λ_c and ℓ_k for systems with detailed chemistry. With knowledge of 5 parameters: T_H, Θ, κ, τ_i, and $dT/dx|_{H,\text{frozen}}$, the critical conditions for thermal ignition near a hot surface are fully defined. The result is a collective effort of over 80 years of theoretical analyses from various authors. Further developments added in this chapter provides the basis for understanding published ignition thresholds for practical hot surface ignition problems.

Chapter 6

NUMERICAL CALCULATION OF Λ_c AND ℓ_k

In this chapter, the characteristic length scales, Λ_c and ℓ_k, derived in Chapter 5 will be determined numerically for various fuels, wall temperatures, and pressures. First, the theoretical configuration analyzed by Thomas and Bowes (1961) will be examined to determine Λ_c and ℓ_k. Then, an alternative and substantially more efficient approach will be described and carried out to determine values of Λ_c and ℓ_k covering several orders of magnitude of the parameter space. The characteristic length scales will be plotted in accordance with the developed hot surface ignition model. The quality of the model and constant of proportionality between the scales will be determined statistically from correlating the numerical data. Lastly, limitations of the ignition model formulation for fuels with substantial exothermic low-temperature chemical pathways will be identified and illustrated.

6.1 The characteristic thermal layer thickness, Λ_c

6.1.1 Calculating Λ_c from the Thomas and Bowes problem

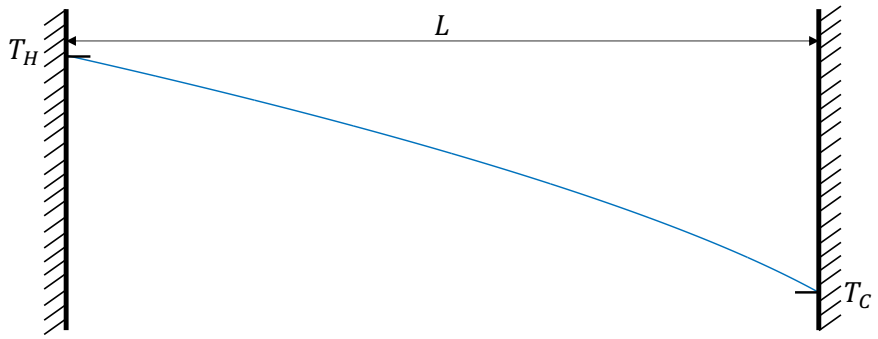


Figure 6.1: The Thomas and Bowes problem.

The most precise approach to finding Λ_c is to solve the one-dimensional problem of a reacting gas slab between two walls separated by some distance, L, and held at some constant temperatures T_H and T_C, as was done analytically by Thomas and Bowes (1961) assuming one-step kinetics and no depletion. We use instead detailed chemical mechanisms and allow for reaction progress and depletion as this is more realistic. A chemically frozen simulation was run to obtain the steady-state temperature profile used as an initial condition. This way, any changes in the thermal

layer and/or thermal runaway is caused by heat release from chemical reaction. A schematic of the problem set up and initial temperature profile is shown in Figure 6.1. Notice the initial temperature profile is not linear as would be predicted from the analytical solution of the standard heat equation. This is because the thermal properties are not constant and are instead a function of temperature. This leads to a near linear decrease in temperature near the hot wall temperature, $T_H \sim 1000$ K, and a more significant role off near the cold wall temperature, $T_C = 300$ K.

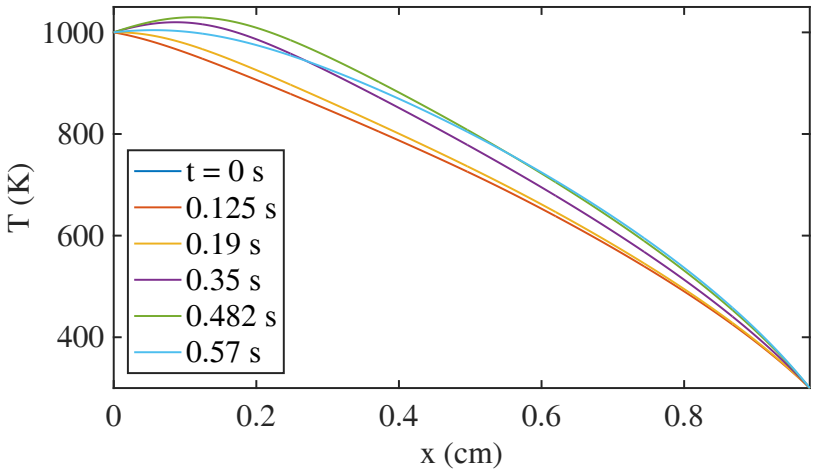


Figure 6.2: Subcritical solution for a mixture of stoichiometric nC_6H_{14}/air at 1 bar with $T_H = 1000$ K, $T_C = 300$ K, $L = 0.976174$ cm.

The critical length, L_c, between the two walls at which an ignition solution can be found can be determined by systematically varying L and observing whether the system ignites or fails to ignite and instead slowly depletes until equilibrium is obtained. This process was carried out for a hot wall temperature of $T_H = 1000$ K and $T_C = 300$ K at 1 bar of pressure for a stoichiometric mixture of nC_6H_{14} and air. A reduced kinetic mechanism for the high temperature oxidation of nC_6H_{14} from the full Dagaut mechanism was used (Dagaut and Cathonnet, 2006). It consists of 62 species and 230 reactions. A series of 33 simulations were run for various L and the results are presented.

Figure 6.2 plots how a typical subcritical solution temperature distribution evolves over time. In this cases, the presented result is near the critical length, with a spacing between the hot and cold walls, $L = 0.976174$ cm. At 0.125 s, the profile is nearly indistinguishable from the prescribed initial temperature profile. However at 0.19 s, an increase in the temperature near the hot wall can be seen. This is a direct result of

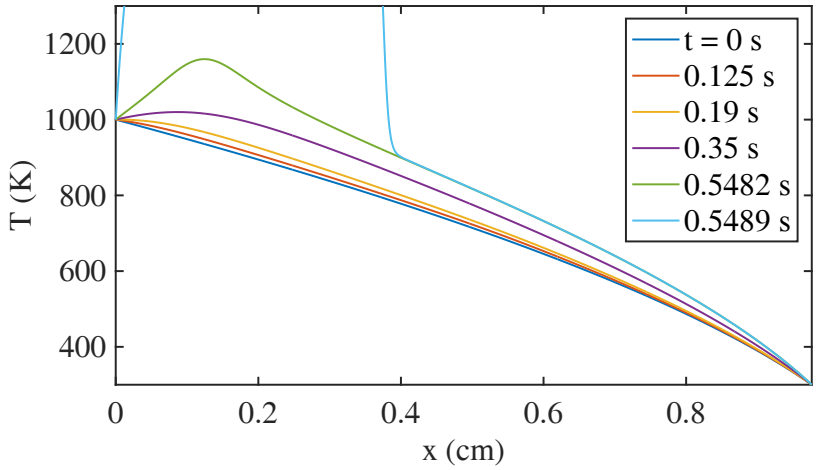


Figure 6.3: Supercritical solution for a mixture of stoichiometric nC_6H_{14}/air at 1 bar with $T_H = 1000$ K, $T_C = 300$ K, $L = 0.976178$ cm.

heat release from chemical reaction. At 0.35 s and 0.482 s, a progressive increase in the entire temperature profile can be seen, with local temperatures in the would-be ignition kernel near the hot wall exceed the wall temperature by 20 K and 30 K, respectively. At 0.57 s, the temperature can be seen dropping again signaling that this selection of L is close to igniting, but is still subcritical. This also highlights the slight inaccuracy of the van't Hoff condition since the solution did not ignite even though gas temperatures exceeded the wall temperature at a certain time by 30 K.

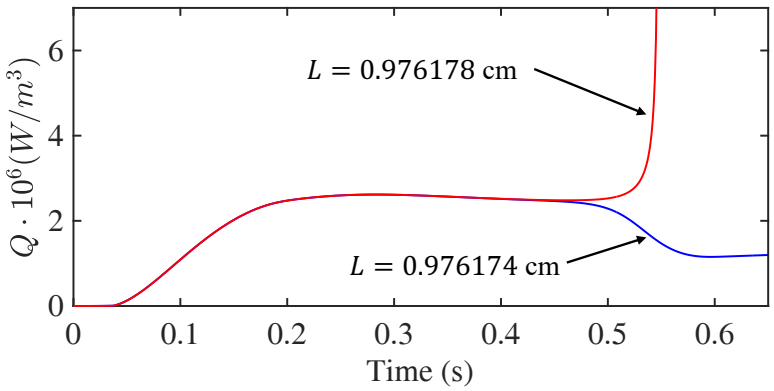


Figure 6.4: Maximum heat release, Q, over time for $L = 0.976174$ cm (subcritical) and $L = 0.976174$ cm (supercritical) cases. nC_6H_{14}/air at 1 bar with $T_H = 1000$ K, $T_C = 300$ K.

If L is increased even slightly, we see a completely different solution. Figure 6.3 plots the temperature profiles at different times for $L = 0.976178$ cm, which is only 0.04 μm larger than the subcritical case. At 0.125 s and 0.19 s, we see similar behavior to the temperature evolution shown for a subcritical solution in Figure 6.2 where a small increase in temperature is seen in the profile, primarily concentrated near the hot wall where chemical reaction and heat release are most significant. A similar ignition kernel is seen at 0.35 s, where the local gas temperature near the hot wall exceeds T_H by 20 K. Past 0.35 s, a different behavior exists. Instead of a slow recession of the temperature back to equilibrium like what was seen in the subcritical case, ignition occurs at 0.5482 s with a rapid increase in temperature about 0.125 cm away from the wall. 0.7 ms later, at 0.5489 s, a flame front can be seen propagating outwards towards the cold wall.

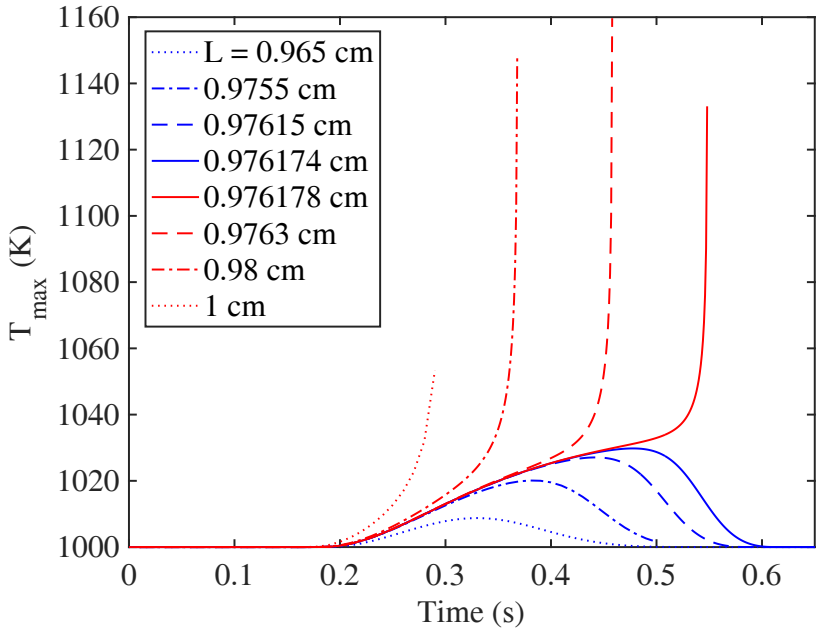


Figure 6.5: Maximum temperature, $T_{\max}$ vs. time for cases near L_c for a mixture of stoichiometric nC_6H_{14}/air at 1 bar with $T_H = 1000$ K and $T_C = 300$ K.

Figure 6.4 plots the maximum heat release from chemical reaction in the domain for the subcritical and supercritical solutions separated by 0.04 μm in L described by Figures 6.2 and 6.3. The curves are nearly indistinguishable for 0.4 s during the cooking phase, where the heat release rises over the first 0.2 s, and stays relatively constant until depletion or thermal runaway. An exceedingly small increase in L (which can be understood as an exceedingly small decrease in the thermal loss),

transitions the solution from a subcritical solution manifold to supercritical one. This also demonstrates the remarkable sensitivity of ignitable systems to certain parameters. This is more easily seen from Figure 6.5 which plots the maximum temperature in the domain over time for a range of L near the critical spacing, L_c. For large L, such as $L = 1$ cm, thermal losses near the hot surface are minimal. Thus, the maximum temperature rises above the wall temperature and ignites quickly, after only 0.3 s. As L is decreased, ignition still occurs, but happens at a much later time. For example, the smallest L resulting in ignition, $L = 0.976178$ cm, ignition occurs after 0.55 s. A further decreasing of L, numerically by as small as 0.04 μm, causes a transition to a subcritical solution where thermal losses are too significant to ignite the mixture before significant depletion occurs.

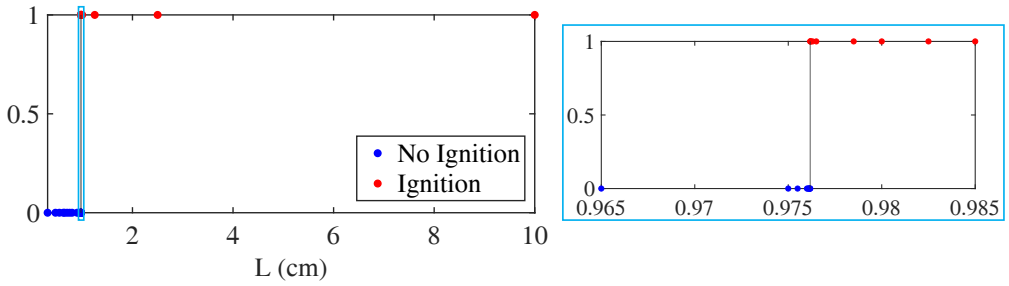


Figure 6.6: Ignition classification vs. L for a mixture of stoichiometric nC_6H_{14}/air at 1 bar with $T_H = 1000$ K and $T_C = 300$ K.

Figure 6.6 plots the ignition classification for all 33 cases simulated for 0.3125 cm $< L <$ 10 cm. A classification of "1" means the configuration ignited whereas a "0" means the configuration did not ignite. A zoomed region shows with more detail, the transition from no ignition cases to ignition cases. From the data, the critical spacing between the hot and cold wall is determined with uncertainty in the sixth decimal point as $L_c = 0.976176$ cm. Thus, the characteristic heat transfer length scale, Λ_c, defined by Eq. (5.64) can be calculated using the prescribed wall temperature, $T_H = 1000$ K and the temperature gradient from the steady-state chemically frozen solution with $L_c = 0.976176$ cm. The steady temperature and temperature gradient profiles are shown in Figure 6.7. At the hot surface, $|dT/dx|_{x=0} = 49720.2 \pm 0.1$ K/m, where the uncertainty is taken as the temperature gradients at the wall from chemically frozen solutions of the two closest sub- and supercritical solutions found numerically at $L = 0.976174, 0.976178$ cm. This uncertainty is $\approx 0.0001\%$ the value of the critical temperature gradient. Therefore, we have high confidence in the number being the correct critical value for this mixture and value for T_H and T_C.

Finally, Λ_c is computed for the stoichiometric nC_6H_{14}/air with $T_H = 1000$ K at 1 bar as $\Lambda_{c,TB} = 0.0201$ m where the subscript TB indicates that it comes from the Thomas and Bowes problem.

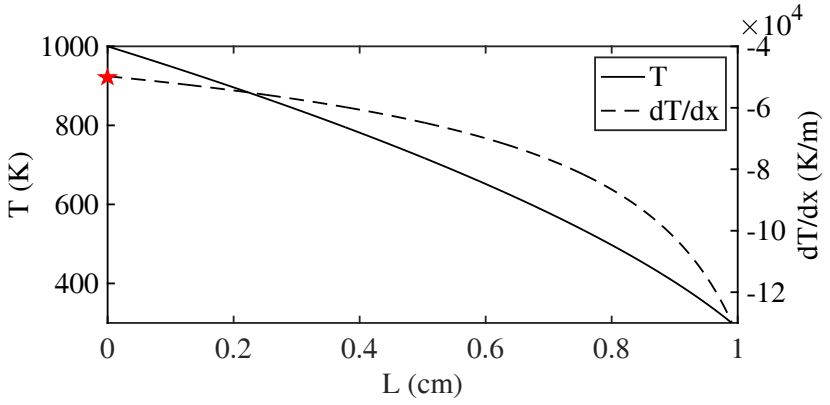


Figure 6.7: Chemically frozen steady-state temperature profile and temperature gradient vs. L for the critical spacing, $L_c = 0.976176$ cm with a mixture of stoichiometric nC_6H_{14}/air at 1 bar with $T_H = 1000$ K and $T_C = 300$ K. The star indicates the critical temperature gradient as theoretically defined in Eq. (5.64).

The single critical value of Λ_c determined for this mixture and thermodynamic state was determined from 33 transient one-dimensional solutions with a detailed kinetic mechanism. To develop a line of criticality for a wide range of fuels, pressures, and surface temperatures, we need many more values of Λ_c. Thus, this process would be quite time and computationally expensive as it requires thousands of dimensional detailed chemical simulations. An alternative approach is necessary to more quickly map the parameter space to find critical Λ_c.

6.1.2 Calculating Λ_c from a diffusing thermal layer

A slightly different one-dimensional problem can be solved to quickly determine Λ_c for a given mixture, pressure, and temperatures, T_H and T_C. Instead of having a reacting gas slab between two walls of fixed temperature, a cold gas is suddenly exposed to a nonreactive heated wall set at temperature T_H on one side and is open to some atmosphere on the other at some cold temperature, T_C and pressure, P. This problem is illustrated schematically in Figure 6.8. A thermal layer develops adjacent to the wall and diffuses away. This simplified problem is similar to what was described by Kumar (1989) to model hydrogen-air ignition near a hot surface, although the emphasis in that study was on extrapolating delay times to obtain a minimum ignition temperature. Instead, we can use the problem to focus on the

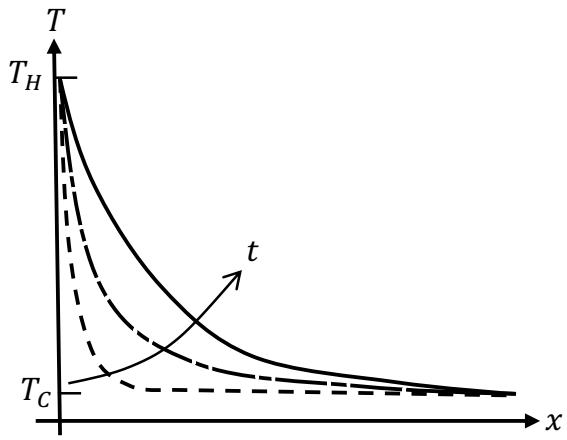


Figure 6.8: Schematic of the one-dimensional diffusing thermal layer problem.

relevant fluid mechanic parameters for hot surface thermal ignition as described by the theoretical framework presented in Chapter 5, the hot wall temperature and temperature gradient. After some delay time, t^*, the thermal layer will grow through a critical thickness where the mixture will ignite. The critical temperature gradient can then be extracted from an equivalent frozen simulation immediately at the wall at t^* as $dT/dx|_c$. By formulating the problem this way, all thermal layer thicknesses are tested with a single simulation to determine the critical point making it significantly more efficient than parametrically varying L as is required by the Thomas and Bowes problem. This approach is valid for obtaining critical conditions in accordance with the theory and should match Λ_c determined from the Thomas and Bowes problem as long as two additional conditions are met:

a. The chemical reaction timescale is sufficiently fast relative to the thermal diffusion timescale such that the correct critical thermal layer thickness can be identified

b. The thermal diffusion timescale is sufficiently fast to reach a critical thermal layer thickness before the mixture undergoes significant reactant depletion and can no longer ignite

To compare with Λ_c found from the Thomas and Bowes problem numerical solution, the diffusing thermal layer problem was simulated for the same conditions: stoichiometric nC_6H_{14}/air, $T_H = 1000$ K, $T_C = 300$ K, and 1 bar. The same reduced kinetic mechanism for the high temperature oxidation of nC_6H_{14} was used. Figure

6.9a plots the temperature distribution at various times for the reacting diffusing thermal layer. For early times, the thermal layer evolves primarily through thermal diffusion as heat release from chemical reaction is still negligible. At 0.36 s, the thermal layer continues diffusing outwards, but evidence of heat release from chemical reaction can be seen close to the hot wall as the van't Hoff condition is reached. Ignition is then classified at 0.4162 s when the gas temperature has exceeded the wall temperature by 150 K as it has been successfully employed by other authors (Melguizo-Gavilanes et al., 2016; Schoeffler and Shepherd, 2023). A short time after, at 0.4167 s, the flame front can be seen running away from the wall through the thermal layer. The equivalent frozen simulation is presented in Figure 6.9b.

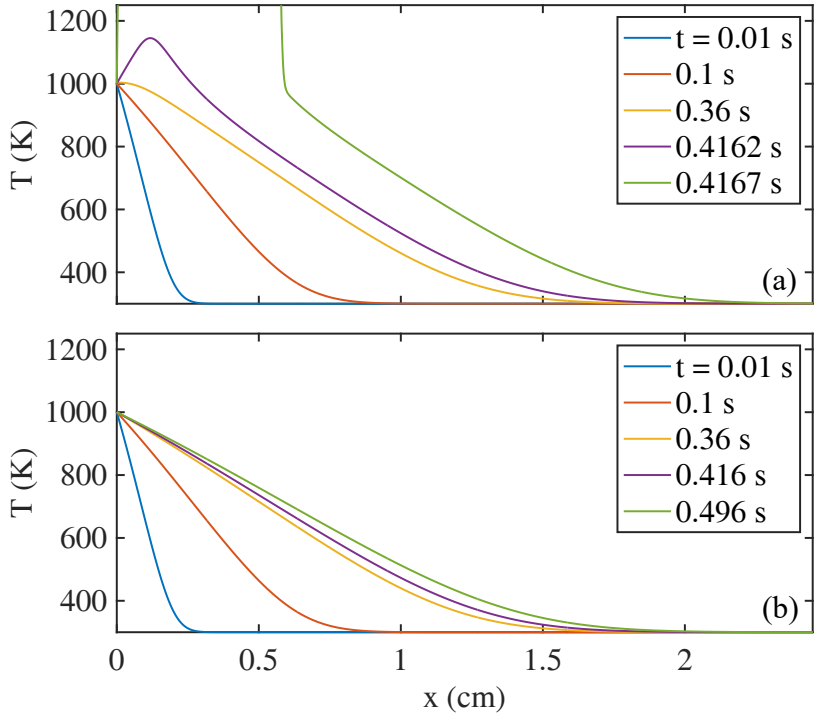


Figure 6.9: Temperature distributions for the diffusing thermal layer problem at various times for (a) reacting and (b) chemically frozen. Stoichiometric nC_6H_{14}/air, T_H = 1000 K, T_C = 300 K, and 1 bar.

Condition (a) presented in the problem formulation can easily be checked. The unsteady heat equation with negligible convective effects an constant properties is written as

$$\frac{\partial T}{\partial t} = \kappa \frac{\partial^2 T}{\partial x^2} \tag{6.1}$$

which has a known analytical solution,

$$T(x,t) = T_H + (T_C - T_H) \cdot \text{erf}\left(\frac{x}{2\sqrt{\kappa t}}\right) \tag{6.2}$$

where the thermal layer thickness grows like $\delta_T \sim \sqrt{\kappa t}$. Thus, the thermal layer growth timescale can be estimated at time ignition time, t^*, as

$$t_{\text{thermal diffusion}} \approx \frac{\delta_T^2(t^*)}{\kappa} \tag{6.3}$$

For the chemically frozen diffusing thermal layer presented for nC_6H_{14}/air in Figure 6.9b, $\delta_T(t^*) \approx 1.5$ cm. For $\kappa \approx 1.8 \cdot 10^{-4}$ m^2/s, $t_{\text{thermal diffusion}} \approx 1.25$ s. As is presented in Section 6.2.2, the chemical timescale can be estimated from the zero-dimensional ignition delay time, τ_i. For this system, $t_{\text{chemical}} \approx \tau_i = 0.0489$ s. $t_{\text{chemical}} << t_{\text{thermal diffusion}}$ by two orders of magnitude. Therefore, condition (a) is satisfied and the diffusing thermal layer formulation should introduce minimal errors in determining the critical Λ_c for this case compared to the Thomas and Bowes formulation.

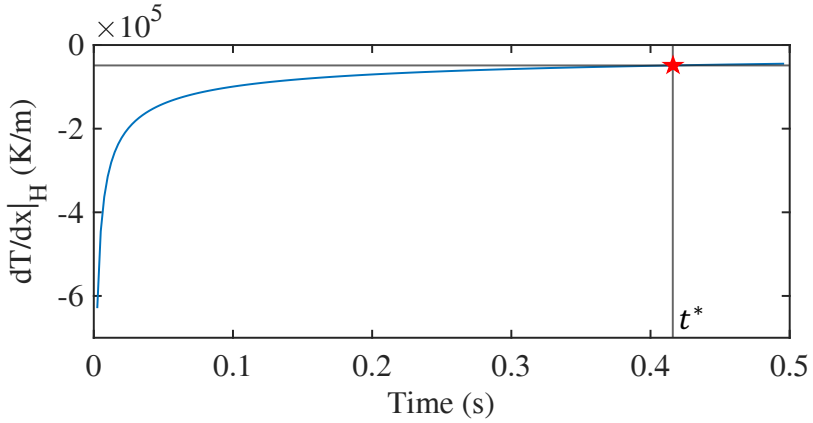


Figure 6.10: Temperature gradient evaluated immediately at the hot wall, $dT/dx|_H$, vs. time from the chemically frozen diffusing thermal layer shown in Figure 6.9b. The star indicates the critical temperature gradient at the wall at t^* determined from the reacting equivalent simulation in Figure 6.9a.

Λ_c can be computed from the temperature gradient immediately at the wall from the frozen flow simulation shown in Figure 6.9b. This is shown in Figure 6.10. The red star indicates $dT/dx|_{H,c}$ defined by the ignition time, t^*. From the plot, $dT/dx|_{H,c} = -48770.9$ K/m and using Eq. (5.64), the characteristic heat transfer length scale is computed as $\Lambda_{c,diffusing} = 0.0205$ m. Comparing with the result

from the Thomas and Bowes problem, Λ_c are in agreement with a difference of 1.9%. We determine that critical values of Λ_c can be obtained from the one-dimensional diffusing thermal layer formulation provided conditions (a) and (b) are met.

To compute critical Λ_c for a wide range of mixtures, temperatures, and pressures, the one-dimensional diffusing thermal layer formulation was used. For each configuration, t_{chemical} was compared with $t_{\text{thermal diffusion}}$ to ensure condition (a) was satisfied. Failure to ignite due to depletion for some cases could be observed from the temperature distributions and therefore, cases breaking condition (b) were omitted from correlation.

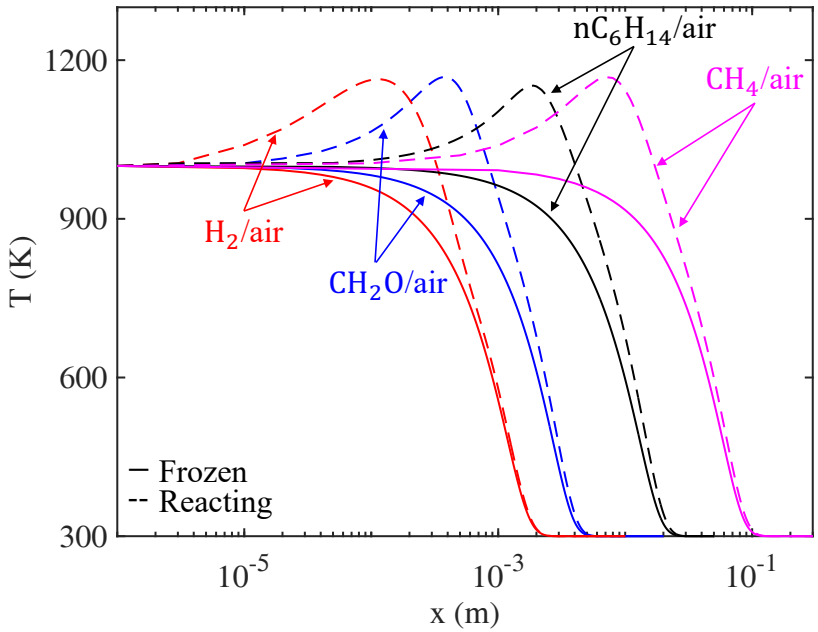


Figure 6.11: Reacting and frozen temperature profiles at the time of ignition, τ, for stoichiometric mixtures of H_2/air, CH_2O/air, nC_6H_{14}/air, and CH_4/air at 1 bar and $T_H = 1000$ K.

Diffusing thermal layers for 57 different mixtures, temperatures, and pressures were simulated in OpenFOAM using the *laminarPimpleSMOKE* custom solver developed by Cuoci et al. (2013a) and Cuoci et al. (2013b). The computational domain size was set to allow the developing thermal layer to be far away from the cold outer boundary, which varied between fuels, temperatures, and pressures. A uniform grid was used where sizes varied to allow sufficient resolution in the ignition kernel ($\sim$ 100 cells). This yielded grid sizes typically from 0.5 μm for the reactive fuels at high temperature and high pressure to 50 μm for low pressures and temperatures

for less reactive fuels. Tested fuels included H_2, CO/H_2, NH_3, CH_2O, CH_4, and nC_6H_{14}. Tested wall temperatures ranged from 1000 K to 1500 K and pressures covered an order of magnitude, ranging from 0.2 bar to 5 bar. A full list of the tested configurations can be found in Appendix D. The ignition delay time was estimated by taking the time at which the gas temperature exceeded the wall temperature by 150 K. Note that this determination of the ignition delay time is empirical and the correct classification of when a given mixture changes from subcritical to supercritical will differ between fuels and thermodynamic states. This can be determined with the Thomas and Bowes model. However, use of defining critical conditions when $t^*(T_{\max} = T_H + 150\ \text{K})$ introduces only small error since $t_{\text{thermal diffusion}} >> t_{\text{chemical}}$. An equivalent frozen simulation was then run for each unique configuration to the determined ignition delay time to find the critical temperature gradient immediately at the wall (114 total simulations: 57 reacting and 57 chemically frozen). In addition to the reduced high temperature kinetic mechanism for nC_6H_{14} previously used, the Foundational Fuel Chemistry Model v1.0 (FFCM1) was used for reacting simulations of H_2, CO/H_2, CH_2O, and CH_4 mixtures (Smith et al., n.d.). The mechanism consists of 38 species and 291 reactions. Reacting simulations with NH_3 used the CRECK mechanism for ammonia oxidation (Stagni et al., 2020; Stagni et al., 2023). It consists of 31 species and 203 reactions.

An example of critical solutions and the equivalent frozen simulations can be seen from Figure 6.11 which plots the temperature profiles at τ for stoichiometric mixtures of H_2/air, CH_2O/air, nC_6H_{14}/air, and CH_4/air at 1 bar and $T_H = 1000$ K. H_2/air mixtures ignited for comparably small thermal layer thicknesses, whereas CH_2O, nC_6H_{14} and CH_4 had increasingly thicker thermal layers at the time of ignition for this thermodynamic condition. Notice also how the size of the ignition kernel grows as the thermal layer thickness grows.

Figure 6.12 plots the computed Λ_c values for all mixtures, wall temperatures, and pressures tested with the one-dimensional diffusing thermal layer model. As the pressure and wall temperature are increased for a given fuel, Λ_c decreases, in some cases up to two orders of magnitude. In general, CH_4 and NH_3 required thicker critical thermal layer thicknesses compared to H_2 and CH_2O mixtures while Λ_c for nC_6H_{14} mixtures lie between. The full range of scales in Λ_c covered by the various fuels and range of wall temperatures and pressures can be visualized, covering four orders of magnitude.

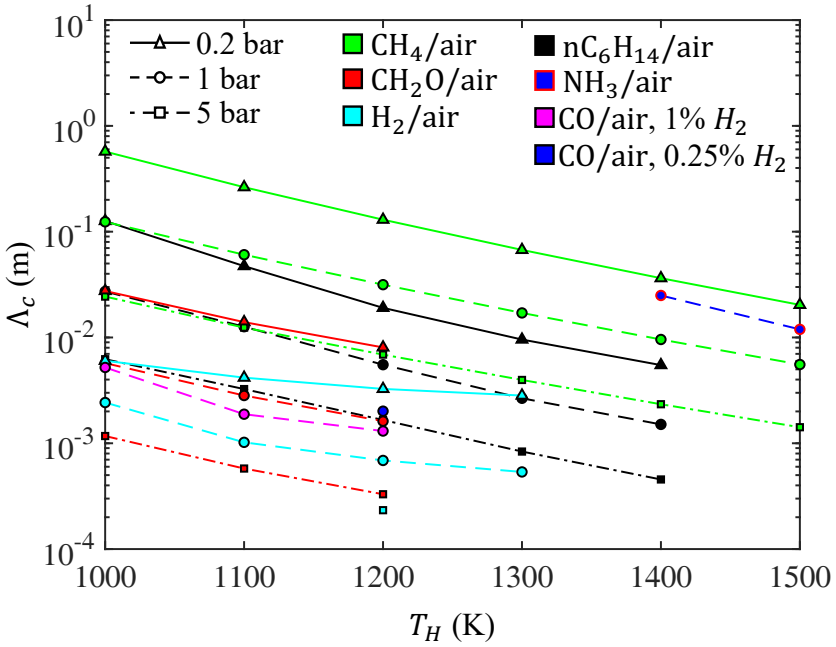


Figure 6.12: Computed Λ_c vs. T_H for all mixtures, wall temperatures, and pressures for the one-dimensional diffusing thermal layer model.

6.2 The characteristic ignition kernel thickness, ℓ_k

6.2.1 The zero-dimensional model

The characteristic ignition kernel thickness, ℓ_k, can be computed from thermodynamic tables and zero-dimensional adiabatic, constant pressure ignition simulations. The equations solved are the unsteady energy equation with only a source term written as

$$\frac{dT}{dt} = -\frac{1}{\rho c_p}\sum_i^N h_i \frac{\dot{\omega}_i W_i}{\rho} \tag{6.4}$$

and an equation for each species, written as

$$\frac{dY_i}{dt} = \frac{\dot{\omega}_i W_i}{\rho} \tag{6.5}$$

where T is the temperature, t is the time, $\dot{\omega}$ is the molar production rate, W is the molecular weight, ρ is the mixture density, c_p is the specific heat capacity at constant pressure, and h is the specific enthalpy. The subscript, i, denotes an individual species and N is the total number of species. The ideal gas law, $P = \rho RT$, was used to calculate the density of the mixture.

Eqs. (6.4) and (6.5) were integrated in MATLAB using the implicit ODE15s variable step, variable order (VSVO) integrator because of its optimization for stiff systems

of ODEs. A relative tolerance of e^{-10} and absolute tolerance of e^{-12} were selected for the integrator. The kinetics and thermochemical properties were computed by Cantera (Goodwin et al., 2021) using chemical mechanisms.

6.2.2 Calculation of the ignition delay time, τ_i

For consistency, the same chemical kinetic mechanisms as those used for the reacting diffusing thermal layer solutions in Section 6.1.2 were used for to compute ℓ_k from the zero-dimensional simulations. Simulations were run for initial temperatures, 900 K< T_0 < 1600 K at 0.2 bar, 1 bar, and 5 bar for stoichiometric mixtures of CH_4, CH_2O, nC_6H_{14}, NH_3, H_2, CO/1% H_2, and CO/0.25% H_2 with air. The zero-dimensional delay time, τ_i, was then estimated from the maximum temperature gradient in time as

$$\tau_i = t\left(\left.\frac{dT}{dt}\right|_{max}\right) \tag{6.6}$$

This is, again, an approximation, but results in negligible errors since the heat release time associated with a rapid increase in temperature is short relative to the time to ignition from the onset of chemical reaction.

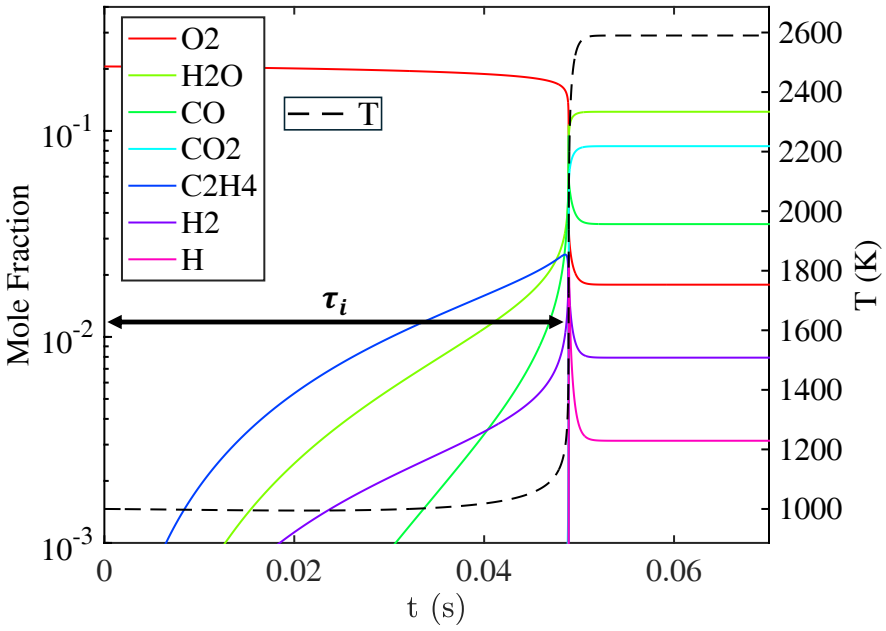


Figure 6.13: Zero-dimensional adiabatic, constant pressure ignition simulation of stoichiometric nC_6H_{14}/air with T_0 = 1000 K at 1 bar. Mole fractions for the top 7 species (ignoring N_2 since it is considered inert) are shown as well as the temperature evolution over time. The ignition delay time, τ_i, is also shown.

Figure 6.13 shows an example zero dimensional adiabatic, constant pressure ignition simulation of stoichiometric nC_6H_{14}/air with T_0 = 1000 K at 1 bar. The temporal evolution of temperature as well as the mole fraction of the top 7 reacting species is shown. From the temperature, we can see a slight dip below T_0 by 5 K in the first $\sim$ 0.03 s prior to thermal runaway. This is typical of heavy hydrocarbon oxidation at high temperature and is attributed to decomposition of the fuel through numerous endothermic cracking reactions. At the end of this pathway is an accumulation of ethene, C_2H_4, and carbon monoxide, CO. Significant water is also formed, but is largely inert after it is formed and does not play a significant role in the thermal runaway process. During ignition rapid, the standard progression of multiplicative OH production and rapid consumption of the O_2 followed by the exothermic reaction CO + OH $\rightarrow$ CO + H drives a rapid increase in temperature from 1000 K to nearly 2600 K. The mixture equilibrates with most significant amounts of products H_2O and CO_2 as well as small amounts of CO, O_2 and H_2. Reaction pathways will vary between different compositions and pressures. However, these differences are accounted for in the analytical model through Θ, κ and τ_i. The ignition delay time can be determined and is illustrated graphically. In this case, τ_i = 0.0489 s.

2,100 total simulations were run to compute τ_i for the 7 fuels examined. High resolution of these curves were required to extrapolate data in the context of computing ℓ_k for arbitrary surface temperatures. Figure 6.14 plots τ_i against the inverse of temperature for the stoichiometric mixtures of the fuels in air at (a) 0.2 bar, (b) 1 bar, and (c) 5 bar. For all pressures and initial temperatures, NH_3 had the largest τ_i followed by CH_4. nC_6H_{14} and CH_2O exhibited progressively lower τ_i compared to NH_3 and CH_4 for a given initial temperature and pressure. Mixtures containing H_2 had relatively low τ_i compared to the other fuels for large initial temperatures. For these fuels, an abrupt increase in τ_i was observed, specifically for 1 bar and 5 bar. Note, the y-axis is logarithmic and covers 10 orders of magnitude which highlights the extreme sensitivity of the ignition delay time on temperature for these mixtures. The transition also occurs for 0.2 bar, but for a much lower temperature than what was included in the parametric study. This crossover temperature was found to transition to higher temperatures as the pressure was increased and can be understood by a shift in dominant reaction pathways from those with HO_2 to those with OH. This is consistent with what has been well documented in the literature (Konnov, 2008; Hashemi et al., 2015). All fuels exhibited a nearly 2 order of magnitude decrease in τ_i as the pressure was increased from 0.2 bar to 5 bar and a nearly 4 order of magnitude decrease from 900 K to 1600 K.

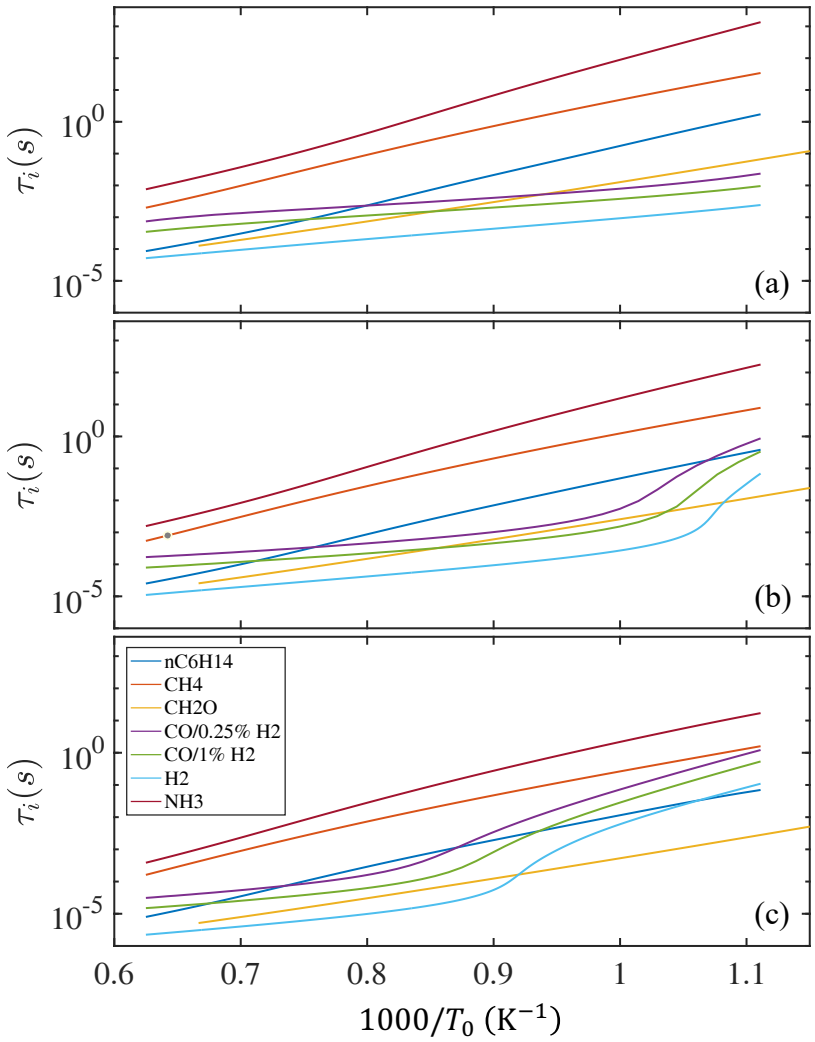


Figure 6.14: Computed ignition delay times as a function of initial temperature for stoichiometric mixtures in air of the tested fuels, nC_6H_{14}, CH_4, CH_2O, CO/0.25% H_2, CO/1% H_2, H_2, and NH_3 for (a) 0.2 bar (b) 1 bar and (c) 5 bar.

τ_i for a given wall temperature, T_H and pressure used for the diffusing thermal layer simulations can then be computed from linear interpolation and used in finding ℓ_k.

6.2.3 Calculation of the thermal diffusivity κ

The thermal diffusivity is defined as the ratio of thermal conductivity to the product of density and heat capacity at constant pressure as $\kappa = \lambda/\rho c_p$. The kinetic mechanisms discussed included thermodynamic and transport data for all species considered.

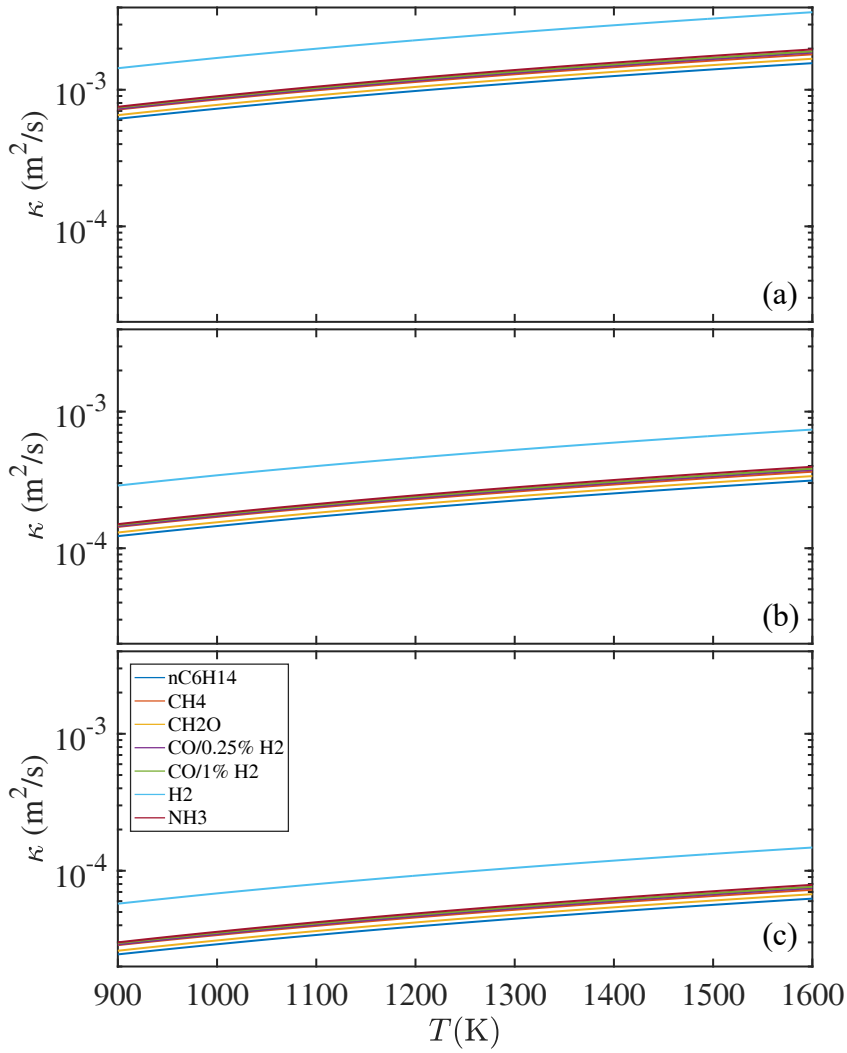


Figure 6.15: Computed thermal diffusivity, κ, as a function of initial temperature for stoichiometric mixtures in air of the tested fuels, nC_6H_{14}, CH_4, CH_2O, CO/0.25% H_2, CO/1% H_2, H_2, and NH_3 for (a) 0.2 bar (b) 1 bar and (c) 5 bar.

Thermodynamic information about c_p for a given molecule, i, is typically given in a "NASA7" polynomial format which tabulates coefficients, a_n, for $c_{p,i} = c_{p,i}(T)$ as

$$\frac{c_{p,i}(T)}{R} = a_1 + a_2 T + a_3 T^2 + a_4 T^3 + a_5 T^4 \tag{6.7}$$

Thermal conductivity for a given molecule is computed using kinetic theory from the Boltzmann equation as

$$\lambda_i = \frac{25}{32} \cdot \frac{k_B}{\sigma_i^2 \Omega^{(2,2)}} \cdot \sqrt{\frac{\pi k_B T}{m_i}} \tag{6.8}$$

where k_B is the Boltzmann constant, σ is the Lennard-Jones diameter, $\Omega^{(2,2)}$ is the collision integral from intermolecular potential interactions, and m_i is the molecular mass. Lennard-Jones parameters needed to define σ and $\Omega^{(2,2)}$ are included in the transport data for all species. The tabulated data for c_p and transport properties can be found in any thermodynamic and transport database, such as Burcat and Ruscic (2005), Yaws (2009), and NIST (2024). Mixture-averaged c_p and λ are then computed as

$$c_p = \sum_i X_i c_{p,i} \qquad ; \qquad \lambda = \sum_i X_i \lambda_i \tag{6.9}$$

With knowledge of the pressure and temperature, ρ can then be computed from the ideal gas law, $\rho = P/RT$. Cantera readily computes the values for ρ, c_p, and λ given a composition, temperature, and pressure. Figure 6.15 plots κ vs T for all tested fuels at (a) 0.2 bar, (b) 1 bar, and (c) 5 bar. Temperature dependence for all fuels is small, with H_2 having the largest κ for all pressures. A two order of magnitude decrease is seen from 0.2 bar to 5 bar. While these changes are modest, they have a secondary effect on the characteristic chemical length scale compared to τ_i, which has significantly larger variation over the same temperature and pressure range.

6.2.4 Calculation of the reduced activation energy, Θ

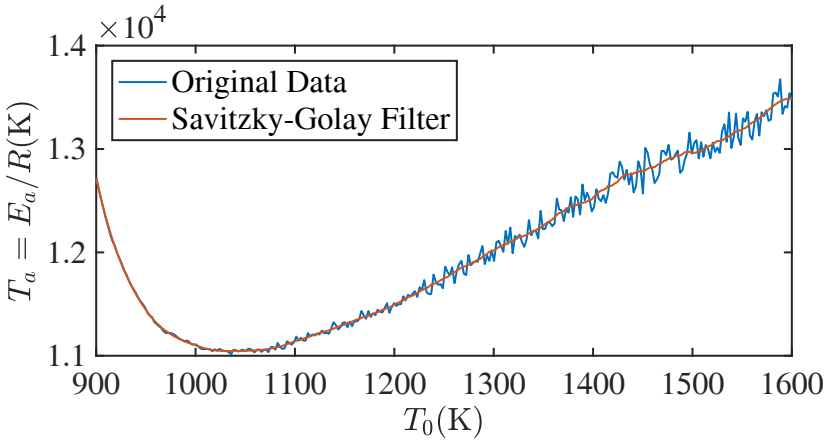


Figure 6.16: Savitzky-Golay filter applied to activation temperature for stoichiometric H_2/air at 0.2 bar.

The activation energy, E_a, used to compute $\Theta = E_a/RT_H$ in solving for ℓ_k can be solved numerically using Eq. (5.21) with the reaction order in Eq. (5.19). The derivatives, $(\partial\tau_i/\partial\rho)_{T_0}$ and $(\partial\tau_i/\partial T_0)_p$ in Eqs. (5.19) and (5.21) can be numerically

estimated using fourth order central differencing as

$$\left(\frac{\partial \tau_i}{\partial \rho_0}\right)_{T_0} \approx \frac{-\tau_{i+2\Delta\rho} + 8\tau_{i+\Delta\rho} - 8\tau_{i-\Delta\rho} + \tau_{i-2\Delta\rho}}{12\Delta\rho} \tag{6.10}$$

$$\left(\frac{\partial \tau_i}{\partial T_0}\right)_{p} \approx \frac{-\tau_{i+2\Delta T} + 8\tau_{i+\Delta T} - 8\tau_{i-\Delta T} + \tau_{i-2\Delta T}}{12\Delta T} \tag{6.11}$$

where $\Delta T = 10$ K and $\Delta\rho = 0.1 \cdot \rho_0$ were chosen empirically based on the best convergence behavior and minimization of noise. It was found that fourth order central differencing produced better convergence of both n and E_a compared to lower order schemes. This is further discussed in Appendix E.

Some noise still exists in computing the derivatives and was filtered out using a Savitzky-Golay filter. Figure 6.16 shows an example of the activation temperature, $T_a = E_a/R$, for a stoichiometric mixture of H_2/air at 0.2 bar along with a Savitzky-Golay filter (3rd order polynomial with 31 point window spacing). Noise fluctuations on the order of 1% can be seen for $T_0 > 1200$ K in the data. This is caused by exceedingly small values of τ_i and machine precision limitations. The Savitzky-Golay fitler was successfully employed to remove this noise.

Since 4th order central differencing requires 4 points, four additional simulations were run to compute each derivative. Therefore, an additional 16,800 simulations were run to solve for the activation energy as a function temperature at 0.2, 1, and 5 bar. Figure 6.17 plots the computed activation temperature, $T_a = E_a/R$, from Eq. (5.21) vs. T_0 for all tested fuels at (a) 0.2 bar, (b) 1 bar, and (c) 5 bar. Non-H_2 fuels have relatively constant T_a across both temperature and pressure. The crossover temperature for H_2 based fuels in this temperature range at 1 bar and 5 bar previously discussed can be seen as a sharp rise in T_a from to as the temperature is decreased.

The activation energies presented in Figure 6.17 can be used to determine whether condition (1) in the analytical model holds. The smallest value of T_a for any of the tested fuels was found to be $\sim 10,000$ K. $-\theta_0$ from the Thomas and Bowes problem can be computed for the bounding temperatures simulated with the diffusing thermal layer. With a cold temperature far from the wall, $T_C = 300$ K and taking this minimum T_a, we find that $-\theta_0 = 7$ and $5.3\bar{3}$ for $T_H = 1000$ K and 1500 K, respectively. A wall temperature of $T_H = 1500$ K yields the lowest value of $-\theta_0$. However, $5.3\bar{3} > 3$. For $-\theta_0 = 5.3\bar{3}$, the difference between the Zeldovich solution and the Thomas and Bowes solution is ~0.1%. Therefore, for all the tested fuels

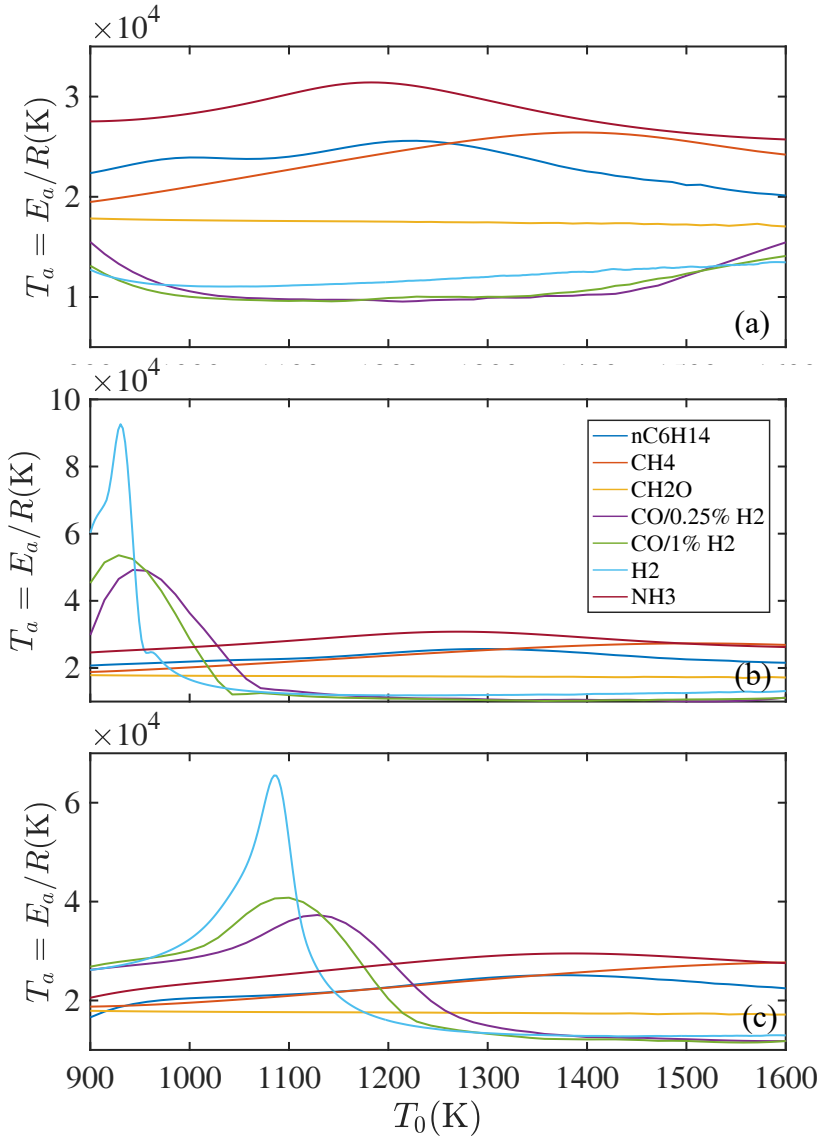


Figure 6.17: Computed activation temperature, $T_a = E_a/R$, as a function of initial temperature for stoichiometric mixtures in air of the tested fuels, nC_6H_{14}, CH_4, CH_2O, CO/0.25% H_2, CO/1% H_2, H_2, and NH_3 for (a) 0.2 bar (b) 1 bar and (c) 5 bar.

and temperature differences in the diffusing thermal layer simulations, a critical temperature gradient for thermal ignition should exist according to theory.

The characteristic chemical length scale, ℓ_k, can then be readily computed for all 57 diffusing thermal layer simulations using the data presented in Figures 6.14, 6.15, and 6.17. Figure 6.18 plots ℓ_k against T_H for all mixtures, wall temperatures, and pressures. Similar to the computed values for Λ_c, as the pressure and wall temperature are increased for a given fuel, ℓ_k decreases. The same trends are

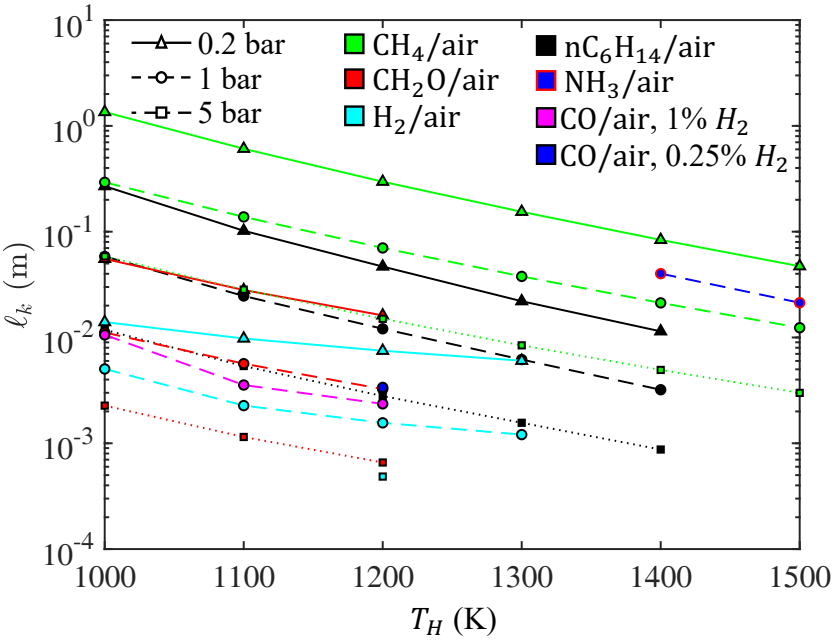


Figure 6.18: Computed ℓ_k vs. T_H for all mixtures, wall temperatures, and pressures for the one-dimensional diffusing thermal layer model.

observed, with CH_4 having the largest ℓ_k for a given pressure and wall temperature followed by NH_3. CH_2O and the H_2 mixtures had the smallest values of ℓ_k with nC_6H_{14} in the middle.

6.3 The line of criticality

After computing Λ_c in Figure 6.12 and ℓ_k in Figure 6.18, the two characteristic length scales can simply be plotted against each other. This is shown in Figure 6.19. Remarkably, all simulation data points collapse over four orders of magnitude and define a line of criticality between sub- and super-critical solutions. For a given (ℓ_k,Λ), a determination of whether a reacting system will ignition can be made based on its relation to the correlated ignition data. That is, if some (ℓ_k,Λ) lie below the correlation, it is subcritical. If it lies above, it is supercritical.

Correlating and statistically analyzing the presented data can be challenging as the results cover such a large range of scales. To this extent, a linear fit between the logarithms can be made as

$$\ln\Lambda_c = 0.97585 \cdot \ln\ell_k - 0.85757 \tag{6.12}$$

where the coefficient of determination, $R^2 = 0.99879$ shows that the variance in

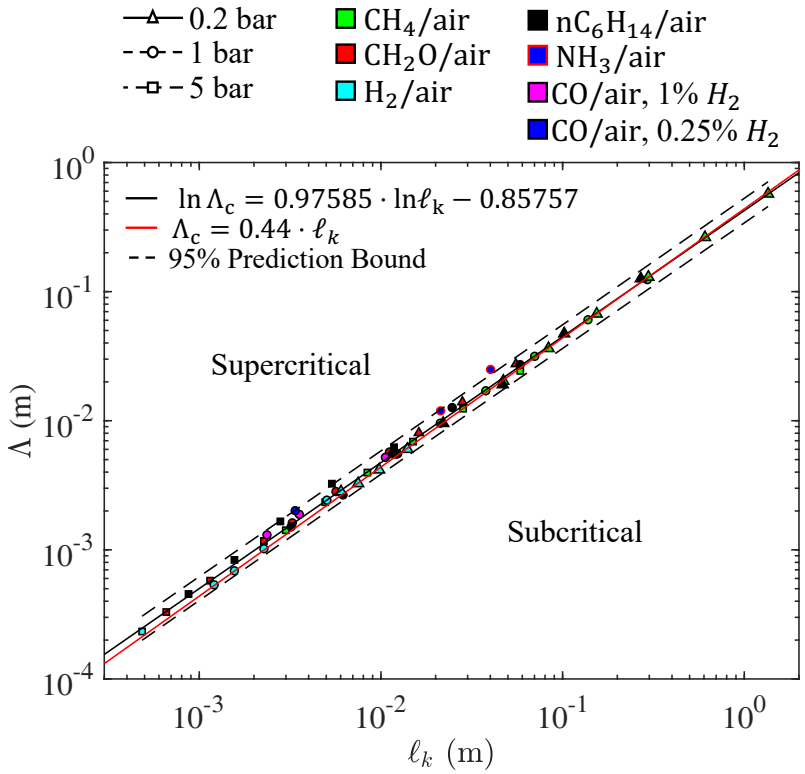


Figure 6.19: Critical values of Λ_c and ℓ_k for the diffusing thermal layer model plotted in $\Lambda - \ell_k$ space.

characteristic scales is remarkably captured by the analytical model. The mean relative error (MRE) also provides a useful metric to assess the variance in the data compared to Eq. (6.12) over a wide range as average error is normalized by the data points themselves. It can be computed as

$$MRE = \frac{1}{n}\sum_{i}^{n}\left|\frac{\Lambda_i - \hat{\Lambda}_i}{\Lambda_i}\right| \tag{6.13}$$

where n is the number of discrete data points. The subscript i denotes a specific data point and $\hat{}$ denotes the predicted value. Therefore, for the fit in Eq. (6.12), MRE = 0.0614 suggesting that the data differs on average from the best fit line by 6.14%. Note, however, that Λ and ℓ_k are both nonlinear functions of temperature, pressure, composition, and the flow field, as Λ encompasses the full non-reactive Navier–Stokes equations and ℓ_k is computed from the stiff and highly nonlinear chemical kinetics. Thus, the difference does not represent the average difference between the predicted and actual ignition temperature. The difference between predicted and actual ignition temperature is significantly smaller which can largely

be attributed to the extreme sensitivity of ℓ_k on the variations in τ_i. This will be shown for various validation cases analyzed in Chapter 7.

To assess the quality of the linear relationship between Λ_c and ℓ_k as predicted in the theoretical analyses (Zeldovich, 1939; Thomas and Bowes, 1961; Law, 2010), a linear best fit line constrained by a zero-intercept is also presented in Figure 6.19 as

$$\Lambda_c = 0.44 \cdot \ell_k \tag{6.14}$$

Providing an R^2 for Eq. (6.14) is not useful as the squared absolute error will disproportionally favor the larger data points. However, the mean relative error can be computed as MRE = 0.0836, suggesting that the data points differ on average from the best fit line by 8.36%.

The results presented in Figure 6.19 suggest a remarkable linear correlation between the two characteristic length scales defined by the theoretical analyses, despite their simple nature. The ratio of characteristic scales defines a critical Damköhler number, $Da_c = \Lambda_c/\ell_k$. In the case of the linear fit, $Da_c = 0.44$. While Eq. (6.14) fits in the 95% prediction bound defined by the logarithmic fit provided in Eq. (6.12), the small differences, especially for small values of ℓ_k, show a slight nonlinearity in the correlated data. Further, the scatter described by the MRE suggests that additional relevant scaling is not captured by the model, such a near wall convection or unsteadiness effects, depletion of the fuel or oxidizer, and production of intermediate products prior to ignition.

6.4 Model limitations: fuels with low-temperature chemistry

One assumption made in the critical (Λ_c, ℓ_k) points presented in Figure 6.19 involves the nC_6H_{14} simulations. The kinetic mechanism used only models the high temperature chemistry as is common practice in mechanism reduction for large fuels. However, we showed in Chapter 4 that the low temperature chemistry has an effect on the structure of the entire thermal layer and ultimately leads to a lower surface ignition temperature than what would otherwise be found from a reacting numerical simulation. This is in violation of the analytical model developed in Chapter 5 which assumes significant chemical reaction only occurs close to the hot surface. Under this assumption, Λ_c can be defined from chemically frozen flow simulations.

The effect of low temperature chemistry on critical (Λ_c, ℓ_k) points for stoichiometric nC_6H_{14}/air was investigated. The 54 species, 265 reaction kinetic mechanism developed for low- and high-temperature ignition studies was used for simulating

the diffusing thermal layer ignition problem. Figure 6.20 plots the temperature distributions for the reacting diffusing thermal layer at various times for T_H = 1000 K, T_C = 300 K, and 1 bar. At 0.01 s, the thermal layer has diffused from the hot wall approximately 2 mm. However, at 0.014 s, a bump in the temperature profile is seen around 750 K. This bump is further discussed chemically in Chapter 4, but can be understood as a heat release purely in the middle of the thermal layer. As time evolves up to and after ignition the bump remains present in the temperature profile. This temperature distribution evolution is in contrast to the high temperature mechanism solution for the same conditions presented in Figure 6.9a where no heat release is observed in the middle of the thermal layer.

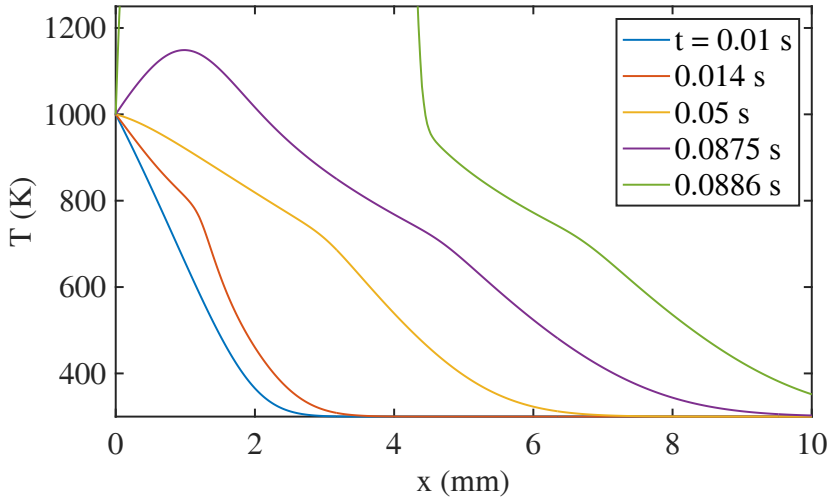


Figure 6.20: Temperature distributions for the reacting-diffusing thermal layer problem at various times for the LTC + HTC kinetic mechanism. Stoichiometric nC_6H_{14}, T_H = 1000 K, T_C = 300 K, and 1 bar.

Figure 6.21 plots the temperature profiles at the time of ignition for 1000 < T_H < 1500 K. As T_H is increased, the thermal layer thickness at time of ignition decreases from ~ 10 mm to ~ 1 mm. Importantly, the bump in the middle of the thermal layer from low temperature chemistry heat release is apparent for 1000 < T_H < 1300 K. For 1300 < T_H < 1500 K, no apparent bump was observed in the low temperature region of the thermal layer. This is because the chemical timescale for high temperature ignition is much faster than the exothermic low temperature chemistry.

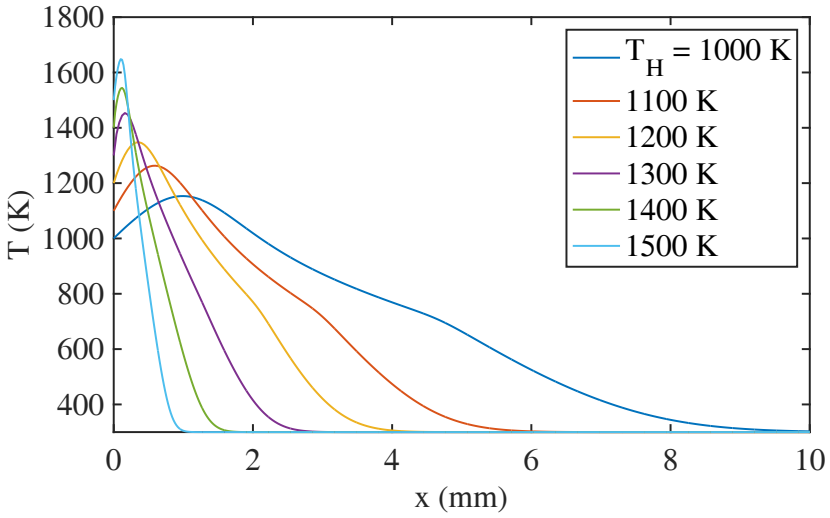


Figure 6.21: Temperature distributions for the reacting-diffusing thermal layer problem at the time of ignition for the LTC + HTC kinetic mechanism. Stoichiometric nC_6H_{14}, $1000 < T_H < 1500$ K, $T_C = 300$ K, and 1 bar.

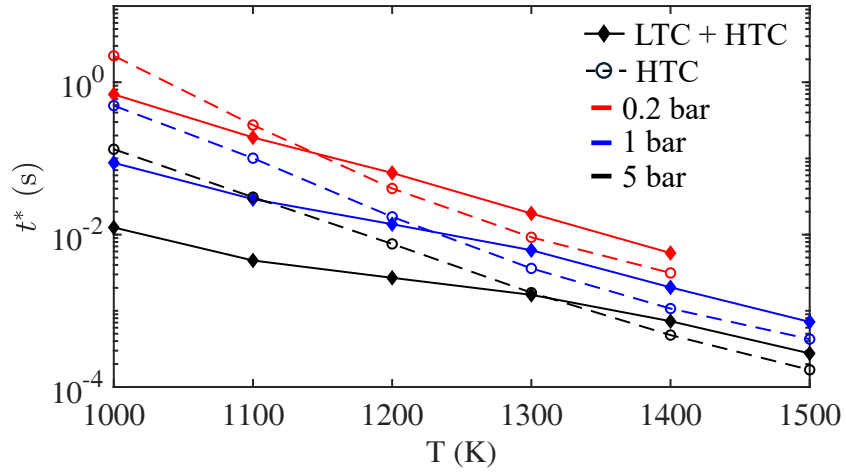


Figure 6.22: Ignition delay time, t^*, vs hot wall temperature for 0.2, 1, and 5 bar for the HT mechanism as well as the LTC + HTC mechanism.

This can further be seen from Figure 6.22 which plots the simulation delay times, t^*, for various hot wall temperatures for 0.2, 1, and 5 bar. Note, t^* is not to be confused with the zero-dimensional delay time, τ_i, discussed extensively in this chapter. In general, as the temperature is increased, the time to ignition decreases. For 0.2 bar, chemical pathways responsible for the NTC region at low temperatures are comparably slow to 1 and 5 bar. Thus, t^*'s exhibit a nearly constant offset between HTC and LTC + HTC mechanisms. This constant offset exists largely due to small

differences in the kinetic mechanism and the discrepancy is recovered through Θ in computing ℓ_k. Between 1100 K and 1200 K, the LTC + HTC mechanism has a subtle flattening of the slope whereas the HTC mechanism continues increasing exponentially with decreasing temperature in an Arrhenius fashion. This flattening effect when including low temperature chemistry is amplified and pushed to higher temperatures ($\sim$ 1300 K) for 1 bar, and further for 5 bar. This can be understood as a stronger NTC effect at elevated pressures. For 5 bar, hot wall temperatures below 1300 K have progressively larger deviations in t^* as the temperature is decreased, up to nearly an order of magnitude at 1000 K.

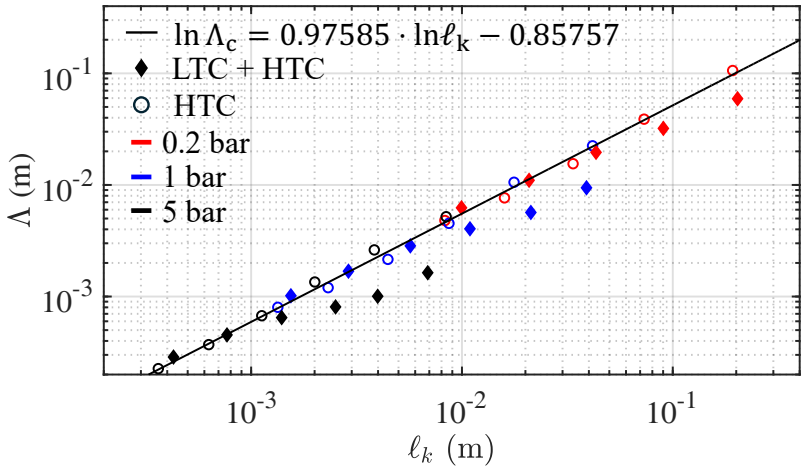


Figure 6.23: Critical (ℓ_k, Λ_c) points for nC_6H_{14}/air simulations using both the HTC mechanism (circles) and LTC + HTC mechanism (diamonds).

Figure 6.23 plots the critical (ℓ_k, Λ_c) points for nC_6H_{14}/air simulations using both the HTC mechanism and LTC + HTC mechanism. A distinct departure from the line of criticality can be seen above hot wall temperatures $T < 1100$ K at 0.2 bar, $T < 1200$ K at 1 bar, and $T < 1300$ K at 5 bar. This happens because the analytical model considers chemical reactions to only occur in a near-wall region where the critical temperature gradient in computing Λ is taken from a chemically frozen simulation. This assumption is quite good for smaller fuels, such as H_2, C_2H_4, etc. that have no NTC region. However for heavier fuels, such as nC_6H_{14}, the low temperature heat release in the middle of the thermal layer reduces the temperature gradient next to the wall. The result is a more easily ignitable mixture that is not incorporated into the analytical model. Therefore, the model will have a tendency to over predict critical ignition temperatures for fuels that have an NTC region. Evidence and quantification of this effect is further provided in Chapters 7 and 8.

6.5 Summary and conclusions

In this chapter, the novel analytical model developed in Chapter 5 is found from simple zero- and one-dimensional numerical simulations of CH_4, CH_2O, H_2, CO/H_2, NH_3, and nC_6H_{14} ignition in air with detailed chemical kinetic mechanisms.

Critical solutions were determined for both the Thomas and Bowes problem as well as a diffusing thermal layer configuration. It was found that the diffusing thermal layer problem could accurately and much more efficiently generate critical solutions to the Thomas and Bowes problem in mapping the parameter space. 57 configurations of surface temperatures, pressures, and fuels were simulated to determine critical values of Λ_c.

Over 18,000 zero-dimensional adiabatic ignition simulations were then run in Cantera to determine the matching critical values of ℓ_k. Plotting the critical solutions in $\Lambda - \ell_k$ space illustrated a remarkable collapse of all 57 configurations to a single line of criticality, where a critical Damköhler number can be defined by the ratio, $Da_c = \Lambda_c/\ell_k$. In the case of the linear fit, $Da_c = 0.44$. Simulations of nC_6H_{14}/air revealed the poorer performance of the analytical model in correlating ignition data for fuels that exhibit an NTC region where exothermic low-temperature chemical pathways affect the structure of the thermal layer.

The result highlights the potential of the analytical model in understanding and predicting critical conditions for ignition near a hot surface as well as limitations for more complicated fuels that exhibit exothermic low-temperature reaction pathways. In the following chapters, this model will be validated against and used to predict critical surface temperatures for ignition in multidimensional numerical simulations and experiments.

Chapter 7

IGNITION MODEL VALIDATION

In this chapter, we will extend the capabilities of the ignition model developed in Chapter 5 and numerically determined in Chapter 6 to demonstrate how it can be used to predict critical ignition temperatures and locations for more realistic, multidimensional systems. First, ignition temperatures and locations determined from several two-dimensional hot surface ignition simulations will be compared against model predictions. Then, previous ignition experiments on a vertical cylinder, flat plate, falling sphere, and glow plug will be modeled numerically. Model predicted ignition temperatures and locations will be compared with the experimentally reported values.

7.1 Application to numerical simulations

The first series of tests developed to validate the line of criticality defined by Eq. (6.12) was to simulate the ignition problem for various fuels and flow configurations.

7.1.1 Configurations

The configurations simulated were forced and natural convection boundary layers as well as stagnation point flow in a two-dimensional domain. Figure 7.1 shows the three configurations tested. The temperature field and instantaneous streamlines are visualized. For the forced convection configuration, the velocity on the left wall is initialized as an inflow condition fixed at U_∞ and the right wall is set as an outflow boundary. The top wall is also set as an outflow boundary. A similar velocity boundary condition was employed for the stagnation point flow. The top boundary was set as an inflow condition at U_∞ and the left and right walls are outflow conditions. For the natural convection problem, the top wall is set as an outflow condition. The bottom and right wall velocity boundary conditions are set using *pressureInletOutletVelocity* in OpenFOAM which sets the tangential velocity as zero gradient and the normal velocity is determined by fixing the total pressure. This allows the thermal layer that forms near the hot surface to determine the inflow velocity as it expels fluid out the top boundary. For all three configurations, the hot surface employs a no slip condition. In the case of the forced and natural convection configurations, the boundary immediately adjacent to the hot surface in the upstream

direction is set as a slip condition to prevent any boundary layer formation upstream of the hot surface. The boundary adjacent to the hot surface in the downstream direction has a no slip condition. Both of these boundaries were set as isothermal at 300 K to isolate the hot surface. For the stagnation point configuration, the two boundaries adjacent to the hot surface had no slip conditions and were set at 300 K.

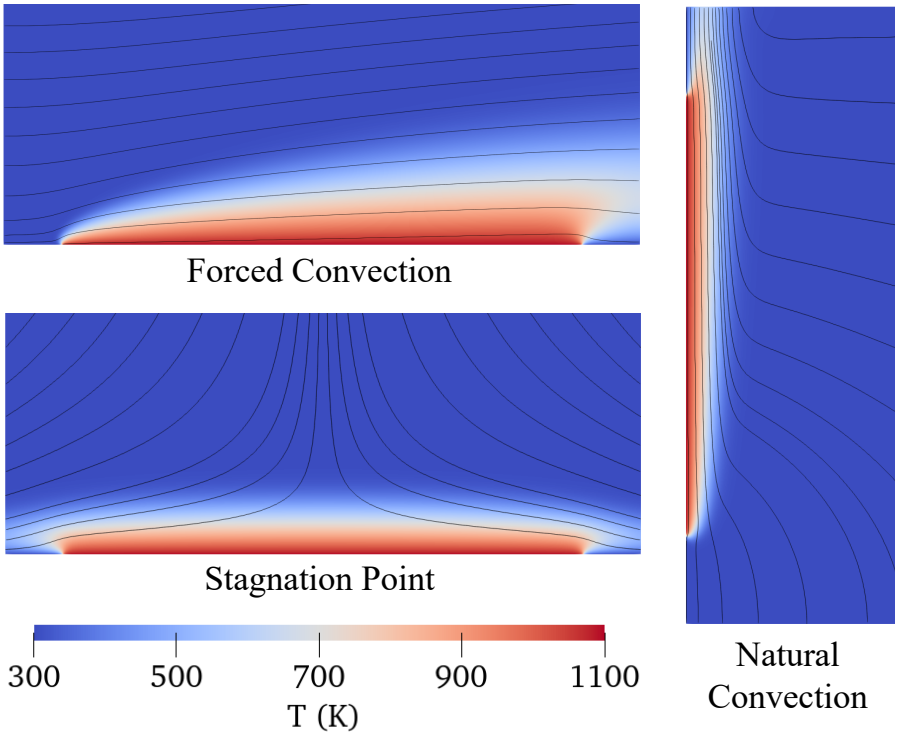


Figure 7.1: Schematics of the forced and natural convection as well as the stagnation point flow configurations.

The domain for all cases was initialized at $T_i = 300$ K. The hot surface itself was ramped at 200 K/s from 300 K until the time of ignition. This approach is similar to the diffusing thermal layer problem in that all values of (ℓ_k, Λ) are simulated at once until the critical pair (ℓ_k, Λ_c) is found as the intersection with the line of criticality. For the stagnation point and forced convection configurations, the velocity was initialized at U_∞ to simulate sudden exposure of a flow field to a hot surface. The natural convection flow field was initialized at rest.

The computational domains consisted of a variable number of cells based on the hot surface length, but typically contained $\sim 300,000$ grid points compressed in the normal direction of the hot surface. The cell size near the wall was ~ 35 μm to resolve the momentum and thermal layers as well as the relevant chemical kinetics for ignition.

For the purposes of validation of the analytical model, a wide range of test conditions were simulated. Three different hot surface lengths, $L = 1, 5$, and 9 cm, were used and for the forced convection/stagnation point problems, three freestream velocities, $U_\infty = 0.01, 0.1$ and 0.5 m/s were examined. All simulations were run at 1 bar of pressure, although three additional simulations were run at 0.2 and 5 bar in the forced convection configuration to observe the pressure dependecne. Tested fuels included stoichiometric mixtures of H_2, nC_6H_{14}, CH_4, and NH_3 with air. The kinetic mechanisms employed were identical to the mechanisms used in the one-dimensional diffusing thermal layer problem to find the line of criticality (Eq. 6.12). The 38 species, 291 reaction FFCM1 mechanism (Smith et al., n.d.) was used for H_2 and CH_4 simulations. The 31 species, 202 reaction CRECK ammonia mechanism (Stagni et al., 2020; Stagni et al., 2023) was used for NH_3 simulations.

The high temperature 62 species, 230 reaction reduced mechanism (Dagaut and Cathonnet, 2006) was used for nC_6H_{14} simulations. The nC_6H_{14} simulations were run before the low-temperature chemistry effects on ignition and the model were fully understood (see Chapter 4). We acknowledge that this mechanism will over predict the ignition temperature compared to the real world since the low-temperature chemistry is not modeled. When the NTC region is modeled, the ignition model will incur errors for (see Section 6.4). However, the simulations presented using the high temperature kinetic mechanism for nC_6H_{14} that excludes LTC modeling is consistent with the analytical model and suffices for validation, at least numerically.

7.1.2 Ignition results

Figure 7.2 plots the temperature field evolution during a typical ignition simulation for the three tested flow configurations. From Figure 7.2a, the ignition event in the forced convection boundary layer flow is seen, characterized by a rapid increase in temperature can be seen at 79.0 mm along the hot surface. In the stagnation point flow in Figure 7.2b, ignition occurs exactly at the center of the hot surface, 45.0 mm. Lastly, in 7.2c, ignition occurs in the natural convection boundary layer near the top, at 45.8 mm. These images are presented to show the ignition behavior for the three flow field configurations. More detailed analysis is presented for all 15 configurations simulated in Appendix G.

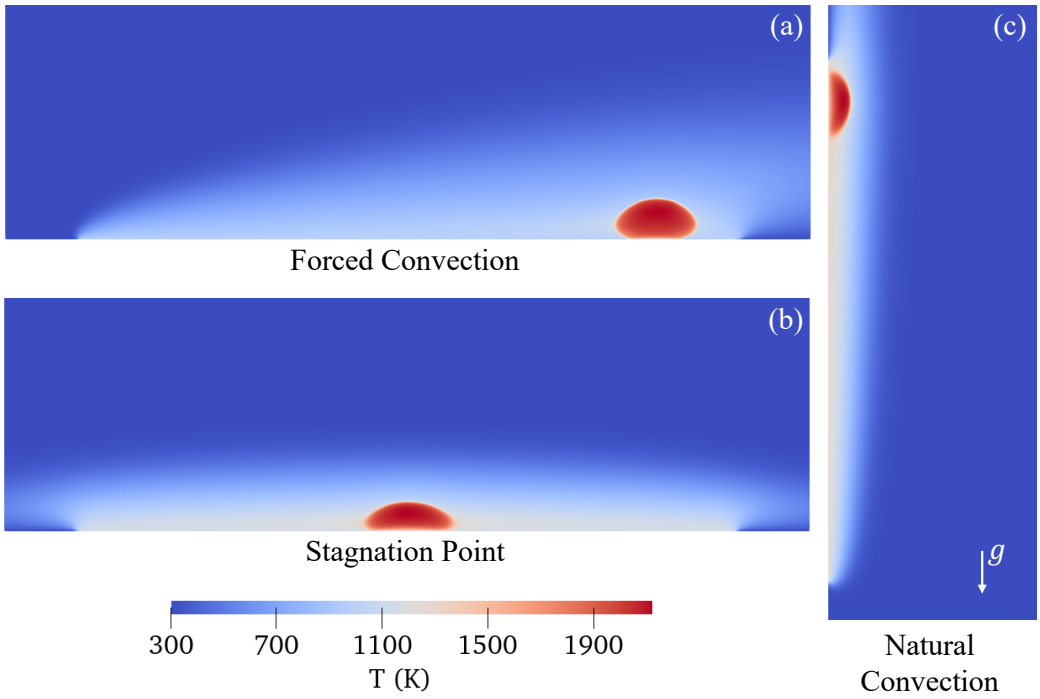


Figure 7.2: Temperature field during an ignition event in a (a) forced convection boundary layer, (b) stagnation point flow, and (c) natural convection boundary layer. For (a) and (b), $L = 9$ cm, $U_\infty = 0.1$ m/s. The surface in (c) was $L = 5$ cm. For all three cases, the mixture was stoichiometric nC_6H_{14}/air at 1 bar.

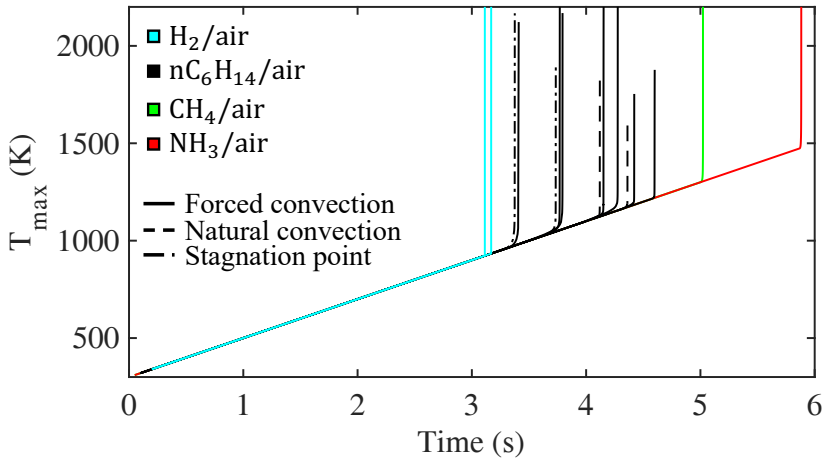


Figure 7.3: Maximum temperature in the domain over time for all two-dimensional simulation cases.

The maximum temperature in the domain over time for all 15 cases is presented in Figure 7.3. For all cases, ignition can be detected as a departure from the linear 200 K/s ramp imposed on the hot surface as the gas temperature thermally runs away. The ignition temperature is then determined as the wall temperature when the gas temperature exceeded it be 150 K. Looking at the fuels, H_2 had the lowest ignition temperature, 936 K, followed by nC_6H_{14}. The CH_4 and NH_3 simulations had significantly higher ignition temperatures compared with H_2 and nC_6H_{14}. This is largely due to the much stronger and more stable C−H and N−H bonds and slow H-abstraction reactions to increase the pool of radicals for thermal runaway. Comparably, H_2 oxidation has simple reaction pathways dominated by chain branching reactions, such as $H + O_2 \rightarrow OH + O$. The larger nC_6H_{14} readily breaks apart at these temperatures which also makes it more easily ignitable compared to CH_4 and NH_3. The NH_3/air forced convection simulation had the highest ignition temperature at 1445 K.

7.1.3 Model predictions

As was stated in the problem formulation, the hot surfaces in this study were ramped at 200 K/s to ramp through the critical wall temperature when a given mixture will ignite in each case. In accordance with the application procedure for the analytical model shown in Figure 5.7, an equivalent chemically frozen variant of the simulation was run for each of the 15 configurations. The wall normal temperature gradient was taken everywhere along the surface at every instance in time. In combination with the surface temperature itself, values for Λ can be determined everywhere on the hot surface spatially and temporally. Similarly, values of ℓ_k can be calculated everywhere on the surface over time. Since the surfaces have an imposed uniform temperature distribution, ℓ_k will only change in time as the surface temperature increases and will be uniform spatially. Values for Θ, τ_i, and κ were computed for each case from zero-dimensional simulations and can be found for each mixture in Appendix F.

Figure 7.4 plots the temporal evolution of (ℓ_k, Λ) pairs everywhere on the surface for three cases shown in Figure 7.2. The line of criticality and 95% prediction bound is shown. Progression of time for $T > 880$ K is illustrated as change in color from 2.9 s (blue) to 4.34 s (red). For all three cases, a rectangular-like solution space is obtained. For a given instance in time, ℓ_k is constant everywhere along the surface and is determined by the temperature. For the forced convection and natural convection cases, as you move downstream from the start of the hot surface, the

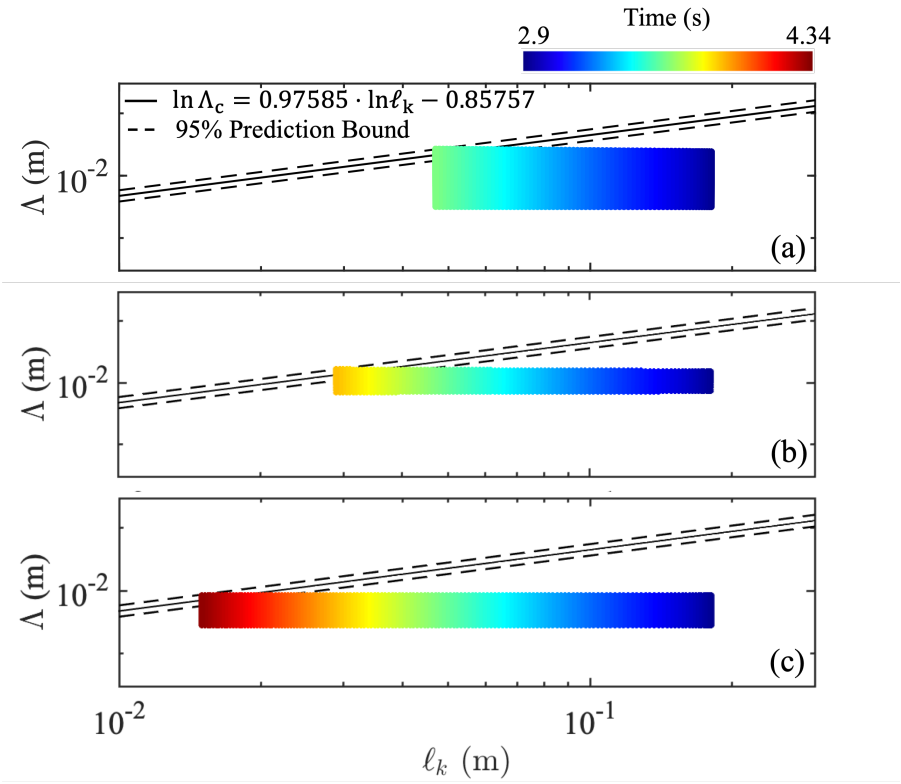


Figure 7.4: Temporal evolution of (ℓ_k, Λ) pairs at every location along the hot surfaces for $T_H > 880$ K for (a) the forced convection simulation described by Figure 7.2a, (b) the stagnation point simulation described by Figure 7.2b, and (c) the natural convection simulation described by Figure 7.2c. The line of criticality described by Eq. (6.12) and 95% prediction bound is shown. The colors represent progression of time from 2.9 s (blue) to 4.34 s (red).

thermal layer grows. For the stagnation point flows, the thermal layer is thickest at the center of the hot surface and gets smaller further away. These effects reduce the local value of the temperature gradient at the wall, thereby increasing Λ. However, this effect is somewhat small compared to the significant change in ℓ_k brought about by the Arrhenius dependence of τ_i on the temperature. As time evolves and the surface temperature increases, ℓ_k decreases. Eventually, the (ℓ_k, Λ) solutions intersect the line of criticality described by Eq. (6.12). Predicted location and surface temperature for ignition can be determined by this critical (ℓ_k, Λ_c) pair. Uncertainty in the model prediction is determined by further intersections with the 95% prediction bounds.

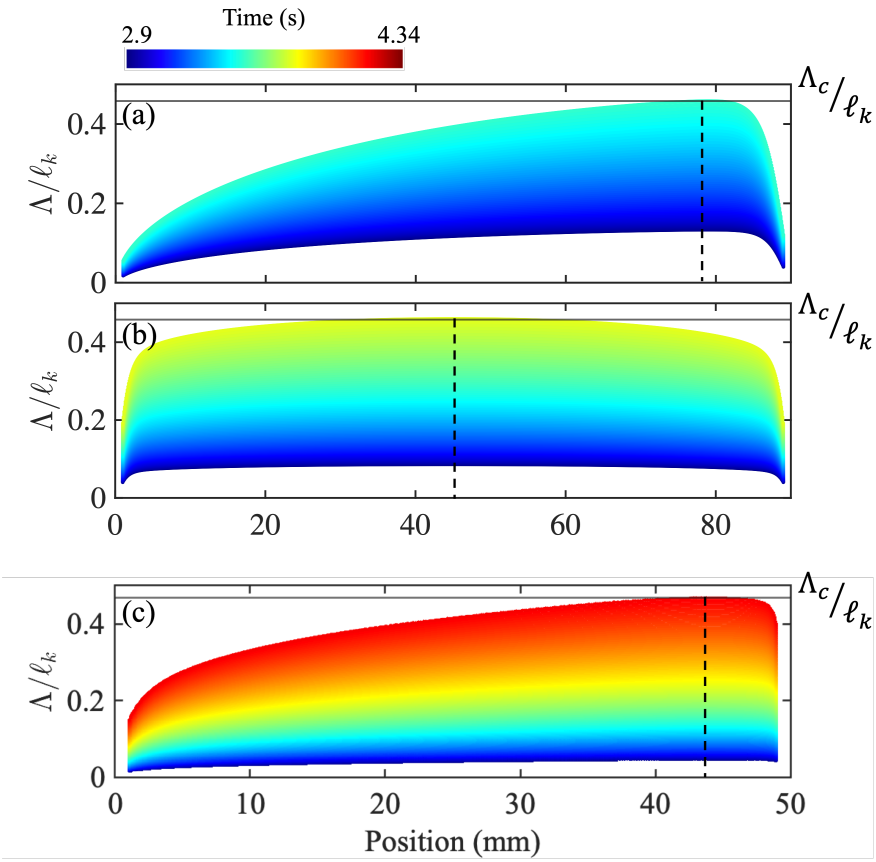


Figure 7.5: Temporal evolution of the ratio Λ/ℓ_k at every location along the hot surfaces for $T_H > 880$ K for (a) the forced convection simulation described by Figure 7.2a, (b) the stagnation point simulation described by Figure 7.2b, and (c) the natural convection simulation described by Figure 7.2c. The critical ratio of Λ_c/ℓ_k from Eq. (6.12) for these values of ℓ_k is shown in addition to a vertical dashed line where the maximum occurs for each case. The colors represent progression of time from 2.9 s (blue) to 4.34 s (red).

Figure 7.5 plots the ratio Λ/ℓ_k against location along the hot surface for the three cases shown in Figure 7.2. The critical ratio Λ_c/ℓ_k described by the line of criticality for these values of ℓ_k is shown along with a vertical dashed line at the location where the maximum occurs for each case. The colors illustrate progression of time from 2.9 s (blue) to 4.34 s (red). Because the wall temperatures are uniform on the surface for a given time, the lines of constant color can be used to understand the effect the fluid mechanics have on the characteristic heat transfer length scale, Λ. As was discussed for Figure 7.4, the forced and natural convection cases see an increase in Λ/ℓ_k as the position is increased. This is a consequence of the thickening thermal layer decreasing the temperature gradient at the wall. A slight decrease is seen at the

end of the hot surface as a consequence of the isothermal cold adjacent boundary cooling the thermal layer through diffusion. For the stagnation point case, the Λ/ℓ_k profiles are symmetric about the center of the hot surface. As the position is increased from zero, Λ/ℓ_k increases and reaches a maximum exactly at the center of the hot surface at 45 mm. As time evolves and the surface temperature increases, the profiles largely shift vertically until it intersects with the critical ratio. Importantly, when Λ/ℓ_k profiles intersect the critical ratio, the position along the hot surface can be extracted and compared with the ignition location in the simulations. For three presented cases, the predicted ignition locations from Figure 7.5 were at (a) 79.0 mm, (b) 45 mm, and (c) 44.4 mm. Remarkably, the predicted ignition location for the forced convection and stagnation point flows match the ignition location from the simulations to the tenth of a millimeter. For the natural convection flow, the model predicted the location low by 1.4 mm (~3%). This could be attributed to a small convection effect on the ignition kernel after it evolves away from the hot wall into the thermal layer.

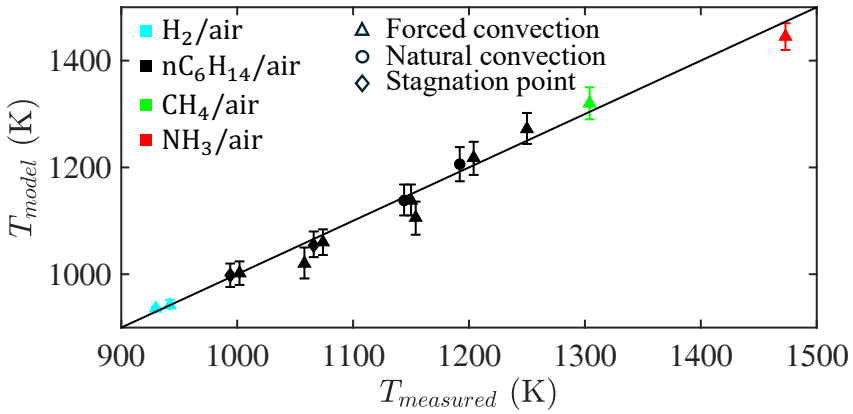


Figure 7.6: Ignition model predicted ignition temperature, T_{model} vs. measured ignition temperature from the detailed ignition simulations, $T_{measured}$.

Figure 7.6 plots the measured ignition temperature against the model predicted ignition temperature for all 15 cases simulated. The error bars are found from intersections of the $\Lambda - \ell_k$ solution space for a given simulation with the 95% prediction bound determined by the model formulation. In general, the uncertainty increases as the temperature increases as a consequence of the Arrhenius dependence of the ignition delay time on temperature. A line with slope of one is shown for reference. We observe good agreement across all cases with an average error of the predicted ignition temperature from the measured value of ΔT = 15.6 K (~ 1.3%

error). This error is significantly smaller than the 6.14% mean relative error found from the scatter of one-dimensional data points used to find the model best fit line which can be attributed to the strong dependence of ℓ_k on the surface temperature. Small variations in surface temperature lead to much larger difference in ℓ_k because of the exponential nature of τ_i.

The results in this section highlight the usefulness of the ignition model developed in Chapter 6. Two preliminary conclusions can be made. First, the model can be successfully extended to, at least, two-dimensional ignition problems with detailed chemistry. Second, the good agreement between the model predictions and numerical simulations indicates that ignition temperatures and locations can be determined quickly and with high accuracy from chemically frozen multi-dimensional flow and zero-dimensional adiabatic, constant-pressure ignition simulations. This highlights the efficiency and usefulness of the ignition model as an engineering correlation.

7.2 Application to experiments

In this section, the viability of the ignition model in predicting critical conditions will be further extended to previously conducted ignition experiments. Four studies were selected as part of the validation set, each with differing complexities in geometry, flow field, and mixture composition to test the ignition model's capabilities. The experimental setups will be modeled numerically to determine Λ and ℓ_k will be computed per usual from zero-dimensional simulations. As always, information on τ_i, κ, and Θ for the mixtures tested can be found in Appendix F.

7.2.1 10 mm vertical cylinder

The 10 mm vertical cylinder ignition experiments performed by Boeck et al. (2017) provide a desirable first test case since the experiment had a simple flow field and the surface temperature distributions were well characterized. In the experiment, ignition of H_2/air, C_2H_4/air, and nC_6H_{14} mixtures was characterized near a 10 mm resistively heated circular cylinder and thresholds were identified. The purposes of the experiment were to develop a simpler and more well-controlled geometry in replacement of a glow plug for ignition studies. The experimental apparatus is reproduced in Figure 7.7. The experiments were performed in a 2.2L closed vessel. A 316 stainless steel circular cylinder was heated internally by a Kanthal A-1 FeCrAl alloy resistance heating wire. The cylinder had an outer diameter of 10 mm and a length of 10 mm ($AR = L/D = 1$). Two 30 mm long insulating quartz glass tubes held the heated stainless steel cylinder to create a continuous geometry and minimize thermal losses.

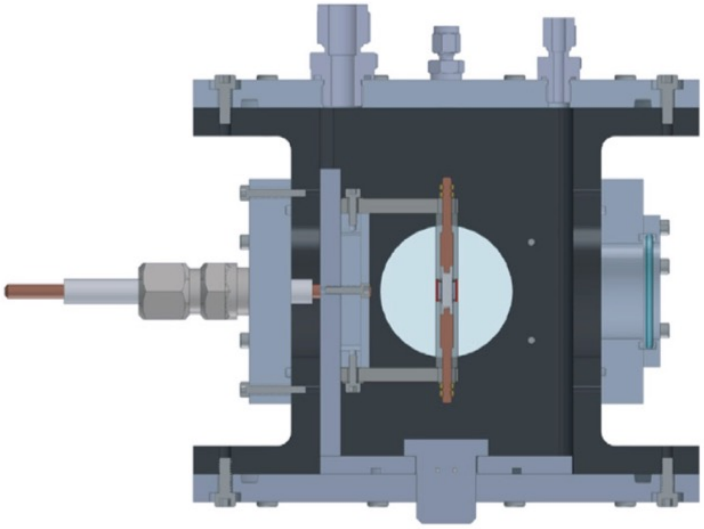


Figure 7.7: Combustion vessel with 10 mm heated cylinder mounted vertically. Reproduced from Boeck et al. (2017).

Scanning pyrometer measurements found that the heated surface temperature was uniform with less than 3% change in temperature between the center and the edges of the stainless steel. It was noted that for a stainless steel surface temperature of 1000 K, a 50 K drop off was observed at the contact between the heated surface and the quartz glass ends. A near linear decrease in temperature from ~950 K to 400 K was reported over the first 10 mm of the quartz glass.

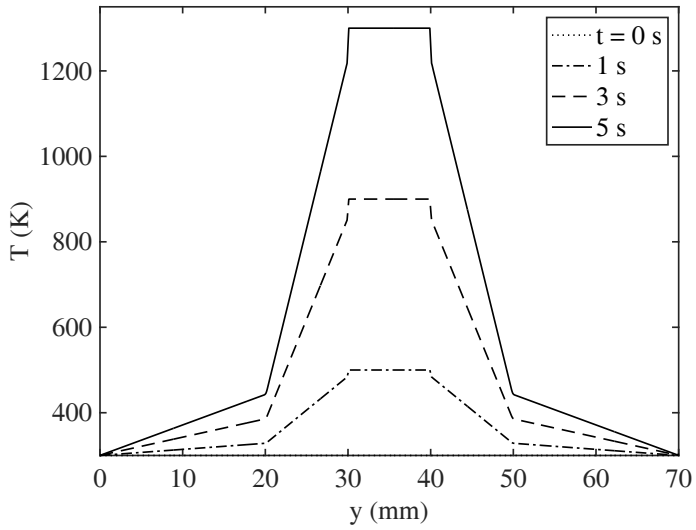


Figure 7.8: Time- and spatially-varying temperature boundary condition used on the surface of the heated vertical cylinder and ends.

The setup described was modeled by a two-dimensional axisymmetric geometry as symmetric thermal layers were observed on either side of the cylinder and ignition was reported to occur randomly in the azimuthal direction. Only the hot surface and quartz glass surfaces were considered as the combustion vessel is sufficiently large such that the system can be considered unconfined. Grid independence could be achieved with 140,000 cells with a geometric scaling in the wall-normal direction. Cells inside the thermal layer were $\sim 45\mu$m.

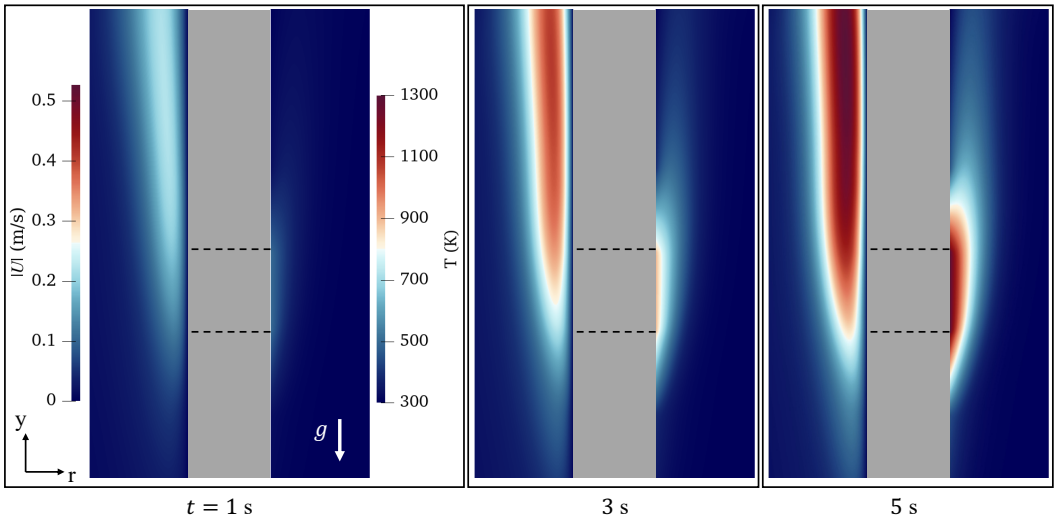


Figure 7.9: Velocity magnitude and temperature fields for the chemically frozen numerical model of the 10 mm cylinder ignition experiment at 1 s, 3 s, and 5 s. The fuel was a stoichiometric mixture of H_2 and air.

The flow was initialized at rest with an initial temperature, T_i = 300 K, and P = 1 bar. A time- and spatially-varying temperature boundary condition was set at the hot surface and holder walls to replicate the surface temperature behavior described in Boeck et al. (2017). This is shown in Figure 7.8. A spatially uniform temperature with a 200 K/s temporal ramp was employed for the hot surface. While this is faster than 10 K/s used in the experiment, it was observed that quasi-steady flow could be achieved for the faster heating rate and accurately reproduces the experimentally measured thermal layers. The temperature distribution in the holder sections at the ends was set as a time-varying piecewise-linear profile. Immediately at the end of the hot surface, a 50 K drop was imposed followed by a linear decrease to 400 K 15 mm away from the center of the hot surface at 3.5 s (1000 K hot surface temperature). The temporal ramp rate was determined as a linear change between 300 K and this imposed condition. From 15 mm to 30 mm, the temperature is

assumed to linearly decrease to 300 K which is fixed at the ends, although the temperature was not measured in this portion of the apparatus experimentally. The effect of different holder temperature boundary conditions on the predicted ignition temperature is examined at the end of the section. A no-slip condition was used on the hot surface and holder walls. The flow was open to the atmosphere at the inlet and outlet boundaries.

Figure 7.9 shows what a typical chemically-frozen flow solution looks like for a stoichiometric mixture of H_2 and air. At 1 s, the cylinder is still relatively cold and the boundary layers are small and with a speed $\sim$ 0.2 m/s near the hot surface. As the wall temperature is ramped in time, the boundary layers grow in size and the max speed reaches a value in excess of 0.5 m/s.

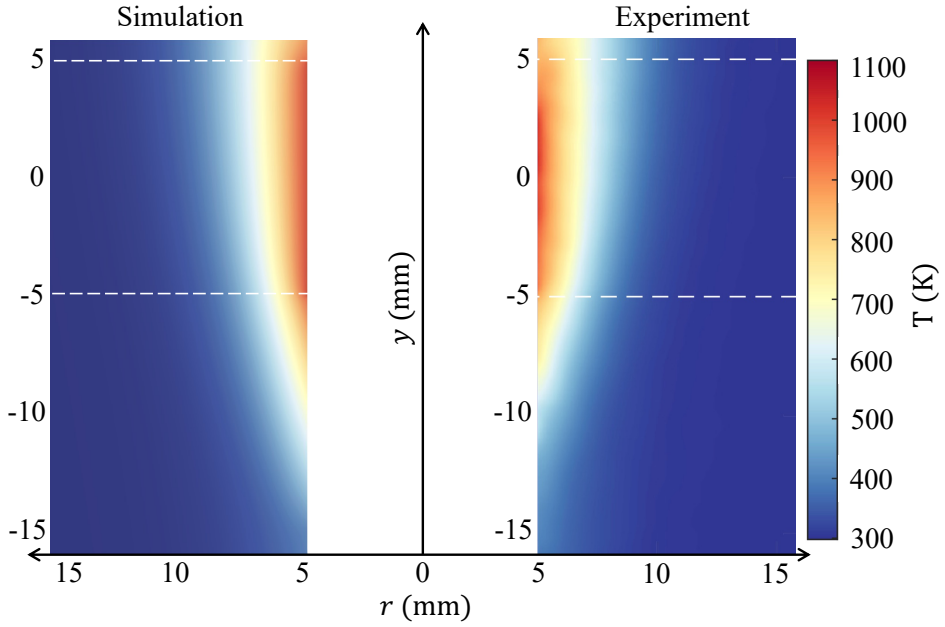


Figure 7.10: Comparison of the temperature field for a stoichiometric H_2/air mixture at a hot wall temperature of 1000 K between simulation and experiment.

The numerical solution can then be compared to an interferogram from the experiment to validate the numerical implementation. Figure 7.10 compares the temperature field for a stoichiometric H_2/air mixture at a hot wall temperature of 1000 K between the numerical model and the experiment. The ends of the hot surface are illustrated as white dashed lines. Good qualitative agreement in the thermal layers is observed, although small hot surface surface temperature differences can be seen in the experiments that is not captured by the numerical model. Comparing the

thermal layer profiles in the center, at $y = 0$ mm in Figure 7.11, the curves lie nearly on top of each other. The thermal layer thickness can be computed as $\delta_{99\%} = 8.5$ mm which is in error of 3.5% to the experimentally measured value.

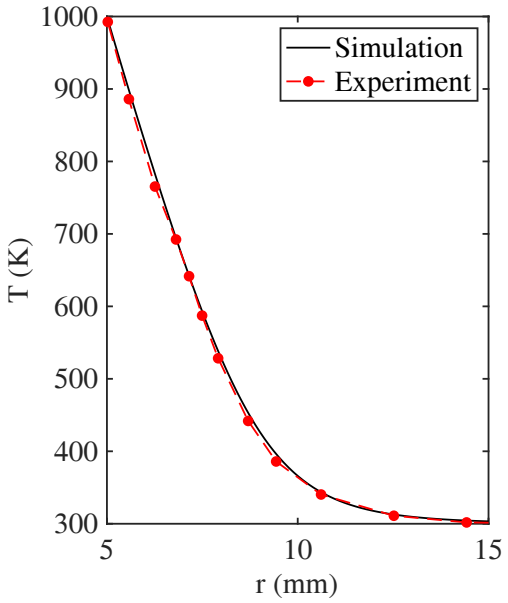


Figure 7.11: Surface normal temperature distribution at the center of the hot surface, $y = 0$ mm.

After validating the numerical implementation, numerous chemically frozen simulations were run at varying fuel concentrations of H_2, C_2H_4, and nC_6H_{14} in air along with the respective zero-dimensional adiabatic constant-pressure ignition simulations. The full 174 species, 1894 reaction CaltechMech mechanism was used for C_2H_4 as the previously used mechanisms were not reduced for ethene. Approximately 260,000 additional zero-dimensional adiabatic, constant pressure ignition simulation were performed to compute ℓ_k for all mixtures in the study. Λ and ℓ_k were computed everywhere on the hot surface over time as the surface temperature was increased, similar to the comparisons with reacting numerical simulations in the previous section. An example of the $\Lambda - \ell_k$ solution space for a stoichiometric mixture of C_2H_4/air is shown in Figure 7.12. Progression of time from 3 s to 4.43 s for $T > 900$ K is represented from a color transition of blue to red. For a given time, as the vertical position is increased, the thermal layer grows in size. Thus, the temperature gradient decreases and Λ increases. However, change in Λ over the entire simulation is relatively small, covering less than an order of magnitude. As time evolves and the surface temperature increases, ℓ_k decreases substantially over three

orders of magnitude. Similar to the comparisons with numerical simulations in the previous section, this is because of the exponential dependence of τ_i on temperature.

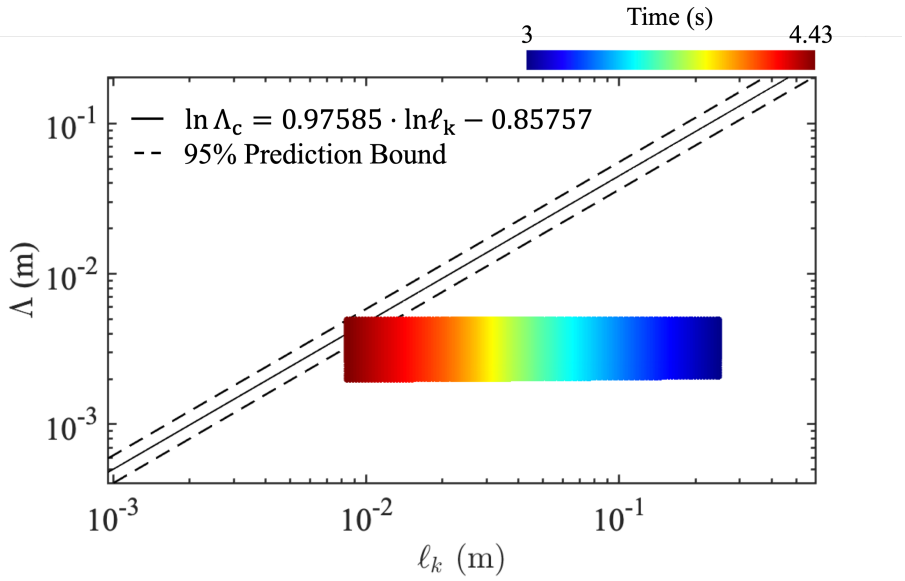


Figure 7.12: Temporal evolution of (ℓ_k, Λ) pairs for a stoichiometric C_2H_4/air mixture at every location on the surface for a temperature $T > 900$ K. The line of criticality and prediction bound is shown. The colors represent progression of time from 3 s (blue) to 4.43 s (red).

A search was performed to find the first instance in time and space where the (ℓ_k,Λ) pairs intersect the line of criticality defined by Eq. (6.12). From this (ℓ_k,Λ_c) pair, the ignition temperature for the system can be backed out from Eqs. (5.64) and (5.68). The same can be performed for the 95% prediction bounds to obtain an critical surface temperature uncertainty bound.

Figure 7.13 plots the temporal evolution of the ratio, Λ/ℓ_k at every location on the hot cylinder for a stoichiometric mixture of C_2H_4/air as a function of vertical position. Again, the colors represent progression of time for $T > 900$ K from 3 s (blue) to 4.43 s (red). For a given time, the temperature is uniform on the surface and Λ/ℓ_k increases with vertical position as the thermal layer grows. The sharpest increase and decrease occurs at the bottom and top of the hot surface, respectively. At the bottom, the thermal layer is initiated and experiences strong temperature gradients. At the top, the holder has a lower temperature that reduces the ratio. The maximum in the spatial profile of Λ/ℓ_k at the time when it intersects the line of criticality provides a prediction for both the critical surface temperature as well as the vertical location. From Figure 7.13, this maxima is shown as a vertical

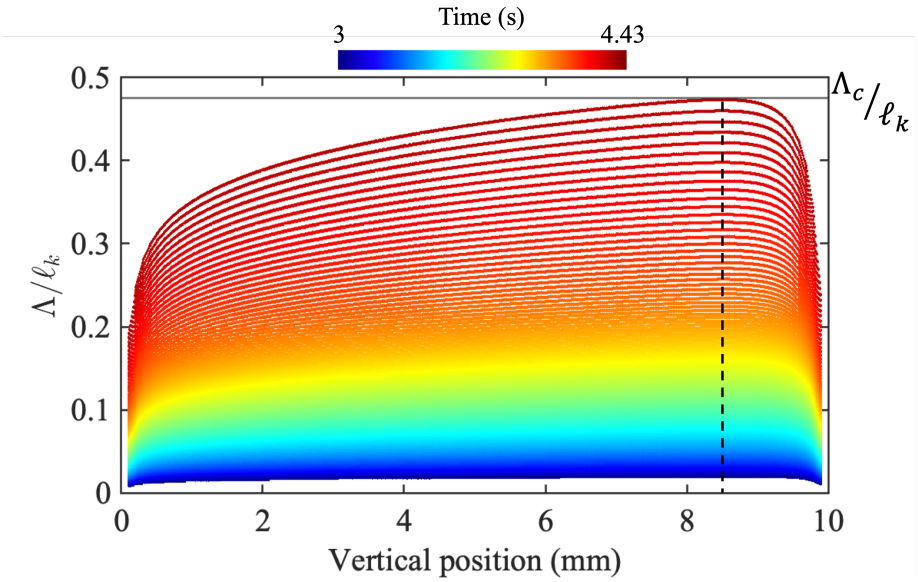


Figure 7.13: Temporal evolution of the ratio, Λ/ℓ_k at every location on the heated cylinder for $T > 900$ K and a stoichiometric mixture of C_2H_4/air as a function of vertical position up until the critical solution is reached. The critical ratio of Λ_c/ℓ_k from Eq. (6.12) for these values of ℓ_k is shown. The colors represent progression of time from 3 s (blue) to 4.43 s (red).

dashed line at 8.5 mm. From Boeck et al. (2017), the experimental ignition location was at approximately 9 mm for all mixtures, although no uncertainty bounds were provided for this location. This yields a 5% difference of the predicted ignition location compared to experimental observation which could be caused by small variations in the surface temperature distribution along the vertical cylinder.

Figure 7.14 plots the predicted ignition temperature using intersections with Eq. (6.12) along with the experimentally measured values for different fuel/air compositions on the 10 mm vertical cylinder. The model predicts the general increase in ignition temperature from ~950 K for H_2 to ~1160 K for C_2H_4 to ~1280 K for nC_6H_{14}, as observed in the experiments. Note the model predicts ignition temperatures without any information from the experiment besides the composition, wall temperature, and chemically frozen temperature gradient. This highlights the generality of the model formulation to accurately predict critical conditions for arbitrary configurations.

From Figure 7.14a, the ignition model predicts a temperature slightly below the measured value for all H_2 mole fractions. A relatively linear increase in predicted temperature from 934 K to 992 K can be seen from 10% to 70% H_2. For H_2

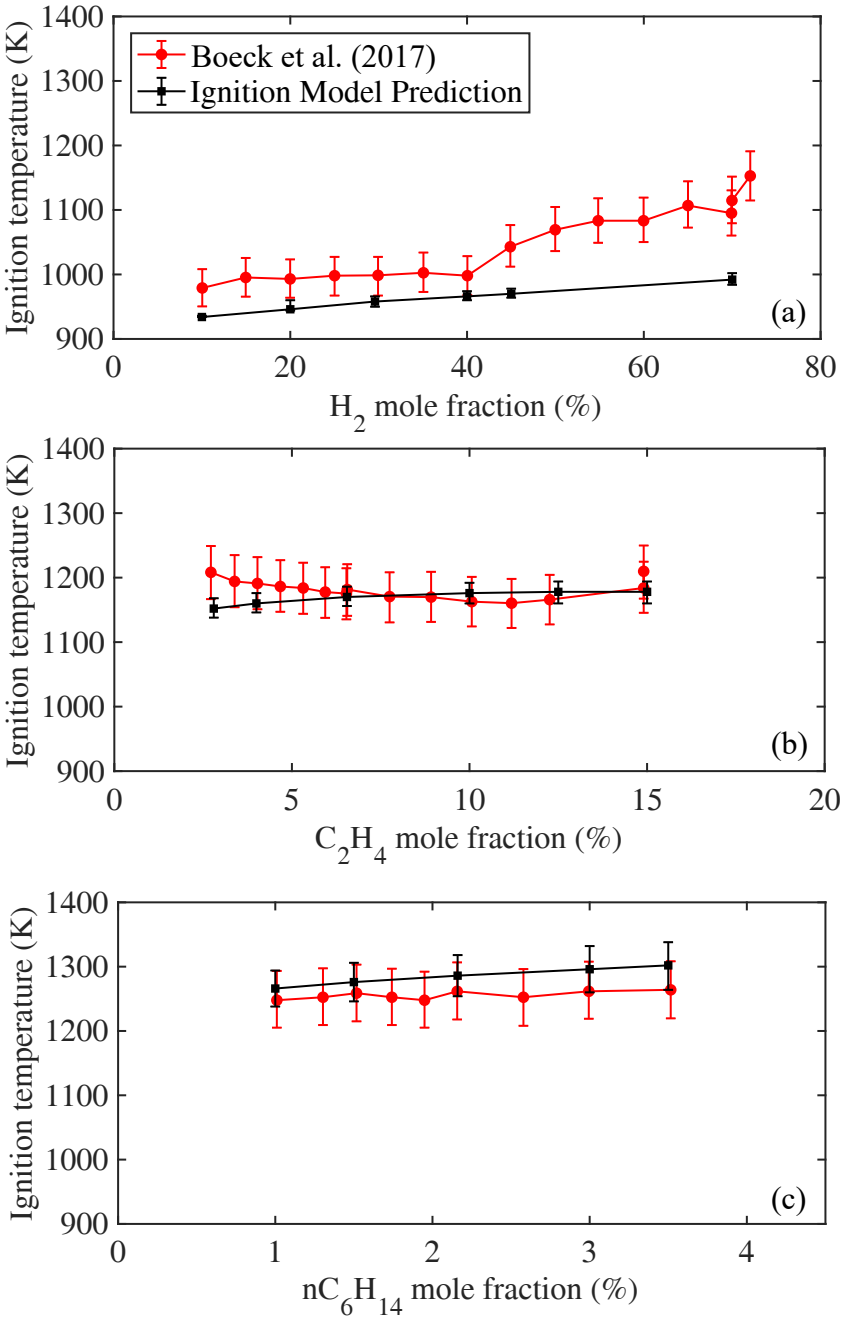


Figure 7.14: Experimentally measured and model predicted hot surface ignition temperature for (a) H_2/air, (b) C_2H_4/air, and (c) nC_6H_{14}/air mixtures.

mole fractions below 40%, the average error in predicted temperature is 41.8 K (4.1%). For H_2 mole fractions above 40%, the model under predicts the ignition temperature more significantly, with an average error of 89 K (8.1%). This result can be explained by an increase in surface chemistry activity for fuel rich H_2/air mixtures

where enhanced recombination of reactive radicals at the surface, primarily H atoms and HO_2 molecules, decrease the radical pool and slow down thermal runaway (Roth et al., 2014). This result has been reported previously by Mével et al. (2019a) in a similar hot surface ignition study on a glow plug where inclusion of H atom and HO_2 molecule destruction at the hot surface in numerical simulations increased the ignition temperature closer to what was observed experimentally. This experiment will be modeled and analyzed later in the chapter.

From Figure 7.14b, the model predicts the ignition temperature for C_2H_4/air mixtures accurately with an average error of 20.8 K (1.6%). Note the model described by Eq. (6.12) has not incorporated any ignition information about C_2H_4. The predicted temperature was insensitive to increases in C_2H_4 ranging from 1152 K to 1178 K at 2.8% and 15% mole fraction, respectively. A similar conclusion can be made from Figure 7.14c. The model accurately predicts the ignition temperature over all tested mole fractions, with an average error of 26.2 K (2.1%). Again, the predicted temperature is insensitive to the nC_6H_{14} mole fraction, with a modest increase from 1266 K to 1302 K at 1% and 3.5%, respectively. While the model predicts the nC_6H_{14} ignition temperature with high accuracy for this experiment, it over predicts the temperature for all mole fractions. This is attributed to exothermic low-temperature reaction pathways occurring in thermal layer far away from the wall at the time of ignition. This phenomenon is discussed in more detail in Chapters 4 and 6.

Alternative holder temperature boundary conditions

The model prediction of critical temperature in Figure 7.14 has substantial agreement with the experiment. To assess the uncertainty in predicted ignition temperature on the imposed holder section boundary condition, two alternative temperature boundary conditions were studied numerically, in addition to the boundary condition in Figure 7.8 to observe the sensitivity on the predicted critical surface temperature. The surface temperature distribution evolutions of these two cases are shown in Figure 7.15. The first was a perfectly isothermal condition set at room temperature, 300 K. The second was an adiabatic boundary condition to simulate no thermal losses on the quartz glass. The evolution of the temperature distribution on the hot surface itself was kept uniform.

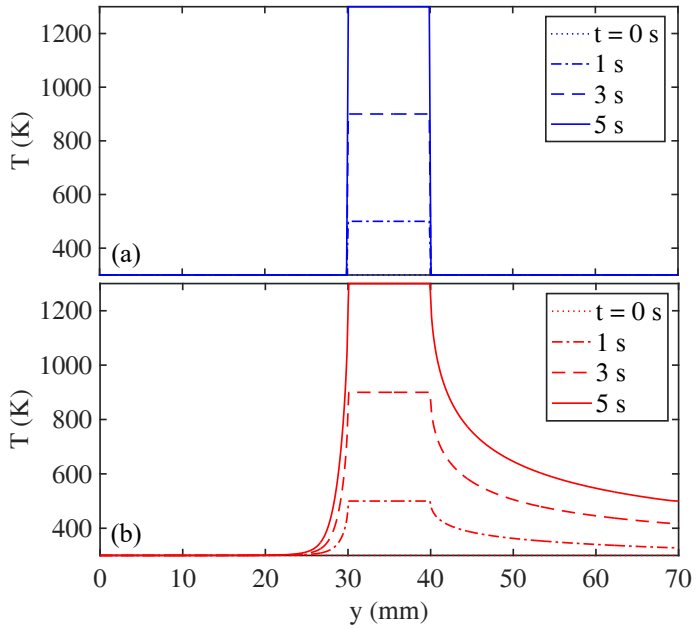


Figure 7.15: Time- and spatially-varying temperature boundary profiles for (a) an isothermal holder temperature and (b) an adiabatic holder temperature.

A stoichiometric mixture of H_2/air was used for the sensitivity study. Figure 7.16 plots the intersection of the (ℓ_k, Λ_c) pairs from the numerical simulations with the analytical model and prediction bounds. Both the isothermal and adiabatic holder temperature boundary conditions lie below the linear temperature distribution boundary condition points. For the isothermal case, this is because the cold boundary cools the thermal layer largely through thermal diffusion, similar to what was observed for the numerical simulations in the previous section. This causes a steeper temperature gradient at the wall near the top of the hot surface where ignition is most likely to occur. The result is a smaller value of both ℓ_k and Λ_c.

For the adiabatic boundary points, the (ℓ_k, Λ_c) pairs are between the isothermal and linear temperature distribution points. In this case, the holder ends do not act as a heat sink. However, it is initialized at room temperature and heats up primarily on the upper portion through convection and thermal diffusion as the hot thermal layer passes it. Comparing to the linear boundary condition in Figure 7.8, the adiabatic boundary temperature decreases much more substantially for a given time as you progress upwards on the holder. The result is a steeper temperature gradient in the upper part of the hot surface where ignition will occur, but to a lesser degree than the isothermal boundary case.

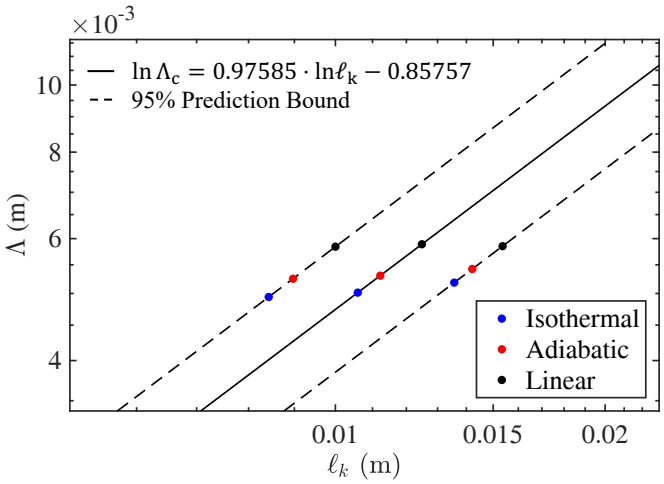


Figure 7.16: Intersections pairs, (ℓ_k, Λ_c) of the numerical solutions with the line of criticality.

Table 7.1: Predicted surface ignition temperature from the ignition model for the three tested temperature boundary conditions for a stoichiometric H_2/air mixture. The uncertainty in predicted temperature given by the temperature range is taken from the intersection of the numerical model with the upper and lower prediction bounds from the ignition model.

Temperature boundary condition	$T_{prediction}$ (K)
Linear	958 [952, 966]
Adiabatic	962 [954, 968]
Isothermal	964 [956, 970]

Table 7.1 presents the predicted ignition temperature from the intersection (ℓ_k, Λ_c) pairs in Figure 7.16 for the three tested temperature boundary conditions with uncertainties provided by the intersection with the upper and lower prediction bounds of the ignition model. The linear temperature boundary profile had the lowest predicted temperature of 958 K whereas the adiabatic and isothermal boundary profiles had predicted temperatures of 962 K and 964 K, respectively. This result is consistent with the decrease in ℓ_k and Λ_c seen for the respective cases. All else being equal, a smaller (ℓ_k, Λ_c) pair will result in a higher ignition temperature. However, the change in temperature between all three cases is only 6 K (0.625%), which is within the uncertainty of the ignition model itself. Thus, the effect of modeling the holder temperature condition in various ways for this particular geometry had negligible effect on the predicted ignition temperature. This further increases the confidence of the results presented in Figure 7.14.

7.2.2 Downward facing hot spots

As part of a more general study to understand ignition due to friction and impact of small particles, Rae et al. (1964) experimentally investigated thermal ignition of a cool CH_4/air mixture suddenly exposed to a downward facing hot surface of varying sizes set to some temperature. This study was chosen as part of the validation set as the experiment was performed with different fuels to Boeck et al. (2017) and exhibited substantially larger ignition temperatures up to 1700 K. The hot surface was created by resistively heating a 0.15 mm thick platinum strip covered by a thin piece of alumina. Surfaces of varying sizes were heated and reported ignition temperature were measured by a disappearing-filament optical pyrometer for varying concentrations of CH_4 in air. Reported ignition delay times were all under 500 ms indicating that ignition occurs during the transient adjustment of the flow to the hot surface exposure.

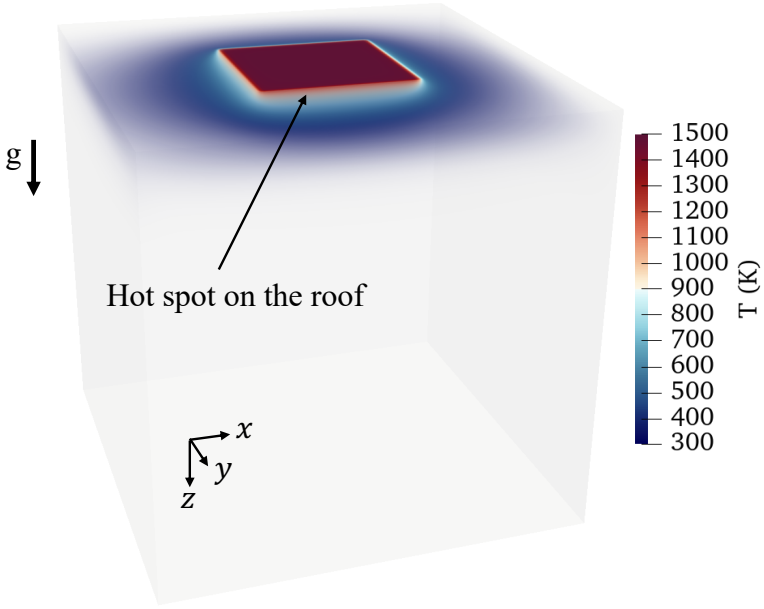


Figure 7.17: Numerical model of a square hot surface suddenly exposed to a cold CH_4/air mixture.

The 3x3 mm and 18x18 mm hot surfaces mounted on the roof of an explosion box in the study were modeled in three-dimensions and simulated for chemically frozen mixtures of CH_4 and air. These surface sizes were selected to achieve the largest range of ignition temperatures observed in the study, ~ 300 K. A schematic of the numerical model is shown in Figure 7.17. A hot surface set to some fixed temperature was initialized on the roof of a box. In-depth measurements of the

temperature uniformity on the hot surface were not reported. Therefore, the hot surface temperature is assumed uniform. The entire upper surface was modeled as a wall to simulate the hot surface setting in the explosion box, employing a no-slip condition. The portion of the upper surface surrounding the hot surface was fixed at room temperature, 300 K. The explosion box used for the experiments was sufficiently large (16 in) relative to the hot surface that the problem can be considered unconfined. Therefore, the side walls and bottom of the computation domain were left as inflow/outflow boundaries to the surrounding atmosphere at 1 bar. The grid consisted of hexahedral cells compressed near the hot surface to a minimum size of 83 μm.

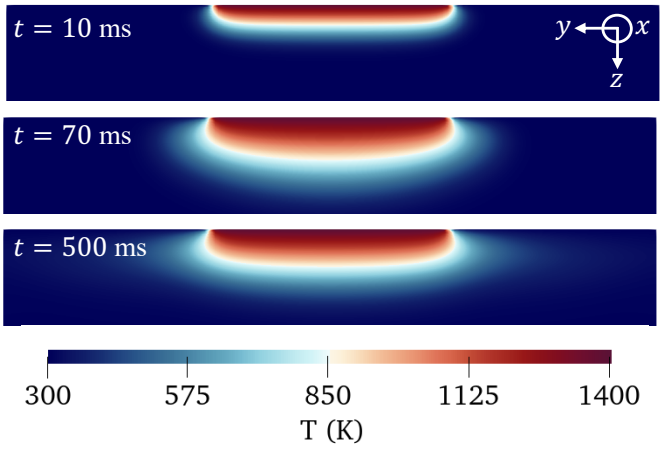


Figure 7.18: Temperature field on a $y-z$ cross-section of the 18x18 mm hot surface at 1402 K suddenly exposed to an 8.0% CH_4/air mixture at 300 K at various instances in time.

The transient flow problem was simulated for 5.6%, 7.1%, and 8.3% CH_4 in air for the 3x3 mm surface and 6.0%, 8.0%, 10.6%, and 12.3% CH_4 in air for the 18x18 mm surface. Figure 7.18 shows the temperature evolution of the gas after suddenly being exposed to a 18x18 mm surface set at 1402 K. At 10 ms, the thermal layer is confined to a thin layer of gas near the wall. At 70 ms, the thermal layer has grown downwards, primarily through thermal diffusion. Far out in time, at 500 ms, a steady solution is obtained with a slightly thinner thermal layer than at 70 ms. This can further be seen from Figure 7.20 which plots the magnitude of the surface normal temperature gradient in the center of the hot surface over time. A rapid decrease in the gradient is seen initially as the thermal layer quickly diffuses downwards. A minimum is obtained around 70 ms. An increase in the gradient can then be seen as the thermal layer thins slightly a result of buoyancy and horizontal thermal diffusion

dissipating the heat from the hot surface. A flattening of the temperature gradient to a steady value can be seen at 500 ms.

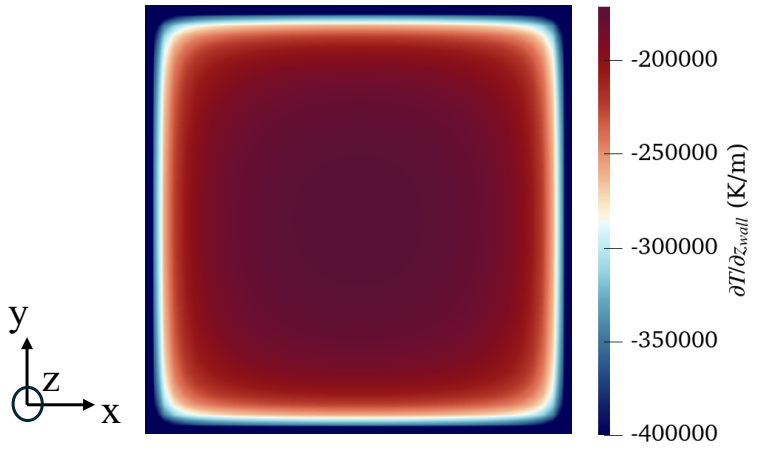


Figure 7.19: Surface normal temperature gradient, $\partial T/\partial z_{wall}$ on the hot surface for $T_H = 1402$ K. Colors near the edges are saturated to show variation near the center.

As with the numerical modeling of other experiments presented in this chapter, a search could be performed across all spacial grid points at every instance in time to find the intersection with the line of criticality. Figure 7.19 shows the typical surface normal temperature gradient on the hot surface. Colors are saturated near the edges to show variation within the interior of the hot surface. This is because the hot surface matches an isothermal cold surface at the edge and so temperature gradients are substantially stronger around the perimeter. A Gaussian-like temperature variation is seen where the smallest value resulting in the thickest thermal layer is exactly at the center of the hot surface. Since the surface is assumed to have a uniform temperature, the center is the location where ignition will occur according to the ignition model. This conclusion is corroborated in the experimental study. Therefore, the search can be made significantly easier by only looking at the temporal variation at the center to determine critical pairs of (ℓ_k, Λ_c), instead of searching across every spatial location.

Since at surface temperatures relevant to this configuration, $T_H > 1400$ K, the chemical timescales approximated from zero-dimensional delay times, $\tau_i < 2$ ms, are much shorter than the flow relaxation timescale ~ 500 ms, ignition will occur during the transient. This is important because the two order of magnitude difference between the timescales implies the quasi-steady inner reactive-diffusive region in the ignition model formulation is satisfied. The reported ignition delay times in

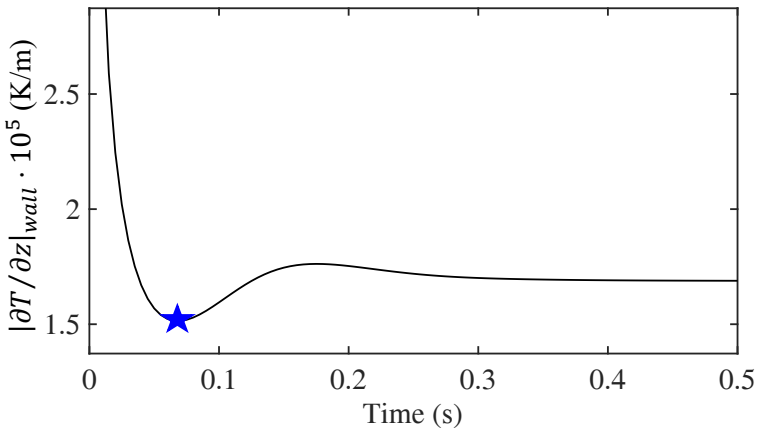


Figure 7.20: The magnitude of the surface normal temperature gradient in the center of the hot surface over time for the 18x18 mm surface with T_H = 1402 K. The star illustrates the minimum gradient in the transient.

Rae et al. (1964) for the experiments support this claim. Therefore, a quasi-steady surface temperature ramp is not sufficient to model this experiment as was done for the numerical simulations and the 10 mm vertical cylinder experiment in previous sections. Instead, simulations must be run for a fixed wall temperature, taking the location where the magnitude of the temperature gradient at the wall is the smallest. This time is taken to obtain the critical temperature gradient used in computing Λ in Eq. (5.64). This time is illustrated as a star in Figure 7.20.

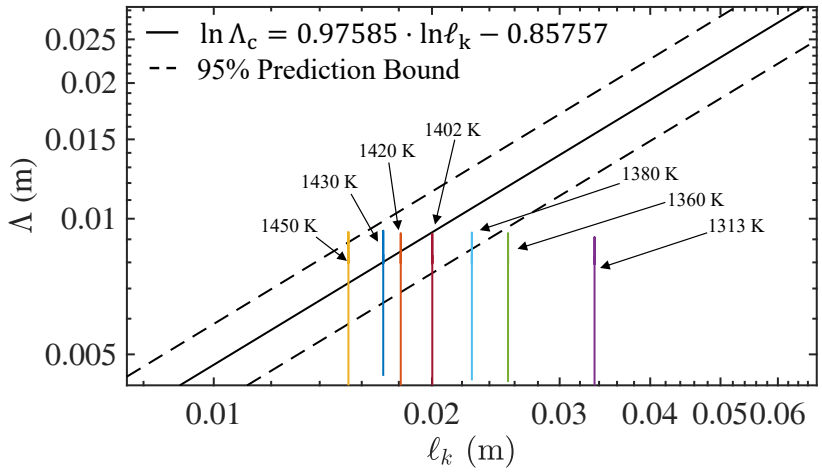


Figure 7.21: Temporal evolution of (Λ, ℓ_k) pairs at the center of the hot surface for seven surface temperatures for the 18x18 mm hot spot with 8.0% CH_4 in air.

The process for determining the critical surface temperature is the following. The (ℓ_k,Λ) pair for a given wall temperature *if* that wall temperature will result in an ignition event can then be computed using the minimum absolute temperature gradient during the transient before the flow becomes steady. The wall temperature can then be increased or decreased based on the relation to the line of criticality and a new (ℓ_k,Λ) pair computed. This process was continued until an intersection with Eq. (6.12) was found. The intersecting pair is deemed the critical (ℓ_k, Λ_c) pair and the ignition temperature can then be predicted and bounded by the model. This is illustrated for the 18x18 mm hot spot with 8.0% CH_4/air in Figure 7.21. The temporal evolution of (Λ, ℓ_k) for seven surface temperatures is shown. Because the wall temperature is fixed for a given simulation, ℓ_k is constant and variation is seen as vertical lines as the Λ changes through the temperature gradient. As the surface temperature is increased, the vertical lines move to the left. This is caused by ℓ_k decreasing as a strong function of temperature. In this case, T_H = 1402 K intersects the line of criticality and is deemed the predicted ignition temperature from the model.

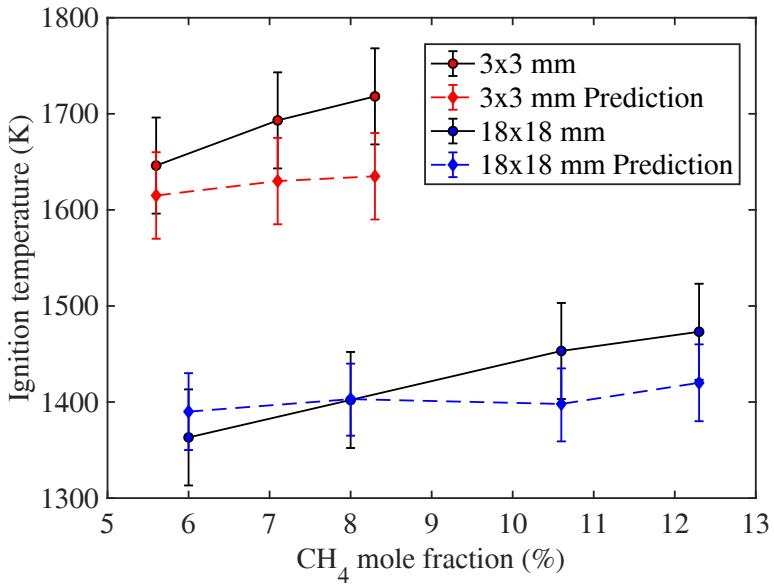


Figure 7.22: Experimentally measured and model predicted hot surface ignition temperature for various CH_4/air mixtures for the 3x3 mm and 18x18 mm surfaces. Uncertainty bars of ±50 K was used for the experimental measurements based on the uncertainty in the pyrometer along with surface reactions induced by surface aging (Rae et al., 1964).

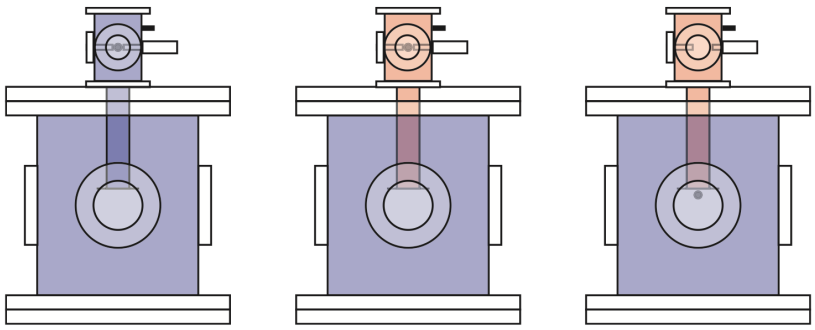
Figure 7.22 plots the experimentally measured and model predicted hot surface ignition temperatures for various CH_4/air mixtures for both the 3x3 mm and 18x18 mm squares. In general, the 3x3 mm hot surface had significantly higher ignition temperatures by $\sim$ 350 K compared to the 18x18 mm hot surface. As the CH_4 mole fraction was increased, the predicted ignition temperature also increased slightly. For the 3x3 mm surface, a 20 K temperature increase was observed between 5.6% and 8.3% CH_4 whereas for the 18x18 mm surface, a 30 K temperature increase was seen between 6% and 12.3%. In comparing the model prediction to the experiments, good agreement can be seen. The model predicts an average temperature error of 34 K (2.4%) for the 18x18 mm surface and 59 K (3.6%) for the 3x3 mm surface.

The larger errors for the smaller surface can be attributed to a number of factors. Without reported surface temperature distributions, a uniform temperature distribution was assumed in the numerical implementation. However, surface temperature differences near the edges of the hot surface could have a significant effect on the critical temperature gradient used to compute Λ_c. This also occurs for the 18x18 mm surface, but likely has less influence as the edge effects are much further away from the center. In addition, as reported in Rae et al. (1964), a catalytic effect could be seen with surface aging, especially at the significantly elevated temperatures needed for ignition, especially for the smaller 3x3 mm surface. These effects could contribute to the under prediction of the ignition model compared to the experiments with the 3x3 mm surface. However, despite these effects, the agreement is still remarkably good differing by only 3.6% on average for the three CH_4/air mixtures with this surface.

7.2.3 Falling sphere

The third study selected in the validation set was the falling sphere experiment conducted at Caltech by Jones et al. (2019). The motivation for the experiment was to better understand ignition thresholds for ejected hot particles inside flammable environments, such as the fuel tank in an aircraft when struck by lightning. This experiment was chosen as part of the validation set because it introduced additional complexities to test the ignition model that aren't prevalent in the experiments on the 10 mm vertical cylinder or small hot spots previously examined in this chapter, such as a curved geometry and temporal variation of the composition.

The experimental setup and procedure, which was originally designed and built by Coronel (2016), is illustrated in Figure 7.23. The apparatus involved dropping



(a) Reactive mixture (b) N_2 addition (c) Sphere drop

Figure 7.23: Schematic for the falling sphere experimental setup and testing procedure. Reproduced from Coronel (2016).

preheated alumina (Al_2O_3) spheres of diameter $d = 6$ mm from an inert N_2 mixture into a reactive one. In this case, three different reacting mixtures of H_2-O_2-N_2 were tested and are presented in Table 7.2. The three mixtures were chosen to represent lean, stoichiometric, and rich conditions where β was selected such that the laminar burning velocity was kept constant and comparable to the sphere fall velocity. The use of alumina as a surface material is ideal as it has nearly no catalytic behavior, which is known to have effects on the ignition temperature for H_2 mixtures as was seen with the 10 mm vertical cylinder experiment.

Table 7.2: Equivalence ratio, Φ, and N_2 fraction, β for the three mixtures of H_2-O_2-N_2. The initial composition is specified as $2\Phi H_2 + O_2 + \beta N_2$.

Equivalence ratio ,Φ	N_2 fraction, β
0.39	2.97
1.0	9
1.35	11.84

A chemically frozen variation of the experiment was simulated in the same axisymmetric geometry as and following the same approach as prescribed by Jones et al. (2019). The experiment was simulated in two parts. First, the free fall of the sphere from rest through the N_2 chamber was simulated for 0.25 s. This time corresponds to the experimental time it took the sphere to reach the optical window from when it was dropped. Then, the free fall of the sphere through the H_2-O_2-N_2 mixtures was simulated for 20 ms. This time corresponds to the time it takes for the sphere to fall across the diameter of the optical window. The gas temperature is initially set at $T_i = 300$ K and $P = 1$ bar. Consistent with the experiment, the sphere surface temperature was set and fixed at T_H. The grid size was compressed near the sphere in the normal direction with local cell sizes of 10 μm.

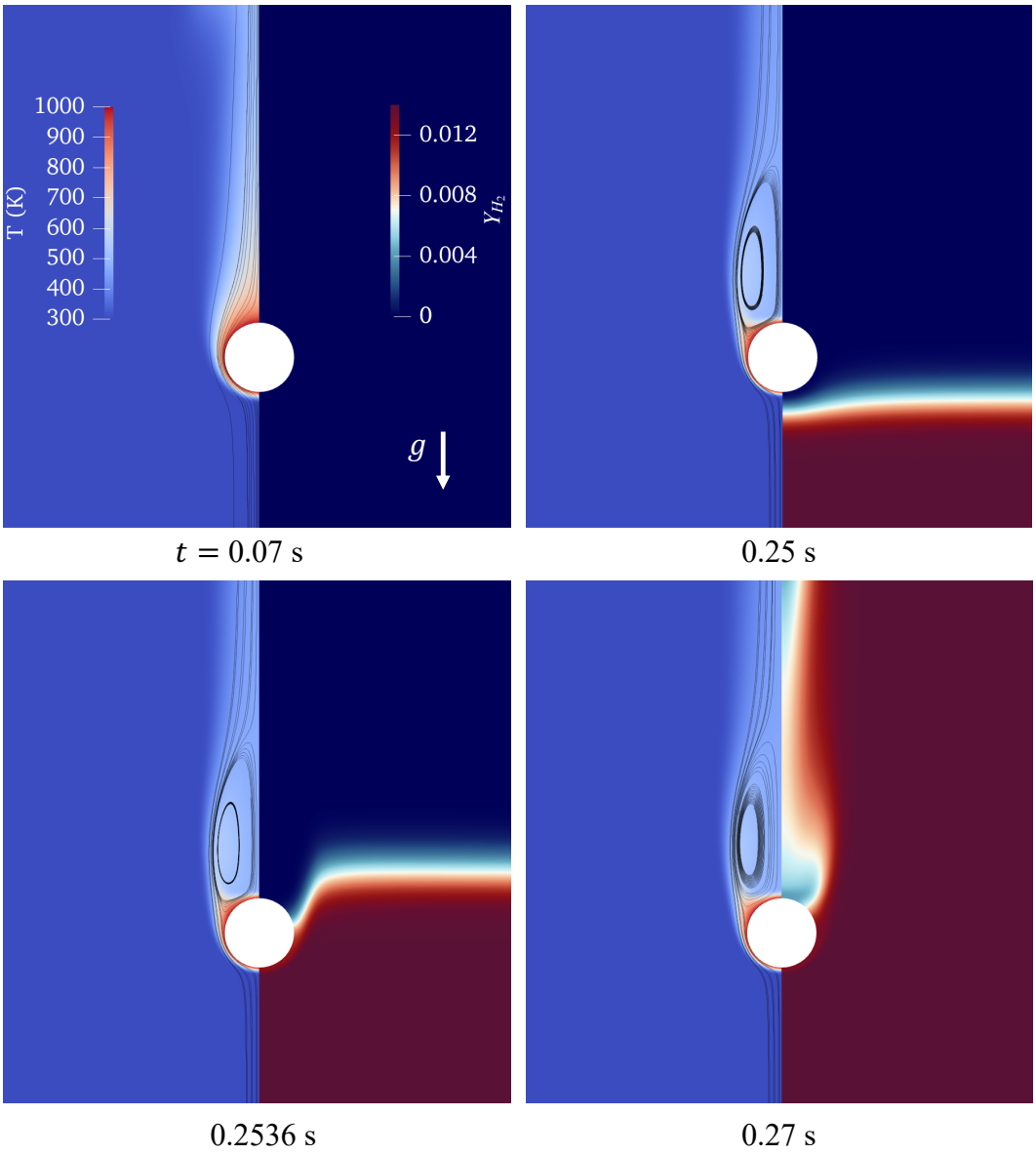


Figure 7.24: Temperature and H_2 mass fraction fields for the numerical model implementation of the falling hot sphere ignition experiment. Instantaneous streamlines are overlaid on the temperature fields.

Figure 7.24 shows an example of the temperature and H_2 mass fraction fields for the numerical implementation of the falling sphere experiment. Instantaneous streamlines are overlaid on the temperature fields. At 0.07 s, the sphere is falling through the inert N_2 mixture and so no H_2 is present. Two stagnation points can be seen from the instantaneous streamlines, one at the leading edge of the sphere and the other 180 degrees around, at the back edge of the sphere. The thermal layer at

the front stagnation point is substantially thinner than at the back stagnation point. As time progresses to 0.25 s, the falling sphere breaches the H_2-O_2-N_2 mixture as can be seen from the H_2 mass fraction field. The rear stagnation point can also be seen moving away from 180 degree location seen for the early time. A recirculation zone emerges behind the sphere. The movement of the stagnation point can be attributed to an increase in flow velocity as the sphere accelerates through free fall and is consistent with what has been discussed extensively by Coronel (2016) and Jones et al. (2019). Over the next 20 ms, the sphere surface sees a shift in concentration from the completely inert N_2 mixture to the reacting mixture. The region immediately behind the sphere takes the longest to equilibrate to the reacting mixture concentration as it is more isolated due to recirculation. Eventually, mass diffusion across streamlines introduces the reacting mixture to the recirculation region.

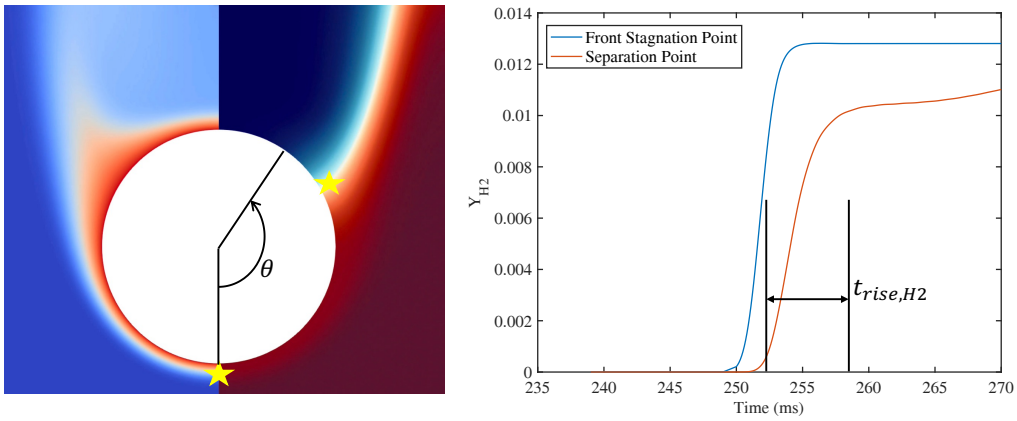


Figure 7.25: Temporal evolution of the H_2 mass fraction at the front stagnation point and separation point along the sphere for $\Phi = 1.0$, $\beta = 9$. The locations are indicated visually with a yellow star.

The variation of concentration temporally along the surface of the sphere is an important point to examine in the context of the ignition model since the inner reactive-diffusive problem is assumed quasi-steady. However, as long as the timescale for change in concentration is sufficiently long relative to the chemical timescale, the model assumptions are still valid. Figure 7.25 plots the temporal evolution of the H_2 mass fraction at the two most important locations around the sphere: the front stagnation point and the separation point. The locations are indicated visually with a yellow star. All else being equal, we expect ignition to occur where the temperature gradient at the wall is minimized. This occurs at the separation point, as can be qual-

itatively observed from the temperature fields shown in Figure 7.24. Therefore, this location is ideal for estimating the concentration evolution timescale. The timescale is estimated from the rise time in the profiles as $t_{rise,H_2} \approx 7$ ms. Comparing to the chemical timescale estimated from the zero-dimensional ignition delay time, $t_{0D,chem} \approx 0.3$ ms. $t_{rise,H_2} > t_{0D,chem}$ by at least an order of magnitude. Therefore, the quasi-steady assumption necessary for the ignition model is satisfied for this experiment. However for less reactive fuels, this assumption may not hold.

Computing ℓ_k for this problem is slightly different than before since the composition is not homogeneous. Instead, surfaces of τ_i, Θ, and κ were computed as a function of initial temperature and nitrogen fraction, β, to populate look-up tables. Similar to before, ℓ_k is computed everywhere on the sphere surface at every instance of time. At each of these points, the temperature is extracted as well as the local fractions of H_2, O_2, and N_2. ℓ_k can then be computed from the zero-dimensional solution surfaces. 67,500 total zero-dimensional adiabatic, constant pressure ignition simulations were run to generate τ_i, Θ, and κ surfaces for the three equivalence ratios. They are provided in Appendix F.

Because this problem is transient, the wall temperature cannot be ramped until the critical solution is found. Instead, a procedure similar to what was performed for the Rae et al. (1964) study discussed previously is employed. Simulations were run for constant and uniform surface temperature spheres and the (ℓ_k, Λ_c) parameter space was searched until a surface temperature was found that yields a single intersection with the line of criticality. Uncertainty bounds for the model is determined by further intersections with the 95% prediction bounds.

Figure 7.26 plots the (ℓ_k, Λ) pairs for every point along the sphere for a surface temperature $T_H = 998$ K, $\Phi = 1.0$, and $\beta = 9$. This surface temperature was selected as it is the critical surface temperature for this configuration determined by its intersection with Eq. (6.12). The progression of time from the breach of the sphere into the reacting mixture at 0.25 s to the end of the simulation at 0.27 s is indicated by a shift from blue to red. For early time, a small θ range of the sphere has the potential to ignite as the sphere has just entered the reacting mixture, as is shown in the flow fields presented in Figure 7.24. These regions are near the front of the sphere, where the thermal layer is exceedingly thin. Thus, Λ is quite small. The mixture in these regions still has a significant amount of N_2 and therefore, ℓ_k is also large. Increasing θ from 0°, both Λ and ℓ_k increase. Λ increases as the thermal layer thickness grows behind the front part of the sphere. ℓ_k increases because the

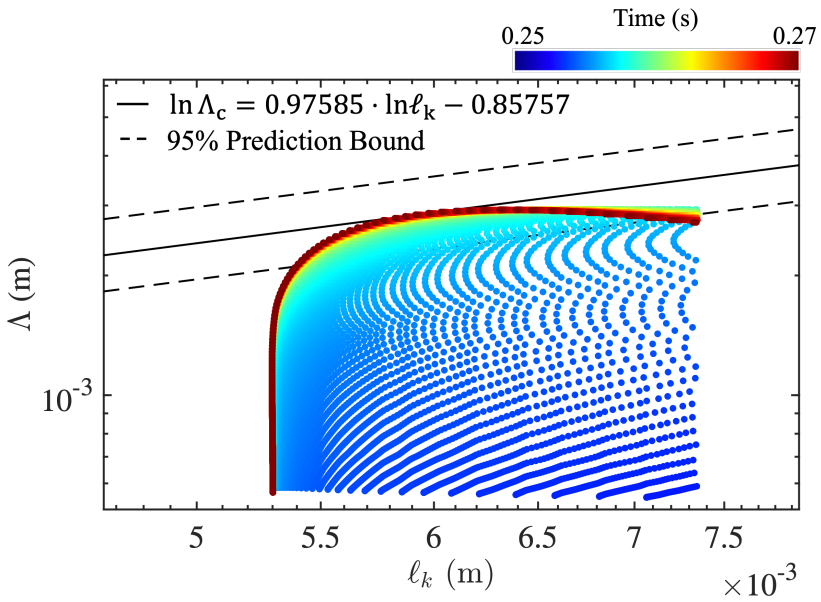


Figure 7.26: Temporal evolution of (ℓ_k, Λ) pairs at every location around the sphere for a surface temperature, T_H = 998 K, with Φ = 1.0 and β = 9. The line of criticality and prediction bound is shown. The colors represent progression of time from 0.25 s (blue) to 0.27 s (red).

mixture changes from the flammable composition near the front of the sphere to pure N_2 at the back. At later times, the sphere is well within the flammable mixture and a larger portion reaches an ignitable local composition, with the majority of the high N_2 concentration locations within the recirculation region behind the sphere. Notice at the end of simulation time, at 0.27 s, there is still a portion of the wake that has a small amount of H_2 that is below the lower flammability limit and thus, does not have the potential to ignite.

The location along the sphere where the configuration reaches a critical solution can be determined by plotting the ratio of the two characteristic scales against the angle around the sphere, θ, and finding the intersection with the line of criticality defined by Eq. (6.12). This is shown in Figure 7.27. The transition of color from blue to red illustrates the evolution of time as the sphere falls through the reacting mixture. For early times, only the first $\sim 30°$ of the sphere are flammable. As time evolves, larger θ become ignitable. A maximum is seen in the ratio of Λ/ℓ_k. The maximum for this surface temperature in this mixture is the first intersection with the line of criticality defined by Eq. (6.12) and is therefore, deemed the critical (ℓ_k, Λ_c) pair. The location is at 119°. This location is expected as the ignition location as it corresponds to the separation point along the sphere which has the smallest

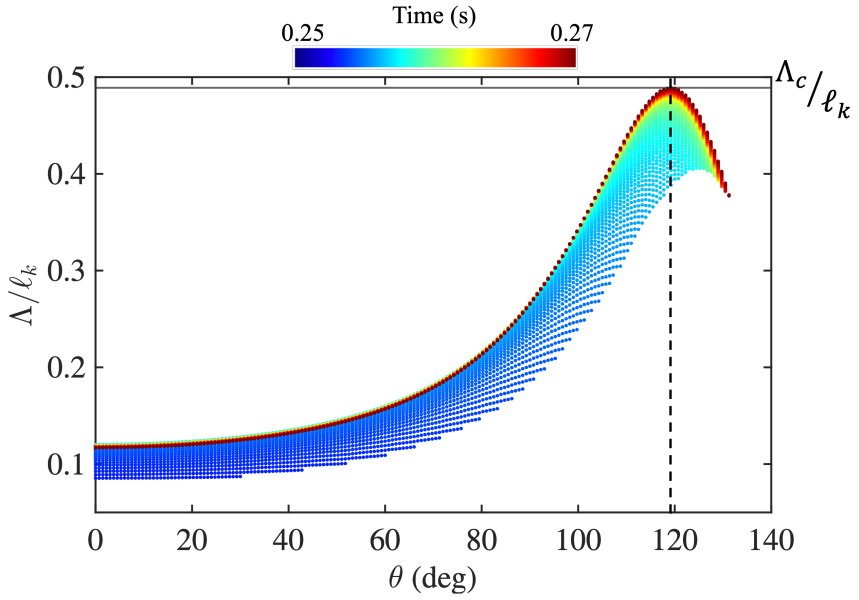


Figure 7.27: Temporal evolution of the ratio, Λ/ℓ_k at every location around the sphere for a surface temperature, $T = 998$ K, with $\Phi = 1.0$ and $\beta = 9$. The critical ratio of Λ_c/ℓ_k from Eq. (6.12) for these values of ℓ_k is shown as well as the θ where the ratio is maximized. The colors represent progression of time from 0.25 s (blue) to 0.27 s (red).

absolute value of the temperature gradient which can be seen graphically from Figure 7.24. This is consistent with the location of ignition found from the experiments and reacting numerical simulations of this problem which was found to be at 120° (Coronel, 2016; Jones et al., 2019). Interestingly, the end of simulation time when the sphere falls out of the optical window experimentally, $130° < \theta < 180°$ is still not ignitable as the concentration of N_2 is still high.

The sphere surface temperature was varied and the critical surface temperature found for the three mixtures in Table 7.2. Figure 7.28 plots the critical sphere surface temperature for ignition as measured experimentally, from detailed kinetics reacting flow simulations, and using the ignition model developed in Chapter 6 for the three mixtures. The uncertainty bounds in the experiment were determined by uncertainty in the pyrometer measurement and by differing kinetic mechanisms in the reacting flow simulations as described by Jones et al. (2019). The uncertainty in the ignition model is taken by the intersection with the 95% prediction bounds of the model. As the equivalence ratio is increased, the ignition temperature increases. In the experiment, the ignition temperature increased 44 K from 963 K to 1007 K. The reacting numerical simulation increased 40 K from 980 K to 1020 K. The analytical

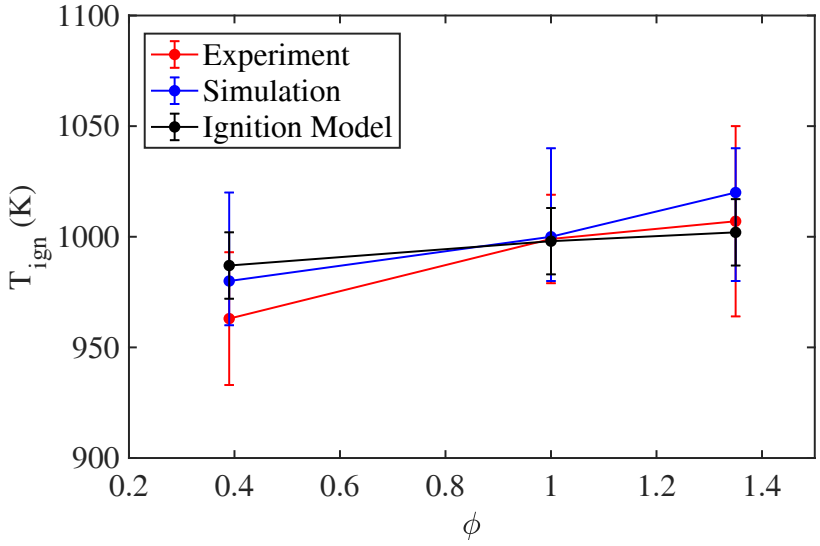


Figure 7.28: Temporal evolution of the H_2 mass fraction at the front stagnation point and separation point along the sphere. The locations are indicated visually with a yellow star. Experimental and simulation data from Jones et al. (2019).

model increased 15 K from 987 K to 1002 K, where the largest deviation with the experiment is 25 K for $\phi = 0.39$. The average difference of the predicted temperature from the ignition model the experiment is 10 K ($\sim$ 1%). This demonstrates that the ignition model can be utilized in predicting ignition for more complicated problems that have surface curvature and mixture inhomogeneities. In the case of a falling hot sphere into flammable mixtures of H_2-O_2-N_2, the model can accurately predict the critical surface temperature for ignition compared to the experiments and numerical simulations with detailed chemistry.

7.2.4 Glow plug

The final configuration selected for the validation data set is the first real-world engineering geometry tested, an Autolite 1110 glow plug. Glow plugs like the Autolite 1110 are commonly used in diesel engines to aid in cold starting. Boettcher (2012) used the glow plug to better understand the effect a rapidly heated surface had on the ignition thresholds in a cold, flammable atmosphere of n-hexane and air. The specific experiments with this setup that will be compared are for mixtures of H_2/air and C_2H_4/air in Mével et al. (2019a) and Mével et al. (2017), respectively. For the present work, it serves as the first engineering geometry validated against the ignition model.

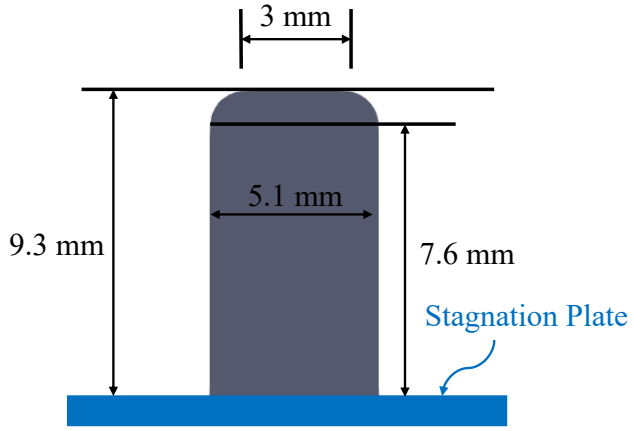


Figure 7.29: Autolite 1110 glow plug schematic.

Figure 7.29 shows the experimental setup with the Autolite 1110 glow plug. The heated area is 9.3 mm in height and 5.1 mm in diameter for the majority of the length. The upper 1.7 mm has a reduction in diameter down to 3 mm. The glow plug is held in place with a stagnation plate that is at a constant temperature.

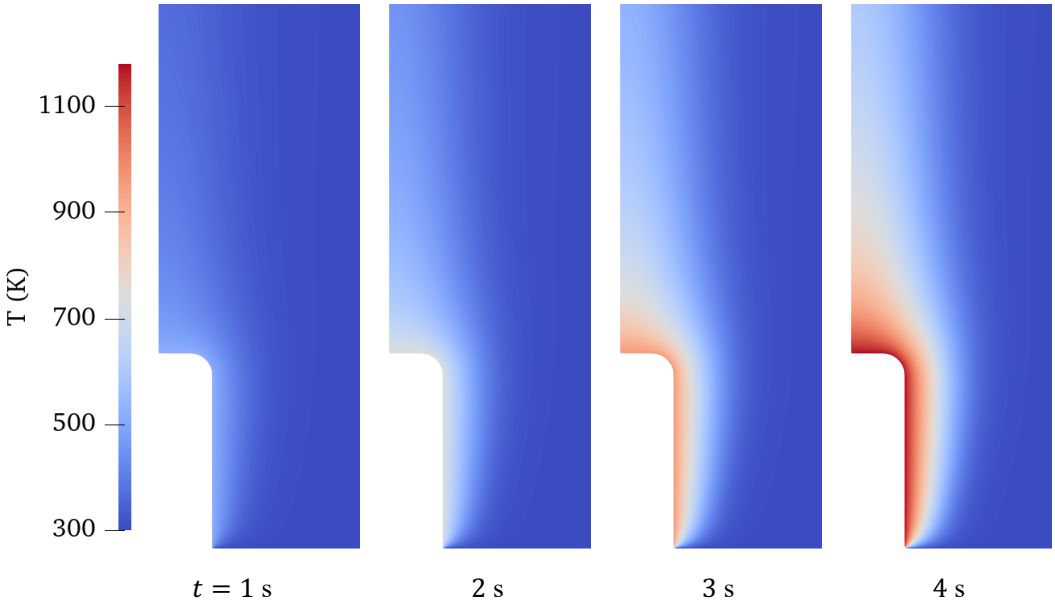


Figure 7.30: Temporal evolution of the temperature field near the glow plug for a stoichiometric mixture of C_2H_4/air.

The glow plug setup was modeled with an axisymmetric two-dimensional geometry. The computational domain consisted of 200,000 cells compressed near the glow plug surface with a minimum cell size of 60 μm. The initial gas state was set at $P = 1$

bar, T_i = 300 K, and U_i = (0, 0) m/s. The surface of the glow plug was heated uniformly from 300 K at 220 K/s to replicate the experiments. Various equivalence ratios of H_2/air and C_2H_4/air were simulated. The simulations were stopped after the solution had passed through the line of criticality.

Figure 7.30 shows what the typical temperature evolution looks like for a simulation, in this case for stoichiometric C_2H_4/air. For early times, such as 1 s, the thermal layer is small since the temperature difference between the glow plug and the surrounding gas is small. As time evolves to 4 s, the surface temperature increases substantially. A well defined thermal layer can be seen where buoyancy convects the heated gas from the bottom of the glow plug up along the sides. The gas at the top of the glow plug is analogous to a hot spot. This geometry is particularly interesting as it is a combination of a heated vertical cylinder and hot spot geometry. This feature will be discussed later in the section.

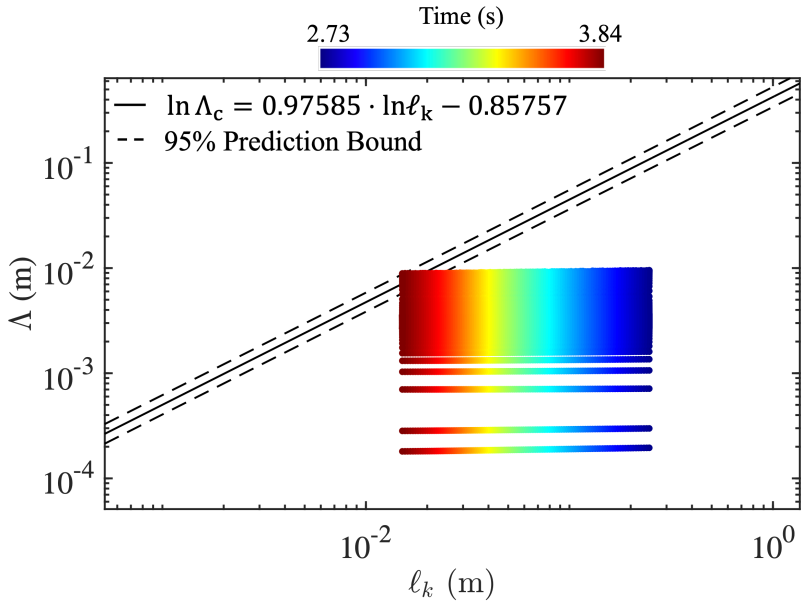


Figure 7.31: Temporal evolution of (ℓ_k, Λ) pairs at every location on the glow plug for a stoichiometric mixture of C_2H_4/air and $T > 900$ K. The line of criticality and prediction bound is shown. The colors represent progression of time from 2.73 s (blue) to 3.84 s (red).

Similar to previous sections, Λ and ℓ_k were computed for every cell on the glow plug surface at every instance of time. Figure 7.31 plots the temporal evolution of (ℓ_k, Λ) pairs at every location on the glow plug for a stoichiometric mixture of C_2H_4/air The colors represent progression of time for $T > 900$ K from 2.73 s (blue) to 3.84 s (red). For a given time, the Λ and ℓ_k pairs move vertically, progressing upwards

along the glow plug from the bottom. This is because a uniform temperature is employed on the glow plug surface and the mixture is homogeneous. Thus, ℓ_k is constant everywhere on the glow plug for a given time. A large increase in Λ can be seen for the first few cells at the bottom of the glow plug. These locations are close to the constant 300 K stagnation plate so the temperature gradients are large. As time evolves and the surface temperature increases, the (ℓ_k, Λ) vertical lines shift to the left as ℓ_k decreases. The predicted ignition temperature can be found from the intersections with the line of criticality and 95% prediction bounds.

The location along the glow plug where the solution becomes critical can also be determined. Figure 7.32 plots the temporal evolution of the ratio of Λ/ℓ_k at every location on the glow plug surface for a stoichiometric mixture of C_2H_4/air against vertical position. The critical ratio of Λ_c/ℓ_k from Eq. (6.12) for these values of ℓ_k is shown. The colors represent progression of time for $T > 900$ K from 2.73 s (blue) to 3.84 s (red). For a given time, as the vertical position is increased, Λ/ℓ_k increases until the curved section at 7.6 mm from the base of the glow plug. This curved surface exhibits a decrease in Λ/ℓ_k until 8.6 mm. Λ/ℓ_k then sharply increases up to the top center of the glow plug at 9.3 mm. This occurs because the temperature gradient on the "hot spot" portion of the glow plug on the top has thick thermal layers with significantly less thermal losses compared to the side. The region from ~8.6 mm to 9.3 mm appears to have a higher density of data points. This is a consequence of the choice of x-axis. The top of the glow plug is flat and exhibits a nearly constant vertical position for a large portion of the glow plug. The location on the glow plug where the solution becomes critical, the ignition location, is exactly at the top center. This is consistent with what was observed in the experiments and detailed chemistry reacting flow simulations presented in Mével et al. (2017).

The existence of two local maxima of Λ/ℓ_k in Figure 7.32 has important implications. From 0 mm to 7.6 mm, the glow plug acts as a hot vertical cylinder whereas it acts as a hot spot on the top. For the presented uniform temperature boundary condition, the predicted ignition location will always be at the top since the absolute value of the temperature gradient is minimized there. However, for large heating rates, the surface temperature distribution can be quite nonuniform with a temperature maximum approximately 7 mm from the base of the glow plug as discussed by various authors (Boettcher, 2012; Mével et al., 2017; Mével et al., 2019a). In these cases, a side ignition is observed instead of on top. While this was not explored in the present work, the occurrence of two local maxima in Figure 7.32 that correspond

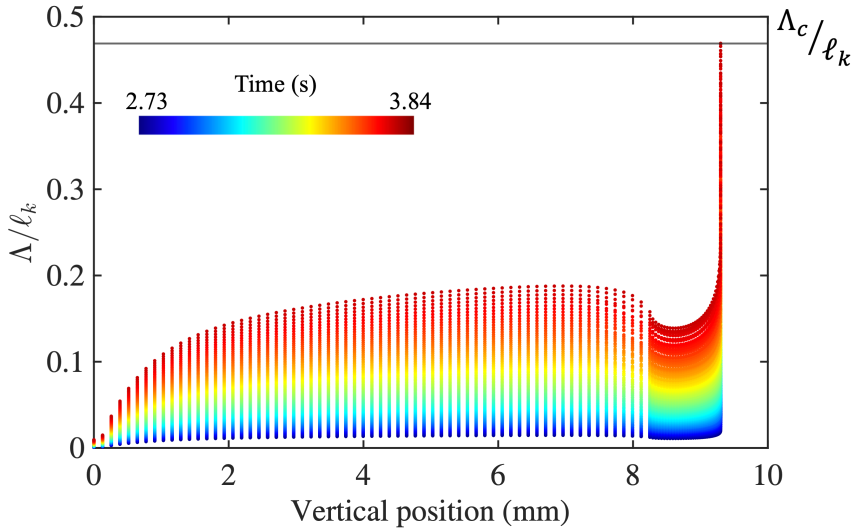


Figure 7.32: Temporal evolution of the ratio, Λ/ℓ_k at every location on the glow plug surface for a stoichiometric mixture of C_2H_4/air as a function of vertical position for $T > 900$ K. The critical ratio of Λ_c/ℓ_k from Eq. (6.12) for these values of ℓ_k is shown. The colors represent progression of time from 2.73 s (blue) to 3.84 s (red).

to the two analogous ignition problems (vertical cylinder and hot spot) allow for a predicted side ignition if the local wall temperature on the side is sufficiently above the temperature on top.

Figure 7.33 plots the ignition temperatures measured experimentally, computed from detailed reacting flow simulations with various kinetic mechanisms, and predicted from the ignition model. From Figure 7.33a shows the results for H_2/air mixtures. Experimentally, the ignition temperature increased from 1012 K with 5% H_2 to 1100 K at 70% H_2. A further increase to 1166 K at 73% H_2 was also seen, likely due to approach of the upper flammability limit. The four kinetic mechanisms used to simulate the problem numerically had ignition temperatures varying by up to 70 K between the GRI and Konnov mechanisms. All mechanisms exhibited a fairly weak dependence on H_2 mole fraction with an increase of roughly 10 K from 10% H_2 to 70% H_2. The GRI mechanism had the best performance in terms of achieving experimentally measured ignition temperatures. The ignition model predicts an ignition temperature in the middle of the numerical simulation results with a slightly stronger H_2 mole fraction dependence ranging from 930 K at 10% H_2 to 955 K at 70% H_2. On average for the cases tested, the predicted ignition temperature differs from the experimental temperature by 113 K. The numerical simulations as well as

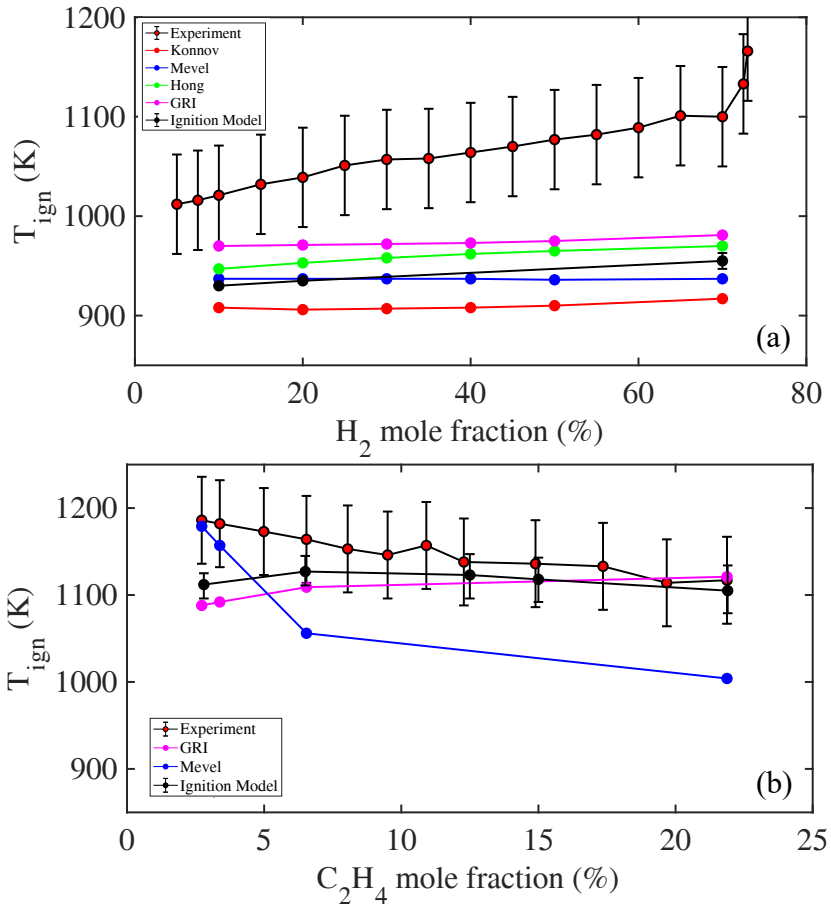


Figure 7.33: Experimentally measured, numerically simulated, and model predicted glow plug ignition temperatures for (a) H_2/air and (b) C_2H_4/air mixtures. Experiments and detailed kinetics reacting flow simulations from Mével et al. (2017) and Mével et al. (2019a). Experimental uncertainties was determined as ±50 K by uncertainty in the pyrometer measurement.

the ignition model predictions all under predict compared to the experiment. This effect is much more substantially pronounced for fuel rich conditions (H_2 fraction > 30 %) and is consistent with what was observed on the 10 mm vertical cylinder studied by Boeck et al. (2017) as both surfaces were made of the same stainless steel. As previously discussed, this is most likely because of increased surface chemistry activity with enhanced recombination of reactive radicals (primarily H and HO_2) at the surface for H_2/air mixtures (Roth et al., 2014; Mével et al., 2019a). Neither the ignition model or the numerical simulations accounted for surface chemistry. We conclude that the ignition model does at least as good as the numerical simulations with detailed chemistry in determining critical surface temperature for ignition.

Figure 7.33b shows the results for C_2H_4/air mixtures. The experimentally measured ignition temperature decreases from 1186 K at 2.7% C_2H_4 to 1117 K at 21.9% C_2H_4. The numerical simulations with the GRI and Mevel kinetic mechanisms exhibited differing ignition temperature behaviors. The GRI mechanism found an increase in ignition temperature with increasing C_2H_4 fraction from 1088 K to 1117 K across the range whereas the Mevel mechanism had a sharp decrease for fuel lean mixtures and an overall decrease across the range from 1179 K to 1004 K. Looking at absolute differences, the Mevel mechanism performed better for fuel lean conditions whereas the GRI mechanism performed better for stoichiometric and fuel rich conditions. The ignition model generally predicted the ignition temperature and trends across the range quite well with an average difference from the experimental value of 31 K. The largest difference came from fuel lean, 2.8% C_2H_4 mixture.

From the predicted ignition temperature results presented in Figure 7.33, the ignition model was found to be a viable and efficient option for determining critical conditions for ignition in the glow plug configuration. The model performs at least as good and in some cases, better than the numerical simulations with detailed chemistry.

7.3 Summary and conclusions

The results presented in this chapter for ignition simulations with detailed chemistry and modeling of past experiments can be summarized from Figure 7.34. The ignition model predictions for critical surface temperature from zero-dimensional simulations and chemically frozen flow, T_{model}, is plotted against the numerically found or experimentally determined ignition temperature, $T_{meausured}$, for all 48 cases tested in the validation set. On average, the temperature difference between the model and numerical simulation/experiment was $\Delta T = 34$ K. In many cases, this uncertainty is well within the uncertainty of the measurement technique. The largest differences were seen for the glow plug and 10 mm vertical cylinder experiments using rich H_2/air mixtures. This discrepancy is a consequence of surface chemistry and has been well documented (Roth et al., 2014; Mével et al., 2019a). Surface chemistry is not accounted for in the ignition model as discussed in assumption (7) outlined in the formulation presented in Chapter 5. Caution should be taken in using the ignition model if surface chemistry effects are expected to be important.

In this chapter, a novel interpretation and application of the developed ignition model in the context of real engineering ignition problems is presented. The model was extensively validated against 48 unique cases with varying fuels, pressures, and

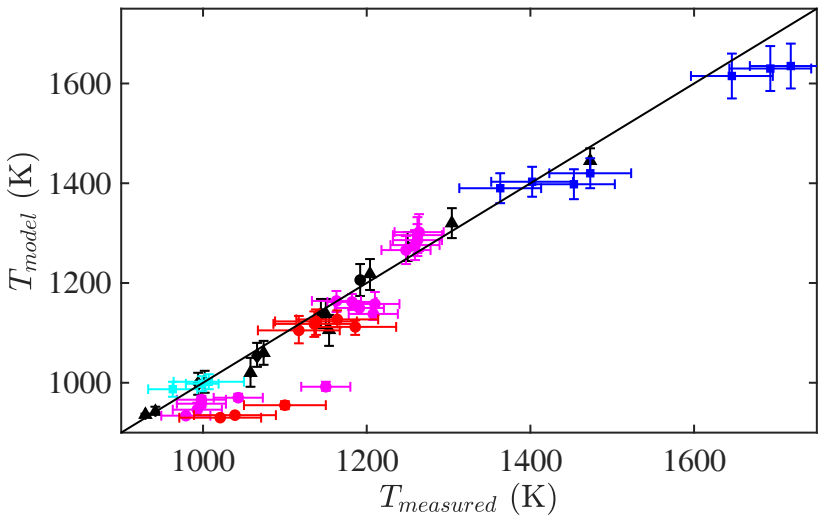


Figure 7.34: Ignition model predicted ignition temperature, T_{model} vs measured ignition temperature, $T_{measured}$ for all experiments and numerical simulations explored in this chapter. Magenta points are for the 10 mm vertical cylinder where experimental ignition temperatures are from Boeck et al. (2019). Blue points are for the downward facing hot spots where experimental ignition temperatures are from Rae et al. (1964). Cyan points are for the falling sphere where experimental ignition temperatures are from Jones et al. (2019). Red points are for the glow plug where experimental ignition temperatures are from Mével et al. (2017) and Mével et al. (2019a). All ignition numerical simulation points are black. Vertical uncertainty bars are computed from the intersections with the 95% prediction interval on the ignition model. Horizontal uncertainty bars are from the uncertainty in the pyrometer measurements.

geometries that resulted in a remarkable agreement between the model predictions and measured ignition temperatures across a nearly 1000 K range. Ignition locations could be predicted for all cases and general analysis of Λ/ℓ_k profiles revealed the unique effect of the fluid mechanics and chemical kinetics on the behavior of each system, such as the capability for side ignition instead of top ignition for the glow plug under specific conditions.

Two big conclusions can be made. First, the model is viable at predicting critical conditions for ignition across a wide range of experimental and numerical test conditions, from falling spheres to glow plugs. This is the first successful unification of theory, numerical simulation, and experiments where the hot surface ignition phenomena is described in terms of a heat transfer length scale and a kinetic length scale. Second, the formulation fully defines the critical conditions for ignition from zero-dimensional reacting simulations and chemically frozen flow simulations.

Provided all 7 assumptions outlined in the model formulation in Chapter 5 are satisfied, critical surface temperatures for a given system can be determined without the need for running the experiment or simulating multidimensional reacting flows.

Chapter 8

IGNITION NEAR A 12.7 CM HOT VERTICAL CYLINDER

8.1 Motivation

In this chapter, ignition near a hot 12.7 cm long vertical cylinder with water-cooled ends will be examined. The ignition model will be used to understand the effects of the geometry, pressure, and composition on the predicted ignition thresholds. The experiment will then be performed for validation.

There are several reasons why this configuration is useful as a test case. First, the 12.7 cm length makes it significantly larger than any of the previous experiments examined. Second, the water cooled ends causes a substantial temperature variation across the heated element itself. None of the previous experiments intentionally had significant temperature variation. Lastly, by using what we learned about the ignition phenomena near a hot surface in Chapters 5, 6, and 7, the experimental test conditions can be carefully selected to achieve a wider range of critical conditions for a single geometry. Specifically, the effect of pressure variation on the ignition temperature will be examined. In addition, the effect of the NTC region present for heavy hydrocarbon fuels on the ignition temperature in relation to the predictions from the ignition model will be quantified.

8.2 Experimental apparatus

For this experiment, the 40 L combustion vessel used previously for many other studies (Coronel, 2016; Jones, 2021; Martin, 2023) was utilized. Specifically, the setup designed and built by Jones (2021) to study nC_6H_{14} ignition on vertical cylinders of varying sizes was used. A schematic of the experimental apparatus is shown in Figure 8.1. The ignition source used for this experiment, tagged cylinder 50C, is a cylinder constructed from 304 stainless steel tubing with copper plugs soldered onto the ends. The cylinder has a total length of 12.7 cm and a diameter of 1.27 cm. The cylinder was mounted vertically and heated resistively using a Magna Power XR5-600 computer controlled DC power supply. The top and bottom ends of the cylinder were kept at 300 K via water cooling using a Thermo-Fisher Scientific NESLAB System III water-to-water heat exchanger to both create the surface temperature variation and to prevent melting of the soldered copper plugs.

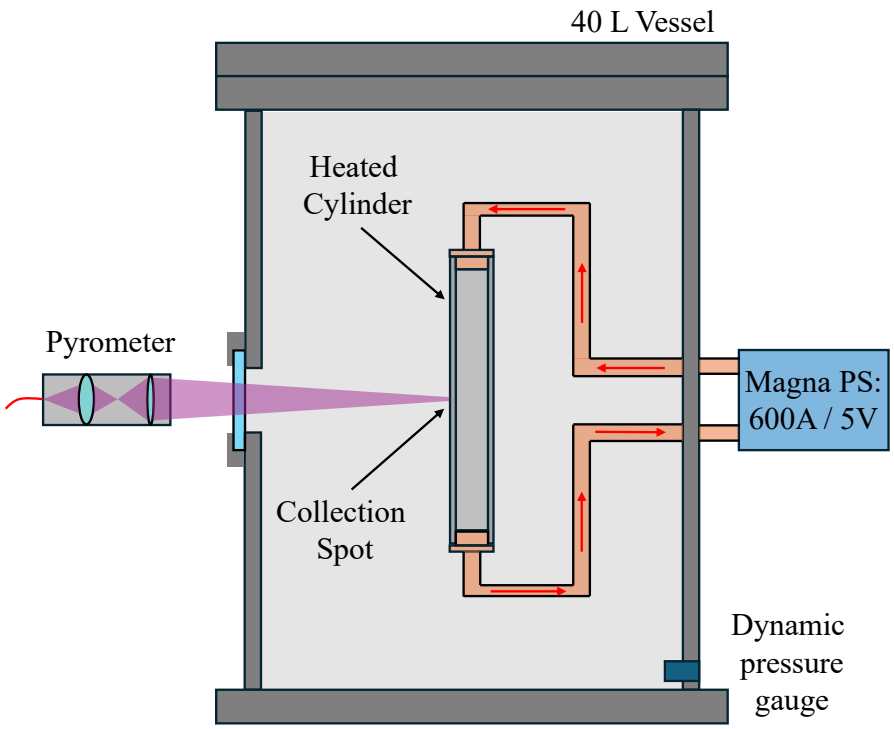


Figure 8.1: Heated cylinder experimental setup.

A KTC-112 vacuum pump was used to remotely evacuate the vessel to < 50 mTorr before running an experiment. An MKS 121AA-0100B pressure transducer was used to fill the reactive atmosphere by the method of partial pressures accurate to 0.01 kPa. To not damage the fill gauges, they are closed during a test. A Kulite piezoresistive sensor was used to measure the dynamic pressure rise during an ignition test.

8.3 Temperature measurements

To obtain confident surface measurements on the stainless steel cylinder, temperature is measured at the center using both a welded thermocouple and optically using a two-color pyrometer.

8.3.1 Thermocouples

Thermocouples were used to measure the temperature at the center of the hot surface. Specifically, a 30 AWG K-type thermocouple was made in the lab by butt-welding chromel and alumel wire using an Orion mPulse arc welder. 30 AWG was used instead of the 24 AWG thermocouples used by previous experiments (Jones, 2021; Martin, 2023) to obtain a faster response time. Care was taken to obtain a high quality junction to ensure accurate temperature measurements.

Because the high temperatures necessary for ignition in this experiment, thermally conductive epoxies are not useful in attaching the thermocouple to the cylinder surface. Instead, the thermocouple was welded directly to the center of the vertical cylinder to achieve a low contact resistance. As a consequence of the design, the surface welds had to be made after the apparatus had been set up inside the vessel. For this purpose, a DCC Corporation Hotspot I spot welder enabled significantly easier surface welding. In previous experiments with these cylinders, the thermocouples were welded to the end of the cylinder upon speculation that it could preemptively trip the thermal layer and affect the ignition results. As will be shown later, for the particular cylinder of interest for this study, cylinder 50C, the thermal layer remained laminar and ignition events still occurred randomly in the azimuthal direction when the thermocouple was welded at the midpoint. This is the preferred weld location as it can be directly compared to the pyrometer without the need for a spatial calibration.

Because the thermocouples are welded directly to the resistively heated element, they experience high current during a test. Analog Devices thermocouple isolation modules (5B37) were used to safely read data from the thermocouple without allowing current from the power supply to damage the computer. Current coupling effects seen by Jones (2021) were mitigated by welding the thermocouple wires perpendicular to the flow of current through the vertical cylinder.

8.3.2 Two-color pyrometer

The idea behind the two-color pyrometer is that temperature measurements can be taken optically at high frequency of the stainless steel cylinder surface. In this experiment, the pyrometer serves as a cross-reference with the thermocouple measurement.

Theory

The idea behind two-color pyrometry, often called ratio pyrometry, is that the radiation emitted from the hot surface can be collected and split into two spectral bands. The intensity of each band can then be measured and the temperature can be determined from the ratio using a calibration curve derived from Planck's law. Unlike conventional single-wavelength pyrometry which requires accurate knowledge of the absolute emissivity of the surface, the two-color approach substantially reduces errors associated with the unknown surface emissivity.

The two-color pyrometer theory is well established as has been discussed extensively by various authors (Michalski and Michalski, 2001; Coronel, 2016; Jones, 2021; Martin, 2023). The irradiance is described by Planck's law as

$$L_\lambda(T) = \frac{\epsilon_\lambda C_1}{\lambda^5[\exp(C_2/\lambda T) - 1]} \tag{8.1}$$

where $C_1 = 8\pi hc^2$, $C_2 = hc/k_B$, L_λ is the irradiance, T is the temperature, λ is the wavelength, h is Planck's constant, c is the speed of light in a vacuum, and k_B is the Boltzmann constant. The spectral emissivity, ϵ_λ, is included as a correction factor for non-ideal bodies. For a perfect black body, $\epsilon_\lambda = 1$. For large temperatures, such as those necessary for hot surface ignition experiments, $\lambda T >> C_2$. Thus, the exponential in the denominator of Eq. (8.1) is large. The Wien approximation (Wien, 1896) can be used to simplify the expression for the irradiance at wavelength λ to

$$L_\lambda(T) = \frac{\epsilon_\lambda C_1}{\lambda^5} \exp(-C_2/\lambda T) \tag{8.2}$$

The total intensity, I, can be found by integrating over the wavelength band $\Delta\lambda$ as

$$I(T) = \int_{\lambda-\Delta\lambda/2}^{\lambda+\Delta\lambda/2} L_\lambda(T) d\lambda \tag{8.3}$$

$$= \frac{\epsilon_\lambda C_1}{\lambda^5} \exp(-C_2/\lambda T)\Delta\lambda \tag{8.4}$$

In the two-color pyrometer formulation, the total intensity is found for two wavelengths. The ratio of intensities can then be written as

$$\frac{I_1}{I_2} = \frac{\epsilon_{\lambda_1}\lambda_2^5\Delta\lambda_1}{\epsilon_{\lambda_2}\lambda_1^5\Delta\lambda_2} \exp\left[\frac{-C_2}{T(1/\lambda_1 - 1/\lambda_2)}\right] \tag{8.5}$$

Assuming the radiation source is a graybody, then the spectral emissivity is considered constant across all wavelengths. In the current formulation, this implies $\epsilon_{\lambda_1} = \epsilon_{\lambda_2}$. The ratio of intensities is then reduced to

$$\frac{I_1}{I_2} = \frac{\lambda_2^5\Delta\lambda_1}{\lambda_1^5\Delta\lambda_2} \exp\left[\frac{-C_2}{T(1/\lambda_1 - 1/\lambda_2)}\right] \tag{8.6}$$

where λ_1, λ_2, $\Delta\lambda_1$, and $\Delta\lambda_2$ are all known and experimentally determined by the band pass filters and detectors. Taking the logarithm of both sides and grouping constant terms yields the fundamental equation used for the two-color pyrometer

$$\ln\left(\frac{I_1}{I_2}\right) = \frac{A}{T} + B \tag{8.7}$$

where $A = C_2/(1/\lambda_1 - 1/\lambda_2)$ and $B = \ln(\lambda_2^5\Delta\lambda_1/\lambda_1^5\Delta\lambda_2)$. In practice, constants A and B will be determined empirically from a calibration.

Two-color pyrometer construction

The two-color pyrometer used for this study was originally built by Jones (2021) and was also used by Martin (2023). It consists of a collection head with two lens. The first lens collects light from a surface 38.1 cm away with a spot diameter of 0.32 cm. The second lens focuses the light onto a multi-mode silica fiber optic cable with a 1 mm core diameter. The light exits the fiber optic cable and is split through a longpass dichroic mirror with a splitting wavelength of 1800 nm. Two narrow bandpass filters at 1705 nm and 1940 nm were placed in front of two PDA10DT photodetectors. The 1940 nm filter had a FWHM of 105 nm and the 1705 nm filter had a FWHM of 97 nm. The two detectors, D_1 and D_2, record I_1 and I_2 as voltages. The detectors were set to sample at 10 kHz to achieve a fast response, while also filtering out higher frequency noise.

Calibration

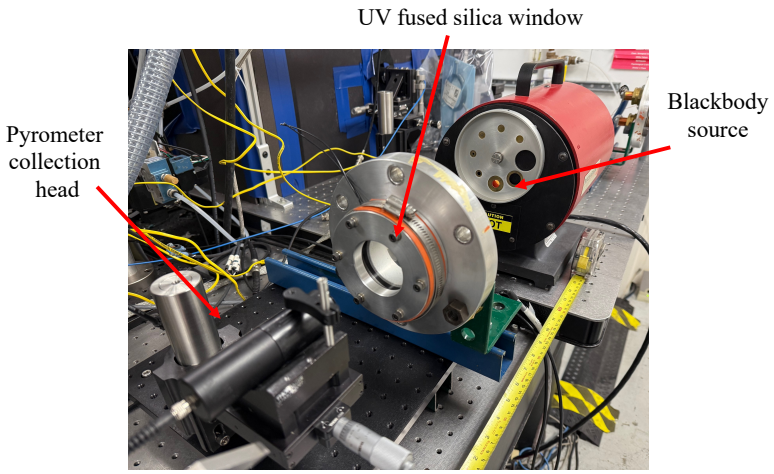


Figure 8.2: Pyrometer calibration setup.

The constants, A and B in Eq. (8.7) were determined empirically by calibrating the ratio of intensities, I_1/I_2 with a Process Sensors BBS1200 blackbody radiation source. Figure 8.2 shows the pyrometer calibration setup. The collection head is pointed and aligned with the BBS1200 blackbody source set at 38.1 cm away. The opening diameter on the blackbody source was set to the closest setting to the 0.32 cm spot size of the collection head at this distance. Importantly, the UV fused silica quartz window from the test vessel must be included to achieve transferable results between calibration and experiment. This is because of slightly nonlinearities in transmission across the wavelengths of interest.

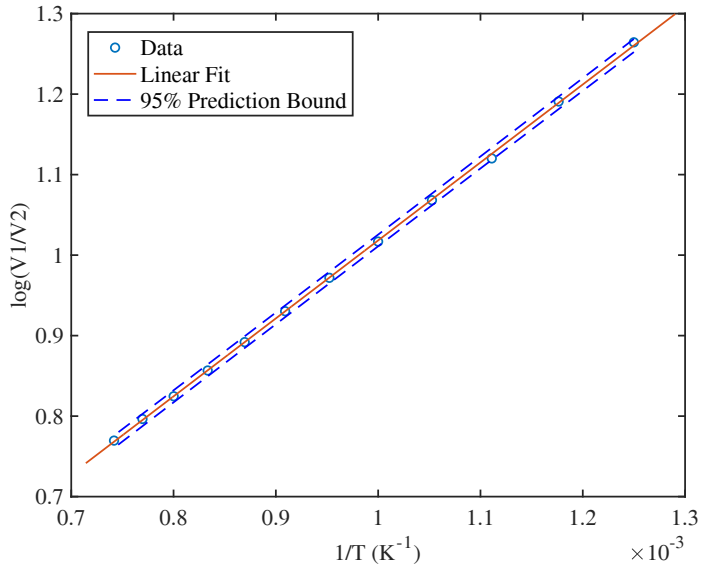


Figure 8.3: Pyrometer calibration.

A pyrometer calibration was taken by increasing the temperature of the BBS1200 from 800 K to 1350 K in 50 K increments. The temperature range is sufficient for measuring surface temperatures in the range of interest for this ignition study. While the BBS1200 could go to higher temperatures, 1350 K is at the limit of the 304 stainless steel cylinder before it starts to flake apart. 10 s of data was collected at each temperature. The ratio of voltages was collected and averaged. These measurements are plotted against the inverse of temperature in Figure 8.3. A linear fit through the data yielded the coefficients of Eq. (8.7), $A = 955.0058$ and $B = 0.0712$. A 95% bound on prediction is also presented and can be used to determine the uncertainty in the pyrometer measurement. In this case, the uncertainty was found to be ±25 K which is consistent with the other studies using this two-color pyrometer (Jones, 2021; Martin, 2023). With the calibration constants, A and B, the surface temperature is then easily found from Eq. (8.7) by solving for temperature as

$$T_s = \frac{A}{\ln(I_1/I_2) - B} \tag{8.8}$$

Temperature measurement validation

The pyrometer measurement of the surface temperature was validated by comparing with the thermocouple measurement at the midpoint of the cylinder. Figure 8.4 plots the pyrometer measurement and thermocouple measurement over time during a typical heating test at constant current. At steady-state the cylinder can be seen

glowing hot and takes roughly 45 s to reach a steady temperature. Before 800 K, the pyrometer measurements are below the noise floor and do not give accurate readings. However, as the temperature increases and the radiation intensity increases, the surface temperature can be readily obtained. The ±25 K uncertainty in the pyrometer measurement defined by the 95% prediction bound on the calibration is included. The results show agreement between the pyrometer and the thermocouple measurement that give high confidence in the surface temperature measurement.

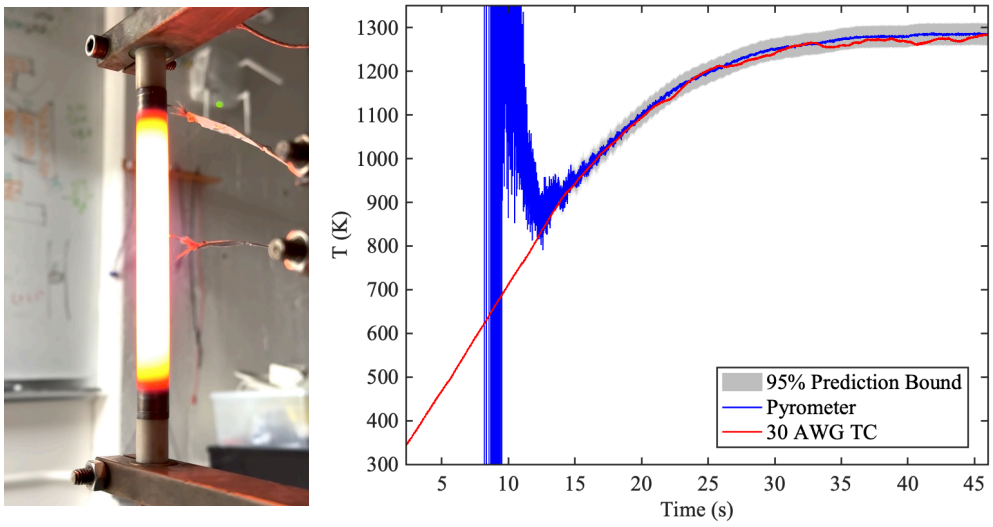


Figure 8.4: Heating test pyrometer and thermocouple temperature measurements over time.

During ignition tests, the pyrometer was used to determine critical surface temperatures. However, the thermocouple was routinely compared against to ensure no drift in the pyrometer calibration or change in surface condition (Martin, 2023) had occurred.

8.4 Test conditions and procedure

To achieve a wide range of ignition temperatures, four fuel/air mixtures were tested at three pressures. 10% H_2/air, stoichiometric C_2H_4/air, stoichiometric nC_5H_{12}/air, and stoichiometric nC_6H_{14}/air. The lean hydrogen mixture was selected instead of stoichiometric to avoid substantial surface chemistry effects that were observed in previous experiments (Boeck et al., 2017; Mével et al., 2019a) and has been extensively discussed in Chapter 7. Both nC_5H_{12} and nC_6H_{14} are known to exhibit an NTC region where dominant exothermic low-temperature reaction pathways exist. This effect leads to errors in the developed ignition model that is discussed

in Chapter 6. However, these errors have not been quantified in the context of predicted ignition temperatures for real systems. These fuels were included in the study to determine the limitations of the ignition model for fuels with this behavior. Stoichiometric CH_4/air mixtures were also initially included, but it was determined that the critical ignition temperatures were in excess of the safe operating temperature of the experimental apparatus.

The three pressures tested were at 0.2 bar, 0.5 bar, and 1 bar. While pressures above atmospheric are desirable for obtaining a larger range of ignition data, structural constraints of the vessel limited the maximum initial pressure to 1 bar. In total, ignition experiments were performed for 12 unique test conditions with duplicate shots being run at each condition to ensure the accuracy of the results from each shot.

Before a test, the vessel was evacuated to below 50 mTorr. Each mixture was then filled by the method of partial pressures in the following order: fuel, N_2, O_2. This order was used as a safety precaution to prevent the possibility of an accidental ignition even in pure fuel/O_2 without any N_2 for dilution. After filling, a mixing fan was switched on in the vessel for 3 minutes to ensure a homogeneous test mixture. A subsequent 3 minutes was taken before heating the cylinder for a test to allow the gas to settle.

Before heating, a dark current measurement was taken with the pyrometer. When it comes time to run a test, everything is controlled from a custom LabView program. A constant current input is sent to the power supply to heat the cylinder slowly, such that it takes 30-60 seconds to pass through the critical temperature. This slow heating rate was selected to allow the fluid mechanics to be quasi-steady with the given surface temperature distribution, but to enable the mixture to always ignite once the critical temperature is reached. Effects of depletion were also minimized due to the size of the combustion vessel. As a result, only a single chemically frozen simulation needed to be run to determine the predicted ignition temperature threshold. The power supply was automatically turned off when either the temperature surpassed 1300 K to prevent damage to the experimental setup or a flame was detected in the vessel. The surface temperature at the time of ignition can then be determined.

8.5 Numerical model

8.5.1 Geometry and boundary conditions

The experimental apparatus was modeled with an axisymmetric geometry in OpenFOAM. Figure 8.5(left) shows the computational domain. The vertical cylinder inside the 40L vessel was simulated. The heated cylinder was originally modeled as free floating in the volume without any modeling of the support structure. In reality, the copper support structure that exists to transfer current to the vertical cylinder as well as the ceramic insulators at the ends will affect the thermal layer, especially near the top. They are incorporated as walls and can be seen in the computational model. All walls in the domain employed a no slip condition.

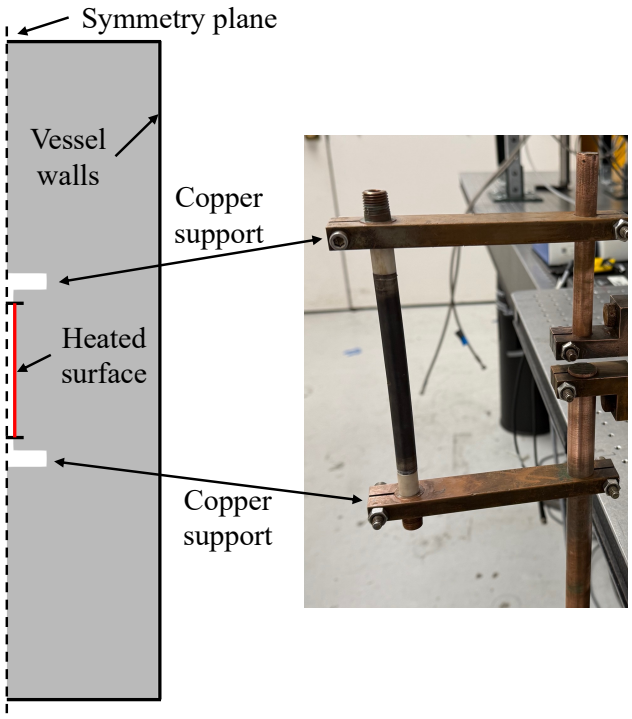


Figure 8.5: 50C axisymmetric computational domain.

8.5.2 Temperature boundary condition

In this experiment, the heated element was designed to have a substantial variation in temperature distribution. The temperature boundary conditions are important to model accurately since we learned in Chapter 7 that the characteristic length scales for ignition, specifically, ℓ_k, is quite sensitive to the local wall temperature. This will affect the intersection point with the ignition model.

On the vessel walls, the temperature was assumed to be isothermal at 300 K. The copper supports and ceramic end pieces were also modeled as isothermal at 300 K. This assumption was checked by measuring the temperature on the copper support as well as on the stainless steel right next to the ceramic during a heating test. Figure 8.6 plots temperature over time for thermocouples mounted at the center and top of the stainless steel as well as on the copper support. The thermocouple at the top is immediately next to the ceramic piece and serves as a good indicator of the ceramic temperature. Over the 60 s test, the cylinder reaches 1050 K at the center. However, the ceramic and copper support only see a 5 K increase, from 300 K to 305 K. Thus, the isothermal 300 K imposed temperature condition is a valid asssumption on these surfaces.

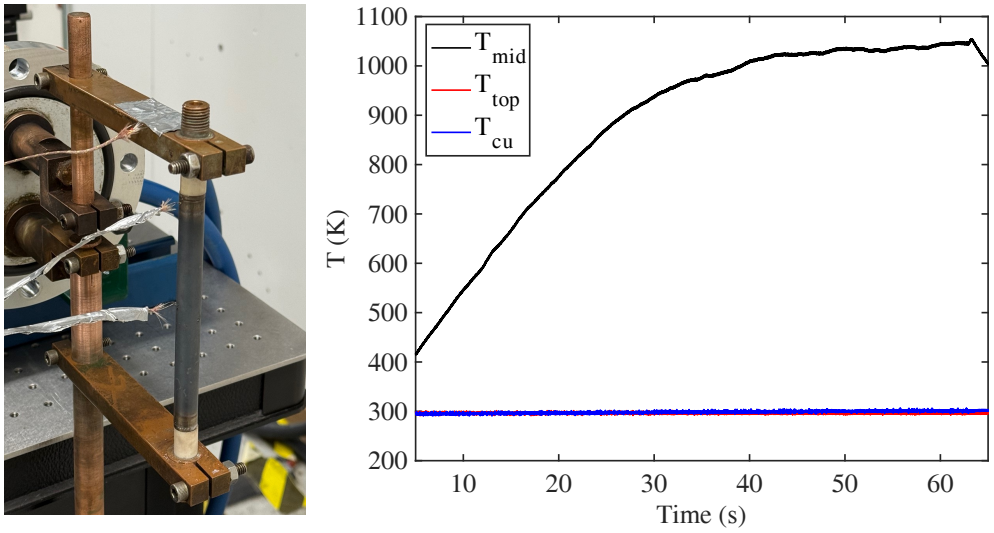


Figure 8.6: Temperature over time at the center, top, and on the copper support during a heating test.

Most importantly, the correct temperature boundary condition on the heated element needs to be used. A spatially and temporally varying temperature on the heated length was imposed along the heated length according to the transient, one-dimensional heat equation. The one-dimensional heat equation along the axial length, y, can be written as

$$\rho c_p \frac{dT}{dt} = \frac{d}{dy}\left(\lambda \frac{dT}{dy}\right) + \frac{I^2}{A_c^2 \sigma_{ss}} - \frac{h(T - T_{ambient})}{w_t} - \frac{\sigma \epsilon_{ss}\left(T^4 - T_{ambient}^2\right)}{w_t} \tag{8.9}$$

which comprises of an unsteady term, a diffusion term, and three source/sink terms. These source/sink terms are the energy added by resistive heating, energy lost to

convection, and energy lost to radiation. ρ is the density, c_p is the the heat capacity at constant pressure, λ is the thermal conductivity, T is the temperature, t is the time, and y is the axial length. I is the current supplied from the power supply, A_c is the cross-sectional area of the cylinder perpendicular to current flow, w_t is the stainless steel wall thickness, σ is the Steffan-Boltzmann constant, σ_{ss} and ϵ_{ss} are the electrical conductivity and emissivity of 304 stainless steel, and h is a convective heat transfer coefficient. The thermodynamic and electrical properties were calculated from tabulated values as a function of temperature (Kim, 1975). h was calculated empirically from the natural convection on vertical plates correlation presented in Churchill and Chu (1975).

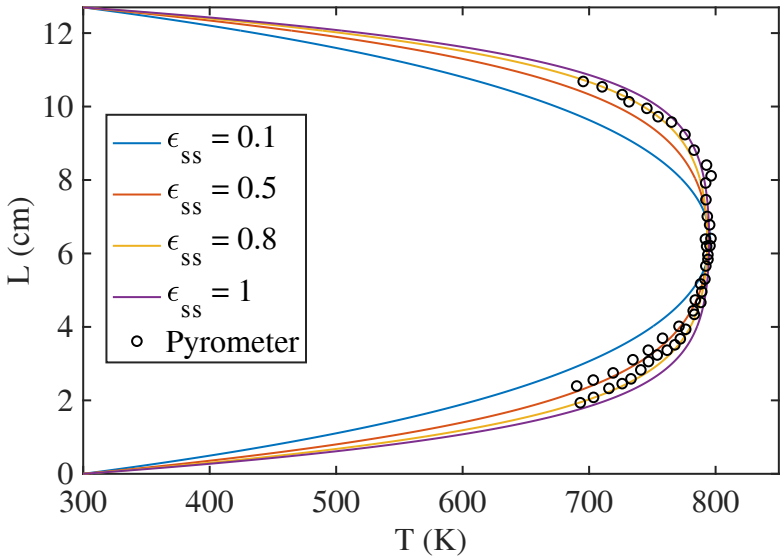


Figure 8.7: Steady heat equation solutions for a surface temperature at the center of 800 K for various values of ϵ_{ss}. Pyrometer measurements are from Jones (2021).

Eq. (8.9) was solved in MATLAB using the method of lines. Central differencing was employed for the spatial derivatives. Time integration was performed using the variable order ODE15s.

The emissivity was determined by fitting the steady-state solution to Eq. (8.9) for various values of ϵ_{ss} with temperature measurements on cylinder 50C presented by Jones (2021). Figure 8.7 plots the steady temperature distributions along the length of the 12.7 cm cylinder for various values of ϵ_{ss}. The experimental pyrometer values for a midpoint surface temperature of 800 K. A low emissivity value produced the sharpest distribution with a distinct peak in temperature at the midpoint. As ϵ_{ss} was increased, the temperature profiles become more flat in the middle before rolling

off to the 300 K ends. Comparing to the experimental pyrometer measurements, $\epsilon_{ss} = 0.8$ yielded the best agreement. Therefore, it was selected when determining the spatial and temporal temperature boundary conditions for the heated element in the numerical model.

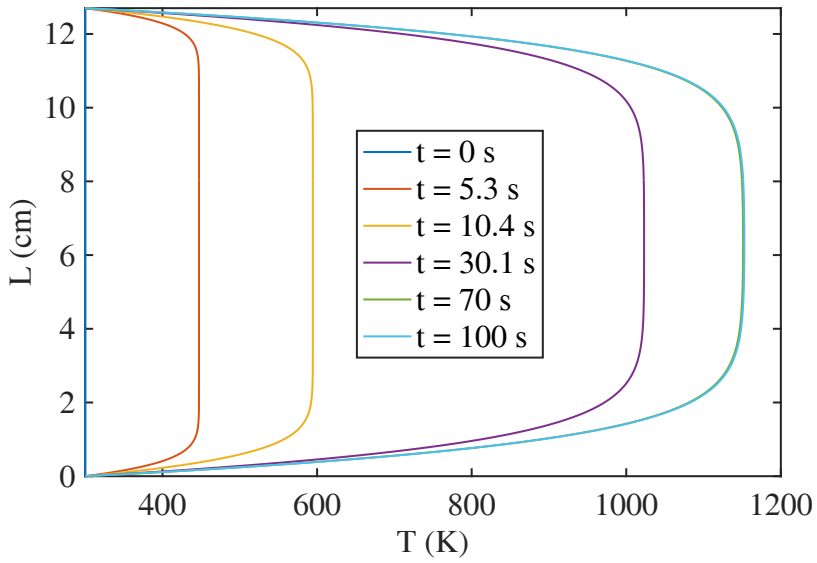


Figure 8.8: Temporal evolution of the temperature from Eq. (8.9) for $I = 235$ A and $\epsilon_{ss} = 0.8$.

Figure 8.8 plots the temporal evolution of the temperature distribution on the cylinder found from solving Eq. (8.9) with $I = 235$ A and $\epsilon_{ss} = 0.8$. The exact value of the current used is not particularly important as long as the timescale between the temperature increase from the heat equation is comparable to what was used for the experiments and the temperatures are sufficient to yield an intersection point with the line of criticality defined by Eq. (6.12). That being said, $I = 235$ A was within 10 A of what was needed to achieve the same temperature experimentally. The small variation is likely due to increased resistance caused by contact points in the copper supports. For early times, the temperature in the center increases quickly. As time evolves to 30.1 s, the temperature reaches 1000 K. It takes another 40 s to reach the steady temperature distribution for this value of I. In this case, $T_{max} = 1153$ K. This slow temperature increase at higher temperatures is caused by the strong T^4 dependence of the radiative loss term.

The spatial and temporally varying temperature distributions described by Figure 8.8 were imposed on the heated element for a majority of the numerical simulations. Temperature profiles for a slightly higher value of I were used for certain mixtures

that required temperatures higher than 1153 K to achieve an intersection with the line of criticality.

8.6 Predicted ignition temperature and location

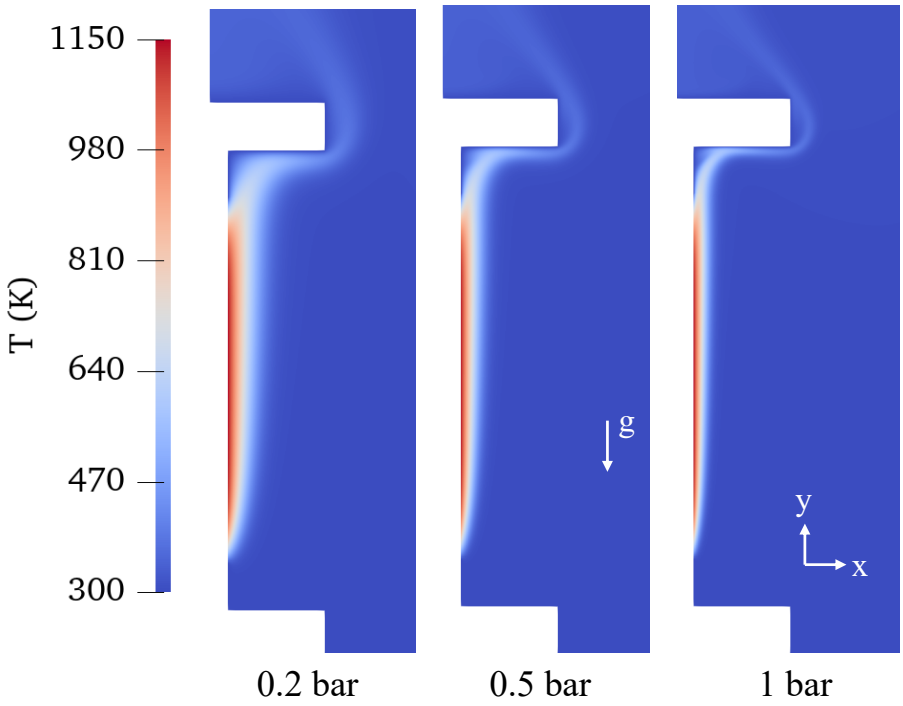


Figure 8.9: Temperature field near the hot vertical cylinder for C_2H_4/air mixtures at 0.2 bar, 0.5 bar, and 1 bar after 60 s of heating.

Chemically frozen flow simulations were run for each of the 12 configurations of composition and pressure. The resulting flow fields were similar in structure. Figure 8.9 shows what the typical thermal layer looks like, in this case for stoichiometric C_2H_4/air at the three tested pressures. The thermal layer develops near the hot surface, entraining cold fluid at the bottom and convecting hot fluid upwards. The importance of including the cold ceramic ends and copper support structure in the modeling can be visualized since the thermal layer must turn the corner when it reaches the lower part of the upper copper support. Because ignition is likely to occur near the top of the hot surface, it is important to include these structural features in the numerical model. The hot gas convecting away from the hot surface has momentum and propagates radially outwards until it reaches the end of the copper support. Buoyancy then causes the hot gas to continue rising past the end of the support.

Comparing the three pressures, 0.2 bar had the thickest thermal layer and lowest velocity boundary layer whereas 1 bar had the thinnest thermal layer and highest velocity boundary layer. These two effects are both a consequence of density variation. At lower pressures, the density is lower and thus the buoyancy force, $f_B = \rho g$, driving convection is lower. Similarly the thermal diffusivity, $\kappa = \lambda/\rho c_p$, scales as the inverse of density. This explains the weaker boundary layers and thicker thermal layers at reduced pressure.

Similar to the analyses presented in Chapter 7, Λ can be computed everywhere along the hot vertical cylinder at every instance in time. ℓ_k are computed for each Λ from the zero-dimensional simulation look-up tables for each mixture and pressure. Data for Θ, τ_i, and κ for each case is presented in Appendix F.

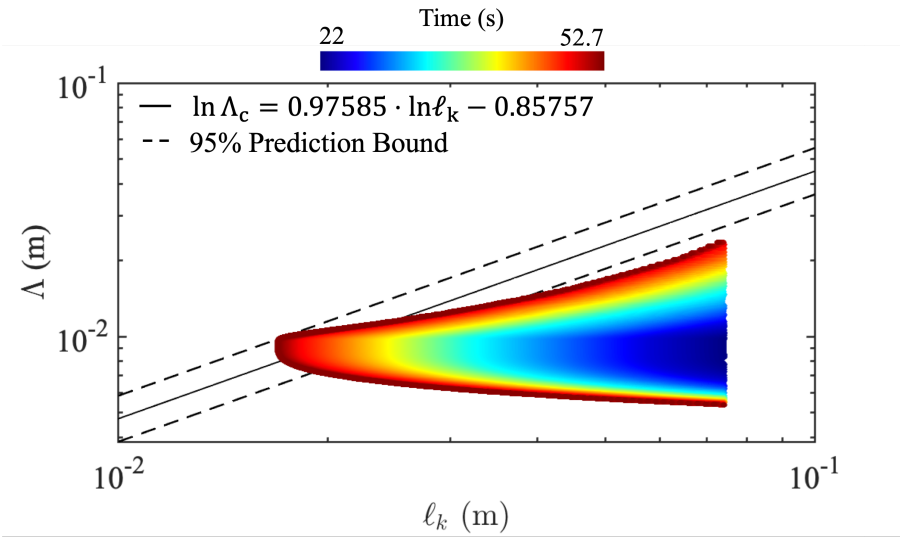


Figure 8.10: Temporal evolution of (ℓ_k, Λ) pairs at every location on the heated portion of the vertical cylinder for C_2H_4/air at 0.5 bar and $T > 900$ K. The line of criticality and prediction bounds are shown. The colors represent progression of time from 22 s (blue) to 52.7 s (red).

Figure 8.10 plots the temporal evolution of (ℓ_k, Λ) pairs at every location on the heated vertical cylinder for C_2H_4/air and $T > 900$ K. The color bar shows the progression of time from 22 s (blue) to 52.7 s (red). For a given time, the solution space takes on a parabolic structure. This can be attributed to the imposed temperature distribution (shown previously in Figure 8.8). At the bottom of the hot surface, the temperature is small. Thus, ℓ_k is large. Progressing vertically, the temperature rises and the thermal layer grows. Therefore, a decrease in ℓ_k and an increase in Λ occurs. Further continuing vertically past the midpoint of the cylinder, the temperature be-

gins to decrease again, but the thermal layer continues to grow. This increases both ℓ_k and Λ and is the cause of the parabolic shape in $\Lambda - \ell_k$ parameter space. For early times (blue), only a small section of the hot cylinder has temperatures high enough to ignite whereas at later times (red), a much larger portion of the surface is potentially ignitable. This causes an increase in size of the parabola as time evolves. At some time, the critical (ℓ_k, Λ_c) pair intersects the line of criticality. The point where this occurs becomes the predicted ignition location and surface temperature.

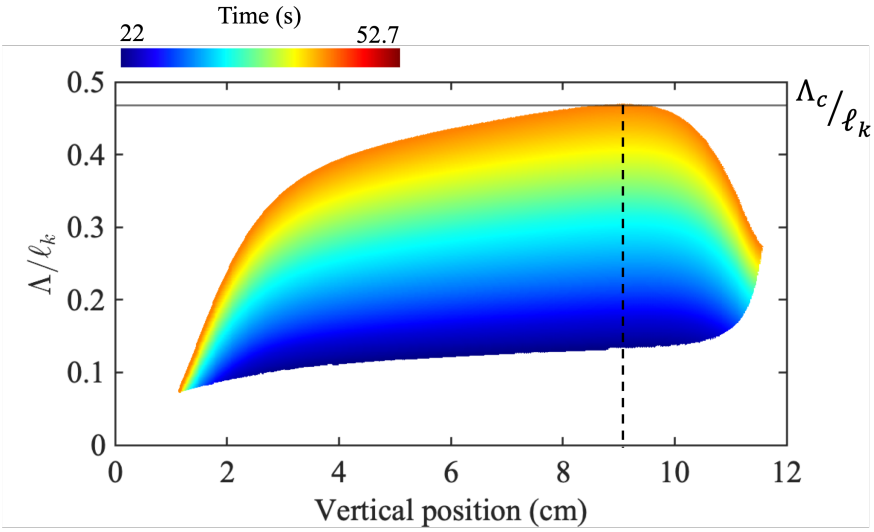


Figure 8.11: Temporal evolution of the ratio, Λ/ℓ_k, at every location on the heated portion of the vertical cylinder for C_2H_4/air at 0.5 bar and $T > 900$ K as a function of vertical position. The critical ratio of Λ_c/ℓ_k from Eq. (6.12) for these values of ℓ_k is shown along with the vertical position where the ratio is maximized. The colors represent progression of time from 22 s (blue) to 52.7 s (red).

Similar to the previous analyses in Chapter 7, it's useful to also plot the temporal evolution of the ratio, Λ/ℓ_k along the hot surface. This is shown in Figure 8.11. As the vertical position is increased, Λ/ℓ_k increases until it reaches a maximum value. As time evolves and the surface temperature rises, it eventually intersects the critical ratio, Λ_c/ℓ_k defined from Eq. (6.12). The location that this occurs is at approximately 9.1 cm from the bottom.

Figure 8.12 plots the predicted ignition temperatures from the model, defined by intersections with Eq. (6.12) for the four fuel/air mixtures and three pressures. The uncertainty bounds are determined by intersections with the 95% prediction intervals on the model. Overall, a 450 K range of ignition temperatures was predicted for this single geometry. For all pressures, nC_6H_{14} had the highest predicted ignition

temperature of 1320 K. As the pressure is increased, the predicted temperature decreases over 100 K to 1211 K. Predicted temperatures for nC_5H_{12} had a similar behavior and temperature range, with ignition temperatures ranging from 1292 K to 1196 K as the pressure is increased. C_2H_4 had a lower predicted ignition temperature and less pressure variation, ranging from 1099 K at 0.2 bar to 1079 K at 1 bar. The decrease in predicted ignition temperature for C_2H_4, nC_5H_{12}, and nC_6H_{14} with increasing pressure can be largely attributed to the increased reactivity of the mixtures at elevated pressures. Mathematically, this equates to a significant decrease in the zero-dimensional ignition delay time, τ_i that decreases the critical value of ℓ_k. κ also has a similar effect on ℓ_k, but to a lesser extent.

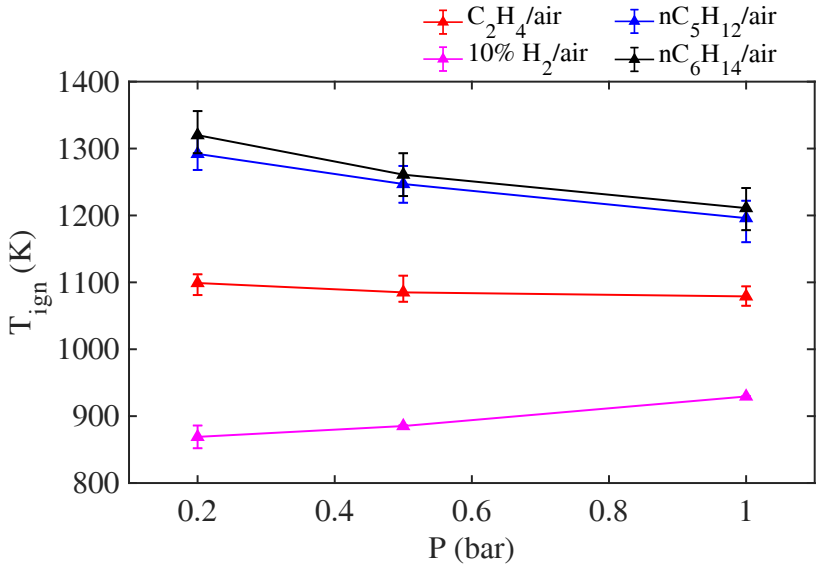


Figure 8.12: Predicted ignition temperatures from the model for all four fuel/air mixtures and three pressures.

The 10% H_2/air mixture had the lowest predicted ignition temperatures ranging from 869 K at 0.2 bar to 929 K at 1 bar. Interestingly, this fuel/air mixture exhibits an increasing in ignition temperature as the pressure is increased. This affect can be attributed to the crossover temperature where the dominant reaction pathways shift from HO_2 to OH reactions (Konnov, 2008; Hashemi et al., 2015). As the pressure is increased, the crossover temperature shifts to a higher temperature, functionally increasing the ignition temperature. This increase in ignition temperature for H_2/air mixtures with increasing pressure for $P < 1$ bar has been observed in the literature for autoignition in a shock tube as well as counterflowing jets (Neer, 1975; Fotache et al., 1995). The results indicate that this effect also occurs for ignition near the 12.7 cm hot vertical cylinder. Note that this increase in ignition temperature with

increasing pressure is particular to low pressures. For $P > 1$ bar, the ignition temperature should follow a similar trend as what was observed for the C_2H_4, nC_5H_{12}, and nC_6H_{14} mixtures, where it decreases with increasing pressure.

8.7 Experimental results

After obtaining the predicted ignition thresholds, the experiments were run on the 12 configurations of composition and initial pressure for validation.

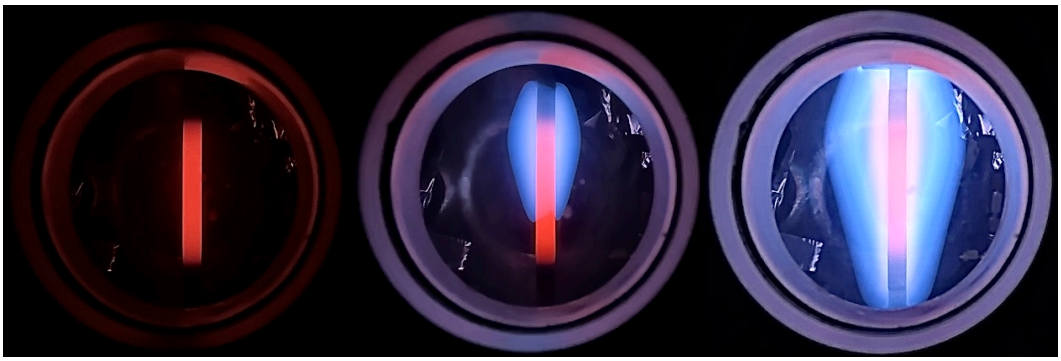


Figure 8.13: Visualization of an ignition event in shot 16. The mixture is stoichiometric C_2H_4/air at 0.5 bar.

Figure 8.13 shows the ignition event and flame propagation for shot 16, which had a mixture of stoichiometric C_2H_4/air at 0.5 bar. All fuels had similar visualizations except for H_2 for which the flame was nearly invisible. The visualization was taken with an iPhone 16 Pro recording 1080p at 240 FPS and 10-bit color depth and was synced with the power supply. At 39.78 s, the hot cylinder can be seen glowing inside the vessel with radiation rolling off near the water cooled ends. Roughly 4 ms later, at 39.784 s, the initial flame can be seen originating from the upper portion of the cylinder, propagating quickly throughout the thermal layer. The blue hue of the flame is attributed to the strong emission of blue light by CH radicals (Karnani and Dunn-Rankin, 2013). This rapid movement of the flame through the thermal layer adjacent to the hot cylinder is expected as the gas temperature is significantly higher, and thus, so is the laminar burning velocity. At 39.788 s, the flame has propagated through the entire length of the cylinder and continues to propagate outwards into the ambient gas. The structured flame propagation is evidence that welding the thermocouple at the midpoint as a second temperature measurement along with the pyrometer does not preemptively trip the thermal layer. Random azimuthal location of ignition events were observed for repeated tests.

This indicates that the thermocouple also does not affect the surface temperature distribution or axisymmetry of the apparatus. This is important in the context of the numerical model simulated in OpenFOAM.

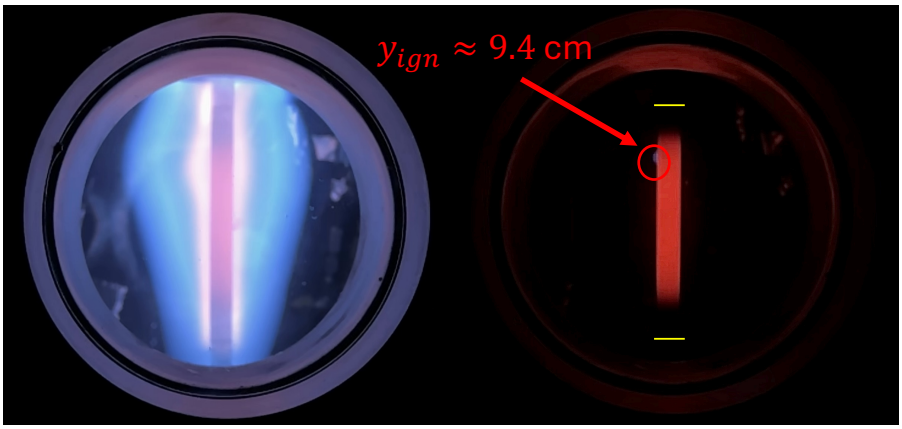


Figure 8.14: Ignition height for shot 18. The mixture is stoichiometric C_2H_4/air at 0.5 bar.

Because the 240 FPS is only fast enough to capture a few frames of the ignition event itself, the location of ignition cannot be determined from the visualization of shot 16. However, numerous shots were run at each condition, each yielding visualizations of the ignition event in different stages. Figure 8.14 (right) shows an image captured of the same mixture and initial pressure for shot 18. A small, faint blue dot can be see immediately next to the hot cylinder which is circled in red. This is the ignition kernel. The axial location of the ignition kernel along the cylinder can be characterized by a linear pixel analysis. The flame propagation in Figure 8.14 (left) is luminous enough to distinguish the ceramic end pieces at the ends of the 12.7 cm heated cylinder. These locations are mapped as yellow lines on Figure 8.14 (right). From these two locations that have a known spacing of 12.7 cm, the ignition location can be extrapolated was found to be $y_{ign} \approx 9.4$ cm.

In comparing to the predicted location determined for this configuration with Figure 8.10, there is a 0.3 cm difference (3.2%) which could be attributed to several factors. First, the heat equation solution shown in Figure 8.8 used in the numerical model assumes an emissivity value, $\epsilon_{ss} = 0.8$. While this value was from fitting experimental pyrometer measurements, it's possible repeated heat cycles increased ϵ_{ss} slightly. As was shown in Figure 8.7, higher values of ϵ_{ss} resulted in flatter temperature profiles which would allow for a predicted ignition location further up the cylinder. Second, after evolving from the wall, the ignition kernel may convect

a small distance vertically prior to thermal runaway. Both of these reasons could be responsible for this small difference between predicted and measured ignition location.

As mentioned, several shots were run at each test condition to ensure accurate determination of the ignition temperature. The repeatability can be seen from Figure 8.15 which plots the temperature at the center of the hot surface measured from the pyrometer for shots 16, 17, and 18. All shots were with stoichiometric C_2H_4/air at 0.5 bar. At 20 s, the surface reaches a sufficient temperature to obtain a pyrometer reading. The temperature continues to increase, up until a sharp decrease of the measurement as a result of the flame propagating over the detection area. This point is determined to be the temperature at the midpoint of the hot surface at the time of ignition. For the three shots at this condition, the ignition temperature varied by 3.3 K (~ 0.3%). In addition, the temperature curves for all three shots are nearly identical. This highlights the repeatability of the heating apparatus and experiment to produce consistent ignition temperatures for a given test condition. The measured temperatures from each shot at a given condition are averaged to determine the ignition temperature. A full shot log can be found in Appendix H.

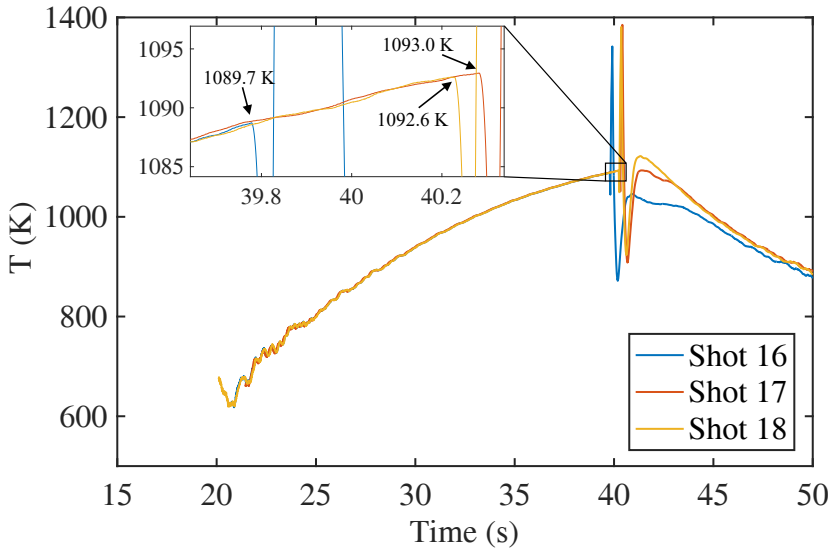


Figure 8.15: Pyrometer temperature measurements for three tests with at the same condition: stoichiometric C_2H_4/air at 0.5 bar.

Table 8.1 provides a summary of the ignition temperatures for the four fuels and three initial pressures. The three hydrocarbon fuels exhibited a decrease in ignition temperature as the pressure was increased. Of the three, C_2H_4 had the lowest

Table 8.1: Summary of temperatures at the center of the vertical cylinder at the time of ignition for the four fuels and three initial pressures. The ±25 K is determined by uncertainty in the pyrometer measurement.

	0.2 bar	**0.5 bar**	**1 bar**
10% H_2	902 K (±25 K)	920 K (±25 K)	950 K (±25 K)
C_2H_4	1143 K (±25 K)	1092 K (±25 K)	1056 K (±25 K)
nC_5H_{12}	1252 K (±25 K)	1184 K (±25 K)	1124 K (±25 K)
nC_6H_{14}	1233 K (±25 K)	1172 K (±25 K)	1114 K (±25 K)

ignition temperatures, ranging from 1056 K at 1 bar to 1143 K at 0.2 bar. Both of the heavy fuels, nC_5H_{12} and nC_6H_{14}, had similar ignition temperatures to each other that were about 100 K higher than C_2H_4 for a given initial pressure. These ignition temperatures ranged from 1114 K at 1 bar to 1252 K at 0.2 bar. For all pressures, 10% H_2 had the lowest ignition temperature, ranging from 902 K at 0.2 bar to 950 K at 1 bar. Similar to what the ignition model predicted in Figure 8.12, an increase in ignition temperature is seen as the initial pressure is increased, opposite what the three hydrocarbon fuels exhibit.

Figure 8.16 plots the pressure increase over time for the four fuel/air mixtures during ignition at (a) 0.2 bar, (b) 0.5 bar, and (c) 1 bar. Ignition and flame propagation is apparent from the rapid increase in pressure. For the hydrocarbon fuels, the pressure rise took about 100 ms to reach a maximum whereas for the 10% H_2 mixture, it took about four times longer. For all mixtures, as the initial pressure was increased from 0.2 bar to 1 bar, the pressure rise during ignition and subsequent flame propagation rose by over a factor of 5, from roughly 130 kPa to 710 kPa for all three hydrocarbon fuels. The 10% H_2 mixture had a significantly lower peak pressure ranging from 43 kPa to 236 kPa over the pressure range. This elongated and lower peak for the 10% H_2 mixtures can be understood from a simple thermodynamic analysis with the ideal gas law. For a constant volume, the pressure rise can be related to the flame temperature as

$$P_f = P_i \cdot \frac{n_f T_f}{n_i T_i} \tag{8.10}$$

where T_f is the temperature behind the flame, P_i and T_i are the initial pressure and temperature, respectively, and P_f is the pressure rise. n_i and n_f are the number of moles of the initial mixture and of the products behind the flame, respectively. For an initial pressure, $P_i = 1$ bar, and $T_i = 298$ K, the adiabatic flame temperature for each

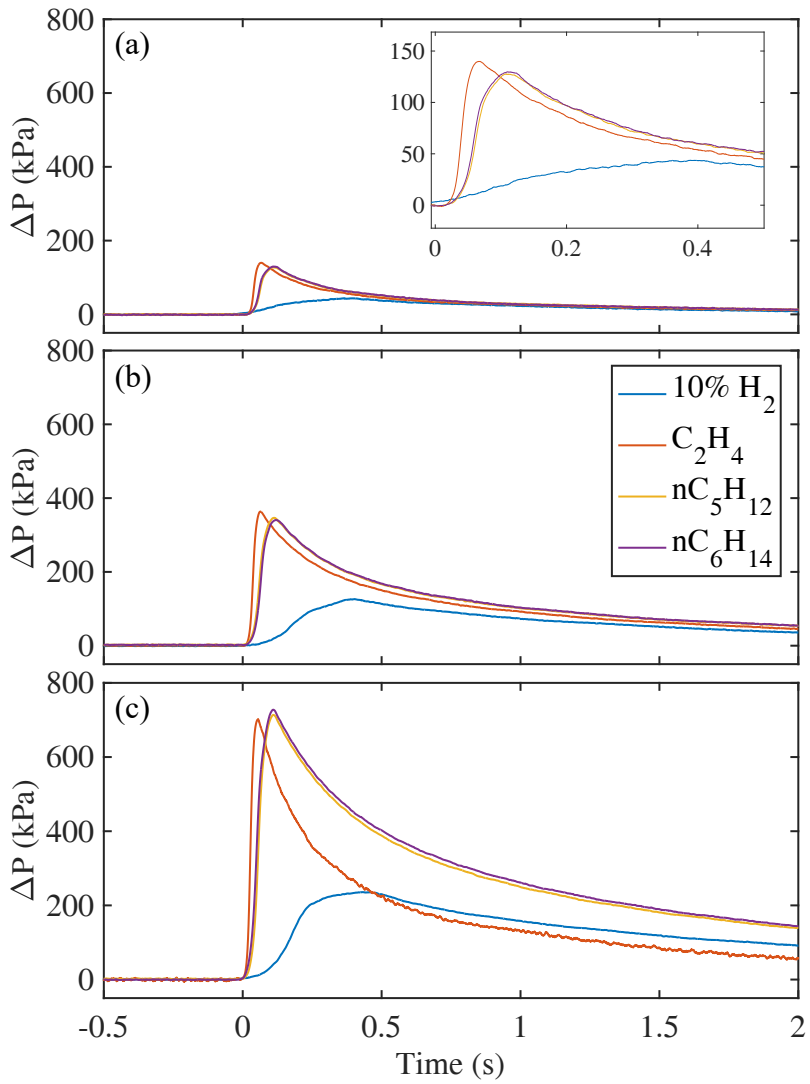


Figure 8.16: Pressure increase over time for the four fuel/air mixtures during ignition at (a) 0.2 bar, (b) 0.5 bar, and (c) 1 bar. Ignition events are all synced to be at $t = 0$ s for comparative analysis

mixture can be computed as $T_{f,10\%H_2} = 1302$ K, $T_{f,C_2H_4} = 2380$ K, $T_{f,nC_5H_{12}} = 2394$ K, and $T_{f,nC_6H_{14}} = 2405$ K. The ratio of n_f/n_i is on the order $O(10^0)$ for these mixtures. Therefore, for the same initial conditions, the pressure rise increases as the flame temperature increases. Because the 10% H_2 mixture is extremely lean, the flame temperature is comparably low. This results in a lower pressure rise. C_2H_4, nC_5H_{12}, and nC_6H_{14} all have similar adiabatic flame temperatures. As a result, the pressure rise is similar for all initial pressures.

The time to peak pressure rise is shortest for the C_2H_4, followed by both nC_5H_{12} and nC_6H_{14} which have nearly identical profiles. The 10% H_2 mixture had the longest time to peak pressure rise. This result is a consequence of flame speed. Qualitatively, the flame speed for stoichiometric C_2H_4 is highest. Stoichiometric nC_5H_{12} and nC_6H_{14} have similar flame speeds that are lower than C_2H_4. Thus, the onset of flame propagation through the mixture takes longer. Typically, H_2/air has substantially higher flame speeds compared to the three other hydrocarbons. However because the mixture is incredibly lean, the flame speed is much lower. This accounts for the significantly longer time to peak pressure rise seen for 10% H_2 in Figure 8.16.

8.8 Ignition temperature comparison

As discussed in the previous section, the ignition location was found experimentally to be at roughly 9.4 cm from the bottom of the cylinder. Because there exists a nonuniform temperature distribution on the surface, the temperature at 9.4 cm will not match the temperature at the midpoint where the pyrometer is focused. This is important because the ignition model discussed in Chapters 5, 6, and 7 uses the *local* wall temperature in calculating Λ and ℓ_k. For comparison with the ignition model, the temperature at 9.4 cm can be approximated using the heat equation presented in Figure 8.8. It was found that the temperature at 9.4 cm was about 14 K lower than what is measured at the center of the vertical cylinder. Thus, for comparison with the ignition model, 14 K is subtracted from the critical ignition temperatures measured via pyrometer in Table 8.1.

The results are shown in Figure 8.17 which compares the ignition temperature calculated from the model against the experimentally measured value for all 12 configurations. For all mixtures, the ignition model predicts the same trends in ignition temperature with pressure. The results for both 10% H_2 and C_2H_4 show good agreement with an average temperature error of $|\Delta T|_{avg} = 20$ K ($\sim 2\%$). As was hypothesized in Chapters 6 and 7 for heavy hydrocarbons, predicted ignition temperature thresholds for nC_5H_{12} and nC_6H_{14} over predict the critical temperature compared to the experimentally measured value. This is because of the NTC region that exists for these fuels where exothermic low temperature reactions create more favorable conditions for high temperature ignition near the hot wall (Chapter 4). On average the error in the predicted ignition temperature for these fuels was found to be $|\Delta T|_{avg} = 89$ K ($\sim 7.4\%$).

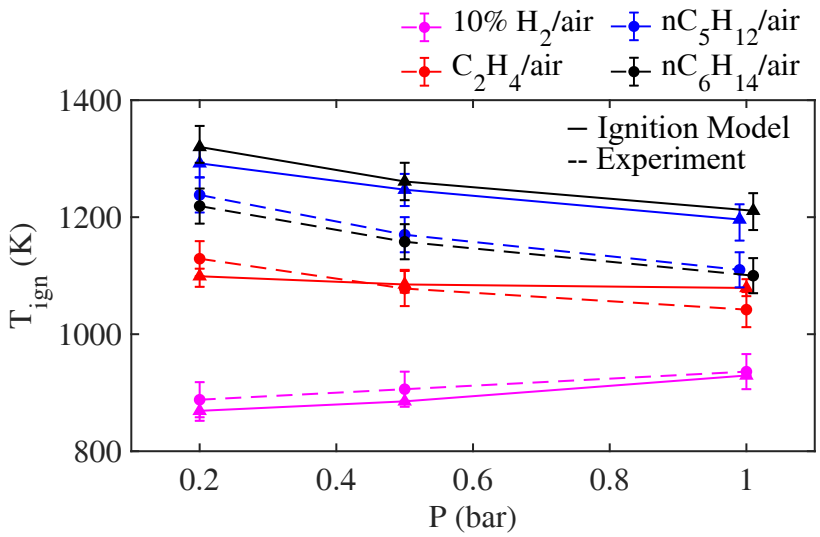


Figure 8.17: Ignition model predicted and experimentally measured ignition temperatures for all four fuel/air mixtures and three pressures

8.9 Summary and conclusions

In this chapter, numerical modeling and experiments were run to understand ignition on a 12.7 cm vertical cylinder with water cooling at the ends. It was found that the ignition temperature for the three hydrocarbon fuels decreased as the initial pressure was increased whereas the hydrogen fuel saw an increase with increasing initial pressure. The 10% H_2/air mixture had the lowest ignition temperature for all pressures while nC_5H_{12} and nC_6H_{14} had the highest ignition temperature.

Use of the ignition model accurately predicted the trend of decreasing ignition temperature for the three hydrocarbon fuels and increasing ignition temperature for H_2 with increasing initial pressure. For the light fuels (10% H_2 and C_2H_4), good agreement with the experiment (2% average error). A larger error (7.4%) was observed for nC_5H_{12} and nC_6H_{14} which was attributed to NTC effects creating more favorable ignition conditions for heavy hydrocarbons that is not accounted for in the ignition model. Comparing the location of ignition yielded a 3% error between the model and the experiment.

Figure 8.18 summarizes the model predictions for all cases analyzed in this thesis. The new data found in this chapter are added and all previous data from Chapter 7 are colored black to emphasize the new data points. The results illustrate the progress we have made on understanding the ignition phenomena near heated surfaces as a whole. For this experiment, the ignition model was shown to accurately describe

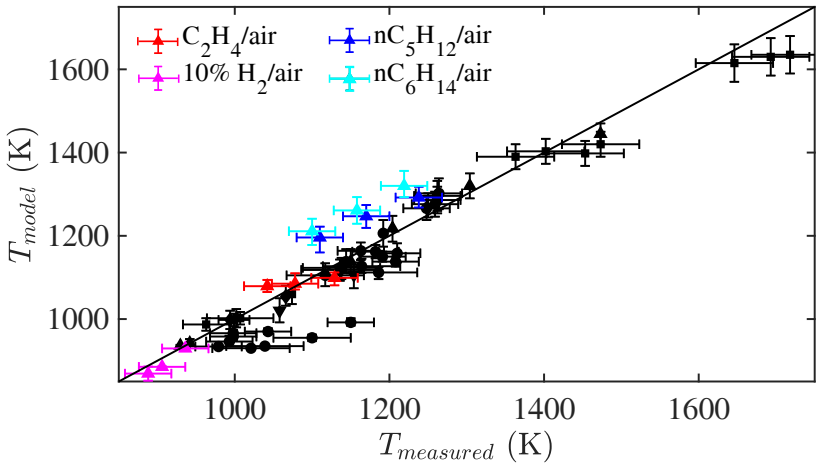


Figure 8.18: Ignition model predicted ignition temperature, T_{model}, vs measured ignition temperature, $T_{measured}$, from the results with the 50C cylinder. All data from Chapter 7 is also included in black. Vertical uncertainty bars are computed from the intersections with the 95% prediction interval on the ignition model. Horizontal uncertainty bars are from the uncertainty in the pyrometer measurements.

the effects of pressure variation on the ignition threshold for four fuels and three pressures. Ignition temperatures spanning over 400 K could be achieved and more importantly, predicted. The presented results provide further validation of the ignition model and present an example of how hot surface ignition problems could be approached in the future for preliminary design and certification of parts in the hazard safety industry.

Further limitations of the ignition model were identified and quantified. In particular, the model over predicts ignition temperatures for more complex fuels that exhibit an NTC region. However, this over prediction was similar for the two NTC fuels examined across the pressure range investigated. While this could imply the low temperature chemistry effects could be empirically corrected for in the model, the full extent of the NTC region on high temperature surface ignition problems remain to be studied and understood in more detail.

Chapter 9

CONCLUSIONS AND FUTURE WORK

9.1 Conclusions

The motivation for this work was to advance understanding of thermal ignition phenomena to mitigate hazards in systems where flammable gases may be present. This goal was pursued through three primary objectives: (1) to characterize the flow field and ignition behavior of fuel during a standardized autoignition temperature (AIT) test, (2) to understand the fundamental physics governing ignition near a hot surface and assess the impact of low-temperature chemistry modeling, and (3) to develop an analytical model for correlating and predicting ignition near hot surfaces for arbitrary fuels, thermodynamic states, and geometries.

First, three-dimensional numerical simulations with realistic transport properties and boundary conditions were used to characterize the nonreactive flow field inside the ASTM-E659 AIT apparatus. Comparison of the simulated temperature field with experimental measurements showed excellent agreement. Within the flask, downward motion of cool air entering from the top creates a dominant toroidal vortex, transporting gas upward along the walls and downward along the centerline. Interestingly, this toroidal vortex in the nonreacting flow was found to be counter-rotating relative to previous observations in closed-vessel reacting flows. This is a consequence of the open-top configuration required in the AIT standard to allow for flame visualization.

Several flask holder heights were investigated to assess their influence on the flow field. While all configurations exhibited the same toroidal structure, the tallest holder produced a substantially more uniform average temperature distribution with smaller and less frequent fluctuations than the shorter holders.

Additional nonreacting flow simulations explored the effect of fuel molecular size and weight on post-injection mixing. Ethene, with its small molecular size and low Schmidt number, mixed rapidly with minimal buoyancy effects. In contrast, heavier fuels such as n-hexane and n-dodecane were strongly affected by gravity and accumulated near the bottom of the flask. These fuels mixed primarily by diffusion and required significantly longer times to achieve uniformity due to their larger Schmidt numbers.

Further simulations incorporating chemical reactivity and a reduced kinetic mechanism for n-hexane autoignition showed that chemical reactions begin gradually near the hot flask walls, forming intermediate species. Ignition initiates as a ring-shaped kernel around the vertical midpoint, where the local fuel-air mixture is rich. A localized two-stage ignition process was observed and characterized through Lagrangian particle tracking. Flame expansion drives unburned fuel out of the flask as a jet through the top opening. The flame quenches at the bottom due to overly rich conditions and instead convects upward, eventually fragmenting into smaller flamelets that exit through the holder. This behavior is consistent with "Mode I" ignition observed in experiments (Martin and Shepherd, 2021; Fouchier and Shepherd, 2025).

A one-dimensional spherically symmetric analog was developed to isolate the influence of temperature gradients on ignition behavior. The simple model confirmed that even small radial temperature differences that are inherent to experimental conditions can shift the ignition location and delay time.

Based on these simulations, several key implications for interpreting published AITs and improving standardized testing procedures can be summarized:

- The downward intrusion of cold air through an open top is inherent in both ASTM-E659 and ISO/IEC testing standards. This introduces temperature and composition fluctuations that influence self-heating and contribute to variability in reported AIT values.
- Variations in implementation of the ASTM-E659 apparatus (e.g., holder geometry) result in different temperature fields and needs to be considered when interpreting published AITs. Standardization of geometric constraints is recommended.
- Current testing practices typically measure temperature at a single point, which may not capture the full temperature range in the flask. More spatially resolved diagnostics would improve the interpretation of AIT values.
- Fuel dispersion depends strongly on both the flow field and fuel physical properties. For short-duration tests, ignition may occur in an incompletely mixed, stratified environment. For long-duration tests, fuel loss could affect the AIT. Mixing and chemical timescales must be considered when comparing AITs across different fuels.

- Asymmetric mixing and temperature gradients produce off-center ignition events, highlighting sensitivity to injection technique. Standardization of fuel injection, such as the automated method proposed in Fouchier and Shepherd (2025), could enhance test reproducibility.

- Different time duration experiments could have significantly different reaction pathways leading to observation variability between tests as identified by Martin and Shepherd (2021) and Fouchier and Shepherd (2025)

- Experimentally observed ignition modes can vary with temperature and fuel quantity, as identified by Martin and Shepherd (2021) and Fouchier and Shepherd (2025). These variations can be linked to underlying changes in ignition dynamics brought about by test duration.

- For temperatures close to the AIT, chemical timescales can be long. Natural convection induced by chemical reaction may become more influential on the ignition behavior, further contributing to published AIT variability.

Second, the fundamental physics of ignition near a hot surface were analyzed for a canonical problem. Ignition emerges from a balance between localized chemical heat release and non-local energy transport. Specifically, an ignition kernel evolves from the wall when thermal diffusion can no longer offset heat release from chemical reaction. Thermal runaway then occurs as a rapid and exothermic conversion of intermediate species into products.

Further simulations with the inclusion of low-temperature kinetic pathways exhibited two-stage ignition, with the first stage driven by low-temperature reactions and the second stage by high-temperature pathways. In contrast, the high-temperature-only mechanism produced a single ignition event. Importantly, the inclusion of low-temperature chemistry significantly reduced the critical surface temperature for ignition. This effect was traced to a quasi-steady band of energy release in the low-temperature region of the thermal layer, originating from the first ignition stage. This band reduces local heat losses, effectively promoting ignition at a lower temperature.

Finally, a hot surface ignition model was developed based on classical theories of ignition, introducing two characteristic length scales, Λ_c and ℓ_k, that describe a critical relation between heat transfer and chemical reaction. We found that these scales could be expressed using results from zero-dimensional ignition delay simulations

and chemically frozen fluid simulations, allowing for tangible application to real systems. To characterize their relationship, a one-dimensional diffusing thermal layer was simulated across a wide range of fuels, pressures, and wall temperatures. Remarkably, all results collapsed onto a single "line of criticality," allowing for a critical Damköhler number to be defined.

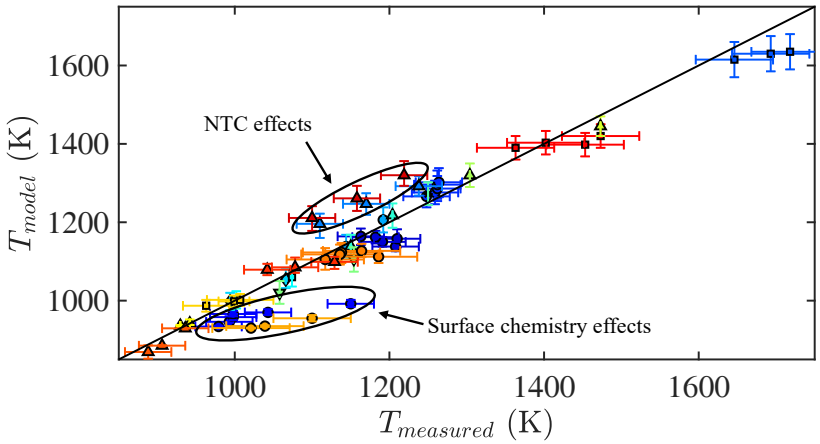


Figure 9.1: Ignition model predicted ignition temperature, T_{model}, vs measured ignition temperature, $T_{measured}$, for all 60 configurations examined in this work. Vertical uncertainty bars are computed from the intersections with the 95% prediction interval on the ignition model. Horizontal uncertainty bars are from the uncertainty in the pyrometer measurements for each respective experiment.

The model's predictive capability was then demonstrated through application to a wide variety of two-dimensional simulations (stagnation point, forced and natural convection) and experimental configurations (heated cylinders, plates, spheres, and glow plugs). Further experiments with a heated vertical cylinder revealed that the model could also capture pressure-dependent ignition behavior across four fuel/air mixtures. The results for all 60 configurations examined are summarized in Figure 9.1 where each color and symbol represent a different series of test data. On average for all the cases, the model predicted ignition temperature differed from the measured value by 40 K (3.4%), demonstrating excellent agreement and marking the first and only successful unification of hot surface ignition theory, simulation, and experiment. This emphasizes a significant improvement over the conventional approach for correlating a wide range of ignition data with surface area as presented in Figure 1.3. However, two model limitations were identified. First, surface chemistry on certain materials may elevate measured ignition temperatures relative to model predictions. Second, the model currently excludes low-temperature chem-

istry, resulting in over predictions for fuels with negative temperature coefficient (NTC) behavior (i.e., heavy hydrocarbons). These effects are emphasized in Figure 9.1

9.2 Future work

9.2.1 Autoignition testing

The present work examined ignition and flow behavior for a single experimentally measured wall temperature distribution. Extending the analysis to a range of wall temperatures would improve understanding of how buoyancy and unsteady flow influence ignition for fuels with large range of AITs.

Incorporating a two-phase numerical model could clarify the effects of vaporization on fuel dispersion, particularly for fuels near or above the Leidenfrost temperature. As observed by Fouchier and Shepherd (2025), the Leidenfrost effect can significantly delay vaporization by creating a stable vapor film at the surface. Additionally, the vaporization process itself may induce flow disturbances that enhance mixing. Both mechanisms could influence fuel distribution and the onset of thermal runaway.

The effect of surface chemistry on autoignition testing is generally inconclusive in the literature. However, as was shown for higher temperature hot surface ignition, it can be quite significant. Surface chemistry may also have an effect on reported AITs. Both an experimental and numerical investigation could be performed to determine the significance of the flask material on the AIT for a given fuel.

At least four ignition modes have been documented in prior AIT studies (Martin and Shepherd, 2021; Fouchier and Shepherd, 2025), classified based on optical emission and temperature traces. However, the physical basis for these distinctions remains unclear. A broader range of reacting flow simulations across fuels, injected fuel volume, and surface temperatures could provide insights. While the current simulations employed wall temperatures just about the AIT to reduce computational time, simulating near-threshold ignition would necessitate simulating much longer durations (several hundred seconds), requiring significant computational resources.

9.2.2 Hot surface ignition modeling and correlation

Expanding the ignition model to include more complex systems, such as aircraft fuel tanks, engines, or auxiliary power units (APUs), would build confidence in its applicability. If successful, this could inform safer and more efficient designs and support revisions to safety certification criteria in the aviation and chemical

industries.

The effect of low-temperature chemistry and surface chemistry could be examined more rigorously and empirical correction factors to the model predictions for relevant systems could be developed. In addition, violation of other assumptions utilized in the theoretical framework could be investigated. The most relevant of which would be the large non-dimensional activation energy assumption. For hot surfaces adjacent to room temperature gas, as was explored in the present work, this assumption was found to be robust for all examined fuels. However, if the gas temperature is increased closer to the hot wall temperature, values of $-\theta_0$ become smaller, inducing larger errors in the critical temperature gradient conclusion found from the theory. The effect this has on the ability to correlate data and predict ignition temperatures has yet to be explored.

The theory itself could be improved to relax current assumptions for broader generality. For instance, the model could be reformulated to incorporate NTC chemistry by introducing a third "middle" layer between the reactive-diffusive and chemically frozen regions in the current theory. This middle region could include a quasi-steady heat release term to represent low-temperature reactions. Similar concepts could also be employed to include surface chemistry effects. Importantly, the model relies on large activation energy asymptotics and a quasi-steady formulation of the problem. In the present work, validation was provided for primarily quasi-steady, laminar flow problems. Transitional and turbulent flows are also relevant to many industrial applications, as demonstrated in laboratory studies of high Rayleigh number convection (Jones, 2021; Martin, 2023). Extending the framework to unsteady flows is therefore necessary for broader applicability. We anticipate that the present formulation may remain valid if turbulence fluctuation timescales are sufficiently long relative to chemical reaction timescales. However, this requires further investigation.

BIBLIOGRAPHY

Accidents in Mines, R. C. on (1867). "Report on the Oaks Colliery Explosion". In: *Parliamentary Papers (UK)* 30.

Arrhenius, S. (1889). "Über die Reaktionsgeschwindigkeit bei der Inversion von Rohrzucker durch Säuren". German. In: *Zeitschrift für Physikalische Chemie* 4, pp. 226–248.

Ashmore, P., B. Tyler, and T. Wesley (1967). "Experimental investigations of conductive and convective heat transfer in relation to thermal ignitions". In: *Symposium (International) on Combustion*. Vol. 11, pp. 1133–1140.

ASTM-E659 (2005). *Standard test method for autoignition temperature of liquid chemicals*. American Society for Testing and Materials.

ASTM-E659-24 (2024). *Standard test method for autoignition temperature of liquid chemicals*. American Society for Testing and Materials.

Bane, S. P. M. (2010). "Spark ignition: experimental and numerical investigation with application to aviation safety". PhD thesis. California Institute of Technology.

Bane, S. P., R. Mével, and J. E. Shepherd (2010a). "Instability of a Flame Front in a Lean H2-N2O Mixture". In: *arXiv preprint arXiv:1010.3255*.

Bane, S., J. Ziegler, and J. Shepherd (2010b). *Development of one-step chemistry models for flame and ignition simulation*. Technical Report GALCITFM:2010.002. California Institute of Technology. URL: http://shepherd.caltech.edu/Reports/FM2010-001.pdf.

Bane, S. et al. (2011). "Flame burning speeds and combustion characteristics of undiluted and nitrogen-diluted hydrogen–nitrous oxide mixtures". In: *International Journal of Hydrogen Energy* 36.16, pp. 10107–10116.

Battin-Leclerc, F. (2008). "Detailed chemical kinetic models for the low-temperature combustion of hydrocarbons with application to gasoline and diesel fuel surrogates". In: *Prog. Energy Combust. Sci.* 34.4, pp. 440–498.

Blanquart, G. et al. (n.d.). *CaltechMech*. URL: https://www.theforce.caltech.edu/CaltechMech/.

Board, C. A. (1964). *Accident Investigation Report: Pan American World Airways, Inc., Clipper Tradewind, Boeing 707-121, N709PA, Elkton, Maryland, December 8, 1963*. https://lessonslearned.faa.gov/PanAm214/PanAm214_AccidentReport.pdf.

Board, N. T. S. (2000). *Aircraft Accident Report: In-Flight Breakup Over the Atlantic Ocean, Trans World Airlines Flight 800, Boeing 747-131, N93119, Near East Moriches, New York, July 17, 1996*. https://www.ntsb.gov/investigations/AccidentReports/Reports/AAR0003.pdf.

Boeck, L. R. et al. (2017). “Ignition of fuel–air mixtures from a hot circular cylinder”. In: *Combustion and Flame* 185, pp. 265–277.

Boeck, L., J. Melguizo-Gavilanes, and J. Shepherd (2019). “Hot surface ignition dynamics in premixed hydrogen–air near the lean flammability limit”. In: *Combust. Flame* 210, pp. 467–478.

Boettcher, P. A. (2012). “Thermal Ignition”. PhD thesis. California Institute of Technology.

BP Deepwater Horizon Oil Spill, N. C. on the (2011). *Deep Water: The Gulf Oil Disaster and the Future of Offshore Drilling*. https://www.govinfo.gov/app/details/GPO-OILCOMMISSION.

Bradley, D., P. H. Gaskell, and X.-J. Gu (1996). “Burning velocities, Markstein lengths, and flame quenching for spherical methane-air flames: a computational study”. In: *Combustion and flame* 104.1-2, pp. 176–198.

Bradley, D. et al. (2000). “The development and structure of flame instabilities and cellularity at low Markstein numbers in explosions”. In: *Combustion and flame* 122.1-2, pp. 195–209.

Burcat, A. and B. Ruscic (2005). *Third Millennium Ideal Gas and Condensed Phase Thermochemical Database for Combustion*. https://garfield.chem.elte.hu/Burcat/burcat.html. Technion - Israel Institute of Technology.

Cairnie, L., A. Harrison, and P. Morgan (1981). “Autoignition in a free convection boundary layer”. In: *Proc. Combust. Inst.* 18, pp. 1799–1806.

Callendar, H. (1927). “Detonation and Dopes”. In: *Engineering* 123, pp. 147, 182, 210.

Campbell, A., S. Cardoso, and A. Hayhurst (2007). “A Comparison of Measured Temperatures with Those Calculated Numerically and Analytically for an Exothermic Chemical Reaction inside a Spherical Batch Reactor with Natural Convection”. In: *Chemical Engineering Science* 62.11, pp. 3068–3082.

Campbell, M. F. et al. (2015). “Constrained reaction volume shock tube study of n-heptane oxidation: Ignition delay times and time-histories of multiple species and temperature”. In: *Proceedings of the Combustion Institute* 35.1, pp. 231–239.

Cavendish, H. (1766). “Three Papers Containing Experiments on Factitious Air”. In: *Philosophical Transactions of the Royal Society of London* 56, pp. 141–184.

Chapman, S. and T. G. Cowling (1990). *The mathematical theory of non-uniform gases: an account of the kinetic theory of viscosity, thermal conduction and diffusion in gases*. Cambridge University Press.

Chenoweth, D. and S. Paolucci (1986). “Natural convection in an enclosed vertical air layer with large horizontal temperature differences”. In: *Journal of fluid mechanics* 169, pp. 173–210.

Churchill, S. W. and H. H. Chu (1975). "Correlating equations for laminar and turbulent free convection from a vertical plate". In: *International journal of heat and mass transfer* 18.11, pp. 1323–1329.

Ciezki, H. and G. Adomeit (1993). "Shock-tube investigation of self-ignition of n-heptane-air mixtures under engine relevant conditions". In: *Combustion and flame* 93.4, pp. 421–433.

Coffee, T. and J. Heimerl (1981). "Transport algorithms for premixed, laminar steady-state flames". In: *Combust. Flame* 43, pp. 273–289.

Commission, F. G. (1906). *Courrières Mine Disaster Report (1906)*.

Coronel, S. et al. (2013). "Laminar burning speed of n-hexane-air mixtures". In: *8th US National Combustion Meeting 2013*. Vol. 3, pp. 2568–2583.

Coronel, S. A. et al. (2018). "Experimental and numerical study on moving hot particle ignition". In: *Combustion and Flame* 192, pp. 495–506.

Coronel, S. A. (2016). "Thermal ignition using moving hot particles". PhD thesis. California Institute of Technology.

Crowl, D. A. and J. F. Louvar (1990). "The PEPCON Explosion: A Case Study in Chemical Process Safety". In: *Chemical Engineering Progress* 86.11, pp. 58–63.

Cuoci, A. et al. (2013a). "A computational tool for the detailed kinetic modeling of laminar flames: Application to C_2H_4/CH_4 coflow flames". In: *Combust. Flame* 160.5, pp. 870–886.

– (2013b). "Numerical modeling of laminar flames with detailed kinetics based on the operator-splitting method". In: *Energy & fuels* 27.12, pp. 7730–7753.

Curran, H. J. (2019). "Developing detailed chemical kinetic mechanisms for fuel combustion". In: *Proc. Combust. Inst.* 37.1, pp. 57–81.

Curtiss, C. F. and J. O. Hirschfelder (1949). "Transport properties of multicomponent gas mixtures". In: *J. Chem. Phys.* 17.6, pp. 550–555.

Cutler, D. (1974). "The ignition of gases by rapidly heated surfaces". In: *Combust. Flame* 22.1, pp. 105–109.

– (1978). "Further studies of the ignition of gases by transiently heated surfaces". In: *Combustion and Flame* 33, pp. 85–91.

Dagaut, P. and M. Cathonnet (2006). "The ignition, oxidation, and combustion of kerosene: A review of experimental and kinetic modeling". In: *Progress in energy and combustion science* 32.1, pp. 48–92.

Davidenko, D., R. Mével, and G. Dupré (2011). "Numerical study of the detonation structure in rich H_2-NO_2/N_2O_4 and very lean H_2-N_2O mixtures". In: *Shock Waves* 21, pp. 85–99.

Davis, S. and C. K. Law (1998). “Determination of and fuel structure effects on laminar flame speeds of C1 to C8 hydrocarbons”. In: *Combustion Science and Technology* 140.1-6, pp. 427–449.

Davy, H. (1815). *On the Fire-Damp of Coal Mines and on Methods of Lighting the Mines so as to Prevent Its Explosion*. Vol. 106. Philosophical Transactions of the Royal Society of London, pp. 1–22. URL: https://doi.org/10.1098/rstl.1818.0001.

Department, U. M. (1913). *Senghenydd Colliery Disaster*. https://www.nmrs.org.uk/mines-map/accidents-disasters/senghenydd-colliery-disaster-1913/.

Dixon, H. B. and H. F. Coward (1909). “The ignition-temperatures of gases”. In: *Journal of the Chemical Society, Transactions* 95. Early experimental study of gas ignition on heated surfaces, pp. 514–543. DOI: 10.1039/CT9099500514. URL: https://doi.org/10.1039/CT9099500514.

Fieweger, K., R. Blumenthal, and G. Adomeit (1997). “Self-ignition of SI engine model fuels: A shock tube investigation at high pressure”. In: *Combustion and Flame* 109.4, pp. 599–619.

Fotache, C. et al. (1995). “An experimental study of ignition in nonpremixed counterflowing hydrogen versus heated air”. In: *Combustion science and technology* 109.1-6, pp. 373–393.

Fouchier, C. and J. Shepherd (2025). “ASTM-E659 Standardized Test Analysis and Results for Synthetic Paraffinic Kerosene”. In: *Journal of Loss Prevention in the Process Industries* 94, p. 105568.

Frank-Kamenetskii, D. A. (1939a). “Diffusion and Heat Transfer in Chemical Kinetics”. In: *Zhurnal Fizicheskoi Khimii* 13, pp. 738–745.

– (1939b). “Calculation of Thermal Explosion Limits”. In: *Acta Physicochemica U.R.S.S* 10, pp. 365–370.

Freyer, F. and V. Meyer (1893). “On the ignition temperatures of explosive gas mixtures”. In: *Z. Phys. Chem* 11, p. 28.

Galloway, R. L. (1882). *A History of Coal Mining in Great Britain*. Contains details on the Felling Colliery and other early firedamp explosions. Macmillan and Co.

Goodwin, D. G. et al. (2021). *Cantera: An Object-oriented Software Toolkit for Chemical Kinetics, Thermodynamics, and Transport Processes*. Version 2.5.1.

Griffin, T. A. et al. (1992). “The influence of catalytic activity on the ignition of boundary layer flows. Part III: Hydroxyl radical measurements in low-pressure boundary layer flows”. In: *Combustion and flame* 90.1, pp. 11–33.

Guard, U. C. (1999). “Chemical hazard response information system (CHRIS)-hazardous chemical data”. In: *Commandant Instruction* 16465.

Harrison, A. and L. Cairnie (1988). "The development and experimental validation of a mathematical model for predicting hot-surface autoignition hazards using complex chemistry". In: *Combustion and flame* 71.1, pp. 1–21.

Hashemi, H. et al. (2015). "Hydrogen oxidation at high pressure and intermediate temperatures: Experiments and kinetic modeling". In: *Proceedings of the Combustion Institute* 35.1, pp. 553–560.

Health, U. and S. Executive (2005). *Buncefield: Why did it happen? The underlying causes of the explosion at the Buncefield oil storage depot, Hemel Hempstead, Hertfordshire, on 11 December 2005*. https://www.hse.gov.uk/comah/buncefield.htm.

Iglesias, I. et al. (2017). "Thermal Explosions in Spherical Vessels at Large Rayleigh Numbers". In: *International Journal of Heat and Mass Transfer* 115, pp. 1042–1053.

Iida, N., O. Kawaguchi, and G. T. Sato (1985). "Premixed flame propagating into a narrow channel at a high speed, part 1: Flame behaviors in the channel". In: *Combustion and flame* 60.3, pp. 245–255.

Industrial Environment, I. (N. I. for and Risks) (2002). *Toulouse AZF Plant Explosion Report*. https://www.ineris.fr/fr/content/toulouse-accident-azf-21-septembre-2001.

Inspectorate, M. (1844). *Report on the Haswell Colliery Explosion*. https://www.durhamrecordoffice.org.uk.

ISO/IEC (2017). *ISO/IEC 80079-20-1: Explosive Atmospheres - Part 20-1: Material Characteristics for Gas and Vapor Classification-Test Methods and Data*. Tech. rep. International Organization for Standardization.

ISO/TC 197 (2015). *ISO/TR 15916:2015(E): Basic considerations for the safety of hydrogen systems*. Tech. rep. ISO/TR 15916:2015(E). Geneva, Switzerland: International Organization for Standardization.

Issa, R. I. (1986). "Solution of the implicitly discretised fluid flow equations by operator-splitting". In: *J. Comput. Phys.* 62.1, pp. 40–65.

Ji, C. et al. (2010). "Propagation and extinction of premixed C5–C12 n-alkane flames". In: *Combustion and Flame* 157.2, pp. 277–287.

Johnson, C. and C. V. Mashuga (2022). "Characterizing the autoignition behavior of simple paraffins and alcohols; comparisons and implications". In: *J. Loss Prev. Process Ind.* 77, p. 104773.

– (2023). "Reconsidering autoignition in the context of modern process safety: Literature review and experimental analysis". In: *J. Loss Prev. Process Ind.* 81, p. 104963.

Jones, D. (1974). "Convective Effects in Enclosed, Exothery Reacting Gases". In: *International Journal of Heat and Mass Transfer* 17.1, pp. 11–21.

Jones, S., J. Melguizo-Gavilanes, and J. Shepherd (2019). "Ignition by moving hot spheres in H2-O2-N2 environments". In: *Proceedings of the Combustion Institute* 37.2, pp. 1597–1604.

Jones, S. M. (2021). "Thermal Ignition by Vertical Cylinders". PhD thesis. California Institute of Technology.

Karnani, S. and D. Dunn-Rankin (2013). "Visualizing CH* chemiluminescence in sooting flames". In: *Combustion and Flame* 160.10, pp. 2275–2278.

Kee, R. J., C. S. Landram, and J. C. Miles (1975). *Natural Convection of a Heat-Generating Fluid Within Closed Vertical Cylinders and Spheres*. Technical Report SAND75-8610. Livermore CA: Sandia Laboratories.

Kee, R. J., M. E. Coltrin, and P. Glarborg (2005). *Chemically reacting flow: theory and practice*. John Wiley & Sons.

Kelley, A. et al. (2011). "Laminar flame speeds of C5 to C8 n-alkanes at elevated pressures: Experimental determination, fuel similarity, and stretch sensitivity". In: *Proceedings of the Combustion Institute* 33.1, pp. 963–970.

Khitrin, L. and S. Goldenberg (1957). "Thermal theory of ignition of gas mixtures: Limiting conditions". In: *Proc. Combust. Inst.* Vol. 6. Elsevier, pp. 545–554.

Kim, C. S. (1975). *Thermophysical properties of stainless steels*. Tech. rep. Argonne National Lab., Ill.(USA).

Kletz, T. and P. Amyotte (2019). *What went wrong?: case histories of process plant disasters and how they could have been avoided*. Butterworth-Heinemann.

Konnov, A. A. (2008). "Remaining uncertainties in the kinetic mechanism of hydrogen combustion". In: *Combustion and flame* 152.4, pp. 507–528.

Kuchta, J. M., A. Bartkowiak, and M. Zabetakis (1965). "Hot Surface Ignition Temperatures of Hydrocarbon Fuel Vapor-Air Mixtures." In: *Journal of Chemical and Engineering Data* 10.3, pp. 282–288.

Kukukova, A., J. Aubin, and S. M. Kresta (2009). "A new definition of mixing and segregation: Three dimensions of a key process variable". In: *Chemical engineering research and design* 87.4, pp. 633–647.

Kumar, R. (1989). "Ignition of hydrogen-oxygen-diluent mixtures adjacent to a hot, nonreactive surface". In: *Combustion and Flame* 75.2, pp. 197–215.

Laurendeau, N. M. (1982). "Thermal ignition of methane-air mixtures by hot surfaces: A critical examination". In: *Combust. Flame* 46, pp. 29–49.

Law, C. K. (2010). *Combustion physics*. Cambridge university press.

Law, C. (1978a). "Ignition of a combustible mixture by a hot particle". In: *AIAA journal* 16.6, pp. 628–630.

– (1978b). "On the stagnation-point ignition of a premixed combustible". In: *International Journal of Heat and Mass Transfer* 21.11, pp. 1363–1368.

Law, C. and C. Sung (2000). “Structure, aerodynamics, and geometry of premixed flamelets”. In: *Progress in energy and combustion science* 26.4-6, pp. 459–505.

Lees, F. (2012). *Lees’ Loss prevention in the process industries: Hazard identification, assessment and control*. Butterworth-Heinemann.

Library, T. S. and Archives (1902). *Fraterville Mine Disaster, Tennessee*. https://teva.contentdm.oclc.org/digital/collection/p15138coll15/id/331.

Liñán, A. et al. (Nov. 2016). “The Slowly Reacting Mode of Combustion of Gaseous Mixtures in Spherical Vessels. Part 1: Transient Analysis and Explosion Limits”. In: *Combustion Theory and Modelling* 20.6, pp. 1010–1028.

Liu, T.-Y. et al. (2010a). “On the Occurrence of Thermal Explosion in a Reacting Gas: The Effects of Natural Convection and Consumption of Reactant”. In: *Combustion and Flame* 157.2, pp. 230–239.

Liu, W. et al. (2010b). “Ignition of n-heptane pool by heated stagnating oxidizing flow”. In: *Combustion and flame* 157.2, pp. 259–266.

Lüth, P., E. Brandes, and T. Stolz (2014). *Interlaboratory Test 2012 - 2013 on the Method EN 14522:2005 "Determination of the Auto Ignition Temperature of Gases and Vapours" - IEC 60079-20-1, Part 7 "Method of Test for Autoignition Temperature: Final Report*. Berlin: BAM, Bundesforschungsanstalt für Materialforschung und -prüfung. ISBN: 978-3-9816380-0-4.

Mallard, H.-L. and F. E. Le Chatelier (1880). “Sur les températures d’inflammation des mélanges gazeux”. fr. In: *Comptes rendus hebdomadaires des séances de l’Académie des sciences* 91, pp. 825–828.

Martin, C. D. and J. E. Shepherd (2021). “Low temperature autoignition of Jet A and surrogate jet fuel”. In: *J. Loss Prev. Process Ind.* 71, p. 104454.

Martin, C. D. (2023). “Experiments in Thermal Ignition: Influence of Natural Convection on Properties of Gaseous Explosions”. PhD thesis. California Institute of Technology.

Mason, W. and R. V. Wheeler (1924). “CCXXXV.—The ignition of gases. Part IV. Ignition by a heated surface. Mixtures of the paraffins with air”. In: *Journal of the Chemical Society, Transactions* 125, pp. 1869–1875.

Matson, A. and R. Dufour (1950). *The Lower Limit of Flammability and the Autogenous Ignition Temperature of Certain Solvent Vapors Encountered in Ovens*. Underwriters’ Laboratories.

Melguizo-Gavilanes, J. et al. (2017a). “Dynamics of ignition of stoichiometric hydrogen-air mixtures by moving heated particles”. In: *international journal of hydrogen energy* 42.11, pp. 7380–7392.

Melguizo-Gavilanes, J. et al. (2017b). "Hot surface ignition of stoichiometric hydrogen-air mixtures". In: *international journal of hydrogen energy* 42.11, pp. 7393–7403.

Melguizo-Gavilanes, J. et al. (June 2019). "Numerical Study of the Transition between Slow Reaction and Ignition in a Cylindrical Vessel". In: *Combustion and Flame* 204, pp. 116–136.

Melguizo-Gavilanes, J. et al. (2016). "Hot surface ignition of n-hexane mixtures using simplified kinetics". In: *Combust. Sci. Technol.* 188.11-12, pp. 2060–2076.

Mendez, F., C. Treviño, and A. Liñán (1986). "Premixed combustion in boundary layers for moderate values of the Zeldovich numbers". In: *Combustion science and technology* 48.3-4, pp. 129–149.

Menon, S. K. et al. (2016). "Hot surface ignition of n-hexane in air". In: *Combustion and Flame* 163, pp. 42–53.

Mével, R. et al. (2017). "Hot surface ignition of ethylene-air mixtures: Selection of reaction models for cfd simulations". In: *10th US National Combustion Meeting*, paper2RK–0098.

Mével, R. et al. (2019a). "Experimental and numerical study of the ignition of hydrogen-air mixtures by a localized stationary hot surface". In: *International Journal of Heat and Fluid Flow* 76, pp. 154–169.

Mével, R. et al. (2019b). "Oxidation of n-hexane in the vicinity of the auto-ignition temperature". In: *Fuel* 236, pp. 373–381.

Meyer, V. and A. Münch (1893). "Ueber ein exactes Verfahren zur Ermittlung der Entzündungstemperatur brennbarer Gasgemische". In: *Berichte der deutschen chemischen Gesellschaft* 26.3, pp. 2421–2432.

Michalski, L. and L. Michalski, eds. (2001). *Temperature measurement*. 2nd ed. Chichester ; New York: J. Wiley. 501 pp. ISBN: 978-0-471-86779-1.

Mines, U. B. of (1891). *Dixonville Mine Explosion, Pennsylvania*. https://arlweb.msha.gov/fatals/pre-1900/DIXONVIL.HTM.

– (1907). *Monongah Mine Disaster, West Virginia*. https://www.msha.gov/mshatime-line/monongah.htm.

National Fire Protection Association (1991). *Fire Protection Guide to Hazardous Materials*. 11th. NFPA 325: Guide to Fire Hazard Properties of Flammable Liquids, Gases, and Volatile Solids. Quincy, MA: National Fire Protection Association.

National Toxicology Program (1992). *National Toxicology Program Chemical Repository Database*. Research Triangle Park, North Carolina.

Neer, M. E. (1975). "Autoignition of flowing hydrogen-air mixtures". In: *AIAA Journal* 13.7, pp. 924–928.

NIST (2024). *NIST Chemistry WebBook, NIST Standard Reference Database Number 69*. https://webbook.nist.gov/.

Ono, S. et al. (1976). "Ignition in a free convection from vertical hot plate". In: *Bul. JSME* 19.132, pp. 676–683.

Paterson, S. (1940). "XLII. The ignition of inflammable gases by hot moving particles: II". In: *The Lon., Edin., and Dub. Phil. Mag. and J. Sci.* 30.203, pp. 437–457.

Pfefferle, L. D. et al. (1989a). "The influence of catalytic activity on the ignition of boundary layer flows Part I: Hydroxyl radical measurements". In: *Combustion and flame* 76.3-4, pp. 325–338.

Pfefferle, L. D. et al. (1989b). "The influence of catalytic activity on the gas phase ignition of boundary layer flows Part II. Oxygen atom measurements". In: *Combustion and Flame* 76.3, pp. 339–349.

Poinsot, T. and D. Veynante (2005). *Theoretical and numerical combustion*. RT Edwards, Inc.

Rae, D., R. Danson, and B. Singh (1964). *The size and temperature of a hot square in a cold plane surface necessary for the ignition of methane*. Tech. rep. Ministry of Power, Safety in Mines Research Establishment.

Ranzi, E. et al. (n.d.). *CRECK Full Kinetic Mechanism*. URL: https://www.creckmodeling.polimi.it/menu-kinetics/menu-kinetics-detailed-mechanisms/107-category-kinetic-mechanisms/405-mechanisms-1911-tot-ht-lt-me/.

Roth, D. et al. (2014). "Ignition by mechanical sparks: ignition of hydrogen/air mixtures by submillimeter-sized hot particles". In: *Combustion Science and Technology* 186.10-11, pp. 1606–1617.

Safety, U. C. and H. I. Board (2007). *Investigation Report: BP Texas City Refinery Explosion and Fire*. https://www.csb.gov/bp-america-refinery-explosion/.

– (2010). *Investigation Report: Valero Refinery Fire, Texas City, TX*. https://www.csb.gov/valero-refinery-fire/.

Sánchez, A. L. et al. (Nov. 2016). "The Slowly Reacting Mode of Combustion of Gaseous Mixtures in Spherical Vessels. Part 2: Buoyancy-induced Motion and Its Effect on the Explosion Limits". In: *Combustion Theory and Modelling* 20.6, pp. 1029–1045. (Visited on 12/29/2024).

Schoeffler and Shepherd (2023). "Thermal Ignition by Millimeter-Scale Surface Hot Spots". In: *Int. Col. Dyn. Exp. Reac. Sys.*

Semenoff, N. (1929). "Kinetics of Chain Reactions." In: *Chemical Reviews* 6.3, pp. 347–379.

Setchkin, N. P. (1954). "Self-ignition temperatures of combustible liquids". In: *Journal of Research of the National Bureau of Standards* 53.1, p. 49.

Silakova, M., V. Smetanyuk, and H. Pasman (2006). *Model, software for calculation of AIT and its validation*. Deliverable No. 18 of SAFEKINEX:SAFe and Efficient hydrocarbon oxidation processes by KINetics and Explosion eXpertise. URL: https://www.morechemistry.com/SAFEKINEX/.

Silver, R. S. (1937). "LXV. The ignition of gaseous mixtures by hot particles". In: *The Lon., Edin., and Dub. Phil. Mag. and J. Sci.* 23.156, pp. 633–657.

Sirignano, W. A. (2010). *Fluid dynamics and transport of droplets and sprays*. Cambridge university press.

Smith, G. P., Y. Tao, and H. Wang (n.d.). *Foundational fuel chemistry model version 1.0 (FFCM-1)*. URL: https://web.stanford.edu/group/haiwanglab/FFCM1/pages/FFCM1.html.

Smyth, K. C. and N. P. Bryner (1997). "Short-duration autoignition temperature measurements for hydrocarbon fuels near heated metal surfaces". In: *Combust. Sci. Technol.* 126.1-6, pp. 225–253.

Society, U. S. H. (1900). *Scofield Mine Disaster, Utah*. https://historytogo.utah.gov/scofield-mine-disaster/.

Spalding, D. and V. Jain (1961). "The theory of steady laminar spherical flame propagation: Analytical solutions". In: *Combust. Flame* 5, pp. 11–18.

Stagni, A. et al. (2020). "An experimental, theoretical and kinetic-modeling study of the gas-phase oxidation of ammonia". In: *Reaction Chemistry & Engineering* 5.4, pp. 696–711.

Stagni, A. et al. (2023). "Low-and intermediate- temperature ammonia/hydrogen oxidation in a flow reactor: Experiments and a wide-range kinetic modeling". In: *Chemical Engineering Journal* 471, p. 144577.

Strang, G. (1968). "On the construction and comparison of difference schemes". In: *SIAM J. Numer. Anal.* 5.3, pp. 506–517.

The Open Foam Foundation (2023). *OpenFOAM*. https://www.openfoam.org/.

Thomas, P. and P. Bowes (1961). "Thermal ignition in a slab with one face at a constant high temperature". In: *Trans. Far. Soc.* 57, pp. 2007–2017.

Thompson, N. (1929). "Autoignition of Flammable Liquids". In: *Industrial Engineering Chemistry* 21.134.

Treviño, C. and F. Méndez (1991). "Asymptotic analysis of the ignition of hydrogen by a hot plate in a boundary layer flow". In: *Combust. Sci. Technol.* 78.4-6, pp. 197–216.

Turner, M. A. et al. (2021). "Resolving flame thickness using high-speed chemiluminescence imaging of OH* and CH* in spherically expanding methane–air flames". In: *Proc. Combust. Inst.* 38.2, pp. 2101–2108.

Turns, S. R. et al. (1996). *Introduction to combustion*. Vol. 287. McGraw-Hill Companies New York, NY, USA.

Tyler, B. and A. Tuck (Feb. 1967). "Heat Transfer to a Gas from a Spherical Enclosure: Measurements and Mechanism". In: *International Journal of Heat and Mass Transfer* 10.2, pp. 251–253.

Tyler, B. (1966). "An experimental investigation of conductive and convective heat transfer during exothermic gas phase reactions". In: *Combust. Flame* 10.1, pp. 90–91.

United Nations Office for the Coordination of Humanitarian Affairs (2020). *Beirut Port Explosion: Situation Report No. 5 (as of 18 August 2020)*. https://reliefweb.int/report/lebanon/beirut-port-explosion-situation-report-no-5-18-august-2020.

USGC (1999). *Autoignition Temperature Table*.

van't Hoff, J. H. (1884). *Études de dynamique chimique*. French. Original publication introducing the van't Hoff equation. Amsterdam: F. Müller & Co. URL: https://archive.org/details/tudesdedynamiqu00hoffgoog.

Volta, A. (1777). *Lettere di Alessandro Volta sull'aria infiammabile nativa delle paludi*. Reprinted in *Lettere e memorie fisiche e storiche*, Milano, 1777.

Westbrook, C. K. and F. L. Dryer (1984). "Chemical kinetic modeling of hydrocarbon combustion". In: *Progress in energy and combustion science* 10.1, pp. 1–57.

Wien, W. (1896). "On the energy distribution in the spectrum of the black-body radiation". In: *Annalen der Physik* 294.8, pp. 662–669. DOI: 10.1002/andp.18962940805.

Yaws, C. L. (2009). *Transport Properties of Chemicals and Hydrocarbons*. William Andrew Publishing.

Zabetakis, M. G., A. L. Furno, and G. W. Jones (1954). "Minimum spontaneous ignition temperatures of combustibles in air". In: *Industrial & Engineering Chemistry* 46.10, pp. 2173–2178.

Zakel, S., E. Brandes, and V. Schröder (2019). "Reliable safety characteristics of flammable gases and liquids–The database CHEMSAFE". In: *J. Loss Prev. Process Ind.* 62, p. 103914.

Zeldovich, Y. B. (1939). "The theory of ignition by a heated surface". In: *Zhurnal Eksperimental'noi i Teoreticheskoi Fiziki* 9.12, pp. 1530–1534.

Zhao, P. et al. (2016). "Initiation and propagation of laminar premixed cool flames". In: *Fuel* 166, pp. 477–487.

Zirwes, T. et al. (2017). "Direct numerical simulation of ignition by hot moving particles". In: *26th International Colloquium on the Dynamics of Explosions and Reactive Systems*.

Appendix A

EFFECTS OF 1,2,4-TRIMETHYLBENZENE ON THE IGNITION OF N-DECANE

A.1 Motivation

The aviation industry is increasingly moving towards adopting Sustainable Aviation Fuels (SAFs) like the candidate Synthetic Paraffinic Kerosene (SPK) to reduce environmental impact. However, these fuels may present new safety challenges. As is shown in Figure A.1, SPK has a lower autoignition temperature by 25-30°C, raising concerns about increased thermal ignition risk. Jet A is composed of roughly 80% heavy alkane compounds and 20% aromatic compounds (Martin and Shepherd, 2021) whereas SPK lacks aromatic content entirely, as confirmed by Kendrick Mass Defect analysis (Fouchier and Shepherd, 2025). This compositional difference may be responsible for the lower ignition resistance observed in SPK.

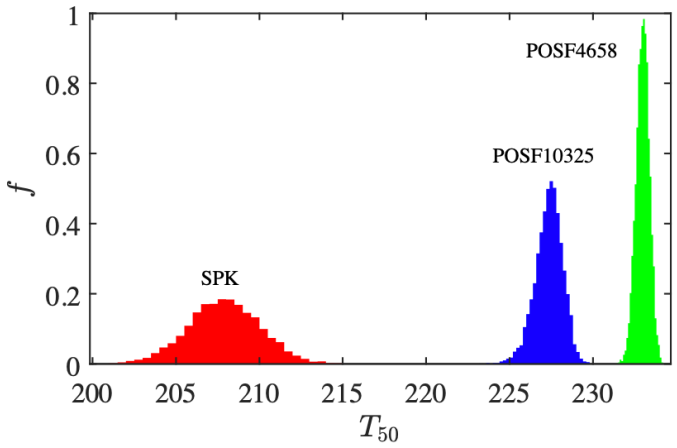


Figure A.1: Autoignition temperature distributions in °C for SPK and two batches of Jet A as experimentally determined in (Fouchier and Shepherd, 2025).

To explore this hypothesis, our laboratory investigated the effect of a common aromatic compound found in Jet A, 1,2,4-trimethylbenzene (1,2,4-TMB), on the ignition of a representative heavy, straight chain alkane in Jet A, nC_9H_{20}. Results from ASTM-E659 testing (Figure A.2) show that increasing the concentration of 1,2,4-TMB delays ignition, suggesting that aromatics may play a stabilizing role. This appendix aims to understand the chemical basis for that behavior through detailed zero-dimensional simulations.

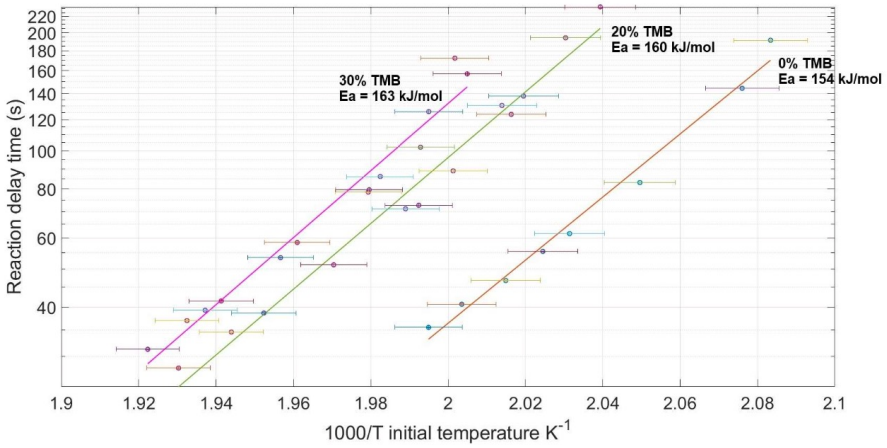


Figure A.2: Internal report of reaction delay time in an ASTM-E659 test for various amounts of 1,2,4-trimethylbenzene in nC_9H_{20}.

A.2 Zero-dimensional ignition results

To understand the reaction delay results shown in Figure A.2, zero-dimensional simulations were performed for mixtures of $nC_{10}H_{22}$/1,2,4-TMB in air. n-Decane ($nC_{10}H_{22}$) was used in the simulations to represent the straight chain alkanes instead of n-nonane (nC_9H_{20}) due to the limited kinetic modeling that exists for the latter. Given their chemical similarity and shared heavy-alkane reaction pathways, n-decane serves as a suitable surrogate. Because the temperatures of interest are very low (~ 500 K), the full 582 species, 21,174 reaction CRECK kinetic mechanism suitable for high and low temperature oxidation of C_1-C_{16} fuels and methyl-esters was used (Ranzi et al., n.d.).

Figure A.3 shows the temporal evolution of major species and temperature for a stoichiometric 70/30 n-decane/1,2,4-TMB mixture ignited at 525 K and 1 bar. A distinct two-stage ignition process is observed with a first-stage temperature rise to ~800 K followed ~400 ms later by a second-stage ignition with a rapid jump to ~2400 K. This behavior is characteristic of straight-chain alkane oxidation at low temperatures and mirrors results previously reported for n-hexane in Chapters 3 and 4 and discussed in Mével et al. (2019a), Battin-Leclerc (2008), and Curran (2019). The first-stage involves low-temperature chain-branching reactions, including O_2 addition to the $nC_{10}H_{21}$ radical and subsequent isomerization, leading to accumulation of peroxy and aldehyde intermediates along with modest heat release. Notably, only limited consumption of 1,2,4-TMB occurs during this stage due to the thermal and structural stability of the aromatic ring.

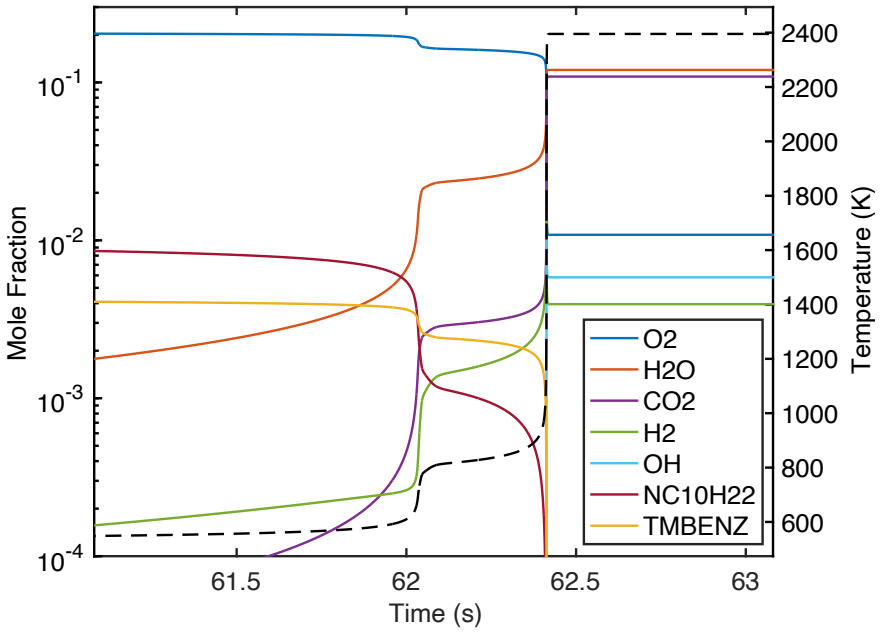


Figure A.3: Temporal evolution of the mole fraction of major species for a stoichiometric mixture of 70% $nC_{10}H_{22}$/30% 1,2,4-TMB in air with T_i = 525 K and P = 1 bar. The temperature evolution is the dashed black line.

To observe the effects on the ignition delay time, a total of 400 simulations were carried out for stoichiometric mixtures of 1,2,4-TMB, n-decane, and air with 0%, 10%, 20%, and 30% 1,2,4-TMB to match the experimental ignition data. The initial temperatures ranged from the autoignition temperature of 479 K (National Fire Protection Association, 1991; USGC, 1999) to 525 K. The ignition delay time for a given simulation was determined by the time when the temporal temperature gradient was maximized. Figure A.4 presents the resulting ignition delay curves. As in the experiments, increasing 1,2,4-TMB content leads to a systematic leftward shift of the delay curves, meaning longer delays at a given initial temperature.

Because the simulation results are from an adiabatic formulation and for a slightly different straight chain alkane fuel, it's challenging to quantitatively compare the effects with the experiment. In the case of the experimental results in Figure A.2, the AIT is determined as the rightmost point on each respective curve as it is the lowest temperature that an ignition event was detected. Numerically however, the system will always ignite if given enough time as a consequence of zero thermal losses. Thus, an initial attempt to quantitatively compare the two figures can be made by defining a critical delay time, τ_{crit}, at the reported AIT for n-decane. From Figure A.4, τ_{crit} = 385 s at the 479 K temperature reported by National Fire

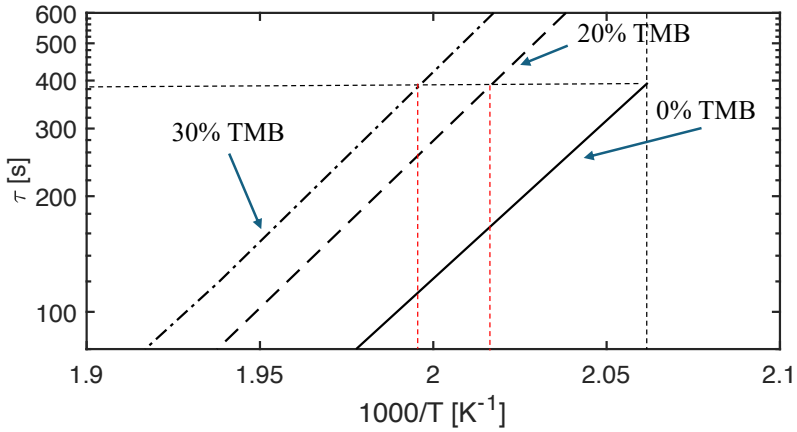


Figure A.4: Computed zero-dimensional ignition delay times for stoichiometric mixtures of 1,2,4-TMB, n-decane, and air for initial temperatures 483 K < T_i < 525 K.

Protection Association (1991) and USGC (1999) as the AIT. Horizontal and vertical dashed black lines are drawn through these two values. If we assume this τ_{crit} that corresponds to the tabulated n-decane/air AIT is the critical delay time for all the mixtures, the relative zero-dimensional estimated AITs can be extrapolated for the mixtures containing 1,2,4-TMB. These temperatures are shown graphically as vertical dashed red lines in Figure A.4.

Table A.1: Experimentally measured and numerically estimated AITs for varying amounts of 1,2,4-trimethylbenzene in n-decane/air.

% 1,2,4-TMB	ASTM-E659 Experimental AIT (°C)	0D Numerical AIT (°C)
0	206	206
10	211	211
20	219	217
30	226	224

Table A.1 compares the AITs as measured experimentally in the ASTM-E659 apparatus and numerically estimated from zero-dimensional simulations. By construction, the AITs between the experiment and simulation match for 0% 1,2,4-TMB. As 1,2,4-TMB is introduced to the mixture, at 10%, the experiment and simulation AITs still match to the nearest kelvin. At 20% 1,2,4-TMB, the experimental AIT was 219°C while the numerical AIT was 217°C (2 K difference). Finally for 20% 1,2,4-TMB, the experimental AIT was 226°C and the numerical AIT was computed as 224°C. (2 K difference). On average for the three 1,2,4-TMB mixtures, the difference between the experimentally measured and numerically estimated AIT was $1.\bar{3}$

K (0.59 % difference). Importantly, the same trend in AIT seen in the experiments is captured by the zero-dimensional model with an increase from 206°C to 224°C.

A.3 Chemical analysis

Having reproduced the ignition delay trends seen in the experiment, the zero-dimensional simulations were further analyzed to identify the chemical mechanisms responsible for the AIT increase with added 1,2,4-TMB. Since the delay between first- and second-stage ignition is only a fraction of a second, we focused on the slow buildup phase leading to the first-stage ignition event.

The dominant low-temperature reaction pathways for n-decane follow well-established alkane oxidation mechanisms, similar to those detailed in Chapter 3 and in Battin-Leclerc (2008). These include H-abstraction from n-decane to form $nC_{10}H_{21}$ radicals, addition of O_2 to form $C_{10}H_{21}O_2$, internal isomerization to hydroperoxyalkyl radicals (QOOH), and subsequent addition of O_2 to form peroxy-hydroperoxides (OOQOOH). culminating in heat release and radical production. These exothermic reactions multiply the radical pool and eventually trigger thermal runaway of the first stage.

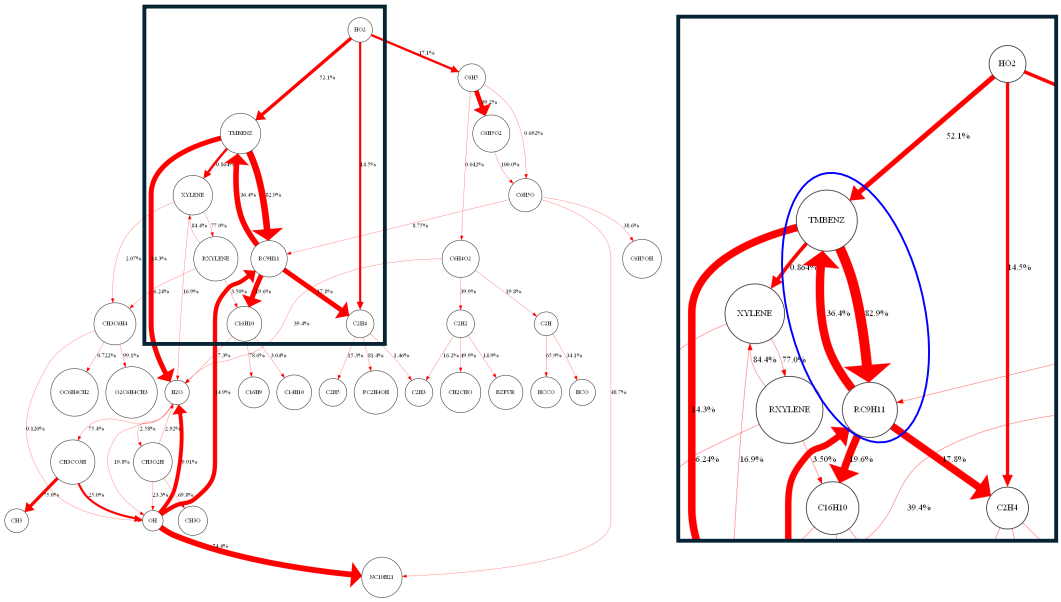


Figure A.5: Efflux of H atoms from HO_2 while the mixture is cooking prior to the first stage ignition event for the simulation presented in Figure A.3. The numbers are the percentage of the total input/output of each molecule. The thickness of the arrow itself represents the magnitude of the flux overall.

To understand how 1,2,4-TMB alters this progression, reaction flux analysis was performed during the pre-ignition phase. Figure A.5 shows the efflux of hydrogen atoms from HO_2, a key chain branching species. While much of the HO_2 drives alkane cracking and peroxy radical formation, approximately 52% is consumed via reactions with 1,2,4-TMB. This suggests that 1,2,4-TMB competes with the alkane for radicals. Closer inspection reveals a more intricate mechanism. A cyclic feedback loop is established between 1,2,4-TMB and its H-abstracted radical form, RC_9H_{11}. As shown in Figure, A.6, the major consumption pathways for 1,2,4-TMB is reaction with OH to form RC_9H_{11} and H_2O. However, unlike alkyl radicals, RC_9H_{11} is resonance-stabilized due to its aromatic ring making it less susceptible to further oxidation. Critically, a substantial fraction of the RC_9H_{11} instead reacts with HO_2 to reform 1,2,4-TMB and release O_2, essentially reversing the initial abstraction. The result is a catalytic loop that consumes reactive OH and HO_2 radicals but yields only thermally stable products such as H_2O, O_2, and the original 1,2,4-TMB. This process is summarized in Figure A.7.

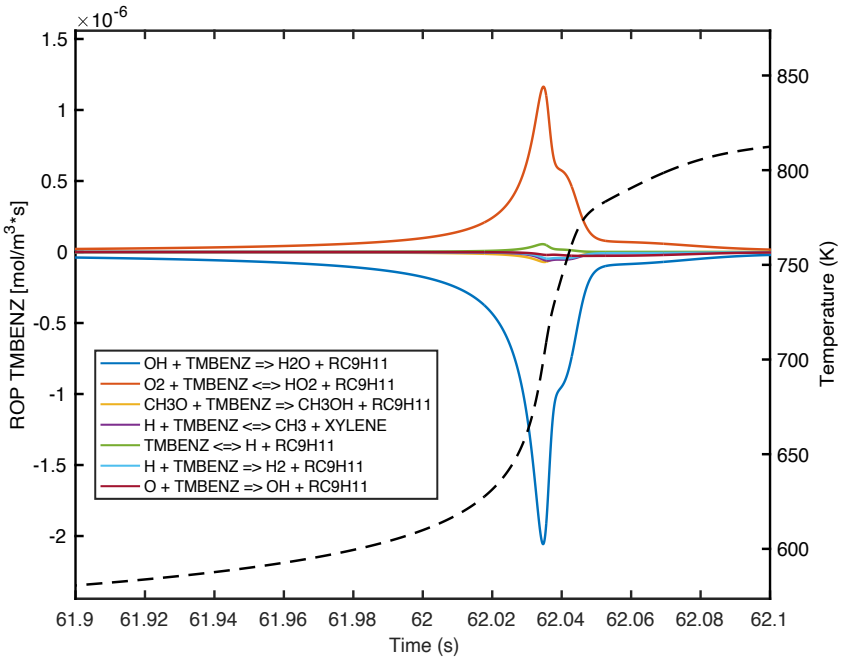


Figure A.6: Rate of production of 1,2,4-TMB for top reactions before and during the first stage ignition event.

This feedback inhibits the chain branching progression by diverting radicals away from exothermic alkane oxidation pathways and reducing the net production of new radicals. In contrast, alkanes typically accelerate runaway by forming hydroperox-

ides and promoting OH multiplication via H_2O_2 decomposition. Thus, 1,2,4-TMB acts as a catalytic inhibitor of ignition. This insight explains the consistent increase in AIT observed experimentally and supports the conclusion that aromatics modulate ignition sensitivity by altering radical pool dynamics during the induction period.

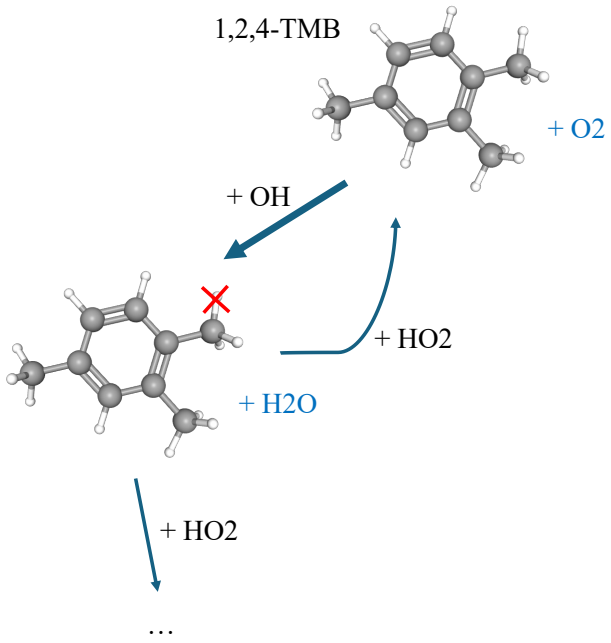


Figure A.7: Visualization of the oxidation pathway of 1,2,4-TMB before and during the first stage ignition event.

A.4 Summary and conclusions

This appendix investigates how the addition of 1,2,4-trimethylbenzene (1,2,4-TMB), a representative aromatic compound in Jet A, affects the ignition behavior of heavy straight-chain alkanes such as n-decane. Motivated by the observed decrease in autoignition temperature (AIT) of a candidate for Sustainable Aviation Fuel (SAF), synthetic paraffinic kerosene (SPK), that contains no aromatic compared to Jet A, zero-dimensional simulations were performed to understand the chemical behavior that contributes to a reduction in the observed AIT. Previous experimental ASTM-E659 tests showed that increasing the proportion of 1,2,4-TMB in n-nonane raises the AIT. Zero-dimensional simulations of n-decane/1,2,4-TMB mixtures confirmed this trend, showing increasing ignition delay times and higher estimated ignition temperatures with more 1,2,4-TMB. Reaction pathway analysis revealed the mechanisms behind such behavior. We found that 1,2,4-TMB acts as a radical sink,

consuming OH and HO_2 radicals without producing significant chain-branching intermediate species necessary for thermal runaway. This catalytic feedback loop stabilizes the mixture compared to pure n-decane/air and delays ignition, explaining the increase in observed AIT.

The findings in this appendix provide a possible explanation for why Synthetic Paraffinic Kerosene (SPK) exhibits a lower autoignition temperature than conventional Jet A. The absence of aromatic compounds in SPK removes a critical ignition-inhibiting component present in Jet A, where aromatics like 1,2,4-trimethylbenzene act as radical sinks and slow the chain-branching reactions that drive thermal runaway. Without these stabilizing species, SPK may ignite more readily under certain conditions, posing challenges for meeting existing safety and certification standards that were established based on the higher AIT of Jet A. These results further suggest that careful reintroduction of aromatic-like compounds, or the design of novel additives that mimic their radical-scavenging behavior without compromising emissions or sustainability goals, could offer a pathway to SAFs with improved ignition resistance. Future development of tailored fuel blends should therefore consider not only molecular weight and volatility, but also chemical structure and reactivity.

Appendix B

REDUCED NC_6H_{14} KINETIC MECHANISM (LTC + HTC)

In this appendix, the reduced kinetic mechanism suitable for low- and high-temperature multidimensional ignition studies is presented. Arrhenius coefficients for all 265 elementary reactions are provided. Low-pressure limit Arrhenius coefficients, TROE parameters as well as third-body efficiencies are also provided for relevant reactions.

Table B.1: Comprehensive list of the 265 elementary reactions used in the reduced nC_6H_{14} mechanism. The table includes pre-exponential factor, A, temperature exponent, n, and activation energy E_a in cal/mol.

No.	Reaction	A	n	E_a (cal/mol)
1	H+O2<=>O+OH	1.040e+14	0.00	15286.81
2	O+H2<=>H+OH	3.820e+12	0.00	7946.94
3	O+H2<=>H+OH	8.790e+14	0.00	19170.65
4	OH+H2<=>H+H2O	2.170e+08	1.52	3456.02
5	2OH<=>O+H2O	3.570e+04	2.40	-2110.42
6	2H(+M)<=>H2(+M)	1.780e+18	-1.00	0.00
7	2H+H2O<=>H2+H2O	5.620e+19	-1.25	0.00
8	O+H(+M)<=>OH(+M)	4.710e+18	-1.00	0.00
9	H+O2(+M)<=>HO2(+M)	5.590e+13	0.20	0.00
10	H2O(+M)<=>OH+H(+M)	6.060e+27	-3.31	120769.60
11	2H2O<=>OH+H+H2O	1.000e+26	-2.44	120160.13
12	HO2+H<=>H2+O2	3.660e+06	2.09	-1450.76
13	HO2+H<=>O+H2O	1.450e+12	0.00	0.00
14	HO2+H<=>2OH	7.080e+13	0.00	301.15
15	HO2+O<=>OH+O2	1.630e+13	0.00	-444.55
16	HO2+OH<=>H2O+O2	2.890e+13	0.00	-499.52
17	2HO2<=>H2O2+O2	1.300e+11	0.00	-1603.73
18	2HO2<=>H2O2+O2	4.200e+14	0.00	11978.97
19	2OH(+M)<=>H2O2(+M)	1.110e+14	-0.37	0.00
20	H2O2+H<=>H2O+OH	1.020e+13	0.00	3577.92
21	H2O2+H<=>HO2+H2	1.210e+07	2.00	5200.76
22	H2O2+O<=>HO2+OH	8.430e+11	0.00	3969.89
23	H2O2+OH<=>HO2+H2O	1.740e+12	0.00	317.88
24	H2O2+OH<=>HO2+H2O	7.590e+13	0.00	7115.20
25	CO+O(+M)<=>CO2(+M)	1.360e+10	0.00	2382.89
26	CO+OH<=>CO2+H	8.000e+11	0.14	7351.82
27	CO+OH<=>CO2+H	8.780e+10	0.03	-16.73
28	CO+HO2<=>CO2+OH	3.010e+13	0.00	22999.52
29	HCO(+M)<=>CO+H(+M)	1.870e+17	-1.00	17000.48
30	HCO+H2O<=>CO+H+H2O	2.240e+18	-1.00	17000.48
31	HCO+H<=>CO+H2	1.200e+14	0.00	0.00
32	HCO+OH<=>CO+H2O	3.020e+13	0.00	0.00
33	HCO+O<=>CO2+H	3.000e+13	0.00	0.00
34	HCO+O2<=>CO+HO2	5.310e+10	0.69	-124.28

Continued on next page

Table B.1 – continued from previous page

No.	Reaction	A	n	E_a
35	T-CH2+O2<=>HCO+OH	9.570e+12	0.00	1737.57
36	T-CH2+O2<=>CH2O+O	3.300e+12	0.00	1737.57
37	T-CH2+O2<=>CO2+H2	3.630e+12	0.00	1737.57
38	T-CH2+HO2<=>CH2O+OH	2.000e+13	0.00	0.00
39	CH2O+H<=>HCO+H2	5.860e+03	3.13	1515.30
40	CH2O+OH<=>HCO+H2O	1.940e+06	2.11	-1687.38
41	CH2O+O<=>HCO+OH	3.900e+13	0.00	3539.67
42	CH2O+O2<=>HCO+HO2	1.000e+14	0.00	40000.00
43	CH2O+HO2<=>HCO+H2O2	5.600e+06	2.00	12000.48
44	CH3+H(+M)<=>CH4(+M)	4.360e+13	0.19	0.00
45	CH3+O<=>CH2O+H	3.320e+13	0.05	-136.23
46	CH3+O<=>HCO+H2	2.220e+13	0.05	-136.23
47	CH3+OH<=>T-CH2+H2O	4.240e+04	2.57	3998.57
48	CH3+O2<=>CH3O+O	1.380e+13	0.00	30521.03
49	CH3+O2<=>CH2O+OH	5.870e+11	0.00	13840.82
50	CH3+O2(+M)<=>CH3O2(+M)	1.010e+08	1.63	0.00
51	CH3O2+CH3<=>2CH3O	1.000e+13	0.00	-1199.81
52	2CH3O2=>2CH3O+O2	1.400e+16	-1.61	1859.46
53	CH3O2+HO2=>CH3O+OH+O2	2.470e+11	0.00	-1570.27
54	CH3O2+CH2O=>CH3O+OH+HCO	1.990e+12	0.00	11670.65
55	CH3+HO2<=>CH3O+OH	1.000e+12	0.29	-685.95
56	CH3+HO2<=>CH4+O2	1.190e+05	2.23	-3023.42
57	CH3+H2O2<=>CH4+HO2	2.450e+04	2.47	5179.25
58	CH3+HCO<=>CH4+CO	2.650e+13	0.00	0.00
59	CH3+CH2O<=>CH4+HCO	3.320e+03	2.81	5860.42
60	CH3+T-CH2<=>C2H4+H	1.000e+14	0.00	0.00
61	2CH3<=>C2H5+H	6.840e+12	0.10	10599.90
62	CH2OH(+M)<=>CH2O+H(+M)	7.370e+10	0.81	39581.74
63	CH3O(+M)<=>CH2O+H(+M)	1.130e+10	1.21	24084.61
64	CH3O+H<=>CH3+OH	4.650e+13	0.28	28.68
65	CH2OH+H<=>CH3+OH	1.820e+13	0.16	112.33
66	CH3O+H<=>CH2O+H2	7.590e+08	1.50	-518.64
67	CH3O+O<=>CH2O+OH	1.000e+13	0.00	0.00
68	CH3O+OH<=>CH2O+H2O	5.000e+12	0.00	0.00
69	CH3O+O2<=>CH2O+HO2	2.290e+03	2.40	413.48
70	CH2OH+O2<=>CH2O+HO2	2.410e+14	0.00	5016.73
71	CH4+H<=>CH3+H2	6.600e+08	1.62	10841.30

Continued on next page

Table B.1 – continued from previous page

No.	Reaction	A	n	E_a
72	CH4+O<=>CH3+OH	1.020e+09	1.50	8599.43
73	CH4+OH<=>CH3+H2O	1.000e+08	1.60	3119.02
74	CH4+T-CH2<=>2CH3	2.460e+06	2.00	8269.60
75	CH3OH(+M)<=>CH3+OH(+M)	2.080e+18	-0.61	92545.41
76	CH3OH+H<=>CH2OH+H2	1.540e+06	2.35	5910.61
77	CH3OH+H<=>CH3O+H2	5.480e+06	2.15	11099.43
78	CH3OH+O<=>CH2OH+OH	3.880e+05	2.50	3099.90
79	CH3OH+OH<=>CH2OH+H2O	5.140e+04	2.62	-681.17
80	CH3OH+OH<=>CH3O+H2O	5.710e+03	2.62	-681.17
81	CH3OH+CH3<=>CH2OH+CH4	4.900e+12	0.01	15078.87
82	CH3OH+HO2<=>CH2OH+H2O2	1.620e-04	4.99	10578.39
83	CH3OH+HO2<=>CH3O+H2O2	8.650e-01	3.89	18413.00
84	HCCO+CH3<=>C2H4+CO	5.000e+13	0.00	0.00
85	HCCO+O=>HCO+CO	7.830e+13	0.00	0.00
86	HCCO+OH=>CO+HCO+H	2.620e+15	-0.41	1006.21
87	HCCO+O2=>CO2+CO+H	4.780e+12	-0.14	1149.62
88	HCCO+O2=>2CO+OH	1.910e+11	-0.02	1022.94
89	C2H2+H(+M)<=>C2H3(+M)	1.710e+10	1.27	2707.93
90	C2H2+O<=>HCCO+H	2.960e+09	1.28	2471.32
91	C2H2+O<=>T-CH2+CO	7.400e+08	1.28	2471.32
92	CH2CO+H<=>HCCO+H2	5.000e+13	0.00	7999.52
93	CH2CO+O<=>HCCO+OH	1.000e+13	0.00	7999.52
94	CH2CO+OH<=>HCCO+H2O	7.500e+12	0.00	2000.48
95	CH2CO+CH3<=>HCCO+CH4	7.500e+12	0.00	12999.52
96	CH2CO+CH3<=>C2H5+CO	9.000e+10	0.00	0.00
97	CH2CO+H<=>CH3+CO	7.770e+08	1.45	2779.64
98	CH2CO+OH<=>CH2OH+CO	5.000e+12	0.00	0.00
99	C2H3+H(+M)<=>C2H4(+M)	6.080e+12	0.27	279.64
100	C2H3+H<=>C2H2+H2	3.000e+13	0.00	0.00
101	C2H3+O<=>CH3+CO	1.030e+13	0.21	-427.82
102	C2H3+OH<=>C2H2+H2O	5.000e+12	0.00	0.00
103	C2H3+O2<=>C2H2+HO2	1.340e+06	1.61	-384.80
104	C2H3+CH3<=>C2H2+CH4	9.030e+12	0.00	-764.82
105	C2H3+O2<=>CH2CHO+O	3.800e+11	0.19	47.80
106	C2H3+O2<=>CH2O+HCO	4.050e+17	-1.86	1166.35
107	C2H3+O2=>CH2O+CO+H	2.220e+16	-1.35	783.94
108	C2H3+H2O2<=>C2H4+HO2	1.210e+10	0.00	-595.12

Continued on next page

Table B.1 – continued from previous page

No.	Reaction	A	n	E_a
109	C2H3+HCO<=>C2H4+CO	9.000e+13	0.00	0.00
110	CH2CHO<=>CH2CO+H	1.320e+34	-6.57	48386.71
111	CH2CHO<=>CH3+CO	6.510e+34	-6.87	47194.07
112	CH2CHO+O<=>CH2O+HCO	3.170e+13	0.03	-394.36
113	CH2CHO+O2=>CH2O+CO+OH	1.810e+10	0.00	0.00
114	CH2CHO+O2=>2HCO+OH	2.350e+10	0.00	0.00
115	CH2CHO+H<=>CH2CO+H2	1.100e+13	0.00	0.00
116	CH2CHO+OH<=>CH2CO+H2O	1.200e+13	0.00	0.00
117	CH2CHO+H<=>CH3+HCO	2.200e+13	0.00	0.00
118	CH2CHO+OH<=>CH2OH+HCO	3.010e+13	0.00	0.00
119	CH2CHO+CH3<=>C2H5+HCO	4.900e+14	-0.50	0.00
120	CH3CHO(+M)<=>CH3+HCO(+M)	2.720e+22	-1.74	86359.94
121	CH3CHO+H=>CH3+CO+H2	1.310e+05	2.58	1218.93
122	CH3CHO+H<=>CH2CHO+H2	2.720e+03	3.10	5205.54
123	CH3CHO+O=>CH3+CO+OH	1.950e+13	0.00	3539.67
124	CH3CHO+OH=>CH3+CO+H2O	9.700e+05	2.11	-1687.38
125	CH3CHO+O2=>CH3+CO+HO2	5.000e+13	0.00	40000.00
126	CH3CHO+HO2=>CH3+CO+H2O2	2.780e-03	4.50	4827.92
127	CH3CHO+CH3=>CH3+CO+CH4	1.550e+00	3.70	4565.01
128	CH3CHO+O<=>CH2CHO+OH	2.920e+12	0.00	1809.27
129	CH3CHO+OH<=>CH2CHO+H2O	6.060e-01	3.90	-1068.36
130	CH3CHO+HO2<=>CH2CHO+H2O2	5.430e-02	4.10	18647.23
131	CH3CHO+CH3<=>CH2CHO+CH4	1.440e+00	3.70	8857.55
132	C2H4+H(+M)<=>C2H5(+M)	1.370e+09	1.46	1355.16
133	C2H4+H<=>C2H3+H2	1.160e+07	2.23	13336.52
134	C2H4+O<=>CH2CHO+H	7.660e+09	0.88	1140.06
135	C2H4+O<=>T-CH2+CH2O	7.150e+04	2.47	929.73
136	C2H4+O<=>CH3+HCO	3.890e+08	1.36	886.71
137	C2H4+OH<=>C2H3+H2O	2.230e+04	2.75	2215.58
138	C2H4+O2<=>C2H3+HO2	4.220e+13	0.00	62100.86
139	C2H4+CH3<=>C2H3+CH4	1.050e+02	3.22	14306.88
140	C2H4+CH3(+M)<=>N-C3H7(+M)	2.550e+06	1.60	5700.29
141	C2H5+H(+M)<=>C2H6(+M)	5.210e+17	-0.99	1579.83
142	C2H5+H<=>C2H4+H2	2.000e+12	0.00	0.00
143	C2H5+OH<=>C2H4+H2O	2.410e+13	0.00	0.00
144	C2H5+O2<=>C2H4+HO2	1.920e+07	1.02	-2033.94
145	C2H5+CH3<=>C2H4+CH4	1.180e+04	2.45	2920.65

Continued on next page

Table B.1 – continued from previous page

No.	Reaction	A	n	E_a
146	C2H5+O<=>CH3+CH2O	3.170e+13	0.03	-394.36
147	C2H5+HO2<=>C2H5O+OH	3.100e+13	0.00	0.00
148	C2H5+HCO<=>C2H6+CO	1.200e+14	0.00	0.00
149	C2H5+HO2<=>C2H6+O2	3.000e+11	0.00	0.00
150	C2H5+HO2<=>C2H4+H2O2	3.000e+11	0.00	0.00
151	C2H5O(+M)<=>CH3+CH2O(+M)	6.310e+10	0.93	17098.47
152	C2H5O+O2<=>CH3CHO+HO2	2.290e+10	0.00	874.76
153	C2H6(+M)<=>2CH3(+M)	1.880e+50	-9.72	107342.26
154	C2H6+H<=>C2H5+H2	1.700e+05	2.70	5740.92
155	C2H6+O<=>C2H5+OH	3.170e+01	3.80	3130.98
156	C2H6+OH<=>C2H5+H2O	1.610e+06	2.22	740.92
157	C2H6+HO2<=>C2H5+H2O2	2.610e+02	3.37	15913.00
158	C2H6+CH3<=>C2H5+CH4	3.450e+01	3.44	10389.58
159	C3H6+H(+M)<=>N-C3H7(+M)	2.500e+11	0.51	2619.50
160	N-C3H7+H<=>C3H6+H2	1.800e+12	0.00	0.00
161	N-C3H7+O<=>C2H5+CH2O	9.600e+13	0.00	0.00
162	N-C3H7+OH<=>C3H6+H2O	2.410e+13	0.00	0.00
163	N-C3H7+O2<=>C3H6+HO2	3.700e+16	-1.63	3417.78
164	N-C3H7+CH3<=>C3H6+CH4	3.310e+12	0.00	-769.60
165	N-C3H7+H(+M)<=>C3H8(+M)	3.610e+13	0.00	0.00
166	C3H8(+M)<=>C2H5+CH3(+M)	1.290e+37	-5.84	97387.67
167	C3H8+H<=>N-C3H7+H2	9.360e+07	1.97	8200.29
168	C3H8+OH<=>N-C3H7+H2O	5.150e+03	2.94	-418.26
169	C3H8+HO2<=>N-C3H7+H2O2	4.760e+04	2.55	16491.40
170	A-C3H4+H<=>C2H2+CH3	8.950e+13	-0.02	11250.00
171	A-C3H4+H<=>A-C3H5	2.010e+49	-10.77	19622.37
172	A-C3H4+O<=>C2H4+CO	9.630e+06	2.05	179.25
173	A-C3H4+OH<=>CH2CO+CH3	4.030e+12	0.00	-198.37
174	C2H3+HCO<=>C2H3CHO	1.800e+13	0.00	0.00
175	C2H3CHO+H=>C2H3+CO+H2	1.310e+05	2.58	1218.93
176	C2H3CHO+O=>C2H3+CO+OH	1.950e+13	0.00	3539.67
177	C2H3CHO+OH=>C2H3+CO+H2O	9.700e+05	2.11	-1687.38
178	C2H3CHO+HO2=>C2H3+CO+H2O2	2.780e-03	4.50	4827.92
179	C2H3CHO+CH3=>C2H3+CO+CH4	1.550e+00	3.70	2413.96
180	C2H3+CH3<=>A-C3H5+H	1.930e+18	-1.25	7669.69
181	A-C3H5+H<=>A-C3H4+H2	9.560e+03	2.80	3291.11
182	A-C3H5+OH<=>A-C3H4+H2O	6.030e+12	0.00	0.00

Continued on next page

Table B.1 – continued from previous page

No.	Reaction	A	n	E_a
183	A-C3H5+CH3<=>A-C3H4+CH4	3.010e+12	-0.32	-131.45
184	A-C3H5+C2H3<=>A-C3H4+C2H4	2.410e+12	0.00	0.00
185	A-C3H5+C2H5<=>A-C3H4+C2H6	9.640e+11	0.00	-131.45
186	2A-C3H5<=>A-C3H4+C3H6	7.500e+11	0.00	0.00
187	A-C3H5+O<=>C2H3CHO+H	1.690e+13	0.03	-394.36
188	A-C3H5+O=>C2H4+CO+H	1.690e+13	0.03	-394.36
189	A-C3H5+O2<=>A-C3H4+HO2	2.060e+04	2.19	17590.82
190	A-C3H5+O2<=>C2H3CHO+OH	3.360e+05	1.81	19189.77
191	A-C3H5+O2=>C2H2+CH2O+OH	9.710e+20	-2.70	24980.88
192	A-C3H5+HO2<=>C3H5O+OH	1.190e+09	1.03	-2249.04
193	C3H5O<=>C2H3CHO+H	1.000e+14	0.00	29098.95
194	C3H5O<=>C2H3+CH2O	2.030e+12	0.09	23561.19
195	C3H5O+O2<=>C2H3CHO+HO2	1.000e+12	0.00	5999.04
196	C3H6<=>A-C3H5+H	3.870e+57	-12.22	113800.19
197	C3H6<=>C2H3+CH3	9.200e+70	-15.96	128551.63
198	C3H6+H<=>C2H4+CH3	2.670e+12	0.47	5432.60
199	C3H6+H<=>A-C3H5+H2	6.030e+05	2.39	4490.92
200	C3H6+OH<=>A-C3H5+H2O	4.190e+13	0.00	4651.05
201	C3H6+O<=>CH2CHO+CH3	8.120e+08	1.25	540.15
202	C3H6+O<=>C2H4+CH2O	3.630e+10	0.82	1828.39
203	C3H6+O<=>A-C3H5+OH	1.430e+02	3.37	174.47
204	C3H6+HO2<=>A-C3H5+H2O2	2.380e+04	2.55	16491.40
205	C3H6+CH3<=>A-C3H5+CH4	4.570e-01	3.65	7153.44
206	C2H4+C2H3<=>C4H6+H	2.150e+12	0.46	14973.71
207	C4H6+O<=>CH2CHO+C2H3	1.620e+09	1.25	540.15
208	C4H6+O<=>A-C3H4+CH2O	7.260e+10	0.82	1828.39
209	N-C6H14=>N-C5H11+CH3	6.030e+18	-0.67	86551.15
210	N-C6H14=>N-C4H9+C2H5	1.620e+22	-1.49	87189.29
211	N-C6H14=>2N-C3H7	2.620e+22	-1.56	87939.77
212	N-C6H14+H=>C6H13+H2	6.160e+07	2.10	5475.62
213	N-C6H14+O=>C6H13+OH	1.420e+06	2.56	3016.25
214	N-C6H14+OH=>C6H13+H2O	7.490e+06	2.09	-623.80
215	N-C6H14+O2=>C6H13+HO2	1.700e+13	0.20	50188.81
216	N-C6H14+HO2=>C6H13+H2O2	6.270e+12	0.21	17698.37
217	C6H13=>N-C4H9+C2H4	3.200e+12	0.13	28881.45
218	C6H13=>N-C3H7+C3H6	5.520e+12	0.17	29913.96
219	C6H13=>C2H5+C4H8	2.760e+12	0.17	29913.96

Continued on next page

Table B.1 – continued from previous page

No.	Reaction	A	n	E_a
220	C6H13=>CH3+C5H10	2.760e+12	0.17	29913.96
221	C6H13=>C6H12+H	1.780e+08	1.63	34474.19
222	C6H13+HO2=>C6H13O+OH	7.000e+12	0.00	-999.04
223	C6H13+CH3O2=>C6H13O+CH3O	7.000e+12	0.00	-999.04
224	C6H13O=>N-C5H11+CH2O	1.190e+18	-1.50	20181.64
225	C6H13O=>N-C4H9+CH3CHO	7.160e+22	-2.78	22997.13
226	C6H13O=>N-C3H7+C2H5+HCO	4.100e+17	-1.31	19502.87
227	C6H13+O2=>C6H13O2	1.360e+13	-0.08	207.93
228	C6H13O2=>C6H13+O2	1.710e+23	-2.33	37839.39
229	C6H13O2=>C6H12OOH	1.830e+05	1.70	19335.56
230	C6H12OOH=>C6H13O2	7.530e+04	1.25	5948.85
231	C6H12OOH=>C6H12+HO2	4.010e+00	3.28	12753.35
232	C6H12OOH=>C6H12O+OH	1.330e+12	-0.74	10172.08
233	C6H12OOH+O2=>C6H13O4	7.710e+12	-0.01	-14.34
234	C6H13O4=>C6H12OOH+O2	2.310e+21	-1.97	36579.83
235	C6H13O4=>OC6H11OOH+OH	6.470e+09	0.18	19839.87
236	OC6H11OOH=>C2H5+CH3CHO+CH2CO+OH	3.260e+09	1.93	38506.21
237	C6H12O+OH=>N-C4H9+CH2CO+H2O	3.680e+12	0.00	0.00
238	C6H12=>N-C3H7+A-C3H5	8.520e+26	-3.39	76505.74
239	C6H12+H=>C6H11+H2	3.700e+13	0.00	3900.57
240	C6H12+OH=>C6H11+H2O	3.000e+13	0.00	1230.88
241	C6H11=>C4H7+C2H4	1.600e+13	0.13	28881.45
242	C6H11=>A-C3H5+C3H6	1.380e+13	0.17	29913.96
243	C6H11=>C2H3+C4H8	1.380e+13	0.17	29913.96
244	N-C5H11=>N-C3H7+C2H4	3.240e+12	0.32	28807.36
245	N-C5H11=>C3H6+C2H5	1.150e+01	3.03	15313.10
246	N-C5H11=>C5H10+H	2.040e+10	0.95	33807.36
247	C5H10=>A-C3H5+C2H5	3.390e+15	0.00	72275.33
248	C5H10+H=>C5H9+H2	3.700e+13	0.00	3900.57
249	C5H10+OH=>C5H9+H2O	3.000e+13	0.00	1230.88
250	C5H9=>A-C3H5+C2H4	1.600e+13	0.13	28881.45
251	C5H9=>C2H3+C3H6	1.380e+13	0.17	29913.96
252	N-C4H9=>C2H5+C2H4	1.600e+13	0.13	28881.45
253	N-C4H9=>C4H8+H	2.040e+10	0.95	33807.36
254	C4H8=>A-C3H5+CH3	3.390e+15	0.00	72275.33
255	C4H8+H=>C3H6+CH3	1.050e+09	1.40	726.58
256	C4H8+H=>C2H5+C2H4	9.020e+08	1.40	2308.80

Continued on next page

Table B.1 – continued from previous page

No.	Reaction	A	n	E_a
257	C4H8+H=>C4H7+H2	3.700e+13	0.00	3900.57
258	C4H8+OH=>C4H7+H2O	3.000e+13	0.00	1230.88
259	C4H7=>C2H4+C2H3	1.000e+11	0.00	37000.48
260	C4H7=>C4H6+H	1.200e+14	0.00	49299.71
261	C4H7+H=>C4H6+H2	3.160e+13	0.00	0.00
262	C4H7+O2=>C4H6+HO2	1.000e+09	0.00	0.00
263	C4H7+CH3=>C4H6+CH4	8.000e+12	0.00	0.00
264	C4H7+HO2=>A-C3H5+CH2O+OH	7.000e+12	0.00	-999.04
265	C4H7+CH3O2=>A-C3H5+CH2O+CH3O	7.000e+12	0.00	-999.04

Table B.2: Subset of reactions that include fall-off behavior, showing low-pressure limit Arrhenius coefficients and TROE parameters for accurate pressure-dependent rate modeling.

No.	Reaction	A_{low}	n_{low}	E_a^{low}	α	T_3 (K)	T_1 (K)	T_2 (K)
9	H+O2(+M)<=>HO2(+M)	2.650e+19	-1.30	0.00	0.700	1.00e-05	1.00e+10	1.00e+10
19	2OH(+M)<=>H2O2(+M)	2.730e+19	-1.50	-2292.10	0.735	9.40e+01	1.76e+03	5.18e+03
25	CO+O(+M)<=>CO2(+M)	1.170e+24	-2.79	4192.20	1.000	1.00e+00	1.00e+07	1.00e+07
44	CH3+H(+M)<=>CH4(+M)	2.790e+34	-5.10	2784.40	0.630	6.10e+01	3.32e+03	1.00e+10
50	CH3+O2(+M)<=>CH3O2(+M)	3.820e+31	-4.89	3432.10	0.045	8.80e+02	2.50e+09	1.79e+09
62	CH2OH(+M)<=>CH2O+H(+M)	3.500e+21	-1.99	23999.00	0.844	9.00e+02	1.00e+00	3.32e+03
63	CH3O(+M)<=>CH2O+H(+M)	6.020e+16	-0.55	18023.00	0.341	2.80e+01	1.00e+03	2.34e+03
75	CH3OH(+M)<=>CH3+OH(+M)	5.390e+51	-9.36	103970.00	0.766	5.95e+01	1.91e+03	9.37e+03
89	C2H2+H(+M)<=>C2H3(+M)	9.060e+31	-4.66	3781.10	0.249	1.21e+01	1.00e+04	5.49e+03
99	C2H3+H(+M)<=>C2H4(+M)	1.400e+30	-3.86	3319.80	0.782	2.08e+02	2.66e+03	6.10e+03
120	CH3CHO(+M)<=>CH3+HCO(+M)	1.630e+59	-11.34	95918.00	0.000	1.00e+00	1.00e+00	-6.70e+02
132	C2H4+H(+M)<=>C2H5(+M)	2.890e+39	-6.64	5769.60	0.260	3.62e+02	1.00e+04	9.10e+03
140	C2H4+CH3(+M)<=>N-C3H7(+M)	3.000e+63	-14.60	18169.00	0.189	2.77e+02	8.75e+03	7.89e+03
141	C2H5+H(+M)<=>C2H6(+M)	1.990e+41	-7.08	6685.00	0.842	1.25e+02	2.22e+03	6.88e+03
151	C2H5O(+M)<=>CH3+CH2O(+M)	4.700e+25	-3.00	16532.00	0.426	3.00e-01	2.05e+03	1.00e+05
153	C2H6(+M)<=>2CH3(+M)	3.720e+65	-13.14	101580.00	0.390	1.00e+02	1.90e+03	6.00e+03
159	C3H6+H(+M)<=>N-C3H7(+M)	6.260e+38	-6.66	7000.50	1.000	1.00e+03	1.31e+03	4.81e+04
165	N-C3H7+H(+M)<=>C3H8(+M)	4.420e+61	-13.55	11358.00	0.315	3.69e+02	3.28e+03	6.67e+03
166	C3H8(+M)<=>C2H5+CH3(+M)	5.640e+74	-15.74	98719.00	0.310	5.00e+01	3.00e+03	9.00e+03

Table B.3: List of third-body enhanced or reduced efficiencies (α_j) specified for collisional stabilization or deactivation, used in pressure-dependent and association reactions.

No.	Reaction	C2H6	CH4	CO	CO2	H2	H2O	N2	O2
6	2H(+M)<=>H2(+M)				0.00	0.00	0.00		
8	O+H(+M)<=>OH+M					2.50	12.00		
9	H+O2(+M)<=>HO2(+M)			1.09	2.18	1.50	11.70		0.89
10	H2O(+M)<=>OH+H(+M)					3.00	0.00	2.00	1.50
19	2OH(+M)<=>H2O2(+M)					2.50	9.00	1.50	
25	CO+O(+M)<=>CO2(+M)			1.75	3.60	2.00	12.00		
29	HCO(+M)<=>CO+H(+M)			1.75	3.60	2.00	0.00		
44	CH3+H(+M)<=>CH4(+M)	3.00	2.00	1.50	2.00	2.00	6.00		
62	CH2OH(+M)<=>CH2O+H(+M)		2.00	1.50	2.00	2.00	6.00		

Continued on next page

Table B.3 – continued from previous page

No.	Reaction	C2H6	CH4	CO	CO2	H2	H2O	N2	O2
63	CH3O(+M)<=>CH2O+H(+M)		2.00	1.50	2.00	2.00	6.00		
75	CH3OH(+M)<=>CH3+OH(+M)	3.00	2.00	1.50	2.00	2.00	6.00		
89	C2H2+H(+M)<=>C2H3(+M)	3.00	2.00	1.50	2.00	2.00	6.00		
99	C2H3+H(+M)<=>C2H4(+M)	3.00	2.00	1.50	2.00	2.00	6.00		
120	CH3CHO(+M)<=>CH3+HCO(+M)	3.00	2.00	1.50	2.00	2.00	6.00		
132	C2H4+H(+M)<=>C2H5(+M)	3.00	2.00	1.50	2.00	2.00	6.00		
140	C2H4+CH3(+M)<=>N-C3H7(+M)	3.00	2.00	1.50	2.00	2.00	6.00		
141	C2H5+H(+M)<=>C2H6(+M)	3.00	2.00	1.50	2.00	2.00	6.00		
151	C2H5O(+M)<=>CH3+CH2O(+M)	3.00	2.00	1.50	2.00	2.00	6.00		
153	C2H6(+M)<=>2CH3(+M)	3.00	2.00	1.50	2.00	2.00	6.00		
159	C3H6+H(+M)<=>N-C3H7(+M)	3.00	2.00	1.50	2.00	2.00	6.00		
165	N-C3H7+H(+M)<=>C3H8(+M)	3.00	2.00	1.50	2.00	2.00	6.00		
166	C3H8(+M)<=>C2H5+CH3(+M)	3.00	2.00	1.50	2.00	2.00	6.00		

Appendix C

ADDITIONAL DATA: HOT SURFACE IGNITION OF DIMETHYL ETHER/AIR

This appendix presents colormaps of the ignition event near a 0.09 m hot surface at 1 bar and U_∞ = 0.1 m/s. The mixture is stoichiometric dimethyl ether (DME)/air. DME is another fuel that exhibits a negative-temperature coefficient (NTC) region with significant low-temperature chemistry as shown in Figure C.1.

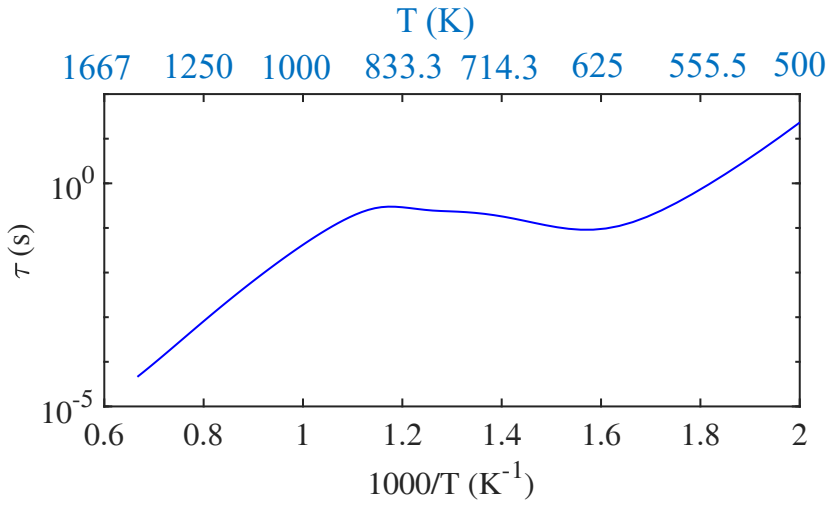


Figure C.1: Zero-dimensional ignition delay times for stoichiometric DME/air at 1 bar.

The simulations were initialized with a steady, fully-developed flow field for a fixed wall temperature to isolate the kinetic effects. Two wall temperatures, T_H = 925 K and T_H = 1000 K were investigated. For the T_H = 1000 K simulation, at t = 0 s, the thermal layer and boundary layer appear normal in Figure C.2. 6.2 ms later, changes in the thermal layer can be seen with a low-temperature flame propagating through the thermal layer. From the streamlines, a separation across this low-temperature flame front is observed. Similar to the results for nC_6H_{14} (Chapter 4), the low-temperature flame fails to fully propagate into the cold gas and stabilizes as an energy release band in the colder portion of the thermal layer. At 0.0634 s and 0.064 s, the high-temperature ignition event is observed closer to the leading edge of the heated surface. From Figures C.3, C.4, and C.5, the low-temperature flame front is seen at t = 0.0062 s as a thin heat release zone in the cold part of the thermal layer,

driven by rapid multiplication of OH molecules and production of intermediate species, like CH_2O. The high-temperature ignition event is characterized by an even larger rise in heat release in a localized region near the hot surface. driven again by a multiplicative production of OH to convert CO and other intermediates like CH_2O to CO_2.

Interestingly, the ignition event occurs in a thinner part of the thermal layer closer to the leading edge compared to results presented in Chapters 4 and 7 as well as Appendix G. This is a direct influence of low-temperature chemistry altering the convective and diffusive losses along the hot surface. The sensitivity of the ignition location can further be seen from the results for $T_H = 925$ K. Influenced by the low-temperature energy release band, the ignition event shifts further downstream compared to the results for $T_H = 1000$ K.

The results for DME/air shown in this appendix further support the generality of a low-temperature energy release band for fuels with an NTC region in the colder parts of the thermal layer near a hot surface. These low-temperature kinetic pathways drastically affect the thermal layer structure and ignition behavior and must be included for accurate numerical modeling.

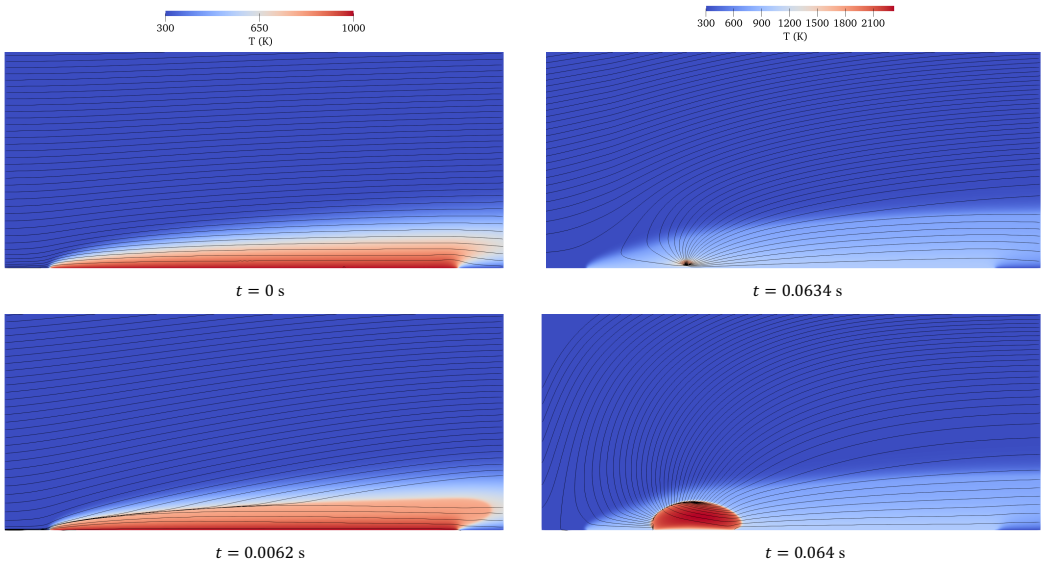


Figure C.2: Temperature field evolution and instantaneous streamlines. $T_H = 1000$ K, $P = 1$ bar, $U_\infty = 0.1$ m/s, and $L = 0.09$ m.

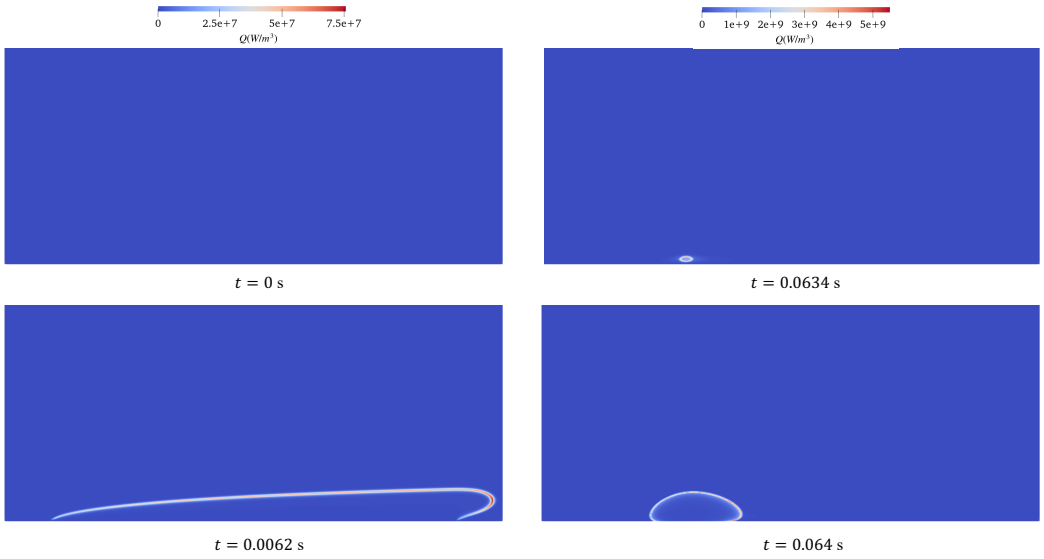


Figure C.3: Heat release field evolution and instantaneous streamlines. $T_H = 1000$ K, $P = 1$ bar, $U_\infty = 0.1$ m/s, and $L = 0.09$ m.

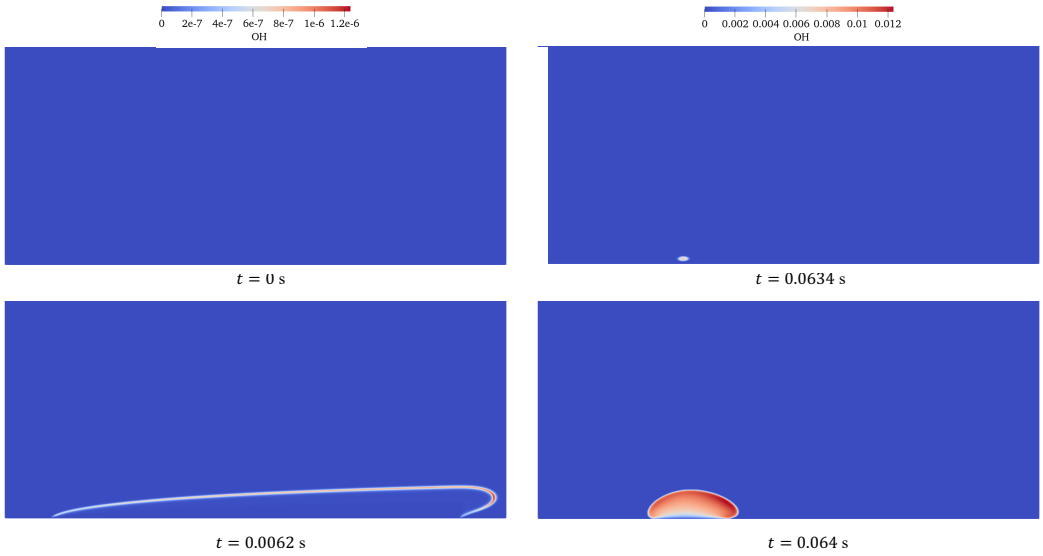


Figure C.4: OH mass fraction field evolution and instantaneous streamlines. T_H = 1000 K, P = 1 bar, U_∞ = 0.1 m/s, and L = 0.09 m.

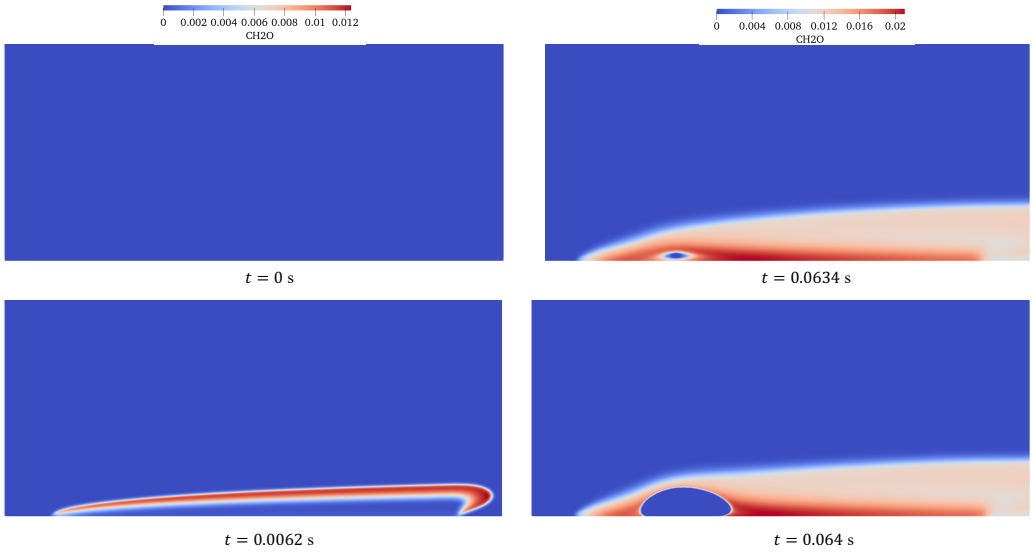


Figure C.5: CH2O mass fraction field evolution and instantaneous streamlines. T_H = 1000 K, P = 1 bar, U_∞ = 0.1 m/s, and L = 0.09 m.

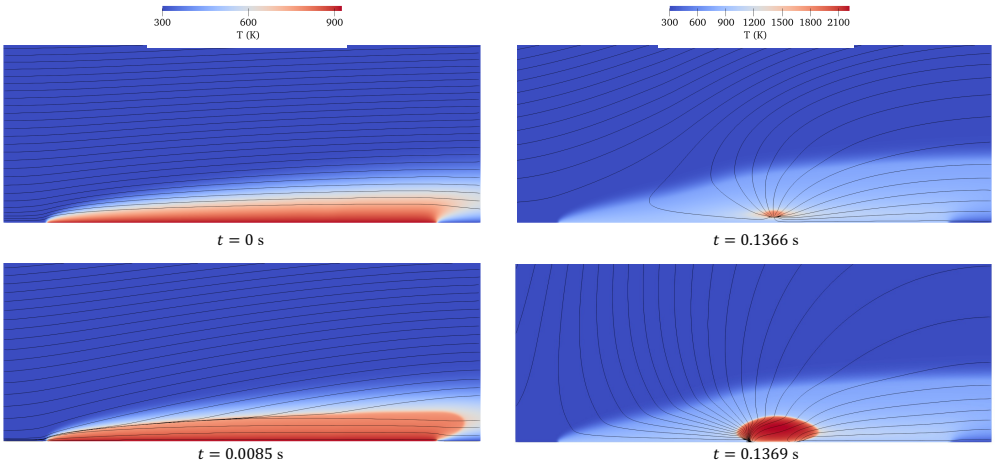


Figure C.6: Temperature field evolution and instantaneous streamlines. $T_H = 925$ K, $P = 1$ bar, $U_\infty = 0.1$ m/s, and $L = 0.09$ m.

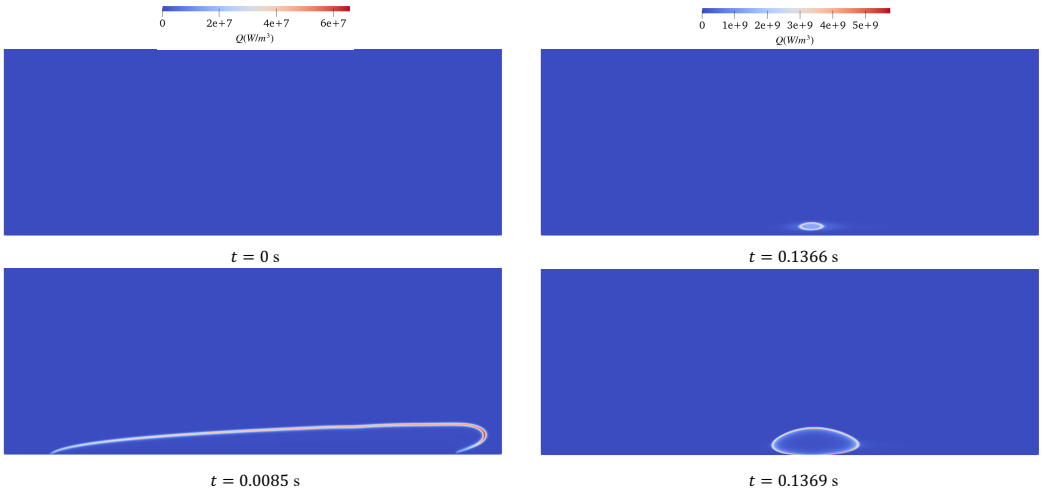


Figure C.7: Heat release field evolution and instantaneous streamlines. $T_H = 925$ K, $P = 1$ bar, $U_\infty = 0.1$ m/s, and $L = 0.09$ m.

Appendix D

ONE-DIMENSIONAL DIFFUSING THERMAL LAYER CONFIGURATIONS

Table D.1: A full list of one-dimensional diffusing thermal layer configurations. The gas mixtures are initially set to 300 K.

Mixture	T_H (K)	P (bar)
Stoichiometric H_2/air	1000	0.2
Stoichiometric H_2/air	1100	0.2
Stoichiometric H_2/air	1200	0.2
Stoichiometric H_2/air	1300	0.2
Stoichiometric H_2/air	1000	1
Stoichiometric H_2/air	1100	1
Stoichiometric H_2/air	1200	1
Stoichiometric H_2/air	1300	1
Stoichiometric H_2/air	1200	5
Stoichiometric CO/air, 1% wt H_2	1000	1
Stoichiometric CO/air, 1% wt H_2	1100	1
Stoichiometric CO/air, 1% wt H_2	1200	1
Stoichiometric CO/air, 0.25% wt H_2	1200	1
Stoichiometric NH_3/air	1400	1
Stoichiometric NH_3/air	1500	1
Stoichiometric CH_2O/air	1000	0.2
Stoichiometric CH_2O/air	1100	0.2
Stoichiometric CH_2O/air	1200	0.2
Stoichiometric CH_2O/air	1000	1
Stoichiometric CH_2O/air	1100	1
Stoichiometric CH_2O/air	1200	1
Stoichiometric CH_2O/air	1000	5
Stoichiometric CH_2O/air	1100	5
Stoichiometric CH_2O/air	1200	5
Stoichiometric CH_4/air	1000	0.2
Stoichiometric CH_4/air	1100	0.2

Mixture	T_H (K)	P (bar)
Stoichiometric CH_4/air	1200	0.2
Stoichiometric CH_4/air	1300	0.2
Stoichiometric CH_4/air	1400	0.2
Stoichiometric CH_4/air	1500	0.2
Stoichiometric CH_4/air	1000	1
Stoichiometric CH_4/air	1100	1
Stoichiometric CH_4/air	1200	1
Stoichiometric CH_4/air	1300	1
Stoichiometric CH_4/air	1400	1
Stoichiometric CH_4/air	1500	1
Stoichiometric CH_4/air	1000	5
Stoichiometric CH_4/air	1100	5
Stoichiometric CH_4/air	1200	5
Stoichiometric CH_4/air	1300	5
Stoichiometric CH_4/air	1400	5
Stoichiometric CH_4/air	1500	5
Stoichiometric nC_6H_{14}/air (HT)	1000	0.2
Stoichiometric nC_6H_{14}/air (HT)	1100	0.2
Stoichiometric nC_6H_{14}/air (HT)	1200	0.2
Stoichiometric nC_6H_{14}/air (HT)	1300	0.2
Stoichiometric nC_6H_{14}/air (HT)	1400	0.2
Stoichiometric nC_6H_{14}/air (HT)	1000	1
Stoichiometric nC_6H_{14}/air (HT)	1100	1
Stoichiometric nC_6H_{14}/air (HT)	1200	1
Stoichiometric nC_6H_{14}/air (HT)	1300	1
Stoichiometric nC_6H_{14}/air (HT)	1400	1
Stoichiometric nC_6H_{14}/air (HT)	1000	5
Stoichiometric nC_6H_{14}/air (HT)	1100	5
Stoichiometric nC_6H_{14}/air (HT)	1200	5
Stoichiometric nC_6H_{14}/air (HT)	1300	5
Stoichiometric nC_6H_{14}/air (HT)	1400	5

Appendix E

CONVERGENCE OF THE REACTION ORDER, n, AND ACTIVATION ENERGY, E_a

The derivatives $\left(\partial\tau_i/\partial\rho\right)_{T_0}$ and $\left(\partial\tau_i/\partial T_0\right)_p$ derived in asymptotic expressions for the reaction order, n, and activation energy, E_a presented in Eqs. (5.19) and (5.21) are recommended by Bane et al. (2010b) to be calculated according to a first order, one-sided differencing scheme as

$$\left(\frac{\partial\tau_i}{\partial\rho_0}\right)_{T_0} \approx \frac{\tau_{i+1}-\tau_i}{T'} \quad ; \quad \left(\frac{\partial\tau_i}{\partial T_0}\right)_p \approx \frac{\tau_{i+1}-\tau_i}{\rho'} \tag{E.1}$$

where τ is the ignition delay time, ρ_0 is the initial density, T_0 is the initial temperature, and p is the pressure. The subscript i indicates the particular "node" where the quantities are computed (i.e., what initial temperature was used to computed the variables). Bane et al. (2010b) recommends $T' = \Delta T = 30$ K and $\rho_0' = \Delta\rho = 0.1\rho_0$ as optimal parameters. In practice, these first-order approximations were found to be insufficient, yielding unconverged values of n and E_a, especially for more complex fuels with more sensitive ignition delay times. In this appendix, reaction order and activation energy solutions will be investigated for three numerical schemes: first order one-sided differencing, second-order central differencing, and fourth-order central differencing. Then, a parametric study on T' and ρ' will be performed to empirically for the higher order differencing schemes to determine the optimal values in terms of convergence and minimization of numerical noise.

E.1 First-, second-, and fourth-order differencing schemes

In addition to the first-order formulation presented in Eq. (E.1), both a two-point second-order central differencing and five-point fourth-order central differencing scheme were tested.

The second-order scheme for the derivatives is defined by

$$\left(\frac{\partial\tau_i}{\partial\rho}\right)_{T_0} \approx \frac{\tau_{i+1}-\tau_{i-1}}{2T'} \quad ; \quad \left(\frac{\partial\tau_i}{\partial T_0}\right)_p \approx \frac{\tau_{i+1}-\tau_{i-1}}{2\rho'} \tag{E.2}$$

Similarly, the fourth order central differencing scheme for the derivatives is defined as

$$\left(\frac{\partial \tau_i}{\partial \rho_0}\right)_{T_0} \approx \frac{-\tau_{i+2\Delta\rho} + 8\tau_{i+\Delta\rho} - 8\tau_{i-\Delta\rho} + \tau_{i-2\Delta\rho}}{12\Delta\rho}$$
$$\left(\frac{\partial \tau_i}{\partial T_0}\right)_{p} \approx \frac{-\tau_{i+2\Delta T} + 8\tau_{i+\Delta T} - 8\tau_{i-\Delta T} + \tau_{i-2\Delta T}}{12\Delta T} \tag{E.3}$$

The reduced CaltechMech mechanism used in Chapter 3 and given in Appendix B was used in zero-dimensional, adiabatic ignition simulations at 1 bar and $900 < T_i < 1500$ K. Figure E.1 plots the activation temperature variation with initial temperature for stoichiometric nC_6H_{14}/air with the three differencing schemes discussed. The recommended values of $T' = \Delta T = 30$ K and $\rho_0' = \Delta\rho = 0.1\rho_0$ were used for the study. The first-order scheme under predicts T_a across the entire temperature range, on average differing from the fourth-order by ~8%. The second-order scheme does significantly better, differing from the fourth-order scheme by only 0.3% on average.

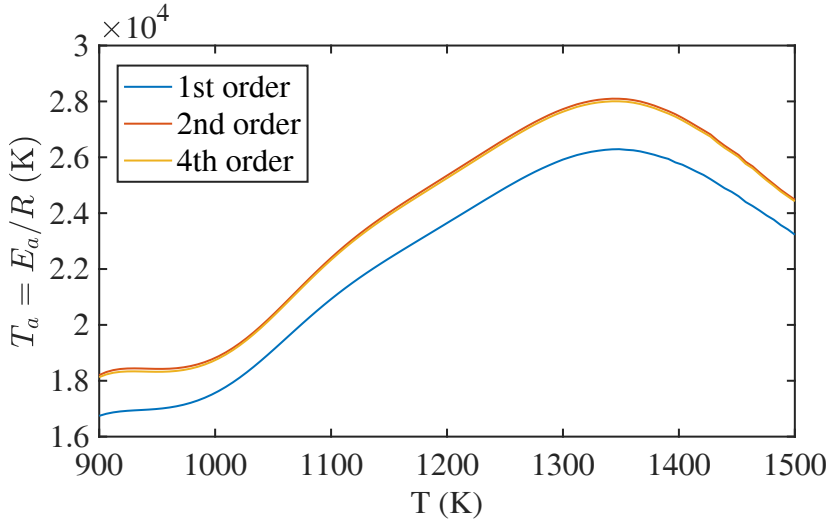


Figure E.1: Activation temperature, $T_a = E_a/R$, variation with initial temperature for a mixture of stoichiometric nC_6H_{14}/air at 1 bar for the three differencing schemes.

The 8% difference seen with the first-order scheme is important to recognize. The characteristic chemical length scale, ℓ_k scales linearly with T_a so converged values are necessary. Therefore, the first-order differencing scheme is deemed insufficient. Both the second- and fourth-order differencing schemes are properly converged. For the purposes of the results in this thesis, the fourth-order scheme is employed for the derivatives in computing n and E_a for the ignition model due to its lower truncation error and reduced numerical noise compared to the second-order scheme.

E.2 Empirical determination of T' and ρ'

Using a different differencing scheme than what was proposed in Bane et al. (2010b) may affect the optimal values of T' and ρ'. Here, two parametric studies will be performed to determine find the optimal T' and ρ' for the employed fourth-order scheme. First, $T' = 10$ K will be fixed and ρ' will be varied to observe the effect on n. Then, $\rho' = 0.1\rho_0$ will be fixed and T' will be varied to observe the effect on T_a.

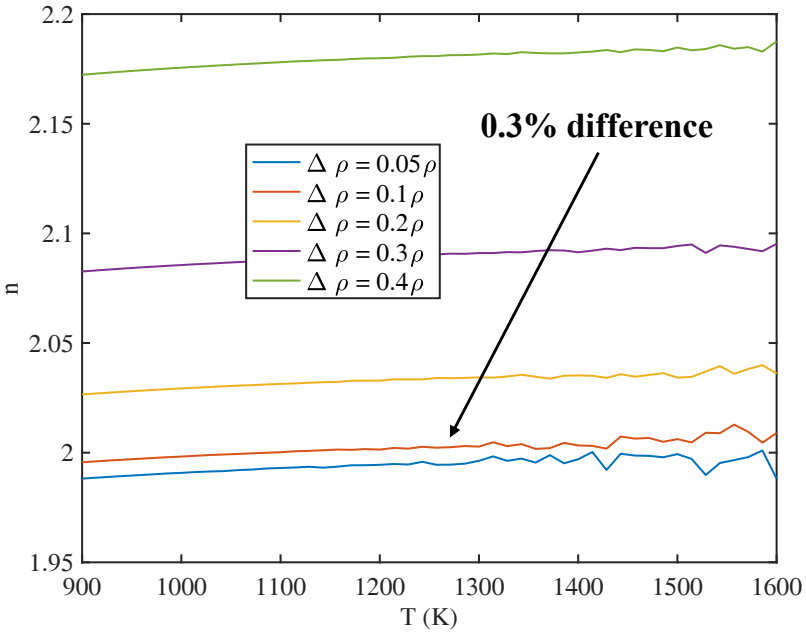


Figure E.2: Reaction order, n, variation with initial temperature for a mixture of stoichiometric CH_2O/air at 1 bar for different values of $\rho' = \Delta\rho$.

This process was carried out for several mixtures, all with similar results. Therefore, results for only one of the mixtures will be presented. Figure E.2 presents the computed reaction orders against temperature for stoichiometric CH_2O/air at 1 bar for $900 < T_0 < 1600$ K. For this mixture, n is fairly constant over the temperature range. However, values for n are quite sensitive to the selection of $\Delta\rho$. For $\Delta\rho = 0.4\rho$, the average difference from the $\Delta\rho = 0.05\rho$ solution is 9.3%. As $\Delta\rho$ is decreased, the accuracy of the derivative approximation increases. However, this increased accuracy comes at a cost. As the difference in initial density shrinks, so does the difference in the computed delay times, τ. This leads to inevitable numerical noise, especially for large temperatures where τ is exceedingly small. As a result, a decrease in noise content is observed as $\Delta\rho$ is increased. The average difference between the $\Delta\rho = 0.1\rho$ and $\Delta\rho = 0.05\rho$ solutions is only 0.3%. Thus,

for the computations in this thesis, $\Delta\rho = 0.1\rho$ was selected and a Savitzky-Golay filter applied to minimize noise and maximize accuracy.

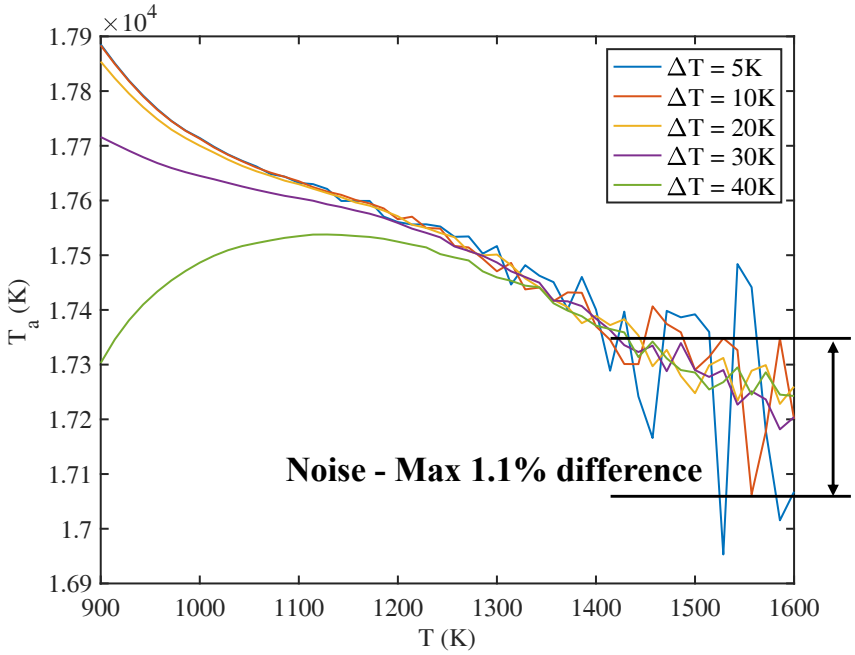


Figure E.3: Activation temperature, $T_a = E_a/R$, variation with initial temperature for a mixture of stoichiometric CH_2O/air at 1 bar for different values of $T' = \Delta T$.

A similar parametric study was performed for computation of T_a for fixed $\Delta\rho = 0.1\rho$ and variable ΔT, as is shown in Figure E.3 for stoichiometric CH_2/air at 1 bar. For low temperatures, the $\Delta T = 40$ K solution differs from the $\Delta T = 5$ K solution by as much as 3.5% and improves as the temperature is increased. Comparably, the $\Delta T = 10$ K solution differs from the $\Delta T = 5$ K solution by only 0.05%. As with the reaction order study, decreasing ΔT better approximates the derivative, but comes at the cost of worse intrusion of numerical noise. In fact, it is even more severe than for the reaction order solutions because there are two sources of noise as both $\left(\partial\tau_i/\partial\rho_0\right)_{T_0}$ and $\left(\partial\tau_i/\partial T_0\right)_p$ are needed to compute T_a whereas the reaction order only requires $\left(\partial\tau_i/\partial\rho_0\right)_{T_0}$. For $\Delta T = 10$ K, the noise in T_a is 1.1% the value itself. Similar to the strategy for computing n, for the computations in this thesis, $\Delta T = 10$ K was selected and a Savitzky-Golay filter applied to minimize noise and maximize accuracy.

Appendix F

τ_i, T_a, AND κ COMPUTATIONS

This appendix presents data for the zero-dimensional ignition delay time and activation temperature,τ_i and $T_a = E_a/R$, as well as the thermal diffusivity κ used for calculation of ℓ_k for all mixtures tested in Chapters 6, 7, and 8. In total over 1,000,000 of these zero-dimensional simulations with detailed chemical mechanisms were run.

F.1 H_2/air mixtures

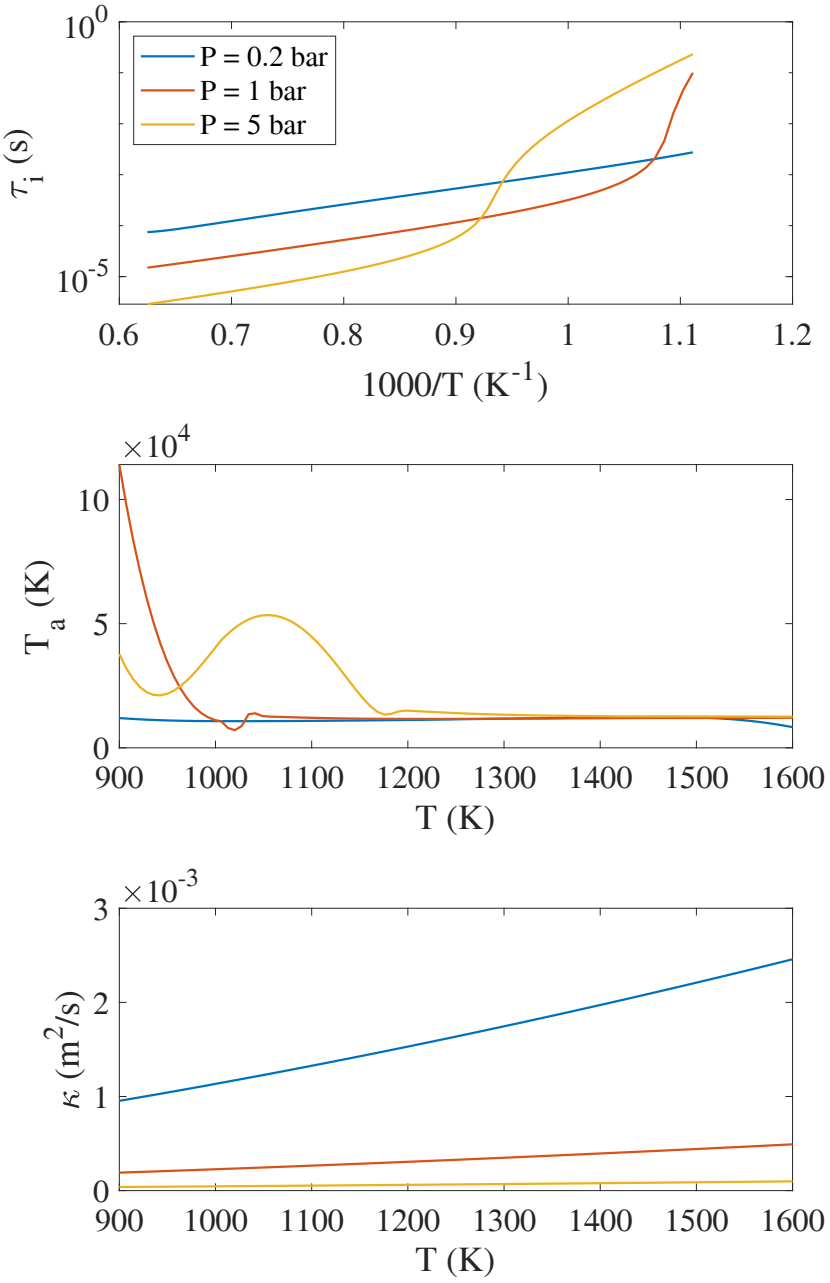


Figure F.1: Computed zero-dimensional ignition delay time τ_i(top), activation temperature $T_a = E_a/R$ (middle), and thermal diffusivity κ (bottom) for 10% H_2/air.

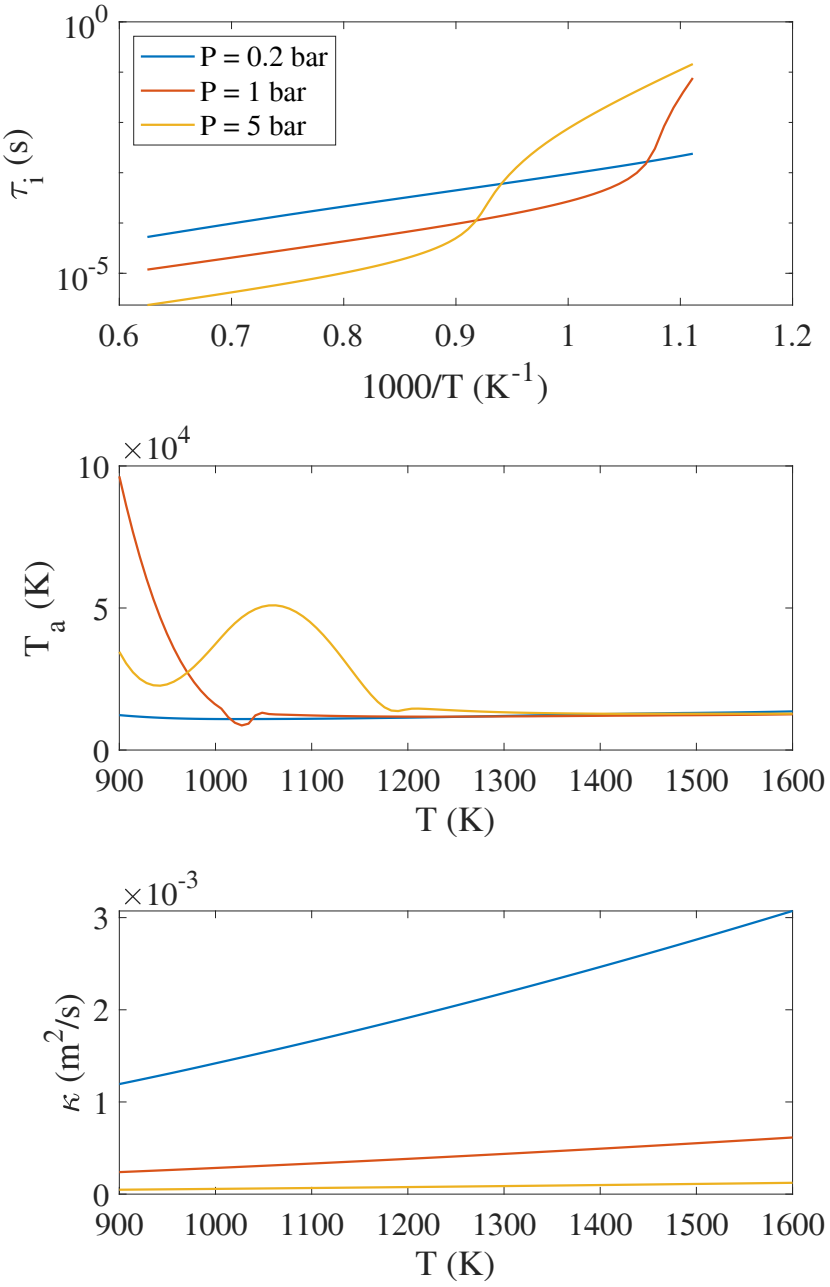


Figure F.2: Computed zero-dimensional ignition delay time τ_i(top), activation temperature $T_a = E_a/R$ (middle), and thermal diffusivity κ (bottom) for 20% H_2/air.

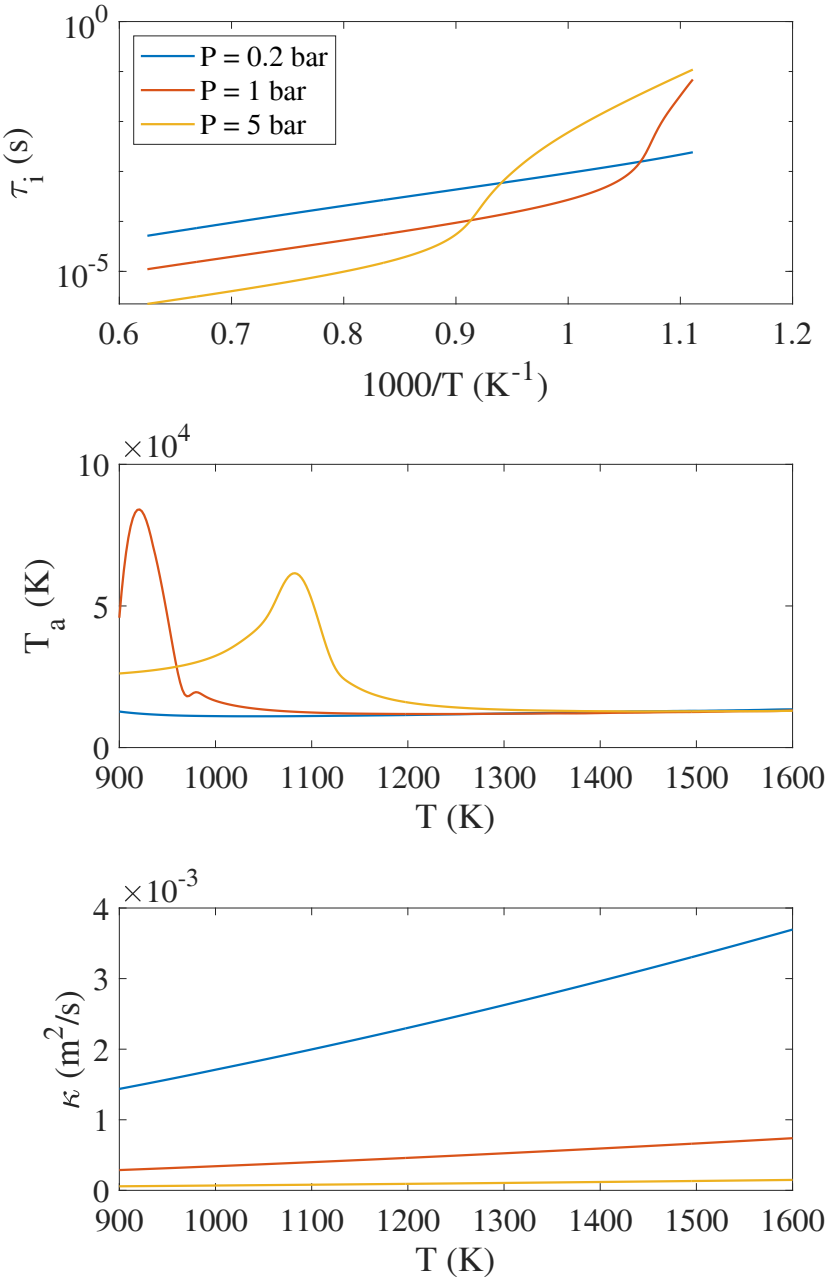


Figure F.3: Computed zero-dimensional ignition delay time τ_i(top), activation temperature $T_a = E_a/R$ (middle), and thermal diffusivity κ (bottom) for stoichiometric H_2/air.

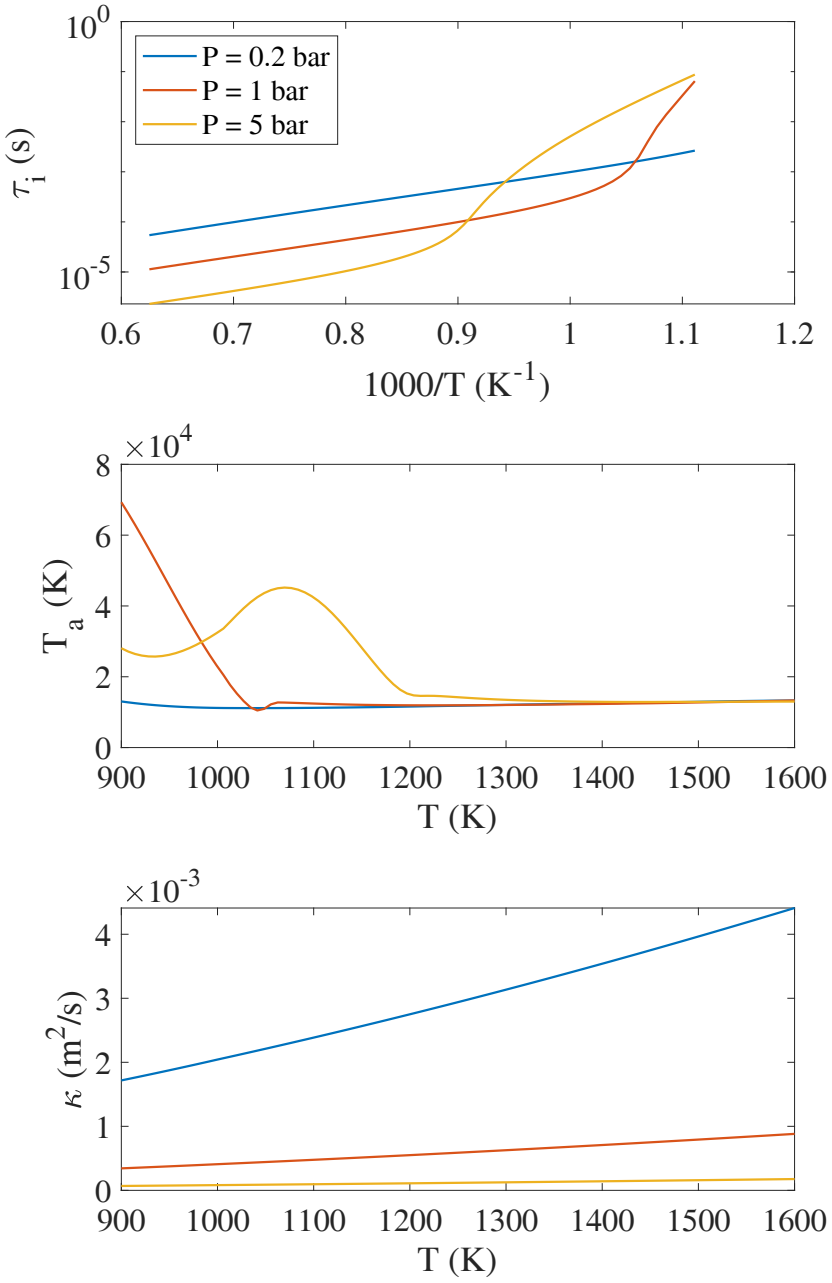


Figure F.4: Computed zero-dimensional ignition delay time τ_i(top), activation temperature $T_a = E_a/R$ (middle), and thermal diffusivity κ (bottom) for 40% H_2/air.

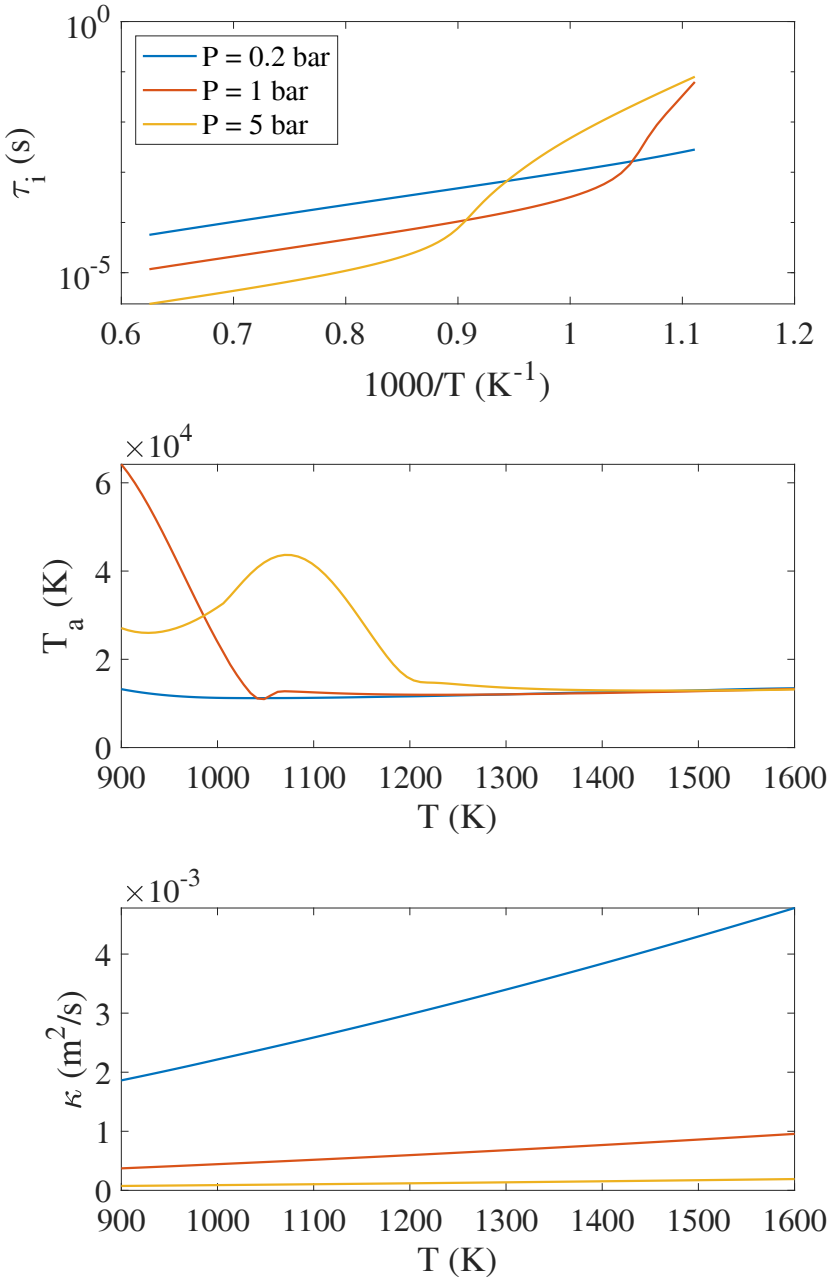


Figure F.5: Computed zero-dimensional ignition delay time τ_i(top), activation temperature $T_a = E_a/R$ (middle), and thermal diffusivity κ (bottom) for 45% H_2/air.

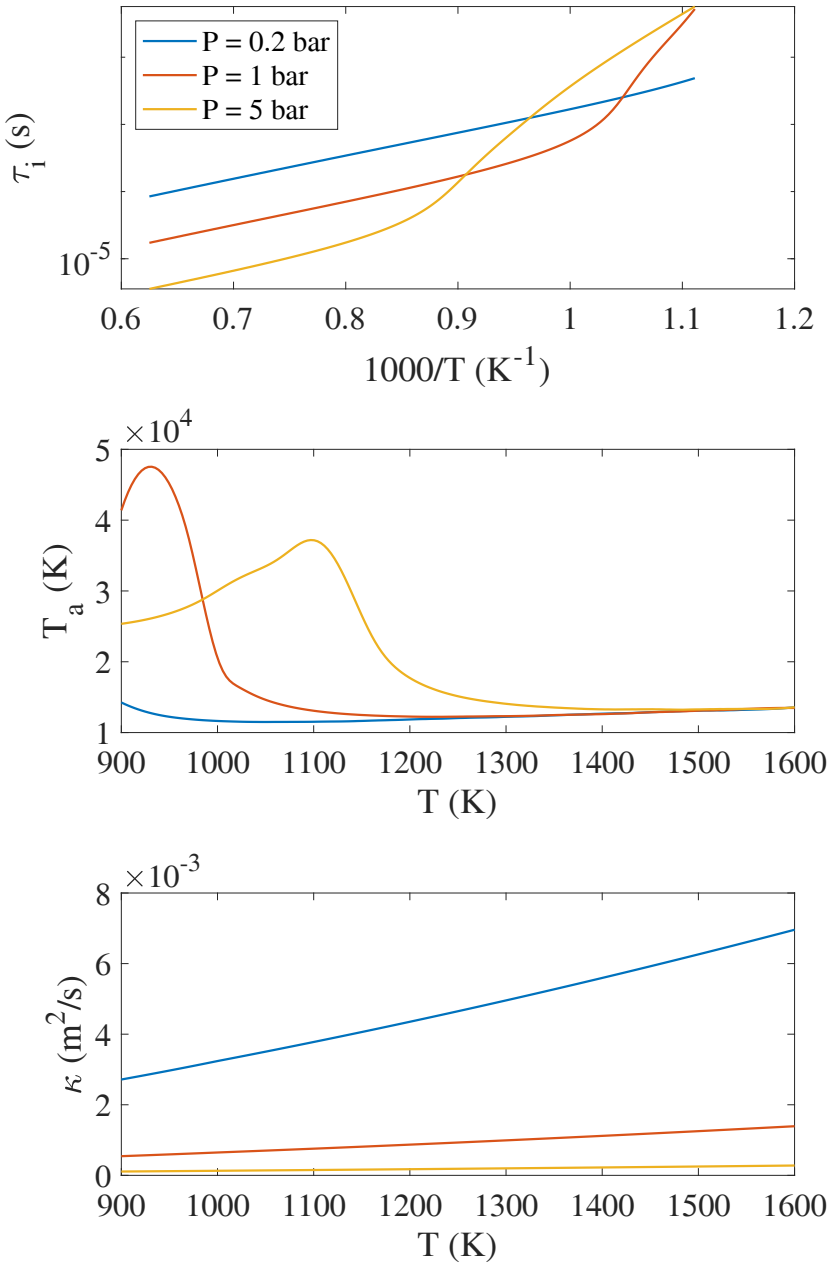


Figure F.6: Computed zero-dimensional ignition delay time τ_i(top), activation temperature $T_a = E_a/R$ (middle), and thermal diffusivity κ (bottom) for 70% H_2/air.

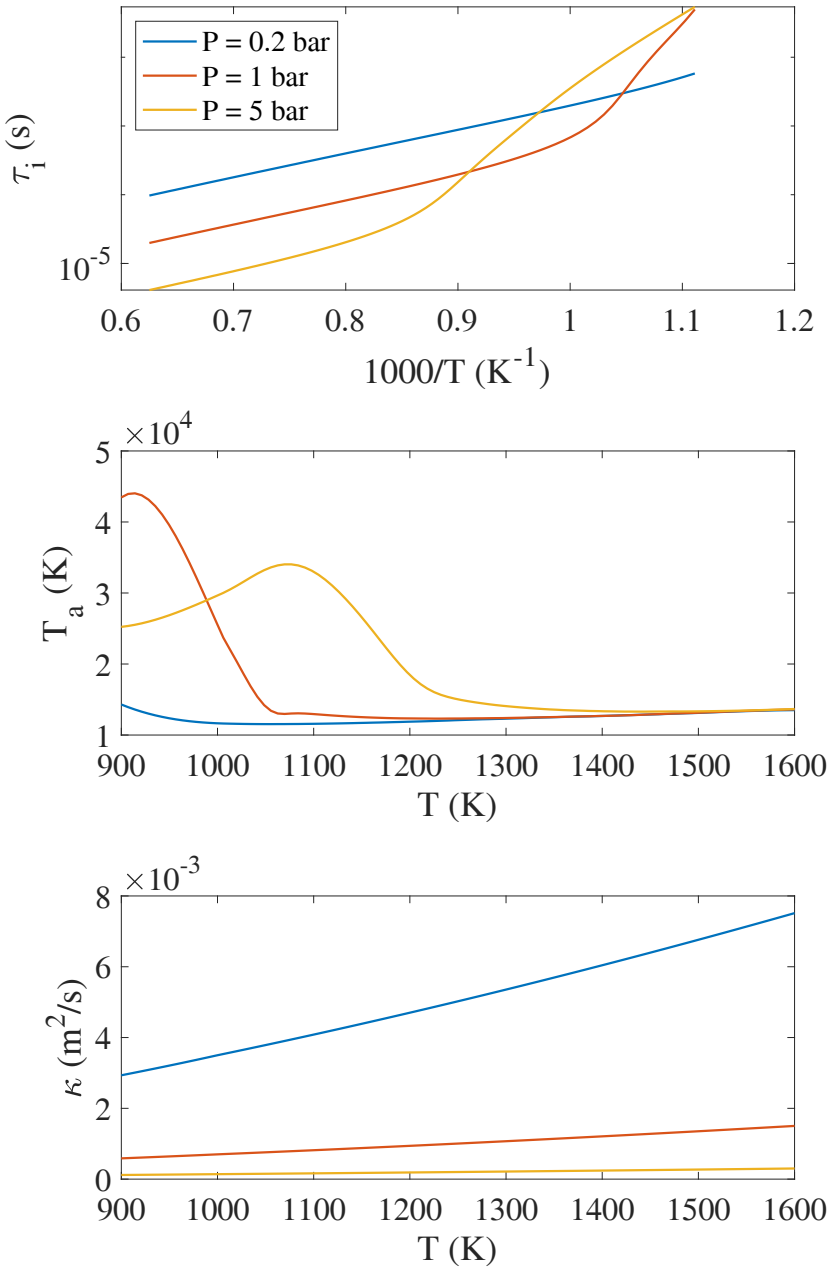


Figure F.7: Computed zero-dimensional ignition delay time τ_i(top), activation temperature $T_a = E_a/R$ (middle), and thermal diffusivity κ (bottom) for 75% H_2/air.

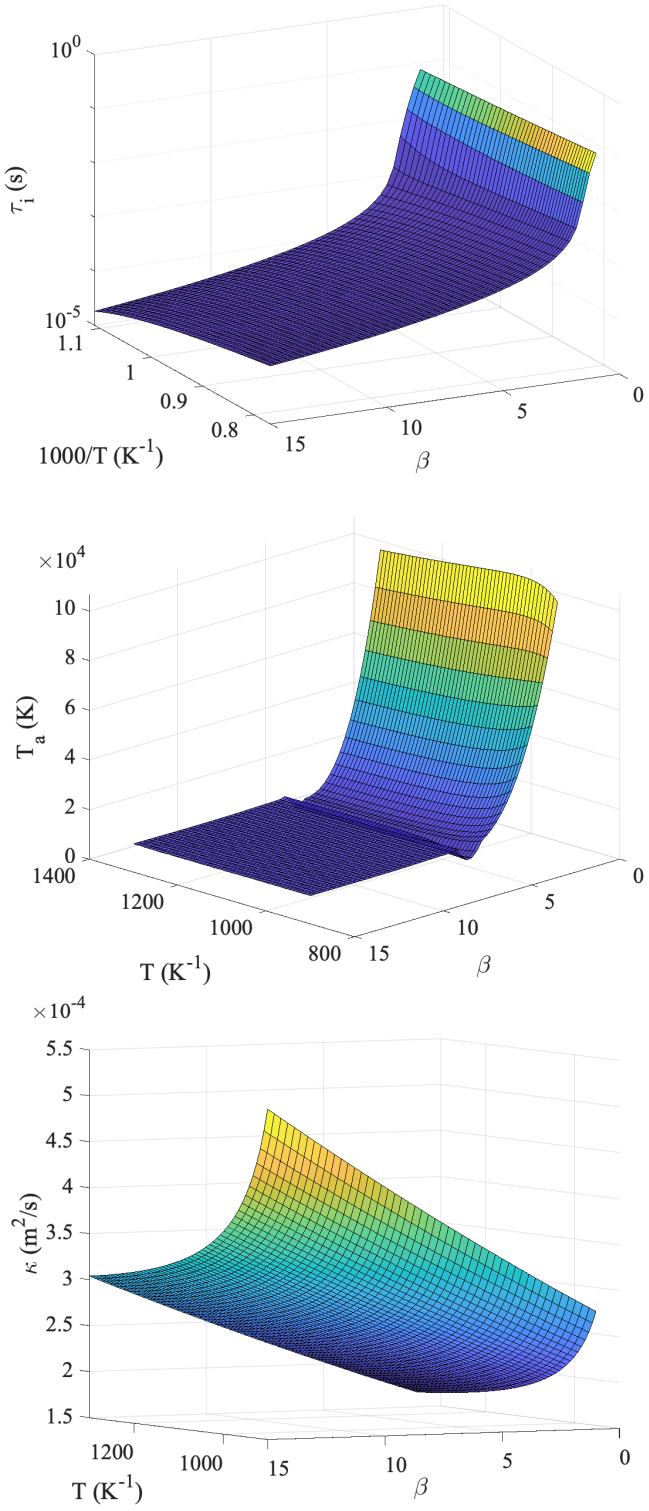


Figure F.8: Computed surfaces for the zero-dimensional ignition delay time τ_i(top), activation temperature $T_a = E_a/R$ (middle), and thermal diffusivity κ (bottom) for a $H_2/O_2/N_2$ mixture as a function of β for an equivalence ratio, $\Phi = 0.39$.

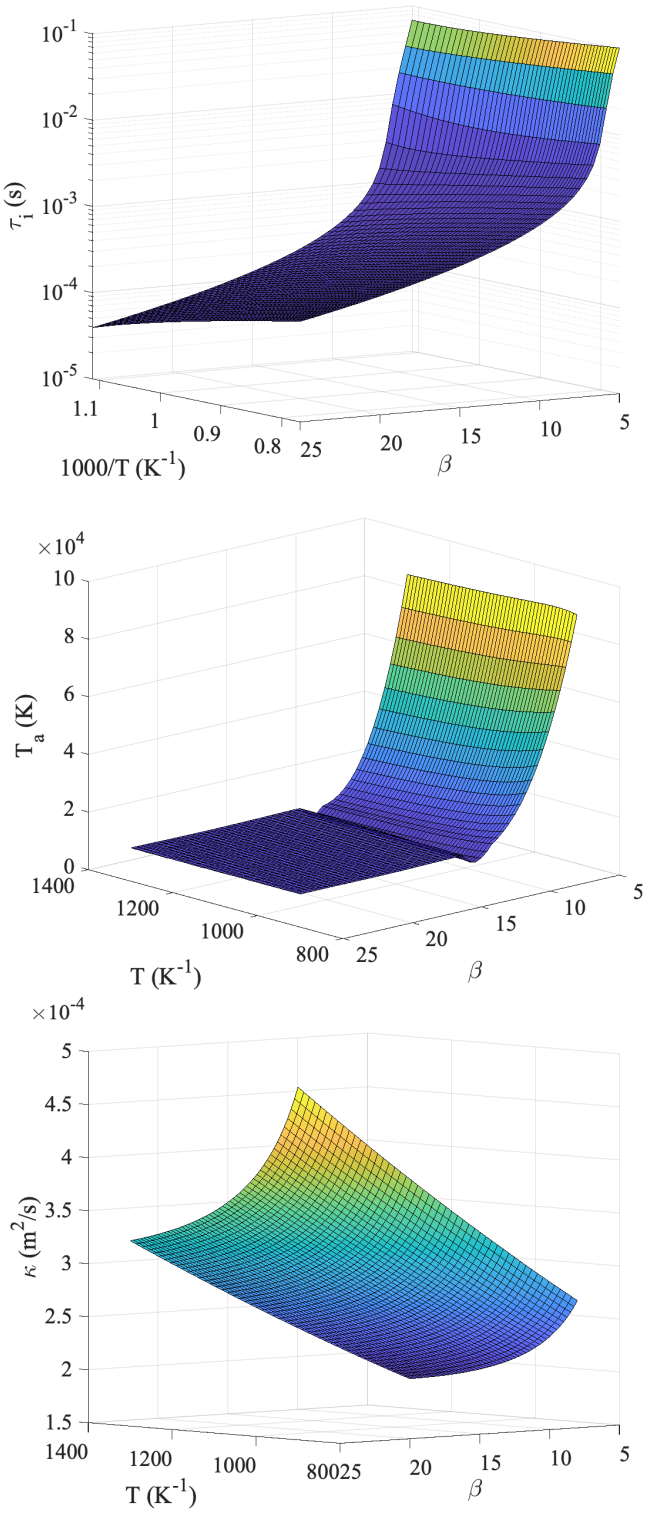


Figure F.9: Computed surfaces for the zero-dimensional ignition delay time τ_i(top), activation temperature $T_a = E_a/R$ (middle), and thermal diffusivity κ (bottom) for a $H_2/O_2/N_2$ mixture as a function of β for an equivalence ratio, $\Phi = 1.0$.

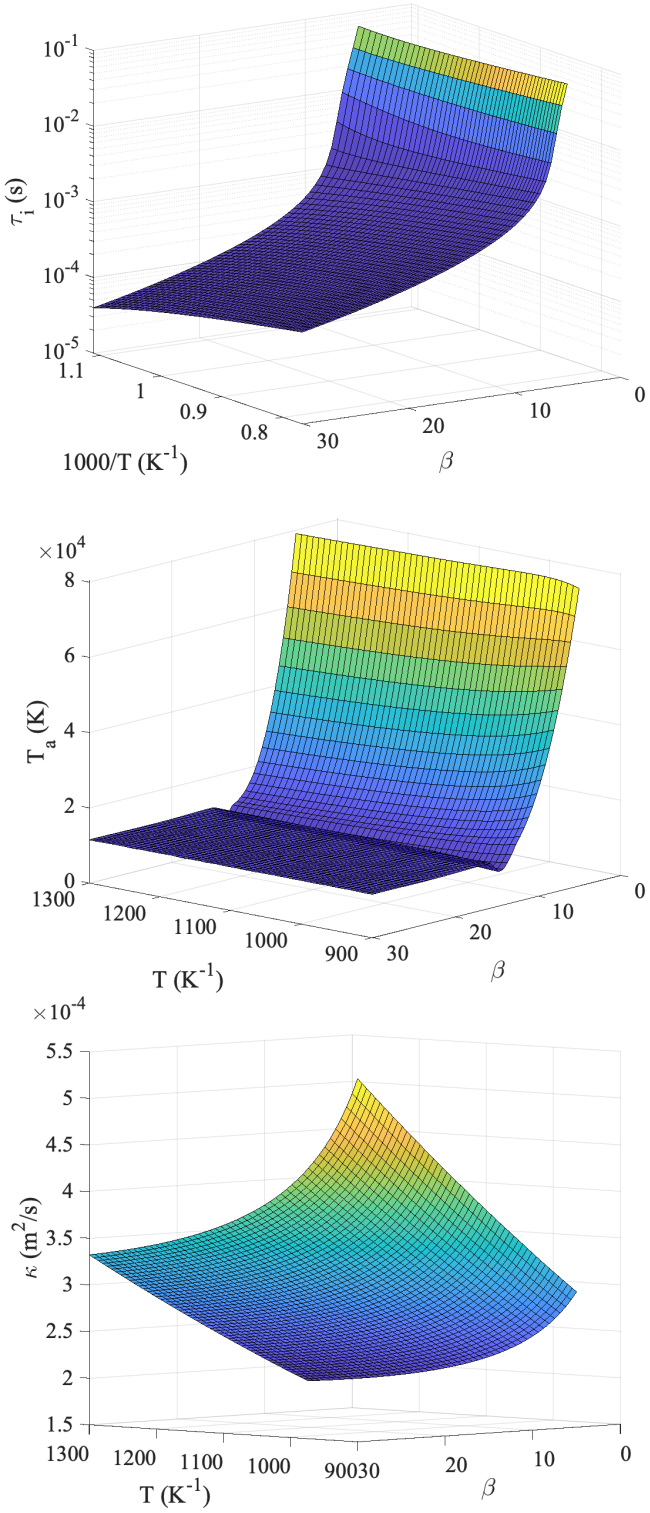


Figure F.10: Computed surfaces for the zero-dimensional ignition delay time τ_i(top), activation temperature $T_a = E_a/R$ (middle), and thermal diffusivity κ (bottom) for a $H_2/O_2/N_2$ mixture as a function of β for an equivalence ratio, $\Phi = 1.35$.

F.2 CO/H_2/air mixtures

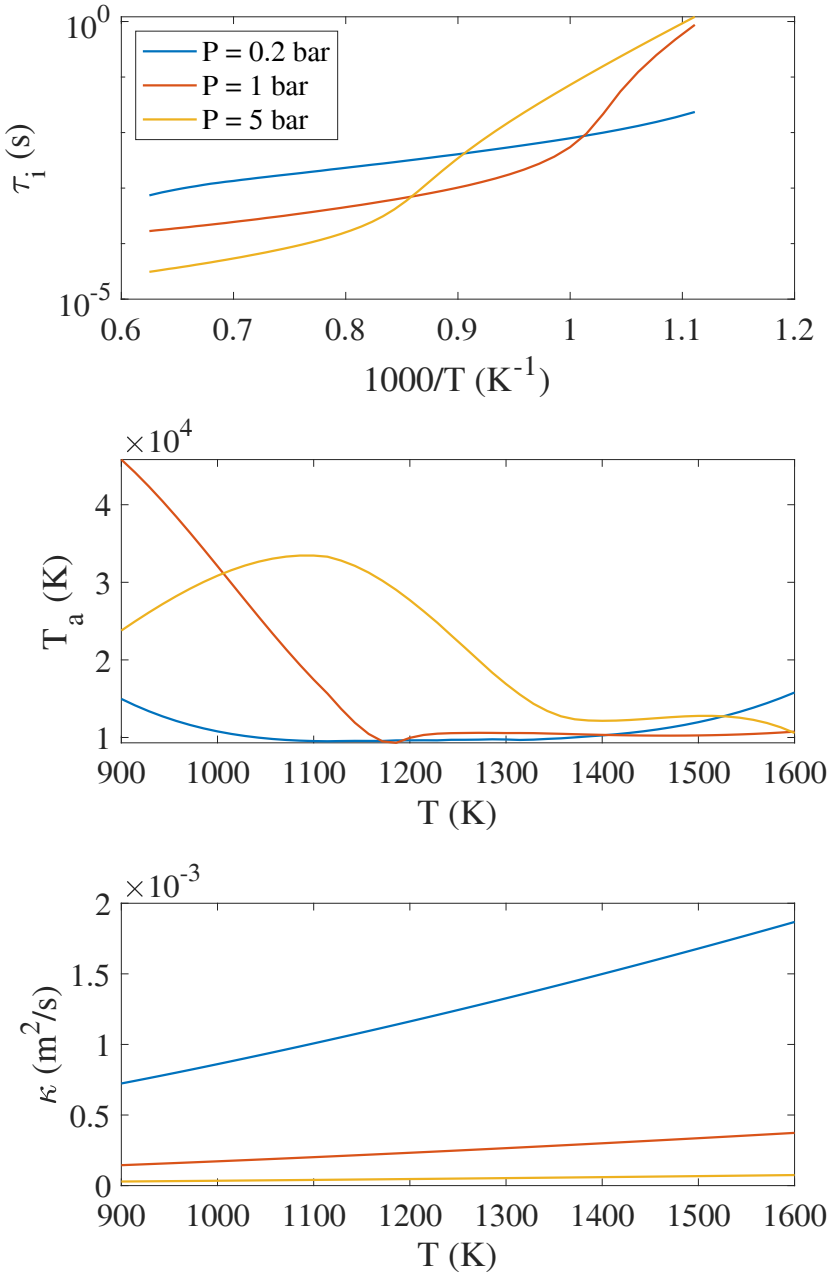


Figure F.11: Computed zero-dimensional ignition delay time τ_i(top), activation temperature $T_a = E_a/R$ (middle), and thermal diffusivity κ (bottom) for CO/0.25%H_2/air.

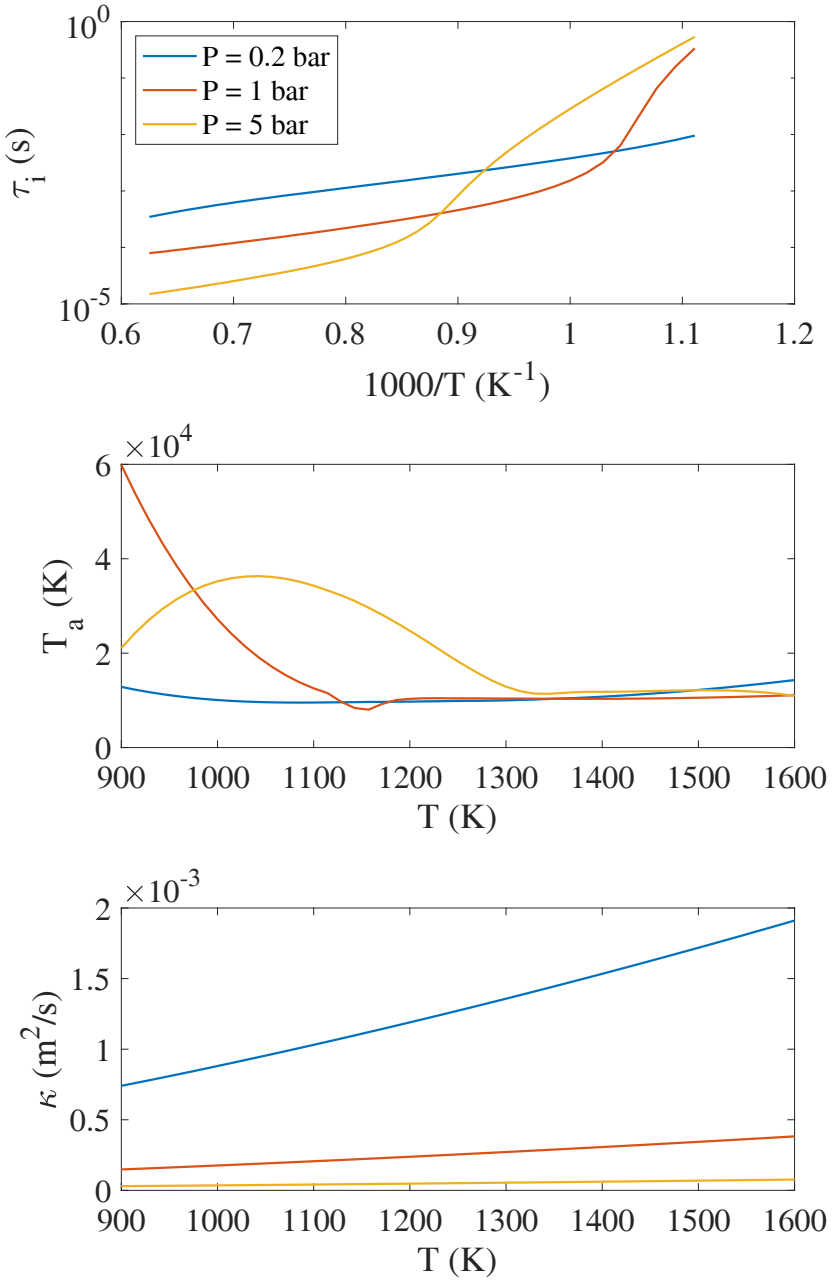


Figure F.12: Computed zero-dimensional ignition delay time τ_i(top), activation temperature $T_a = E_a/R$ (middle), and thermal diffusivity κ (bottom) for CO/1%H_2/air.

F.3 CH_4/air mixtures

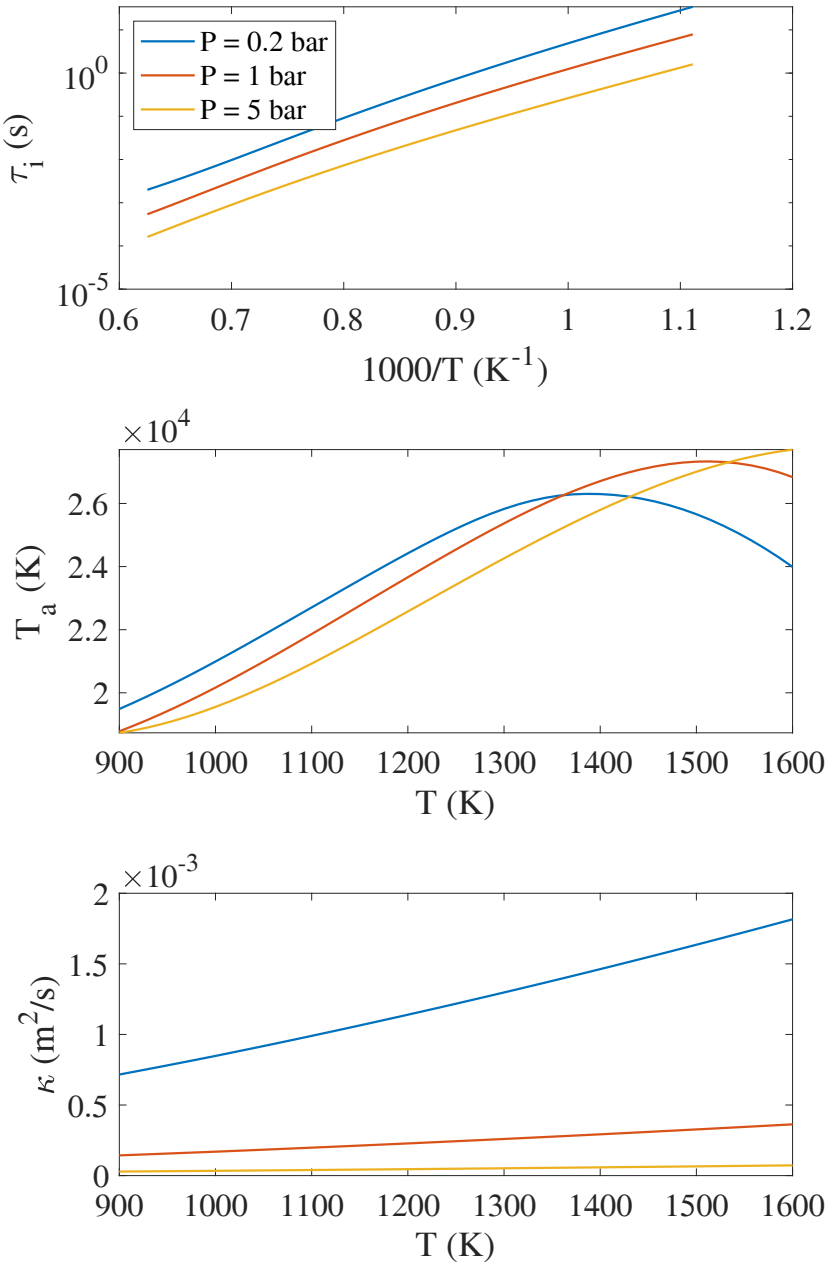


Figure F.13: Computed zero-dimensional ignition delay time τ_i(top), activation temperature $T_a = E_a/R$ (middle), and thermal diffusivity κ (bottom) for stoichiometric CH_4/air.

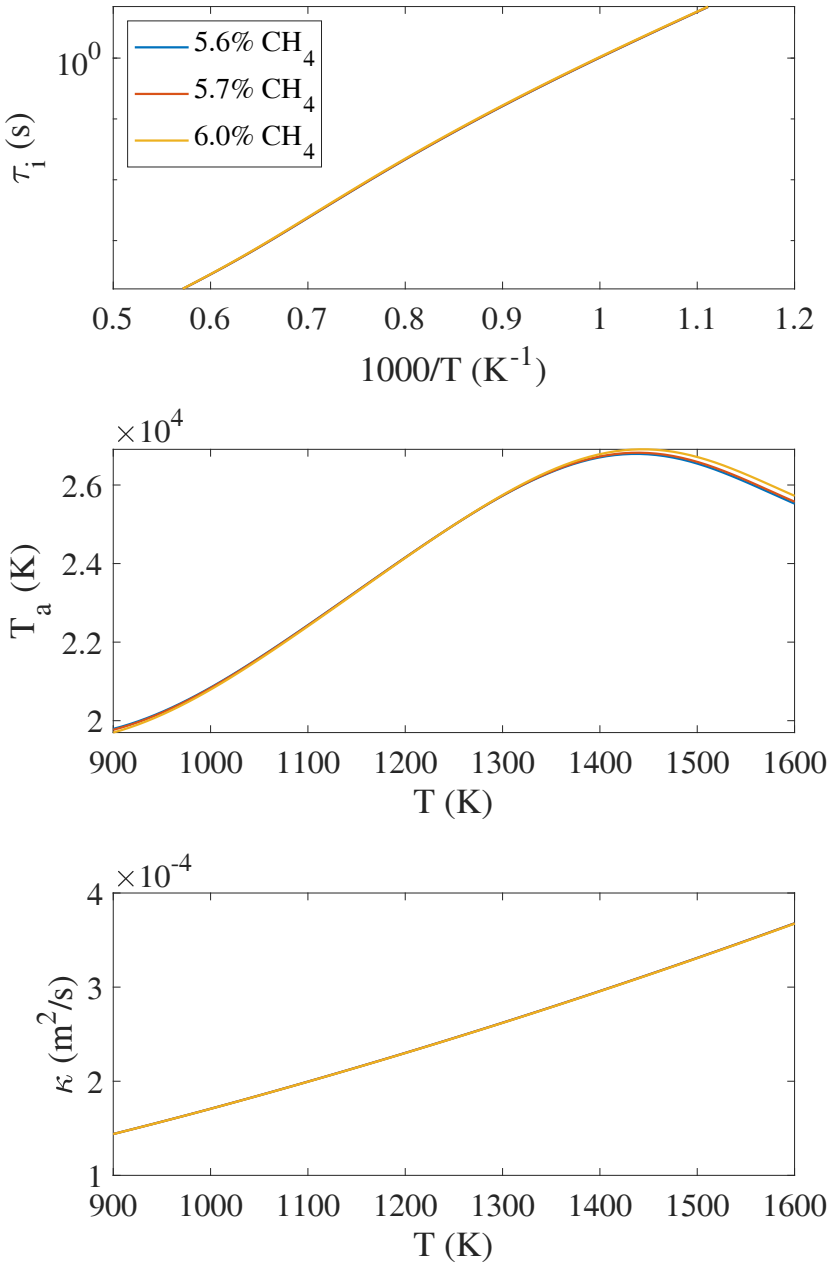


Figure F.14: Computed zero-dimensional ignition delay time τ_i(top), activation temperature $T_a = E_a/R$ (middle), and thermal diffusivity κ (bottom) for 5.6%, 5.7%, and 6.0% CH_4/air at 1 bar.

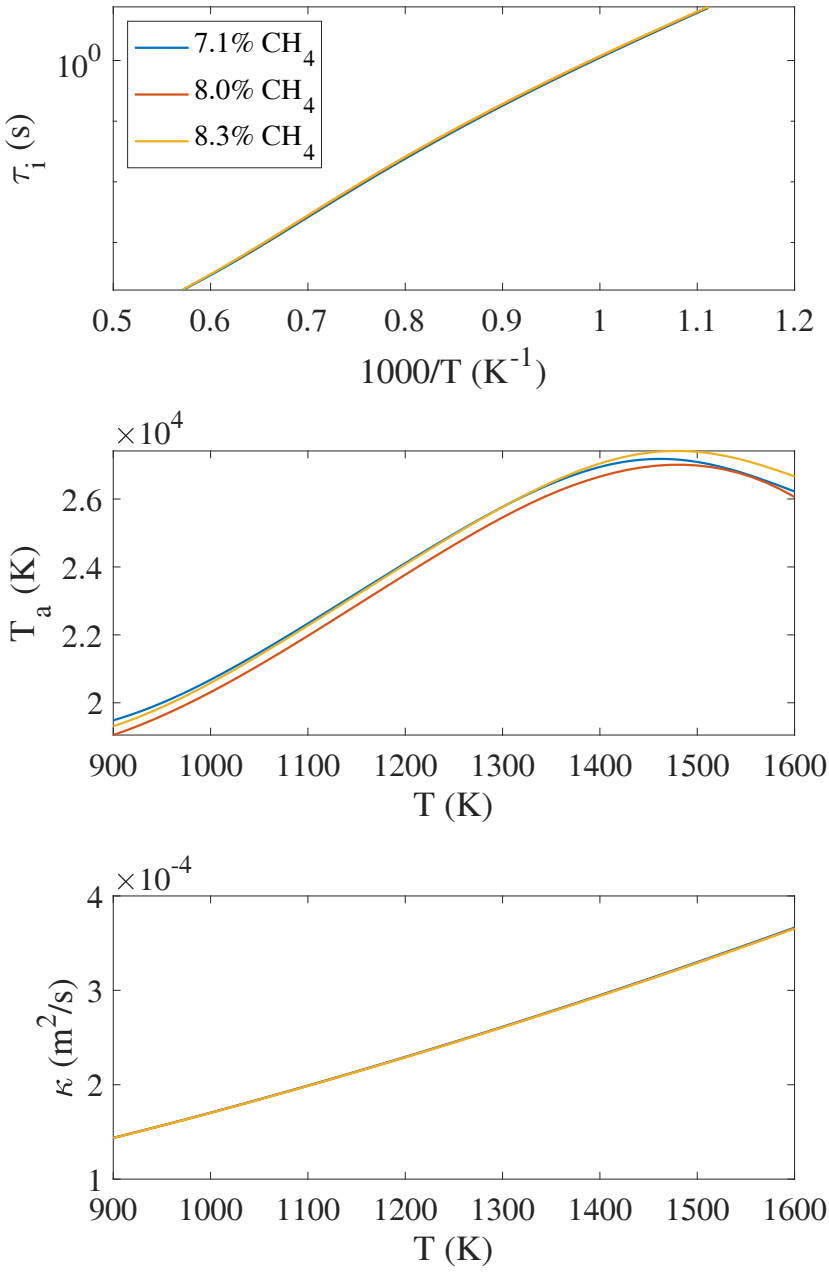


Figure F.15: Computed zero-dimensional ignition delay time τ_i(top), activation temperature $T_a = E_a/R$ (middle), and thermal diffusivity κ (bottom) for 7.1%, 8.0%, and 8.3% CH_4/air at 1 bar.

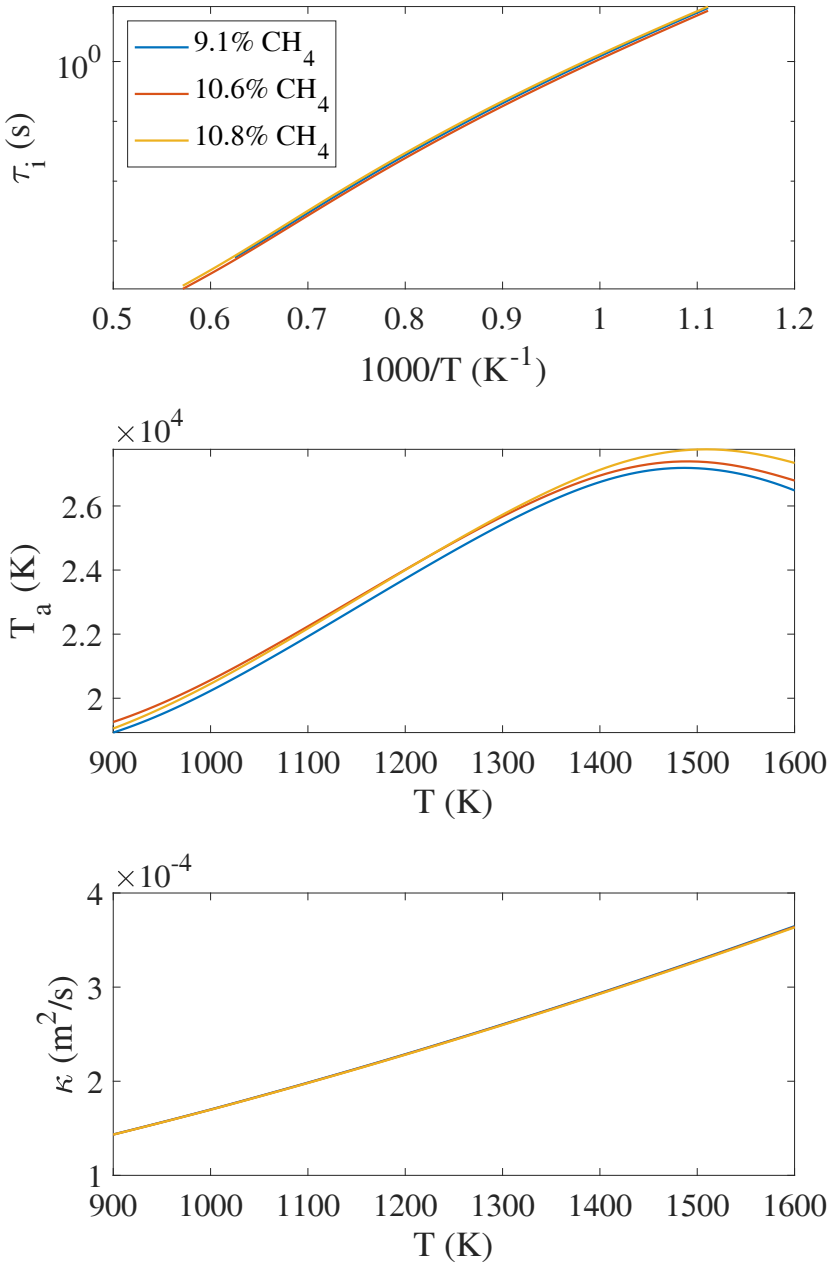


Figure F.16: Computed zero-dimensional ignition delay time τ_i(top), activation temperature $T_a = E_a/R$ (middle), and thermal diffusivity κ (bottom) for 9.1%, 10.6%, and 10.8% CH_4/air at 1 bar.

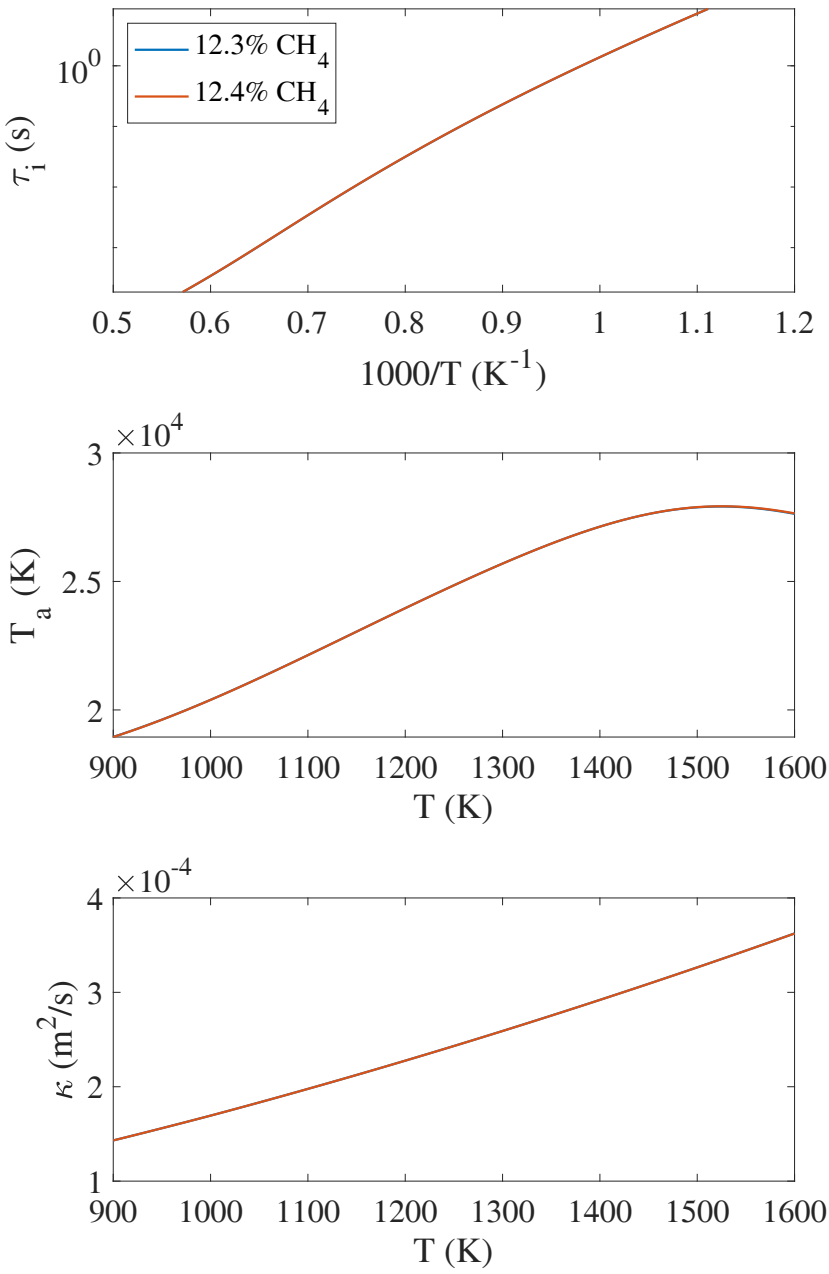


Figure F.17: Computed zero-dimensional ignition delay time τ_i(top), activation temperature $T_a = E_a/R$ (middle), and thermal diffusivity κ (bottom) for 12.3% and 12.4% CH_4/air at 1 bar.

F.4 CH_2O/air mixtures

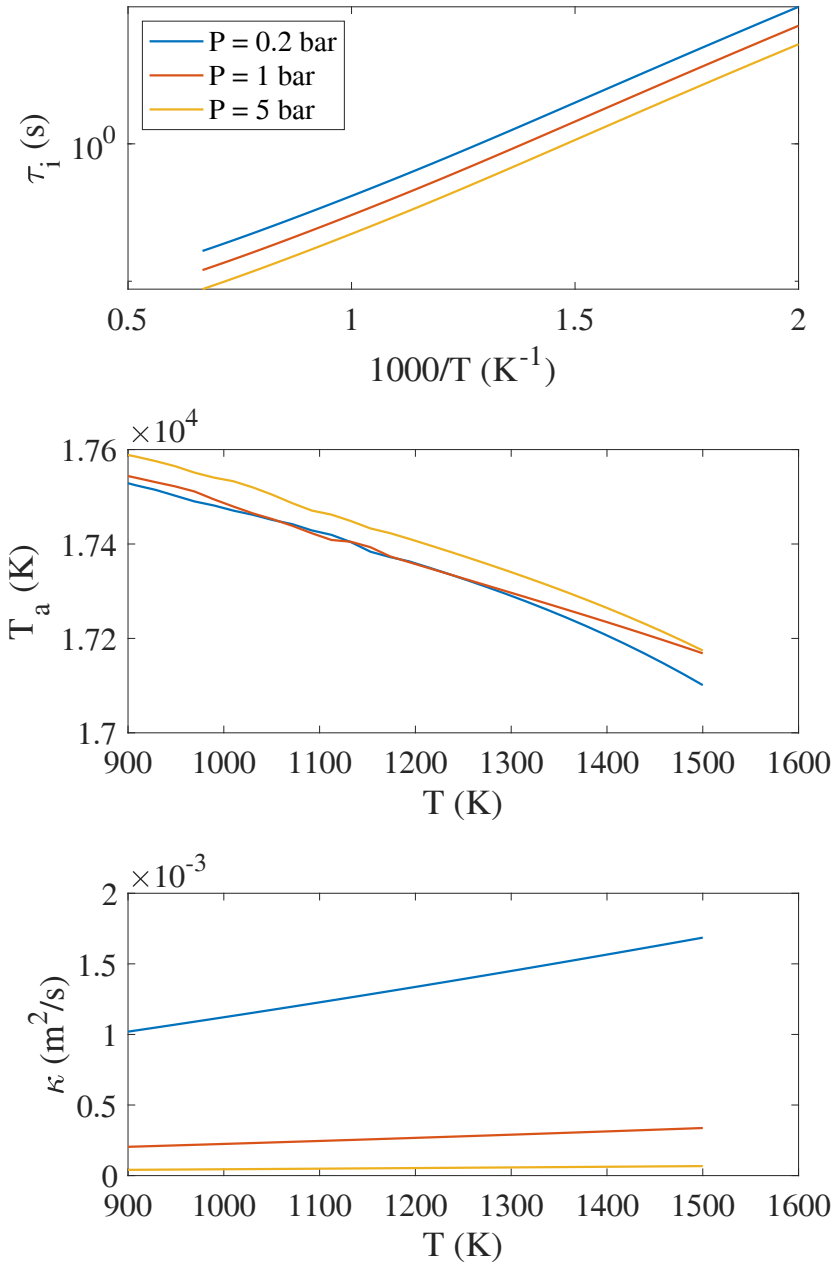


Figure F.18: Computed zero-dimensional ignition delay time τ_i(top), activation temperature $T_a = E_a/R$ (middle), and thermal diffusivity κ (bottom) for stoichiometric CH_2O/air.

F.5 C_2H_4/air mixtures

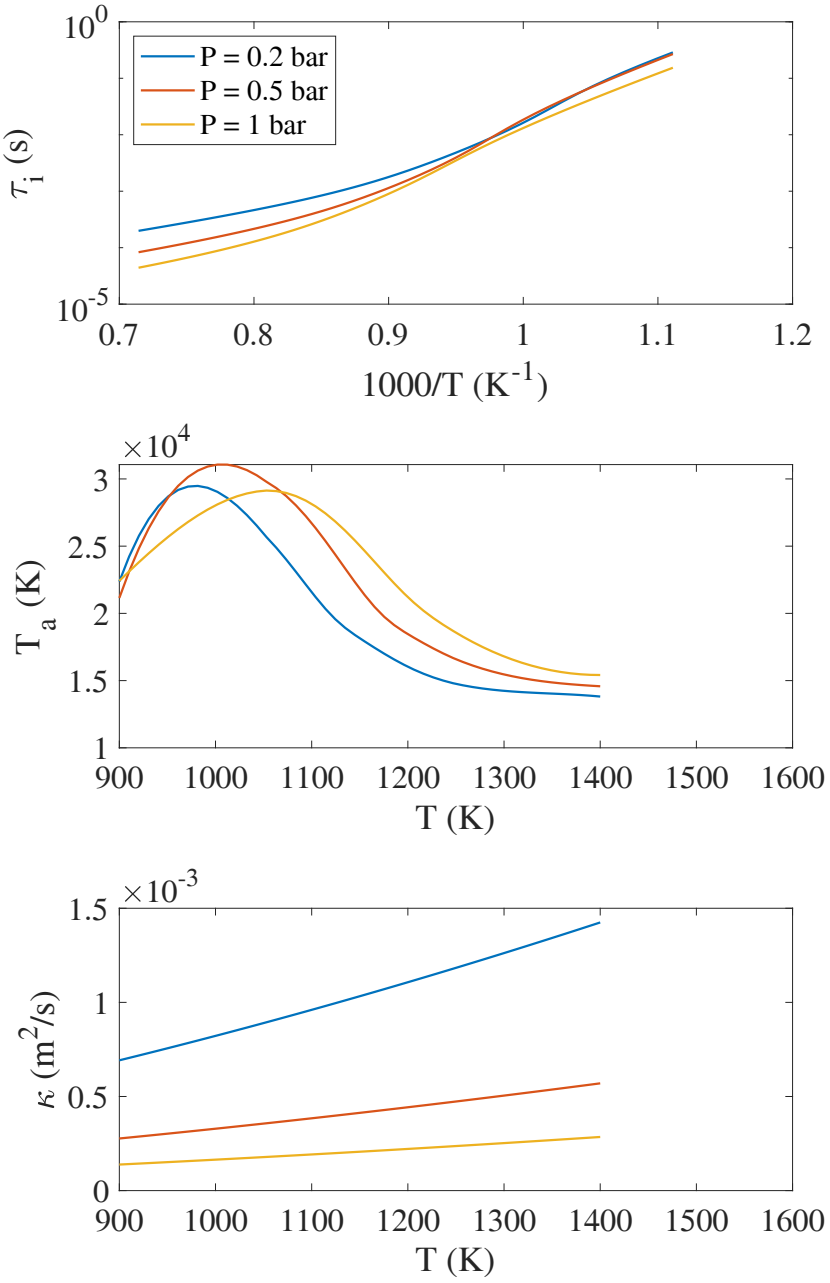


Figure F.19: Computed zero-dimensional ignition delay time τ_i(top), activation temperature $T_a = E_a/R$ (middle), and thermal diffusivity κ (bottom) for stoichiometric C_2H_4/air.

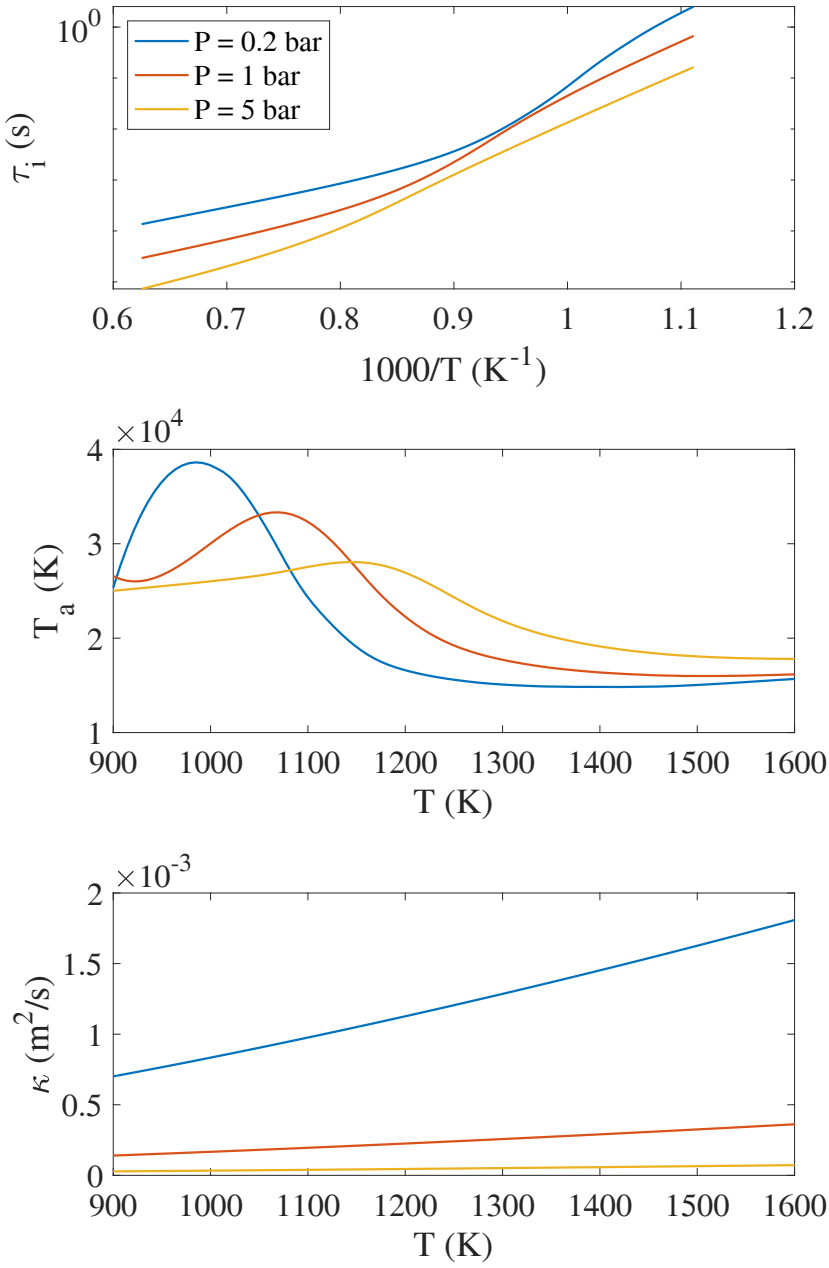


Figure F.20: Computed zero-dimensional ignition delay time τ_i(top), activation temperature $T_a = E_a/R$ (middle), and thermal diffusivity κ (bottom) for 2.8% C_2H_4/air.

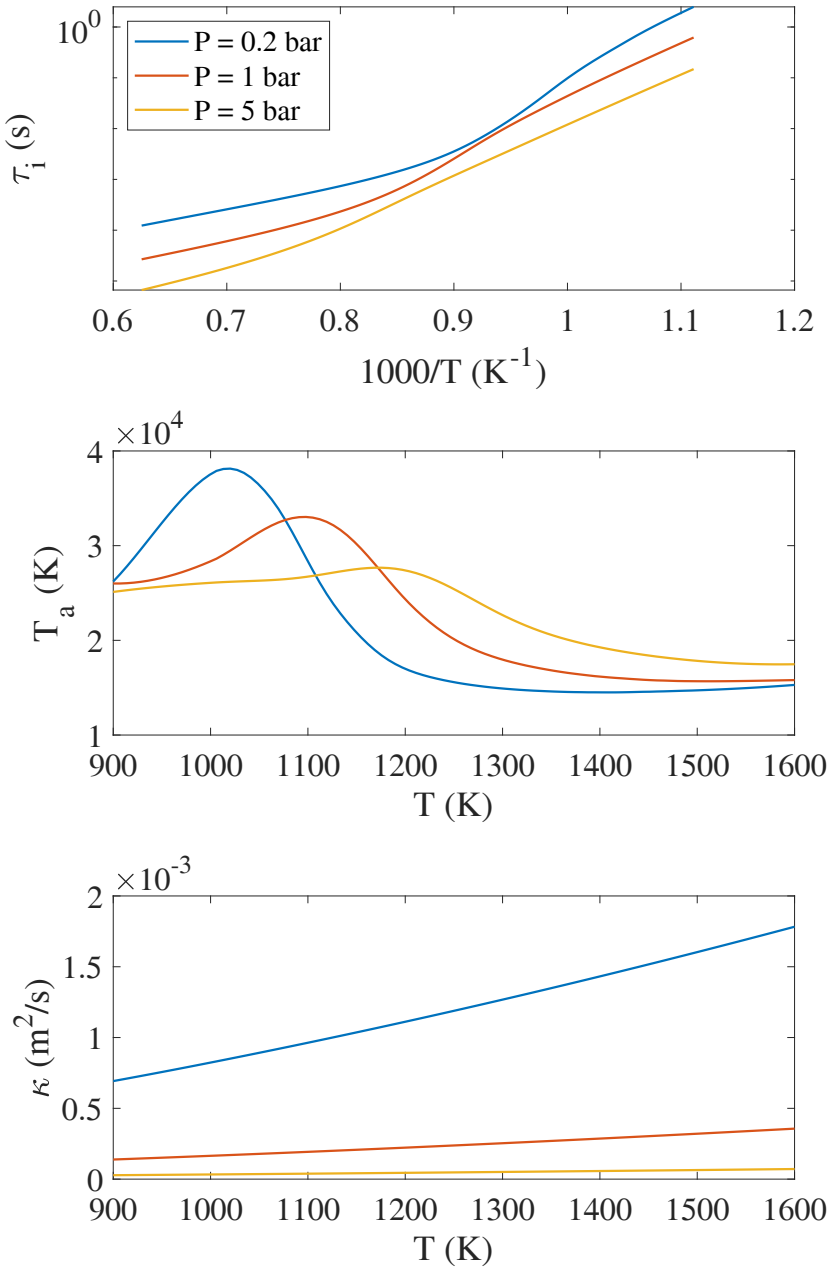


Figure F.21: Computed zero-dimensional ignition delay time τ_i(top), activation temperature $T_a = E_a/R$ (middle), and thermal diffusivity κ (bottom) for 4% C_2H_4/air.

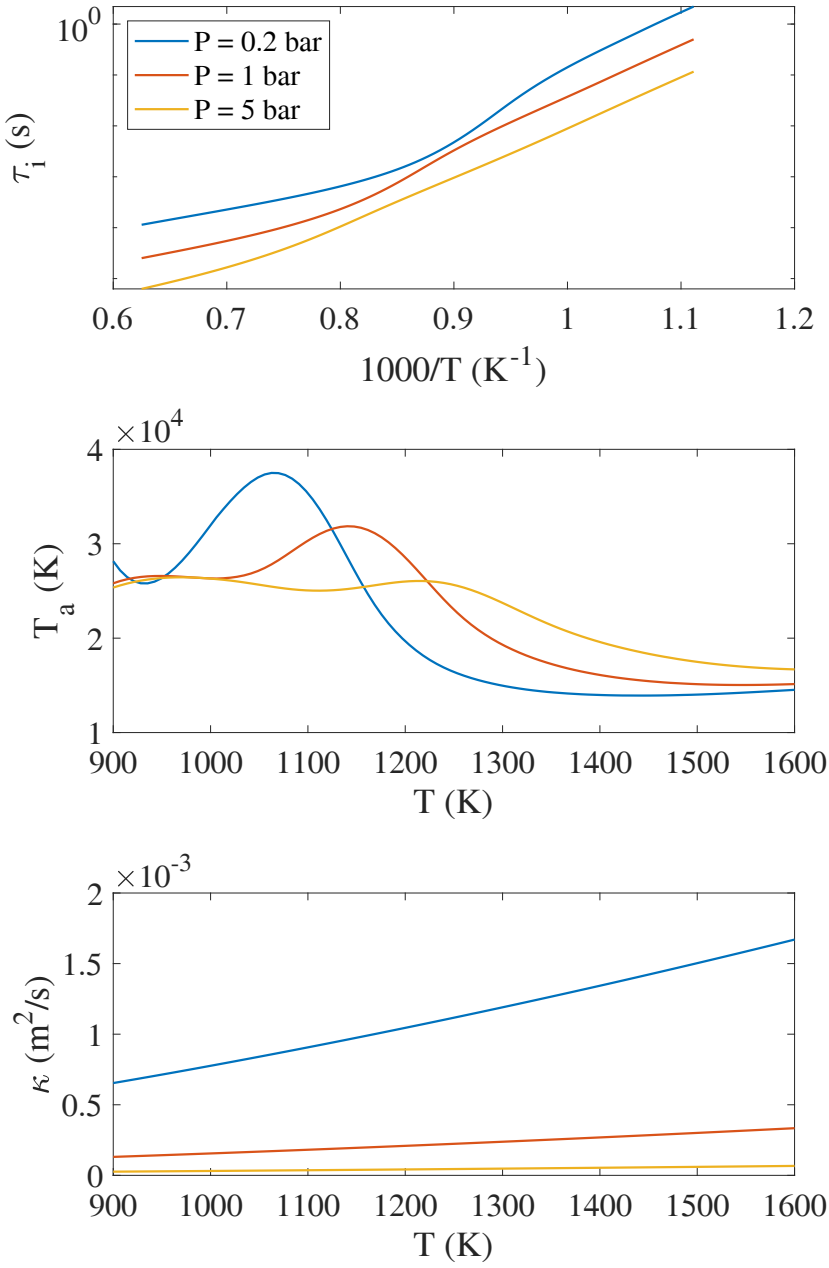


Figure F.22: Computed zero-dimensional ignition delay time τ_i(top), activation temperature $T_a = E_a/R$ (middle), and thermal diffusivity κ (bottom) for 10% C_2H_4/air.

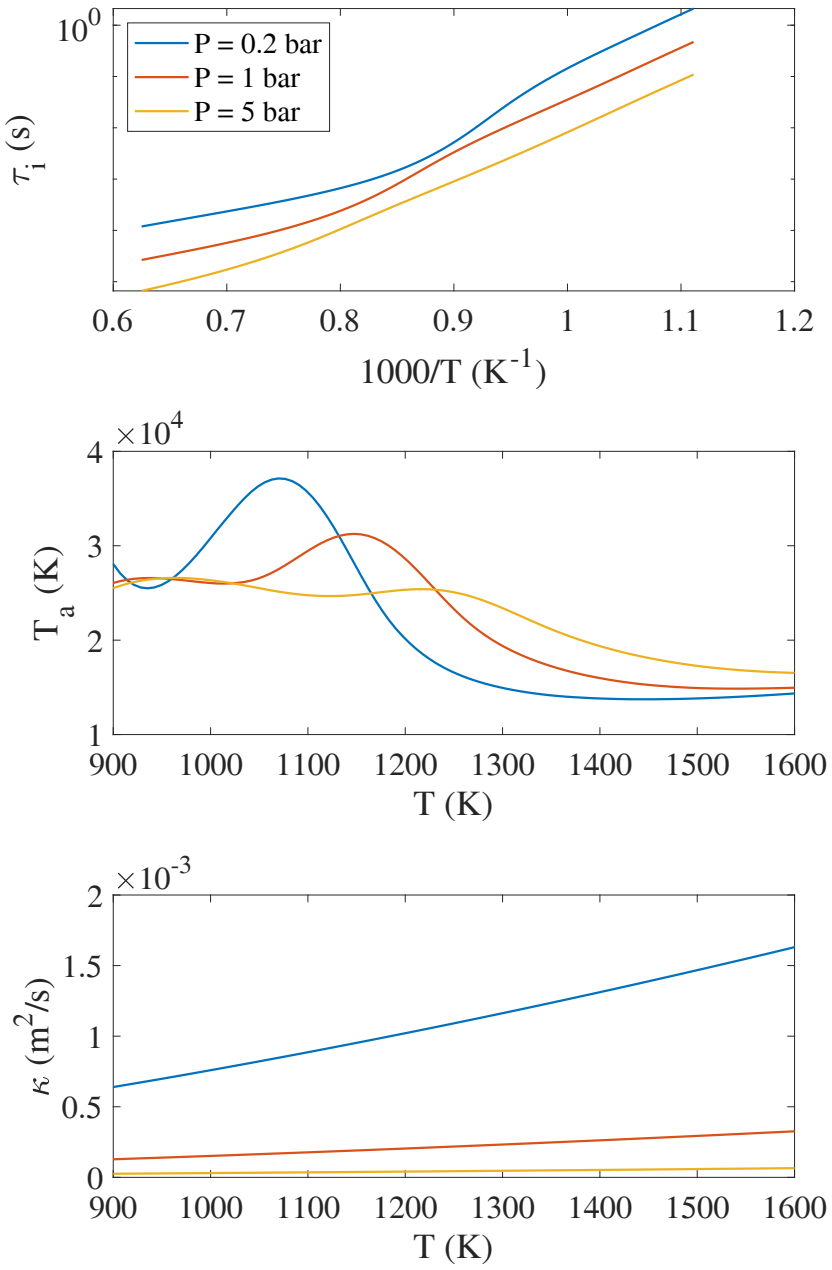


Figure F.23: Computed zero-dimensional ignition delay time τ_i(top), activation temperature $T_a = E_a/R$ (middle), and thermal diffusivity κ (bottom) for 12.5% C_2H_4/air.

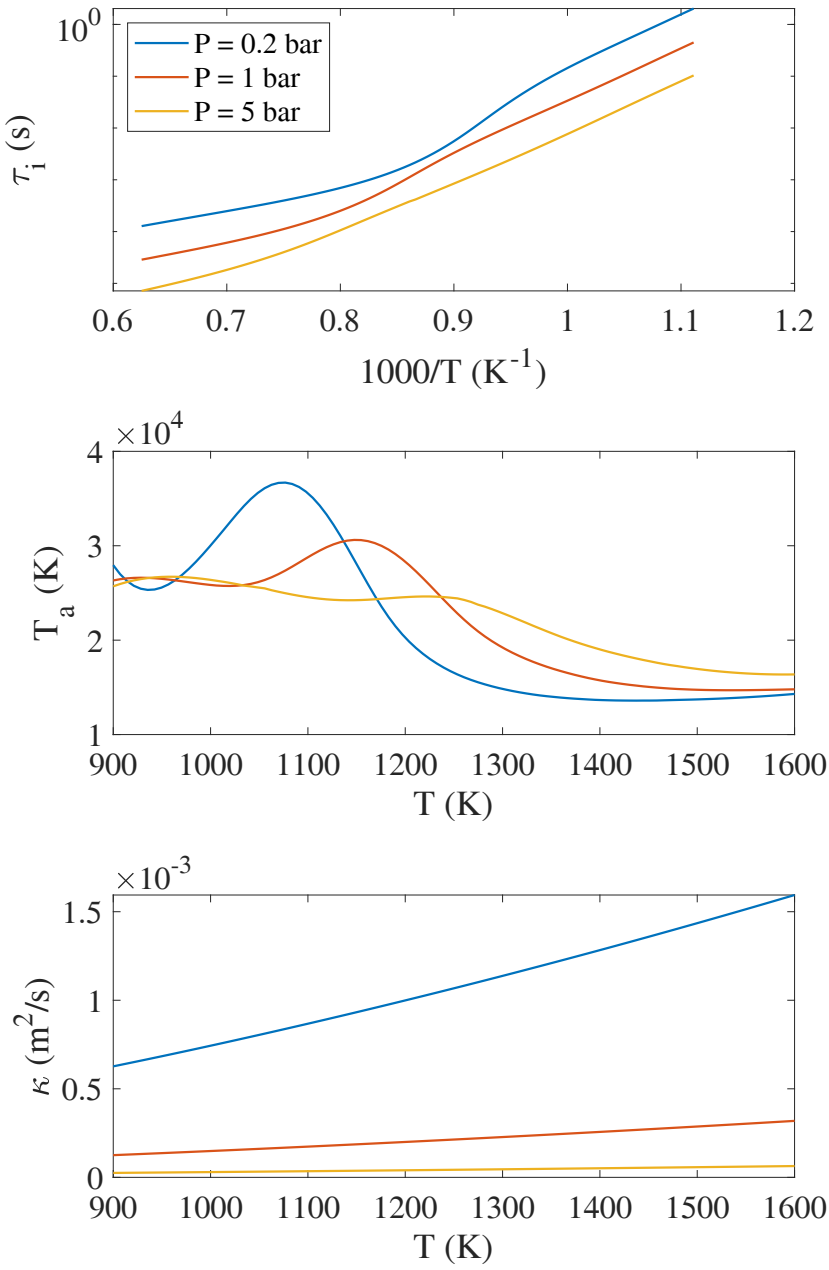


Figure F.24: Computed zero-dimensional ignition delay time τ_i(top), activation temperature $T_a = E_a/R$ (middle), and thermal diffusivity κ (bottom) for 15% C_2H_4/air.

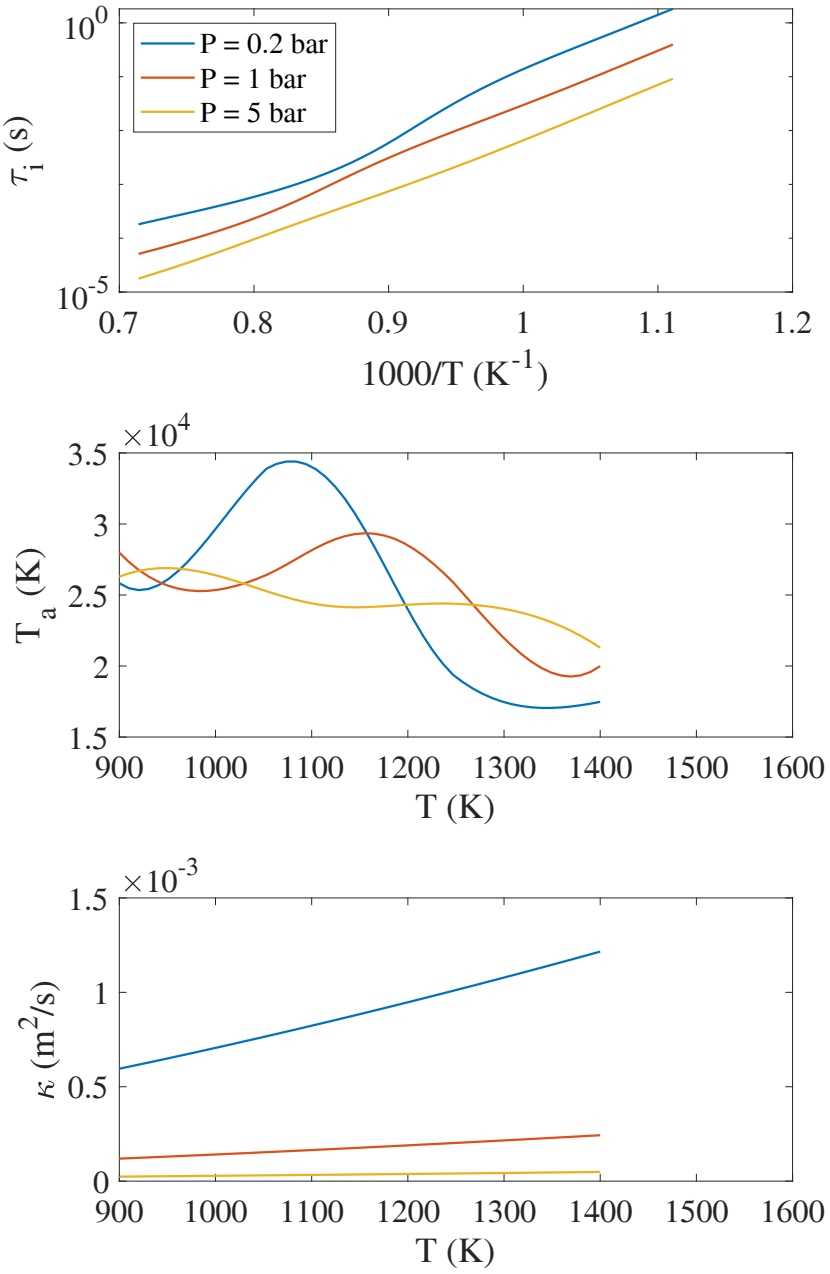


Figure F.25: Computed zero-dimensional ignition delay time τ_i(top), activation temperature $T_a = E_a/R$ (middle), and thermal diffusivity κ (bottom) for 21.9% C_2H_4/air.

F.6 nC_5H_{12}/air mixtures

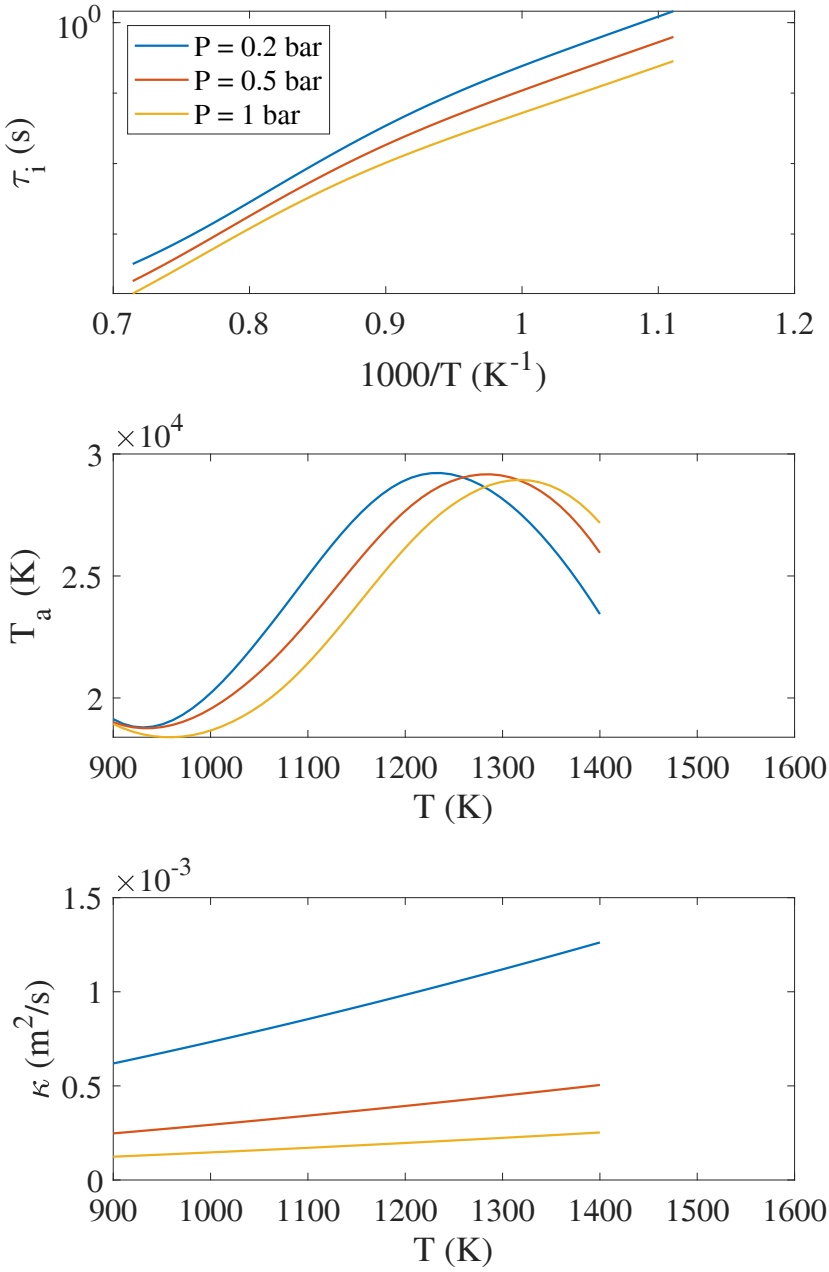


Figure F.26: Computed zero-dimensional ignition delay time τ_i(top), activation temperature $T_a = E_a/R$ (middle), and thermal diffusivity κ (bottom) for stoichiometric nC_5H_{12}/air.

F.7 nC_6H_{14}/air mixtures

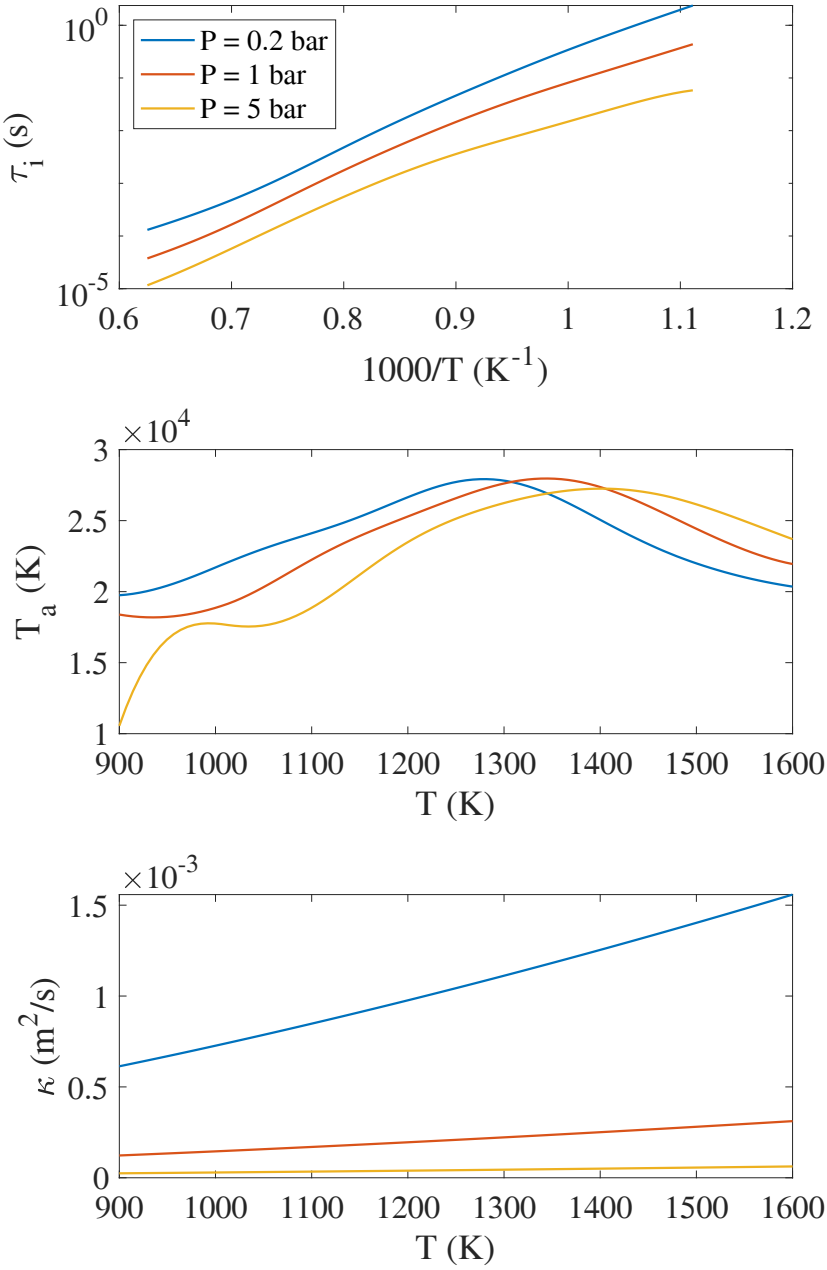


Figure F.27: Computed zero-dimensional ignition delay time τ_i(top), activation temperature $T_a = E_a/R$ (middle), and thermal diffusivity κ (bottom) for stoichiometric nC_6H_{14}/air.

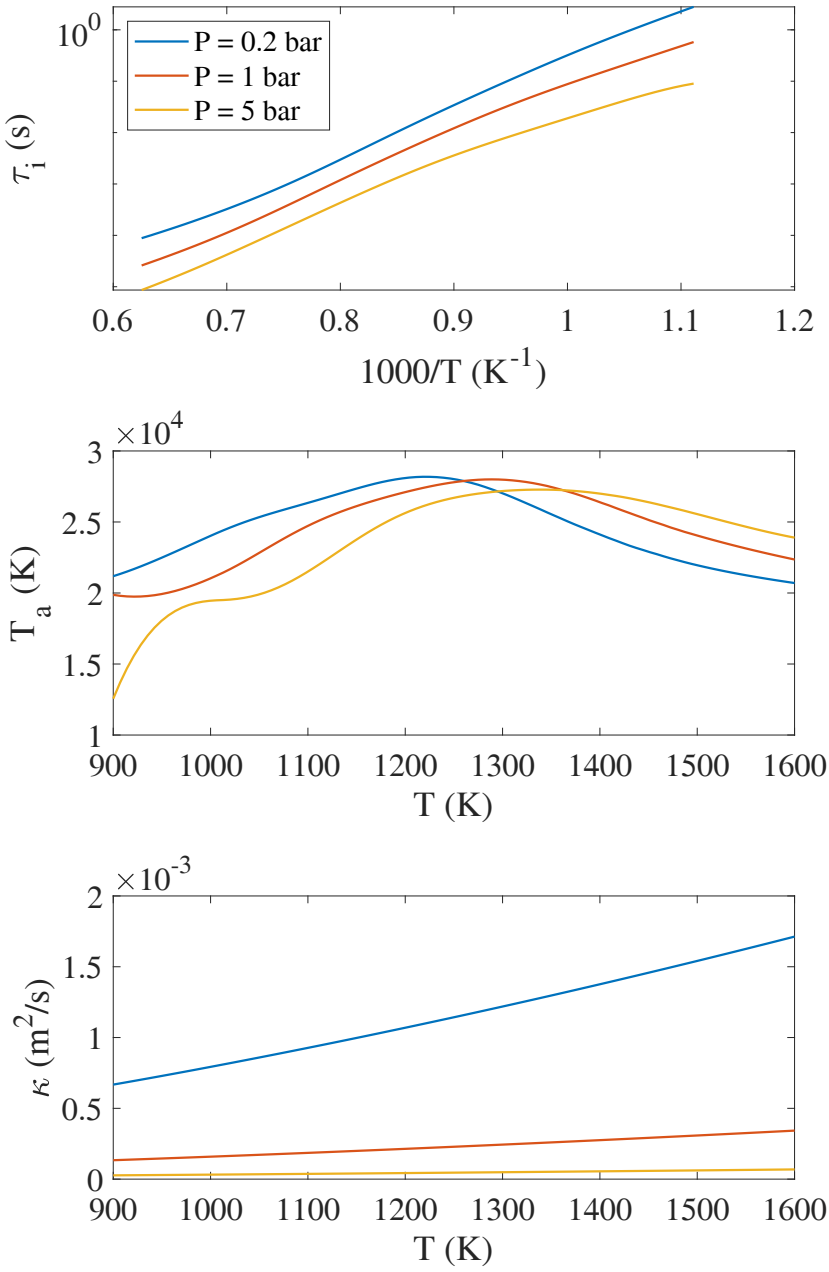


Figure F.28: Computed zero-dimensional ignition delay time τ_i(top), activation temperature $T_a = E_a/R$ (middle), and thermal diffusivity κ (bottom) for 1% nC_6H_{14}/air.

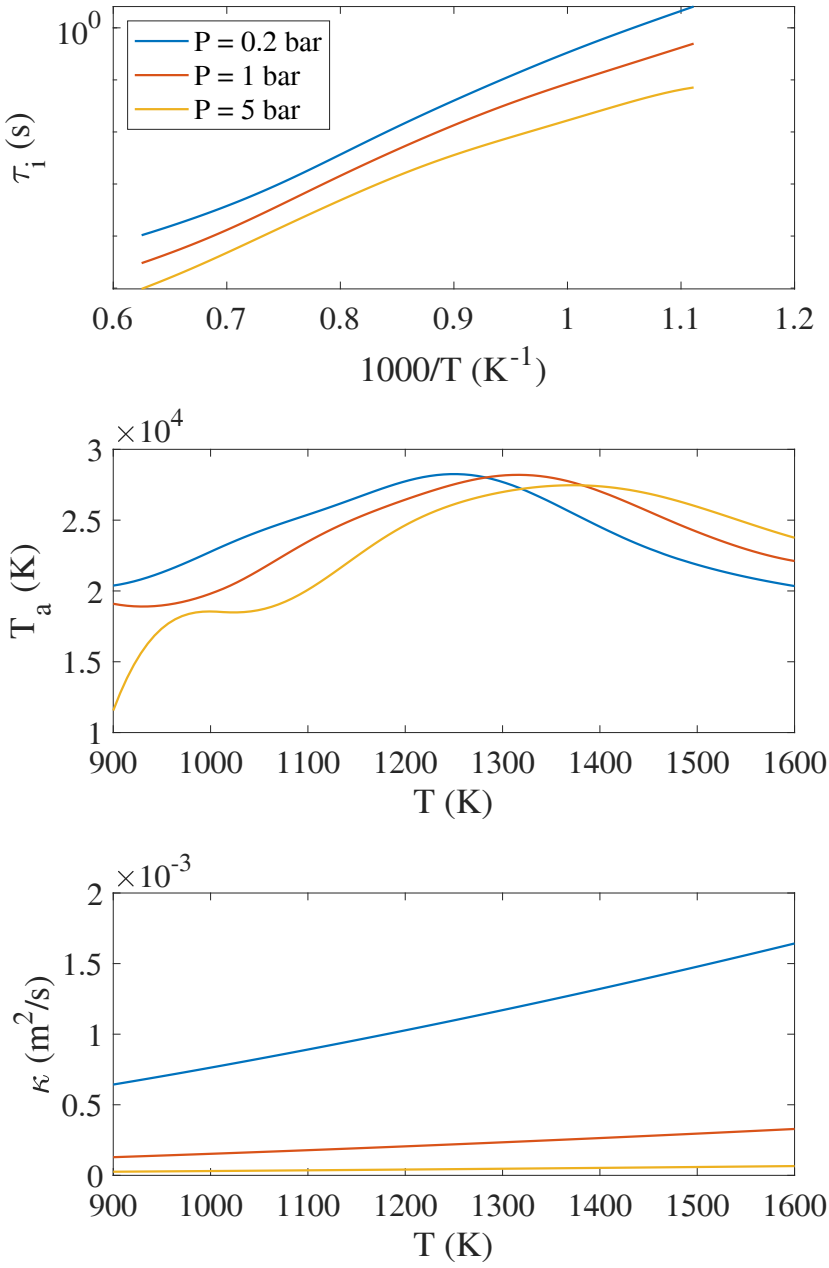


Figure F.29: Computed zero-dimensional ignition delay time τ_i(top), activation temperature $T_a = E_a/R$ (middle), and thermal diffusivity κ (bottom) for 1.5% nC_6H_{14}/air.

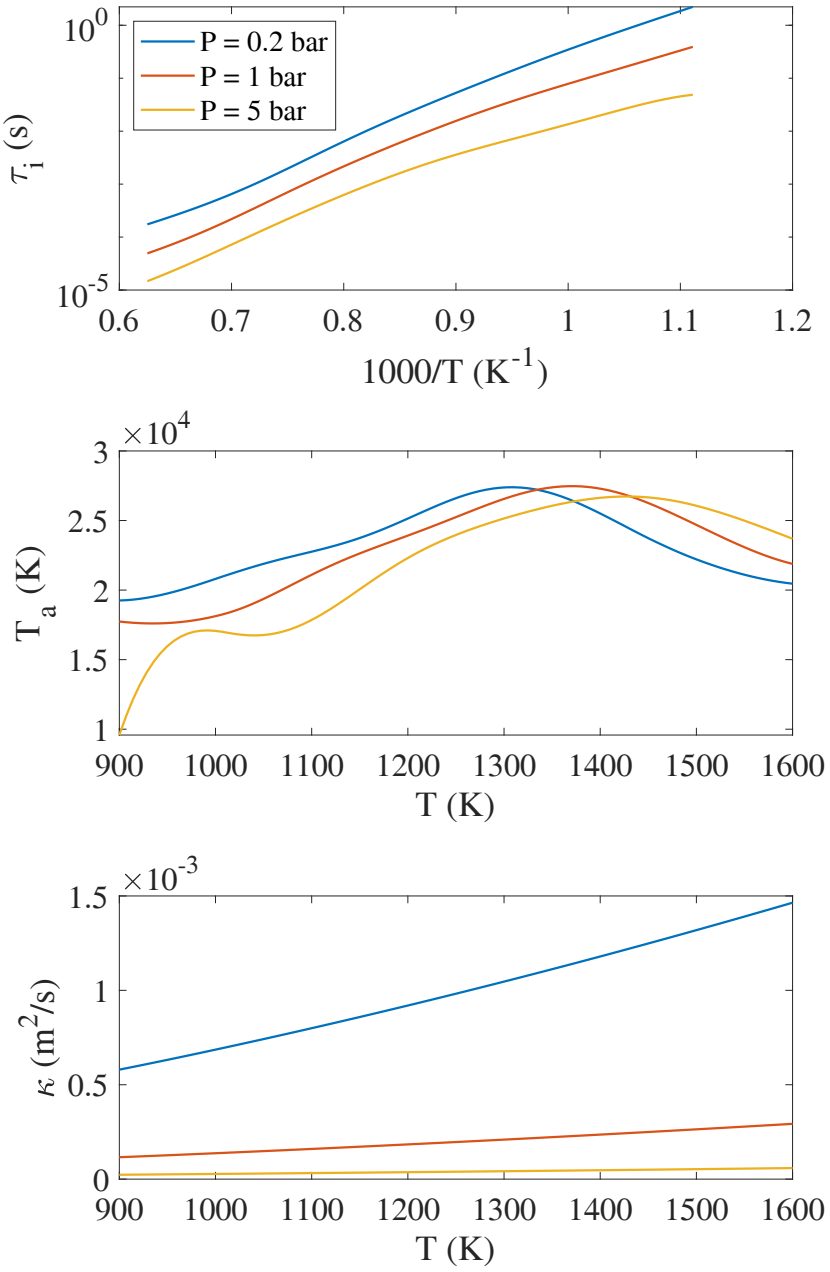


Figure F.30: Computed zero-dimensional ignition delay time τ_i(top), activation temperature $T_a = E_a/R$ (middle), and thermal diffusivity κ (bottom) for 3% nC_6H_{14}/air.

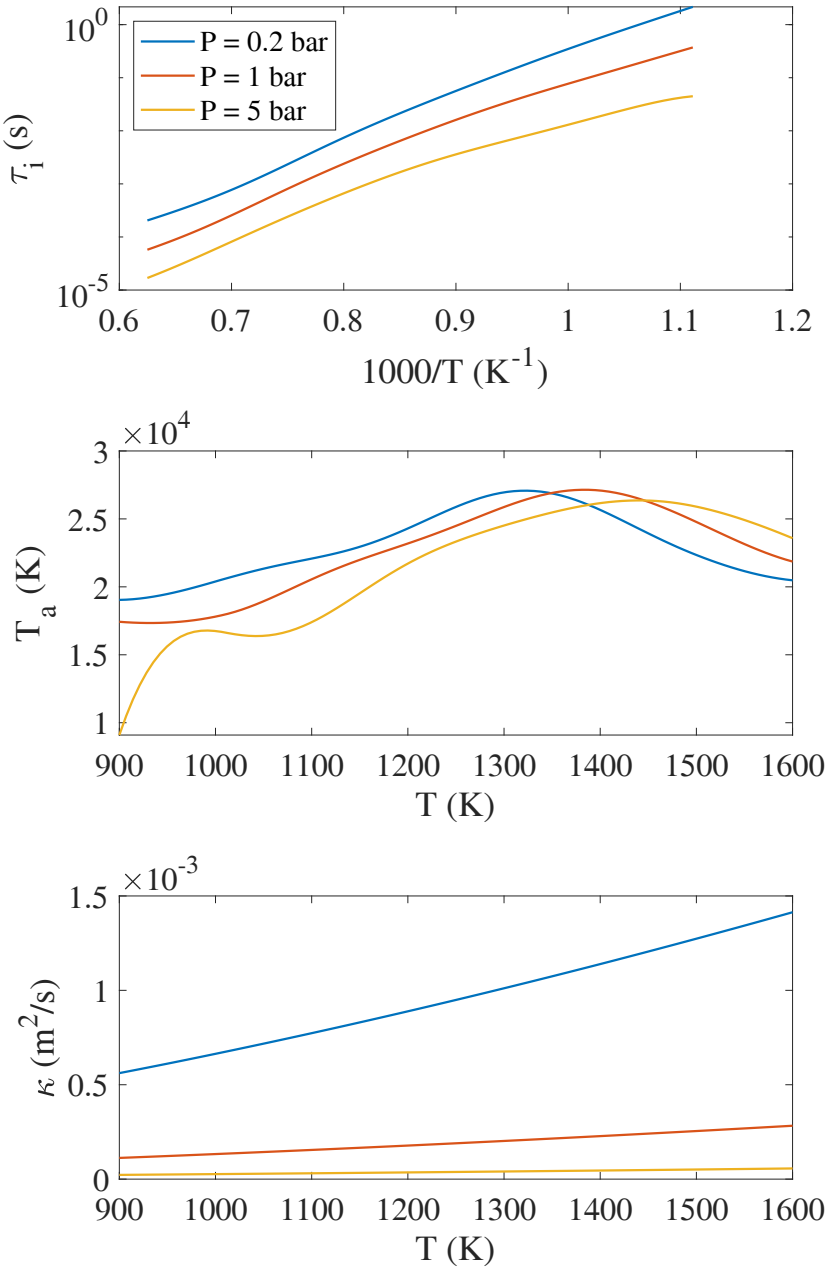


Figure F.31: Computed zero-dimensional ignition delay time τ_i(top), activation temperature $T_a = E_a/R$ (middle), and thermal diffusivity κ (bottom) for 3.5% nC_6H_{14}/air.

F.8 NH_3/air mixtures

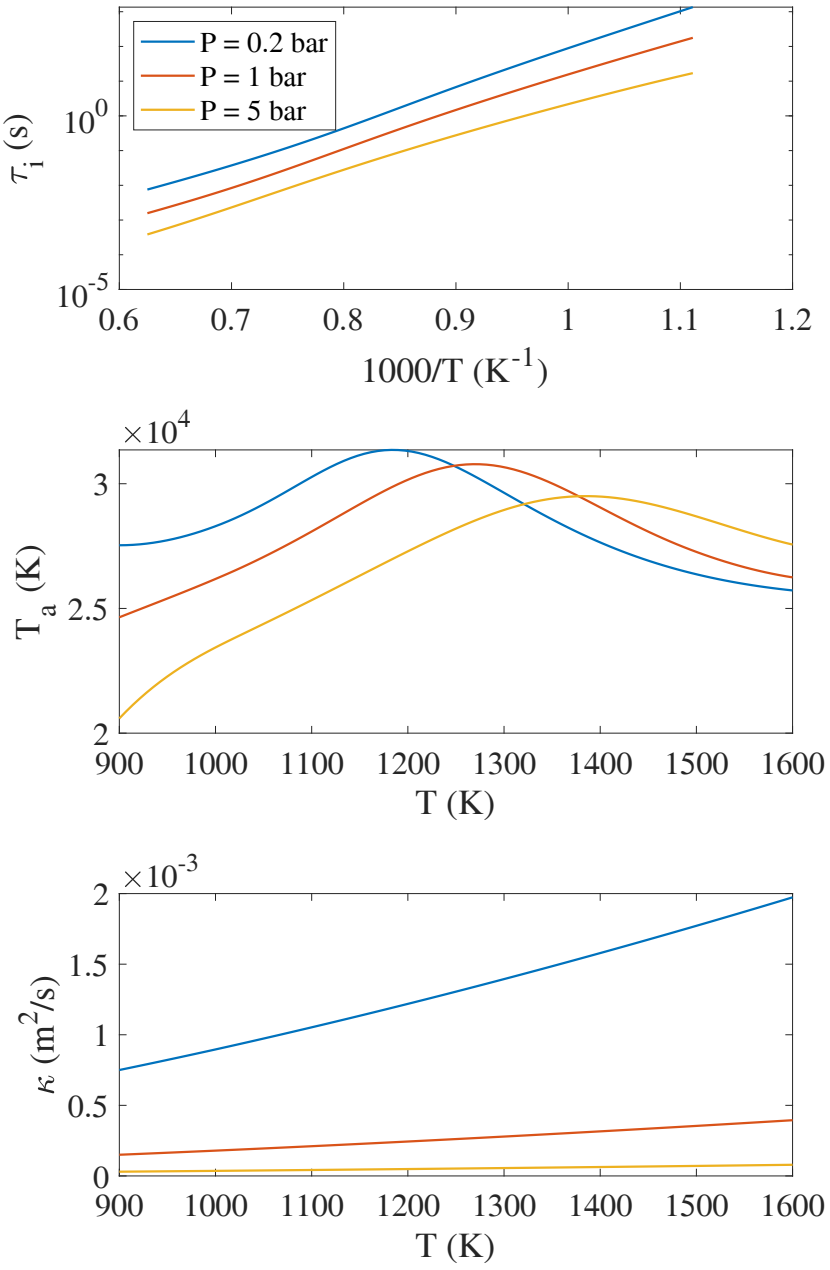


Figure F.32: Computed zero-dimensional ignition delay time τ_i(top), activation temperature $T_a = E_a/R$ (middle), and thermal diffusivity κ (bottom) for stoichiometric NH_3/air.

Appendix G

ADDITIONAL DATA: TWO-DIMENSIONAL IGNITION SIMULATIONS

This appendix presents additional data for all 15 configurations of geometry, pressure, hot surface length, freestream velocity, and fuel investigated in the numerical study in Chapter 7. Specifically the temperature field evolutions are shown leading up to ignition. The geometric configurations are for natural convection, stagnation point, and forced convection flows for nC_6H_{14}, H_2, CH_4, and NH_3 with air.

G.1 nC_6H_{14}/air

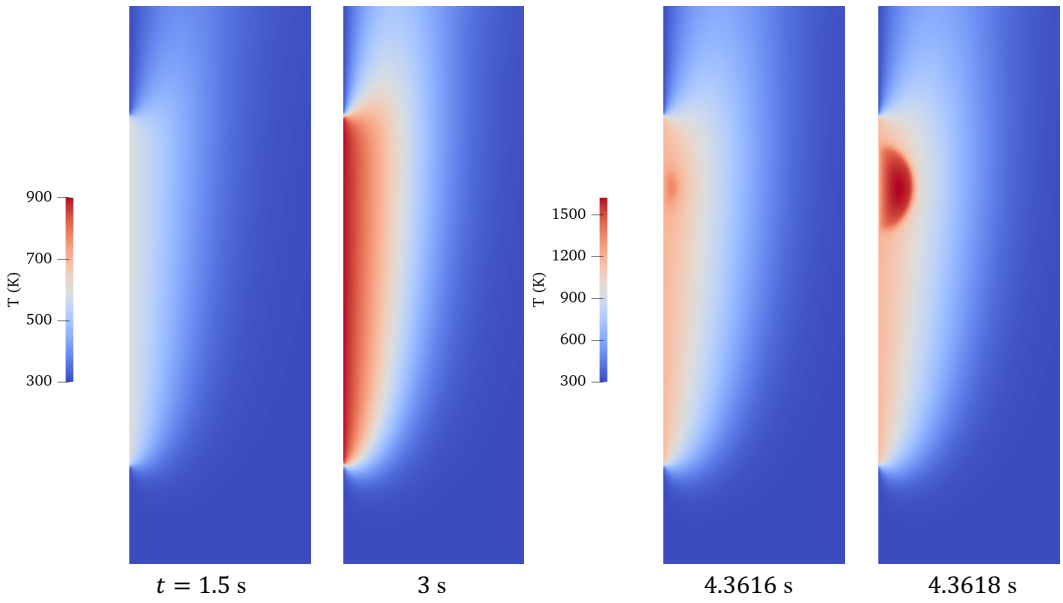


Figure G.1: Natural convection: Temperature field evolution during the ignition event. $P = 1$ bar, $L = 0.01$ m.

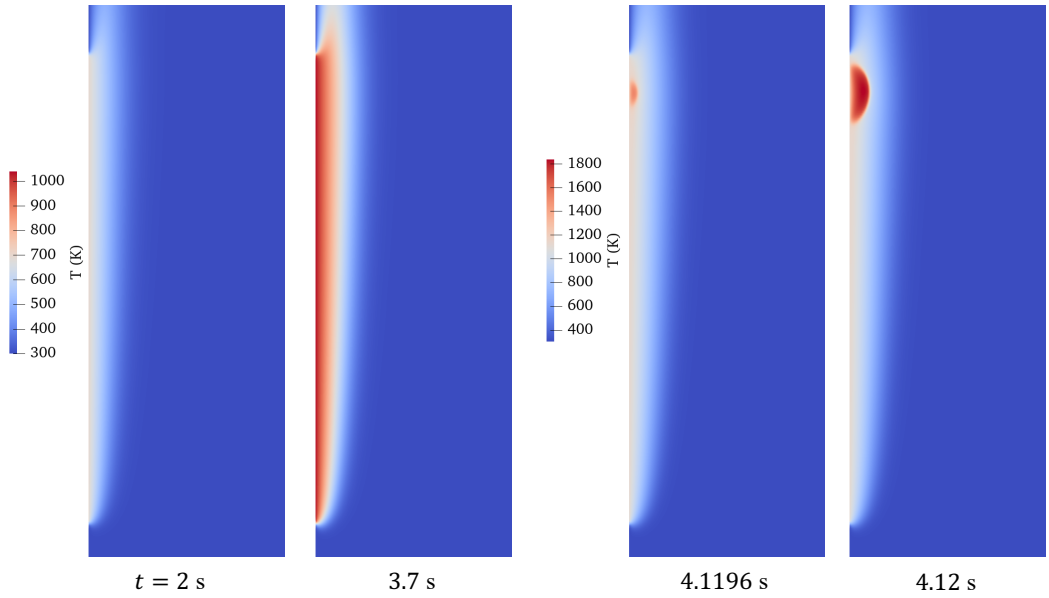


Figure G.2: Natural Convection: Temperature field evolution during the ignition event. $P = 1$ bar, $L = 0.05$ m.

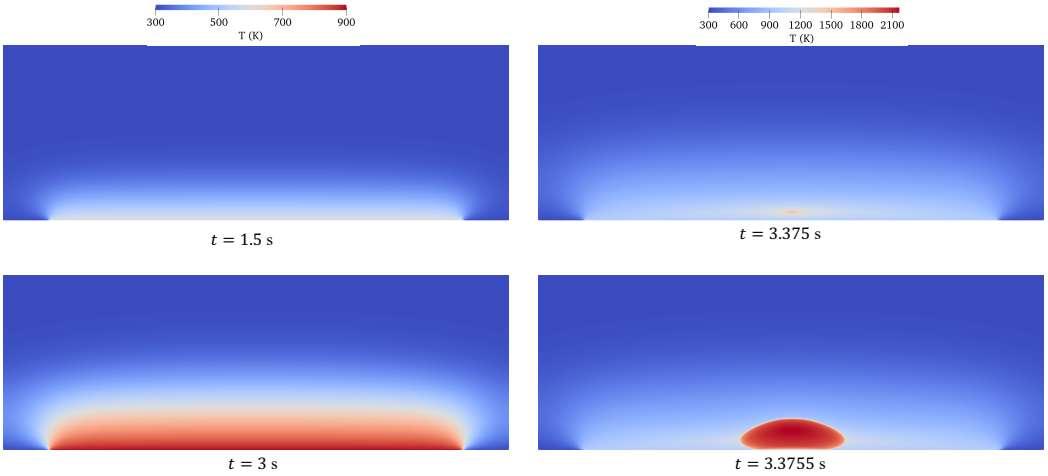


Figure G.3: Stagnation point: Temperature field evolution during the ignition event. $P = 1$ bar, $L = 0.09$ m, $U_\infty = 0.01$ m/s.

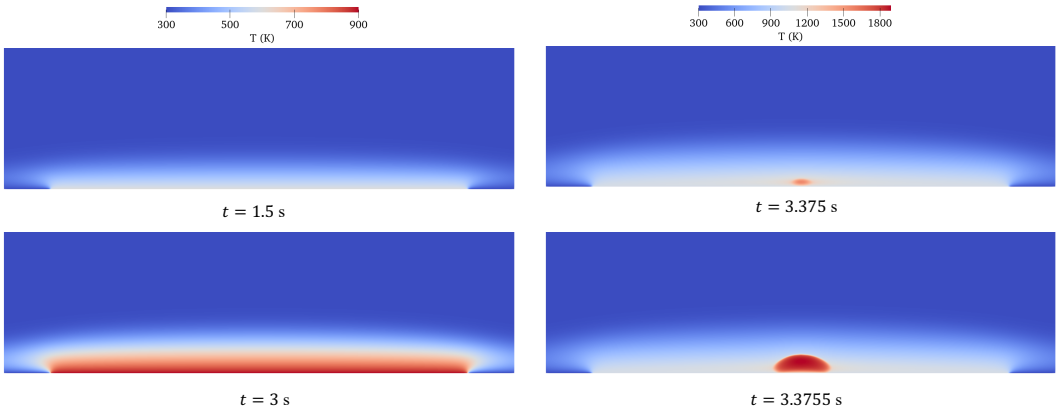


Figure G.4: Stagnation point: Temperature field evolution during the ignition event. $P = 1$ bar, $L = 0.09$ m, $U_\infty = 0.1$ m/s.

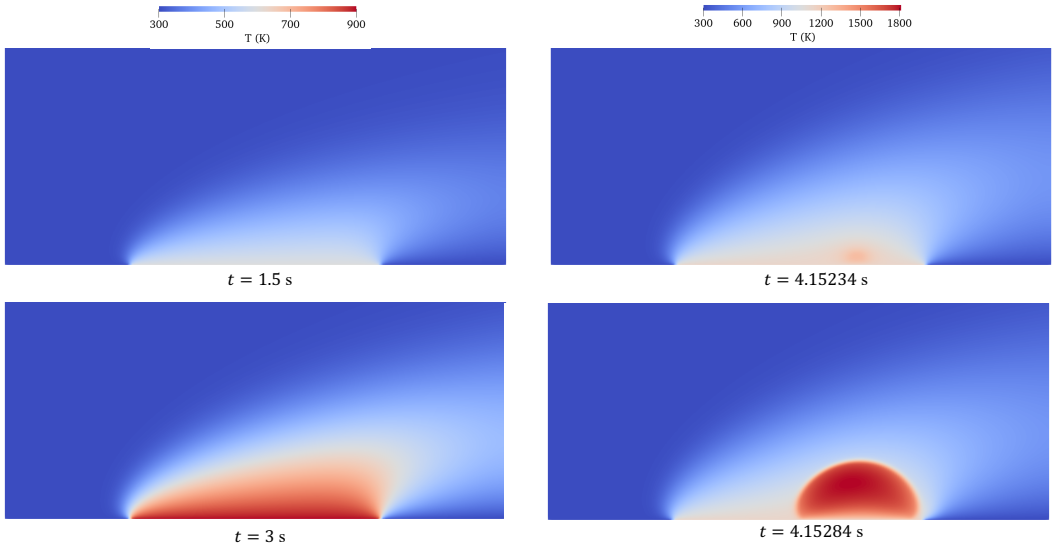


Figure G.5: Forced convection: Temperature field evolution during the ignition event. $P = 1$ bar, $L = 0.01$ m, $U_\infty = 0.1$ m/s.

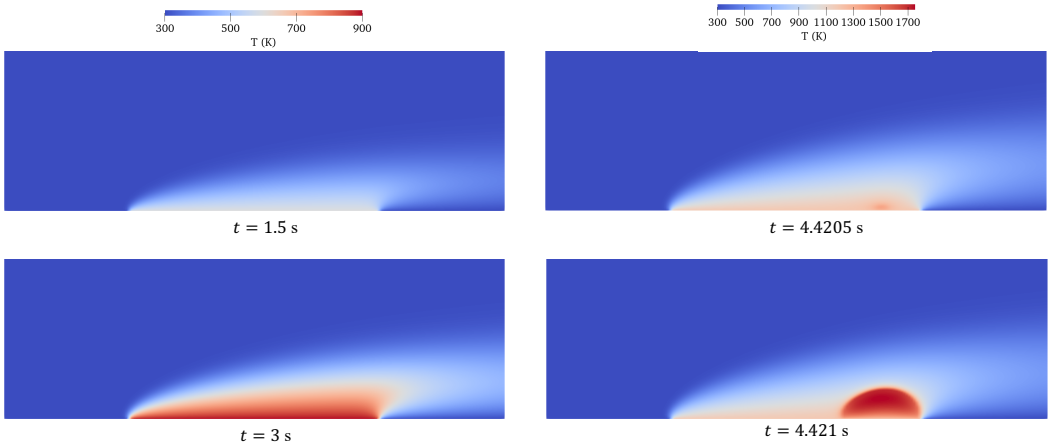


Figure G.6: Forced convection: Temperature field evolution during the ignition event. $P = 1$ bar, $L = 0.01$ m, $U_\infty = 0.5$ m/s.

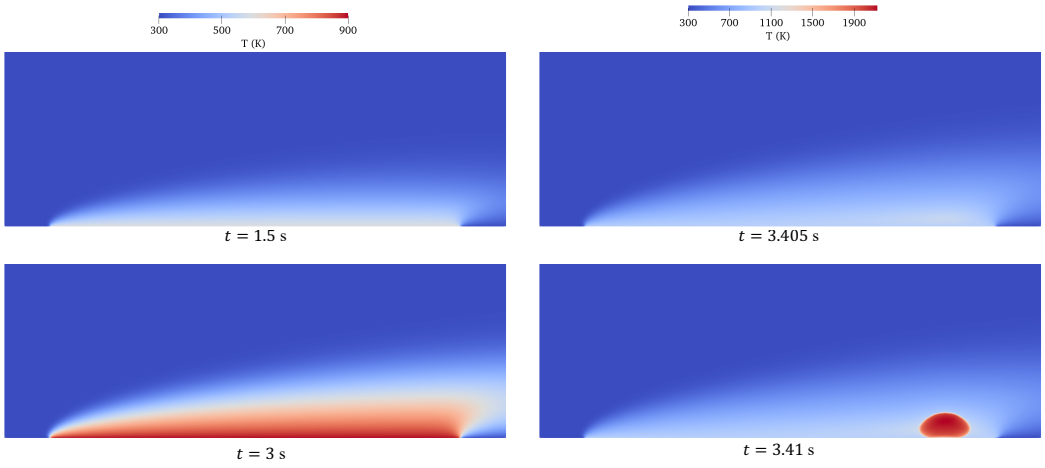


Figure G.7: Forced convection: Temperature field evolution during the ignition event. $P = 1$ bar, $L = 0.09$ m, $U_\infty = 0.1$ m/s.

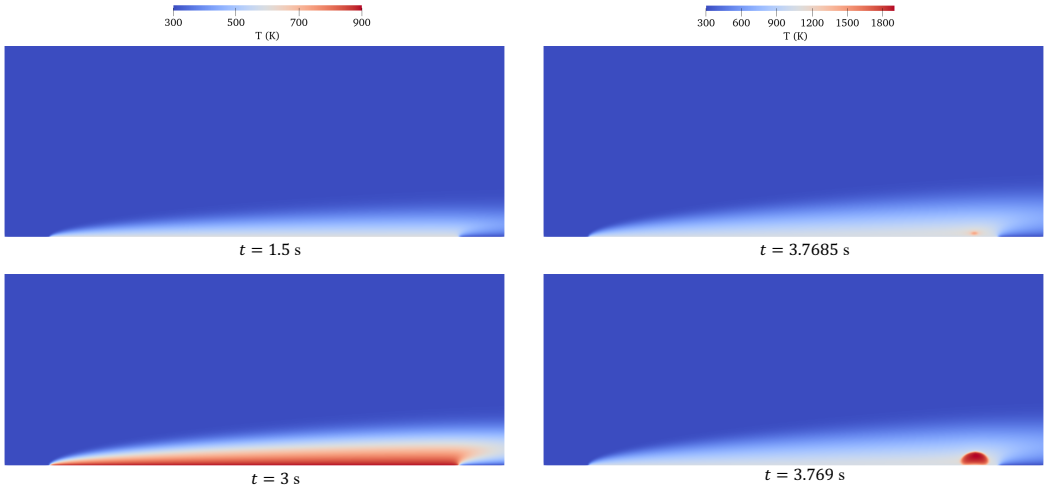


Figure G.8: Forced convection: Temperature field evolution during the ignition event. $P = 1$ bar, $L = 0.09$ m, $U_\infty = 0.5$ m/s.

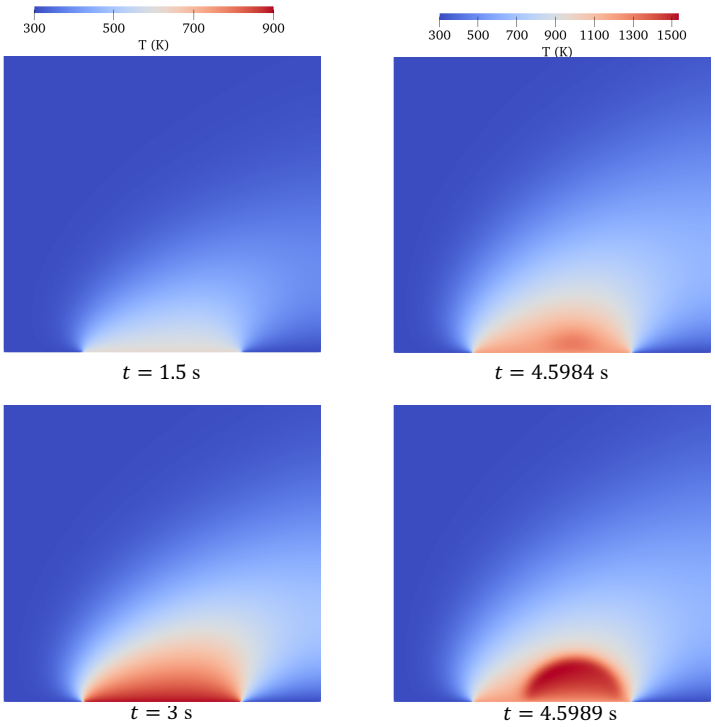


Figure G.9: Forced convection: Temperature field evolution during the ignition event. $P = 0.2$ bar, $L = 0.01$ m, $U_\infty = 0.1$ m/s.

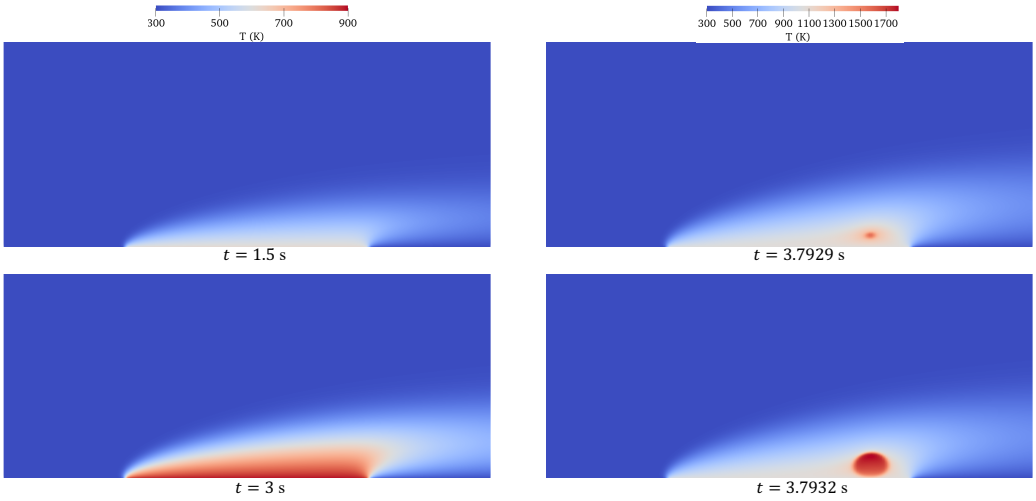


Figure G.10: Forced convection: Temperature field evolution during the ignition event. $P = 5$ bar, $L = 0.01$ m, $U_\infty = 0.1$ m/s.

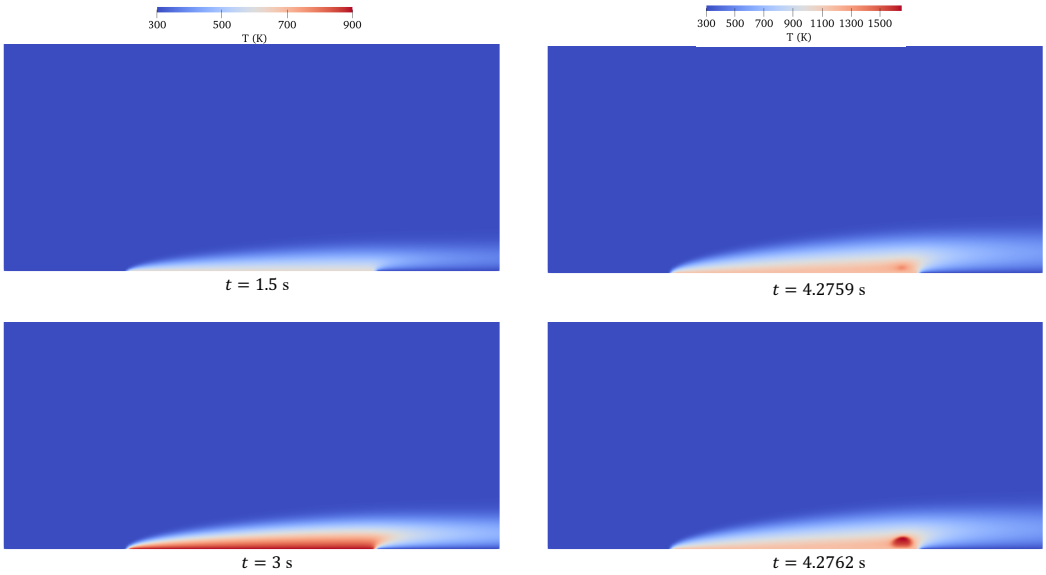


Figure G.11: Forced convection: Temperature field evolution during the ignition event. $P = 5$ bar, $L = 0.01$ m, $U_\infty = 0.5$ m/s.

G.2 H_2/air

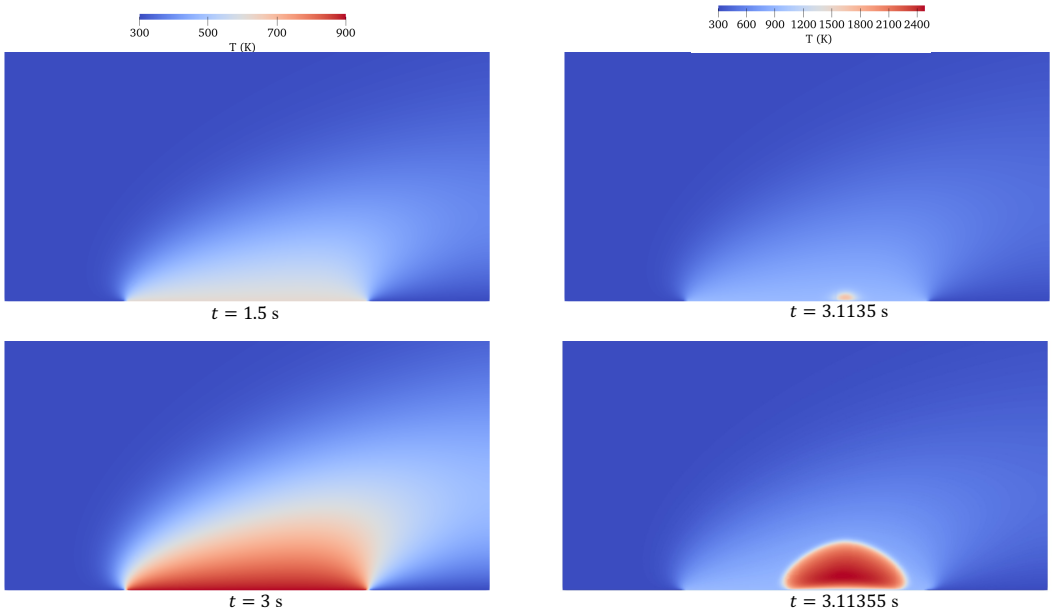


Figure G.12: Forced convection: Temperature field evolution during the ignition event. $P = 1$ bar, $L = 0.01$ m, $U_\infty = 0.1$ m/s.

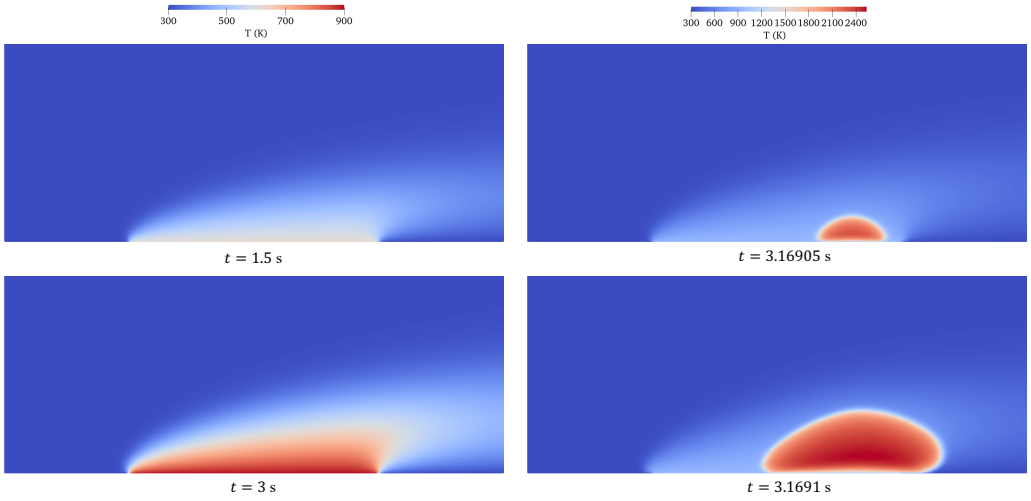


Figure G.13: Forced convection: Temperature field evolution during the ignition event. $P = 1$ bar, $L = 0.01$ m, $U_\infty = 0.5$ m/s.

G.3 CH_4/air

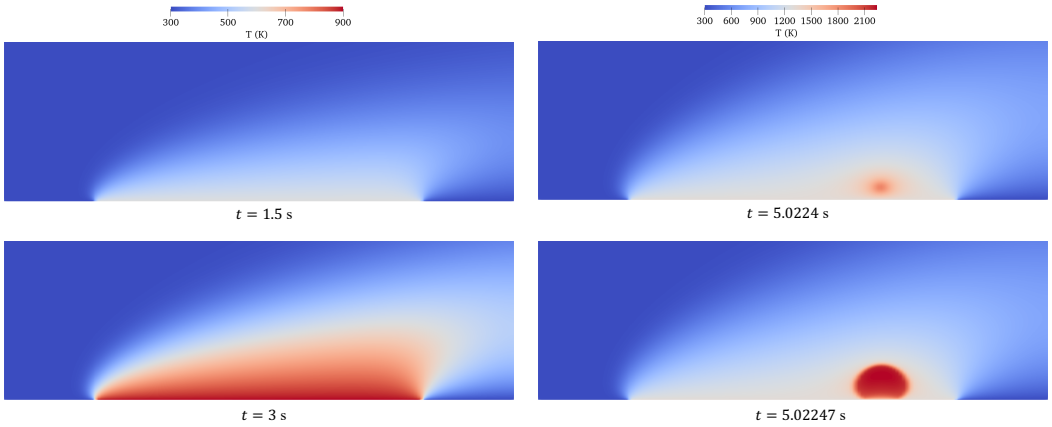


Figure G.14: Forced convection: Temperature field evolution during the ignition event. $P = 1$ bar, $L = 0.018$ m, $U_\infty = 0.1$ m/s.

G.4 NH_3/air

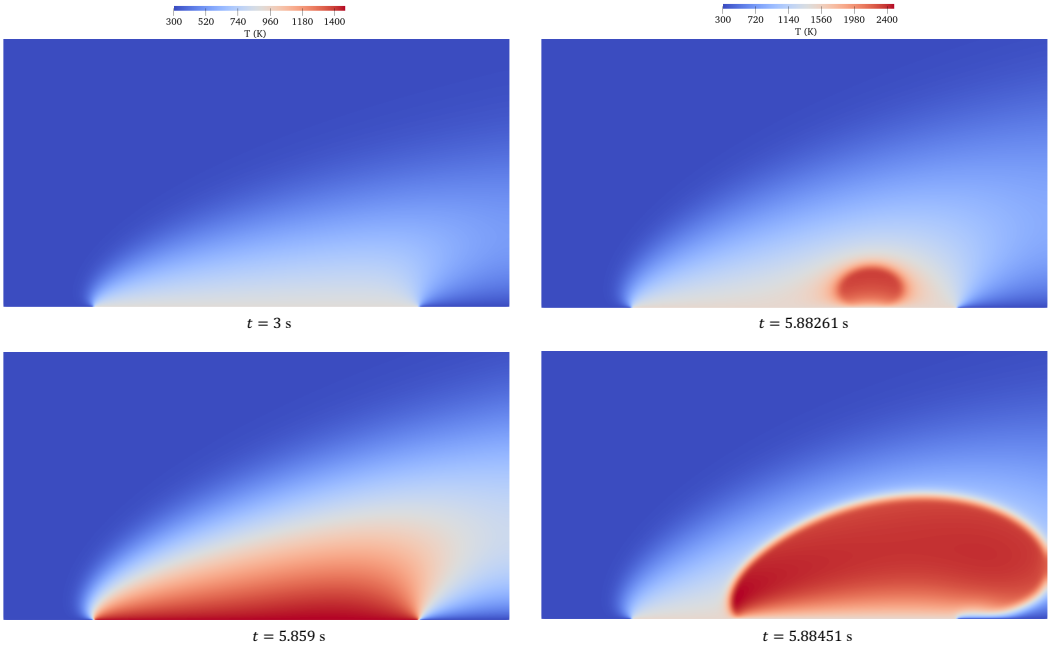


Figure G.15: Forced convection: Temperature field evolution during the ignition event. $P = 1$ bar, $L = 0.018$ m, $U_\infty = 0.1$ m/s.

Appendix H

50C EXPERIMENTAL SHOT LOG

Table H.1: Shot log for ignition experiments on the 12.7 cm vertical cylinder (tagged 50C). T_{ign} is the pyrometer measured value at the center of the cylinder.

Shot number	Mixture	P_{fuel} (torr)	P_{N_2} (torr)	P_{total} (torr)	T_{ign} (K)	P_{max} (bar)
1	nC_6H_{14}/air	16.4	603.9	760	–	–
2	nC_6H_{14}/air	16.5	603.9	760	–	–
3	nC_6H_{14}/air	16.5	603.8	759.4	–	–
4	nC_6H_{14}/air	16.6	603.8	765.6	1114	8.1
5	nC_6H_{14}/air	16.4	603.9	760	1114	8.4
6	C_2H_4/air	49.7	610	760	1056	8.3
7	C_2H_4/air	49.7	610.8	759.7	1045	8.7
8	C_2H_4/air	49.6	610.8	759	1054	8.5
9	C_2H_4/air	49.7	610.8	760	1071	8.7
10	CH_4/air	72.3	615.5	760	–	–
11	CH_4/air	72.3	615.6	760	–	–
12	C_2H_4/air	10.1	122.2	152	1141	1.7
13	C_2H_4/air	10.1	122.2	152	1143	1.6
14	C_2H_4/air	10.1	124.4	152.1	1147	1.6
15	C_2H_4/air	10.0	122.3	152	1138	1.6
16	C_2H_4/air	25	305.4	380.1	1089	4.1
17	C_2H_4/air	24.9	305.5	380	1093	4.1
18	C_2H_4/air	24.9	305.4	380	1093	4.1
19	nC_5H_{12}/air	19.7	603.5	760	1126	8.1
20	nC_5H_{12}/air	19.6	603.5	760.2	1120	8.1
21	nC_5H_{12}/air	3.8	121.1	152.1	1252	1.5
22	nC_5H_{12}/air	3.8	121.3	152	1252	1.5
23	10% H_2/air	76.1	616.3	760	950	3.4
24	10% H_2/air	76.2	616.4	760.1	949	3.4
25	10% H_2/air	15.4	123.4	152	899	0.64
26	10% H_2/air	38.2	308.2	380	920	1.8
27	nC_5H_{12}/air	9.7	302.2	380	1189	4.0
28	nC_5H_{12}/air	9.7	302.2	380.1	1181	3.9
29	nC_5H_{12}/air	9.7	302.7	380.1	1180	3.9
30	nC_6H_{14}/air	8.2	301.9	380	1169	4.0
31	nC_6H_{14}/air	8.2	301.9	380	1171	3.8
32	nC_6H_{14}/air	3.3	121	152.1	1232	1.6
33	nC_6H_{14}/air	3.3	120.8	152	1232	1.5